Heinrich Heine
Universität
Düsseldorf

Modifications of Fumarate-Based Aluminum and Zirconium Metal-Organic Frameworks for Enhanced Gas Adsorption and Adsorption-Driven Heat Transformation Applications

Inaugural thesis presented to the Faculty of Mathematics and Natural Sciences
of Heinrich-Heine-University Düsseldorf
for the degree of

Doctor of Philosophy (Ph.D.) in Natural Sciences

by

Tobie J. Matemb Ma Ntep

from Cameroon, Yaoundé

Düsseldorf, December 2019

from the Institute for Inorganic and Structural Chemistry

at the Heinrich-Heine-University Düsseldorf

Printed by permission of the Faculty of Mathematics and Natural Sciences of Heinrich-Heine-University Düsseldorf

Examiners:

1. Prof. Dr. Christoph Janiak
2. Prof. Dr. Christian Ganter

Date of the oral defense: 19.12.2019

To Many Genius

who will never be known because no one dared to give them a chance

Eidesstattliche Erklärung

Ich versichere an Eides statt, dass die Dissertation von mir selbstständig und ohne unzulässige fremde Hilfe unter der Beachtung der „Grundsätze zur Sicherung guter wissenschaftlicher Praxis“ an der Heinrich-Heine-Universität Düsseldorf erstellt worden ist. Die aus fremden Quellen direkt oder indirekt übernommenen Gedanken sind als solche kenntlich gemacht. Die Arbeit wurde bisher weder im Inland noch im Ausland in gleicher oder ähnlicher Form einer anderen Prüfungsbehörde vorgelegt. Es wurden keine früheren erfolglosen Promotionsversuche unternommen.

……………………. ……………………

Ort, Datum Unterschrift

Acknowledgments

I first of all express my deepest gratitude to my supervisor, Prof. Dr. Christoph Janiak, for giving me the opportunity right from Cameroon to join and work within his research group. Thank you very much for your thorough training and time given to me, as well as your trust; it has left a permanent impact regarding the development of my scientific skills.

I also thank Prof. Dr. Christian Ganter for accepting to co-supervise my Ph.D. research work. Thank you for your prompt help whenever I needed any from you.

I address my sincere gratitude to the German Academic Exchange Service (DAAD) for sponsoring my travel and stay in Germany through a doctoral scholarship from April 2016 to September 2018.

I thank Bastian Moll for conducting the Raman spectroscopy measurement for so many of my samples. Your contribution was great.

My gratitude also to Dr. Helge Reinsch (Christian-Albrechts-Universität zu Kiel) who solved the structures of the new obtained materials in this work from powder X-ray data by Rietveld refinement. I highly value your contribution to this work. Thank you for a nice collaboration.

My gratitude goes to Dr. Hergen Breitzke (Technische Universität Darmstadt) for conducting the solid-state NMR spectroscopy experiments for many of my samples. Thanks for your expertise; it has been determinant to this work.

I thank Dr. Sebastian-Johannes Ernst (Fraunhofer Institute for Solar Energy Systems, Freiburg) for conducting the multicycle ad-/desorption stability test of aluminum muconate, as well as the theoretical calculations of performance.

I thank Emrah Hastürk for all his contribution by conducting several gas sorption experiments and training me to the use of adsorption devices. Thank you very much for your availability.

I thank Serkan Gökpinar for training me in the use of equipment in the lab and within the group. Thanks for your availability and contribution to make me feel at home in the group.

My gratitude goes to Carsten Schlüsener and Dr. Laura Schmolke for measuring several SEM-EDX and XPS analyses, respectively.

I thank especially Mrs. Claudia Schäfer, Mrs. Birgit Tommes, Mrs. Annette Ricken, Mr. Marcell Demandt and Mrs. Jutta Bourgeois for all their technical support.

I express my gratitude to all the AC1 group members for the friendly atmosphere and readiness to help. I especially think of Niels Tannert, Anna Goldman, Simon Millan, Ülkü Kökcam-Demir, Philipp Brandt, Alexander Nuhnen, Tim-Oliver Knedel, Irina Gruber, Bahareh Natheghi, Anna Christin Kautz, Christian Jansen, Simon-Patrick Höfert, Vasily Gvilava, Alexa Schmitz, Yangyang Sun, Beatriz Giesen, Moritz Steinert, Alex Spieß, Stephanie Bügel, Ilka Simon, Secil Öztürk, Saskia Menzel, Dennis Woschko, Olga Koikolainen, Dr. Nader de Souza Amadeu, Dr. Jun Liang, Dr. Mahsa Armaghan, Dr. Marvin Siebels, Dr. Dennis Dietrich, Dr. Sebastian Glomb, Dr. Sandra Nießing and Dr. Vera Vasylyeva-Shor. I had spent among you during the last three years, remarkable moments of long lasting memories.

Last but not the least, I am very grateful to my wife Lucie Matemb and our children who allowed me to conduct my Ph.D. research far away for more than three years. Thank you for bearing the sacrifice and for your supportive love.

To all whose names deserve to be and have not been mentioned here, I sincerely say thank you!

List of publications

The work presented in this cumulative thesis was done from October 2016 to September 2019 at the Institute for Inorganic Chemistry and Structural Chemistry I of the Heinrich-Heine-University Düsseldorf, under the supervision of Prof. Dr. Christoph Janiak. From this work resulted the following publications:

1. Realizing the Potential of Acetylenedicarboxylate by Functionalization to Halofumarate in Zr^{IV} Metal-Organic Frameworks.
   Tobie J. Matemb Ma Ntep, Helge Reinsch, Bastian Moll, Emrah Hastürk, Serkan Gökpinar, Hergen Breitzke, Carsten Schlüsener, Laura Schmolke, Gerd Buntkowsky, and Christoph Janiak, *Chem. Eur. J.* **2018**, *24*,14048–14053.
   DOI: 10.1002/chem.201802838

2. Acetylenedicarboxylate and In Situ Generated Chlorofumarate-Based Hafnium(IV)−Metal−Organic Frameworks: Synthesis, Structure, and Sorption Properties.
   Tobie J. Matemb Ma Ntep, Helge Reinsch, Carsten Schlüsener, Anna Goldman, Hergen Breitzke, Bastian Moll, Laura Schmolke, Gerd Buntkowsky, and Christoph Janiak, *Inorg. Chem.* **2019**, *58*, 16, 10965-10973.
   DOI: 10.1021/acs.inorgchem.9b01408

3. Halogen Functionalization of Aluminium Fumarate Metal–Organic Framework via In Situ Hydrochlorination of Acetylenedicarboxylic Acid.
   Tobie J. Matemb Ma Ntep, Wei Wu, Hergen Breitzke, Carsten Schlüsener, Bastian Moll, Laura Schmolke, Gerd Buntkowsky, and Christoph Janiak, *Aust. J. Chem*. **2019**, *72*, 835–841.
   DOI: 10.1071/CH19221

(Contribution upon invitation to the special issue for Professor Richard Robson in commemoration of his seminal contribution to science, in particular to the foundation of MOF chemistry)

4. Acetylenedicarboxylate-based cerium(IV) metal-organic framework with **fcu** net topology: a potential material for air cleaning from toxic halogen vapors.

   Tobie J. Matemb Ma Ntep, Helge Reinsch, Jun Liang, and Christoph Janiak, *Dalton Trans*. **2019**, *48*, 15849–15855.

   DOI: 10.1039/c9dt03518d

5. Designing a new aluminium muconate metal-organic framework (MIL-53-muc) as a methanol adsorbent for sub-zero temperature heat transformation applications.

   Tobie J. Matemb Ma Ntep, Helge Reinsch, Philipp P. C. Hügenell, Sebastian-Johannes Ernst, Emrah Hastürk and Christoph Janiak, *J. Mater. Chem. A*, **2019**, *7*, 24973–24981.

   DOI: 10.1039/c9ta07465a

6. Facile In Situ Halogen Functionalization via Triple-Bond Hydrohalogenation: Enhancing Sorption Capacities through Halogenation to Halofumarate-based Zr(IV)-Metal-organic Frameworks.

   Tobie J. Matemb Ma Ntep, Hergen Breitzke, Laura Schmolke, Carsten Schlüsener, Bastian Moll, Simon Millan, Niels Tannert, Ilias El Aita, Gerd Buntkowsky, and Christoph Janiak, *Chem. Mater.* **2019,** *31*, 21, 8629–8638.

   DOI: 10.1021/acs.chemmater.9b00524

Zusammenfassung

Die vorliegende kumulative Thesis umfasst sechs wissenschaftliche Artikel, welche über verschiedene Modifikationen von Fumarat-basierten Metall-organischen Gerüstverbindungen (engl. metal-organic frameworks, MOFs) mit **fcu** und MIL-53 analogen Topologien berichten. Ziel der vorliegenden Thesis war die Untersuchung von Effekten durch Linearisierung und der zweifachen Verlängerung des Fumarat-Linkers auf die Gasadsorptions-, Wasserdampf- und Alkoholdampf-Sorptionseigenschaften im Vergleich zu den ursprünglichen MOFs Aluminium- bzw. Zirkoniumfumarat (MIL-53-Fum, MOF-801). Hierbei wurde besonders auf potentielle Anwendungen in der Gasspeicherung/-separation und in Wärmetransformationsprozessen eingegangen.

Zunächst wurden drei neue isostrukturelle Acetylendicarboxylat (Adc)-basierte Zirkonium(IV), Hafnium(IV) und Cerium(IV)-MOFs, gekennzeichnet als M-HHU-1 M = Zr, Hf, Ce) mit der vollständigen Summenformel $[M_6(\mu_3\text{-}O)_4(\mu_3\text{-}OH)_4(Adc)_6]$, hergestellt und vollständig charakterisiert (HHU steht für Heinrich-Heine-Universität). Die drei MOFs wurden als mikrokristalline Pulver erhalten und ihre Strukturen mittels Pulver-Röntgendiffraktometrie (PXRD) und anschließender Rietveldverfeinerung bestimmt.

Die MOFs M-HHU-1 bestehen aus oktaedrischen $[M_6(\mu_3\text{-}O)_4(\mu_3\text{-}OH)_4]^{12+}$ Clustern, welche jeweils über zwölf Adc-Linker mit anderen anorganischen Einheiten verknüpft sind. Dies führt zu mikroporösen Materialien mit **fcu** Netztopologie, welche mit dem prototypischen MOF UiO-66 vergleichbar ist. Ihre permanente Mikroporosität wurde mittels Stickstoffsorption bestimmt, was M-HHU-1 zum ersten berichteten Adc-basierten MOF mit experimentell bestätigter, permanenter Porosität macht. Ihre hohe Hydrophilie konnte über Typ I Wasserdampf-Sorptionsisothermen gezeigt werden. Die Adsorptionsisothermen von CO_2 und H_2 zeigen bemerkenswert hohe isosterische Adsorptionsenthalpien (bei Anfangsbeladung) von 47 beziehungsweise 9 kJ mol^{-1}, welche auf die Anwesenheit einer $–C{\equiv}C–$ Dreifachbindung im Netzwerk zurückzuführen sind. Diese macht es Ce-HHU-1 auch möglich, Br_2-Dämpfe zu chemisorbieren, wohingegen I_2-Dämpfe chemi- und physisorbiert werden. Daher könnte das Material potentiell in der Reinigung von toxischen Halogendämpfen aus der Luft angewendet werden.

Weiterhin wurde eine neue Strategie für eine einfache Halogenfunktionalisierung der Fumarat-basierten MOFs mittels in-situ Hydrohalogenierung von Acetylendicarbonsäure entwickelt. Diese Methode wurde nach der Beobachtung der Reaktionen von Zirkonium- oder Hafniumhalogeniden (MX_4; M= Zr, Hf; X = Cl, Br, I) mit Acetylendicarbonsäure in Wasser unerwarteterweise entdeckt. Hierbei wird die Acetylendicarbonsäure quantitativ einer ungewöhnlichen in-situ Linkertransformation zum Halofumarat unterzogen, welche über eine *trans*-Addition von HX (X = Cl, Br und I) an die –C≡C– Dreifachbindung abläuft.

Die HX-Addition und die anschließende Ausbildung der MOFs erfolgen in einer Eintopf-Reaktion, bei der in-situ halogenierte Linker mit gelösten Zirkonium- bzw. Hafniumionen reagieren und zu vier neuartigen mikroporösen Zr-HHU-2-X (X = Cl, Br, I) und Hf-HHU-2-Cl MOFs führen, welche eine **fcu** Topologie aufweisen. Hierbei werden die sekundären Baueinheiten des UiO-Typs $[M_6O_4(OH)_4]^{12+}$ zwölffach über die Halofumarat-Linker miteinander verknüpft. Dieser Ansatz wurde ausgeweitet um Aluminiumfumarat (MIL-53-Fum) in einer chloro-funktionalisierten Variante herzustellen. Dazu wurde Acetylendicarbonsäure mit Aluminiumchlorid in der Anwesenheit von Essigsäure als Modulator zur Reaktion gebracht. Hierbei wurde ein neues mikroporöses MOF, bezeichnet als MIL-53-Fum-Cl, mit der Formel [Al(OH)(Fum-Cl)] (Fum-Cl = chloro-Fumarat), erhalten. Dabei ist die Struktur, welche analog zu MIL-53-Fum ist, aus Ketten von *trans*-eckenverknüpften AlO_6 Oktaedern aufgebaut, welche über die Chlorofumarat-Linker zu einem Netzwerk verknüpft werden. Dieses Netzwerk weist eindimensionale Kanäle mit rautenförmigem Querschnitt auf. Im Vergleich zu nicht-halogeniertem MOF-801 führen die Chloro-Gruppen in Zr-HHU-2-Cl zu einer erhöhten Hydrophilie, wie auch zu einer erhöhten Gasaufnahme von 21 Gew.% SO_2, 24 Gew.% CH_4, 44 Gew.% CO_2 und 154 Gew.% N_2. Die Gassorptionseigenschaften des Zr-HHU-2-Cl deuten auf eine Eignung für die CO_2-, N_2- und SO_2-Aufnahme sowie Trennung hin, während aus den Wasserdampf-Sorptionsisothermen eine hohe Wärmespeicherungskapazität von 500 kJ kg^{-1} folgt, was das Material vielversprechend für eine Anwendung in Adsorptions-basierten Wärmebatterien (adsorption-based thermal batteries (ATB)) und zur Luftentfeuchtung macht. Hf-HHU-2-Cl absorbiert CO_2 mit einer isosterischen Wärmeenthalpie von 39 kJ mol^{-1} und absorbiert durch Chlorofunktionen an der Porenoberfläche molekularen Ioddampf ausschließlich als Polyiodid-Anionen. Analog erhöhen die funktionellen Chlorogruppen in den Poren von MIL-53-Fum-Cl die Kapazität und Affinität der Gassorptionen (CO_2, CH_4 und H_2) im Vergleich zum nicht-funktionalisierten MIL-53-Fum. Durch die Funktionalisierung resultiert auch ein zweifacher Anstieg der selektiven Adsorption von CO_2 über CH_4 im Vergleich zu MIL-53-Fum.

Abschließend wurde basierend auf der zweifachen isoretikulären Erweiterung des Aluminiumfumarats ein neues Aluminium-basiertes MOF hergestellt. Hierbei wurde *trans,trans*-Muconat als Linker eingesetzt und das entstandene MOF als MIL-53-Muc benannt, da es isostrukturell zum prototypischen Aluminiumterephthalat (Al-MIL-53-Bdc) ist und somit aus Ketten von *trans*-eckenverknüpften $AlO_4(OH)_2$ Oktaedern besteht. Die einzelnen Ketten werden durch die Muconat Linker verbrückt, hieraus resultiert ein mikroporöses Netzwerk mit rautenförmigen, eindimensionalen Poren. Kennzeichnend sind die hohe spezifische BET-Oberfläche (S_{BET}) von 1750 $m^2\ g^{-1}$, eine Typ V (S-förmige) Methanolsorptionsisotherme mit einem steilen Anstieg im relativen Druckbereich von 0.05–0.15 und eine maximale Aufnahmekapazität von 0.5 $g\ g^{-1}$.

Das hergestellte Material besitzt eine hohe Stabilität, welche über 50 Ad- und Desorptionszyklen von Methanol nachgewiesen werden konnte, wodurch sich MIL-53-Muc als ein vielversprechendes Adsorbens für Adsorptionswärmepumpen und Adsorptionskühler herausstellt. Die Beurteilung der Leistungsfähigkeit des Materials für diese Prozesse erfolgte anhand der Leistungszahl (engl. coefficient of performance, COP). Für MIL-53-Muc konnten hohe COP_H-Werte von über 1.5 bei niedrigen Evaporationstemperaturen von bis zu -5 °C beim Heizvorgang, während sehr niedrige Temperaturen von bis zu -10 °C im Kühlmodus erreichbar sind. Hierbei wird weiterhin ein hoher COP_C von bis zu 0.73 erreicht.

Das Arbeitspaar MIL-53-Muc/Methanol übertrifft die meisten literaturbekannten Arbeitspaare für Adsorptions-basierte Wärmepumpen und Kühler bei Temperaturen unterhalb von 0 °C. Des Weiteren ist MIL-53-Muc unter hydrothermalen Bedingungen stabil und zeigt vorteilhafte Wasseradsorptionseigenschaften, die das Material für die autonome Feuchtigkeitskontrolle vielversprechend erscheinen lassen.

Summary

The present thesis is a cumulative of six scientific articles reporting different modifications of fumarate-based metal-organic frameworks (MOFs) with **fcu** and MIL-53-type topologies. The objective was to investigate the effect of the linearization and twofold extension of the fumarate linker on the gas, water and alcohol vapor adsorption properties for the parent aluminum and zirconium fumarate (MIL-53-Fum and MOF-801), with respect to their potential application for gas storage/separation and heat transformation processes.

At first instance, three new isostructural acetylenedicarboxylate (Adc)-based zirconium(IV)-, hafnium(IV)- and cerium(IV)-MOFs denoted as M-HHU-1 (M = Zr, Hf, Ce) and of formulas $[M_6(\mu_3\text{-}O)_4(\mu_3\text{-}OH)_4(Adc)_6]$, were synthesized and fully characterized (HHU stands for Heinrich-Heine-Universität). The three MOFs were obtained as microcrystalline powder and their structure was determined from powder X-ray diffraction (PXRD) data and Rietveld refinement. Their structure consists of octahedral $[M_6(\mu_3\text{-}O)_4(\mu_3\text{-}OH)_4]^{12+}$ clusters, each of which is connected to other inorganic units by twelve Adc linkers to give microporous materials with **fcu** net topology like the prototypical UiO-66. Their permanent microporosity was established from nitrogen sorption experiment, making M-HHU-1 to be the very first reported Adc-based MOFs with experimentally demonstrated permanent porosity. Their high hydrophilicity was displayed by a type I water vapor sorption isotherm, while the adsorption of CO_2 and H_2 in M-HHU-1 features a remarkably high zero-coverage isosteric heat of adsorption above 47 and 9 kJ mol^{-1}, respectively, attributed to the presence of the –C≡C– triple-bond in the framework. The latter also allows for Ce-HHU-1 to capture and irreversibly chemisorb Br_2 vapors, as well as both chemi- and physisorb I_2 vapors in an effective manner, making this material potentially applicable for air cleaning from toxic halogen vapors.

Furthermore, a new strategy was developed for a facile halogen functionalization of fumarate-based MOFs via in situ hydrohalogenation of acetylenedicarboxylic acid. This approach was unexpectedly discovered when reacting zirconium or hafnium halides (MX_4; M = Zr, Hf; X = Cl, Br, I) in water with acetylenedicarboxylic acid. The latter quantitatively undergoes an unusual in-situ linker transformation to halofumarate via *trans*

addition of HX to the -C≡C- triple-bond. This HX addition and MOF formation happen in a one-pot reaction, that is, the in-situ generated halogenated linker reacts with zirconium/hafnium ions in solution to yield four new microporous Zr-HHU-2-X (X = Cl, Br, I) and Hf-HHU-2-Cl MOFs with **fcu** topology, containing the UiO-type $[M_6O_4(OH)_4]^{12+}$ secondary building units twelvefold connected by halofumarate linkers. This approach was extended to chloro-functionalize aluminum fumarate (MIL-53-Fum) by reacting acetylenedicarboxylic acid with aluminum chloride in the presence of acetic acid as crystallization modulator. A new microporous MOF denoted as MIL-53-Fum-Cl, with formula [Al(OH)(Fum-Cl)] (Fum-Cl = chlorofumarate) was obtained, which structure analogous with MIL-53-Fum, is built up from chains of *trans*-corner-sharing AlO_6 octahedra, linked together by chlorofumarate to form a framework having one-dimensional channels with lozenge-shaped cross-section. When compared to the non-halogenated zirconium fumarate (MOF-801), the chloro-functional groups in Zr-HHU-2-Cl result in increased hydrophilicity, as well as increased gas uptakes of 21% SO_2, 24% CH_4, 44% CO_2, 154% N_2. The gas sorption properties of the chlorinated Zr-HHU-2-Cl material indicate its suitability for CO_2, N_2, SO_2 capture and separation, while its water sorption profile yields a high heat storage capacity of 500 kJ kg^{-1}, making it promising for adsorption-based thermal batteries (ATB) and dehumidification applications. Hf-HHU-2-Cl also adsorbs CO_2 with an isosteric heat of adsorption of 39 kJ mol^{-1}, as well as adsorbs molecular iodine vapor exclusively as polyiodide anions due to grafted chloro-functions on the pore surface. Similarly, the chloro-functional groups decorating the pores of MIL-53-Fum-Cl enhance the gas (CO_2, CH_4 and H_2) sorption capacities and affinity compared to the non-functionalized MIL-53-Fum. The functionalization also results in a twofold increase in the selective adsorption of CO_2 over CH_4 compared to MIL-53-Fum.

Finally, an isoreticular twofold expansion of aluminum fumarate was designed and synthesized using the *trans,trans*-muconate linker to form a new aluminum metal-organic framework (MOF) termed as MIL-53-Muc. MIL-53-Muc is isostructural to the prototypical aluminum terephthalate (Al-MIL-53-Bdc) and is therefore built up from chains of *trans*-corner-sharing $AlO_4(OH)_2$ octahedra connected by muconate linkers to a microporous network with lozenge-shaped one-dimensional channeled pores. MIL-53-Muc Features a high BET specific surface area of 1750 m^2 g^{-1}, a type V (S-shaped) stepwise methanol adsorption isotherm stepping at 0.05–0.15 relative pressure range, a high methanol uptake capacity of about 0.5 g g^{-1} and methanol stability over 50 assessed ad/desorption cycles. Therefore, MIL-53-Muc is revealed as a promising adsorbent applicable for adsorption-based heat transformation applications. The performance evaluation indicates that high coefficient of performance COP_H values above 1.5 could be reached for the evaporator operating at temperature as low as -5 °C under heat pump conditions, while very low temperatures down to -10 °C could be achieved for refrigeration/ice making with COP_C values up to 0.73 under cooling conditions. This makes MIL-53-Muc/methanol outperforming most other working pairs for adsorption-based cooling and heating applications under sub-zero temperature conditions. Furthermore, MIL-53-Muc is hydrothermally stable and presents a favorable water sorption profile making this material also suitable for application in autonomous indoor humidity control.

List of abbreviations

Adc	Acetylenedicarboxylate
AHP	Adsorption Heat Pump
AHT	Adsorption Heat Transformation
ATB	Adsorption Thermal Battery
Bdc	Benzene-1,4-dicarboxylate
BET	Brunauer-Emmett-Teller
CFC	Chlorofluorocarbon
COP	Coefficient of Performance
CP	Coordination Polymer
DMF	*N*,*N'*-Dimethylformamide
EDX	Energy Dispersive X-ray spectroscopy
Fum	Fumarate
HHU	Heinrich-Heine-Universität
HKUST	Hong Kong University of Science and Technology
IR	Infrared spectroscopy
IRMOF	Isoreticular Metal-Organic Framework
MIL	Materials of Institute Lavoisier
MOF	Metal-Organic Framework
Muc	Muconate
PXRD	Powder X-ray Diffraction
SBU	Secondary Building Unit
SEM	Scanning Electron Microscopy
ssNMR	Solid-state Nuclear Magnetic Resonance spectroscopy
TDC	Thermally Driven Chiller
TGA	Thermogravimetric analysis
UiO	Universitetet i Oslo/ University of Oslo
XPS	X-ray Photoelectron Spectroscopy

Table of contents

Chapter 1

Introduction

1.1 Traditional air conditioning systems and drawbacks

Maintaining pleasant living conditions with variable weather including extreme summer and winter has triggered the development of technologies to regulate indoor space temperature.[1] Among these technologies are heat exchangers, namely heat pumps and chillers, which are used not only for air conditioning purpose but also for refrigeration and production of hot water.[2] The demand for cooling devices (for air conditioning and refrigeration) has increased during the last years. This trend is very likely to continue due to global warming resulting in recurrence of extreme heat peaks during summer.[3]

The most frequently used air conditioning systems and refrigerators operate on electricity or fossil fuels and are therefore heavy energy consumers, as more than 50% of modern buildings energy consumption originates from air conditioning processes.[4] The number of used air conditioning systems is even expected to triple over the next 30 years, particularly due to increased income and urbanization/living standards in developing countries, most of which are located in tropical or subtropical regions of the world.[5,6] In addition, traditional air conditioners constitute a considerable source of domestic and industrial carbon dioxide (CO_2) emission. Furthermore, traditional heat exchangers have compressors using chlorofluorocarbons (CFCs) as cooling agents, which are known to be toxic, flammable and harmful to the environment. These facts expose the drawbacks in using traditional heat exchangers in a context of worldwide energy crisis, global warming and environmental challenges.[7,8] For this reasons, there is an urgent need to look for alternatives to these systems.

---

[1] Y. I. Aristov, *Fut. Cit. & Env.* **2015**, *1*: 10.

[2] T. Núñez, W. Mittelbach, H.-M. Henning, *Appl. Therm. Eng*. **2007**, *27*, 2205–2212.

[3] European Commission Energy. Projected primary energy consumption in 2020 (NL); http://ec.europa.eu/energy/efficiency/eed/reporting_en.htm (accessed 17-01-2015).

[4] Eurostat Database for Energy Statistics. http://ec.europa.eu/eurostat/web/energy/publications (accessed 17-01-2015).

[5] D. Lefebvre, F. H. Tezel, *Renew. Sust. Energ. Rev.* **2017**, *67*, 116–125.

[6] International Energy Agency, World Energy Outlook. 2011, p696; http://www.iea.org/publications/freepublications/publication/weo2011_web.pdf (accessed 17-01-2015).

[7] S. Maeda, K. Thu, T. Maruyama, T. Miyazaki, *Appl. Sci*. **2018**, *8*, 2061.

[8] M. Isaac, D. P. van Vuuren, *Energy Policy* **2009**, 37, 507−521.

1.2 Adsorption-based heat transformation as alternative to traditional heat exchangers

To address the problem of hazardous and energy-intensive cooling devices, alternative solutions for heat reallocation are currently been developed, namely thermally driven adsorption chillers (TDCs) and adsorption heat pumps (AHPs).[9,10] TDCs and AHPs are indeed driven by solar heat or waste heat from industrial processes, which would otherwise be simply released to the environment. Furthermore, they use environmentally benign coolants such as water, ethanol or methanol.[11] TDCs and AHPs can therefore significantly help to minimize primary energy consumption and greenhouse gas emissions generated by industrial or domestic cooling.

The working principle of AHPs and TDCs is depicted in Figure 1. It is based on the evaporation and subsequent reversible adsorption of a coolant onto a porous material. The process releases heat during the working cycle and the fluid is desorbed and re-condensed under low temperature heating (solar heat or waste heat) during the regeneration cycle.[12]

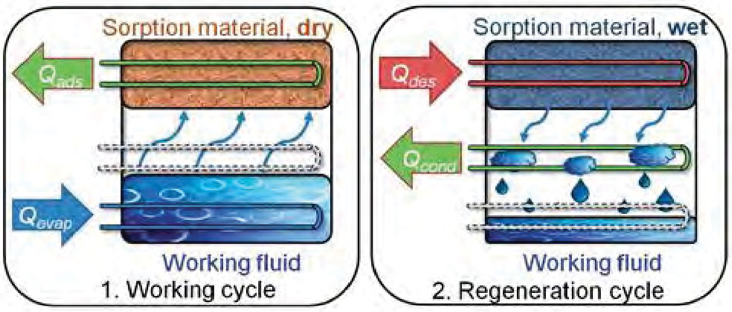

Figure 1. Working principle of adsorption-based heat exchangers. In the working cycle (1), the coolant is evaporated by taking up the heat of evaporation Q_{evap} from the ambient. The fluid vapor is subsequently adsorbed on the porous material, releasing adsorption heat Q_{ads}. In the regeneration cycle (2), a driving heat Q_{des} is applied to the saturated adsorbent resulting in the desorption of the fluid. The desorbed vapors condense at a medium temperature level, releasing condensation heat Q_{cond}. Q_{evap} is exploited for cooling in TDCs, while Q_{ads} and Q_{cond} are exploited for heating in AHPs. Reproduced with permission from ref 12. Copyright 2014 RSC.

---

[9] H.-M. Henning, *Appl. Therm. Eng.* **2007**, *27*, 1734−1749.

[10] C. A. Balaras, G. Grossman, H.-M. Henning, C. A. Infante Ferreira, E. Podesser, L. Wang, E. Wiemken, *Renewable Sustainable Energy Rev.* **2007**, *11*, 299−314.

[11] R.Z. Wang, R.G. Oliveira, *Prog. Energy Combust. Sci.* **2006**, *32*, 424–458.

[12] F. Jeremias, D. Fröhlich, C. Janiak, S. K. Henninger, *New J. Chem.* **2014**, *38*, 1846–1852.

It is obvious from their principle, that the efficiency of heat transformation devices depends primarily on the performance of the porous adsorbent material used.[13]

1.3 Adsorbent materials in adsorption-based heat transformation processes

1.3.1 Criteria for good materials

The adsorbent-adsorbate working pair applied in an adsorption-driven heat exchanger is of key importance to achieve the best performing device.[14] The choice of a promising working pair applicable for adsorption-based heat transformation depends on four main criteria: (i) the adsorption profile should yield an S-shaped (type V) stepwise isotherm, with the step located in the relative pressure range P/P_0 = 0.05–0.4. A steep uptake step displays the highest thermodynamic efficiency, since only a small change in the relative sorbate pressure is needed for a large loading. The system can therefore be easily switched between the working and regeneration cycle by small temperature difference adjustment, as it leads to a change of the relative pressure. There should be minimal or better no hysteresis loop between the adsorption and desorption branches (ii) The adsorbate uptake should be high, which requires materials with large pores and high surface area. However, the pores should not be too large to avoid hysteresis originating from mesopores. (iii) The temperature of desorption should be low (80–120 °C) or ultralow (<80 °C) to increase the efficiency and to make use of solar heat, industrial waste heat or district heat. (iv) The material has to be thermally and hydrolytically stable to avoid its degradation under applied temperatures or hydrolysis under the ubiquitous moist. In addition, the adsorbent should feature stability over multiple sorbate adsorption-desorption cycles. The stability should correspond to the targeted life span of the devise (e.g. 30000 cycles for an estimated operational life of 10 years).[15,16]

So far, various inorganic porous solids like silica gel, aluminophosphates (AlPO) and zeolites have been investigated and utilized as sorbent materials in commercial sorption-based heat pumps and chillers. However, these conventional adsorbents require

---

[13] S. K. Henninger, F. P. Schmidt, H.-M. Henning, *Appl. Therm. Eng*. **2010**, *30*, 1692–1702.

[14] W. Li, X. Xia, M. Cao, S. Li, *J. Mater. Chem. A* **2019**, *7*, 7470–7479.

[15] M. F. de Lange, K. J. F. M. Verouden, T. J. H. Vlugt, J. Gascon, F. Kapteijn, *Chem. Rev.* **2015**, *115*, 12205−12250.

[16] M. H. Bagheri, S. N. Schiffres, *Langmuir* **2018**, *34*, 4, 1908–1915.

either very high desorption temperatures (e.g., hydrophilic zeolites like NaA or 13X) or feature an unwanted linear isotherm shape (e.g., silica gel) that limits the exchangeable amount of water/adsorbate (Figure 2).[17,18,19] Beside these purely inorganic porous materials, hybrid inorganic-organic materials, the so called metal-organic frameworks (MOFs) are an emerging class of microporous materials of interest.[20]

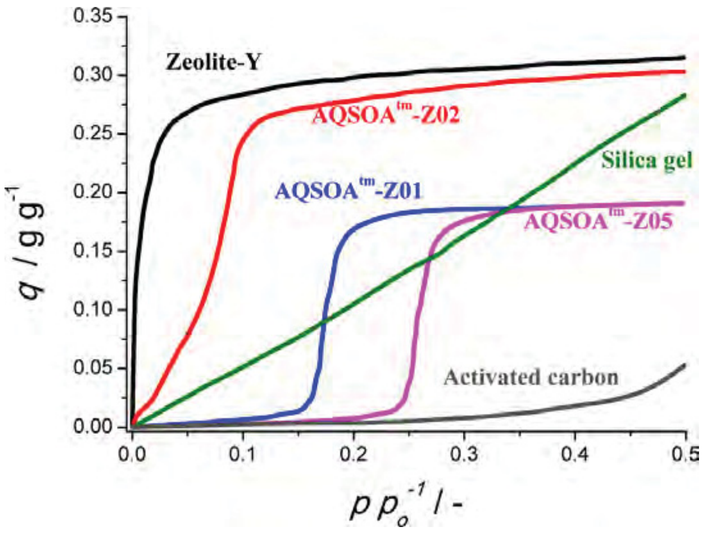

Figure 2. Water adsorption isotherms of commercially employed adsorbents. Reproduced with permission from ref 40. Copyright 2015 American Chemical Society.

1.3.2 Metal-organic frameworks (MOFs) as promising materials in sorption- based heat transformation

Metal-organic frameworks (MOFs) also termed as porous coordination polymers (CPs), represent a relatively new class of porous materials that have attracted tremendous attention over the past years. MOFs are constructed by joining metal ions or metal-containing clusters, the so-called secondary building units (SBUs), with polytopic organic linkers (e.g. di, tri-, or tetracarboxylate ligands), using strong coordinative bonding to create open crystalline frameworks with permanent porosity (Figure 3a).[21] An example is UiO-66 (UiO stands for University in Oslo), a prototypical Zr(IV)-MOF which was first

---

[17] L.W. Wang, R.Z. Wang, R.G. Oliveira, *Renew. Sust. Energ. Rev.* **2009**, *13*, 518–534.

[18] Y. I. Aristov, *Appl. Therm. Eng.* **2013**, *50*, 1610–1618.

[19] S. K. Henninger, S.-J. Ernst, L. Gordeeva, P. Bendix, D. Fröhlich, A. D. Grekova, Lucio Bonaccorsi, Y. Aristov, J. Jaenchen, *Renew. Energ.* **2017**, *110*, 59–68.

[20] S. Cui, M. Qin, A. Marandi, V. Steggles, S. Wang, X. Feng, F. Nouar, C. Serre, *Sci. Rep.* **2018**, *8*, 15284.

[21] C. Janiak, J. K. Vieth, *New J. Chem.* **2010**, *34*, 2366–2388.

reported in 2008 by Lillerud *et al*. The UiO-66 framework is built up from $[Zr_6(\mu_3\text{-}O)_4(\mu_3\text{-}OH)_4]^{12+}$ octahedral secondary building units (SBUs) connected each by twelve bridging benzene-1,4-dicarboxylate (Bdc) linkers, resulting in a three dimensional arrangement of micropores with **fcu** topology, containing large octahedral cages and smaller tetrahedral cages (Figure 3b).[22]

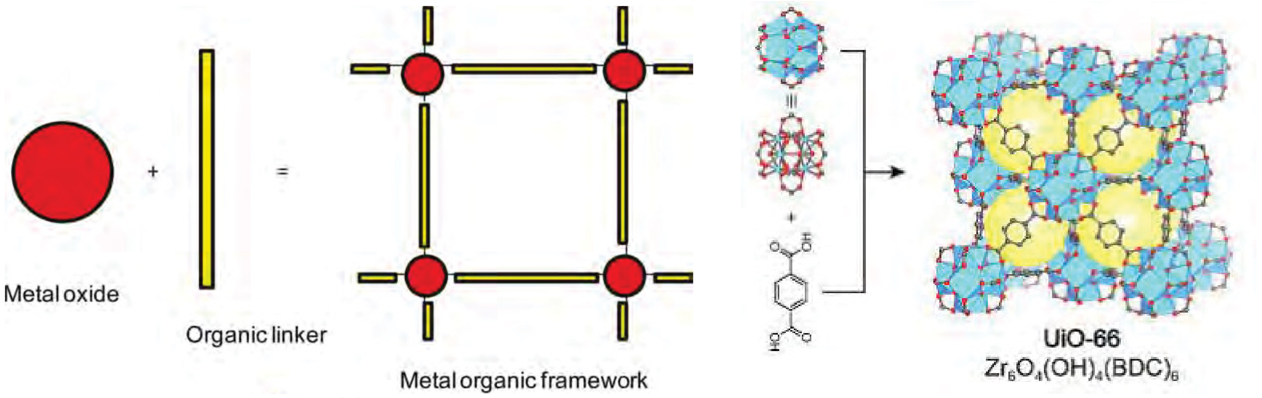

(a) (b)

Figure 3. (a) Building blocks and building scheme of MOFs, (b) the example of UiO-66. Adapted with permission from ref 33. Copyright 2019 John Wiley and Sons.

Figure 4 gives a summary of some SBUs and Figure 5 shows some well-known linkers employed in the construction of MOFs.

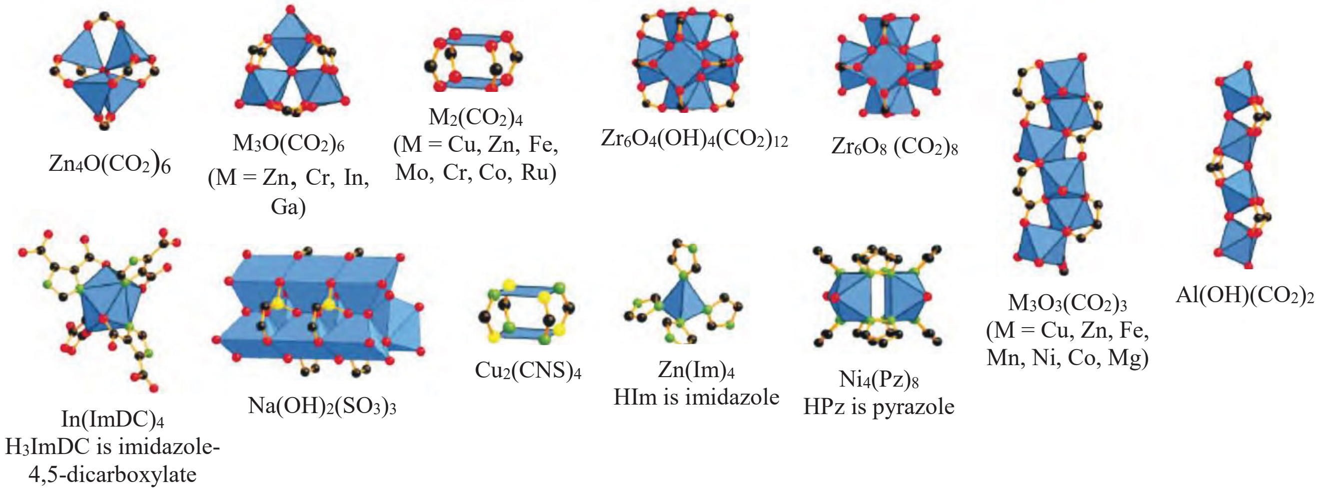

Figure 4. Some common inorganic secondary building units used in the construction of MOFs (the polyhedra demonstrate the metal coordination). Reproduced from ref 31. Copyright 2013 American Association for the Advancement of Science.

---

[22] J. H. Cavka, S. Jakobsen, U. Olsbye, N. Guillou, C. Lamberti, S. Bordiga, K. P. Lillerud, *J. Am. Chem. Soc.* **2008**, *130*, 13850–13851.

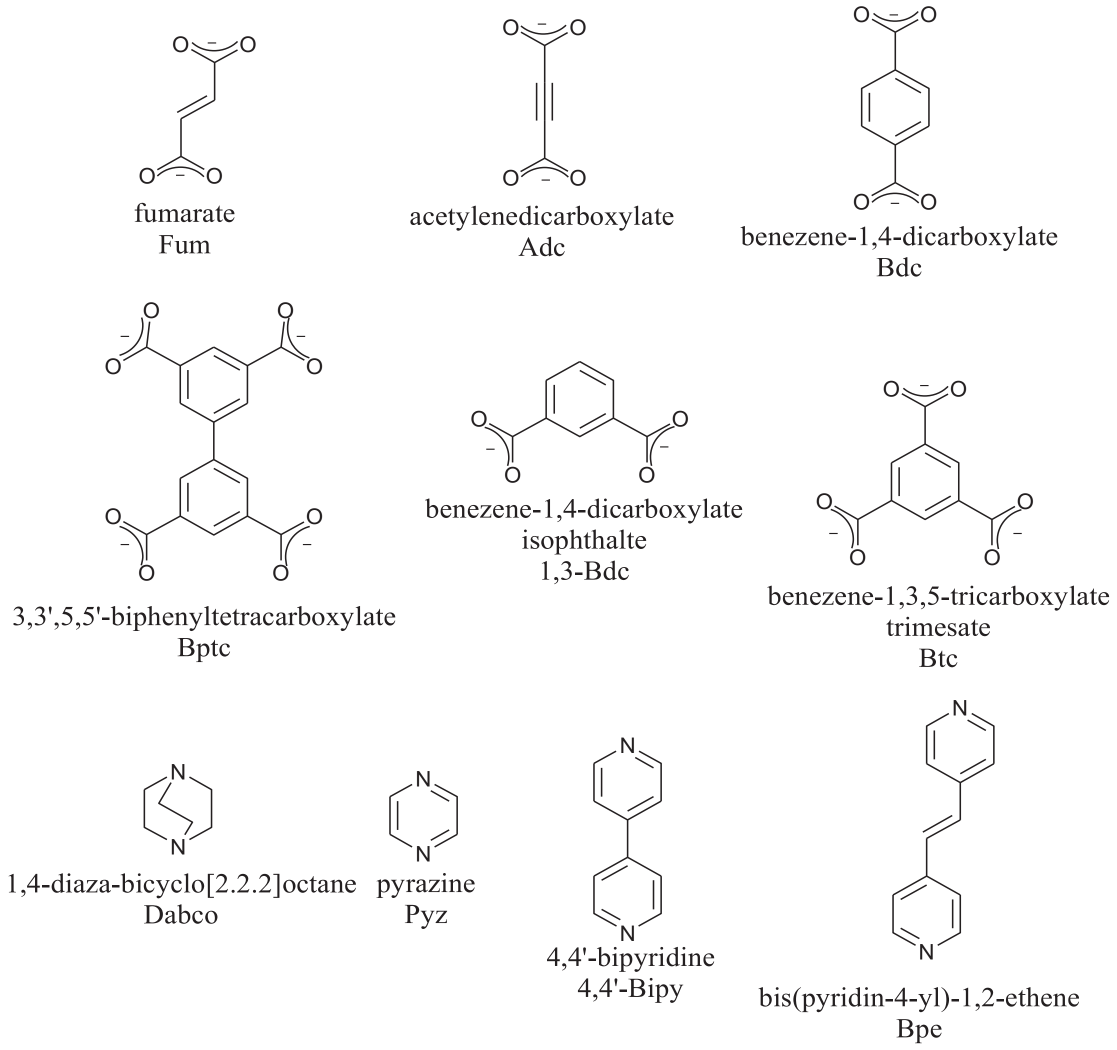

fumarate
Fum

acetylenedicarboxylate
Adc

benezene-1,4-dicarboxylate
Bdc

3,3',5,5'-biphenyltetracarboxylate
Bptc

benezene-1,4-dicarboxylate
isophthalte
1,3-Bdc

benezene-1,3,5-tricarboxylate
trimesate
Btc

1,4-diaza-bicyclo[2.2.2]octane
Dabco

pyrazine
Pyz

4,4'-bipyridine
4,4'-Bipy

bis(pyridin-4-yl)-1,2-ethene
Bpe

Figure 5. Some organic linkers used in the construction of MOFs.

MOFs are mostly synthesized by solvothermal methods, whereby metal salt and organic molecules are dissolved in a solvent.[23] Afterwards, the mixture is heated at or above the boiling point of the solvent in a special closed chemical reactor (e.g. Teflon-lined autoclave). The MOF then precipitates as microcrystalline powder or is obtained as single crystals under the elevated pressure caused by the solvent vapor.[24] Variations made to the traditional solvothermal method result in other synthesis nomenclatures as follows:

- In the *hydrothermal synthesis*, water is the employed solvent instead of organic solvents.

---

[23] C. Dey, T. Kundu, B. P. Biswal, A. Mallick, R. Banerjee, *Acta Cryst*. **2014**, *B70*, 3–10.

[24] P. Pachfule, R. Das, P. Poddar, R. Banerjee, *Cryst. Growth Des*. **2011**, *11*, 1215–1222.

- In the *microwave-Assisted* synthesis the mixture is heated with microwave irradiation, rather than conventional electric heating in an oven, as done in the typical solvothermal synthesis.
- In the *non-solvothermal synthesis*, the reaction mixture is heated below the boiling temperature of the solvent or under reflux, or the reaction is carried out at room temperature.

Other synthesis methods of MOFs include sonochemical, electrochemical, and mechanochemical synthesis.[25] Whatever the synthesis method used, the formation of the MOF occurs when the metal-oxo cluster, the so called SBU is formed in situ, meanwhile the organic ligands are often deprotonated and connect to the SBUs. The connectivity of the SBUs and linkers determine the structure and topology of the obtained framework. After the synthesis, the product is washed to remove impurities and by-products. Afterwards, activation procedures are carried out to empty the pores of the MOF prior to the porosity-based characterizations or utilizations. The activation procedure usually consists of exchanging the solvent of synthesis in the pores of the MOF against a more volatile solvent and then heating the solid under vacuum. In the case of chemically and thermally fragile frameworks, other procedures like supercritical CO_2 drying are used. This means to circumvent applying elevated temperatures for the pores outgassing.[26]

One advantage of MOFs compared to zeolites, aluminophosphates, activated carbons and silica gels, is that they can feature very high surface areas, pore size and volume. For instance, NU-110 is a MOF that displays a record BET surface area of about 7100 $m^2\ g^{-1}$, which is higher than any porous material.[27] In addition, the vast variety of building units and connection modes afford a great number of different architectures. Furthermore, the pore size can be easily tuned just by controlling the length of the organic ligand, as well as their pore walls can be functionalized for specific applications via ligand design.

Regarding their tunability, two main strategies are commonly used to tune MOFs chemistry and pore size:

---

[25] N. Stock and S. Biswas, *Chem. Rev.* **2012**, *112*, 933–969.

[26] J. E. Mondloch, O. Karagiaridi, O. K. Farha, J. T. Hupp, *CrystEngComm* **2013**, *15*, 9258–9264.

[27] O. K. Farha, I. Eryazici, N. C. Jeong, B. G. Hauser, C. E. Wilmer, A. A. Sarjeant, R. Q. Snurr, S. T. Nguyen, A, Ö, Yazaydin, J. T. Hupp, *J. Am. Chem. Soc.* **2012**, *134*, 15016−15021.

- The *functionalization*. The chemistry of the MOF can be fine-tuned by decorating the pores with functional groups like $–NH_2$, –Cl, –Br, $–NO_2$, $–SO_3H$, –OH, etc. This can be done pre-synthetically by performing the synthesis using organic ligands bearing pending functional groups. The functionalization can also be done by means of post-synthetic modification (PSM) of pre-constructed parent MOF (Figure 6).[28] Finally, the functionalization can be done in situ, whereby the linker or cluster functionalization and MOF formation occur in a one-pot reaction.[29]

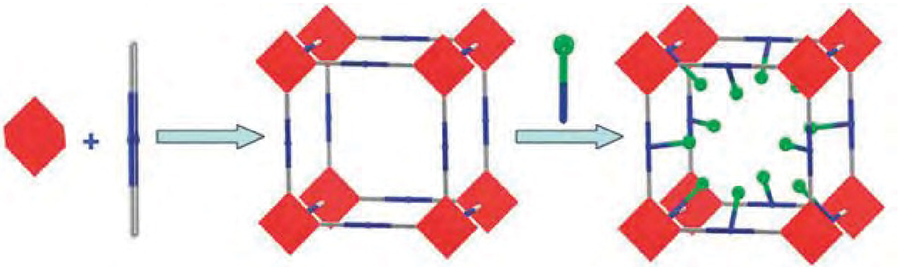

Figure 6. Illustration of the concept of post-synthetic modification of MOFs. Reproduced with permission from ref 28. Copyright 2009 Royal Society of Chemistry.

- The *Isoreticulation*. Also known as reticular synthesis, its principle is to construct isotopic frameworks of predetermined structure, with varying pore sizes by using linkers with the same connectivity but different lengths or functionality.[30] A typical example is the isoreticular metal-organic framework (IRMOF) series based on the MOF-5 structure, with $Zn_4(\mu_4\text{-}O)$ tetrahedra joined by linear dicarboxylate linkers to give a series of extended 3D cubic frameworks with increasing pore sizes and functionalities (Figure 7).

  It is noteworthy that the isoreticular frameworks are usually obtained under similar synthesis mixtures and conditions.[31] For instance, UiO-type MOFs are usually synthesized by the so-called *modulated synthesis*, whereby $ZrCl_4$ or $ZrOCl_2$ is reacted with a linear dicarboxylic acid by addition to the reaction mixture of a monocarboxylic acid (formic, acetic, trifluoroacetic, benzoic acid etc.) as crystallization modulator. It is assumed that the modulator induces initial in situ formation of soluble monomeric $\{Zr_6O_4(OH)_4(RCOO)_{12}\}$ clusters, which then lead

---

[28] Z. Wang, S. M. Cohen, *Chem. Soc. Rev.* **2009**, *38*, 1315–1329.

[29] X. Kong, T. He, Y. Zhang, X. Wu, S. Wang, M. Xu, G. Si, J. J. Li, *Chem. Sci.* **2019**, *10*,3949–3955.

[30] O. M. Yaghi, M. O'Keeffe, N. W. Ockwig, H. K. Chae, M. Eddaoudi, K. Kim, *Nature* **2003**, *423*, 705–714.

[31] Hiroyasu Furukawa, Kyle E. Cordova, Michael O'Keeffe, Omar M. Yaghi, *Science* **2013**, *341*, 1230444.

to network growth through a slower dynamic exchange between the modulator and the linker units. Thus modulation is now commonly used to induce highly crystalline products, controlling crystals size and morphology with enhanced reproducibility of synthesis procedure.[32]

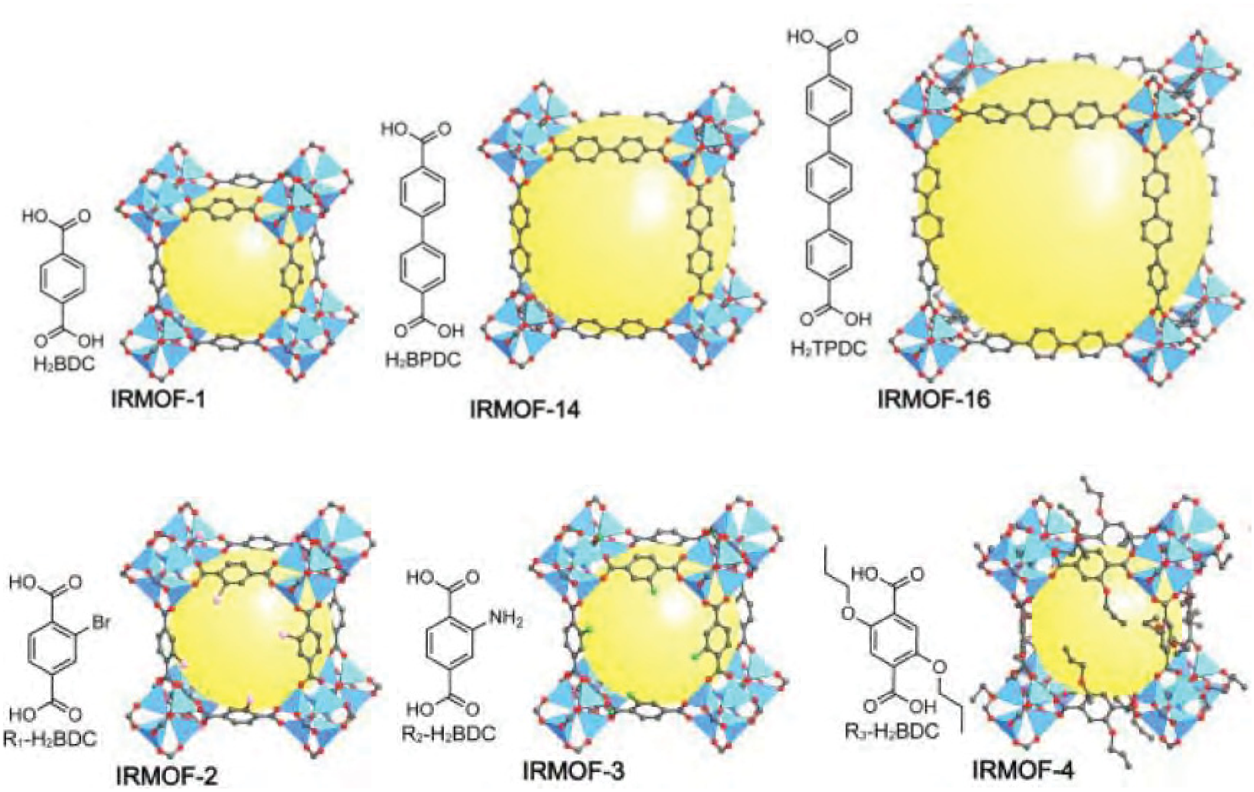

Figure 7. Isoreticular MOF series (IRMOF) based on the structure of MOF-5 (also termed IRMOF-1). Using extended linkers gives isoreticular expanded frameworks. H_2Bdc derivatives decorated with various substituents yield isoreticular functionalized frameworks, both of **pcu** topology.[33] Reproduced with permission from ref 33. Copyright 2019 John Wiley and Sons.

Metal-organic frameworks have already been investigated for a wide range of potential applications including gas storage and separation,[34] heterogeneous catalysis,[35] drug delivery,[36] sensing,[37] proton conduction.[38] More recently, MOFs have started to be

---

[32] A. Schaate, P. Roy, A. Godt, J. Lippke, F. Waltz, M. Wiebcke, P. Behrens, *Chem. Eur. J.* **2011**, *17*, 6643–6651.

[33] O. M. Yaghi, M. J. Kalmutzki, C. S. Directcks, Introduction to Reticular Chemistry: Metal-Organic Frameworks and Covalent Organic Frameworks, Wiley-VCH, Weinheim, **2019**.

[34] S. Chavan, J. G. Vitillo, D. Gianolio, O. Zavorotynska, B. Civalleri, S. Jakobsen, M. H. Nilsen, V. Valenzano, C. Lamberti, P. P. Lillerud, S. Bordiga, *Phys. Chem. Chem. Phys.* **2012**, *14*, 1614–1626.

[35] F.Vermoortele, B. Bueken, G. Le Bars, B. Van de Voorde, M. Vandichel, K. Houthoofd, A. Vimont, M. Daturi, M. Waroquier, V. Van Speybroeck, C. Kirschhock, D. De Vos, *J. Am. Chem. Soc.* **2013**, *135*, 11465−11468.

[36] X. Zhu, J. Gu, Y. Wang, B. Li, Y. Li, W. Zhao, J. Shi, *Chem. Commun.* **2014**, *50*, 8779–8782.

investigated as adsorbents for their potential application in adsorption-based heat transformation processes.[39,40] Since the first works of Henninger, Janiak *et al.* in 2009, a significant increasing number of works are reported in this regard. This is due to the possibility to fine-tune the adsorbate sorption profile in MOFs, especially because MOFs can feature higher fluid uptake compared to other adsorbents (Figure 8).[41,42] However, some challenges have to be circumvented before MOFs can practically be used for efficient AHT.

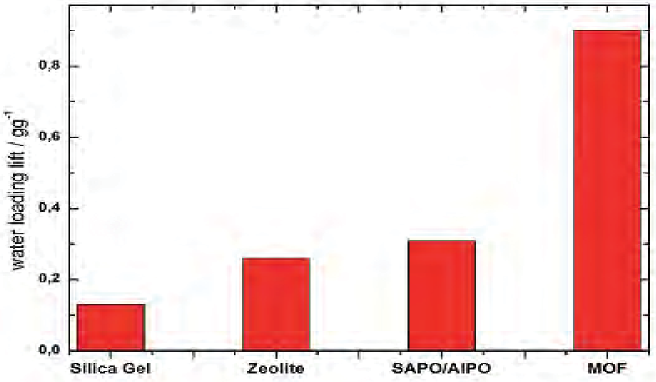

Figure 8. Illustration of the possible water loading lift for different material classes within a typical heat transformation cycle. Graphic reproduced with permission from ref 42. Copyrigth 2012 Wiley-VCH Verlag GmbH & Co.KGaA.

1.3.3 Challenges to overcome for the practical use of MOFs

Before MOFs can be practically used for heat transformation applications, some critical issues have to be addressed including the hydrothermal stability, the long-term multicycle ad/desorption stability, the increasing of the adsorption capacity while remaining in the realm of microporosity, the cost and sustainability of production.

(i) **The hydrolytic and multicycle stability**. Before a MOF can be considered for practical application, its robustness toward moist exposure should be established. This is

---

[37] I. Stassen, B. Bueken, H. Reinsch, J. F. M. Oudenhoven, D. Wouters, J. Hajek, V. Van Speybroeck, N. Stock, P. M. Vereecken, R. Van Schaijk, D. De Vos, R. Ameloot, *Chem. Sci.* **2016**, *7*, 5827–5832.

[38] G. K. H. Shimizu, J. M. Taylor, S. Kim, Science **2013**, *341*, 354–355.

[39] S. K. Henninger, H. A. Habib, C. Janiak, *J. Am. Chem. Soc.* **2009**, *131*, 2776–2777.

[40] M. F. de Lange, K. J. F. M. Verouden, T. J. H. Vlugt, J. Gascon, F. Kapteijn, *Chem. Rev.* **2015**, *115*, 12205−12250.

[41] A. Cadiau, J. S. Lee, D. D. Borges, P. Fabry, T. Devic, M. T. Wharmby, C. Martineau, D. Foucher, F. Taulelle, C.-H. Jun, Y. K. Hwang, N. Stock, M. F. De Lange, F. Kapteijn, J. Gascon, G. Maurin, J.-S. Chang, C. Serre, *Adv. Mater.* **2015**, *27*, 4775–4780.

[42] K. Henninger, F. Jeremias, H. Kummer, C. Janiak, *Eur. J. Inorg. Chem.* **2012**, 2625–2634.

due to the ubiquitous nature of water. Most landmark MOFs based on divalent metal cation such as zinc terephthalate (MOF-5), copper(II) trimesate (HKUST-1) and Ni(Bdc)(Ted)$_{0.5}$ (Bdc = Benzene-1,4-dicarboxylate, Ted = triethylenediamine) degrade upon exposure to various degree of moist.[43] It was shown that this instability largely depends on the ligand-metal interactions, where the carboxylate substitution by water usually leads to the collapse of the framework. In order to enhance the stability of the framework, high-valence metal ions such as Al^{3+}, Fe^{3+}, Zr^{4+}, Cr^{3+}, Ti^{4+} are used.[44] This reduces the liability of the bond simply by increasing the electrostatic interaction between the metal ions and the ligands. Hence, Zr-UiO-66, MIL-100 (Al, Fe) and Cr-MIL-101 were reported as water stable MOFs.[45] The hydrolytic stability is usually assessed by stirring a sample of the MOF for a certain length of time in water, and afterwards, measuring the powder X-ray diffraction (PXRD) pattern and porosity of the sample post-treatment. However, when the MOF is intended for application in AHT, it should be ascertained that the material retains its crystallinity and adsorption capacity under long term multiple adsorption-desorption cycles. UiO-66 and zirconium fumarate (MOF-801) for instance have the reputation of high chemical, thermal and hydrolytic stabilities. However, the coexistence of often large amount of various types of (missing linker or missing cluster)-defects within their framework could compromise their otherwise high hydrothermal stability.[46,47] These MOFs therefore, on account of large amount of defects, often gradually deteriorate over multiple water adsorption-desorption cycles.[48]

(ii) **Increasing the porosity within the microporosity range**. The adsorption capacity of the MOF is a key parameter influencing the efficiency of a heat exchanger. Therefore, increasing the porosity of MOFs is of prime importance. However, MOFs with very large pores would yield hysteresis loops between the adsorption and desorption branches of their adsorbate isotherm. For example, Al-MIL-100 and Cr-MIL-101 are mesoporous MOFs featuring extremely high water sorption uptake (0.6–0.75 and 1.0–1.5 g g^{-1} respectively), but their water sorption isotherms exhibit a large hysteresis loop arising from capillary condensation effect, and many uptake steps, which are unfavorable for efficient AHT

---

[43] N. C. Burtch, H. Jasuja, K. S. Walton, *Chem. Rev.* **2014**, *114*, 20, 10575–10612.
[44] M. Bosch, M. Zhang, H. Zhou, *Adv. Chem.* **2014**, *182327*, 1–8.
[45] F. Jeremias, A. Khutia, S. T. Henninger, C. Janiak. *J. Mater.* Chem. **2012**, *22*, 10148–10151.
[46] G. C. Shearer, S. Chavan, S. Bordiga, S. Svelle, U. Olsbye, K. P. Lillerud, *Chem. Mater.* **2016**, *28*, 11, 3749-3761.
[47] J. Choi, Li-Chiang Lin, Jeffrey C. Grossman, *J. Phys. Chem. C* **2018**, *122*, 10, 5545–5552.
[48] F. Jeremias, V. Lozan, S. K. Henninger, C. Janiak, *Dalton Trans*. **2013**, *42*, 15967–15973.

(Figure 9).[49] Precisely, the capillary condensation occurs when the pore diameter of the MOF is larger than the so-called *critical diameter* D_C. The critical diameter of water is $D_C = 2.1$ nm, while that of methanol is $D_C = 3.5$ nm. Nonetheless, framework flexibility of microporous MOFs could also induce a hysteresis between the adsorption and desorption.[50,51]

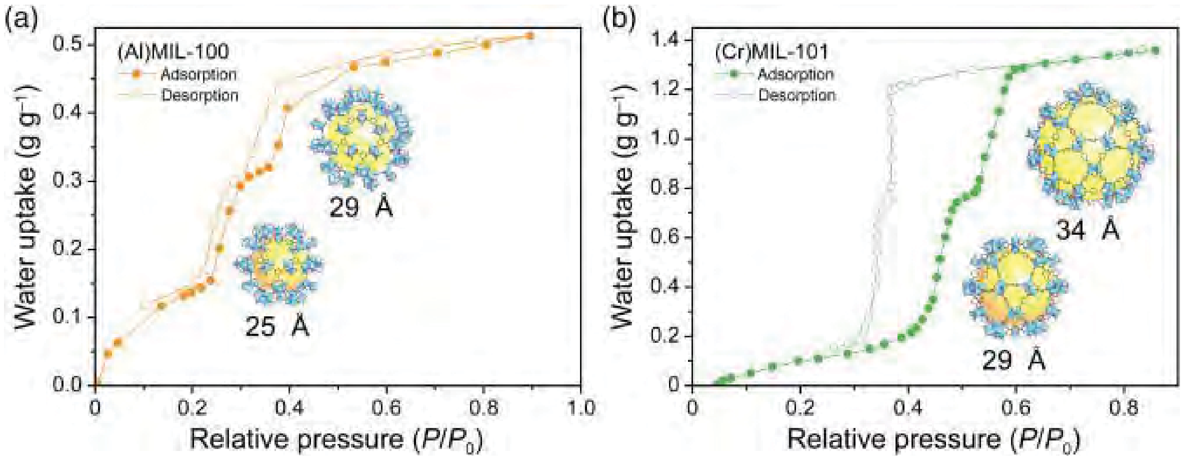

Figure 9. Typical water sorption isotherms of mesoporous MOFs. A large hysteresis loop is observed and two distinct steps corresponding to the filling of two differently sized cages in the **mtn** type structures of (a) MIL-100 and (b) MIL-101. Filled and open symbols represent the adsorption and desorption, respectively. Reproduced with permission from ref 33. Copyright 2019 John Wiley and Sons.

(iii) **The cost and sustainability in the production.** Producing MOFs at affordable cost and in an environment-friendly way is of prime importance, when aiming at their practical use in industry. This requires that they are prepared from inexpensive and benign chemicals. Using organic ligands obtainable from biomass, water as solvent, nontoxic metal ions, low reaction temperature and short reaction time are therefore some of the aspects to target.[52,53] This will allow an affordable production cost of AHPs and TDCs, and eventually speed up their commercial success. In addition, the aspect of shaping MOFs powders into practically usable semi-industrial macroscopic solids should also be taken into consideration.[54]

---

[49] J. Ehrenmann, S. K. Henninger, C. Janiak, *Eur. J. Inorg. Chem.* **2011**, 471–474.

[50] M. F. de Lange, B. L. van Velzen, C. P. Ottevanger, K. J. F. M. Verouden, L.-C. Lin, T. J. H. Vlugt, J. Gascon, F. Kapteijn, *Langmuir* **2015**, *31*, 12783−12796.

[51] J. Canivet, A. Fateeva, Y. Guo, B. Coasne, D. Farrusseng, *Chem. Soc. Rev.* **2014**, *43*, 5594–5617.

[52] H. Reinsch, *Eur. J. Inorg. Chem.* **2016**, 4290–4299.

[53] S. Wang, C. Serre, *ACS Sustainable Chem. Eng*. **2019**, *7*, 11911−11927.

[54] D. Bazer-Bachi, L. Assié, V. Lecocq, B. Harbuzaru, V. Falk, *Powder Technol.* **2014**, *255*, 52–59.

1.3.4 Fumarate-based aluminum and zirconium MOFs in adsorption heat transformation

Aluminum- and zirconium-based MOFs have recently attracted attention on account of their high thermal, hydrolytic and chemical stabilities, as well as the low toxicity of these metals.[55,56] Aluminum fumarate for instance, is one of the first commercialized Al-MOFs due to its easy and inexpensive synthesis route at large scale.[57] The fumaric acid used for its synthesis is a biologically occurring and economical molecule which is found as a food additive (E297).

Aluminum fumarate, commercialized under the trademark Basolite A520 is also named MIL-53-Fum because it is isostructural to the aluminum terephthalate MOF Al-MIL-53-Bdc. The MIL-53 framework is built up from chains of *trans*-corner sharing AlO_6 octahedra, linked together by fumarate to form lozenge-shaped one-dimensional pores having about 5.7 × 6.0 $Å^2$ free dimension (see structure in Figure. 10).[58] The short fumarate linker in this material yields narrow pores (ultramicroporous MOF), which are beneficial with respect to the optimum adsorption of some gases/vapors like CO_2 and water. For example, MIL-53-Fum and zirconium fumarate (MOF-801) display both an S-shaped water sorption isotherm in spite of their structural differences (Figure 10 (a) & (b)).

MOF-801, crystallizes in an **fcu** net topology, consisting of octahedral $[Zr_6O_4(OH)_4]^{12+}$ SBUs each connected by twelve fumarate linkers to yield a three-dimensional framework with octahedral cages of 7.4 Å diameter and two slightly differently sized tetrahedral cages with pore diameters 4.8 and 5.6 Å respectively (see structure in Figure 10).[59] The high hydrophilicity of these MOFs is displayed by a steep water uptake at low relative pressure range of $P/P_0 = 0.2–0.3$ (for MIL-53-Fum) and 0.05–0.1 (for MOF-801), which is favorable for application in thermally driven adsorption heat exchangers. This hydrophilicity was attributed to the small pores which dictate the easy water molecules interaction with the framework and

---

[55] M. Gaab, N. Trukhan, S. Maurer, R. Gummaraju, U. Müller, *Microporous Mesoporous Mater.* **2012**, *157*, 131–136.

[56] S. Yuan, J.-S. Qin, C. T. Lollar, H.-C. Zhou, *ACS Cent. Sci*. 2018, 4, 440−450.

[57] M. Gaab, N. Trukhan, S. Maurer, R. Gummaraju, U. Müller, *Microporous Mesoporous Mater*. **2012**, *157*, 131–136.

[58] E. Alvarez, N. Guillou, C. Martineau, B. Bueken, B. Van de Voorde, C. Le Guillouzer, P. Fabry, F. Nouar, F. Taulelle, D. de Vos, J. S. Chang, K. H. Cho, N. Ramsahye, T. Devic, G. Maurin, C. Serre, *Angew, Chem. Int. Ed.* **2015**, *54*, 3664–3668.

[59] H. Furukawa, F. Gándara, Y.-B. Zhang, J. Jiang, W. L. Queen, M. R. Hudson, O. M. Yaghi, *J. Am. Chem. Soc*. **2014**, *136*, 4369−4381.

formation of hydrogen-bonds between neighboring water molecules. In addition, the short fumarate linker enables to minimize or even cancel the hysteresis loop between the water adsorption and desorption branches in MIL-53-Fum and MOF-801 compared to what is observed for their respective terephthalate parent MOFs MIL-53-BDC and UiO-66.

Aluminum fumarate was the first MOF reported with a very high hydrothermal and multicycle water ad/desorption stability over 4500 cycles (Figure 11b). Nevertheless, the water sorption isotherm reported by Jeremias *et al* shows an undesirable hysteresis loop (Figure 11a) which would lower the efficiency of the heat exchanger.[60] MOF-801 was also proven to be stable over six (06) water ad/desorption cycles and promises applicability for adsorption thermal batteries (ATB), water harvesting from air and adsorption cooling.[59,61,62]

---

[60] F. Jeremias, D. Fröhlich, C. Janiak, S. K. Henninger, *RSC Adv*. **2014**, *4*, 24073–24082.

[61] H, Kim, S. Yang, S. R. Rao, S. Narayanan, E. A. Kapustin, H. Furukawa, A. S. Umans, O. M. Yaghi, E. N. Wang, *Science* **2017**, *356*, 430–434.

[62] M. V. Solovyeva, L. G. Gordeeva, T. A. Krieger, Y. I. Aristova, *Energy Convers. Manag.* **2018**, *174*, 356–363.

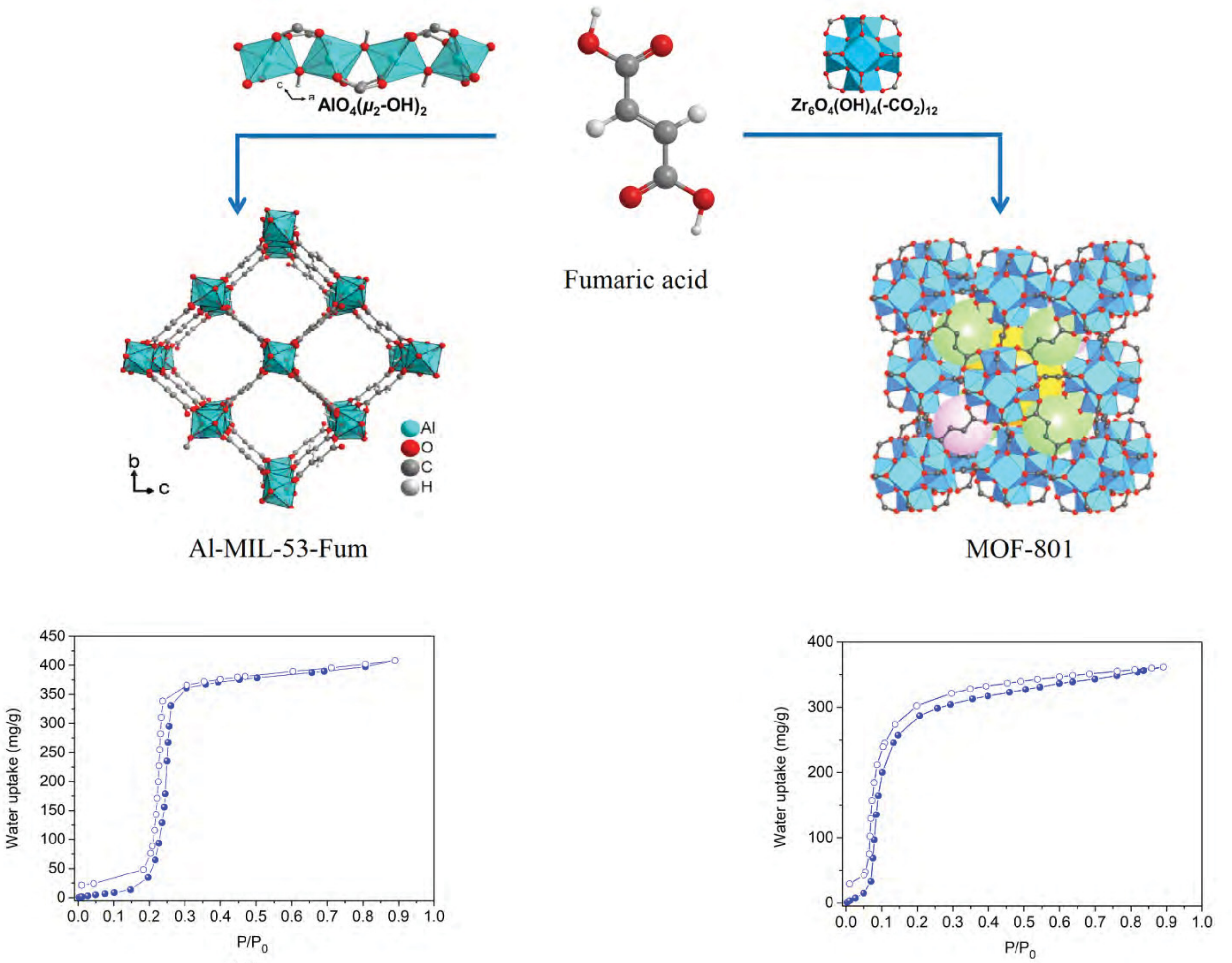

(a)

(b)

Figure 10. Scheme of formation of MIL-53-Fum with MIL-53-type topology and MOF-801 with the **fcu** topology, from the same fumaric acid ligand. (a) and (b) show the water sorption isotherms of MIL-53-Fum and MOF-801 respectively. The two MOFs display water sorption isotherms with S-(type V) stepwise shape (the isotherms were measured within this work).

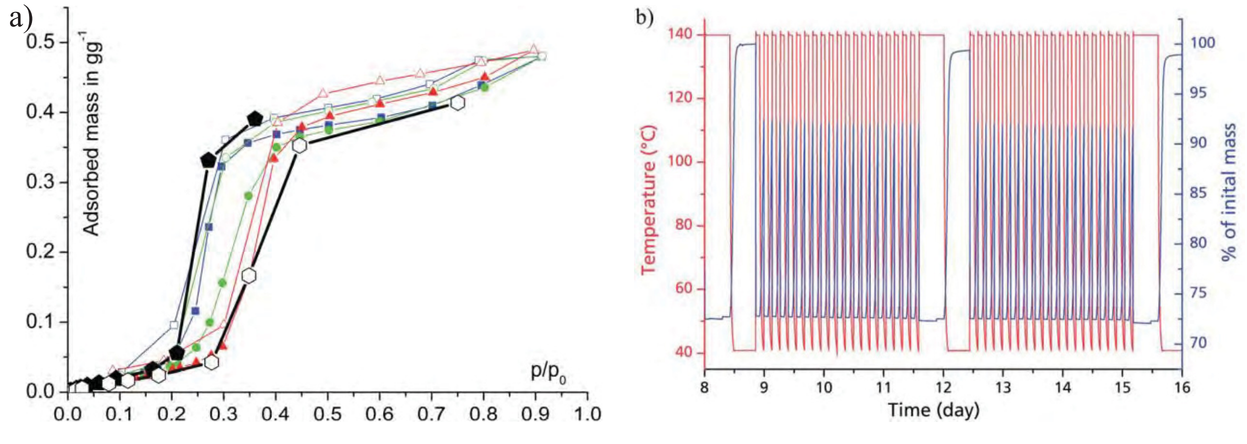

Figure 11. (a) Water sorption isotherms and (b) thermogravimetric water adsorption/desorption cycling experiments for 40cycles of MIL-53-Fum, showing that this material maintains its integrity and capacity during the process. Reproduction permission from ref 60. Copyright 2014 RSC.

1.4 Motivation and objectives of this work

Although MIL-53-Fum and MOF-801 feature interesting water adsorption profiles regarding AHT applications, their capacities are however still small (0.4 and 0.36 g g^{-1} for MIL-53-Fum and MOF-801, respectively) compared to MOFs potentialities. Some structural modifications on MIL-53-Fum and MOF-801 could help improving the capacity of resulting materials and therefore their performance toward AHT. Four modification approaches could be thought of, including:

- The *linearization* of the fumarate linker by replacing it with the acetylenedicarboxylate linker in the **fcu** and MIL-53 structures.
- The *ligand functionalization* of the fumarate liker with halogen (–Cl, –Br, –I) substituents.
- The *twofold extension* of the fumarate linker by using the *trans*,*trans*-muconate linker.
- The *metal substitution* by using other metal cations, namely cerium(IV) and hafnium(IV).

The modification strategies used in this work are summarized in Scheme 1.

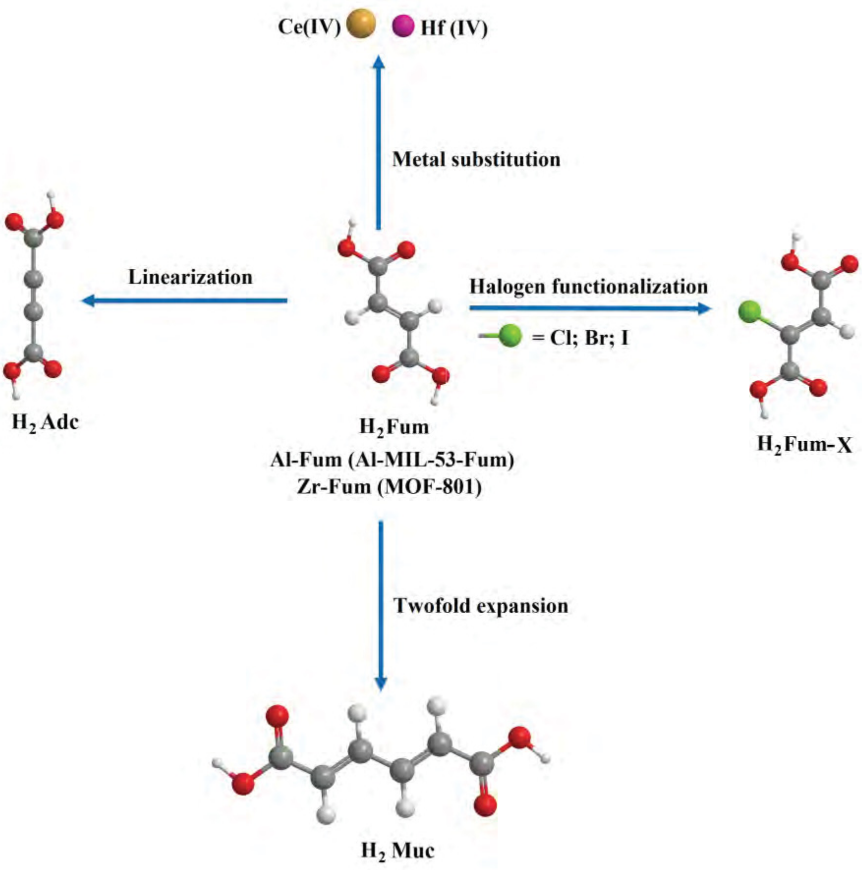

Scheme 1. Modification strategies of the fumarate linkers and metal substitution employed in this work.

The general objective of this research work was to synthesize new hydrothermally stable metal-organic frameworks based on acetylenedicarboxylate, muconate linkers, and Al^{3+}, Zr^{4+}, Hf^{4+} and Ce^{4+} metal cations. Afterwards, to evaluate the applicability of the obtained materials for adsorption-based heat transformation, as well as for gas capture, storage and separation. It should be noted that, although it was not part of the initial objective, an unexpected halofumarate formation from in situ hydrohalogenation of acetylenedicarboxylic acid was discovered during this work. The halofumarate-based MOFs thereof obtained were also evaluated for the aforementioned applications.

The specific objectives are:

- To synthesize and determine the structure of new MOFs, namely aluminum acetylenedicarboxylate, zirconium acetylenedicarboxylate, hafnium acetylenedicarb oxylate, cerium acetylendedicarboxylate, zirconium and aluminum halofumarate, aluminum muconate.

- To determine their chemical and thermal stabilities in view of their possible applicability as porous materials.
- To determine their porosity and adsorption properties toward vapors like water (H_2O) and methanol (CH_3OH) or gases like carbon dioxide (CO_2), methane (CH_4), hydrogen (H_2) and sulfur dioxide (SO_2).
- To evaluate promising MOFs among them as adsorbent for adsorption-driven heat pumps (AHPs) and adsorption thermally driven chillers TDCs.

The report of results obtained is presented in the following chapter (chapter 2) of this thesis as a cumulative of scientific articles published in scientific peer reviewed journals.

Chapter 2

Cumulative Part

2.1 Realizing the potential of acetylenedicarboxylate by functionalization to halofumarate in Zr(IV) metal-organic frameworks

Tobie J. Matemb Ma Ntep, Helge Reinsh, Bastian Moll, Emrah Hastürk, Serkan Gökpinar, Hergen Breitzke, Carsten Schlüsener, Laura Schmolke, Gerd Buntkowsky, and Christoph Janiak

Chem. Eur. J. **2018**, *24*, 14048–14053.

DOI: 10.1002/chem.201802838

Impact factor 2018: 5.16

Before investigating how the water sorption profile of MIL-53-Fum and MOF-801 would change by linearizing the fumarate (Fum) linker into acetylenedicarboxylate (Adc), the new acetylenedicarboxylate-based aluminum MIL-53-type and zirconium UiO-type MOFs had first to be synthesized. However, one should first overcome the challenge of dealing with the thermally labile acetylenedicarboxylic acid under solvothermal conditions usually involved for the synthesis of these MOFs families. Acetylenedicarboxylic acid decomposes easily in solution at elevated temperatures above 100 °C. This limitation could explain why no experimentally porous MOF based on the otherwise simple Adc linker was yet reported. Several attempts to obtain a MIL-53 analogue aluminum acetylenedicarboxylate were unsuccessful. In this paper, the synthesis conditions were determined to successfully obtain the first Adc-based MOF with experimentally proven permanent porosity, namely zirconium acetylenedicarboxylate (Zr-HHU-1; HHU stands for **H**einrich-**H**eine-**U**niversität Düsseldorf), which has the same structure as UiO-66. The main challenge to circumvent for access the porosity of this MOF was during the activation process. Classical activation by heating at elevated temperatures leads to the collapse of the framework. The supercritical CO_2 drying was found to be the best option to de-solvate the material's pores.

Unexpectedly, it was observed that the same reaction mixture for the formation of Zr-HHU-1 leads rather to the formation of a different MOF containing the chlorofumarate linker. When the reaction is conducted in water instead of DMF, acetylenedicarboxylic acid undergoes an in situ hydrochlorination to chlorofumaric acid and then to a zirconium chlorofumarate MOF (Zr-HHU-2) in a one-pot reaction. It is worth noting that, detecting and determining the nature of this transformation was challenging because the two MOFs (Zr-HHU-1 and Zr-HHU-2) have the same structure and display similar PXRD patterns. It took about one third of the time invested on this whole research project to detect and fully determine the transformation and the nature of the new linker. By combining Raman spectroscopy, solid-state NMR (ssNMR), SEM-EDX, XPS and TGA analyses, the linker in Zr-HHU-2 was unambiguously elucidated as substituted (chloro-)fumarate. Obtaining the later result is not trivial. As a matter of facts, a work was published about six months after the release of this article, where the authors claim not to have observed the linker transformation under the same synthesis mixture and conditions as in this work.[63] However, no Raman spectrum was provided in their work to demonstrate the presence of acetylenedicarboxylate in the obtained material. The Raman spectroscopy in this work is the basic analysis to proof the presence or transformation of acetylenedicaboxylate in the MOF. The –C≡C– triple-bond exhibits in the Raman spectrum a very strong and remarkable band at 2250 cm^{-1}, which disappears whenever the bond is transformed. Detailed results of this work are found in the article that follows.

Author´s contribution to the work:

- Idea and setting of the synthesis procedures.
- Synthesis and preparation of the samples for further characterization.
- Characterizations including PXRD experiment, TGA, chemical stability test, N_2 sorption and porosity parameters determination, other gas/vapor sorption (H_2O, CO_2 and H_2) experiments.
- Organization of other analyses (Raman, ssNMR, SEM-EDX and XPS), data analysis/interpretations and treatment.
- Samples activations prior characterizations and MOF digestion prior liquid NMR analysis.
- Fitting of adsorption isotherms with the 3P-SIM software and determination of the isosteric heat of adsorption.

---

[63] Y. Wang, S. Yuan, Z. Hu, T. Kundu, J. Zhang, S. B. Peh, Y. Cheng, J. Dong, D. Yuan, H.-C. Zhou, D. Zhao, *ACS Sustainable Chem. Eng*. **2019**, *7*, 7118−7126

- Writing of the manuscript, drawing of figures and responses to reviewers during the review process.

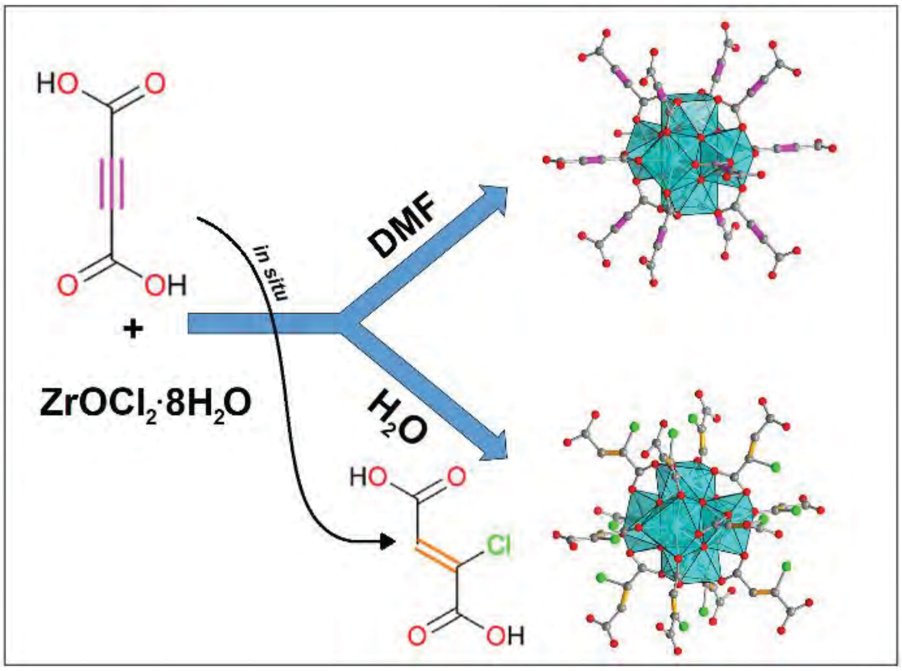

ChemPubSoc Europe

DOI: 10.1002/chem.201802838

CHEMISTRY
A European Journal
Communicatio

Check for updates

Metal–Organic Frameworks

Realizing the Potential of Acetylenedicarboxylate by Functionalization to Halofumarate in Zr^{IV} Metal–Organic Frameworks

Tobie J. Matemb Ma Ntep,[a] Helge Reinsch,[b] Bastian Moll,[a] Emrah Hastürk,[a] Serkan Gökpinar,[a] Hergen Breitzke,[c] Carsten Schlüsener,[a] Laura Schmolke,[a] Gerd Buntkowsky,[c] and Christoph Janiak*[a]

Abstract: A strategy was developed to obtain from acetylenedicarboxylic acid either an acetylenedicarboxylate-based Zr^{IV} metal–organic framework (MOF) with **fcu** topology or a halo-functionalized-MOF-801 through in situ ligand hydrohalogenation. The new materials feature exceptionally high hydrophilicity and CO_2/H_2 adsorption energetics. The acetylenedicarboxylate linker and its functionalizable triple-bond discloses its potential in the engineering of microporous materials with targeted properties.

Acetylenedicarboxylic acid (H_2ADC) should be an interesting linker for metal–organic frameworks because of its rigidity and its alkyne function,[1] the latter being a basis for various modifications by addition reactions. It was demonstrated that post-halogenation was possible in zirconium-based MOFs containing alkyne moieties, with retention of structure topology.[2] The ADC^{2-} linker was already used to construct the smallest member of the IRMOF (isoreticular MOF) series, namely IRMOF-0, consisting of a two-fold interpenetrated MOF-5 type network with low thermal stability relative to the other IRMOFs.[3,4] Except for IRMOF-0 no other (potentially porous) MOFs but solely densely packed coordination polymers or molecular metal complexes with ADC have been reported to the best of our knowledge.[5] The scarcity of MOFs with the ADC^{2-} linker can be understood from the often high temperature (above 100 °C) at which many MOFs are obtained,[6] which is not compatible with the thermal sensitivity of acetylenedicarboxylic acid in solution.[7] Acetylenedicarboxylic acid decomposes in solution above 110 °C. IRMOF-0 and coordination polymers with ADC^{2-} were obtained at room temperature either in solution by slow evaporation, by diffusion or by mechanochemical methods (see Table S1 in the Supporting Information).

The in situ ADC transformation presents an easy access to MOFs with substituted fumarate linkers, for example, to 2-chlorofumarate MOFs for which the linker as the acid is otherwise very expensive (50 mg of 2-chlorofumaric acid presently cost 144 EUR, compared to 25 g of H_2ADC for 210 EUR from Sigma-Aldrich).

The design and construction of MOFs were significantly advanced with the introduction of reticular synthesis. Its principle is to construct isotopic frameworks of predetermined structure, with varying pore sizes by using linkers with the same connectivity but different lengths.[8] A typical example is the UiO isoreticular MOFs series based on UiO-66 structure, consisting of octahedral $[Zr_6(\mu_3\text{-}O)_4(\mu_3\text{-}OH)_4]^{12+}$ secondary building units (SBUs), which are twelvefold joined by linear dicarboxylate linkers to give a series of extended 3D **fcu** frameworks with increasing pore sizes.[9] Acetylenedicarboxylate is the shortest straight dicarboxylate linker that can be used to make a MOF with UiO-66 topology, since oxalic acid reacts with Zr^{4+} ions to a polymeric structure, which does not feature the $Zr_6O_4(OH)_4$ inorganic building block.[10] However, no UiO-type MOF based on this linker is yet reported.

As a contribution to fill this gap in the UiO family, we herein report for the first time the successful synthesis at mild temperature and characterization of a contracted member of the UiO family using acetylenedicarboxylate as linker with zirconium(IV) as metal cation. The interest of using acetylenedicarboxylate as linker lies in providing a smaller pore analogue of UiO-66, what was suggested by Rowsell et al. to be a necessity with respect to applications such as hydrogen storage; smaller pores account for moderately stronger adsorbent–adsorbate interactions.[11] Pore size contraction was also suggested as one strategy to improve carbon dioxide sorption performance in MOFs.[12]

The reaction of acetylenedicarboxylic acid with $ZrOCl_2 \cdot 8\,H_2O$ in DMF at 85 °C in the presence of acetic acid yielded the new MOF **HHU-1** of ideal formula $[Zr_6(\mu_3\text{-}O)_4(\mu_3\text{-}OH)_4(ADC)_6]\cdot$solv (Scheme 1) as microcrystalline powder with a morphology of

---

[a] *T. J. M. Ma Ntep, B. Moll, E. Hastürk, S. Gökpinar, C. Schlüsener, L. Schmolke, Prof. Dr. C. Janiak*
Institut für Anorganische Chemie und Strukturchemie
Heinrich-Heine-Universität Düsseldorf
Universitätsstrasse 1, 40225 Düsseldorf (Germany)
E-mail: janiak@uni-duesseldorf.de

[b] *Dr. H. Reinsch*
Institut für Anorganische Chemie, Christian-Albrechts-Universität zu Kiel
Max-Eyth-Strasse 2, 24118 Kiel (Germany)

[c] *Dr. H. Breitzke, Prof. Dr. G. Buntkowsky*
Eduard-Zintl-Institut für Anorganische und Physikalische Chemie
Technische Universität Darmstadt
Alarich-Weiss- Strasse. 4, 64287 Darmstadt (Germany)

Supporting information and the ORCID identification number(s) for the author(s) of this article can be found under: https://doi.org/10.1002/chem.201802838.

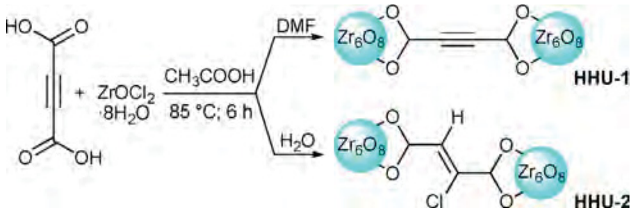

Scheme 1. Reaction of acetylenedicarboxylic acid to the UiO-type MOFs **HHU-1** or **HHU-2** (by in situ HCl addition) depending on the solvent.

octahedrally to cubic shaped crystallites with less than 0.5 μm diameter (by scanning electron microscopy, SEM Figure S3 in the Supporting Information). This shape is quite common for microcrystals of Zr-based MOFs with UiO topology.[13] **HHU-1** could not be obtained as crystalline materials without acetic acid modulation. (**HHU** stands for Heinrich-Heine-University Düsseldorf.)

When the reaction of acetylenedicarboxylic acid with $ZrOCl_2{\cdot}8\,H_2O$ was carried out in water at 85 °C in the presence of acetic acid, an unexpected in situ linker transformation to chlorofumarate by addition of HCl to the C≡C triple bond of ADC took place,[14] as evidenced by the isolation of the UiO-type MOF Zr^{IV}-Fum-Cl of ideal formula $[Zr_6(\mu_3\text{-}O)_4(\mu_3\text{-}OH)_4(\text{Fum-Cl})_6]{\cdot}\text{solv}$ (**HHU-2**). Such an in situ addition reaction to acetylenedicarboxylate, yielding a substituted fumarate linker, during MOF synthesis is described here for the first time and realizes the potential of this otherwise unstable acid for the formation of important functionalized fumarate linkers in MOFs.[15]

In the diagnostic Raman spectrum of **HHU-1** (Figure S2) the band at 2225 cm^{-1} is ascribed to the stretching vibration of the C≡C triple bond of the linker. The powder-X-ray diffraction (PXRD) pattern of **HHU-1** resembles that of UiO-66 (Figure 1), with reflections shifted to lower diffraction angles due to a smaller lattice constant of the new material. This is in agreement with the shorter acetylenedicarboxylate linker compared to terephthalate in UiO-66. Indeed, following fumarate, acetylenedicarboxylate is the next smallest linear and rigid dicarboxylate linker, about 1.8 Å shorter than benzene-1,4-dicarboxylate (Scheme S1 in SI). The ADC-based MOF **HHU-1** corresponds therefore to the third most contracted UiO series member, after zirconium squarate[16] and zirconium fumarate (MOF-801).[17] **HHU-1** fills a gap between zirconium fumarate and UiO-66 in the isoreticular UiO series.

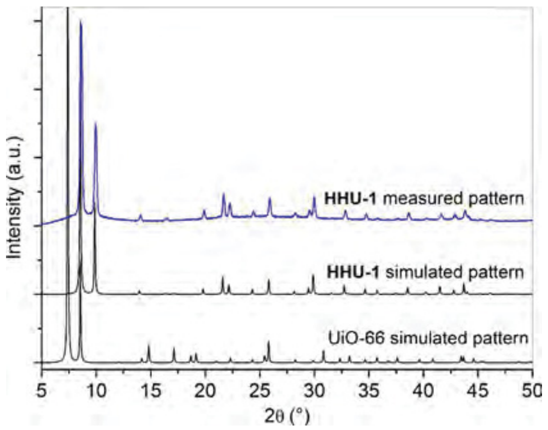

Figure 1. Experimental and simulated PXRD patterns of **HHU-1** in comparison with UiO-66 (simulated from deposited cif-file; CCDC 837796 contains the supplementary crystallographic data for this compound. These data are provided free of charge by The Cambridge Crystallographic Data Centre).

The structure of **HHU-1** was determined from powder diffraction data with $a=17.925(3)$ Å in space group $Fm\bar{3}m$ using the crystal structure of the terephthalate UiO-66 as a starting point (see the Supporting Information for further details). The UiO-type hexanuclear $[Zr_6O_4(OH)_4]^{12+}$ SBU with the attached ADC linkers and the face-centered cubic (fcc) packing diagram of the **fcu** network are shown in Figure 2. The contact diameters for the surrounding van der Waals radii of the octahedral and tetrahedral cages are about 9.6 and 5.8 Å diameter, respectively, with a triangular window diameter 4.4 Å (Figure S14 in the Supporting Information).

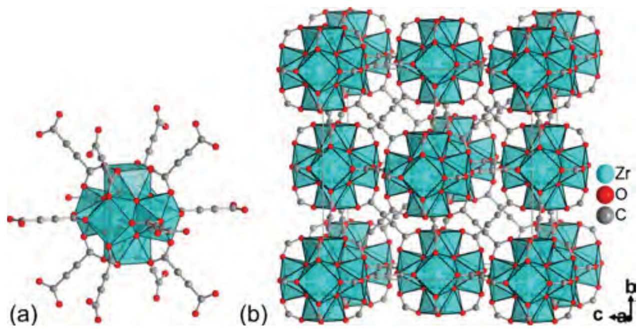

Figure 2. (a) Secondary building unit of $\{Zr_6(O)_4(OH)_4\}$ with the 12 surrounding and connecting acetylenedicarboxylate linkers and the edge-sharing square-antiprismatic ZrO_8 coordination as polyhedra. (b) fcc packing diagram of the **fcu** framework in **HHU-1**. The refined guest atoms are not shown for clarity.

Argon and nitrogen sorption experiments at 87 and 77 K, respectively, (Figure S21 in Supporting Information) yielded Brunauer–Emmett–Teller (BET) surface areas of 619 and 551 m^2 g^{-1} with a pore volume for pore diameters less than 20 nm of 0.38 and 0.29 cm^3 g^{-1}, respectively for **HHU-1** (Table S5).

A theoretical pore volume investigation with the program CrystalExplorer, a "void" calculation with Mercury and a "calc void/solv" calculation with Platon (see Table S8, Supporting Information) suggest a specific pore volume between 0.33 and 0.34 cm^3 g^{-1}, which is between the experimental values of **HHU-1** from Ar and N_2 sorption of 0.38 and 0.29 cm^3 g^{-1}, respectively (Table S5). A surface area calculation by CrystalExplorer on the other hand gives a specific surface area of 1700–1880 m^2 g^{-1}, whereby overestimating the experimental surface area. From our experience with CrystalExplorer, such an overestimation by a factor of 2–3 is common. The theoretical calculation probably counts adjacent, nearby or opposite surfaces of micropores twice, which in reality will be covered by only one Ar atom or N_2 molecule. The adsorbed gas–surface interactions in small micropores will occur at both ends of the Ar atom or N_2 molecule or if the gas species is adsorbed on one surface region the opposite surface region in such a narrow micropore will be blocked and is no longer accessible for another Ar atom or N_2 molecule. The lower surface area from (larger) N_2 sorption versus (smaller) Ar sorption supports this notion.

HHU-1 and Zr-fumarate (MOF-801) have very similar cell constants and unit cell volumes ($a = 17.9239(3)$ Å versus 17.9309(4) Å and $V = 5758.4(3)$ Å^3 versus 5765.09 Å^3, respectively), yet the BET surface area and porosity of **HHU-1** was found significantly smaller than for MOF-801 (Table S5). This could be due to a higher linker flexibility and thereby better adaption to guest molecules in MOF-801 together with a larger number of linker defects, which both would give rise to a better ultramicropore access and higher porosity. Alternatively, pore blocking effects could have lowered the access and porosity in **HHU-1**.

Water vapor adsorption was measured at 20 °C for **HHU-1** to determine the hydrophilicity and give insight about the chemical environment inside the pores. **HHU-1** unexpectedly displays a Type Ib water sorption isotherm, with a hysteresis loop between the adsorption and desorption branches (Figure 3 and Figure S25). A Type I or Ib adsorption isotherm for water vapor is rather unusual in MOFs without functionalization (as for example in UiO-type MOF-804 ($Zr_6O_4(OH)_4[BDC\text{-}(OH)_2]_6$)).[18,19] A Type I water vapor adsorption isotherm is given by hydrophilic microporous zeolites, whereas less hydrophilic/more hydrophobic MOFs display a Type V S-shaped isotherm.[20,21] This indicates a higher hydrophilicity of **HHU-1** compared to MOF-801 (Zr-fumarate) and UiO-66 for which the water sorption S-shaped isotherms show a hydrophobic region (up to $P/P_0 < 0.1$ for MOF-801 and $P/P_0 < 0.3$ for UiO-66) due to the hydrophobicity of the linker (as judged by the decreasing solubility of the acid H_2ADC, H_2Fum and H_2BDC in water). The high affinity of the ADC linker for water is probably due to the C≡C triple bond.[1]

The early water uptake at $P/P_0 = 0.05$ for **HHU-1** is larger than for MOF-801 and UiO-66. The water uptake of **HHU-1** of 205 mg g^{-1} (at $P/P_0 = 0.9$) correlates with the micropore volume of 0.19 cm^3 g^{-1} (Table S5), as do the comparable water uptakes of MOF-801 and UiO-66 with 280 mg g^{-1} and 375 mg g^{-1} at micropore volumes of 0.27 and 0.33 cm^3 g^{-1}, respectively.

The more pronounced hysteresis for **HHU-1** in comparison to UiO-66 and MOF-801 is a further indicator of the hydrophilicity of this MOF, where most of the adsorbed water will be in the first or second hydrogen-bonded coordination sphere of the hydrophilic $Zr_3(\mu_3\text{-}OH)$, $Zr_3(\mu_3\text{-}O)$, and $Zr_2(\mu\text{-}O_2C)$ sites. Together with a possible structural adjustment of the framework as a result of very strong H_2O–MOF interactions, the hydrogen-bonded water is kinetically slower to desorb. We note that the initial hydrophilic regions of the sorption isotherms of UiO-66 and MOF-801 up to the steep increase also have a more pronounced hysteresis than the isotherm after the increase.

The possibility to understand and tune the hydrophilicity of MOFs is important for the possible technological application in cycling water sorption for heat transformation.[21,22] Specifications for thermally driven adsorption chillers and adsorption heat pumps can vary depending on the evaporation temperature, the heat rejection and condenser temperature as well as the desorption temperature (range), which are possible for the specific application. Hence, different MOF materials are desirable in order to cover different working windows. Also, further understanding is needed on how to fine-tune MOFs for potential heat transformation applications under different boundary conditions.[21,22]

The CO_2 uptake of **HHU-1** is in agreement with its surface area and pore volume in comparison to other MOFs (Table S7). From the CO_2 sorption experiments at 195, 273, and 293 K (Figure S27) the isosteric heat of CO_2 adsorption (Q_{st}) was estimated by applying the Clausius–Clapeyron expression using the sorption isotherms measured at 273 and 293 K (Figure 4 a).[23]

The isosteric heat of CO_2 adsorption at zero coverage (Q^0_{st}) is 60 kJ mol^{-1}. This value is more than double the Q^0_{st} values of the parent UiO-66 (28 kJ mol^{-1}) as well as that of functionalized UiO-66-NH_2 (29.4 kJ mol^{-1}), UiO-66-$(OH)_2$ (30 kJ mol^{-1}), UiO-66-$(COOH)_2$ (34 kJ mol^{-1})[24] and is thus the largest reported value of Q^0_{st} for UiO type MOFs. It is also the largest reported value so far for all MOFs without amine functionalization or open metal sites.[25]

The Q^0_{st} value of **HHU-1** is also unexpectedly more than double the Q^0_{st} value for Zr-fumarate (MOF-801, $Q^0_{st} <$ 30 kJ mol^{-1}).[26] This high Q^0_{st} value for **HHU-1** clearly is not

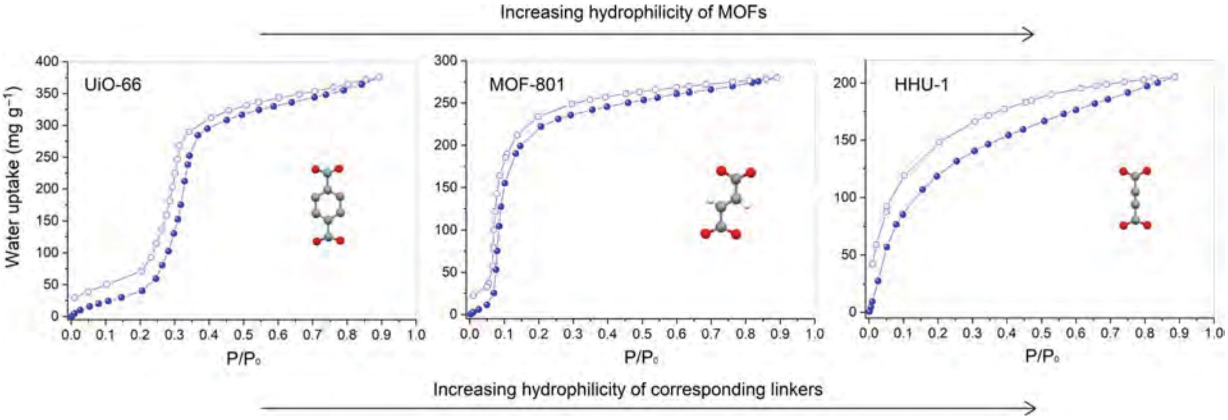

Figure 3. Comparative water sorption isotherms of UiO-66, MOF-801 and **HHU-1** (further details in the Supporting Information).

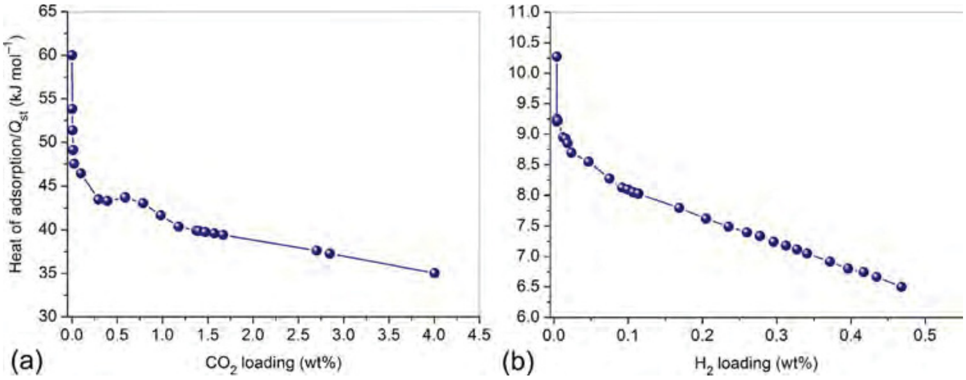

Figure 4. Isosteric heat of **HHU-1** for (a) CO_2 adsorption (from adsorption data at 273 and 293 K) and (b) H_2 adsorption (from adsorption data at 77 and 87 K).

only due to the small micropores, when compared to the similar pore system in MOF-801, but due to the synergistic effects of the triple bond C≡C, the pore confinement, and the μ_3-OH groups on Zr-oxo clusters in **HHU-1**. The latter two factors are already known to increase CO_2 adsorption in MOFs[12,27] but the triple bond adds a strong enhancement in such small micropores. Note that, despite the drop of Q_{st} with CO_2 loading, even at 4 wt% CO_2 Q_{st} is about 35 kJ mol^{-1}, which is higher than Q^0_{st} for UiO-MOFs (vide supra) and well above the heat of liquefaction (condensation) of bulk CO_2 with 17 kJ mol^{-1}.[28] The isosteric heat of H_2 at zero adsorption (Q^0_{st}) of **HHU-1** calculated from adsorption isotherms at 77 and 87 K (Figure S29) is above 10 kJ mol^{-1} (Figure 4b), which is comparable to Q^0_{st} for the parent UiO-66 (10 kJ mol^{-1}).[29]

Concerning the unusual in situ linker transformation in $[Zr_6(\mu_3\text{-}O)_4(\mu_3\text{-}OH)_4(\text{Fum-Cl})_6]\cdot$solv (**HHU-2**), this was first hinted at by the PXRD pattern, which is similar to that of zirconium fumarate (MOF-801) (Figure 5). The transformation was confirmed by Raman spectroscopy analysis with complete disappearance of the C≡C stretching band at about 2250 cm^{-1} (Figure 6).[2]

In the ^{13}C solid state (ss)NMR spectrum of **HHU-2** in Figure S34, the signals at about 140 and 130 ppm chemical shift are attributable to two carbons of a non-symmetrically bonded C=C double bond. The ^{1}H ssNMR spectrum (Figure S35) shows a signal at about 6.9 ppm corresponding to one proton bonded to the C=C double bond. The signal at 170 ppm in the ^{13}C ssNMR displays a shoulder more visible in the FSLG-HETCOR spectrum. This is ascribed to carbons of the two different carboxylates of the ligand, appearing at slightly different chemical shifts. This is consistent with the non-symmetrically bonded nature of the double bond. Signals at about 180 and 20 ppm are assignable to carbons of –COO and –CH_3 from coordinated acetate.

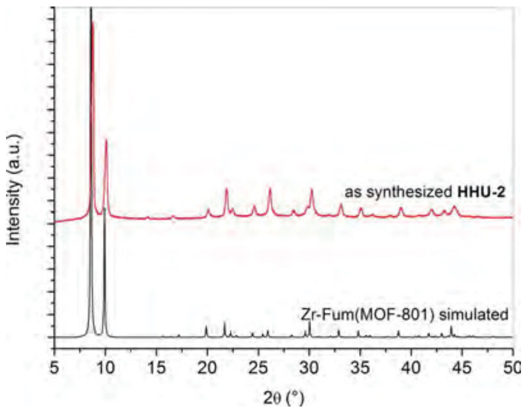

Figure 5. PXRD pattern of as-synthesized **HHU-2** comparison with MOF-801 simulated PXRD pattern from deposited cif-files. CCDC 1002676 contains the supplementary crystallographic data for this compound. These data are provided free of charge by The Cambridge Crystallographic Data Centre.

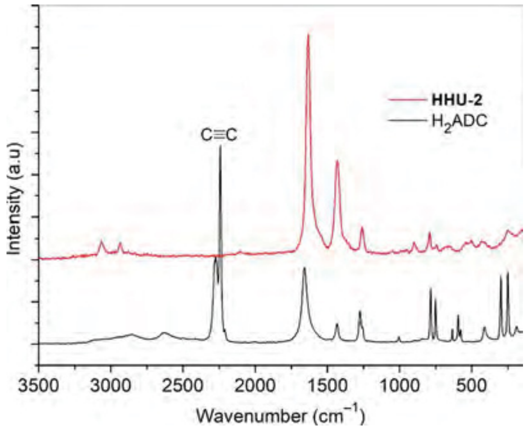

Figure 6. Raman spectrum of **HHU-2** in comparison with that of acetylenedicarboxylic acid.

Furthermore, the ^{1}H/^{13}C correlations seen in the FSLG-HETCOR spectrum recorded with 200 µs contact time, (Figure S36) possess the expected correlations within the terminal CH_3COO ligand, and two more correlations from the protons at 2.2 and 1.8 ppm onto carbons at 170 ppm. These correlations can be assigned to the protons from μ_3-OH and acetate groups coordinated to the zirconium clusters. Then these protons are in the vicinity of the carboxylate carbon atoms of the bridging chlorofumarate linker (Figure S34) and therefore these expected correlation peaks are an additional strong indicator for the **HHU-2** configuration. No detection of a second phase is seen from the PXRD and solid-state NMR spectroscopy analyses, excluding occurrence of insoluble side products, for example, due to linker polymerization.

To prove the addition of HCl (exclude the addition of H_2O) the presence of chlorine was shown by X-ray photoelectron spectroscopy (XPS) through the Cl_{2p} peak at 200.4 eV binding energy (Figure S8). This value is indicative of organic chlorine.[30] SEM with energy-dispersive X-ray spectroscopy (EDX) elemental mapping confirms the even distribution of Cl and Zr across the entire **HHU-2** sample with a molar atomic Zr:Cl ratio of $\approx$1: 0.8 (Figure S6, Table S2 in the Supporting Information). The deviation from the ideal 1:1 Zr:Cl ratio corroborates with the calculated 1.5 missing linkers per Zr_6 cluster from TGA and solution NMR (see the Supporting Information for details).

HHU-2 is thermally stable to about 300 °C and has chemical stability comparable to MOF-801 (Figures S16 and S19), unlike **HHU-1**.

A water vapor sorption isotherm of **HHU-2** (Figure S26) showed an early uptake with overall Type Ib isotherm, similar to **HHU-1**. Argon sorption yielded a BET surface area of 460 $m^2 g^{-1}$ with a total and micropore volume of 0.22 $cm^3 g^{-1}$ and 0.15 $cm^3 g^{-1}$, respectively.

We think that this work will open the field of substituted fumarate linkers supplementing the already important (non-substituted) basic fumarate linker. To date, only one methyl-functionalized version of zirconium fumarate has been reported, namely zirconium mesaconate.[31] Substituting fumarate with less bulky and polar group like chlorine rationally has the advantage of tuning the pore chemistry for selective gas adsorption, while preserving the MOF-801 porosity. Generating the chlorofumarate in situ during MOF formation compared to post-synthesis reduces reaction steps, cost, and time. Although **HHU-1** may be limited towards practical application due to its low thermal and chemical stability, **HHU-2** combines good thermal and chemical stability. Together with its chloro-functionalized micropores, the high hydrophilicity and Type I water sorption isotherm make **HHU-2** a prospective material for technological applications including gas/hydrocarbon separation by selective adsorption, dehumidification, adsorption-driven heat transformation[21,22] and water harvesting from air.[32] Ongoing work is currently being carried out in our group, to investigate **HHU-2** for some of these applications.

Experimental Section

Experimental and synthesis procedures; IR, Raman, NMR, XPS, and EDX spectra; gas/vapor sorption isotherms, gas sorption modeling; pore size distribution; PXRD patterns of chemical stability tests; TGA, SEM images; EDX maps; crystallographic data and cif files can be found in the Supporting Information.

Acknowledgements

We thank the German Academic Exchange Service (DAAD) for funding to T.J.M.M.N. and the Federal Ministry of Education and Research (BMBF) for project Optimat, grant no. 03SF0492C.

Conflict of interest

The authors declare no conflict of interest.

Keywords: acetylenedicarboxylate · gas adsorption · hydrophilicity · in situ functionalization · metal–organic frameworks

[1] a) O. K. Farha, C. E. Wilmer, I. Eryazici, B. G. Hauser, P. A. Parilla, K. O'Neill, A. A. Sarjeant, S. T. Nguyen, R. Q. Snurr, J. T. Hupp, *J. Am. Chem. Soc.* **2012**, *134*, 9860 – 9863; b) D. J. Tranchemontagne, K. S. Park, H. Furukawa, J. Eckert, C. B. Knobler, O. M. Yaghi, *J. Phys. Chem. C* **2012**, *116*, 13143 – 13151.
[2] R. J. Marshall, S. L. Griffin, C. Wilson, R. S. Forgan, *J. Am. Chem. Soc.* **2015**, *137*, 9527 – 9530.
[3] D. J. Tranchemontagne, J. R. Hunt, O. M. Yaghi, *Tetrahedron* **2008**, *64*, 8553 – 8557.
[4] M. Eddaoudi, J. Kim, N. Rosi, D. Vodak, J. Wachter, M. O'Keeffe, O. M. Yaghi, *Science* **2002**, *295*, 469 – 472.
[5] a) F. Hohn, I. Pantenburg, U. Ruschewitz, *Chem. Eur. J.* **2002**, *8*, 4536 – 4541; b) R. Ahlers, U. Ruschewitz, *Solid State Sci.* **2009**, *11*, 1058 – 1064.
[6] N. Stock, S. Biswas, *Chem. Rev.* **2012**, *112*, 933 – 969.
[7] J. Li, T. B. Brill, *J. Phys. Chem. A* **2002**, *106*, 9491 – 9498.
[8] O. M. Yaghi, M. O'Keeffe, N. W. Ockwig, H. K. Chae, M. Eddaoudi, K. Kim, *Nature* **2003**, *423*, 705 – 714.
[9] J. H. Cavka, S. Jakobsen, U. Olsbye, N. Guillou, C. Lamberti, S. Bordiga, K. P. Lillerud, *J. Am. Chem. Soc.* **2008**, *130*, 13850 – 13851.
[10] R. Baggio, M. T. Garland, M. Perec, *Inorg. Chem.* **1997**, *36*, 737 – 739.
[11] J. L. C. Rowsell, O. M. Yaghi, *Angew. Chem. Int. Ed.* **2005**, *44*, 4670 – 4679; *Angew. Chem.* **2005**, *117*, 4748 – 4758.
[12] Q. Wang, J. Bai, Z. Lu, Y. Pan, X. You, *Chem. Commun.* **2016**, *52*, 443 – 452.
[13] A. Schaate, P. Roy, A. Godt, J. Lippke, F. Waltz, M. Wiebcke, P. Behrens, *Chem. Eur. J.* **2011**, *17*, 6643 – 6651.
[14] H. Billetter, I. Pantenburg, U. Ruschewitz, *Acta Crystallogr. Sect. E* **2006**, *62*, m881 – m883.
[15] A. H. Assen, Y. Belmabkhout, K. Adil, P. M. Bhatt, D.-X. Xue, H. Jiang, M. Eddaoudi, *Angew. Chem. Int. Ed.* **2015**, *54*, 14353 – 14358; *Angew. Chem.* **2015**, *127*, 14561 – 14566.
[16] B. Bueken, H. Reinsch, N. Reimer, I. Stassen, F. Vermoortele, R. Ameloot, N. Stock, C. E. A. Kirschhock, D. De Vos, *Chem. Commun.* **2014**, *50*, 10055 – 10058.
[17] G. Wissmann, A. Schaate, S. Lilienthal, I. Bremer, A. M. Schneider, P. Behrens, *Microporous Mesoporous Mater.* **2012**, *152*, 64 – 70.
[18] H. Furukawa, F. Gándara, Y.-B. Zhang, J. Jiang, W. L. Queen, M. R. Hudson, O. M. Yaghi, *J. Am. Chem. Soc.* **2014**, *136*, 4369 – 4381.
[19] J. Canivet, A. Fateeva, Y. Guo, B. Coasnec, D. Farrusseng, *Chem. Soc. Rev.* **2014**, *43*, 5594 – 5617.
[20] M. Thommes, K. Kaneko, A. V. Neimark, J. P. Olivier, F. Rodriguez-Reinoso, J. Rouquerol, K. S. W. Sing, *Pure Appl. Chem.* **2015**, *87*, 1051 – 1069.
[21] F. Jeremias, D. Fröhlich, C. Janiak, S. K. Henninger, *New J. Chem.* **2014**, *38*, 1846 – 1852.
[22] H. Kummer, F. Jeremias, A. Warlo, G. Füldner, D. Fröhlich, C. Janiak, R. Gläser, S. K. Henninger, *Ind. Eng. Chem. Res.* **2017**, *56*, 8393 – 8398; D. Fröhlich, E. Pantatosaki, P. D. Kolokathis, K. Markey, H. Reinsch, M. Baumgartner, M. A. van der Veen, D. E. De Vos, N. Stock, G. K. Papadopoulos, S. K. Henninger, C. Janiak, *J. Mater. Chem. A* **2016**, *4*, 11859 – 11869; C. Janiak, S. K. Henninger, *Chimia* **2013**, *67*, 419 – 424.
[23] H. J. Park, M. P. Suh, *Chem. Sci.* **2013**, *4*, 685 – 690.
[24] Z. Hu, Y. Peng, Z. Kang, Y. Qian, D. Zhao, *Inorg. Chem.* **2015**, *54*, 4862 – 4868.
[25] K. Sumida, D. L. Rogow, J. A. Mason, T. M. McDonald, E. D. Bloch, Z. R. Herm, T.-H. Bae, J. R. Long, *Chem. Rev.* **2012**, *112*, 724 – 781.
[26] Z. Hu, I. Castano, S. Wang, Y. Wang, Y. Peng, Y. Qian, C. Chi, X. Wang, D. Zhao, *Cryst. Growth Des.* **2016**, *16*, 2295 – 2301.
[27] a) H. Wu, Y. S. Chua, V. Krungleviciute, M. Tyagi, P. Chen, T. Yildirim, W. Zhou, *J. Am. Chem. Soc.* **2013**, *135*, 10525 – 10532; b) R. E. Morris, P. S.

Wheatley, *Angew. Chem. Int. Ed.* **2008**, *47*, 4966 – 4981; *Angew. Chem.* **2008**, *120*, 5044 – 5059.
[28] S. Keskin, T. M. van Heest, D. S. Sholl, *ChemSusChem* **2010**, *3*, 879 – 891.
[29] C. Zlotea, D. Phanon, M. Mazaj, D. Heurtaux, V. Guillerm, C. Serre, P. Horcajada, T. Devic, E. Magnier, F. Cuevas, G. Férey, P. L. Llewellyn, M. Latroche, *Dalton Trans.* **2011**, *40*, 4879 – 4881.
[30] E. Papirer, R. Lacroix, J.-B. Donnet, G. Nan, P. Fioux, *Carbon* **1995**, *33*, 63 – 72.
[31] M. SK, S. Bhowal, S. Biswas, *Eur. J. Inorg. Chem.* **2015**, 3317 – 3322.
[32] M. J. Kalmutzki, C. S. Diercks, O. M. Yaghi, *Adv. Mater.* **2018**, DOI: https://doi.org/10.1002/adma.201704304.

Manuscript received: June 4, 2018
Revised manuscript received: June 22, 2018
Accepted manuscript online: June 25, 2018
Version of record online: August 22, 2018

CHEMISTRY
A European Journal

Supporting Information

Realizing the Potential of Acetylenedicarboxylate by Functionalization to Halofumarate in Zr^{IV} Metal–Organic Frameworks

Tobie J. Matemb Ma Ntep,[a] Helge Reinsch,[b] Bastian Moll,[a] Emrah Hastürk,[a] Serkan Gökpinar,[a] Hergen Breitzke,[c] Carsten Schlüsener,[a] Laura Schmolke,[a] Gerd Buntkowsky,[c] and Christoph Janiak*[a]

chem_201802838_sm_miscellaneous_information.pdf

Table of contents

- Selected list of coordination polymers based on acetylenedicarboxylate linker
- Methods and Syntheses of Materials
- Scanning electron microscopy images
- Additional structure images of HHU-1
- Thermal and chemical analyses
- Nitrogen and argon sorption analyses
- Theoretical surface area and pore volume
- Images from Mercury void calculations
- Fitting of CO_2 / H_2 adsorption isotherms with the Toth model for HHU-1
- Solid-state and solution ^1H and ^{13}C NMR spectroscopy of HHU-2 (Zr-Fum-Cl)
- References

Selected list of coordination polymers based on acetylenedicarboxylate linker

Table S1. Some reported ADC-based coordination polymers, synthesis conditions and stabilities

Coordination polymer	Synthesis procedure	Thermal stability	Ref.
$[Cu\{ADC\}(H_2O)_3]\cdot H_2O$	RT slow evaporation from water	Decomposes at RT in air	[1]
$Co(C_2(ADC)(H_2O)_4\cdot 2H_2O$	RT slow evaporation from water	Stable till about 200°C	[2]
$Zn_4O(ADC)_4(Et_3N)_6$	RT in DMF	Decomposes at 120°C	[3]
$[Cd\{C_2(COO)_2\}(H_2O)_3]\cdot H_2O$	RT in water	Decomposes at RT in air	[4]
$Mg(ADC)(H_2O)_2$	Mechanochemical, 70°C	Stable till about 200°C	[5]
CaADC	Mechanochemical, 50°C	Decomposes above 50°C	[5]
PbADC·H2O	RT diffusion	Stable till about 250°C	[6]
$[Ce_2(ADC)_3(H_2O)_6]\cdot 2H_2O$	RT diffusion	Stable till about 250°C	[7]
$Sr[C_2(COO)_2]$	RT diffusion	Stable till 440 °C	[8]
$[Bi(ADC)_{2/4}(ADC)_{3/3}(H_2O)_2]\cdot 2H_2O$	RT slow evaporation from water	Stable till 150 °C	[9]

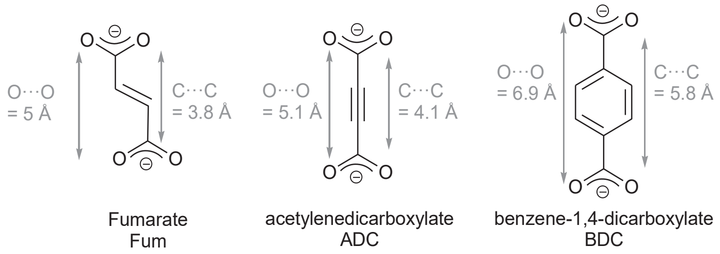

Scheme S1. Comparison of axial dimensions between fumarate, acetylenedicarboxylate and benzene-1,4-dicarboxylate.

Methods and Syntheses of Materials

Methods:

Chemicals used in this work. Acetone (purity ≥ 99.5 %), zirconium oxychloride octahydrate ($ZrOCl_2\cdot 8H_2O$, purity 99.99 %) were obtained from Sigma Aldrich; acetylenedicarboxylic acid (H_2ADC, purity 97 %) was obtained from abcr; N,N-Dimethylformamide (DMF; analytical reagent grade) was obtained from Fischer Chemical; acetic acid (purity 100 %) was obtained from VWR Chemicals. All chemicals were used without further purification.

Analytical techniques. Infrared (IR) spectra were obtained on a Bruker FT-IR Tensor 37 Spectrometer in the 4000-550 cm^{-1} region with 2 cm^{-1} resolution as KBr disks. **Raman spectra** were obtained on a Bruker MultiRAM-FT Raman spectrometer equipped with a Nd:YAG-laser (wavelength 1064 nm). All Raman spectra were measured in solid state for 2500 scans with a laser power between 10-20 mW. **Chlorine elemental analysis** was carried out by Mikroanalytisches Laboratorium Kolbe, Mülheim a. d. Ruhr, Germany. **Powder X-ray diffraction (PXRD)** data was collected on a Bruker D2 Phaser diffractometer using a flat sample holder (also a flat silicon, low background sample holder) and Cu Kα_1/α_2 radiation with λ = 1.5418 Å at 30 kV covering 2theta angles 5-80° over a time of 2 h, that is 0.01 °/sec. Diffractograms were obtained on flat layer sample holders where at low angle the beam spot is strongly broadened so that only a fraction of the reflected radiation reaches the detector which leads to low relative intensities measured at $2\theta < 7°$. **Thermogravimetric analyses (TGA)** were carried out at a ramp rate of 10 °C/min in a N_2 flow with a Netzsch Thermo-Microbalance Apparatus TG 209 F3 Tarsus. **Scanning electron microscopy (SEM)** images were obtained using a Jeol JSM-6510LV QSEM advanced electron microscope with a LaB_6 cathode at 5–20 keV. The samples for SEM imaging were coated with gold using a Jeol JFC 1200 fine-coater (20 mA for 25 s). **X-ray photoelectron spectroscopy, XPS–(ESCA–)** measurement was performed with a Fisons/VG Scientific ESCALAB 200X xp–spectrometer, operating at 70–80 °C, a pressure of 7.0×10^{-9} bar and a sample angle of 33°. Spectra were recorded using polychromatic AlKα excitation (11 kV, 20 mA) and an emission angle of 0°. Calibration of the XPS was carried out by recording spectra with Al Kα X–rays from clean samples of copper, silver and gold at 50 eV and 10 eV pass energies and comparison with reference values. Conventional **CP MAS solid state NMR** measurements were carried out at room temperature on a Bruker AVANCE II$^+$ spectrometer at 400 MHz proton resonance frequency, employing a Bruker 4 mm double resonance probe. ^{13}C CP MAS spectra were recorded utilizing ramped CP-MAS sequences at spinning rates of 12 kHz. Contact time was set to 1.5 ms and tppm decoupling with a 15° phase jump was applied during data acquisition.[10] ^{13}C spectra were referenced with respect to TMS (tetramethylsilane). **Frequency switched Lee Goldburg (FSLG) CP MAS HETCOR** spectra were recorded at 12 kHz and contact times of 2 ms, 500 µs (not shown), and 200 µs (Figure 36). The tppm decoupling sequence with a 15° phase jump was applied during data acquisition. ^1H spectra were recorded utilizing the Bruker background suppression sequence at 12 kHz, and were referenced with respect to TMS (tetramethylsilane).

Supercritical CO_2 drying was performed using an automated Leica EM CPD300 critical point dryer. As-synthesized samples were transferred into the sample holder which was inserted in the sample chamber of supercritical CO_2 dryer containing ethanol as exchanging fluid. The temperature was lowered to 10 °C, and the chamber was filled with liquid CO_2 (ultrahigh grade CO_2 with a siphon from Air-Gas Inc was used). The sample was soaked for about 7 hours, venting for five minutes every two hours (99 exchange cycles). The chamber was then heated to 40 °C, and the supercritical CO_2 was bled off at a rate of 1 mL/min until the chamber reached ambient pressure. The chamber was opened and the dried samples were used for sorption experiments.

Prior to the gas sorption measurements, each sample was activated by supercritical CO_2 ($scCO_2$) exchange involving ninety-nine exchange cycles with ethanol for seven hours. This was followed by outgassing in high vacuum for 1 h at room temperature. This activation procedure was adopted to accommodate the thermal sensitivity of these compounds.

For **gas sorption studies** nitrogen, hydrogen and argon isotherms were measured on a Quantachrome Autosorb iQ MP at 77 K (N_2, H_2) and 87 K (Ar), respectively. The temperature of 87 and 100 K was set by a Cryocooler or Cryosync temperature controller from Qantachrome. The specific surface area was calculated from the nitrogen sorption isotherms using the Brunauer-Emmett-Teller (BET) equation. The pore size distribution traces were calculated by Density Functional Theory (DFT) of the NovaWin 11.03 software using the "N_2 at 77 K on carbon, slit pore, nonlinear functional theory (NLDFT) equilibrium" model. CO_2 isotherms were measured using a Micromeritics ASAP 2020 automatic gas sorption analyzer equipped with oil-free vacuum pumps (ultimate vacuum <10^{-8} mbar) and valves, which guaranteed contamination free measurements. The sample was connected to the preparation port of the sorption analyzer and degassed under vacuum until the outgassing rate, i.e., the rate of pressure rise in the temporarily closed manifold with the connected sample tube, was less than 2 μTorr/min at the specified temperature of 80 °C. After weighing, the sample tube was then transferred to the analysis port of the sorption analyzer. Enthalpies of CO_2 and H_2 adsorption were calculated respectively from ASAP and iQ software packages by applying the Clausius-Clapeyron expression using the sorption isotherms data collected at 273 K and 293 K (for CO_2) / at 77 K and 87 K (for H_2). All gases for the sorption measurements were of ultrapure grades (99.999%, 5.0).

Fits of adsorption isotherms were performed using the software DynaSim V 1.1.0.5 by Quantachrome GmbH 2015. DynaSim is a tool for interpretation and evaluation of experimental data from dynamic experiment.

Water vapor sorption isotherms were measured gravimetrically at 20 °C on a VSTAR^{TM} vapor sorption analyzer (Model number Vstar4-0000-1000-XS) from Quantachrome. For this purpose, about 25 mg of activated sample were introduced in the measuring cell and connected to the analysis port of the analyzer.

General synthesis procedure. Zirconium(IV)-ADC (**HHU-1**) with the acetylenedicarboxylate (ADC) linker was prepared following the modulated synthesis approach. UiO type MOFs are usually synthesized by addition to the reaction mixture of a monocarboxylic acid (formic, acetic, trifluoroacetic, benzoic acid etc.) as modulator. It is assumed that modulators induce initial in situ formation of soluble monomeric $\{Zr_6O_4(OH)_4(RCOO)_{12}\}$ clusters, which then lead to network growth through a slower dynamic exchange between the modulator and the linker units. Thus modulation is now commonly used to induce highly crystalline products, controlling crystals size and morphology with enhanced reproducibility of synthesis procedure.[11] In our case, acetic acid was employed as modulator in DMF or water as solvent, while $ZrOCl_2·8H_2O$ was used as metal source.

[Zr_6(μ_3-O_4)(μ_3-OH)$_4$(ADC)$_6$] (HHU-1, Zr-ADC)

A portion of 320 mg (1 mmol) of $ZrOCl_2·8H_2O$ was ultrasonically dissolved in a solvent mixture of DMF/acetic acid (2.5 mL / 2.5 mL) (corresponding to 32 mmol DMF / 44 mmol acetic acid). 114 mg (1 mmol) of acetylenedicarboxylic acid were added to the reaction mixture which was further sonicated till a limpid solution was obtained. The resulting mixture was sealed in a 10 mL screw-capped glass vial which was stored for 6 h in an oven preheated at 85 °C. After cooling to room temperature, white precipitate was separated from the mother liquor by centrifugation, before being redispersed and centrifuged twice in fresh DMF (5 mL). The solid was washed with acetone (5 mL) for 2 h and centrifuged three consecutive times, then dried at room temperature in air. Yield: 292 mg (94%) based on the Zr salt.

The solvent in the pores of as-synthesized sample was removed by supercritical CO_2 ($scCO_2$) drying. This was followed by outgassing under dynamic vacuum for 1 h at room temperature, to yield the activated sample.

[Zr_6(μ_3-O)$_4$(μ_3-OH)$_4$(chlorofumarate)$_6$] (HHU-2, Zr-Fum-Cl)

In a typical synthesis, 640 mg (2 mmol) of $ZrOCl_2·8H_2O$ were dissolved in a solvent mixture of distilled water/acetic acid (5 mL/5 mL) (corresponding to 280 mmol DMF / 88 mmol acetic acid). 228 mg (2 mmol) of acetylenedicarboxylic were added to the reaction mixture which was ultrasonicated for 2 min. The resulting mixture was introduced in a 25 mL screw-capped Duran glass vial and stored for 6 h in an oven preheated at 85 °C. After cooling to room temperature, white precipitate was separated from mother liquor by centrifugation, re-dispersed and centrifuged in distilled water (3×10 mL) and in methanol (3×10 mL). Afterwards the product was dried in air. Yield: 576 mg (95.7 %) based on the zirconium salt. Chlorine elemental analysis calcd. for $Zr_6C_{22}H_{40}O_{44}Cl_5 \equiv [Zr_6O_4(OH)_5(OOC\text{-}CH{=}CCl\text{-}COO)_{4.5}(H_3CCOO)_{1.5}(OH)_{1.5}]·13H_2O$: Cl 9.41%; found: Cl 9.83%.

$[Zr_6O_4(OH)_5(OOC\text{-}CH{=}CCl\text{-}COO)_{4.5}(H_3CCOO)_{1.5}(OH)_{1.5}]·13H_2O$ is based on the approximate 1:0.8 molar Zr:Cl ratio from SEM-EDX (Figure S6, Table S2 in the SI) and the 1:1 Fum-Cl^{2-} : H_3CCOO^- proton integral ratio in the solution ^1H NMR of **HHU-2** (Figure S38). The necessary charge equilibration is then obtained with an additional 1.5 OH^- ligands The water content of $13H_2O$ represents 13 wt% which was confirmed by TGA of the dried and stored under air sample. Hydrophilic MOFs can adsorb water from ambient air during storage, waiting time and preparation before weighing for elemental analysis under ambient air conditions. The water content of 13 H_2O was based on the water loss seen in the thermogravimetric analysis (TGA).

Infrared spectroscopy

The strong absorption bands in the FT-IR spectrum (Figure S1) at around 1590-1610 and 1360-1390 cm^{-1}, can be ascribed to the asymmetric and symmetric –COO^{-} -stretching vibrations of the coordinated linker. The bands at 1651, 1600, and 1661 cm^{-1} are ascribed to –C=O stretching vibration of residual DMF solvent in the pores. The broad band centered at about 3400 cm^{-1} is ascribed to stretching vibrations of water molecules.

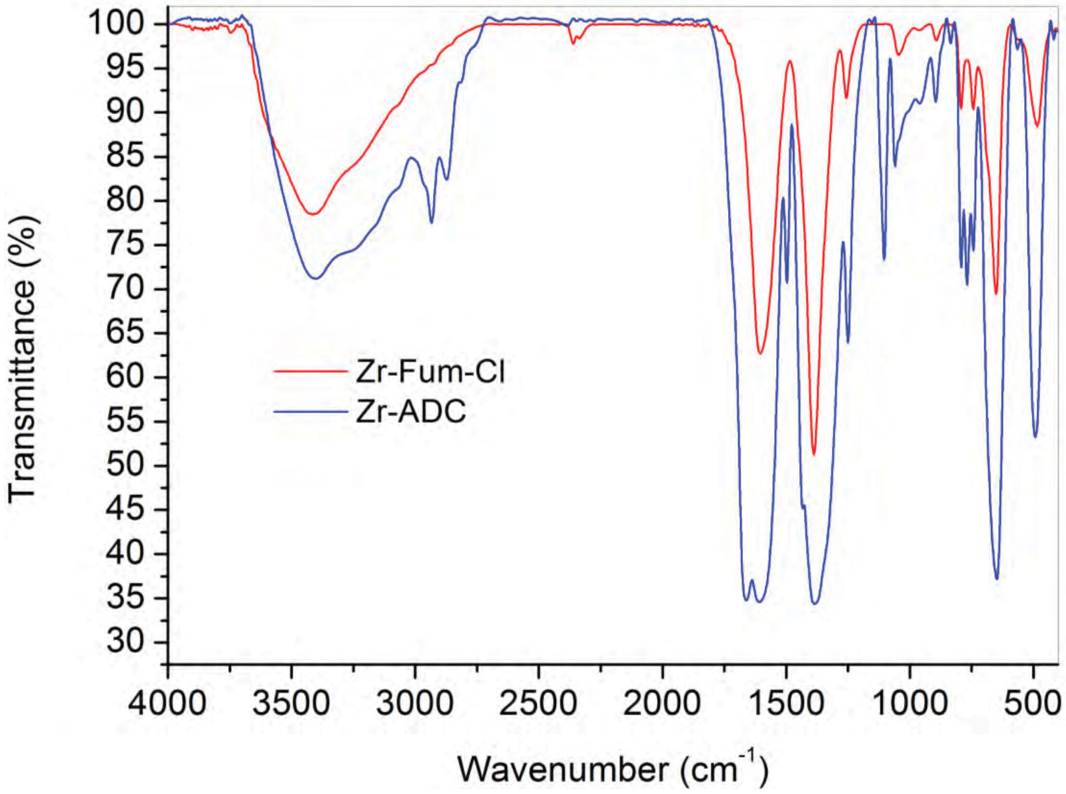

Figure S1. IR spectrum of **HHU-1** (Zr-ADC) and **HHU-2** (Zr-Fum-Cl).

Raman spectroscopy

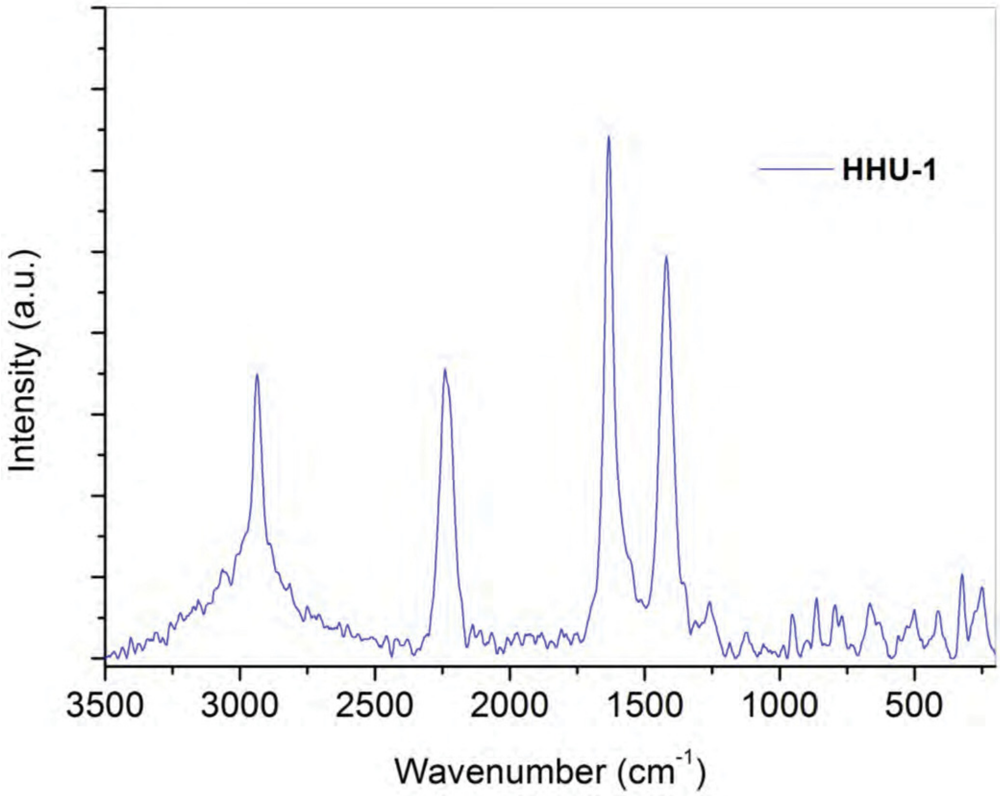

Figure S2. Raman spectrum of **HHU-1** (Zr-ADC). The band at about 1400 cm^{-1} is assignable to the vibrations of coordinated –COO^{-}. The band centered at 2900 cm^{-1} can be ascribed to the vibration of H_3C-C group of the acetate modulator probably coordinated at missing linker sites.

Scanning electron microscopy images

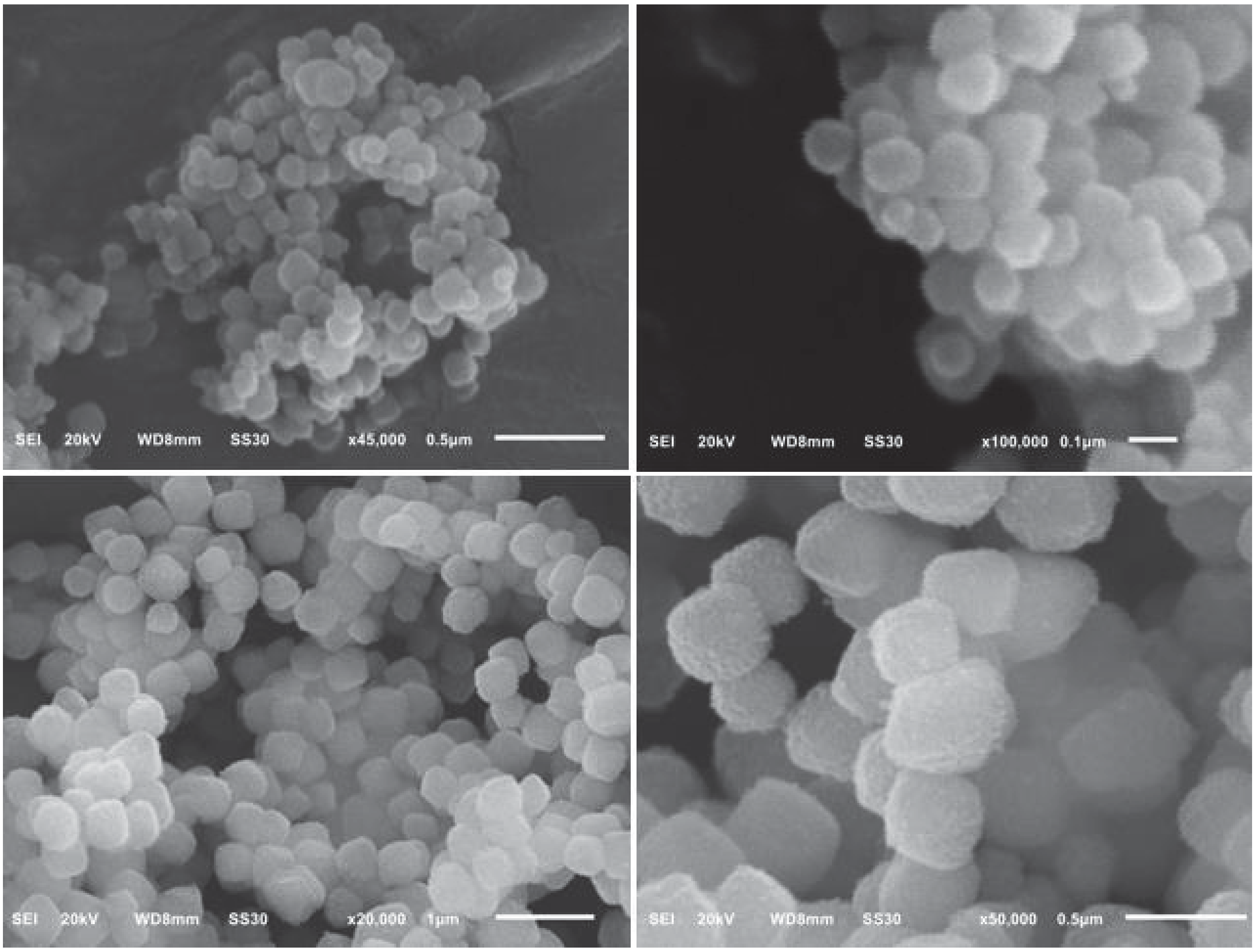

Figure S3. SEM images of **HHU-1** (Zr-ADC).

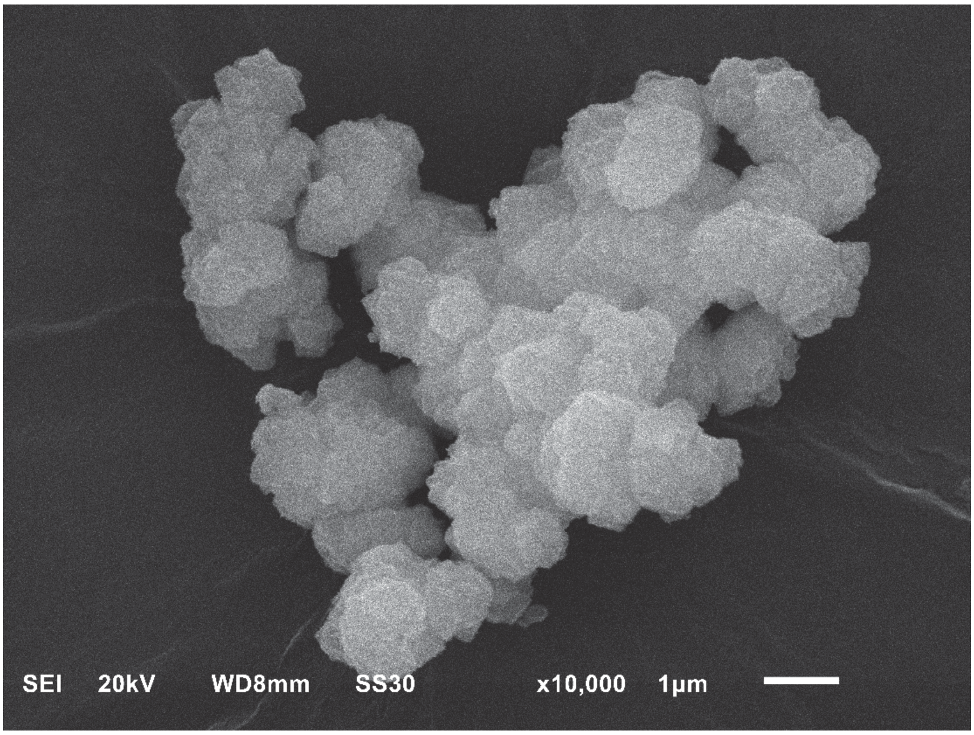

Figure S4. SEM images of **HHU-2** (Zr-Fum-Cl).

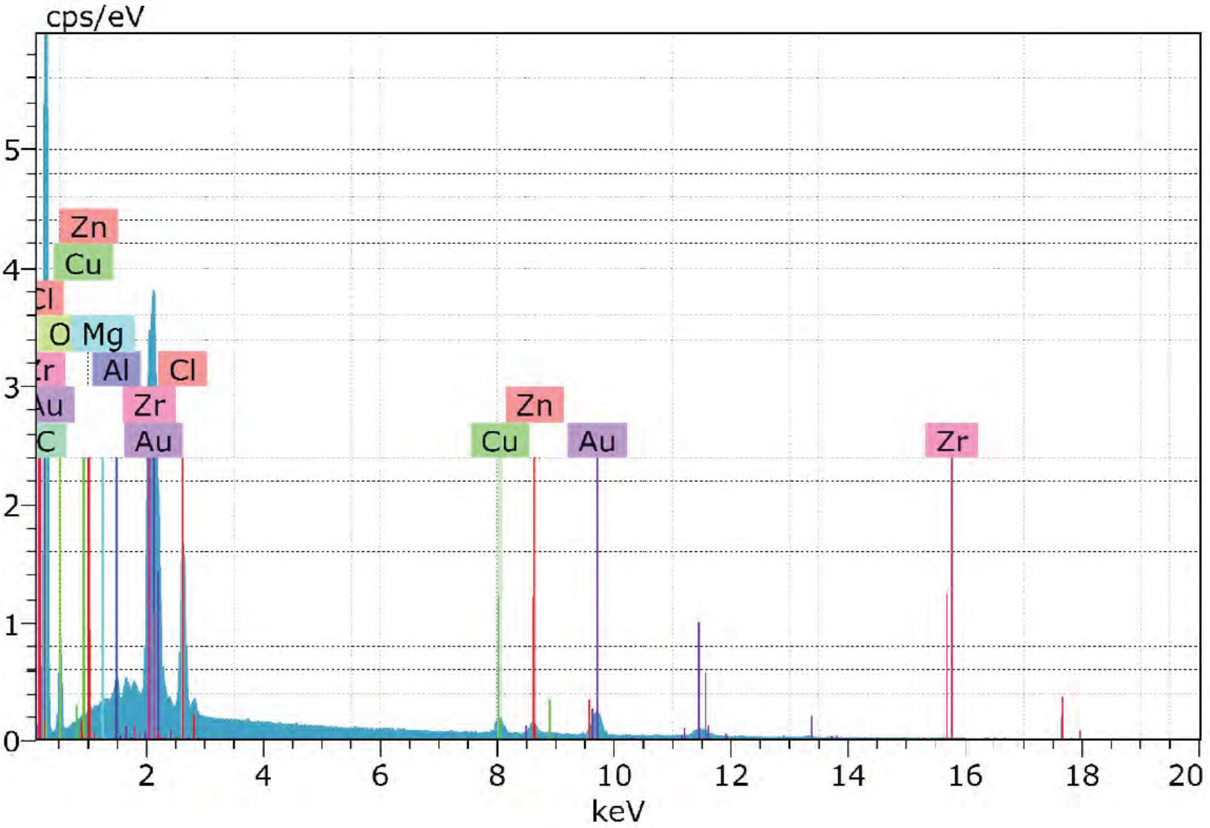

Figure S5. EDX spectrum of **HHU-2** (Zr-Fum-Cl).

Table S2. Atomic and Weight % of C, O, Cl and Zr for **HHU-2** (Zr-Fum-Cl)

```
Spektrum: TM073 1

El OZ   Serie   unn. C norm. C Atom. C Fehler (1 Sigma)
               [Gew.%] [Gew.%]  [At.%]          [Gew.%]
-------------------------------------------------------
C   6  K-Serie   66.75   63.71   87.58            8.05
Au 79  L-Serie   14.45   13.79    1.16            0.50
Zr 40  L-Serie    9.58    9.15    1.66            0.40
O   8  K-Serie    7.34    7.00    7.23            1.23
Cl 17  K-Serie    3.14    3.00    1.40            0.14
Cu 29  K-Serie    1.74    1.66    0.43            0.09
Zn 30  K-Serie    1.41    1.34    0.34            0.08
Al 13  K-Serie    0.28    0.26    0.16            0.04
Mg 12  K-Serie    0.08    0.08    0.05            0.03
-------------------------------------------------------
       Summe:  104.76  100.00  100.00
```

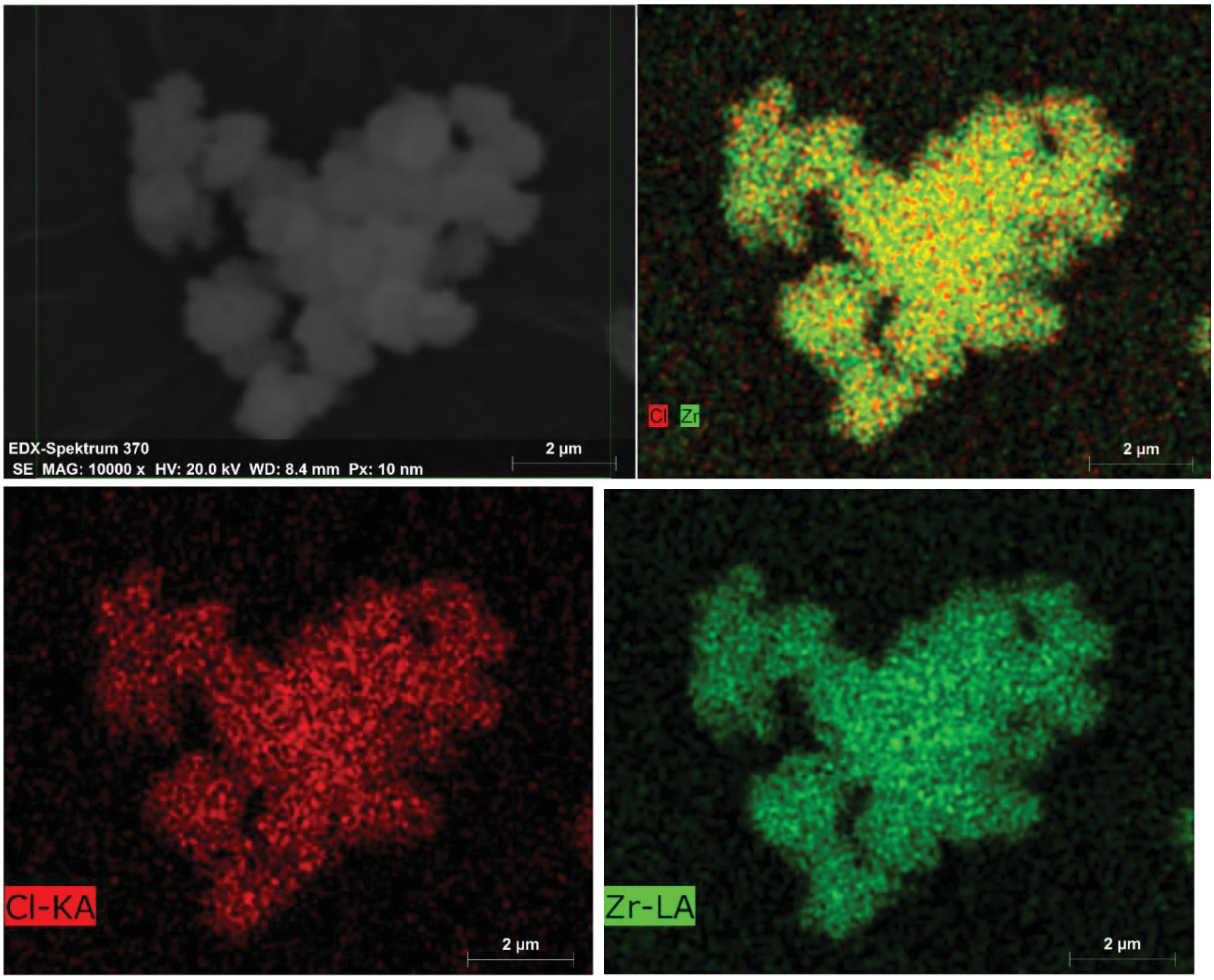

Figure S6. EDX elemental maps of **HHU-2** (Zr-Fum-Cl).

X-ray Photoelectron Spectroscopy (XPS)

After observing the obvious transformation of the triple bond of the initial H_2ADC ligand into a double bond in a new ligand by Raman spectroscopy, and the mono-substituted nature of the double bond indicated by NMR spectroscopy, XPS analysis was conducted in order to identify the nature of the substituent. Prior to the analysis, the sample was thoroughly washed with water for 2 days to ensure removal of all impurities

Interestingly, is the presence of chlorine of which the Cl_{2p} peak appears in the XP spectrum at 200.36 eV binding energy (Figure S8). This value suggests the presence in the compound of organic chlorine (covalently bonded), since the binding energy of inorganic chloride is usually expected at lower binding energy values (typically in the range 197-199 eV). This is consistent with the presence of a =C-Cl vibration band at about 743 cm^{-1} in the IR spectrum (Figure S1).[12] Assignments of all peaks of the survey XP spectrum are found in Table S3.

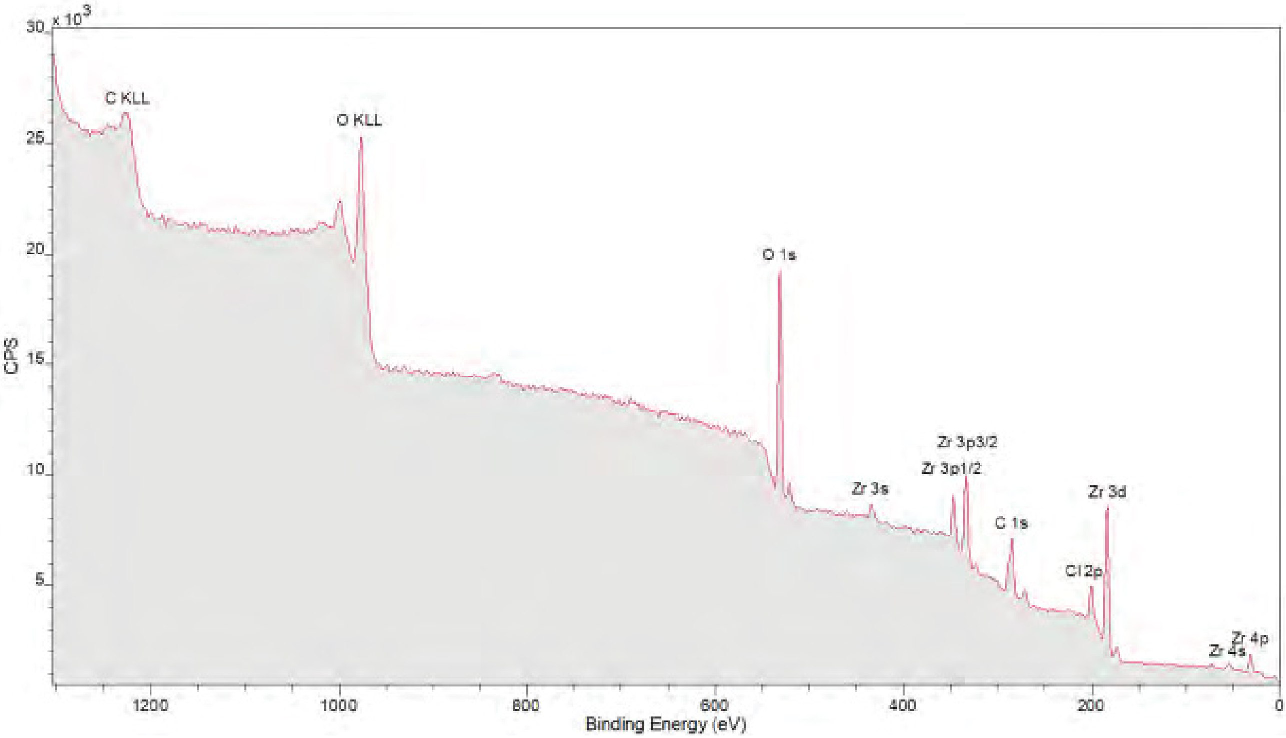

Figure S7. XPS survey spectrum of **HHU-2** (Zr-Fum-Cl) surface.

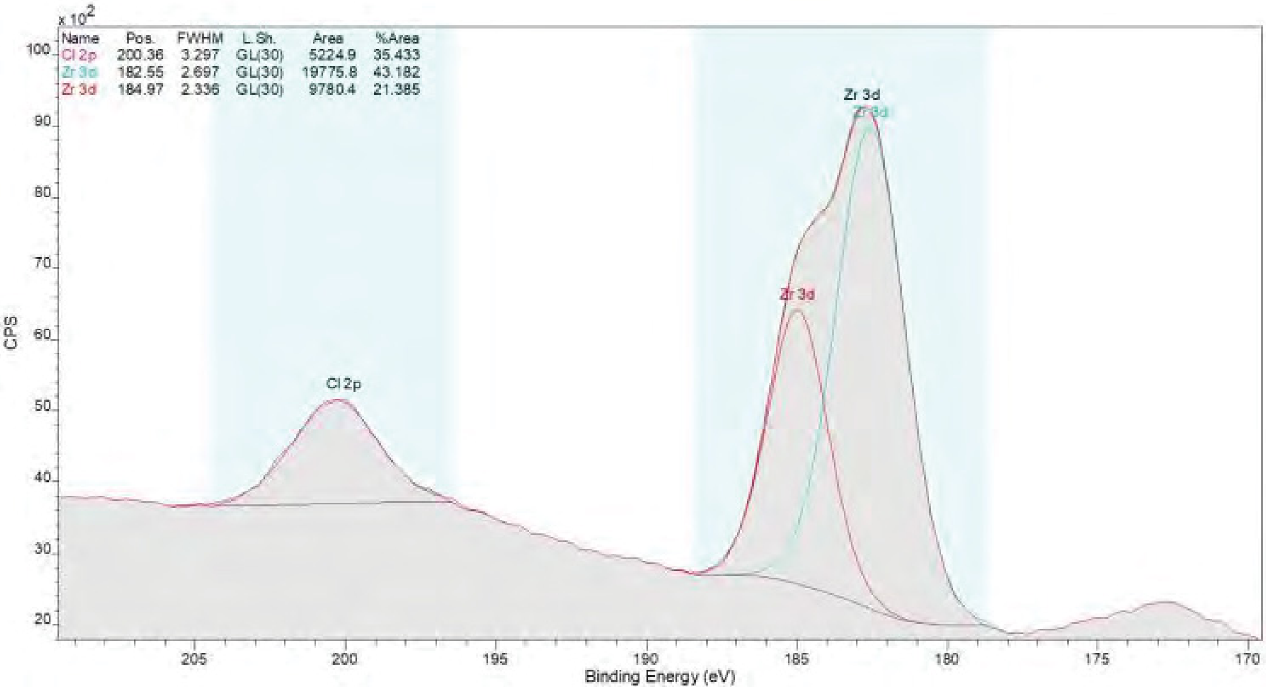

Name	Pos.	FWHM	L.Sh.	Area	%Area
Cl 2p	200.36	3.297	GL(30)	5224.9	35.433
Zr 3d	182.55	2.697	GL(30)	19775.8	43.182
Zr 3d	184.97	2.336	GL(30)	9780.4	21.385

Figure S8. High resolution XPS core-level spectrum of **HHU-2** (Zr-Fum-Cl) in the region of Cl 2p and Zr 3d.

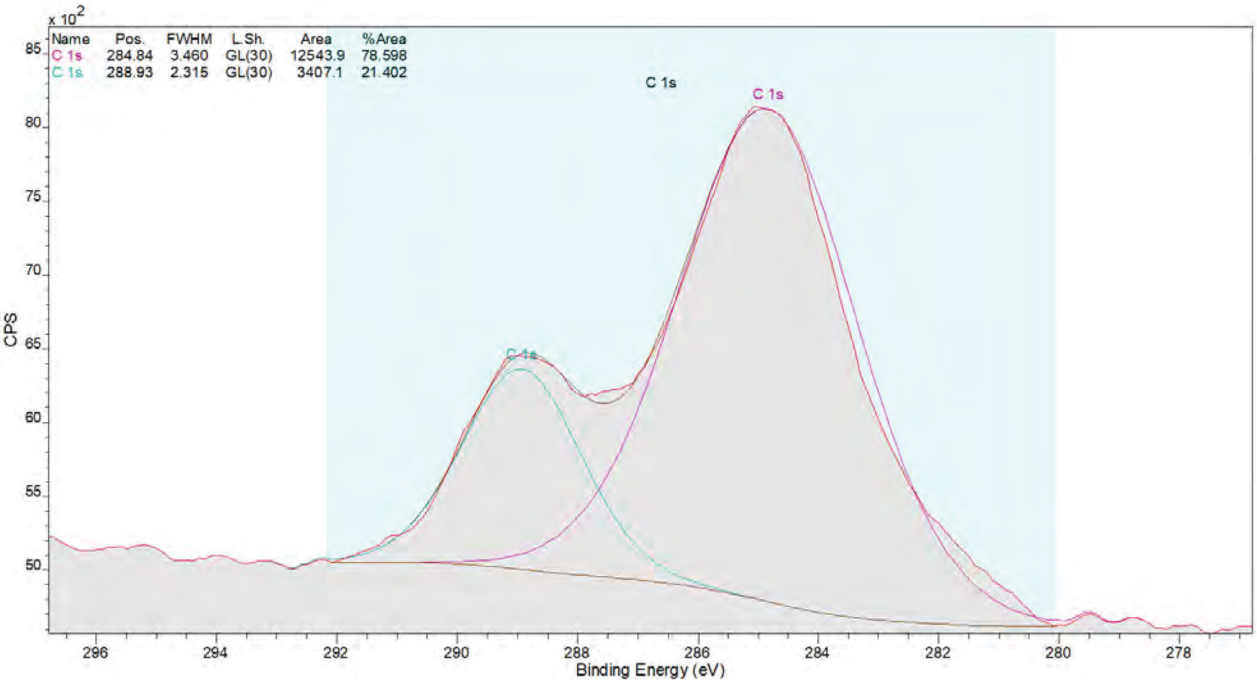

Name	Pos.	FWHM	L.Sh.	Area	%Area
C 1s	284.84	3.460	GL(30)	12543.9	78.598
C 1s	288.93	2.315	GL(30)	3407.1	21.402

Figure S9. High resolution XPS core-level spectrum of **HHU-2** (Zr-Fum-Cl) in the region of C 1s.

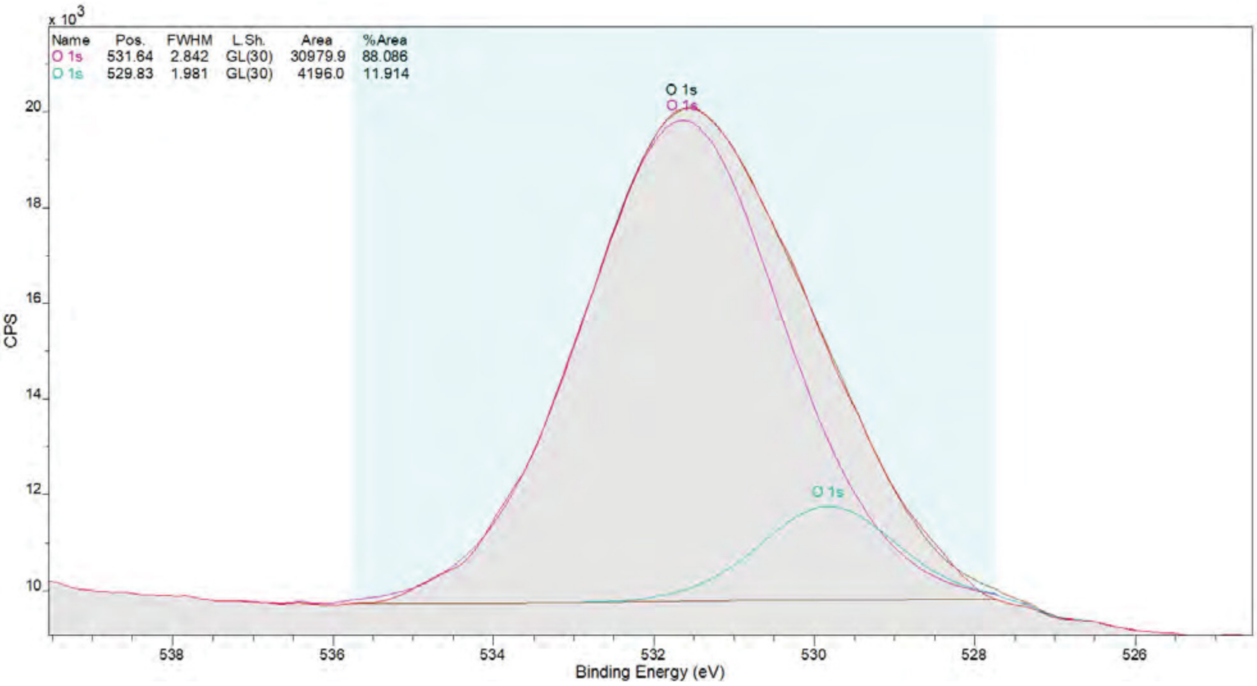

Figure S10. High resolution XPS core-level spectrum of **HHU-2** (Zr-Fum-Cl) in the region of O 1s.

Table S3. XP spectrum peaks assignments

Element	Orbital	Binding Energy	Area	RSF	Area/RSF	Assignment
C	1s	284.84	12543.9	1	12543.9	C-C
		288.93	3407.1	1	3407.1	Carboxyl
O	1s	529.83	4196	2.93	1432.08191	M-Ox
		531,64	30979.9	2.93	10573.3447	org. C-O
Cl	2p	200.36	5224.9	2.29	2281.61572	organic Cl
Zr	3d 3/2	182.55	19775.8	7.04	2809.0625	Zr-O
	3d 5/2	184.97	9780.4	7.04	1389.26136	

Crystal Structure refinement of HHU-1 (Zr-ADC)

PXRD patterns were measured in transmission geometry on a STOE Stadi MP, equipped with a Dectris Mythen detector and using monochromated CuKα_1 radiation, and could be successfully indexed using TOPAS academics[13] with cubic *F*-centered cells (a = 17.925(3) Å for **HHU-1** (Zr-ADC), extinction conditions suitable for space group $Fm\bar{3}m$). A suitable starting model for Rietveld refinement was established using the crystal structure of the terephthalate UiO-66 as a starting point. The lateral atoms of the benzene core of the linker molecules were removed after imposing the indexed cell parameters and the structure was optimized by force-field calculation using the universal force field as implemented in the Materials Studio software.[14] The thus obtained models were refined by Rietveld methods using TOPAS. All atoms were freely refined using one temperature factor for the framework and one temperature factor for the guest atoms, respectively. The occupancy of the linker molecules was also freely refined. Residual electron density inside the pores was identified by Fourier synthesis and attributed to guest molecules, modeled by oxygen atoms of refinable occupancy. These guest atoms (G*n*) should be considered placeholders for any kind of solvent molecules. The freely refined linker occupancy converged to ≈ 0.6 for **HHU-1** (Zr-ADC). It must be mentioned that the modelling of the guest atoms could easily affect this linker occupancy and thus this value should be carefully interpreted. Some relevant parameters are summarized in Table S4 and the final plots are shown in Figure S11. Crystallographic data for the structural analysis **HHU-1** (Zr-ADC) have been deposited with the Cambridge Crystallographic Data Centre (CCDC 1831552).

Table. S4. Selected parameters for the Rietveld refinement of **HHU-1** (Zr-ADC).

Compound	HHU-1 (Zr-ADC)
Crystal system	cubic
Space group	$Fm\bar{3}m$
$a = b = c$ / Å	17.9239(3)
$\alpha = \beta = \gamma$ / °	90
V / Å^3	5758.4(3)
R_{wp} / %	4.3
R_{Bragg} / %	1.2
GoF	2.0

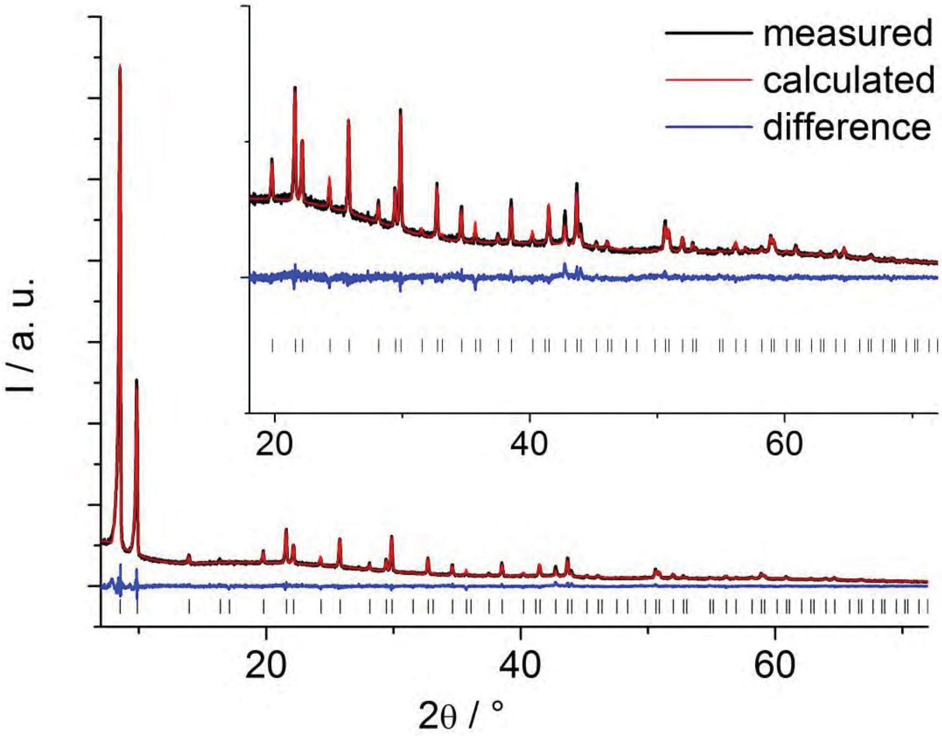

Figure S11. Final Rietveld plot for **HHU-1** (Zr-ADC). The black curve represents the measured data, the red curve is the theoretical data and the blue curve indicates the difference. Vertical black bars mark the allowed Bragg reflection positions.

Additional structure images of HHU-1 (Zr-ADC)

As previously reported for UiO-66, the MOF consist of hexanuclear $[Zr_6O_4(OH)_4]^{12+}$ secondary building units (SBUs). The SBU is constructed of six Zr atoms defining a regular octahedron, in which the triangular faces alternatively are spanned by μ_3-O and μ_3-OH capping groups. Together with the oxygen atoms of the carboxylate groups, each Zr atom has a square-antiprismatic coordination environment, thus yielding a hexanuclear cluster of a six vertex-sharing ZrO_8 square antiprismatic polyhedra (Figure 12). The octahedral SBUs are twelve-fold interconnected by acetylene-dicarboxylate linkers in a face-centered cubic arrangement, resulting in a porous three-dimensional **fcu** network (Figure 2 in manuscript). The octahedral and tetrahedral cages/voids are depicted in Figure S13 and S14.

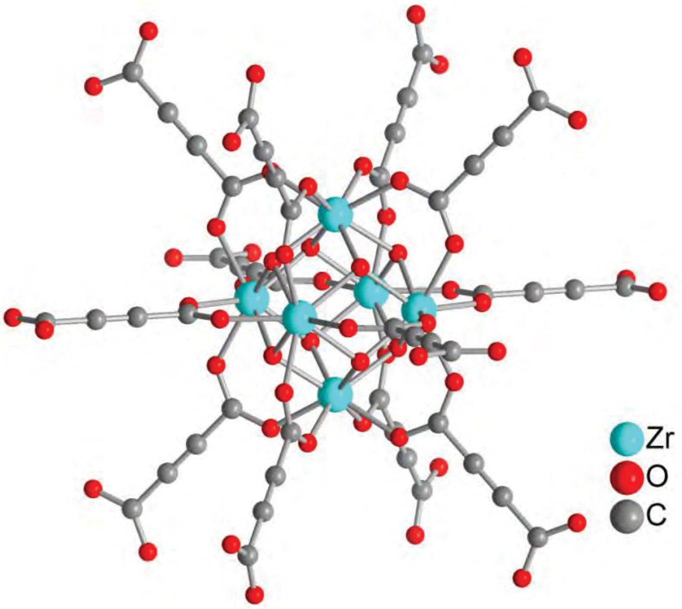

Figure S12. Secondary building units of the octahedral clusters $\{Zr_6(O)_4(OH)_4\}$ with the 12 surrounding and connecting acetylene-dicarboxylate linkers.

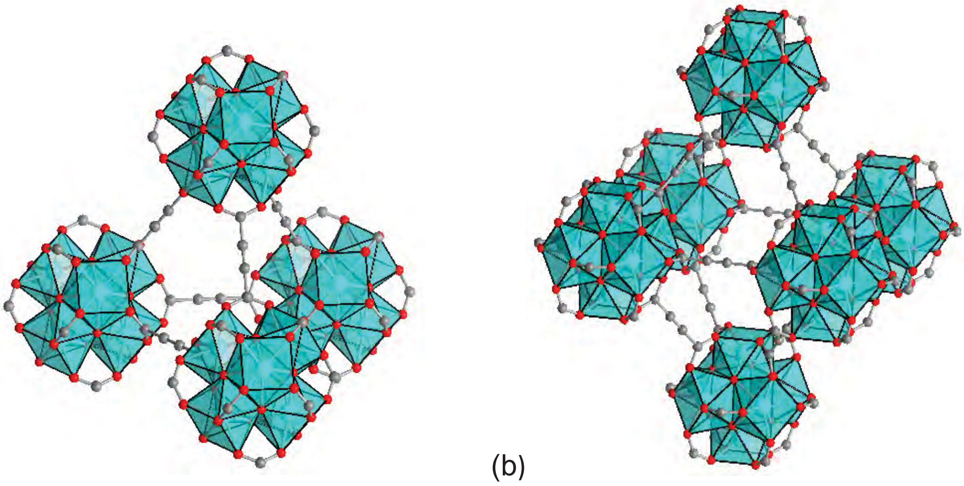
(a) (b)

Figure S13. Tetrahedral (a) and octahedral (b) voids in **HHU-1** (Zr-ADC) framework

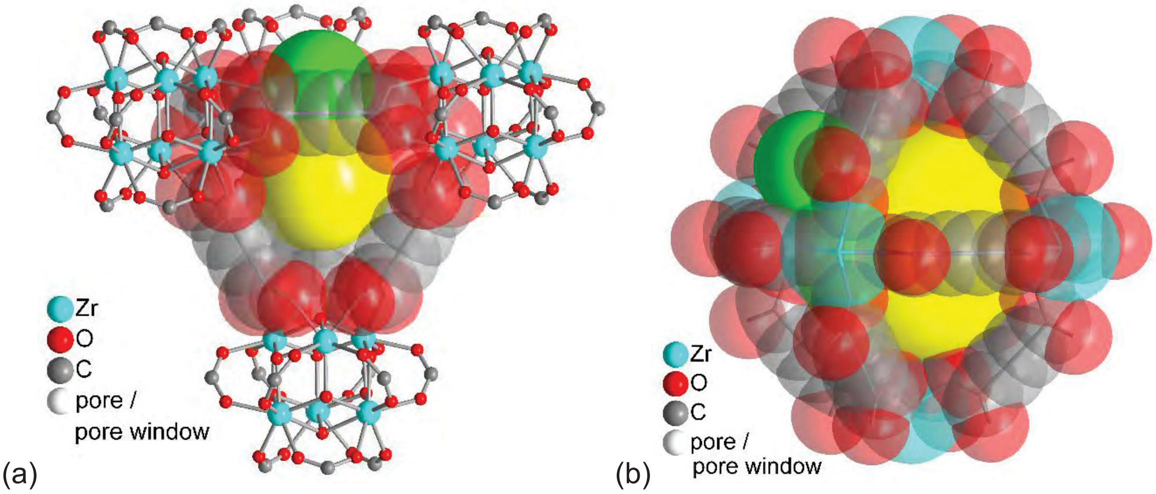

(a) (b)

Figure S14. (a) Tetrahedral and (b) octahedral cavity with the surrounding ligand and metal atoms in space-filling mode with van der Waals radii. The diameter of the yellow spheres which approach the van-der-Waals surface of the surrounding atoms are 5.8 Å (tetrahedral) and 9.6 Å (octahedral), respectively, with a window diameter (green sphere) of 4.4 Å.

Thermal and chemical stability analyses

Thermogravimetric (TG) analysis was carried out in a nitrogen atmosphere for investigation of the thermal stability. The TG trace (Figure S15) of **HHU-1** (Zr-ADC) shows thermal stability till about 180 °C, after which the material decomposes. This rather low thermal stability can be rationally attributed to the low thermal stability of the acetyledicarboxylate linker. Solid acetylenedicarboxylic acid is known to decompose at 180 °C. A similar result was also observed for the IRMOF series with MOF-5 topology, in which the smallest member IRMOF-0 based on ADC^{2-} linker begins to decompose at only 120 °C, unlike other members of this IRMOF family which show stability up to 400 °C or higher.[3]

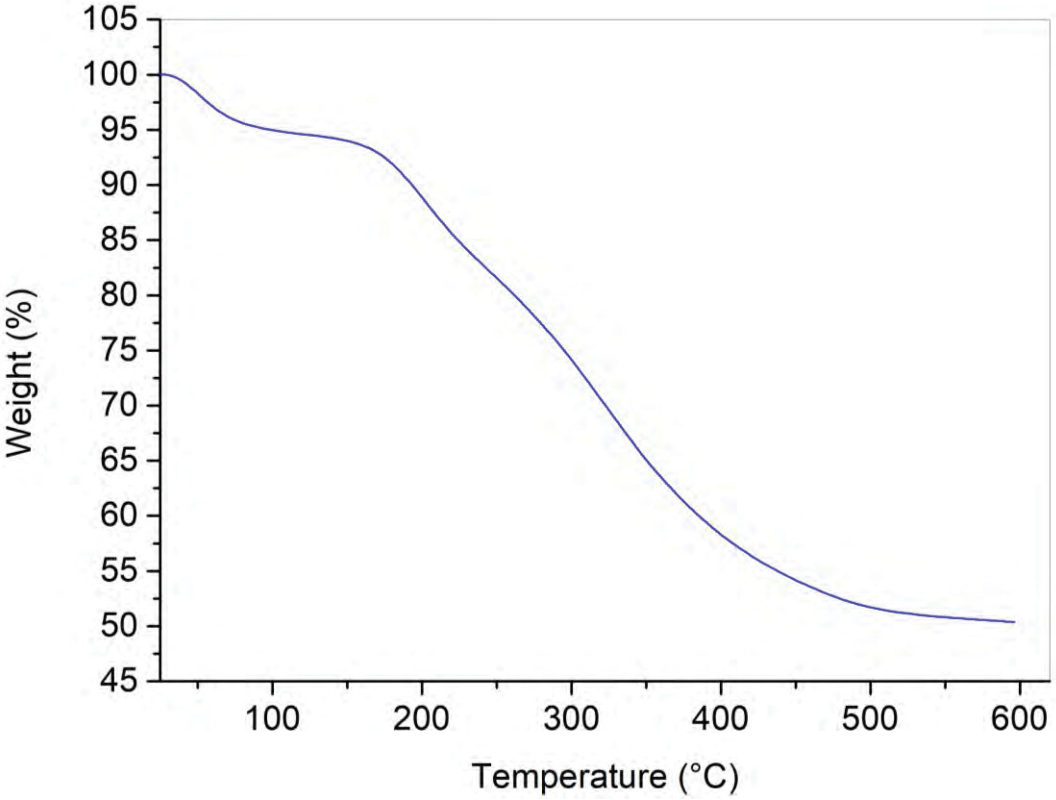

Figure S15. TG trace of **HHU-1** (Zr-ADC).

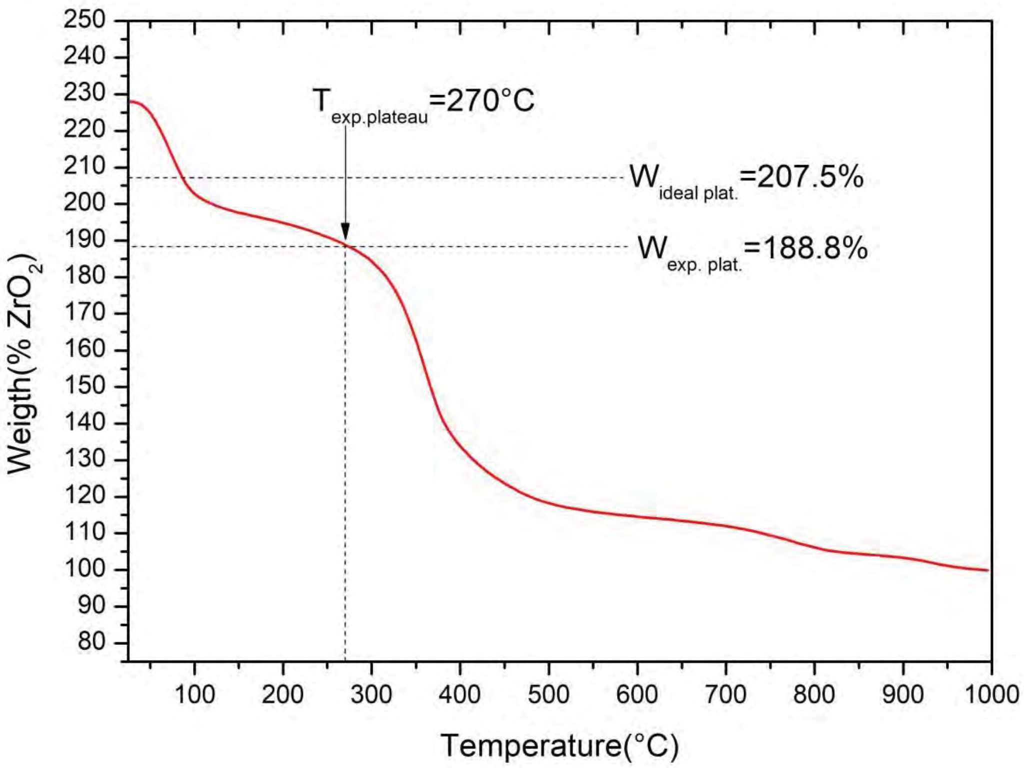

Figure S16. TG trace of **HHU-2** (Zr-Fum-Cl).

The TGA trace (Figure S16) shows that **HHU-2** (Zr-Fum-Cl) is stable up to about 300 °C. The TGA trace of washed and air dried **HHU-2** presents two well resolved weight loss steps. The first step occurring between 25 °C and 150 °C can be assigned to the evaporation of guest methanol and water molecules from the pores, accompanied by a broad endothermic peak in the DSC trace. Three successive close endotherms are observed in DSC trace (Figure S17) in the temperature range ca. 210-270 °C without evidence of a well resolved step, but rather a continuous loss. This can tentatively be assigned to the removal of the coordinated acetate ligand and the dehydroxylation of the Zr_6 cornerstones. The acetate was indeed revealed from ssNMR to be coordinatively connected to Zr-oxo cluster in the MOF. These transformations are already well established during the thermal decomposition of Zr-based UiO type MOFs. The second step occurring between 280 °C and 500 °C can be attributed to an exothermal decomposition of the linker to yield zirconium carbonate as was already reported for zirconium fumarate. Further two light weight losses occur at about 750 °C and 950 °C respectively, that we tentatively ascribed to final decomposition of the zirconium carbonate in two steps, yielding ZrO_2 with release of CO_2.

The presence of acetate coordinated to the Zr-oxo cluster suggested the presence in the framework of missing linker defects. TGA and DSC were used to determine the missing linker ratio per $Zr_6O_4(OH)_4$ cluster following the method previously reported.[15 It was obtained from this method that 1 (calc.1.05) linker out of 6 is missing per Zr_6 unit. This result is in agreement with that obtained from EDX spectroscopy (calc. 0.96). Noteworthy is the presence in the DSC trace of three endothermic peaks in the dehydroxylation region (210-270 °C). This suggests the coexistence in the framework of three distinct cornerstones, which we hypothetically attributed to be Zr_6 clusters without defects, Zr_6 clusters with defects capped with acetate and Zr_6 cluster with defects capped with water molecules. The presence of water molecules capping some defects could explain the very broad desolvation endotherm till about 185 °C.

- Missing linker defect calculation (according to Shearer *et al.*[15])

The ideal (defect-free) **HHU-2** (Zr-Fum-Cl) MOF formula would be $[Zr_6O_4(OH)_4(\text{Fum-Cl})_6]$.

The dehydroxylated form $Zr_6O_6(\text{Fum-Cl})_6$ would yield 6 ZrO_2 solid residue upon complete decomposition.

Masse of solid residue: $6 \times M(ZrO_2) = 736.34$ g

Molar mass of ideal **HHU-2** (Zr-Fum-Cl): $M[Zr_6O_6(\text{Fum-Cl})_6] = 1534.35\ \text{g mol}^{-1}$, a factor of 2.075 higher than solid residue.

The ideal plateau of dehydroxylated MOF should then be found at 207.52% on the TG trace normalized to 100% solid residue i.e $Wt_{\text{ideal plat.}} = 207.52\%$ and $W_{\text{end}} = 100\%$.

The experimental plateau of final dehydroxylation is found at $T_{\text{exp.plat.}} = 270$ °C, as indicated by the end endotherm of dehydroxylation on the DSC trace. Which correspond to a weight $Wt_{\text{exp.plat.}} = 188.8\%$.

A value for expected weight loss per Fum-Cl linker out of $NL_{\text{ideal}} = 6$ linkers is:

$Wt_{\text{pL.teo}} = (Wt_{\text{ideal plat.}} - W_{\text{end}}) / NL_{\text{ideal}} = (207.52 - 100) / 6 = 17.92\%$

The number of experimental linkers per Zr_6 cluster is:

$NL_{\text{exp.}} = 6 - x = (Wt_{\text{exp. plat.}} - W_{\text{end}}) / Wt_{\text{pL.theo}} = (188.8 - 100) / 17.92 = 4.95$ and then the number of linker defeciencies per Zr_6 cluster is $x = 1.05$

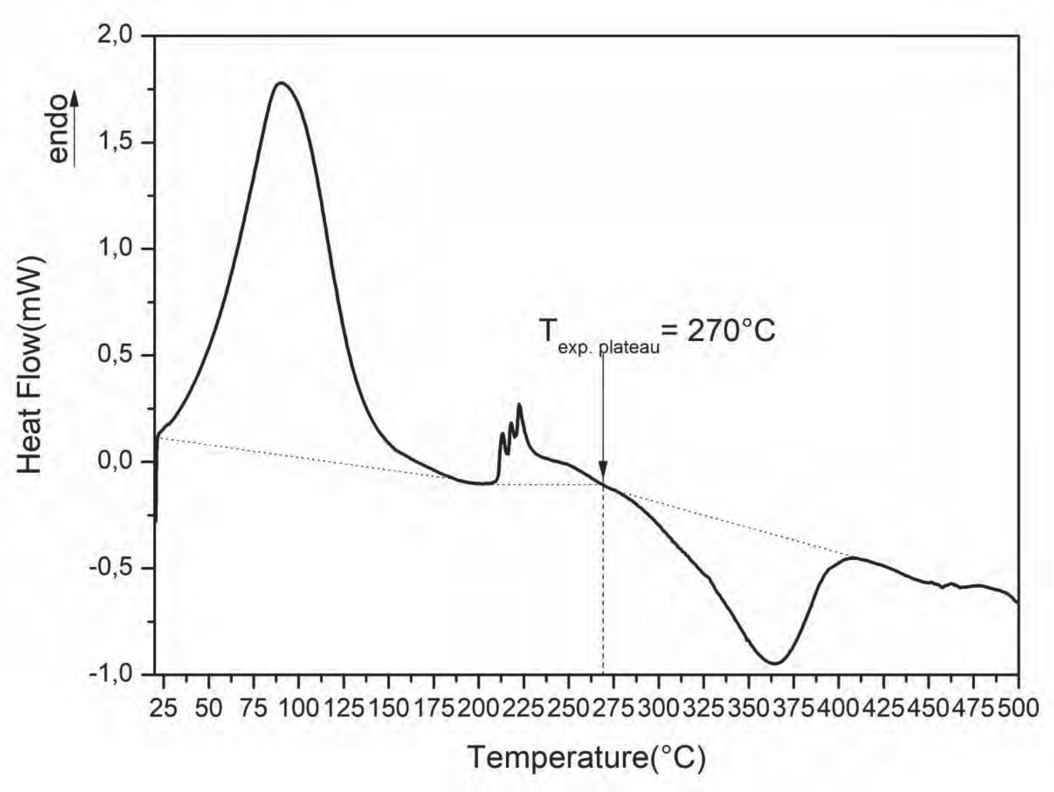

Figure S17. DSC trace of **HHU-2** (Zr-Fum-Cl).

- Chemical stability

The chemical stability of **HHU-1** (Zr-ADC) was investigated by stirring at room temperature for 24h samples in different solvents and aqueous solutions including water, methanol, acetone, DMF, ethanol, aqueous 0.1 mol/L HCl and 0.01 mol/L NaOH. By PXRD (Figure S18) it is evident that **HHU-1** (Zr-ADC) loses most of its crystallinity. **HHU-1** (Zr-ADC) has thus a rather moderate chemical stability compared to the parent UiO-66.

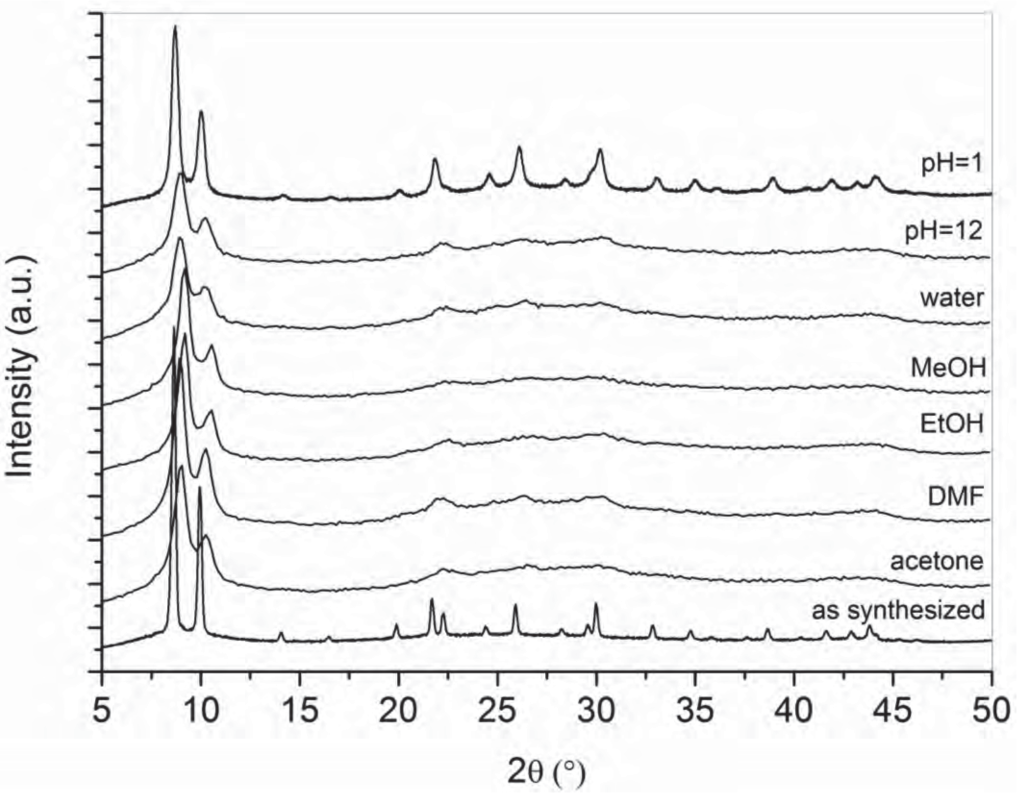

Figure S18. PXRD patterns of **HHU-1** (Zr-ADC) after stirring in different solutions/solvents for 24 h at room temperature.

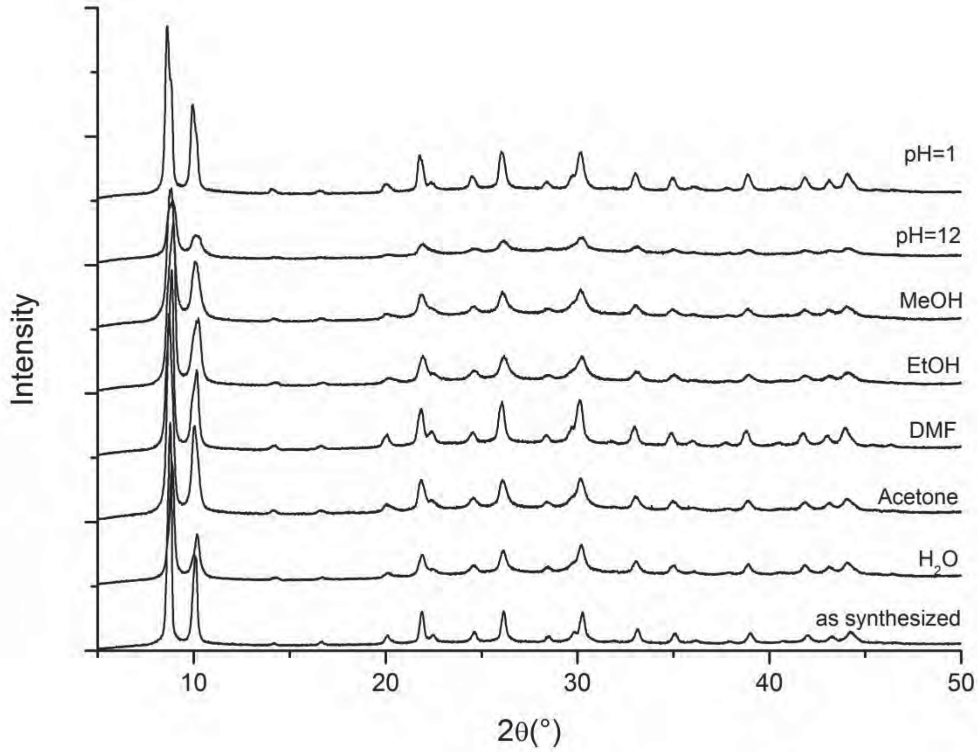

Figure S19. PXRD patterns of **HHU-2** (Zr-Fum-Cl) after stirring in different solutions/solvents for 24h.

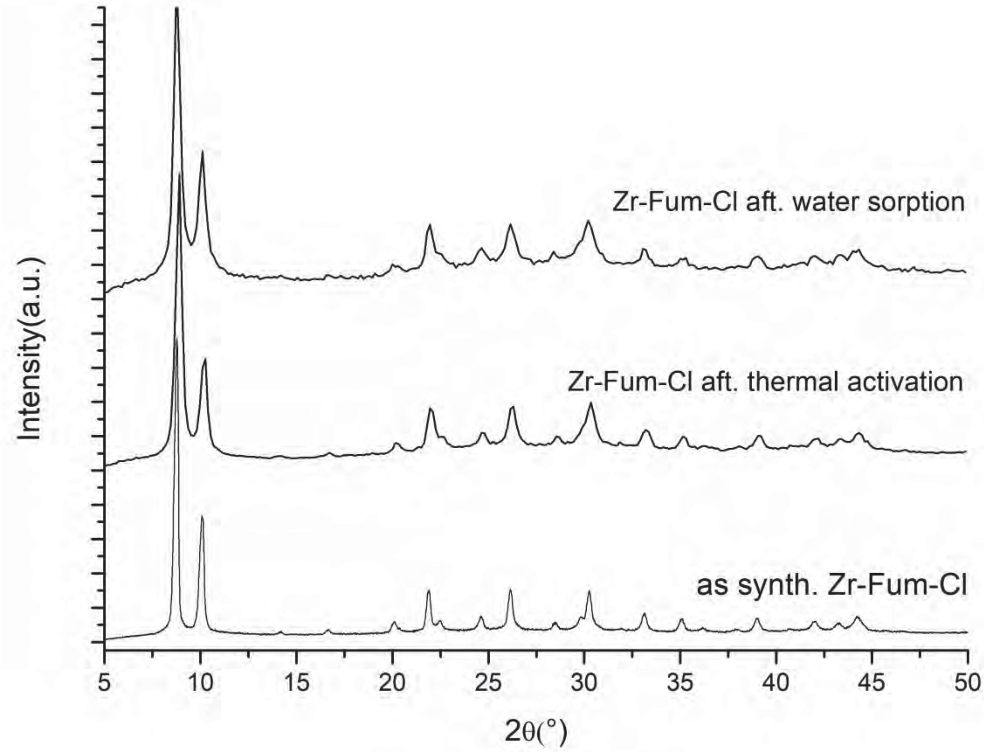

Figure S20. PXRD patterns of **HHU-2** (Zr-Fum-Cl) after thermal activation at 110°C and after water sorption in comparison to that of as-synthesized sample.

It is noticeable that Zr-Fum-Cl is stable in all this solutions as its crystalllinity was retained, except in aqueous NaOH (pH=12) for which a sensible loss of crystallinity is observed. So the chemical stability of Zr-Fum-Cl follows the same trend with others Zr-based MOFs like Zr-fumarate.

Nitrogen and argon sorption analyses

Argon is an alternative adsorptive for surface area determination at 87 K, i.e., at liquid argon temperature. Argon does not have a quadrupole moment. At 87 K, a cross-sectional area, σ_m(Ar), of 0.142 nm^2 is usually assumed. Because of the absence of a quadrupole moment and the higher temperature, σ_m(Ar) is less sensitive to differences in the structure of the adsorbent surface. Furthermore, argon adsorption at 87 K offers advantages in particular for micropore analysis.[16] At 87 K, argon fills narrow micropores at significantly higher relative pressures in comparison with nitrogen at 77 K. This leads to accelerated equilibration and permits the measurement of high resolution adsorption isotherms. Argon adsorption at 87 K allows a much more straightforward correlation to be obtained between the pore filling pressure and the confinement effect (depending on pore width and shape), particularly important for zeolitic materials, metal organic frameworks (MOFs) and others.[16]

For **HHU-1** (Zr-ADC) the N_2 and Ar isotherms in Figure S21 are of Type Ib at lower and Type II at higher relative pressure, the latter due to interparticle macropore condensation.

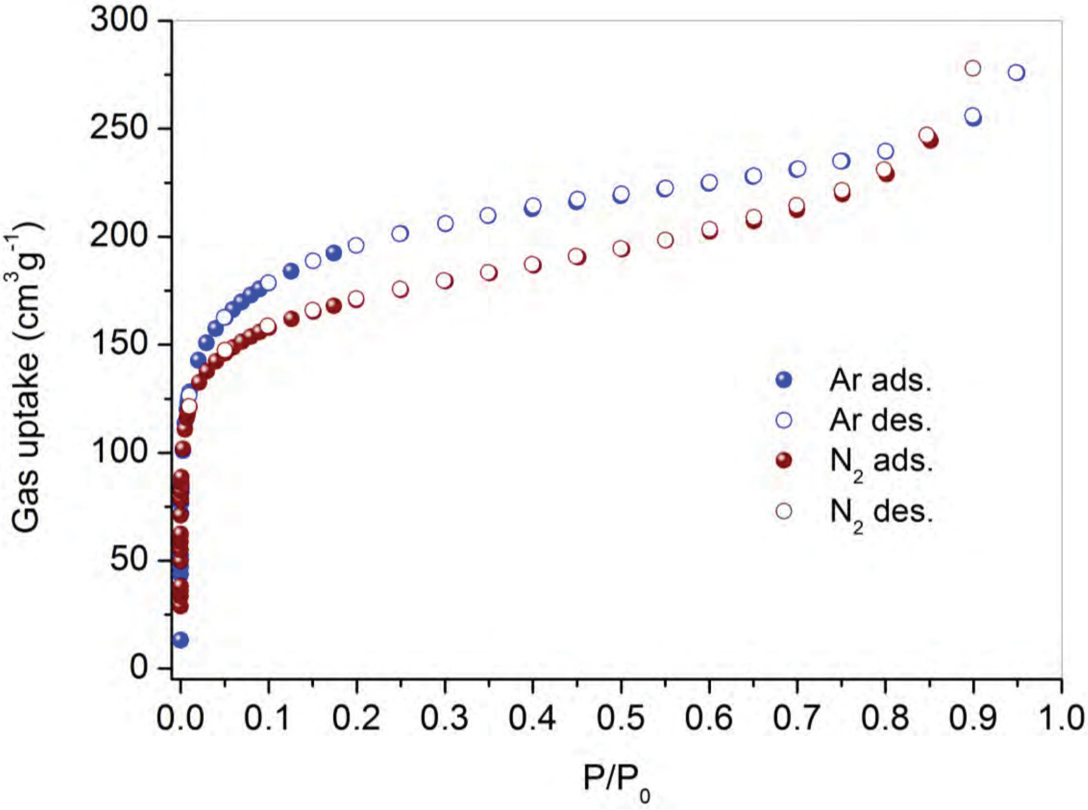

Figure S21. Nitrogen (77 K) and argon (87 K) sorption isotherms of **HHU-1**.

Table S5. Porosity data of **HHU-1** and related Zr-MOFs from Ar and N_2 sorption.

Adsorptive	**S_{BET} [m^2g^{-1}] [a]**	**$S_{micro\text{-}BET}$ [m^2g^{-1}] [b]**	**S_{Ext} [m^2g^{-1}] [c]**	**$V_{pore\ (total)}$ [cm^3g^{-1}] [d]**	**$V_{pore\ (NLDFT)}$ [cm^3g^{-1}] [e]**	**$V_{pore\ (micro)}$ [cm^3g^{-1}] [f]**
Ar	619	457	162	0.38	0.26	0.19
N_2	551	457	94	0.29	0.43	0.19
Comparison to MOF-801 (Zr-fumarate)[g]						
N_2 [h]	790 [i]	684	106	0.39	0.36	0.27
Comparison to UiO-66 (Zr-benzene-dicarboxylate)						
N_2	1031	949	81	0.44	0.41	0.33

[a] BET surface areas (S_{BET}) were obtained from five adsorption points in the pressure range pp_0^{-1}=0.001-0.05. [b] Micropore areas ($S_{micro\text{-}BET}$) were obtained by t-plot and V-t-method. [c] External area (S_{Ext}) refers to all area that does not originate from micropores and it includes meso- and macropores, i.e. pores > 2nm. Obtained by t-plot and V-t-method. [d] Total pore volumes ($V_{pore\ (total)}$) were derived at pp_0^{-1} = 0.95 for pores ≤ 20 nm. [e] Pore volumes from NLDFT ($V_{pore\ (NLDFT)}$) were calculated using 'N_2 at 77 K on carbon, slit pore, NLDFT equilibrium' model. See Figure S22 for the pore size distribution. [f] Micropore volume ($V_{pore\ (micro)}$) refers to volume that originates only from micropores, obtained by V-t-method with thickness method 'DeBoer'. All correlation coefficients (r) within calculations were >0.999. [g] MOF-801 is the second smallest Zr-MOF with **fcu** topology, containing two crystallographically independent tetrahedral cavities, with slightly different sizes of 5.6 Å and 4.8 Å diameter and an octahedral cavity of 7.4 Å diameter. [h] Synthesized by acetic acid modulation, from reference [17]. [i] Reported surface areas for MOF-801 range from up to 960 m^2 g^{-1} [18] down to 590 m^2 g^{-1}.[17]

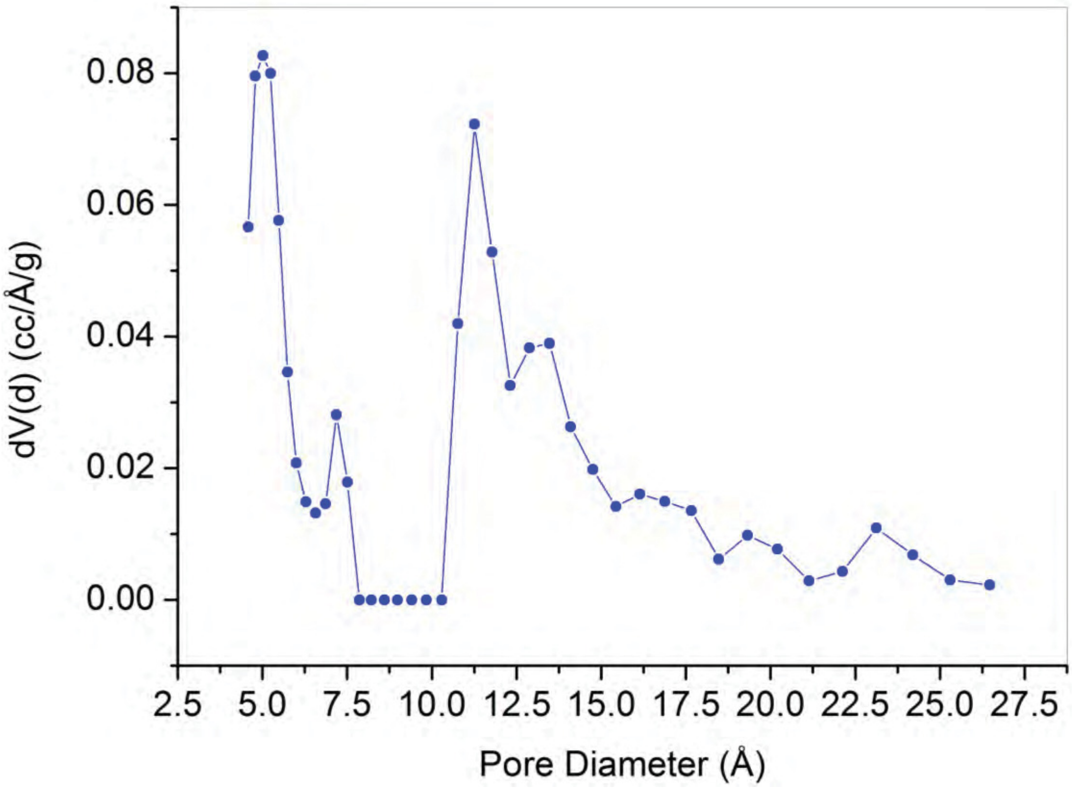

Figure S22. Pore size distribution analysis of **HHU-1** (Zr-ADC) MOF from Ar sorption isotherm with the NLDFT model.

Table S6. Porosity parameters of HHU-2 (Zr-Fum-Cl).

Adsorptive	S_{BET} $[m^2g^{-1}]$ [a]	$S_{micro\text{-}BET}$ $[m^2g^{-1}]$ [b]	S_{Ext} $[m^2g^{-1}]$ [c]	$V_{pore\ (total)}$ $[cm^3g^{-1}]$ [d]	$V_{pore\ (NLDFT)}$ $[cm^3g^{-1}]$ [e]	$V_{pore\ (micro)}$ $[cm^3g^{-1}]$ [f]
Ar	460	383	77	0.22	0.27	0.143
N2	450	390	60	0.25	0.23	0.15

[a] BET surface areas (S_{BET}) were obtained from five adsorption points in the pressure range pp_0^{-1}=0.001-0.05. [b] Micropore areas ($S_{micro\text{-}BET}$) were obtained by t-plot and V-t-method. [c] External area (S_{Ext}) refers to all area that does not originate from micropores and it includes meso- and macropores, i.e. pores > 2nm. Obtained by t-plot and V-t-method. [d] Total pore volumes ($V_{pore\ (total)}$) were derived at pp_0^{-1} = 0.95 for pores ≤ 20 nm. [e] Pore volumes from NLDFT ($V_{pore\ (NLDFT)}$) were calculated using ‘N_2 at 77 K on carbon, slit pore, NLDFT equilibrium’ model. See Figure S24 for the pore size distribution. [f] Micropore volume ($V_{pore\ (micro)}$) refers to volume that originates only from micropores, obtained by V-t-method with thickness method ‘DeBoer’. All correlation coefficients (r) within calculations were >0.999.

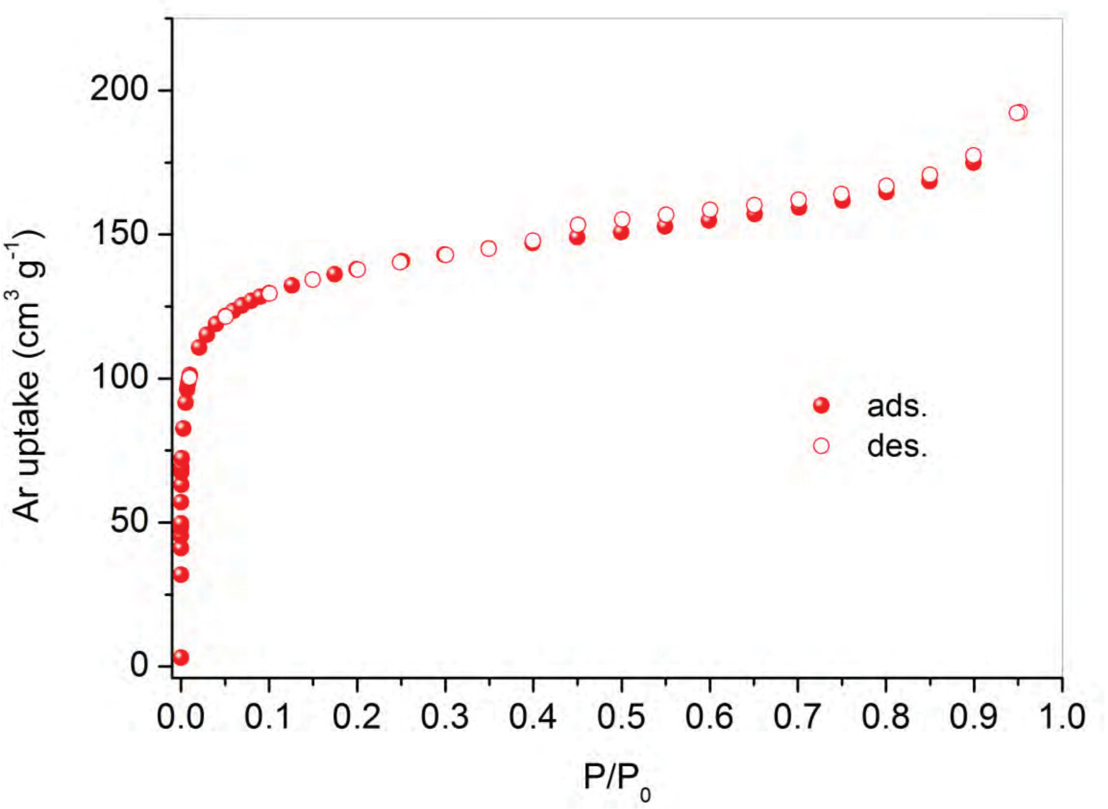

Figure S23. Argon sorption isotherms of **HHU-2** (Zr-Fum-Cl) at 87 K.

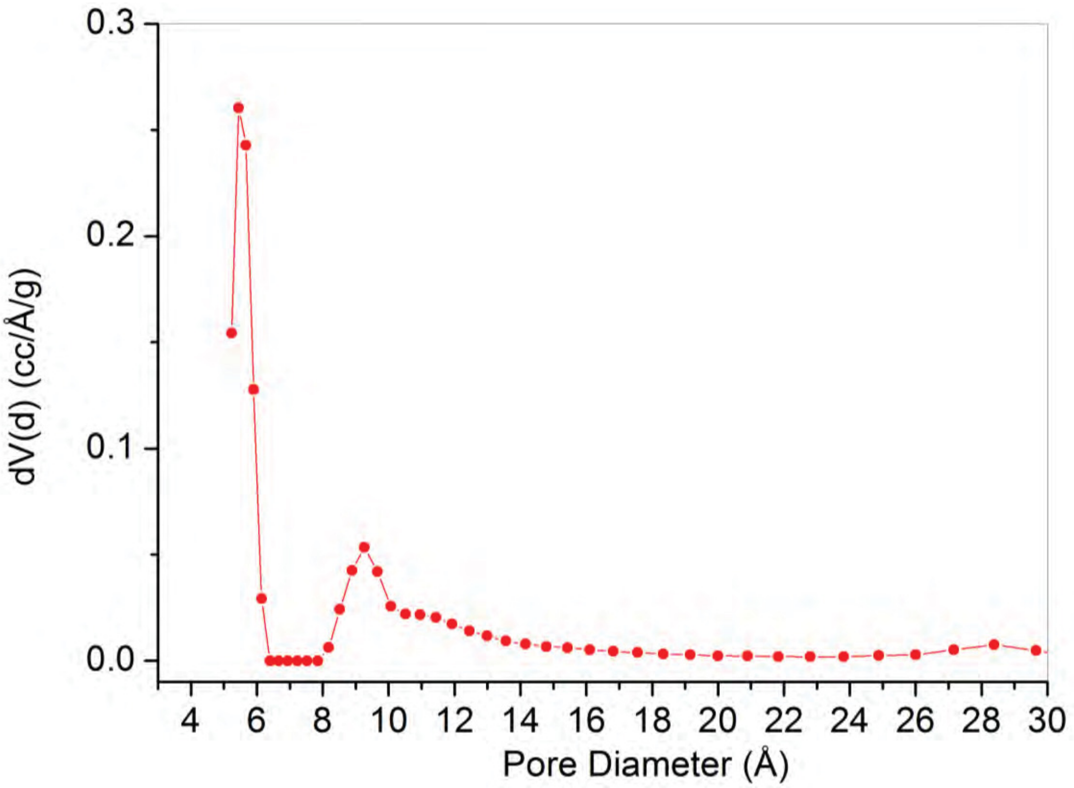

Figure S24. Pore size distribution analysis of **HHU-2** (Zr-Fum-Cl) from Ar sorption isotherm with the QSDFT model.

Water vapor sorption analyses

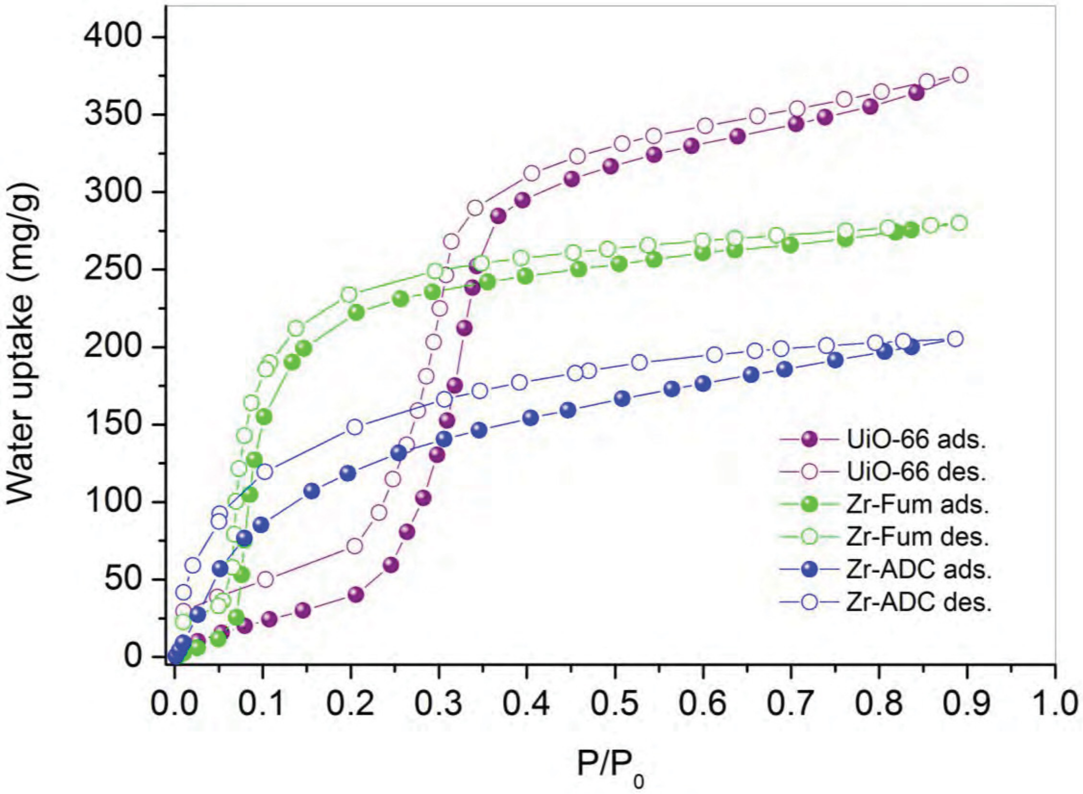

Figure S25. Water ad- and desorption isotherm for **HHU-1** (Zr-ADC), MOF-801 (Zr-fumarate) and UiO-66.

MOF-801 and UiO-66 have been synthesized according to previously reported procedure.[18] Their PXRD patterns were positively matched to the respective simulated diffractograms. Their BET surface areas from N_2 adsorption were determined as 790 m^2 g^{-1} and 1295 m^2 g^{-1} for MOF-801 and UiO-66 respectively.

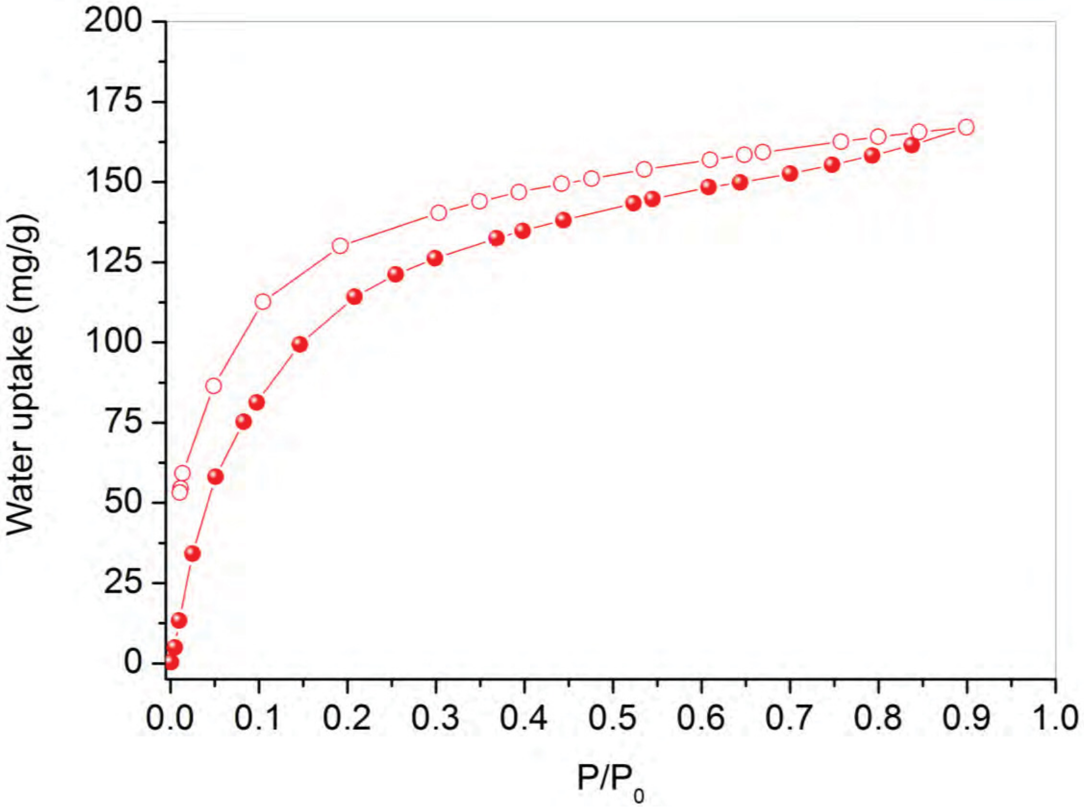

Figure S26. Water vapor sorption isotherms of **HHU-2** (Zr-Fum-Cl) at 20 °C.

CO_2 sorption analyses

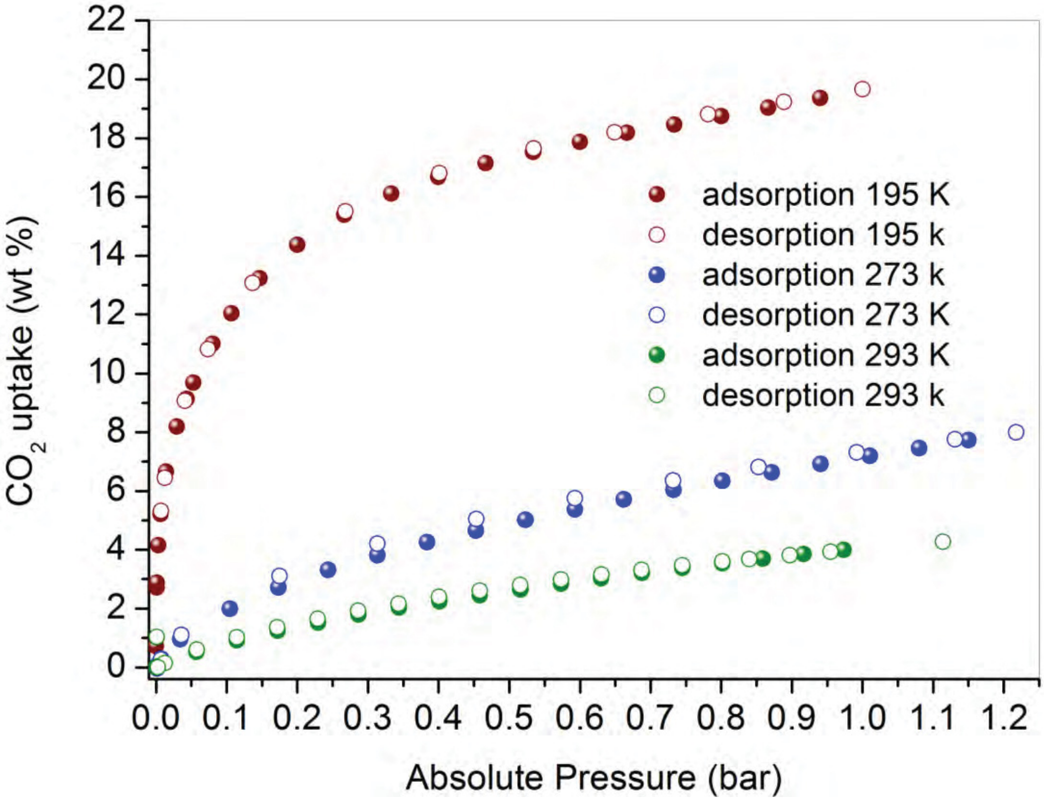

Figure S27. CO_2 sorption isotherms of **HHU-1** (Zr-ADC) at 195, 273 and 293 K.

As shown in Figure S27, the CO_2 adsorption of **HHU-1** (Zr-ADC) displays reversible type I isotherms. At 1 bar, the CO_2 uptakes are 19.65 wt% (4.46 mmol g^{-1}), 7.45 wt% (1.69 mmol g^{-1}), 4 wt% (0.9 mmol g^{-1}) at 195 K, 273 K and 293 K, respectively, without reaching saturation. The CO_2 uptake of **HHU-1** is lower than that of the parent UiO-66 MOF (2.88 mmol l^{-1}, at 273 K and 1 bar)[19], which is in agreement with a lower surface area and pore volume of **HHU-1** compared to UiO-66. However, the CO_2 sorption capacity of **HHU-1** is comparable to many Zr-MOFs and other MOFs reported (Table S7).

To investigate the total CO_2 sorption capacity of **HHU-1**, high-pressure CO_2 adsorption experiment was performed at 293 K up to 20 bar. The CO_2 uptake (Figure S28) is 72.7 wt% at 293 K and 20 bar. Nevertheless, the CO_2 adsorption saturation was not still reached at such a high pressure. Indeed, the Toth fit of CO_2 sorption isotherm indicates the maximum loading to be 79.6 wt% (18.1 mmol g^{-1}) at 293 K (see Table S9).

Table S7. Lower-Pressure CO_2 adsorption capacities in MOFs at 273 K, 1 bar and isosteric (Q_{st}) heat of adsorption

Chemical formula	**Common name**	**BET**[a]	**Langmuir**[a]	**CO_2 capacity**[b]	**- Q^o_{st}**[c]	**Ref.**
$Zn_4O(BDC)_3$	MOF-5	2300		6.6	34[d]	20
$Co_4(m\text{-}OH_2)_4(MTB)_2$	SNU-15	356		7	-	21
$Cu_2(CNBPDC)_2(DMF)_2$	MOF-601	-	980	7.3	-	22
$[Zr_6(\mu_3\text{-}O_4)(\mu_3\text{-}OH)_4(BDC\text{-}(COOH)_2)_6]$	UiO-66-$(COOH)_2$	-	217	7.48	33.6[e]	19,23
$[Zr_6(\mu_3\text{-}O_4)(\mu_3\text{-}OH)_4(BDC\text{-}Cl_2)_6]$	UiO-66-$(Cl)_2$	-	609	7.39	-	19
$[Zr_6(\mu_3\text{-}O_4)(\mu_3\text{-}OH)_4(BDC)_6]$	UiO-66	1434		15.51	28[e]	19,24
$[Zr_6(\mu_3\text{-}O_4)(\mu_3\text{-}OH)_4(BDC\text{-}NH_2)_6]$	UiO-66-NH_2	1220		19.62	29.4[e]	22
$[Zr_6(\mu_3\text{-}O_4)(\mu_3\text{-}OH)_4(BDC\text{-}(OH)_2)_6]$	UiO-66-$(OH)_2$	705		12.21	30.1[e]	23
$[Zr_6(\mu_3\text{-}O_4)(\mu_3\text{-}OH)_4(ADC)_6]$	**HHU-1** (Zr-ADC)	617		7.45	60[e]	This work

[a] $m^2 \cdot g^{-1}$; [b] wt%; [c] $kJ \cdot mol^{-1}$; [d] Q^o_{st} calculated by fitting with Freundlich isotherm model; [e] Q^o_{st} calculated with Clausius-Clapeyron equation.

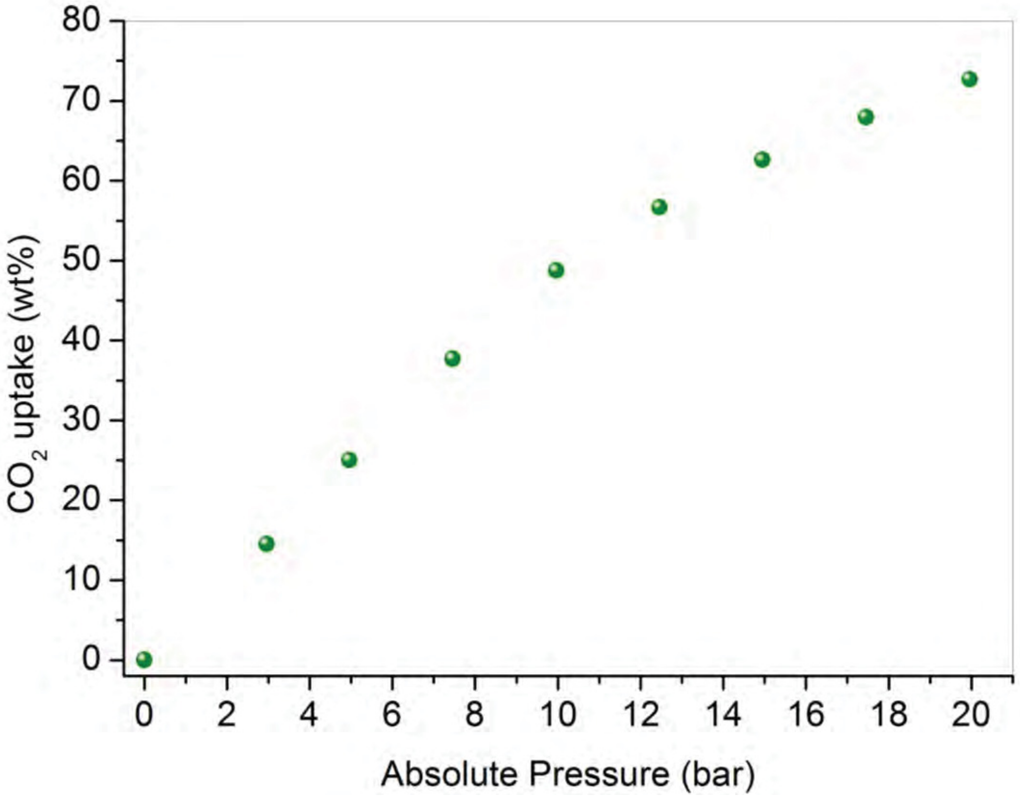

Figure S28. High pressure CO_2 adsorption isotherm of **HHU-1** (Zr-ADC) at 293 K.

H_2 sorption analyses

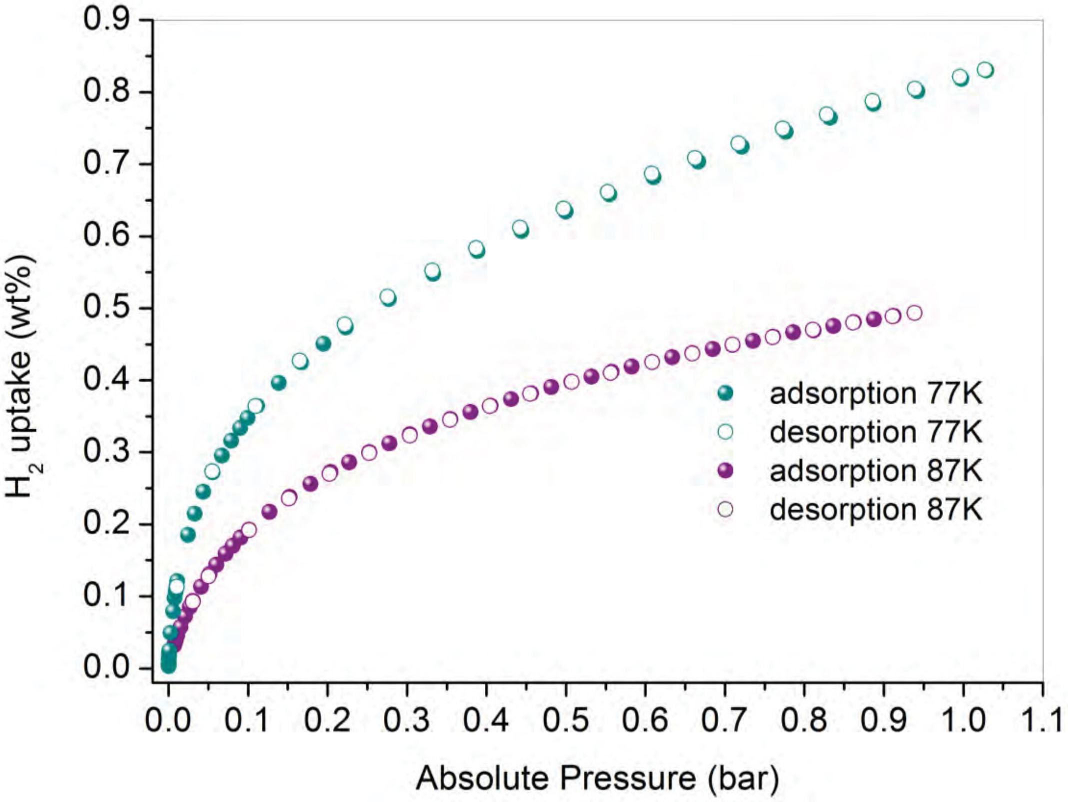

Figure S29. H_2 sorption isotherms of **HHU-1** (Zr-ADC) at 77 and 87 K.

The hydrogen sorption of **HHU-1** (Zr-ADC) MOF was measured at 77 K and 87 K respectively. The measured sorption isotherms (Figure S29) show a fully reversible Type I behavior, as evidenced by the complete coincidence of the adsorption and desorption curves. At 1 bar, H_2 uptakes are 0.83 wt% (4.10 mmol g^{-1}) and 0.5 wt% (2.47 mmol g^{-1}) at 77 and 87 K respectively. The H_2 uptake is lower than that of parent UiO-66(Zr) (1.6 wt% at 77K, 1bar), which is in agreement with a lower surface area. However the H_2 sorption performance of **HHU-1**, when normalized to the BET surface area (4.10 mmol g^{-1} / 618 m^2 g^{-1} = 0.0066 mmol / m^2) is higher than that of UiO-66 (7.92 mmol g^{-1} / 1434 m^2 g^{-1} = 0.0055 mmol / m^2) at 77 K and 1 bar.[24] Furthermore, the H_2 adsorption isotherms show a steep increase up to 1 bar and do not reach saturation to that pressure. Therefore, higher H_2 uptakes would be expected at elevated pressures. The maximum H_2 loading at this temperature is estimated from the Toth isotherm model to 1.57 wt% (see below).

The isosteric heat of H_2 at zero adsorption (Q^0_{st}) of **HHU-1** (Zr-ADC) of slightly above 10 kJ mol^{-1} is comparable with the zero-coverage heat of H_2 adsorption for the parent UiO-66(Zr) (10 kJ mol^{-1}).[25] In both MOFs the enthalpy of adsorption (Q_{st}) decreases rapidly to about 7 kJ mol^{-1} (cf. Fig. 4b in manuscript). This indicates the presence of a small amount of strong binding sites. It was indeed demonstrated that μ_3-OH hydroxyl groups of $Zr_6O_4(OH)_4$ SBU are the strongest binding sites of H_2 in UiO-66 and UiO-67.[26] The similarity in enthalpy of adsorption profile of two MOFs suggests that the interaction between H_2 and μ_3-OH groups of the $\{Zr_6O_4(OH)_4\}$ SBU in UiO(Zr)-type MOFs plays a key role in the enthalpy of H_2 adsorption. The pore size reduction in the case of **HHU-1** (Zr-ADC) does not contribute to enhance the enthalpy of H_2 adsorption. Zlotea *et al.* obtained relatively low enthalpies of adsorption for UiO-66(Zr)-NH_2 (7 kJ mol^{-1}) and UiO-66(Zr)-$(CF_3)_2$ (6.5 kJ mol^{-1}) in spite of pore confinement. It was suggested that this decrease in heat of H_2 adsorption could result from the steric shielding of the strong binding sites by the presence of –NH_2 and –$(CF_3)_2$.[25] However, the heat of adsorption for H_2 calculated from the Toth fits of the H_2 adsorption isotherms (12 kJ mol^{-1}) is higher than that obtained from the Clausius-Clapeyron expression (see below).

Theoretical surface area and pore volume

The theoretical surface area and pore volume of the 3D framework **HHU-1** (Zr-ADC) was calculated using the program CrystalExplorer[27] following the methodology outlined in ref.[28], by a 'Void' calculation with Mercury[29] and by a 'Calc Void/Solv' calculation with Platon.[30] The calculated values are listed in Table S8.

Table S8. Surface areas and pore volumes for **HHU-1** (Zr-ADC).

	HHU-1		
Z, $M_{formula\ unit}$ (g mol^{-1}), V ($Å^3$) from Rietveld structures; cf. Table 1 in main manuscript formula unit: $Zr_6(O)_4(OH)_4(O_2CCCCO_2)_6$ = $C_{24}H_4O_{32}Zr_6$ (H not refined)	4, 1351.6, 5758.40(33)		
CrystalExplorer calculation	isovalue		
surface area	0.002	0.0003	
- $S_{unit\ cell}$ ($Å^2$)	1683	1547	
- specific (m^2 g^{-1}) [a]	1875	1723	
pore volume			
- $V_{unit\ cell}$ ($Å^3$)	2925	1875	
- specific (cm^3 g^{-1}) [a]	0.326	0.209	
Mercury 'Void' calculation			
(probe radius 1.2 Å, grid spacing 0.7 Å)	calc. using solvent accessible surface		
void volume $V_{unit\ cell}$ ($Å^3$) [b] (% of unit cell volume) [b] - specific (cm^3 g^{-1}) [a]	1255 (22) 0.140		
	calc. using contact surface		
void volume $V_{unit\ cell}$ ($Å^3$) [b] (% of unit cell volume) [b] - specific (cm^3 g^{-1}) [a]	2917 (51) 0.325		
Platon 'Calc Void/Solv' calculation			
tot. pot. solv. area volume (SAV) ($Å^3$) (% of unit cell vol.) - specific pore volume (cm^3 g^{-1}) from SAV [a]	3078 (53) 0.343		

Comment on the results from CrystalExplorer:

Figure S30 illustrates the iso-surface areas at 0.002 and 0.0003 au around the pore/channel windows.

The 0.0003 au calculated surface area is seen as a better choice for estimating the internal surface area in porous materials than the 0.002 isosurface.[28] The value of 0.002 au corresponds approximately to a smoothed van der Waals surface and 0.0003 au seems to be more appropriate for mapping "empty" space in molecular crystals.[28] From the above comparison in Table S8 it is, however, apparent that the isovalue of 0.002 gives a better match in the pore volumes, which are also derived from Mercury and Platon.

The calculated surface area presents an upper bound which can be approached but it will be physically unrealistic to expect that the experimental measurements will surpass the calculated value.

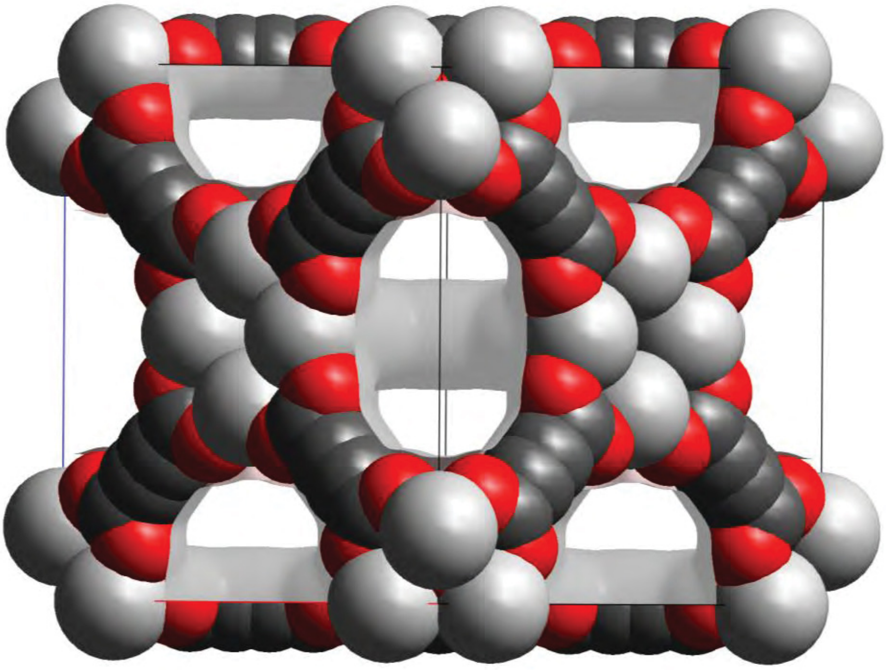

(a)

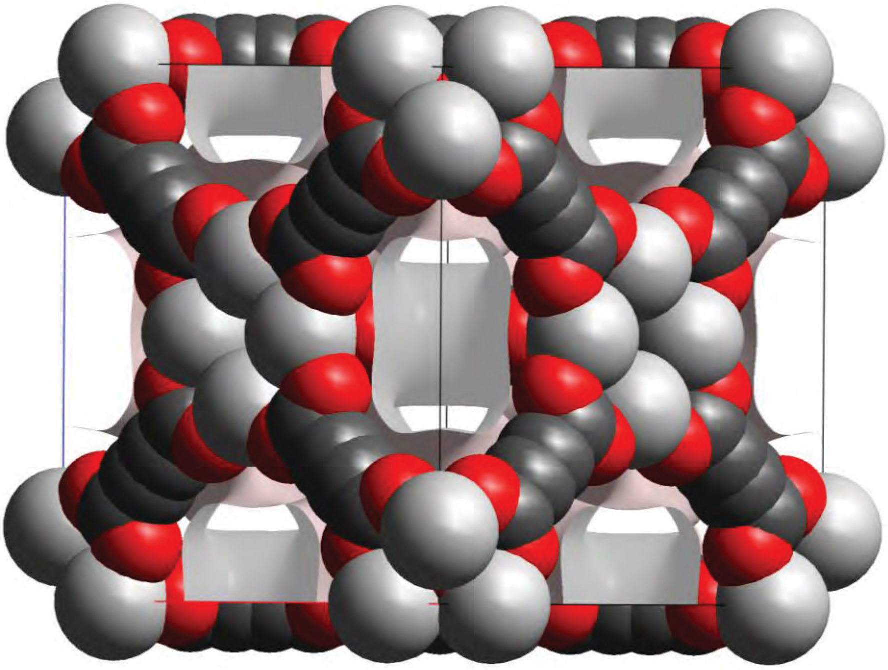

(b)

Figure S30. Void surfaces (a) 0.002 au and (b) 0.0003 au around pore windows in **HHU-1** (Zr-ADC) superimposed on space-filling representations of the unit cell content. From the (vertical) axis length of 17.92 Å, the open channel cross-sections are measured to about 2.1 x 4.2 Å (0.002 au) and 0.8 x 2.8 Å (0.0003 au).

Images from Mercury void calculations

In Mercury[29] voids can be calculated using two different methods:

- Calculate voids using Contact Surface maps the volume that can be occupied by the full probe (including its radius) and thus gives an estimate of the volume that could be filled by solvent or guest molecules.

- Calculate voids using Solvent Accessible Surface gives the volume which can be occupied by the centre of a probe of a given radius.

- A full description of these two different surfaces and the ways in which they can be used is given in: L. J. Barbour, *Chem. Commun.* **2006**, 1163–1168.

(The dimensions of the crystallograpic axes are given to facilitate the estimate of the cross-sections of the pore apertures.)

HHU-1 (Zr-ADC)**:** Probe radius 1.2 Å, grid spacing 0.7 Å; three-dimensional pore system

a=b=c/(Å)	17.9239(3)

void with *solvent accessible surface*:

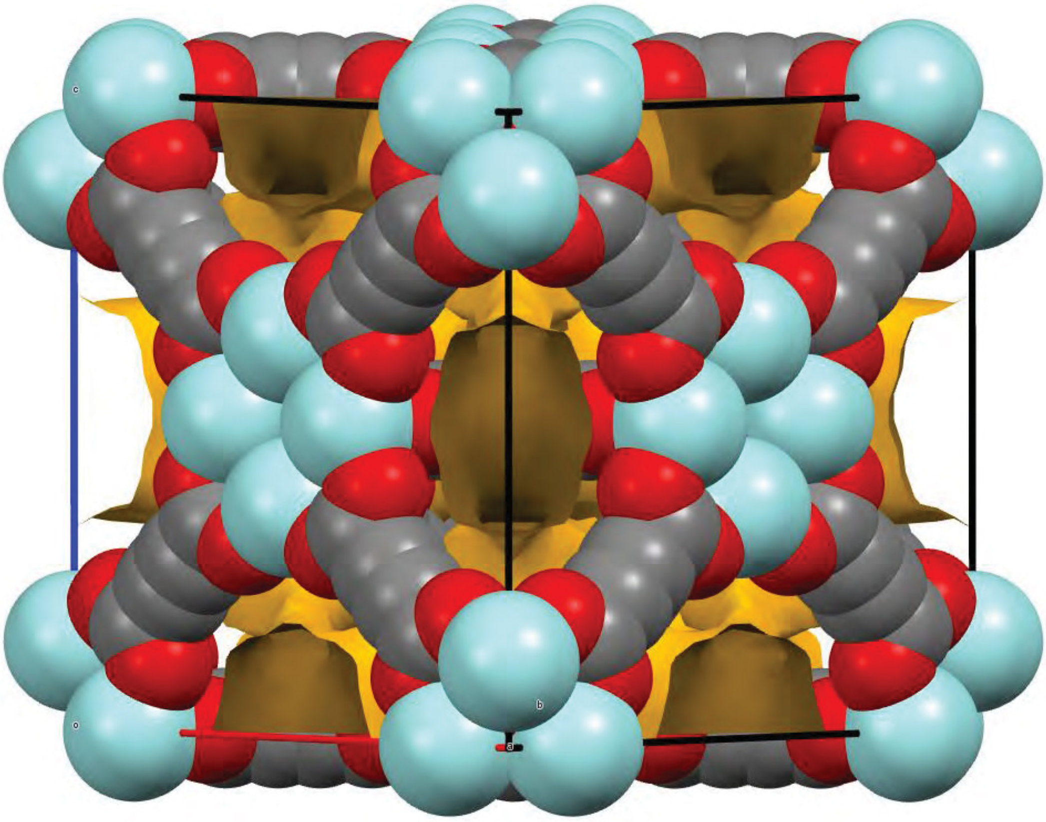

void with *contact surface:*

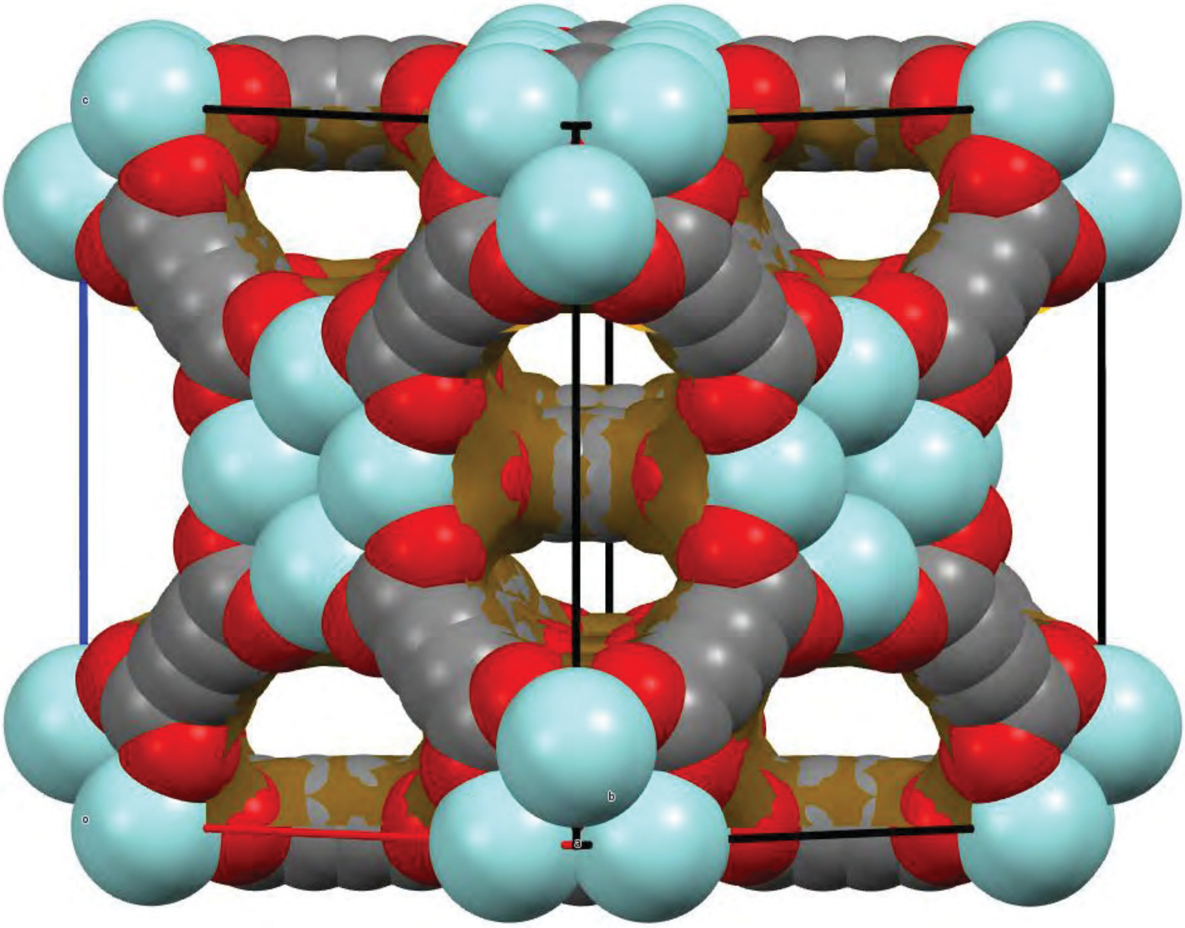

Figure S31a and b. Images from Mercury void calculations for compound **HHU-1**.

Fitting of CO_2 and H_2 adsorption isotherms with the Toth model for HHU-1

CO_2 and H_2 adsorption isotherms of **HHU-1** (Zr-ADC) were fitted with several adsorption isotherm models including Henry, Toth, Freundlich, LAI, SIPS, Dual-site Langmuir, and DS Langmuir SIPS models. For this purpose, adsorption isotherms for each gas, collected at three different temperatures were fitted to the assessed model. The isotherm model was validated based on the best correlation coefficient R^2. For the best fitting adsorption model, were calculated the affinity constant and maximal loading at each temperature and the heat of adsorption. The Toth model showed the best fitting to experimental data both for CO_2 and H_2. Toth fit traces are given in Figure S32 and S33 and fitting parameters obtained are summarized in Table S9.

The Toth equation has the form: $q = q_{max} \cdot K \cdot p / [\, 1 + (K \cdot p)^t]^{1/t}$

Where q is the amount adsorbed, q_{sat} is the amount adsorbed at saturation / maximal loading, p is the equilibrium pressure, K is the Toth constant and t the Toth exponent. K and t describe the heterogeneity of the adsorbent surface.[31]

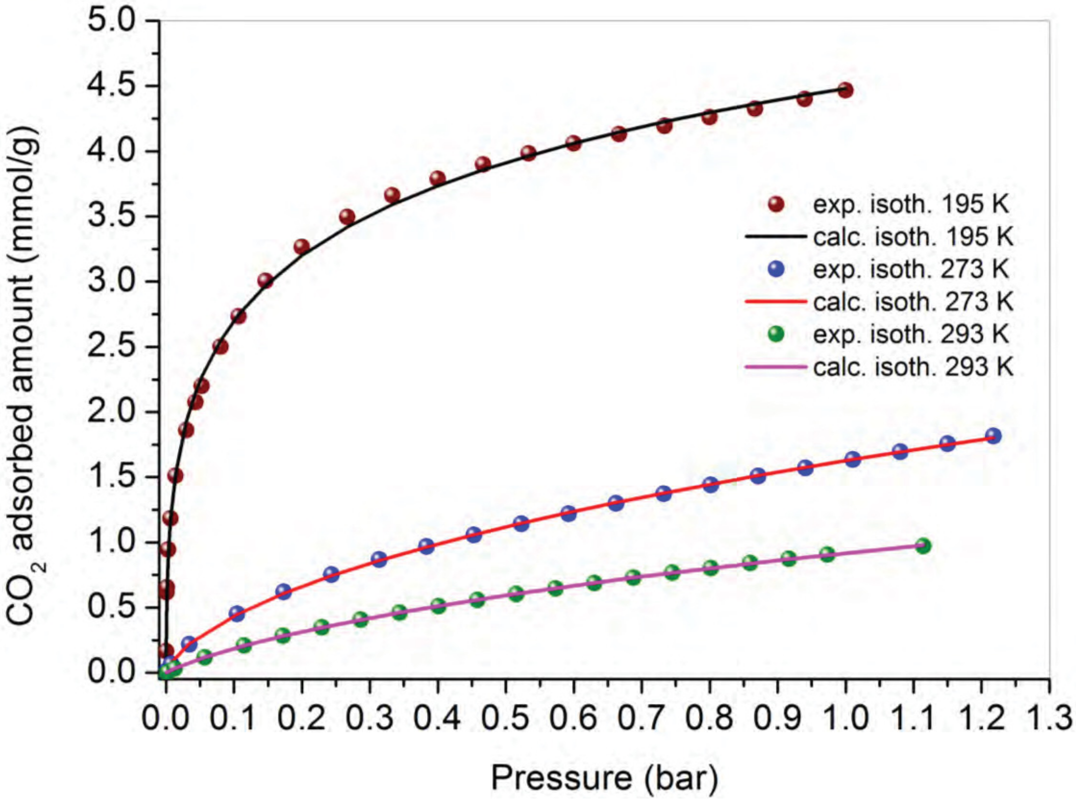

Figure S32. Experimental CO_2 adsorption isotherms of **HHU-1** (Zr-ADC) with corresponding Toth model fits at 195, 273 and 293 K respectively.

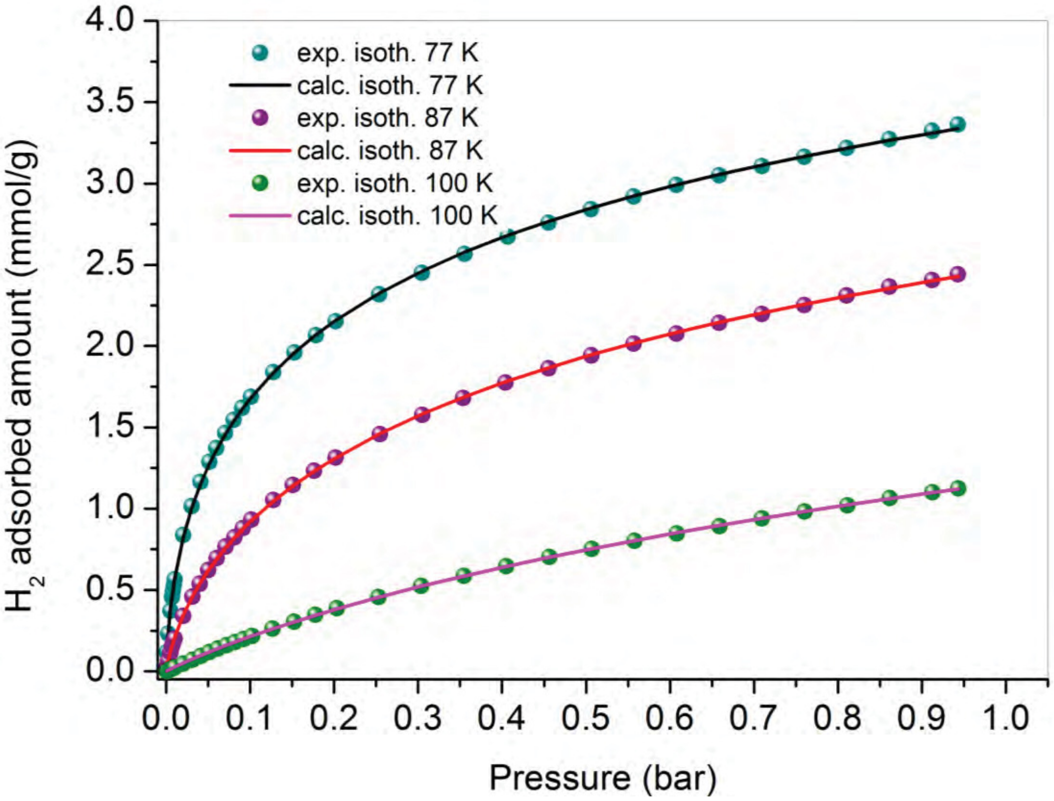

Figure S33. Experimental H_2 adsorption isotherms of **HHU-1** (Zr-ADC) with corresponding Toth model fits at 77, 87 and 100 K respectively.

Table S9. Obtained Toth fitting parameters of CO_2 and H_2 adsorption isotherms for **HHU-1**

Gas	**CO_2**			**H_2**		
Temperature	195 K	273 K	293 K	77 K	87 K	100 K
Toth exponent	0.1801	0.3264	0.4830	0.291826	0.3955	0.6252
correlation coefficient R^2	0.999090	0.999810	0.999925	0.999908	0.999942	0.999949
affinity constant / bar^{-1}	3648	2.2	0.88	43.7	6.5	0.58
maximal loading / mmol g^{-1} [a]	61.8	42.3	18.1	7.8	6.6	4.7
heat of adsorption / KJ mol^{-1}	41.0			12.1		

[a] amount adsorbed at saturation, that is maximal loading for the asymptotic curvature of the adsorption isotherm.

Solid-state and solution ^{1}H and ^{13}C NMR spectroscopy of HHU-2 (Zr-Fum-Cl)

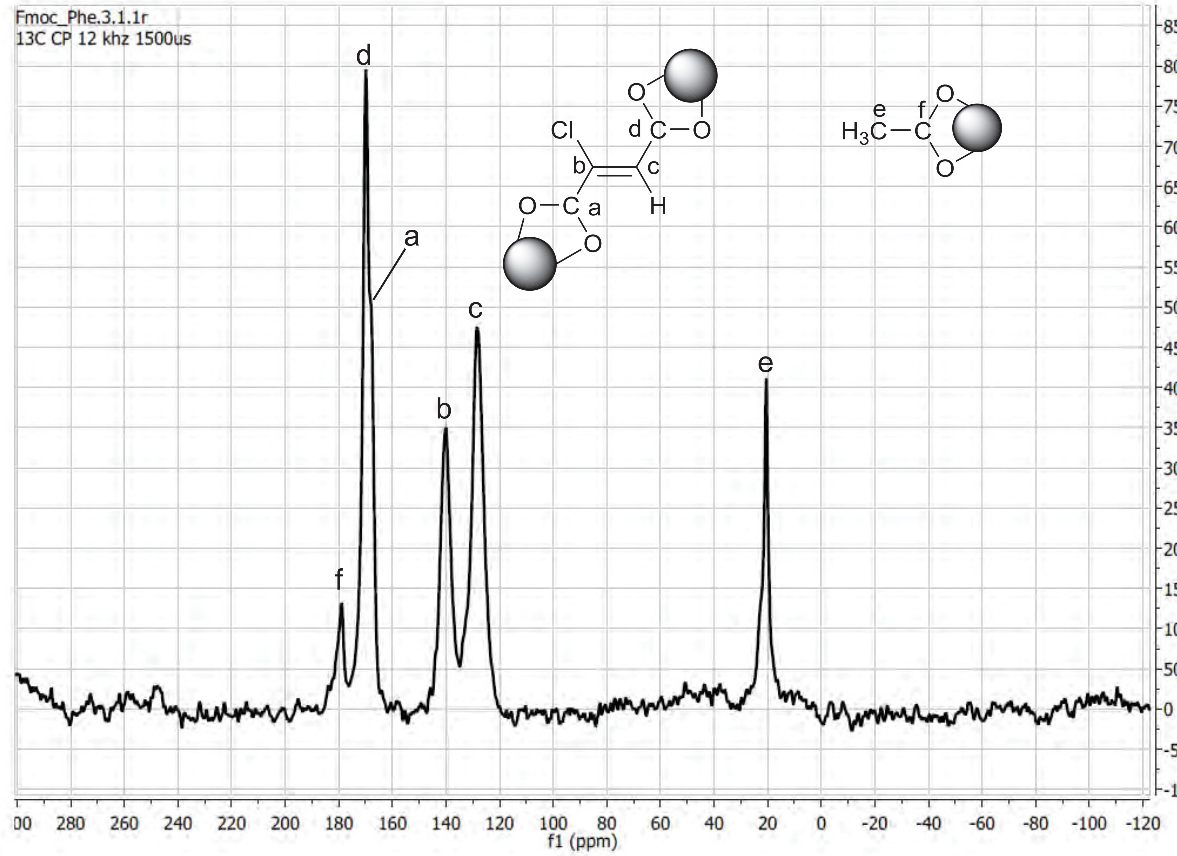

Figure S34. ^{13}C CP MAS solid-state NMR spectrum of **HHU-2** (Zr-Fum-Cl).

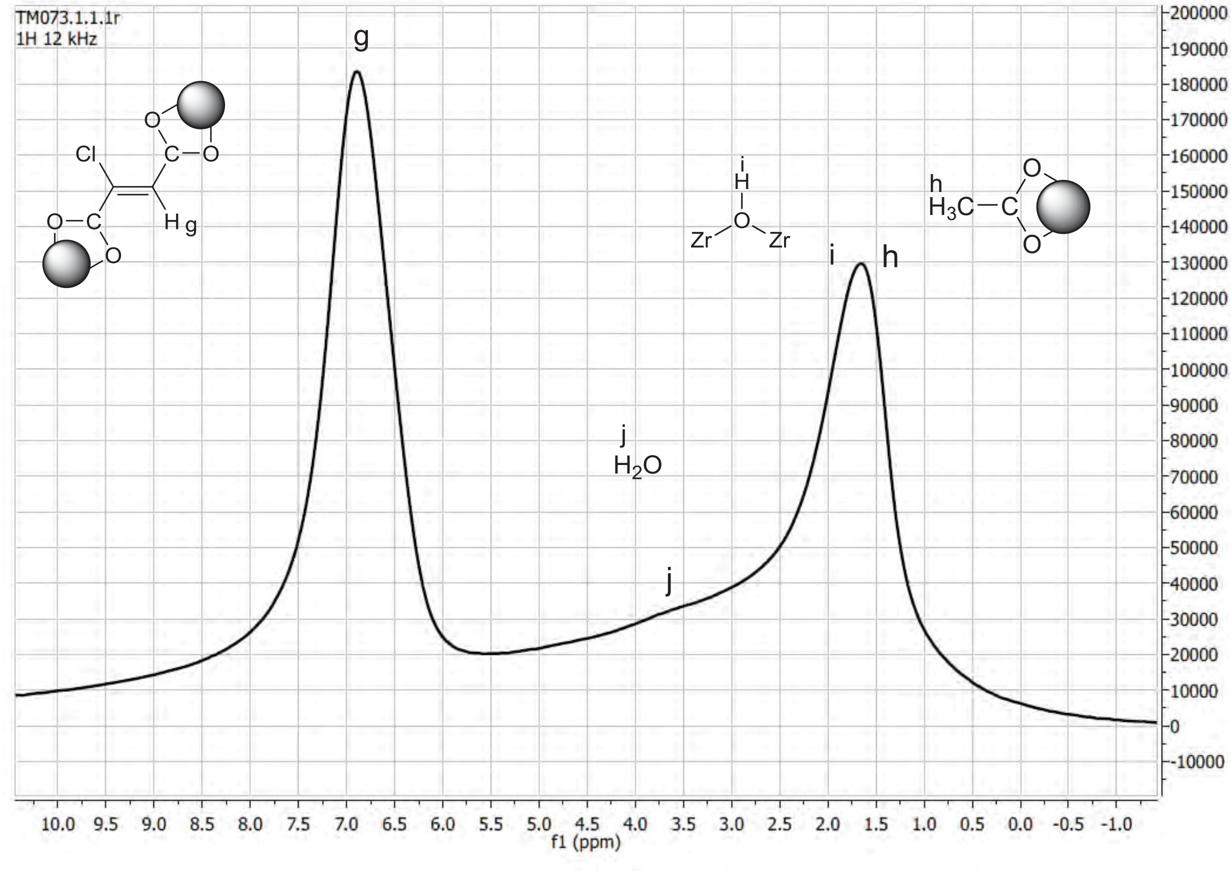

Figure S35. ^{1}H solid-state NMR spectrum of **HHU-2** (Zr-Fum-Cl).

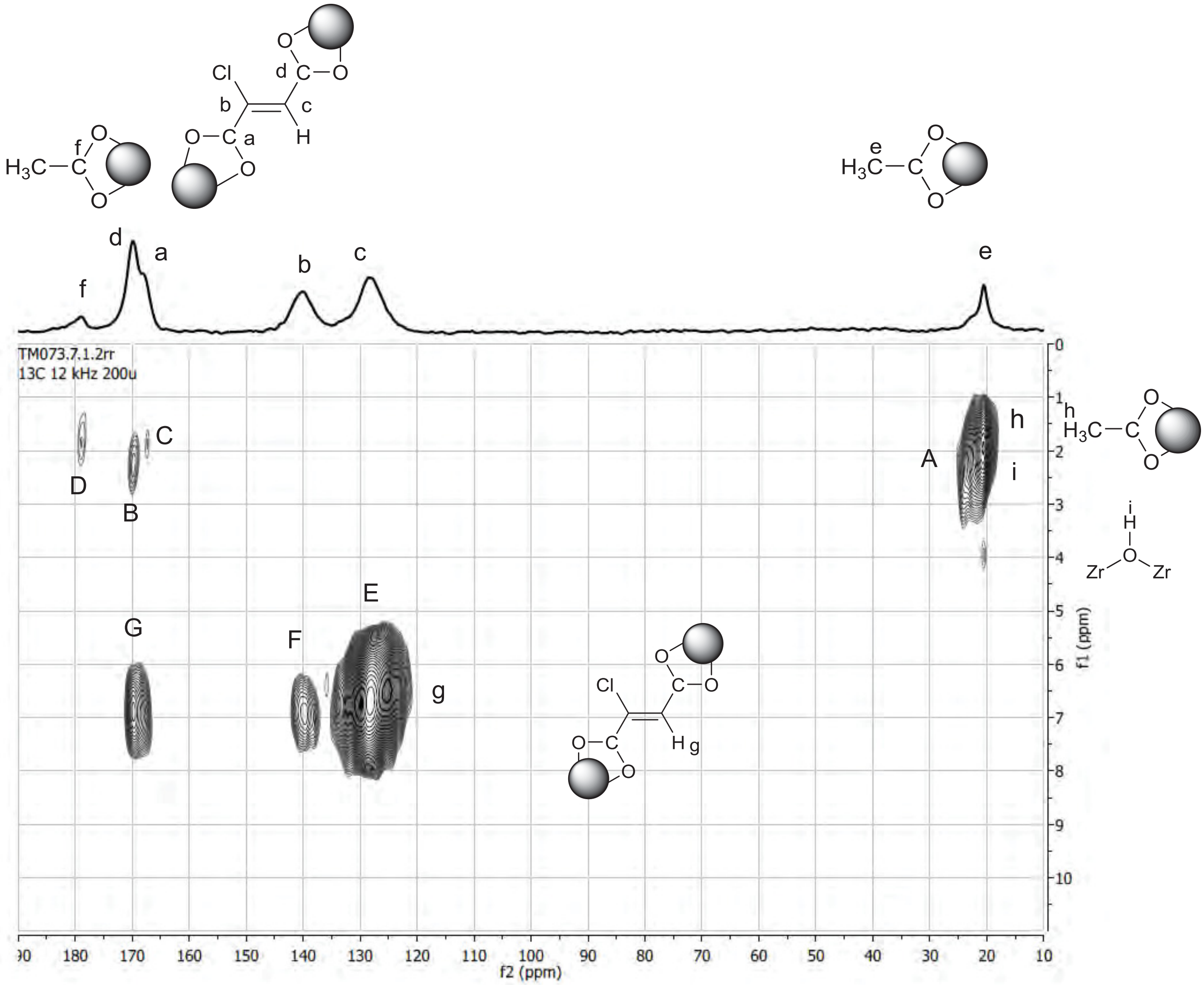

Figure S36. ^{1}H-^{13}C FSLG-HETCOR CP MAS of **HHU-2** (Zr-Fum-Cl) at 12 kHz spinning speed and 200 µs contact time.

The ^{1}H/^{13}C FSLG-HETCOR spectrum recorded with 200 µs contact time (Figure S36) shows the expected intra-ligand correlations (A and D) of the coordinated CH_3COO^- modulator. Further, the protons at at 2.2 ppm and 1.8 ppm correlate with the carbon atoms at 170 ppm. These correlations B and C are ascribed to the protons of µ$_3$-OH groups on the Zr-clusters and the acetate-CH_3 groups, which are in the vicinity of the carboxylates (carbon atoms a and d) of the bridging chlorofumarate ligand. The correlations A to D are depicted below. Therefore these correlations are an additional strong indicator for the **HHU-2** configuration with a bridging Fum-Cl^{2-} ligand and terminal acetate and µ$_3$-hydroxido ligands.

A: correlation

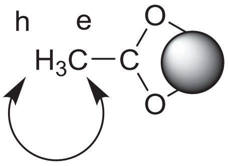

B: correlation

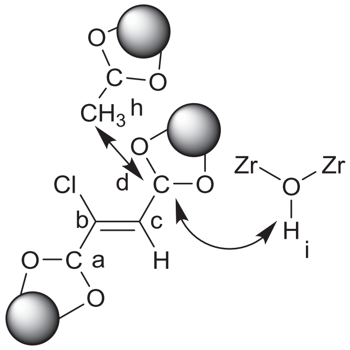

C: correlation

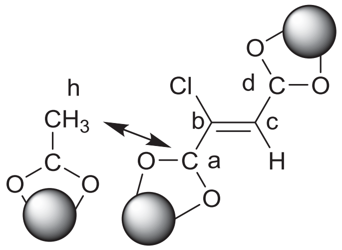

D: correlation

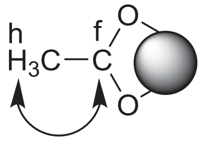

E: correlation g ↔ c

F: correlation g ↔ b

G: correlation g ↔ d

Prior to solution NMR analysis, **HHU-2** (Zr-Fum-Cl) MOF was digested as follows. 6 mg of MOF and 6.11 mg CsF (cesium fluoride) were suspended in DMSO-d_6 (0.65 mL). A drop of aqueous DCl (35 wt%) was added. As soon as the light yellow solid of **HHU-2** had dissolved (after 5-15 min), K_2CO_3 was added to neutralize the acid.[32]

The solution ^{1}H NMR spectrum (Figure S38) shows a 1:1 ratio for the olefinic Fum-Cl and the acetate CH_3 protons. Such a molar 1:1 ratio correlates with 4.5 OOC-CH=CCl-COO-linkers and 1.5 H_3CCOO ligands. The necessary charge equilibration is then obtained with an additional 1.5 OH^- ligands to give the formula $[Zr_6O_4(OH)_5(OOC\text{-}CH{=}CCl\text{-}COO)_{4.5}(H_3CCOO)_{1.5}(OH)_{1.5}]$

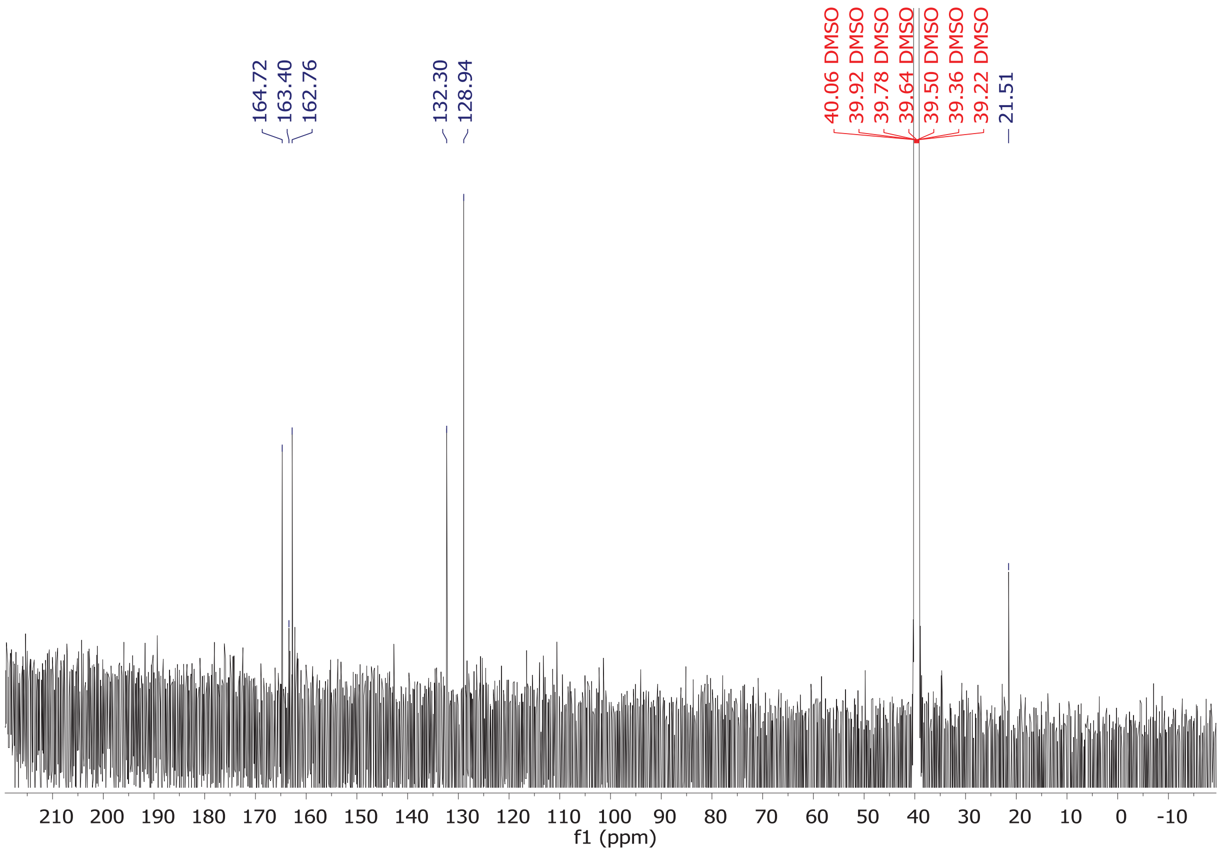

Figure S37. Solution ^{13}C NMR spectrum of digested **HHU-2** (Zr-Fum-Cl) in DMSO-d_6.

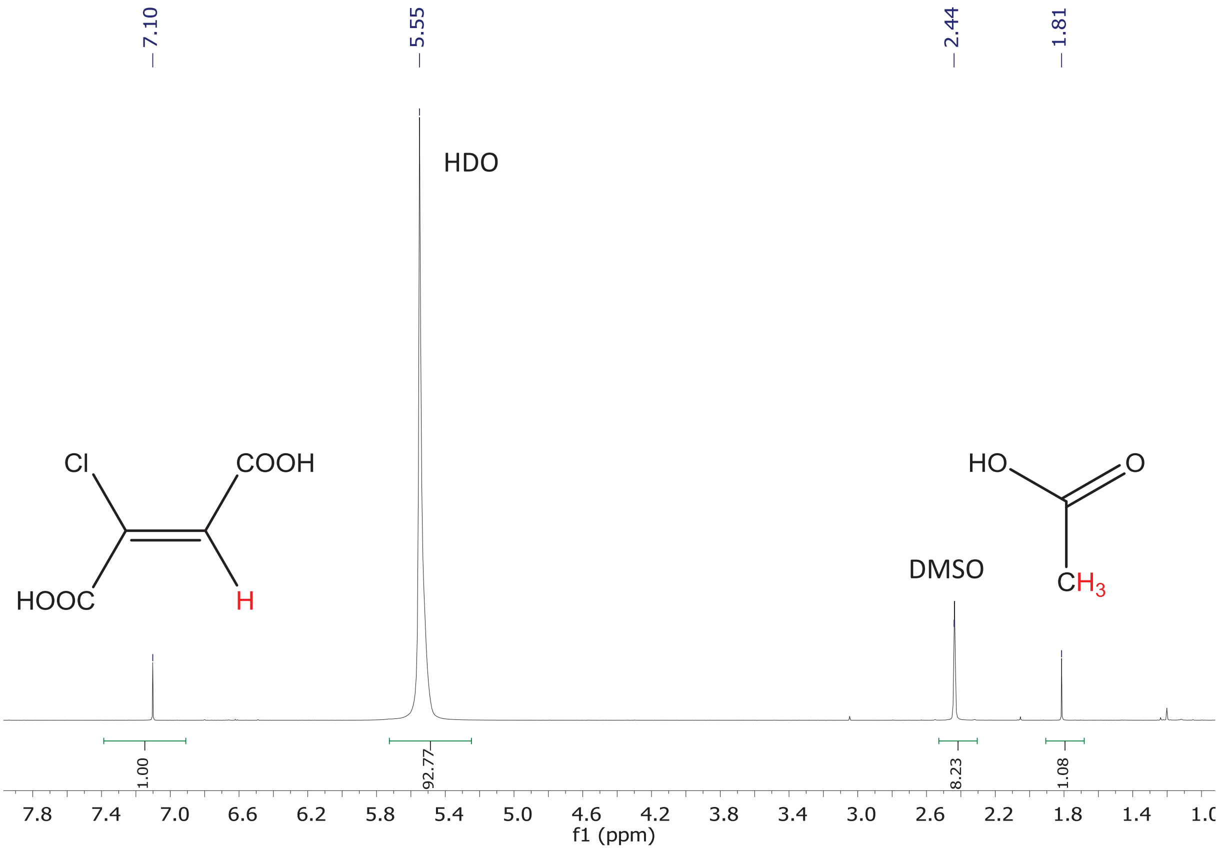

Figure S38. Solution ^{1}H NMR spectrum of digested **HHU-2** (Zr-Fum-Cl) in DMSO-d_6.

REFERENCES

---

[1] H.Billetter, F. Hohn, I.Pantenburg, U. Ruschewitz, *Acta Cryst. C* **2003**, *59*, 130-131.

[2] I. Pantenburg, U. Ruschewitz, *Z. Anorg. Allg. Chem*. **2002**, *628*, 1697-1702.

[3] D. J. Tranchemontagne, J. R. Hunt, O. M. Yaghi, *Tetrahedron* **2008**, *64*, 8553-8557.

[4] U. Ruschewitz, I. Pantenburg, *Acta Cryst. C* **2002**, *58*, 483-484.

[5] I. Stein, U. Ruschewitz, *Z. Anorg. Allg. Chem.* **2010**, *636*, 400-404.

[6] A. Schuy, I. Stein, U. Ruschewitz, *Z. Anorg. Allg. Chem.* **2010**, *636*, 1026-1031.

[7] A. Michaelides, S. Skoulika, *Crystal Growth Des.* **2005**, *5*, 529-533.

[8] F. Hohn, I. Pantenburg, U. Ruschewitz, *Chem. Eur. J.* **2002**, *8*, 4536-4541.

[9] S. Busch, I. Stein, U. Ruschewitz, *Z. Anorg. Allg. Chem.* **2012**, *638*, 2098-2101.

[10] A. E. Bennett, C. M. Rienstra, M. Auger, K. R. G. Lakshmi Griffin, *J. Chem. Phys.* **1995**, *103*, 6951-6958.

[11] A. Schaate, P. Roy, A. Godt, J. Lippke, F. Waltz, M. Wiebcke, P. Behrens, *Chem. Eur. J.* **2011**, *17*, 6643-6651.

[12] A. De Lorenzi, S. Giorgianni, R. Bini, *Mol. Phys.* **1999**, *96*, 101-108.

[13] Coelho Software, Topas Academics 4.2, 2007.

[14] Accelrys Materials Studio Version 5.0, San Diego, CA, 2009.

[15] G. C. Shearer, S. Chavan, S. Bordiga, S. Svelle, U. Olsbye, K. P. Lillerud, *Chem. Mater.* **2016**, *28*, 3749-3761.

[16] M. Thommes, K. Kaneko, A. V. Neimark, J. P. Olivier, F. Rodriguez-Reinoso, J. Rouquerol, K. S. W. Sing, *Pure Appl. Chem.* **2015**, *87*, 1051-1069.

[17] Hu, I. Castano, S. Wang, Y. Wang, Y. Peng, Y. Qian, C. Chi, X. Wang, D. Zhao, *Cryst. Growth Des.* **2016**, *16*, 2295-2301.

[18] H. Furukawa, F. ndara, Y-B. Zhang, J. Jiang, W. L. Queen, M. R. Hudson, O. M. Yaghi, *J. Am. Chem. Soc.* **2014**, *136*, 4369-4381.

[19] S. Biswas, P. Van Der Voort, *Eur. J. Inorg. Chem.* **2013**, 2154-2160.

[20] Z. Zhao, Z. Li, Y. S. Lin, *Ind. Eng. Chem. Res.* **2009,** *48,* 10015–10020.

[21] Y. E. Cheon, M. P. Suh, *Chem. Commun*. **2009**, 2296-2298.

[22] H. Furukawa, J. Kim, N. W. Ockwig, M. O'Keefe, O. M. Yaghi, *J. Am. Chem. Soc*. **2008**, *130*, 11650-11661.

[23] Z. Hu, Y. Peng, Z. Kang, Y. Qian, D. Zhao, *Inorg. Chem*. **2015**, *54*, 4862−4868.

[24] H. R. Abid, H. H.-M. Tian, Ang, M. O. Tade, C. E. Buckley, S. Wang, *Chem. Engin. J.* **2012**, *187*, 415-420.

[25] C. Zlotea, D. Phanon, M. Mazaj, D. Heurtaux, V. Guillerm, C. Serre, P. Horcajada, T. Devic, E. Magnier, F. Cuevas, G. Férey, P. L. Llewellyn, M. Latroche, *Dalton Trans.* **2011**, *40*, 4879-4881.

(26) S. Chavan, J. G. Vitillo, D. Gianolio, O. Zavorotynska, B. Civalleri, S. Jakobsen, M. H. Nilsen, L. Valenzano, C. Lamberti, K. P. Lillerud, S. Bordiga, *Phys. Chem. Chem. Phys.* **2012**, *14*, 1614-1626.

(27) *CrystalExplorer17*, Version 3.1; M. J. Turner, J. J. McKinnon, S. K. Wolff, D. J. Grimwood, P. R. Spackman, D. Jayatilaka, M. A. Spackman,: University of Western Australia, 2017. http://hirshfeldsurface.net

(28) M. J. Turner, J. J. McKinnon, D. Jayatilaka, M. A. Spackman, *CrystEngComm* **2011**, *13*, 1804-1813.

(29) Mercury CSD 3.9, program for crystal structure visualisation, exploration and analysis from the Cambridge Crystallographic Data Center, Copyright CCDC 2001-2016, http://www.ccdc.cam.ac.uk/mercury/

(30) Spek, A. L. Structure validation in chemical crystallography *Acta Crystallogr. D* **2009**, *65*, 148–155; PLATON – A Multipurpose Crystallographic Tool, Utrecht University, Utrecht, The Netherlands, Spek, A. L. **2008**; Windows implementation: Farrugia, L. J. University of Glasgow, Scotland, Version 40608, **2008**.

(31) A. P. Terzyk, J. Chatłas, P. A. Gauden, G. Rychlicki, P. Kowalczyk, *J. Colloid Interface Sci.* **2003**, *266*, 473-476.

(32) P. Roy, A. Schaate, P. Behrens, A. Godt, *Chem. Eur. J.* **2012**, *18*, 6979-6985.

2.2 Acetylenedicarboxylate and in situ generated chlorofumarate-based hafnium(IV)-metal-organic frameworks: synthesis, structure and sorption properties

Tobie J. Matemb Ma Ntep, Helge Reinsch, Carsten Schlüsener, Anna Goldman, Hergen Breitzke, Bastian Moll, Laura Schmolke, Gerd Buntkowsky, and Christoph Janiak

Inorg. Chem. **2019**, *58*, 10965−10973.

DOI: 10.1021/acs.inorgchem.9b01408

Impact factor 2018: 4.85

Because hafnium and zirconium have very similar chemical properties, many reported Zr-metal-organic frameworks have their hafnium-based analogues. It was expected that the results obtained with acetylenedicarboxylic acid when reacting with zirconium could also be obtained with hafnium. As anticipated, a new Adc-based Hf^{IV}-MOF with **fcu** topology was obtained under modulation with acetic acid in DMF, that is, an analogue of Zr-HHU-1. When the reaction was conducted in water instead, and using $HfCl_4$ salt in place of $HfOCl_2$, the product was rather a hafnium chlorofumarate resulting from an in situ hydrochlorination of acetylenedicarboxylate. Two new MOFs were denoted as Hf-HHU-1 and Hf-HHU-2 for the Adc-based and Fum-Cl-based Hf-MOFs, respectively. These MOFs have broadly the same properties as their Zr analogues, albeit with lower adsorption capacities per weight due to the larger molar mass of Hf compared to Zr. Detailed results of this work are found in the articles that follows.

Author´s contribution to the work:

- Idea and setting of the syntheses procedures.
- Synthesis and preparation of the samples for further characterization.
- Characterizations including PXRD experiments, TGA, chemical stability test, nitrogen sorption and porosity parameters determination, other gas/vapor sorption (H_2O, CO_2 and I_2) experiments.
- Organization of other analyses (Raman, ssNMR, SEM-EDX and XPS), data analysis/interpretations and treatment.
- Samples activations prior characterizations and MOF digestion prior liquid NMR analysis.

- Fitting of adsorption isotherms and determination of the isosteric heat of CO_2 adsorption.
- Writing of the manuscript, drawing of figures and responses to reviewers during the review process.

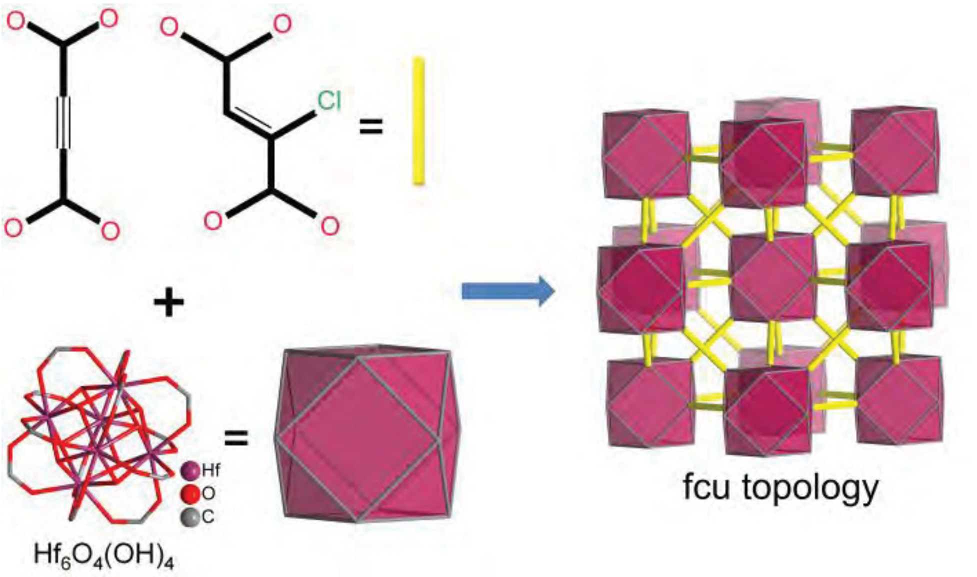

Inorganic Chemistry
Article
Cite This: Inorg. Chem. 2019, 58, 10965−10973
pubs.acs.org/IC

Acetylenedicarboxylate and In Situ Generated Chlorofumarate-Based Hafnium(IV)−Metal−Organic Frameworks: Synthesis, Structure, and Sorption Properties

Tobie J. Matemb Ma Ntep,† Helge Reinsch,‡ Carsten Schlüsener,† Anna Goldman,† Hergen Breitzke,§ Bastian Moll,† Laura Schmolke,† Gerd Buntkowsky,§ and Christoph Janiak*,⊥,†

†Institut für Anorganische Chemie, Heinrich-Heine-Universität Düsseldorf, D- 40204 Düsseldorf, Germany
‡Institut für Anorganische Chemie, Christian-Albrechts-Universität, Max-Eyth-Straße 2, 24118 Kiel, Germany
§Eduard-Zintl-Institut für Anorganische und Physikalische Chemie, Technische Universität Darmstadt, Alarich-Weiss-Straße. 4, D-64287 Darmstadt, Germany
⊥Hoffmann Institute of Advanced Materials, Shenzhen Polytechnic, 7098 Liuxian Boulevard, Nanshan District, Shenzhen, China

Supporting Information

ABSTRACT: New acetylenedicarboxylate (ADC) and chlorofumarate (Fum-Cl) based hafnium-metal−organic frameworks have been synthesized by alternatively reacting acetylenedicarboxylic acid in DMF or water with appropriate hafnium salt, in the presence of acetic acid modulator. The two materials of respective ideal formulas $[Hf_6O_4(OH)_4(ADC)_6]$ (Hf-HHU-1) and $[Hf_6O_4(OH)_4(Fum\text{-}Cl)_6]$ (Hf-HHU-2) have been structurally characterized by powder X-ray diffraction to be UiO-66 isostructural, consisting of octahedral $[Hf_6O_4(OH)_4]^{12+}$ secondary building units each connected to other units by 12 ADC or Fum-Cl linkers into a microporous network with **fcu** topology. This structure was confirmed by Rietveld refinement. Hf-HHU-2 is formed by *in situ* hydrochlorination of acetylenedicarboxylic acid to chlorofumarate. Its presence has been determined by combined Raman spectroscopy, solid-state NMR, scanning electron microscopy, energy dispersive X-ray and X-ray photoelectron spectroscopies. Hf-HHU-1 and Hf-HHU-2 exhibit very high hydrophilicity as revealed by their water sorption profiles, meanwhile Hf-HHU-2 adsorbs CO_2 with an isosteric heat of 39 kJ mol^{-1}. Hf-HHU-2 also adsorbs molecular iodine vapor exclusively as polyiodide anions due to grafted chloro-functions on the pores surface. It has been observed that defective nanodomains with **reo** tolopology can be introduced in the structure of Hf-HHU-2 by variation of the linker to metal-salt molar ratio.

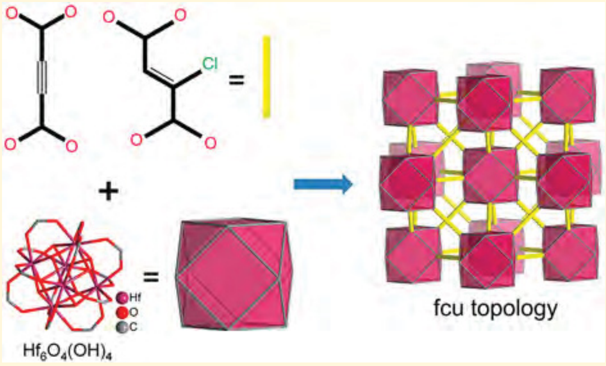

INTRODUCTION

Hafnium and zirconium have very similar chemical properties.[1] Hf^{4+} has the same d^0 electronic configuration and nearly identical radius with Zr^{4+}. As consequence, Hf-based MOFs usually show isostructural Zr-based counterparts.[2,3] This chemical resemblance is also displayed in the engineering of Zr- and Hf-metal−organic frameworks (MOFs). MOFs are porous materials formed by linking metal−oxido clusters with organic ligands into three-dimensional potentially porous networks.[4] Zirconium(IV)-based metal−organic frameworks (Zr-MOFs) with polycarboxylate ligands have high hydrothermal and chemical stabilities,[5−7] making them promising porous materials for possible applications in heterogeneous catalysis,[8,9] gas storage and separation,[10−12] drug delivery,[13] sensing,[14,15] water harvesting from air,[16] and adsorption-based heat transformations.[17,18] The robust Zr−O bonds on the highly charged and oxophilic Zr(IV) cations account for these enhanced stabilities compared to MOFs based on low valence metal cations.[19,20]

Prototypical Zr-MOFs are based on the isoreticular UiO structures which are constructed by linking 12-fold-connected octahedral $[Zr_6(\mu_3\text{-}O)_4(\mu_3\text{-}OH)_4]$ clusters with linear dicarboxylates into a network with **fcu** topology.[21] By using the same organic linkers and the same synthesis conditions, the zirconium precursor salt ($ZrCl_4$ or $ZrOCl_2$) can be replaced by a hafnium salt ($HfCl_4$ or $HfOCl_2$). Thus, nearly each UiO Zr-MOF can also be obtained in its Hf-MOF version containing octahedral $[Hf_6(\mu_3\text{-}O)_4(\mu_3\text{-}OH)_4]$ clusters.[22] The known Hf-based analogues of Zr-MOFs include Hf-UiO-66,[23] Hf-UiO-66-NH_2,[24] Hf-UiO-67,[25] and Hf-Fum.[26]

Received: May 14, 2019
Published: July 31, 2019

DOI: 10.1021/acs.inorgchem.9b01408
Inorg. Chem. 2019, 58, 10965−10973

We recently reported the synthesis of the first acetylenedicarboxylate-based Zr-MOF, namely HHU-1 (HHU stands for Heinrich-Heine-Universität Düsseldorf) which is isoreticular with the well-known UiO-66 (cf. Scheme 1).[27] We also demonstrated that using water as solvent in the synthesis instead of DMF, yields rather a halogen-functionalized zirconium fumarate MOF (HHU-2-Cl) based on the *in situ* generated halofumarate linker, which is derived from the hydrohalogenation of acetylenedicarboxylic acid. The chloro-substituted zirconium fumarate MOF (HHU-2-Cl) featured an increased hydrophilicity and gas sorption capacities compared to parent zirconium fumarate. However, most especially, a strong affinity with iodine vapor was noticed for this halogenated material, which could be exploited for radioactive iodine storage.

Scheme 1. Reaction of Acetylenedicarboxylic Acid with $HfOCl_2$ in DMF or $HfCl_4$ in Water to UiO-Type Hafnium MOFs with Acetylenedicarboxylate Linker (Hf-HHU-1) or in Situ Formed Chlorofumarate Linker (Hf-HHU-2)

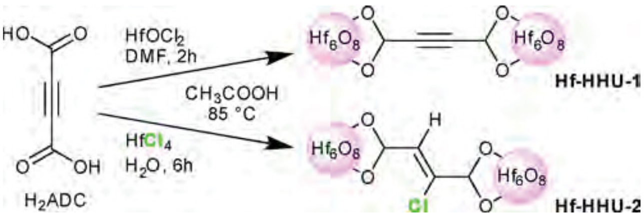

Given the close similarity in chemical properties of hafnium and zirconium, and the fact that most Zr-MOFs have Hf-based analogs, we were motivated to investigate the extensibility of our previous findings with zirconium using this time hafnium salts. Hence, we herein report the synthesis, structure and characterization of the first acetylenedicarboxylate-based UiO-type Hf-MOF and in situ generated chlorofumarate-based Hf-MOF (Scheme 1). We investigate their stabilities, porosity, and defect features, as well as their water, iodine, and CO_2 adsorption properties.

RESULTS AND DISCUSSION

Synthesis and Characterizations. The reaction at 85 °C of a mixture containing acetylenedicarboxylic acid, hafnium oxychloride, and acetic acid as modulating agent in anhydrous DMF, yielded within 2 h the new acetylenedicarboxylate-based MOF Hf-HHU-1 of ideal formula $[Hf_6(\mu_3\text{-}O)_4(\mu_3\text{-}OH)_4(ADC)_6]$ (ADC = acetylenedicarboxylate) (Scheme 1). This material was obtained as a microcrystalline powder. The use of DMF as solvent was guided by most reports of modulated synthesis of Zr- and Hf-MOFs, which are carried out in DMF. Still, it took us several months to find the right conditions (concentration of reactants, temperature, reaction time, molar ratios) that gave the desired Hf-HHU-1 phase. Therefore, no other solvents were tried.

The strong absorption bands in the FT-IR spectra (Figure S1, Supporting Information) at around 1590−1610 and 1360−1390 cm^{-1}, can be ascribed to the asymmetric and symmetric $-CO_2$ stretching vibrations of coordinated linker. The bands at 1651 cm^{-1} is ascribed to $-C{=}O$ stretching vibration of residual DMF solvent in the pores. In the Raman spectrum of activated Hf-HHU-1 (Figure 1), the band at 2225 cm^{-1} is ascribed to the vibrations of the $-C{\equiv}C-$ triple bond of the linker (Figure S2, Supporting Information). This band is absent in the Raman spectrum of Hf-HHU-2 (Figure 1). This indicates the transformation of the triple bond, and therefore the transformation of the acetylenedicarboxylate linker into a new linker.

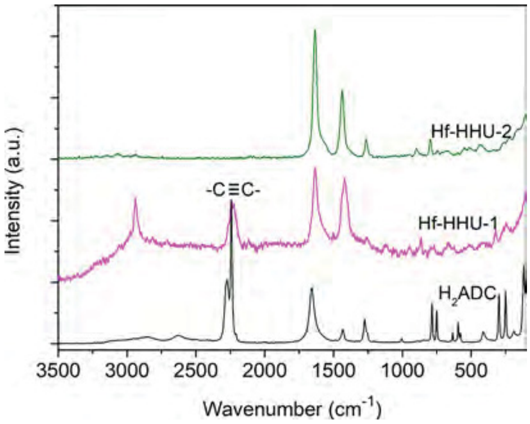

Figure 1. Raman spectrum of Hf-HHU-1 (pink) and Hf-HHU-2 (green) compared with acetylenedicarboxylic acid (black). A complete disappearance of the band assigned to the $-C{\equiv}C-$ triple bond is observed in Hf-HHU-2. The band at about 3000 cm^{-1} is ascribed to the methyl groups ($-CH_3$) of residual DMF in the pores of Hf-HHU-1.

When the reaction was carried out in water using instead hafnium chloride as metal salt, the new MOF Hf-HHU-2 of ideal formula $[Hf_6(\mu_3\text{-}O)_4(\mu_3\text{-}OH)_4(\text{Fum-Cl})_6]$ (Fum-Cl = 2-chlorofumarate) was obtained as highly microcrystalline powder (Scheme 1). Hf-HHU-2 results from an in situ transformation of acetylenedicarboxylic acid to 2-chlorofumaric acid (*vide infra*), and the new linker reacts readily with hafnium clusters in solution to yield the new MOF. A similar in situ linker transformation was previously obtained by us when reacting zirconium chloride with H_2ADC in water, yielding a chlorofumarate-based Zr-MOF, namely Zr-HHU-2.[27] This transformation indicates that the first step of the modulated reaction consists of the formation of soluble hafnium acetate clusters with release of HCl in solution. The $-C{\equiv}C-$ triple-bond of H_2ADC then undergoes a hydrochlorination (addition of released HCl) to a chloro-functionalized double-bond containing linker. Hf-HHU-2 is finally formed when 2-chlorofumaric acid substitutes acetate on the hafnium−oxido−hydroxido clusters.[28] The high solubility of HCl in water, coupled with the dissociation to H_3O^+ and Cl^- could justify why this transformation is favored in water. Other authors obtained hydrohalogenation of acetylenedicarboxylic acid to halofumarate in water in the formation of copper(II) chlorofumarate and lithium hydrogen iodofumarate coordination polymers.[29]

The powder X-ray pattern of Hf-HHU-1 resembles that of Zr−acetylenedicarboxylate, Zr-HHU-1 and the diffractogram of Hf-HHU-2 resembles that of Zr−chlorofumarate, Zr-HHU-2 and both HHU-1 and HHU-2 patterns resemble each other in view of the same underlying UiO-topology (Figure 2).

The solid-state NMR (ssNMR) analysis was conducted on as-synthesized sample of Hf-HHU-2 to identify the nature of the in situ formed linker in the MOF. The ^{13}C CPMAS spectrum (Figure S3 in Supporting Information) displays two peaks at 129 and 140 ppm which are typical for olefinic carbons. Water was exchanged by methanol during the washing process. As the ssNMR analysis was conducted with the air-

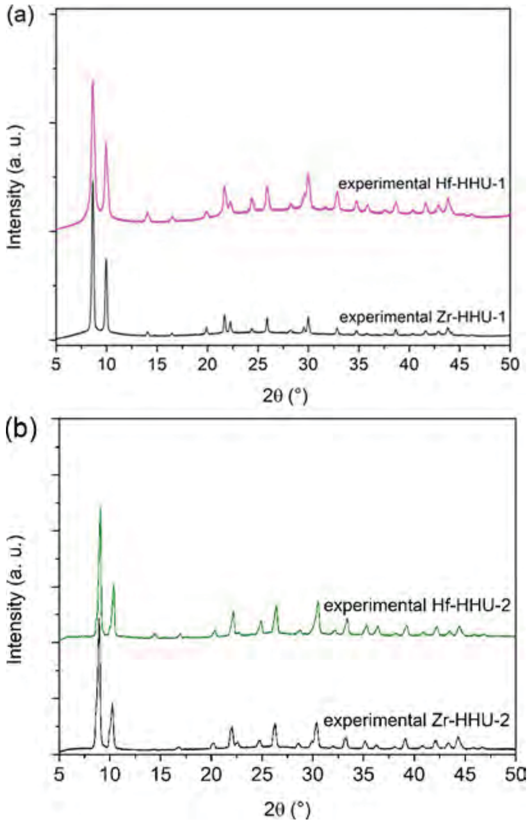

Figure 2. Powder XRD pattern of (a) Hf-HHU-1 in comparison with experimental pattern of Zr-HHU-1[27] and (b) Hf-HHU-2 in comparison with experimental pattern of Zr-HHU-2.

dried, non-activated sample, methanol solvent in the pores appears in the spectra.

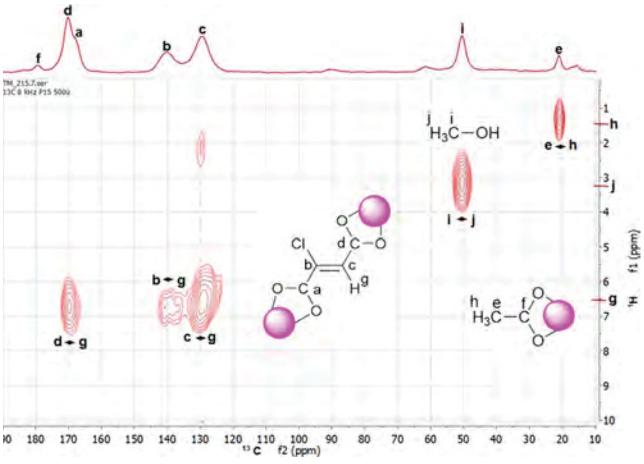

Figure 3. $^1H-^{13}C$ FSLG-HETCOR CP MAS of Hf-HHU-2 at 8 kHz spinning speed and 500 μs contact time.

It is observed in the FSLG-HECTOR spectra (Figure 3) a very strong correlation of the carbon at 129 ppm with a proton at 6.5 ppm. Clearly, this carbon is bonded to a hydrogen atom (=C−H). Meanwhile, the carbon at 140 ppm has a very weak correlation with the same proton, indicating that it is not bonded to a hydrogen atom. The carbon peaks at 170, 50, and 20 ppm shift are respectively ascribed to the carboxylate of the linker, the methanol solvent in the pores and methyl group of acetate modulator coordinated at linker defective sites. The ssNMR spectra of Hf-HHU-2 are very similar to those obtained for Zr-HHU-2,[27] confirming that the transformation leads to the formation of the same new linker as that observed in the zirconium-based analogue.

From the HETCOR CP MAS of Hf-HHU-2 (Figure 3), we can rule out the presence of protonated acetic acid modifier in the pores. The carboxyl group carbon signals appear around 170 ppm. All proton shifts could be assigned. If the acetic acid would be protonated then there should be a correlation from the proton to the carboxyl region, which is only present there and which correlates to no other carbon signal, except maybe weakly to the methyl group of the acetic acid. There is, however, no correlation of the carboxylate carbon signals of acetate at 179 ppm with any proton. This allows to conclude that the modifier is not found in the material as acetic acid, but only as coordinated acetate.

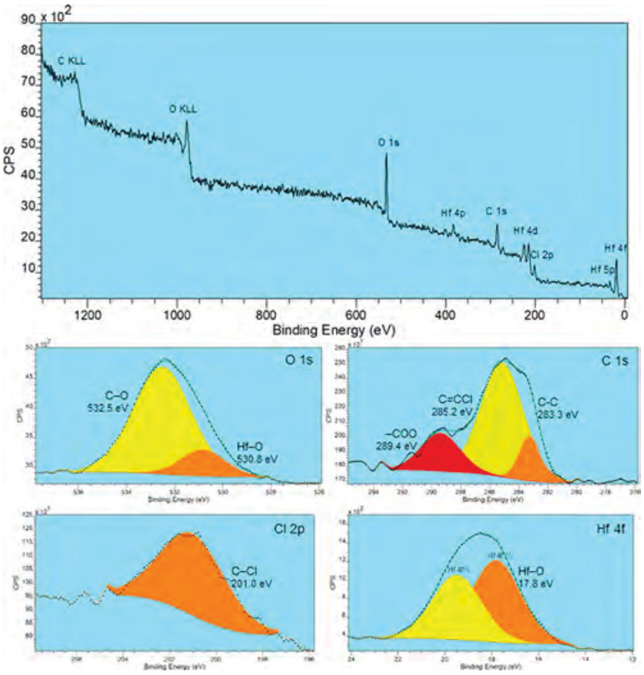

Figure 4. XPS survey spectrum and high-resolution core-level in the region of O 1s, C 1s, Cl 2p, and Hf 4f of Hf-HHU-2.

The X-ray photoelectron spectroscopy (XPS) of a thoroughly washed and activated sample of Hf-HHU-2 (Figure 4) shows the presence of chlorine in the material. The high resolution XPS core level spectrum (Figure 4) displays the Cl_{2p} peak at 201 eV binding energy, which is indicative of organic chlorine (C−Cl). The inorganic chloride (Cl^-) Cl_{2p} peak would appear at about 198 eV binding energy.[30] These results prove occurrence of a hydrochlorination (addition of HCl) on the ADC triple bond to a chlorofumarate containing MOF. The deconvoluted Hf spectrum shows two peaks at 17.8 and 19.5 eV binding energy, corresponding respectively to $4f_{7/2}$ and $4f_{5/2}$ components of hafnium in the oxidation state Hf^{IV}.[31] Fitting the C 1s spectrum reveals three components which can be assigned to the carboxylate's carbon −COO (289.4 eV), the chlorine-bonded olefinic carbon =C−Cl (285.2 eV) and the hydrogen-bonded olefinic carbon =C−H (283.3 eV). The high-resolution O 1s spectrum (Figure 4) shows two components attributable to the carboxylate oxygen C−O

(530.5 eV) and the oxygen of the hafnium cluster Hf−O (530.8 eV).[32,33]

Since the sample of our material is not a flat surface, the XPS analysis, which is known to be a surface probe of the material, can be considered more for qualitative elemental determination, indicating the presence and type of C and O atoms in the material. A quantification of the different carbon and oxygen species is not possible. The typical surface impurities could not be removed by cleaning the MOF surface with Ar^+ sputtering or etching. In both cases, the MOF material would decompose. Furthermore, the intensity of the C 1s signal is not high enough for a more detailed analysis. Quantitative discrepancy like in the ratio of the respective species should therefore not be surprising.

Furthermore, scanning electron microscopy (SEM) coupled with electron-dispersive X-ray spectroscopy (EDX) elemental mapping (Figure S8 in the Supporting Information) shows that chlorine, as well as hafnium, is evenly distributed across the entire sample.

Thermal and Chemical Stabilities. The thermal stabilities of Hf-HHU-1 and Hf-HHU-2 (both as synthesized) were evaluated by thermogravimetric analysis. The thermogravimetric curves in Figure S10 reveal that Hf-HHU-1 is thermally stable until less than 200 °C, while Hf-HHU-2 is stable until about 300 °C. The low thermal stability of Hf-HHU-1 is attributable to the thermal liability of H_2ADC, which decomposes at 180 °C in its solid state. The low thermal stability of Hf-HHU-1 is attributable to the thermal liability of H_2ADC, which decomposes at 180 °C in its solid state. Furthermore, the thermal stability of ADC-based Hf-HHU-1 (less than 200 °C) is in agreement with the large majority of metal−ADC compounds.[34] A noteworthy exception is Sr−ADC ($Sr[C_2(COO)_2]$) where a thermal stability up to about 450 °C was reported.[35] Hf-HHU-1 and Hf-HHU-2 display thermal stabilities similar to those of Zr-HHU-1 and Zr-HHU-2 respectively.

The chemical stability of new materials was assessed by stirring a sample of each 24 h in various solvents and solutions. The crystallinity monitoring from the PXRD patterns of samples after these experiments reveals that Hf-HHU-1 has a low chemical stability in water, methanol, ethanol, acetone, and aqueous solution of pH = 12 (Figure S11, Supporting Information). An increased crystallinity was instead noticed in aqueous solution of pH = 1. Hf-HHU-2 shows good chemical stability in all aforementioned solutions, as the material maintains its full crystallinity after each chemical treatment (Figure S11, Supporting Information).

Crystal Structure. The structure of Hf-HHU-1 was determined from powder diffraction data. Crystallographic data for the structural analyses of Hf-HHU-1 have been deposited with the Cambridge Crystallographic Data Center (CCDC 1915835).

Hf-HHU-1 is isostructural with its previously reported zirconium-based analogue Zr-HHU-1 and crystallizes in the space group $Fm\overline{3}m$. Its crystal structure consists therefore of hexanuclear $[Hf_6O_4(OH)_4]^{12+}$ secondary building units (SBUs). The SBU is constructed of six Hf atoms defining a regular octahedron, in which the triangular faces alternatively contain μ_3-O and μ_3-OH capping groups. Together with the oxygen atoms of the carboxylate groups, each Hf atom has a square-antiprismatic coordination environment, thus yielding a hexanuclear cluster of six vertex-sharing HfO_8 square antiprismatic polyhedra (Figure 5a). The octahedral SBUs are 12-fold interconnected by acetylenedicarboxylate linkers in a face-centered cubic arrangement, resulting in a porous three-dimensional **fcu** network (Figure 5b and Figure 6) with octahedral and tetrahedral cages of about 9.6 and 5.8 Å diameter respectively (Figure 5c,d).

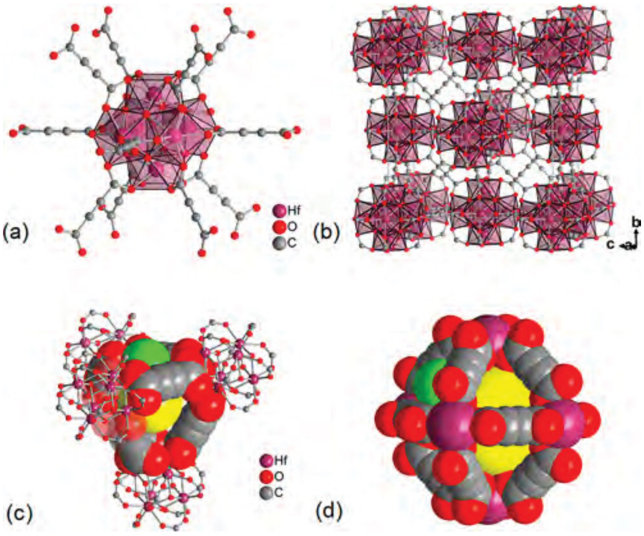

Figure 5. (a) Secondary building unit of $\{Hf_6O_4(OH)_4\}$ with the 12 surrounding and connecting acetylenedicarboxylate linkers and the edge-sharing square-antiprismatic HfO_8 coordination as polyhedra (b) fcc packing diagram of the **fcu** network in Hf-HHU-1, (c) tetrahedral cage, and (d) octahedral cage with available pore (yellow ball) and triangular windows (green ball).

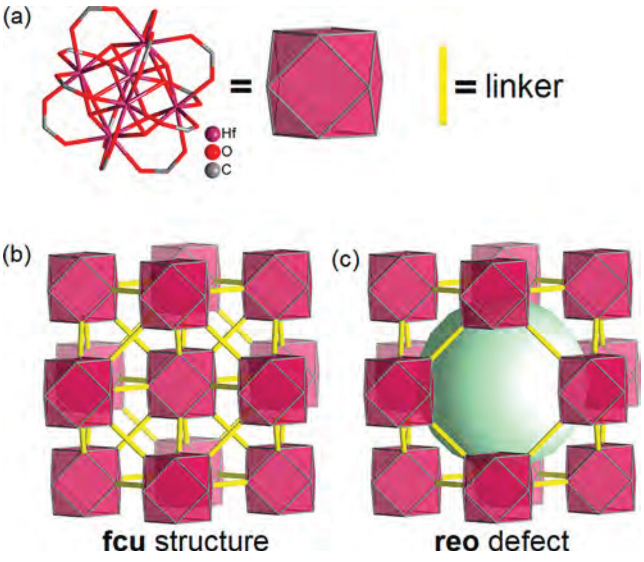

Figure 6. Network topology image of Hf-HHU-1 and Hf-HHU-2. (a) $\{Hf_6O_4(OH)_4(O_2C)_{12}\}$-SBU as polyhedra and connecting linkers (acetylenedicarboxylate or chlorofumarate, respectively) as yellow rods to give (b) the **fcu** topology network and eventually (c) defective missing cluster regions with **reo** topology.

Hf-HHU-2 being isostructural with zirconium chlorofumarate is also a UiO-type MOF like Hf-HHU-1. Its structure is best rationalized by replacing the acetylenedicarboxylate linker in Hf-HHU-1 structure by the chlorofumarate linker. Depending on the H_2ADC to $HfCl_4$ molar ratio of the initial mixture, differences were noticed in the PXRD pattern of Hf-HHU-2.

When the H_2ADC to $HfCl_4$ molar ratio was 3:1, that is with excess linker, the PXRD pattern corresponds to the **fcu** topology similar to zirconium chlorofumarate (Figure 2b). Meanwhile, three diffuse less-intense reflections systematically appeared at about 5, 7, and 11° 2θ angles (Figure 7), when the initial reactants mixture was made of 1:1 H_2ADC to $HfCl_4$ molar ratio. Such diffuse reflections were previously observed for Zr/Hf-UiO-66, and are associated with the presence of correlated defect nanoregions with **reo** topology in the structure (Figure S16).[36] These defect nanoregions result from missing clusters and linkers.[36,37] A PXRD pattern of the **reo** topology with a halofumarate linker was simulated and compared to our experimental PXRD pattern of Hf-HHU-2 from a 1:1 linker to metal molar ratio. It is noticeable that the three more visible diffuse reflections at 5, 7, and 11° fit well with the (101), (110), and (200) reflections of the **reo** MOF.

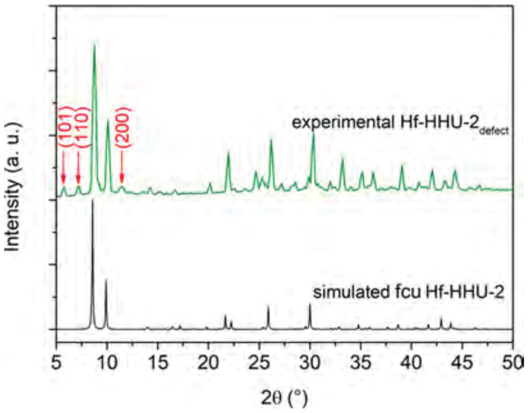

Figure 7. PXRD pattern of Hf-HHU-2 containing defective nanodomains with reo topology (green) and simulated pattern of the **fcu** topology for Hf-HHU-2 (black). The pattern of Hf-HHU-2_{defect} shows the coexistence of the bulk framework of **fcu** topology and minor **reo** topology. From the latter the clearly visible (101), (110), and (200) reflections are indicated (see the pattern of **reo** topology in Figure S16, Supporting Information). Their low intensities reflect the minor contribution of the **reo** nanodomains within the major **fcu** bulk phase (cf. ref 35).

Porosity and Gas Adsorption Properties. *Nitrogen Adsorption.* In order to investigate their porosity, nitrogen sorption experiments were conducted on activated samples of Hf-HHU-1 and Hf-HHU-2 at 77 K. The resulting isotherms shown in Figure 8 correspond to the type Ib isotherm according to IUPAC classification,[38] which indicates the microporous nature of both materials. From the isotherms obtained, the BET (Brunauer−Emmett−Teller) surface area was calculated to 476 and 541 $m^2\ g^{-1}$, while the total pore volume was estimated to 0.20 and 0.25 $cm^3\ g^{-1}$ for Hf-HHU-1 and Hf-HHU-2, respectively. The respective specific surface area and porosity of Hf-HHU-1 and Hf-HHU-2 are contradictory to expectations. Hf-HHU-2 was expected to have a lower surface area and porosity than Hf-HHU-1 due to steric occupation of chloro functions in the pores compared to free pores in Hf-HHU-1. The linear and hydrogen-free ADC linker should provide more space than the chlorofumarate linker in corresponding MOFs. This discrepancy could be explained by residual DMF solvent in small pores of Hf-HHU-1, therefore reducing nitrogen access during the adsorption experiment. DMF is usually difficult to be completely evacuated from small pores, mostly when the activation process does not involve elevated temperatures.[39,40] This was confirmed by the elemental analysis of the activated sample showing the presence of nitrogen, which is due to residual DMF in the pores of the material. From the CHN analysis, about 1 DMF molecule per formula unit of $[Hf_6(\mu_3\text{-}O)_4(\mu_3\text{-}OH)_4(ADC)_6]$ can be estimated.

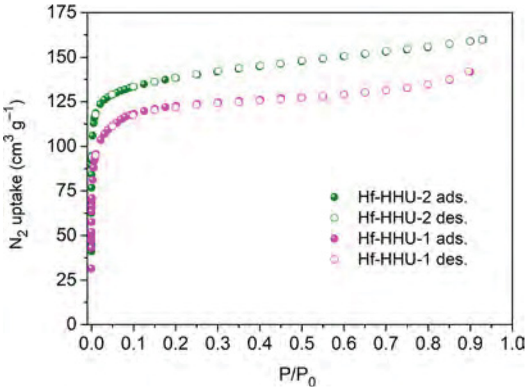

Figure 8. Nitrogen sorption isotherms of Hf-HHU-1 and Hf-HHU-2 at 77 K.

In order to have more clues on the porosity of Hf-HHU-1, the surface area and pore volume were also theoretically estimated from the crystallographic data using Materials Studio.[41] The theoretically accessible surface area calculated for a probe molecule with the kinetic diameter of nitrogen (3.64 Å) amounts to 707 $m^2\ g^{-1}$ and the corresponding theoretical micropore volume amounts to 0.26 $cm^3\ g^{-1}$.

Water Sorption and Hydrophilicity. In order to investigate their hydrophilicity, water vapor sorption was measured at 20 °C for Hf-HHU-1 and Hf-HHU-2. The two materials display water sorption isotherms close to type Ib (Figure 9), with some hysteresis loop between the adsorption and desorption branches. This corresponds to a high hydrophilicity of these two materials, indicating very strong H_2O-MOFs interactions. The respective isotherm shapes of Hf-HHU-1 and Hf-HHU-2 are similar to isotherms obtained for Zr-HHU-1 and Zr-HHU-2 respectively. This is expected as these MOFs are isostructural to their zirconium counterparts, differing only in their metal cation and gravimetric porosities. The strong interaction of water molecules with the framework was attributed to the effect of −C≡C− triple bond and functional chlorine on the

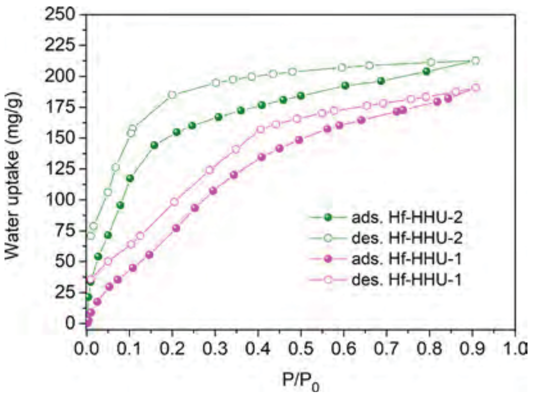

Figure 9. Water vapor sorption isotherms of Hf-HHU-1 and Hf-HHU-2 at 20 °C (filled symbols adsorption, empty symbols desorption).

inner pore surface of Zr-HHU-1 and Zr-HHU-2, respectively. However, the polar chlorine function seems to induce a stronger hydrophilicity as judged by a steeper slope of the adsorption isotherm at lower relative pressure values. The water adsorption capacities at P/P_0 = 0.9 are 190 and 212 mg g^{-1} for Hf-HHU-1 and Hf-HHU-2, respectively (Table 1). These values agree with obtained pore volumes from nitrogen sorption.

Table 1. Summary of Surface Area, Porosity Characteristics, and Water Uptakes of Hf-HHU-1 and HF-HHU-2

material	S_{BET} ($m^2 g^{-1}$)[a]	$V_{total\ pore}$ (cm^3 g^{-1})[b]	$V_{micropore}$ (cm^3 g^{-1})[c]	water uptake (mg g^{-1})[d]
Hf-HHU-1	476	0.20	0.17	190
Hf-HHU-2	541	0.25	0.18	212
Hf-HHU-2_{defect}	302	0.13	0.10	150

[a] Obtained from seven points in the pressure range P/P_0 = 0.001–0.05. [b] Derived at P/P_0 = 0.9 for pores smaller than 20 nm. [c] Volume that originates only from micropores, obtained by the $V-t$ method with thickness method "DeBoer". [d] Uptake at P/P_0 = 0.9.

Comparatively, Hf-HHU-1 and Hf-HHU-2 display lower specific (mass based) nitrogen sorption capacities and BET surface areas as well as water uptake capacities (Table 1), than their zirconium analogs (see Table S4, Supporting Information). This is expected as the hafnium MOFs have a higher molecular weight, due to the higher atomic mass of Hf over Zr. However, the corresponding analogs display similar shapes of water sorption isotherms and a similar high hydrophilicity (see Figure S17 in the Supporting Information), which is in agreement with their isostructural nature.

The presence of defects in Hf-HHU-2_{defect} could influence the material properties. It can also be the basis of further postsynthetic modifications.[42] The porosity and water sorption of Hf-HHU-2 and Hf-HHU-2_{defect} were compared. Surprisingly, Hf-HHU-2_{defect} displays a lower surface area (302 m^2 g^{-1}), pore volume (0.13 cm^3 g^{-1}), and water uptake compared to Hf-HHU-2 (Figure S17, Supporting Information). This is contradictory to expectations. It is expected that defective linkers and clusters sites should yield more space and therefore higher specific surface area. Such erratic behavior was also observed in the study of correlated defect nanoregions in Hf-UiO-66, whereby a decrease in BET surface area and pore volume was obtained with increasing defect content.[36] This result points out that defective nanodomains could have more complexity than has yet been elucidated. Furthermore, Hf-HHU-2_{defect} displays a type I adsorption water sorption isotherm (Figure S18, Supporting Information) indicating a higher hydrophilicity compared to Hf-HHU-2. The latter rather shows a lower sloped type Ib isotherm with a two-step filling of pores of distinct sizes. It was also observed that the defective Hf-HHU-2_{defect} has a reduced stability compared to the nondefective material. The PXRD pattern (Figure S19, Supporting Information) after the water sorption experiment shows amorphization of the sample containing defective nanodomains. This indicates the collapse of the framework under the water ad/desorption stress. On the contrary, the nondefective sample retains its full crystallinity after the water sorption experiment, attesting its hydrolytic stability (Figure S19, Supporting Information). This is not surprising as defects in MOFs are known to compromise their stability.[43] The hydrolytic instability of Hf-HHU-2_{defect} could be due to water molecules coordinating strongly to the metal clusters at defective nanodomain sites. This results in the collapse of the framework when the strongly attached water molecules are removed during the desorption. However, even the sample without clusters defect nanoregions do contain some level of missing linker defects. This is substantiated by the presence of acetate modulator in ssNMR spectra (Figure 3 and Figure S3, Supporting Information). The acetate would coordinate the Hf-clusters at missing linker sites. The amount of missing linker defective sites was evaluated from solution NMR experiment (Figure S4 in Supporting Information). From the relative integration of protons from the linker and acetic acid modulator in the ^{1}H spectrum, the number of missing linker molecules was calculated to 0.5 missing linker per {Hf_6}-cluster in Hf-HHU-2 (calculation details in the Supporting Information).

Furthermore, CO_2 sorption experiments were conducted on Hf-HHU-2 at 273 and 293 K, respectively. The isosteric heat (Q_{st}) of CO_2 adsorption was determined by applying the Clausius–Clapeyron equation using the isotherm data obtained at 273 and 293 K (see details in Supporting Information). The CO_2 sorption isotherms obtained are shown in Figure 10a. At 1 bar, the CO_2 adsorption capacity of Hf-HHU-2 is 2.27 mmol g^{-1} (9.1 wt %) and 1.6 mmol g^{-1} (6.5 wt %) at 273 and 298 K, respectively. Figure 10b displays the trace of the isosteric heat (Q_{st}) *of* CO_2 with increasing CO_2 loading. It shows that the isosteric heat of adsorption at zero coverage ($Q^0{}_{st}$) is 39 kJ mol^{-1}. The value of the isosteric heat

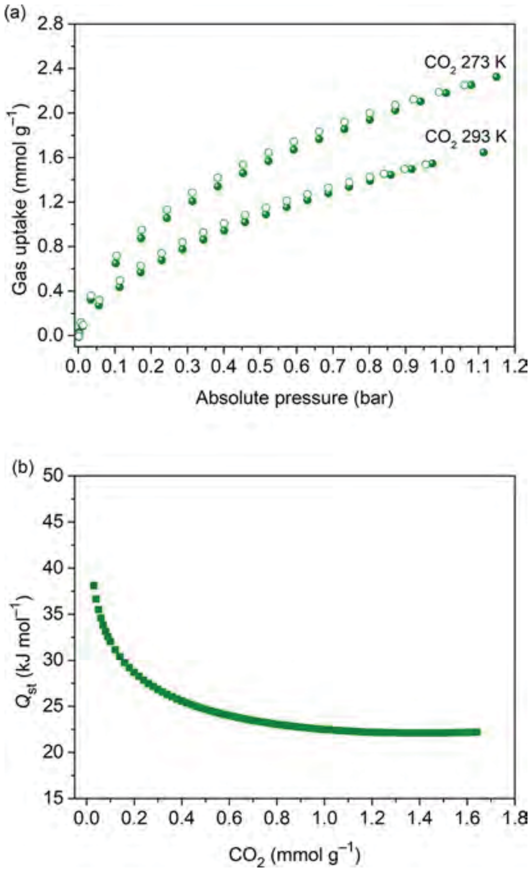

Figure 10. (a) CO_2 sorption isotherms of Hf-HHU-2 at 273 and 293 K. (b) Plot of isosteric heat of CO_2 adsorption from isotherms data at 273 and 293 K.

of adsorption abruptly drops after the strong binding sites (μ_3-OH, μ_3-O, and μ_3-Cl) are saturated to converge to a value of about 20 kJ mol^{-1} at higher loadings.

Iodine Adsorption. Iodine vapor adsorption experiment was conducted gravimetrically at 20 °C with an activated sample of Hf-HHU-2. The iodine adsorption was evidenced by a gradual change of the sample color from white to dark brown (see photograph Figure S20 in the Supporting Information). The plot of iodine uptake with time shown in Figure 11a reveals that iodine is gradually adsorbed and reaches a plateau after about 10 days, corresponding to an iodine adsorption capacity of 0.65 g g^{-1}.

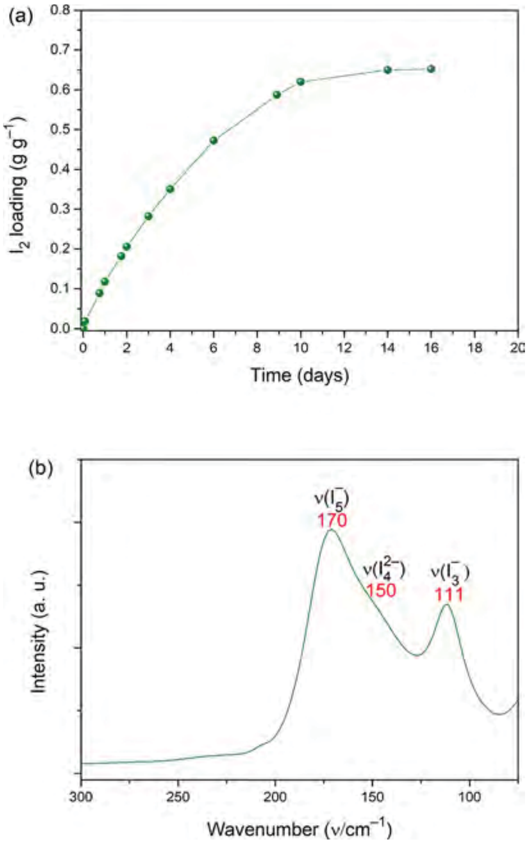

Figure 11. (a) Gravimetric iodine vapor adsorption trace of Hf-HHU-2. (b) Raman spectrum of iodine-loaded Hf-HHU-2 in the wavenumber range 300−50 cm^{-1}.

In order to investigate the interactions of iodine with the material and the adsorption mechanism, Raman spectroscopy analysis was conducted on iodine-loaded samples of Hf-HHU-2. In Figure 11b and Figure S22, Supporting Information, the Raman spectrum of the iodine-loaded sample I_2@Hf-HHU-2 displays additional signals compared to the spectrum of unloaded Hf-HHU-2, namely two strong bands at 111 and 170 cm^{-1}. These bands are characteristic vibrations of I_3^- and I_5^- polyiodides, respectively. A shoulder is also visible at 150 cm^{-1}, which is attributable to the vibration of the I_4^{2-} anion.[44,45] The Raman absorption for neutral I_2 would be expected at 180 cm^{-1}. Thus, Hf-HHU-2 adsorbs iodine vapor exclusively as polyiodide as no band for the molecular I_2 vibration was observed at 180 cm^{-1}.

The formation of polyiodide chains in neutral I_2-adducts is known. The ß-cyclodextrin inclusion complex with iodine is a typical example, whereby (neutral I_2) iodine molecules, once adsorbed, dissociate heterolytically to form polyiodide anionic species.[46] Such a reaction is also known to occur between iodine and amylase or with O and N macrocycles.[47] A plausible mechanism of formation is based on a donor−acceptor interaction, whereby I_2 interacts with a donor atom (D). The D···I_2 adduct can further evolve into a $(D\text{-}I)^+\cdot I^-$ species, which then leads to the formation of I_3^-, I_4^{2-} or I_5^- from various combinations of I^- with I_2. Due to their high electronegativity, halogen atoms in molecular entities are the basis of inter and intramolecular interaction known as *halogen bonding*.[48] Therefore, the Cl atom of the linker may act as donor atom toward adsorbed iodine −Cl···I_2 that evolves to $-(Cl\cdot\cdot I)^+\cdot I^-$, leading to further formation of I_3^-, I_4^{2-}, or I_5^- from various combinations of I^- with I_2.

The PXRD pattern of iodine-loaded I_2@Hf-HHU-2 and washed samples (Figure S23, Supporting Information) shows that Hf-HHU-2-Cl maintains its structural integrity upon adsorption and desorption of iodine vapor. The presence of hafnium in Hf-HHU-2, its hydrothermal stability, its strong affinity for iodine due to chloro-functionality, and its iodine adsorption capacity of 0.65 g g^{-1} makes it a potential material for long-term iodine capture and sequestration.

■ CONCLUSIONS

In summary, two new Hf-MOFs based on acetylenedicarboxylate and chlorofumarate linkers have been obtained. The solvent used for the synthesis was found to direct the nature of the product. Hafnium acetylenedicarboxylate was obtained in DMF, while hafnium chlorofumarate was obtained in water from an in situ transformation of H_2ADC, that is a hydrochlorination consisting of addition of HCl on the −C≡C− triple-bond of H_2ADC. The high crystallinity of the new materials enabled to determine their structure from PXRD and Rietveld refinement to be UiO-66 analogues. The porosity investigated by means of nitrogen sorption reveals that these materials are microporous as expected. Meanwhile the type Ib water sorption isotherms for both materials disclose their high hydrophilicity, with an additional enhancement noticed on account of chloro-functions in Hf-HHU-2. The CO_2 and iodine adsorption properties were further investigated on Hf-HHU-2, as well as formation of clusters defect nanoregions with **reo** topology in its framework when the reaction mixture contains a linker to metal−salt molar ratio of 1:1. We have hence obtained that the halogen MOFs functionalization via in situ hydrohalogenation of acetylenedicarboxylic acid triple bond is also implementable with hafnium-based MOFs like those recently developed for Zr-MOFs.

■ ASSOCIATED CONTENT

Ⓢ Supporting Information

The Supporting Information is available free of charge on the ACS Publications website at DOI: 10.1021/acs.inorgchem.9b01408.

Experimental methods and syntheses, IR, Raman, NMR, XPS, and SEM-EDX spectra, TGA and chemical stability tests, structure details and cif-file, nitrogen and water sorption isotherms also in comparison to Zr-HHUs and of cluster defective Hf-HHU-2, iodine adsorption related photographs, and isosteric heat of CO_2 adsorption (PDF)

Accession Codes

CCDC 1915835 contains the supplementary crystallographic data for this paper. These data can be obtained free of charge via www.ccdc.cam.ac.uk/data_request/cif, or by emailing data_request@ccdc.cam.ac.uk, or by contacting The Cambridge Crystallographic Data Centre, 12 Union Road, Cambridge CB2 1EZ, UK; fax: +44 1223 336033.

AUTHOR INFORMATION

Corresponding Author

*(C.J.) E-mail: janiak@uni-duesseldorf.de.

ORCID

Helge Reinsch: 0000-0001-5288-1135
Gerd Buntkowsky: 0000-0003-1304-9762
Christoph Janiak: 0000-0002-6288-9605

Notes

The authors declare no competing financial interest.

ACKNOWLEDGMENTS

We thank the German Academic Exchange Service (DAAD) for funding to T.J.M.M.N. and the Federal Ministry of Education and Research (BMBF) for project Optimat, Grant No. 03SF0492C.

REFERENCES

(1) Kerr, J. A. In *CRC Handbook of Chemistry and Physics*, 81st ed.; Lide, D. R., Ed.; CRC Press: Boca Raton, FL, 2000.

(2) Bon, V.; Senkovska, I.; Baburin, I. A.; Kaskel, S. Zr- and Hf-Based Metal-Organic Frameworks: Tracking Down the Polymorphism. *Cryst. Growth Des.* **2013**, *13*, 1231−1237.

(3) Bon, V.; Senkovskyy, V.; Senkovska, I.; Kaskel, S. Zr- and Hf-Based Metal-Organic Frameworkswith reo-Topology. *Chem. Commun.* **2012**, *48*, 8407−8409.

(4) Janiak, C.; Vieth, J. K. MOFs, MILs and More: Concepts, Properties and Applications for Porous Coordination Networks (PCNs). *New J. Chem.* **2010**, *34*, 2366−2388.

(5) DeCoste, J. B.; Peterson, G. W.; Jasuja, H.; Glover, T. G.; Huang, Y.-G.; Walton, K. S. Stability and Degradation Mechanisms of Metal-Organic Frameworks Containing the $Zr_6O_4(OH)_4$ Secondary Building Unit. *J. Mater. Chem. A* **2013**, *1*, 5642−5650.

(6) Kandiah, M.; Nilsen, M. H.; Usseglio, S.; Jakobsen, S.; Olsbye, U.; Tilset, M.; Larabi, C.; Quadrelli, E. A.; Bonino, F.; Lillerud, K. P. Synthesis and Stability of Tagged UiO-66 Zr-MOFs. *Chem. Mater.* **2010**, *22*, 6632−6640.

(7) Marshall, R. J.; Griffin, S. L.; Wilson, C.; Forgan, R. S. Stereoselective Halogenation of Integral Unsaturated C-C Bonds in Chemically and Mechanically Robust Zr and Hf MOFs. *Chem. - Eur. J.* **2016**, *22*, 4870−4877.

(8) Vermoortele, F.; Bueken, B.; Le Bars, G.; Van de Voorde, B.; Vandichel, M.; Houthoofd, K.; Vimont, A.; Daturi, M.; Waroquier, M.; Van Speybroeck, V.; Kirschhock, C.; De Vos, D. Synthesis Modulation as a Tool To Increase the Catalytic Activity of Metal-Organic Frameworks: The Unique Case of UiO-66(Zr). *J. Am. Chem. Soc.* **2013**, *135*, 11465−11468.

(9) Gomes Silva, C.; Llabrés i Xamena, F. X.; Corma, A.; García, H.; et al. Water Stable Zr-Benzenedicarboxylate Metal-Organic Frameworks as Photocatalysts for Hydrogen Generation. *Chem. - Eur. J.* **2010**, *16*, 11133−11138.

(10) Chavan, S.; Vitillo, J. G.; Gianolio, D.; Zavorotynska, O.; Civalleri, B.; Jakobsen, S.; Nilsen, M. H.; Valenzano, V.; Lamberti, C.; Lillerud, K. P.; Bordiga, S. H_2 Storage in Isostructural UiO-67 and UiO-66 MOFs. *Phys. Chem. Chem. Phys.* **2012**, *14*, 1614−1626.

(11) Lv, X.-L.; Tong, M.; Huang, H.; Wang, B.; Gan, L.; Yang, Q.; Zhong, C.; Li, J.-R. A High Surface Area Zr(IV)-Based Metal-Organic Framework Showing Stepwise Gas Adsorption and Selective Dye Uptake. *J. Solid State Chem.* **2015**, *223*, 104−108.

(12) Shen, J.; Liu, G.; Huang, K.; Li, Q.; Guan, K.; Li, Y.; Jin, W. UiO-66-Polyether Block Amide Mixed Matrix Membranes for CO_2 Separation. *J. Membr. Sci.* **2016**, *513*, 155−165.

(13) Zhu, X.; Gu, J.; Wang, Y.; Li, B.; Li, Y.; Zhao, W.; Shi, J. Inherent Anchorages in UiO-66 Nanoparticles for Efficient Capture of Alendronate and its Mediated Release. *Chem. Commun.* **2014**, *50*, 8779−8782.

(14) Wei, Z.; Gu, Z.-Y.; Arvapally, R. K.; Chen, Y.-P.; McDougald, R. N., Jr.; Ivy, J. F.; Yakovenko, A. A.; Feng, D.; Omary, M. A.; Zhou, H.-C. Rigidifying Fluorescent Linkers by Metal-Organic Framework Formation for Fluorescence Blue Shift and Quantum Yield Enhancement. *J. Am. Chem. Soc.* **2014**, *136*, 8269−8276.

(15) Stassen, I.; Bueken, B.; Reinsch, H.; Oudenhoven, J. F. M.; Wouters, D.; Hajek, J.; Van Speybroeck, V.; Stock, N.; Vereecken, P. M.; Van Schaijk, R.; De Vos, D.; Ameloot, R. Towards Metal-Organic Framework Based Field Effect Chemical Sensors: UiO-66-NH_2 for Nerve Agent Detection. *Chem. Sci.* **2016**, *7*, 5827−5832.

(16) Kim, H.; Yang, S.; Rao, S. R.; Narayanan, S.; Kapustin, E. A.; Furukawa, H.; Umans, A. S.; Yaghi, O. M.; Wang, E. E. Water Harvesting from Air with Metal-Organic Frameworks Powered by Natural Sunlight. *Science* **2017**, *356*, 430−434.

(17) Jeremias, F.; Lozan, V.; Henninger, S. K.; Janiak, C. Programming MOFs for Water Sorption: Amino-Functionalized MIL-125 and UiO-66 for Heat Transformation and Heat Storage Applications. *Dalton Trans.* **2013**, *42*, 15967−15973.

(18) Jeremias, F.; Fröhlich, D.; Janiak, C.; Henninger, S. K. Water and Methanol Adsorption on MOFs for Cycling Heat Transformation Processes. *New J. Chem.* **2014**, *38*, 1846−1852.

(19) Wang, S.; Wang, J.; Cheng, W.; Yang, X.; Zhang, Z.; Xu, Y.; Liu, H.; Wu, Y.; Fang, M. A Zr Metal-Organic Framework Based on Tetrakis(4-carboxyphenyl) Silane and Factors Affecting the Hydrothermal Stability of Zr-MOFs. *Dalton Trans.* **2015**, *44*, 8049−8061.

(20) Mondloch, J. E.; Katz, M. J.; Planas, N.; Semrouni, D.; Gagliardi, L.; Hupp, J. T.; Farha, O. K. Are Zr_6-Based MOFs Water Stable? Linker Hydrolysis *vs.* Capillary-Force-Driven Channel Collapse. *Chem. Commun.* **2014**, *50*, 8944−8946.

(21) Cavka, J. H.; Jakobsen, S.; Olsbye, U.; Guillou, N.; Lamberti, C.; Bordiga, S.; Lillerud, K. P. A New Zirconium Inorganic Building Brick Forming Metal Organic Frameworks with Exceptional Stability. *J. Am. Chem. Soc.* **2008**, *130*, 13850−13851.

(22) Waitschat, S.; Fröhlich, D.; Reinsch, H.; Terraschke, H.; Lomachenko, K. A.; Lamberti, C.; Kummer, H.; Helling, T.; Baumgartner, M.; Henninger, S.; Stock, N. Synthesis of M-UiO-66 (M = Zr, Ce or Hf) Employing 2,5-Pyridinedicarboxylic Acid as a Linker: Defect chemistry, Framework Hydrophilisation and Sorption Properties. *Dalton Trans* **2018**, *47*, 1062−1070.

(23) Jakobsen, S.; Gianolio, D.; Wragg, D. S.; Nilsen, M. H.; Emerich, H.; Bordiga, S.; Lamberti, C.; Olsbye, U.; Tilset, M.; Lillerud, K. P. Structural Determination of a Highly Stable Metal-Organic Framework with Possible Application to Interim Radioactive Waste Scavenging: Hf-UiO-66. *Phys. Rev. B: Condens. Matter Mater. Phys.* **2012**, *86*, 125429.

(24) Hu, Z.; Nalaparaju, A.; Peng, Y.; Jiang, J.; Zhao, D. Modulated Hydrothermal Synthesis of UiO-66(Hf)-Type Metal-Organic Frameworks for Optimal Carbon Dioxide Separation. *Inorg. Chem.* **2016**, *55*, 1134−1141.

(25) Xydias, P.; Spanopoulos, I.; Klontzas, E.; Froudakis, G. E.; Trikalitis, P. N. Drastic Enhancement of the CO_2 Adsorption Properties in Sulfone-Functionalized Zr- and Hf-UiO-67 MOFs with Hierarchical Mesopores. *Inorg. Chem.* **2014**, *53*, 679−681.

(26) Hu, Z.; Castano, I.; Wang, S.; Wang, Y.; Peng, Y.; Qian, Y.; Chi, C.; Wang, X.; Zhao, D. Modulator Effects on the Water-Based Synthesis of Zr/Hf Metal-Organic Frameworks: Quantitative Relationship Studies between Modulator, Synthetic Condition, and Performance. *Cryst. Growth Des.* **2016**, *16*, 2295−2301.

(27) Matemb Ma Ntep, T. J.; Reinsch, H.; Moll, B.; Hastürk, E.; Gökpinar, S.; Breitzke, H.; Schlüsener, C.; Schmolke, L.; Buntkowsky, G.; Janiak, C. Realizing the Potential of Acetylenedicarboxylate by

Functionalization to Halofumarate in Zr^{IV} Metal-Organic Frameworks. *Chem. - Eur. J.* **2018**, *24*, 14048−14053.

(28) (a) Zahn, G.; Zerner, P.; Lippke, J.; Kempf, F. L.; Lilienthal, S.; Schröder, C. A.; Schneider, A. M.; Behrens, P. Insight into the Mechanism of Modulated Syntheses: In Situ Synchrotron Diffraction Studies on the Formation of Zr-fumarate MOF. *CrystEngComm* **2014**, *16*, 9198−9207. (b) Marshall, R. J.; Hobday, C. L.; Murphie, C. F.; Griffin, S. L.; Morrison, C. A.; Moggach, S. A.; Forgan, R. S. Amino Acids as Highly Efficient Modulators for Single Crystals of Zirconium and Hafnium Metal-Organic Frameworks. *J. Mater. Chem. A* **2016**, *4*, 6955−6963.

(29) (a) Billetter, H.; Pantenburg, I.; Ruschewitz, U. Copper(II) Chlorofumarate Trihydrate. *Acta Crystallogr., Sect. E: Struct. Rep. Online* **2006**, *E62*, m881−m883. (b) Billetter, H.; Pantenburg, I.; Ruschewitz, U. Lithium Hydrogen Iodofumarate Monohydrate. *Acta Crystallogr., Sect. E: Struct. Rep. Online* **2005**, *E61*, m1857−m1859.

(30) (a) Papirer, E.; Lacroix, R.; Donnet, J.-B.; Nansé, G.; Fioux, P. XPS Study of the Halogenation of Carbon black - part 2 Chlorination. *Carbon* **1995**, *33* (I), 63−72. (b) Li, Y.; Chen, H.; Voo, L. Y.; Ji, J.; Zhang, G.; Zhang, G.; Zhang, F.; Fan, X. Synthesis of Partially Hydrogenated Graphene and Brominated Grapheme. *J. Mater. Chem.* **2012**, *22*, 15021−15024.

(31) Alivio, T. E. G.; De Jesus, L.; Dennis, R. V.; Jia, Y.; Jaye, C.; Fischer, D. A.; Singisetti, U.; Banerjee, S. Atomic Layer Deposition of Hafnium(IV) Oxide on Graphene Oxide: Probing Interfacial Chemistry and Nucleation by using X-ray Absorption and Photoelectron Spectroscopies. *ChemPhysChem* **2015**, *16*, 2842−2848.

(32) Alexander, S.; Morrow, L.; Lord, A. M.; Dunnill, C. W.; Barron, A. R. Branched Hydrocarbon Low Surface Energy Materials for Superhydrophobic Nanoparticle Derived Surfaces. *J. Mater. Chem. A* **2015**, *3*, 10052−10059.

(33) Zhan, G.; Zeng, H. C. Synthesis and Functionalization of Oriented Metal-Organic-Framework Nanosheets: Toward a Series of 2D Catalysts. *Adv. Funct. Mater.* **2016**, *26*, 3268−3281.

(34) (a) Billetter, H.; Hohn, F.; Pantenburg, I.; Ruschewitz, U. $[CuC_2(COO)_2\}(H_2O)_3]\div H_2O$, the First Copper Complex of Acetylenedicarboxylic Acid. *Acta Crystallogr., Sect. C: Cryst. Struct. Commun.* **2003**, *59*, m130−m131. (b) Pantenburg, I.; Ruschewitz, U. $Co(C_2(COO)_2)(H_2O)_4\div 2H_2O$ and $Co(C_2(COO)_2)(H_2O)_2$: Two CoordinationPolymers of the Acetylenedicarboxylate Dianion. *Z. Anorg. Allg. Chem.* **2002**, *628*, 1697−1702. (c) Tranchemontagne, D. J.; Hunt, J. R.; Yaghi, O. M. Room Temperature Synthesis of Metal-Organic Frameworks: MOF-5, MOF-74, MOF-177, MOF-199, and IRMOF-0. *Tetrahedron* **2008**, *64*, 8553−8557. (d) Ruschewitz, U.; Pantenburg, I. $[Cd\{C_2(COO)_2\}(H_2O)_3]\div H_2O$, the First Cadmium Salt of Acetylenedicarboxylic Acid. *Acta Crystallogr., Sect. C: Cryst. Struct. Commun.* **2002**, *58*, m483−m484. (e) Stein, I.; Ruschewitz, U. Mechanochemical Synthesis of New Coordination Polymers with Acetylenedicarboxylate as Bridging Ligand. *Z. Anorg. Allg. Chem.* **2010**, *636*, 400−404. (f) Schuy, A.; Stein, I.; Ruschewitz, U. PbADC and $PbADC\div H_2O$: Two Coordination Polymers with Acetylenedicarboxylate (ADC^{2-}) as Bridging Ligand. *Z. Anorg. Allg. Chem.* **2010**, *636*, 1026−1031. (g) Michaelides, A.; Skoulika, S. Reactive Microporous Rare-Earth CoordinationPolymers that Exhibit Single-Crystal-to-Single-Crystal Dehydration and Rehydration. *Cryst. Growth Des.* **2005**, *5*, 529−533. (h) Busch, S.; Stein, I.; Ruschewitz, U. Hydrate Isomerism in Coordination Polymers of Bismuth and Acetylenedicarboxylate. *Z. Anorg. Allg. Chem.* **2012**, *638*, 2098−2101.

(35) Hohn, F.; Pantenburg, I.; Ruschewitz, U. $Sr[C_2(COO)_2]$: The First Anhydrous Salt of Acetylenedicarboxylic Acid. *Chem. - Eur. J.* **2002**, *8*, 4536−4541.

(36) Cliffe, M. J.; Wan, W.; Zou, X.; Chater, P. A.; Kleppe, A. K.; Tucker, M. G.; Wilhelm, H.; Funnell, N. P.; Coudert, F.-X.; Goodwin, A. L. Correlated Defect Nanoregions in a Metal-Organic Framework. *Nat. Commun.* **2014**, *5*, 4176.

(37) Shearer, G. C.; Chavan, S.; Bordiga, S.; Svelle, S.; Olsbye, U.; Lillerud, K. P. Defect Engineering: Tuning the Porosity and Composition of the Metal-Organic Framework UiO-66 via Modulated Synthesis. *Chem. Mater.* **2016**, *28*, 3749−3761.

(38) Thommes, M.; Kaneko, K.; Neimark, A. V.; Olivier, J. P.; Rodriguez-Reinoso, F.; Rouquerol, J.; Sing, K. S. W. Physisorption of Gases, with Special Reference to the Evaluation of Surface Area and Pore Size Distribution (IUPAC Technical Report). *Pure Appl. Chem.* **2015**, *87*, 1051−1069.

(39) Mondloch, J. E.; Karagiaridi, O.; Farha, O. K.; Hupp, J. T. Activation of Metal-Organic Framework Materials. *CrystEngComm* **2013**, *15*, 9258−9264.

(40) Howarth, A. J.; Peters, A. W.; Vermeulen, N. A.; Wang, T. C.; Hupp, J. T.; Farha, O. K. Best Practices for the Synthesis, Activation, and Characterization of Metal-Organic Frameworks. *Chem. Mater.* **2017**, *29*, 26−39.

(41) Düren, T.; Millange, F.; Férey, G.; Walton, K. S.; Snurr, R. Q. Calculating Geometric Surface Areas as a Characterization Tool for Metal-Organic Frameworks. *J. Phys. Chem. C* **2007**, *111* (42), 15350−15356.

(42) Taddei, M. When Defects Turn into Virtues: The Curious Case of Zirconium-Based Metal-Organic Frameworks. *Coord. Chem. Rev.* **2017**, *343*, 1−24.

(43) Thornton, A. W.; Babarao, R.; Jain, A.; Trousselet, F.; Coudert, F.-X. Defects in Metal-Organic Frameworks: A Compromise Between Adsorption and Stability? *Dalton Trans.* **2016**, *45*, 4352−4359.

(44) Yushina, I. D.; Kolesov, B. A.; Bartashevich, E. V. Raman Spectroscopy Study of New Thia- and Oxazinoquinolinium Triodides. *New J. Chem.* **2015**, *39*, 6163−6170.

(45) Deplano, P.; Ferraro, J. R.; Mercuri, M. L.; Trogu, E. F. Structural and Raman Spectroscopic Studies as Complementary Tools in Elucidating the Nature of the Bonding in Polyiodides and in Donor-I2 Adducts. *Coord. Chem. Rev.* **1999**, *188*, 71−95.

(46) Mohanambe, L.; Vasudevan, S. Insertion of Iodine in a Functionalized Inorganic Layered Solid. *Inorg. Chem.* **2004**, *43*, 6421−6425.

(47) Semnani, A.; Shamsipur, M. Spectrophotometric Study of the Complexation of Iodine with Macrocycles in Chloroform Solution. *J. Chem. Soc., Dalton Trans.* **1996**, 2215−2218.

(48) Cavallo, G.; Metrangolo, P.; Milani, R.; Pilati, T.; Priimagi, A.; Resnati, G.; Terraneo, G. The Halogen Bond. *Chem. Rev.* **2016**, *116*, 2478−2601.

Supporting Information

Acetylenedicarboxylate and In Situ Generated Chlorofumarate-Based Hafnium(IV)-Metal-Organic Frameworks: Synthesis, Structure, and Sorption Properties

Tobie J. Matemb Ma Ntep,[†] Helge Reinsch,[‡] Carsten Schlüsener,[†] Anna Goldman,[†] Hergen Breitzke,[§] Bastian Moll,[†] Laura Schmolke,[†] Gerd Buntkowsky,[§] and Christoph Janiak*[⊥,†]

[†] Institut für Anorganische Chemie, Heinrich-Heine-Universität Düsseldorf, D- 40204 Düsseldorf, Germany

[‡] Institut für Anorganische Chemie, Christian-Albrechts-Universität, Max-Eyth-Straße 2, 24118 Kiel, Germany

[§] Eduard-Zintl-Institut für Anorganische und Physikalische Chemie, Technische Universität Darmstadt, Alarich-Weiss-Straße. 4, D-64287 Darmstadt, Germany

[⊥] Hoffmann Institute of Advanced Materials, Shenzhen Polytechnic, 7098 Liuxian Blvd, Nanshan District, Shenzhen, China

* Corresponding author: E-mail: janiak@uni-duesseldorf.de; Fax: + 49-211-81-12287; Tel: +49-211-81-12286

Additional email addresses:

tobie.matemb.ma.ntep@uni-duesseldorf.de; hreinsch@ac.uni-kiel.de; carsten.schluesener@uni-duesseldorf.de; anna.goldman@uni-duesseldorf.de; breitzke@chemie.tu-darmstadt.de; bastian.moll@uni-duesseldorf.de; laura.schmolke@uni-duesseldorf.de; gerd.buntkowsky@chemie.tu-darmstadt.de

Table of Contents

- Experimental Section
- Infrared and Raman Spectroscopy Analyses
- Solid State and Solution NMR of Hf-HHU-2
- Determination of Acetate to Halofumarate (Fum-Cl) Linker Ratio in Hf-HHU-2 MOF from Solution ^{1}H NMR
- X-ray Photoelectron Spectroscopy (XPS) Analyses of Hf-HHU-2
- Scanning Electron Microscopy and Energy Dispersive X-ray Spectroscopy (EDX) Analyses of Hf-HHU-2
- Thermogravimetric analyses of Hf-HHU-1, -2
- Chemical Stability Tests of Hf-HHU-1, -2
- Structure Details of Hf-HHU-1, -2
- Comparison of Nitrogen and Water Vapor Sorption Characteristics of Hf-HHUs and Zr-HHUs
- Nitrogen and Water Sorption Isotherms of Hf-HHU-2 Containing Cluster Defect Nanodomains with reo Topology
- Iodine Adsorption for Hf-HHU-2
- Determination of the Isosteric Heat of CO_2 Adsorption
- References

Experimental Section

Materials and Methods. Acetylenedicarboxylic acid (H_2ADC, purity 97%) was purchased from Alfa Aesar; hafnium chloride ($HfCl_4$, purity 99%) was purchased from Acros Organics; hafnium oxychloride hydrate ($HfOCl_2 \cdot xH_2O$, purity 99.9%) was purchased from Sigma-Aldrich; N,N-dimethylformamide (DMF, analytical reagent grade) and methanol (analytical reagent grade) were purchased from Fischer Chemical; acetic acid (purity >99.9%) was purchased from VWR Chemicals; iodine (I_2, purity 99.5 %) was purchased from Grüssing. All chemicals were used without further purification.

Infrared (IR) spectra were obtained on a Bruker FT-IR Tensor 37 Spectrometer in the 4000-550 cm^{-1} region with 2 cm^{-1} resolution as KBr disks. Raman spectra were obtained on a Bruker MultiRAM-FT Raman spectrometer equipped with a Nd:YAG-laser (wavelength 1064 nm).

All Raman spectra were measured in solid state for 2500 scans with a laser power between 10-20 mW.

Powder X-ray diffraction (PXRD) data was collected on a Bruker D2 Phaser diffractometer using a flat silicon low background sample holder and Cu $K\alpha1/\alpha2$ radiation with $\lambda = 1.5418$ Å at 30 kV covering 2theta angles 5-50° over a time of 1 h, that is 0.01 °/sec. Diffractograms were obtained on a flat layer sample holder where at low angles the beam spot is strongly broadened so that only a fraction of the reflected radiation reaches the detector which leads to low relative intensities measured at $2\theta<7°$. Therefore, PXRD data for Rietveld refinement was measured in transmission geometry using a STOE Stadi MP equipped with a Mythen detector and using Cu $K\alpha_1$ radiation.

Thermogravimetric analyses (TGA) were carried out at a ramp rate of 10 °C/min in a N_2 flow with a Netzsch Thermo-Microbalance Apparatus TG 209 F3 Tarsus.

Scanning electron microscopy (SEM) images were obtained using a Jeol JSM-6510LV QSEM advanced electron microscope with a LaB6 cathode at 5–20 keV. The samples for SEM imaging were coated with gold using a Jeol JFC 1200 fine-coater (20 mA for 25 s).

X-ray photoelectron spectroscopy, XPS–(ESCA–) measurement was performed with a Fisons/VG Scientific ESCALAB 200X XP–spectrometer, operating at 70–80 °C, a pressure of $7.0x10^{-9}$ mbar and a sample angle of 33°. Spectra were recorded using polychromatic AlKα excitation (11 kV, 20 mA) and an emission angle of 0°. Calibration of the XPS was carried out by recording spectra with Al Kα X–rays from clean samples of copper, silver and gold at 50 eV and 10 eV pass energies and comparison with reference values. Fitting of the experimental XP spectra was done with the program CasaXPS, version 2.3.19PR1.0, copyright 1999-2018 Casa Software Ltd.

Conventional CP MAS solid state NMR measurements were carried out at room temperature on a Bruker AVANCE II+ spectrometer at 400 MHz proton resonance frequency, employing a Bruker 4 mm double resonance probe. ^{13}C CP MAS spectra were recorded utilizing ramped CP-MAS sequences at spinning rates of 8 kHz. Contact time was set to 1.5 ms and tppm decoupling with a

15° phase jump was applied during data acquisition.[1] ^{13}C spectra were referenced with respect to TMS (tetramethylsilane). Frequency switched Lee Goldburg (FSLG) CP MAS HETCOR spectra were recorded at 8 kHz and contact times of 2 ms, 500 µs (not shown), and 200 µs (Figure 36). The tppm decoupling sequence with a 15° phase jump was applied during data acquisition. ^{1}H spectra were recorded utilizing FSLG homonuclear decoupling, applying the same LG field strength and step width as for the FSLG HETCOR spectra. ^{1}H shift values of the direct dimension of these spectra were utilized to reference the indirect dimensions of the FSLG HETCOR spectra. The direct dimensions of the ^{1}H spectra were referenced with respect to TMS.

Solution ^{1}H, ^{13}C spectra were measured with a Bruker Avance III-300 (300 MHz). Prior to solution NMR analysis, an activated sample of Hf-HHU-2 was digested as follows: 15 mg of MOF and 10 mg of CsF (caesium fluoride) were suspended in DMSO-d_6 (0.65 mL). 5 drops of aqueous DCl (35 wt% in D_2O) were added. As soon as the light yellow solid of MOF was dissolved (after 15-30 min), 12 mg K_2CO_3 was added to neutralize the acid.[2]

Water vapor sorption isotherms were measured at 20 °C on a VSTARTM vapor sorption analyzer (Model number Vstar4-0000-1000-XS) from Quantachrome. For this purpose, about 25 mg of activated sample were introduced in the measuring cell and connected to the analysis port of the analyzer.

For porosity studies, nitrogen isotherms were measured on a Quantachrome Autosorb iQ MP at 77 K (N_2). The temperature of 77 K was set by a liquid nitrogen bath. The specific surface area was calculated from the nitrogen sorption isotherms using the Brunauer-Emmett-Teller (BET) equation. BET surface areas (S_{BET}) were obtained from five adsorption points in the pressure range P/P_0 = 0.001-0.05. Total pore volumes ($V_{pore\ (total)}$) were derived at $P/P_0 = 0.95$ for pores of diameter ≤ 20 nm. Micropore volume ($V_{pore\ (micro)}$) which refers to volume that originates only from micropores, was obtained by V-t-method with thickness method 'DeBoer'. All correlation coefficients (r) within calculations were >0.999.

CO_2 isotherms were measured using a Micromeritics ASAP 2020 automatic gas sorption analyzer equipped with oil-free vacuum pumps (ultimate vacuum $<10^{-8}$ mbar) and valves, which guaranteed contamination free measurements. The sample was connected to the preparation port of the sorption analyzer and degassed under vacuum until the outgassing rate, i.e., the rate of pressure rise in the temporarily closed manifold with the connected sample tube, was less than 2 µTorr/min at the specified temperature of 120 °C or room temperature. After weighing, the sample tube was then transferred to the analysis port of the sorption analyzer. Enthalpies of CO_2 adsorption were calculated from ASAP software packages by applying the Clausius-Clapeyron expression using the sorption isotherms data collected at 273 K and 293 K.

Synthesis Procedure.

Synthesis of [$Hf_6(\mu_3\text{-}O)_4(\mu_3\text{-}OH)_4(ADC)_6$], Hf-HHU-1. In a solvent mixture of DMF/acetic acid (2.5 mL/2.5 mL), were consecutively ultrasonically dissolved 409.5 mg (1 mmol) of hafnium oxychloride octahydrate ($HfOCl_2 \cdot 8H_2O$) and 114 mg (1 mmol) of acetylenedicarboxylic acid (H_2ADC). The resulting limpid solution was sealed in a screw-capped glass vial which was stored for 2 h in an oven preheated at 85 °C. After cooling to room temperature, white precipitate was separated from mother liquor, before being washed and centrifuged twice in fresh DMF (5 mL). DMF was exchanged by dispersing the solid three consecutive times in acetone (5m L) and centrifuging, then drying at room temperature in air. Yield: 230 mg.

The solvent in the pores of as-synthesized sample was removed by supercritical CO_2 ($scCO_2$) drying. This was followed by outgassing under dynamic vacuum for 1 h at room temperature, to yield the activated sample. This activation procedure was adopted to account for the thermal sensitivity of Hf-HHU-1. Attempts to activate this material at temperatures above 100 °C lead to amorphization of the material (see Figure S12).

Elemental analysis obtained for activated Hf-HHU-1: found C 15.10, H 1.96, N 0.80; calc. for [$Hf_6(O_4)(OH)_4(C_4O_4)_6$]($C_3H_7NO$)($H_2O$)$_{10}$: C 15.24, H 1.47, N 0.66%.

Synthesis of [$Hf_6(\mu_3\text{-}O)_4(\mu_3\text{-}OH)_4(Fum\text{-}Cl)_6$], Hf-HHU-2. In a solvent mixture of water/acetic acid (2.5 mL/2.5 mL), were consecutively ultrasonically dissolved 320 mg (1 mmol) of hafnium chloride ($HfCl_4$) and 114 mg (1 mmol) or 342 mg (3 mmol) of acetylenedicarboxylic acid (H_2ADC). The resulting limpid solution was sealed in a screw-capped glass vial which was stored for 6 h in an oven preheated at 85 °C. After cooling to room temperature, white precipitate was separated from mother liquor, washed and centrifuged thrice in fresh water (5 mL). The solid was re-dispersed three consecutive times in methanol and centrifuged, then dried at room temperature in air. Yield: 343 mg.

The as-synthesized sample was heated 6 h at 120 °C under dynamic vacuum to yield the activated sample.

Iodine Adsorption. About 30 mg of activated samples of Hf-HHU-2 were distributed in a small open vial, while about 100 mg I_2 crystals were distributed in a second open vial. The two vials were transferred together in a vessel that was charged with nitrogen. The vessel was then sealed to ensure a closed system and stored at room temperature. Iodine uptake was measured by the gravimetric method after regular adsorption times.

Infrared and Raman Spectroscopy Analyses

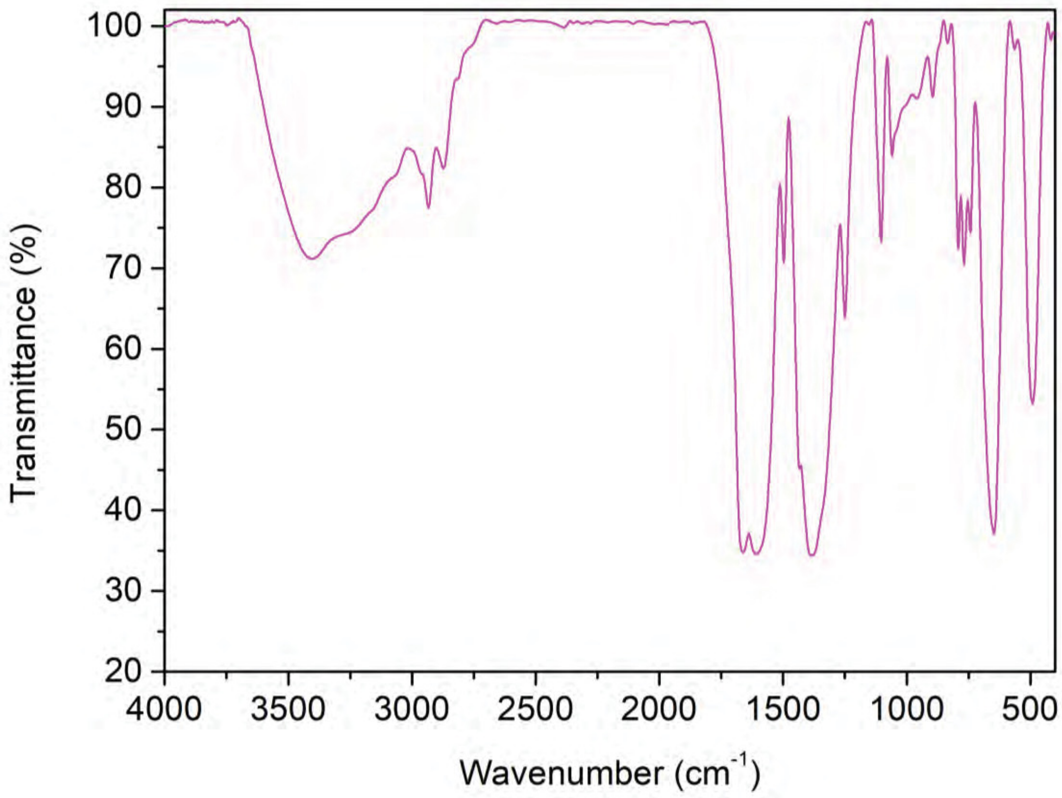

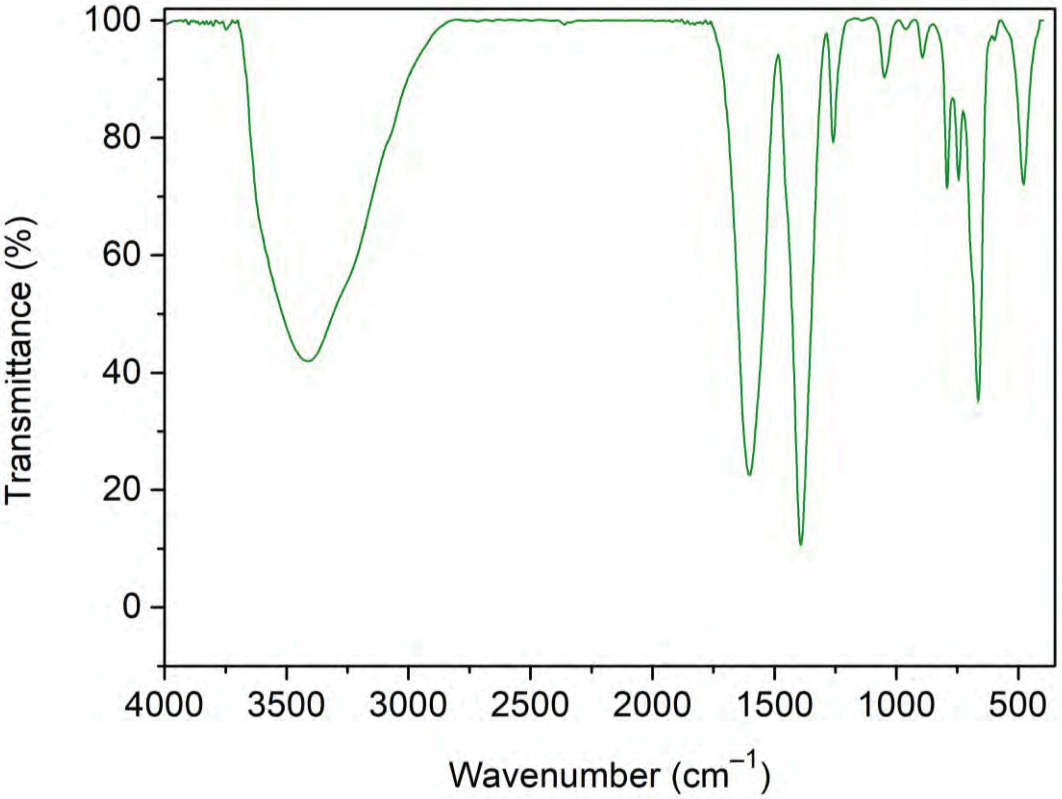

Figure S1. IR spectra of as-synthesized Hf-HHU-1 (top) and Hf-HHU-2 (bottom).

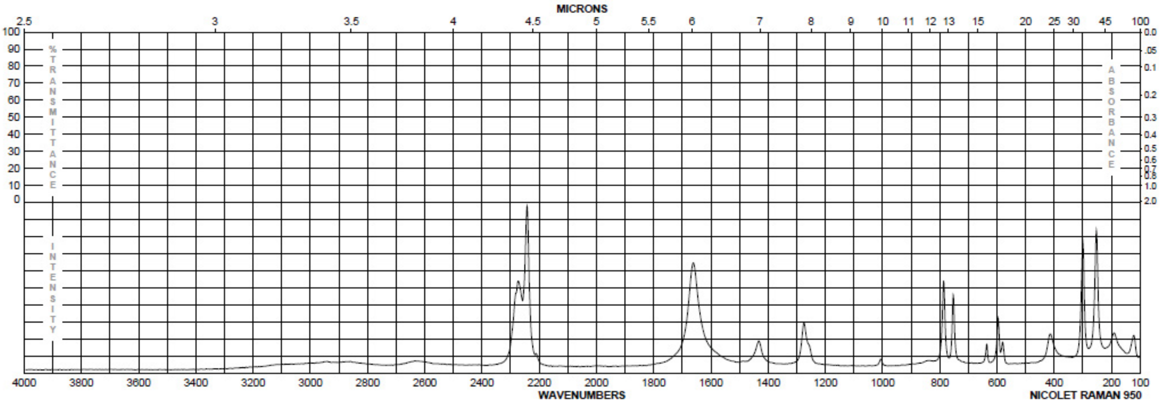

Figure S2. Raman spectrum of H_2ADC obtained from the purchase web page of Sigma Aldrich (www.sigmaaldrich.com/catalog/product/aldrich/a15207?lang=de&region=DE). Our pristine H_2ADC that was purchased from Alfa Aesar displays the same feature. The compound is very hygroscopic. Thus, water adsorption together with hydrogen bonding to the -COOH groups will change the C≡C stretching frequency.

Solid State and Solution NMR of Hf-HHU-2

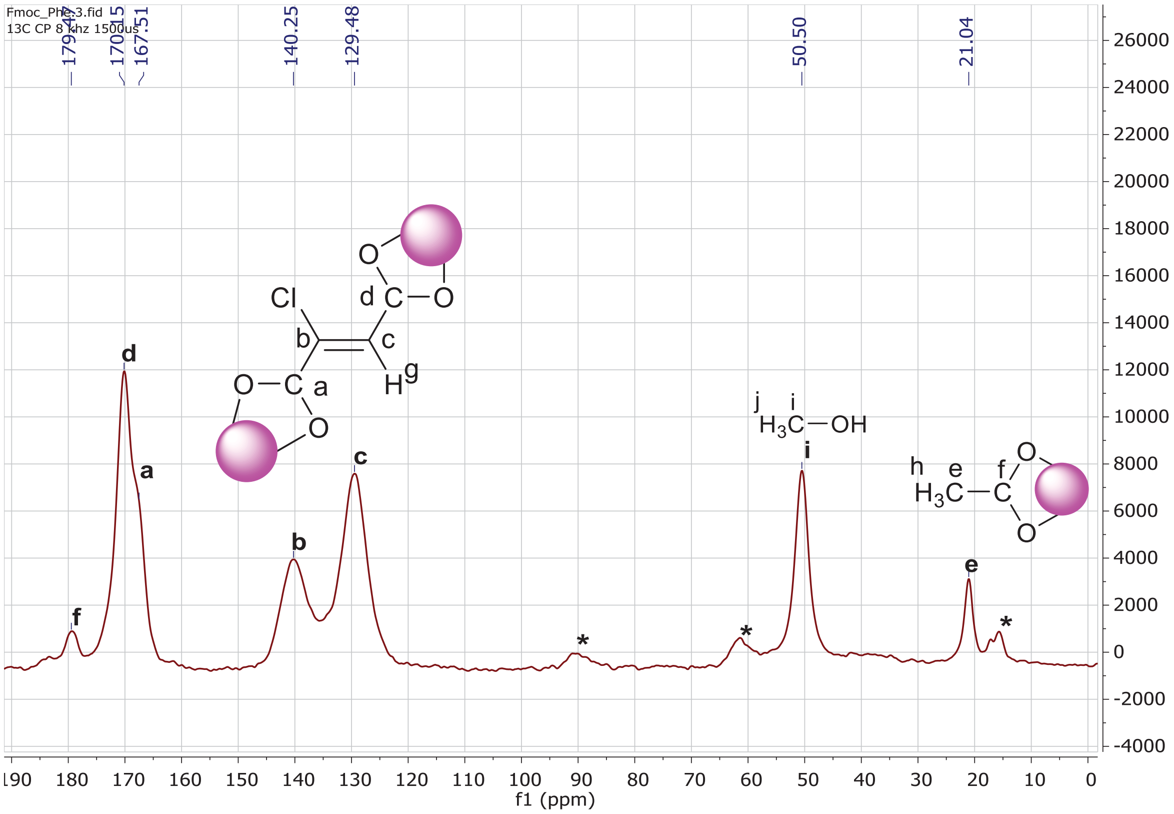

Figure S3. ^{13}C CP MAS solid-state NMR spectrum of Hf-HHU-2. The stars indicate spinning sidebands.

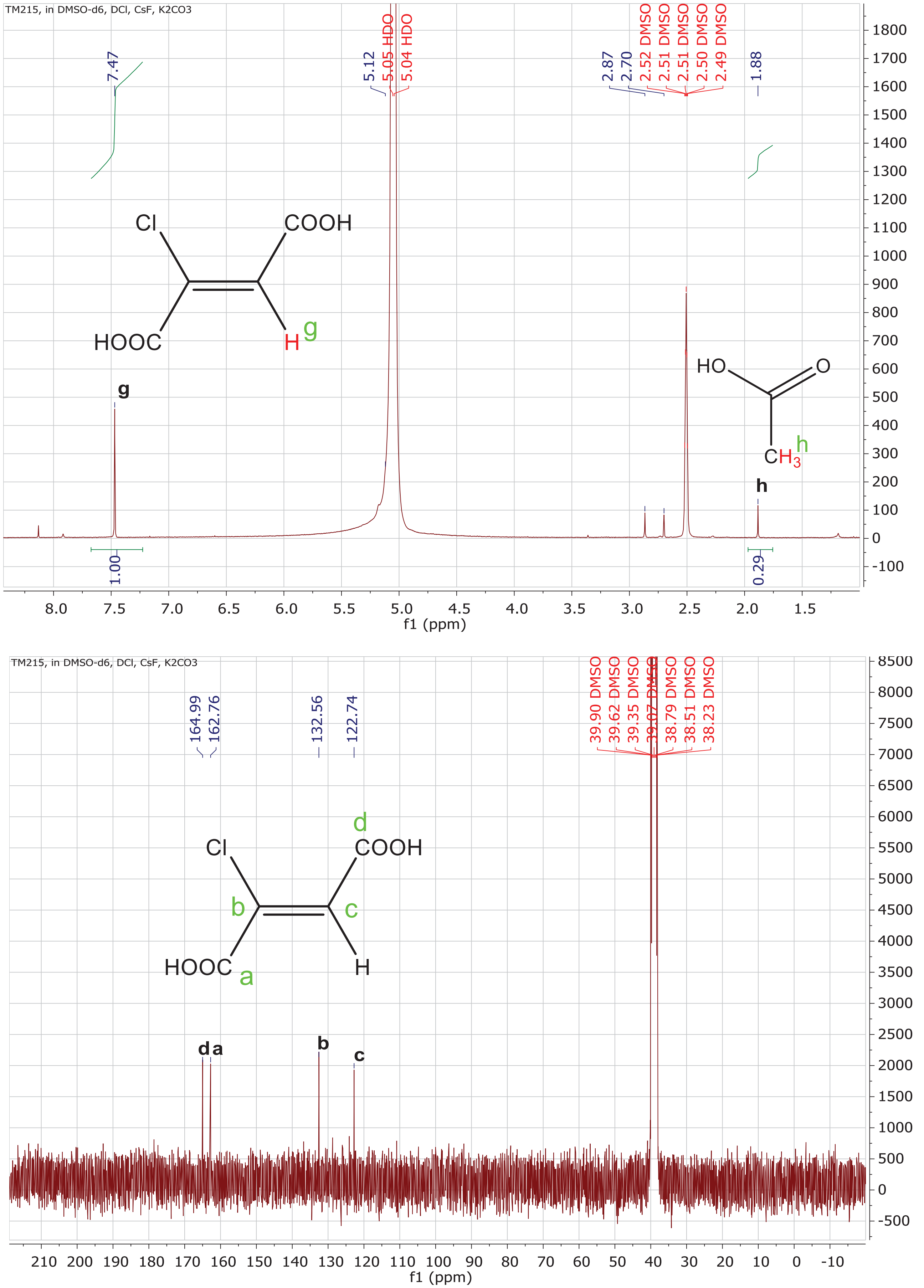

Figure S4. Solution ^{1}H (top) and ^{13}C (bottom) NMR spectra of digested Hf-HHU-2 in DMSO-d_6 (300 Hz).

Determination of Acetate to Halofumarate (Fum-Cl) Linker Ratio in Hf-HHU-2 MOF from Solution ^{1}H NMR

$$\frac{Acetate}{Fum-\mathrm{x}}\,\text{molar ratio} = \frac{\left(\frac{Integration\ of\ acetate\ signal}{Number\ of\ protons\ per\ acetate}\right)}{\left(\frac{Integration\ of\ Fum-X\ signal}{Number\ of\ protons\ per\ Fum-X}\right)}$$
$$= \left(\frac{Integ.\,of\ acet.}{3}\right) \times \left(\frac{1}{Integ.\,of\ Fum-X}\right)$$

Hence, the acetate to linker molar ratios is calculated to 0.096 for Hf-HHU-2.

Considering the unit formula $[Hf_6O_4(OH)_{4+x}(Fum\text{-}Cl)_{6-x}(Ac)_x]$ where *x* is the number of missing linker on the $\{Hf_6\}$-cluster per unit formula:

$$\frac{Ac}{Fum-\mathrm{x}}\,\text{molar ratio} = m_R = \frac{x}{6-x}\,, \qquad \text{which leads to} \quad x = \frac{6 \times m_R}{1+m_R}$$

Corresponding amount of missing linker per $\{Hf_6\}$-cluster in the unit formula is 0.53 missing linker per hafnium cluster for Hf-HHU-2.

X-ray Photoelectron Spectroscopy (XPS) Analyses of Hf-HHU-2

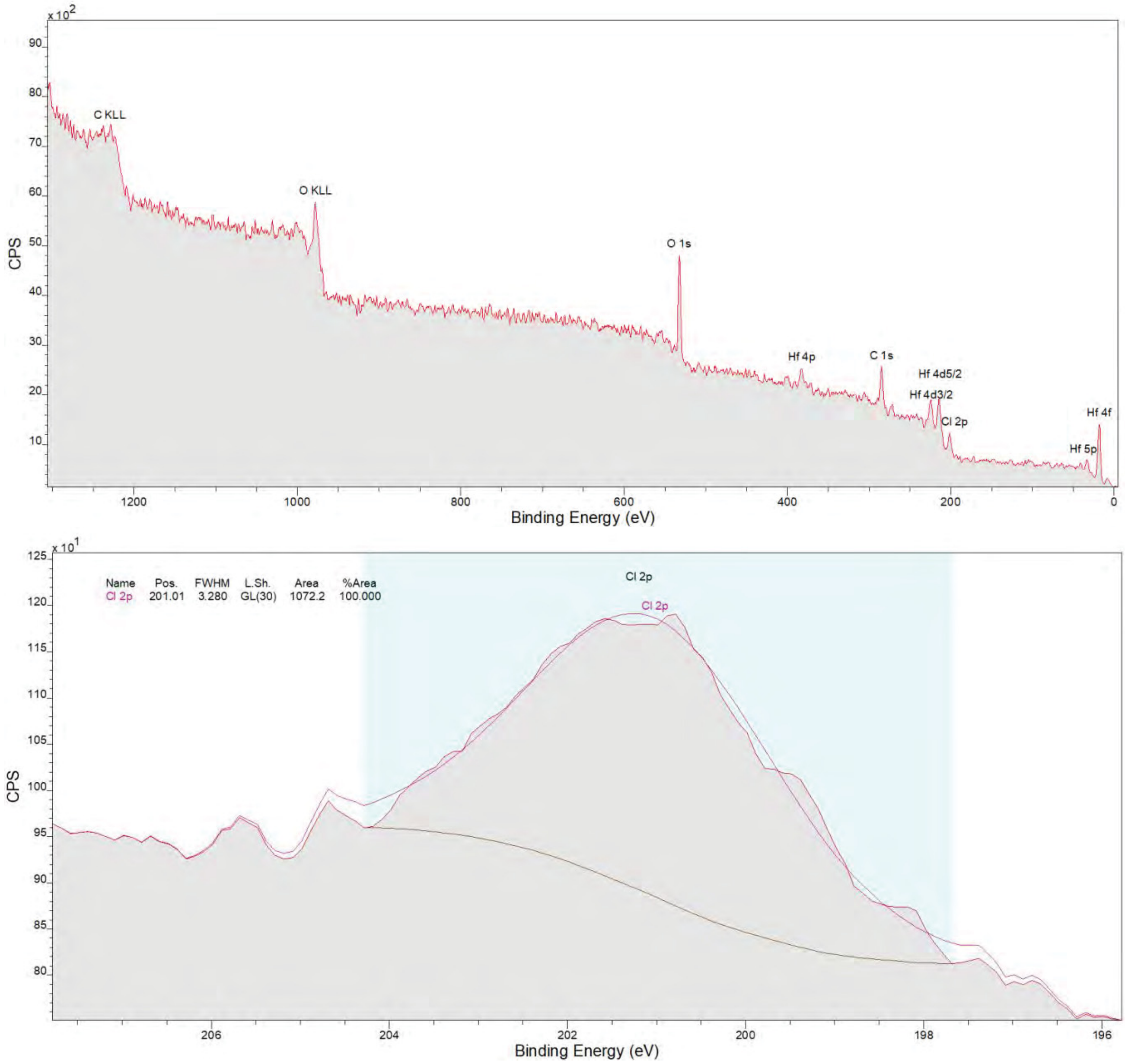

Figure S5. XPS survey spectrum surface and high resolution XPS core-level spectrum of Hf-HHU-2 (Hf-Fum-Cl) in the region of Cl 2p.

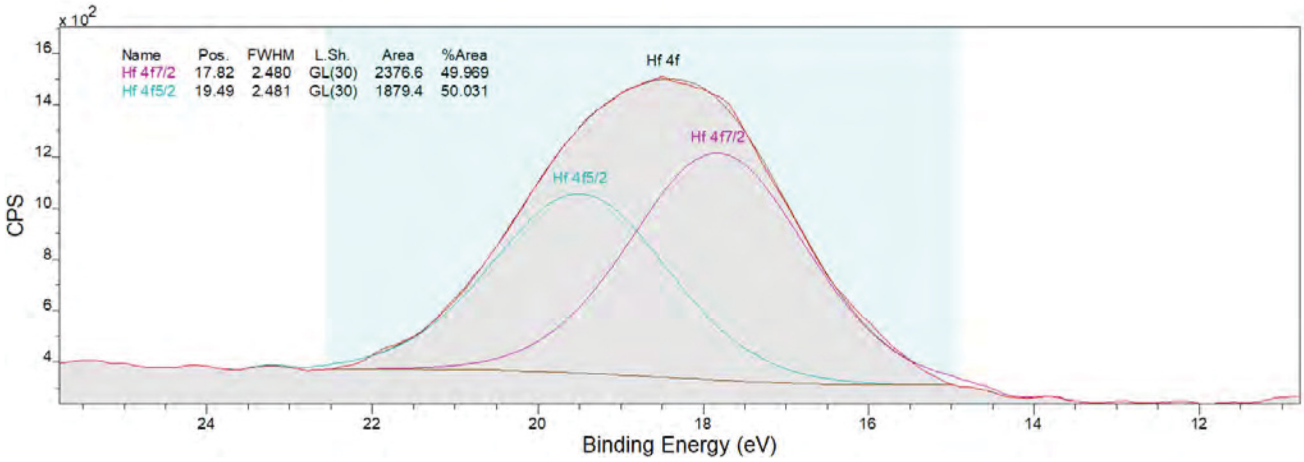

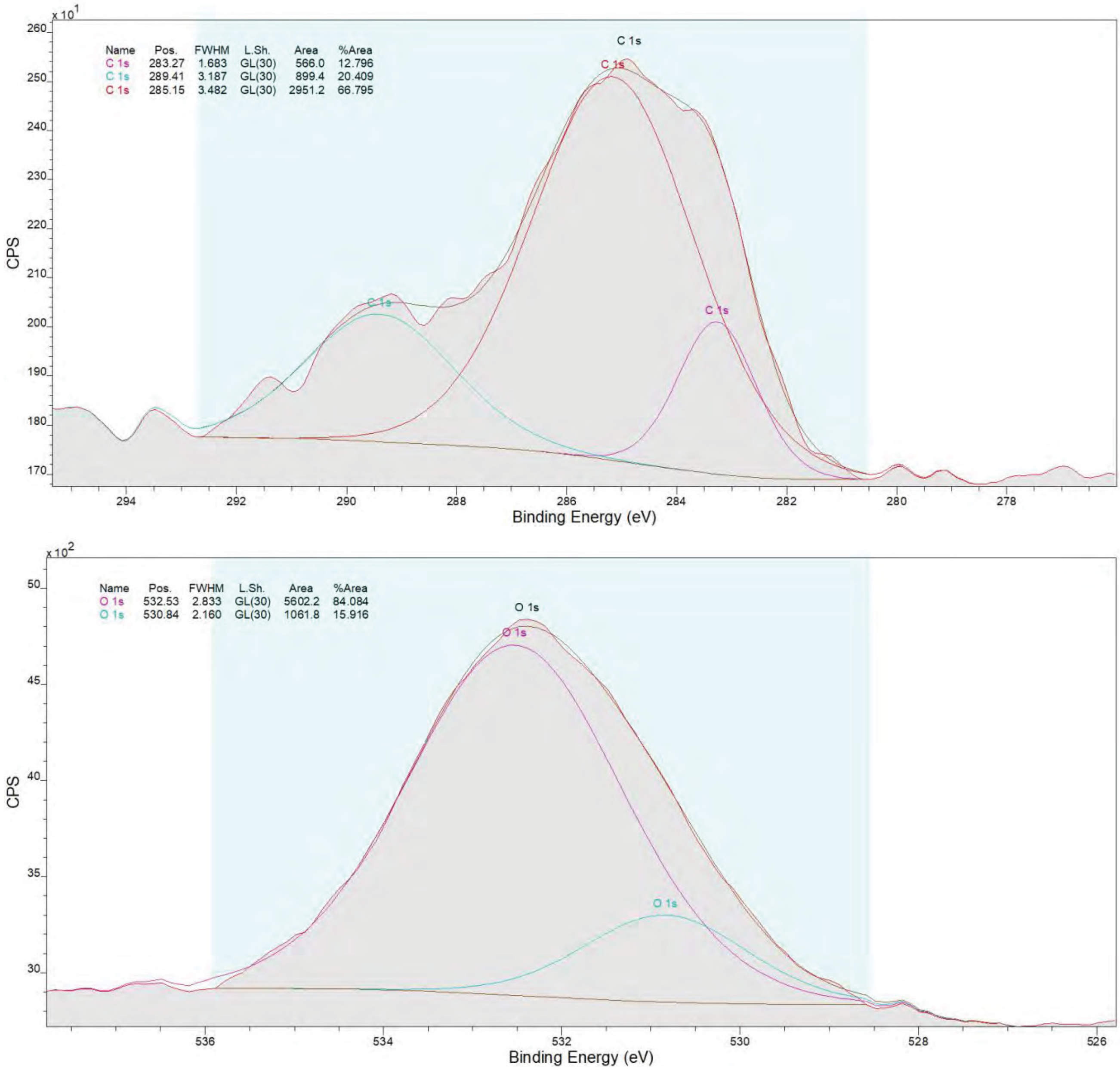

Figure S6. High resolution XPS core-level spectrum of Hf-HHU-2 in the region of Hf 4f, C 1s and O 1s (top to bottom, respectively).

Table S1. XP spectrum peaks assignments of Hf-HHU-2

Element	Orbital	Binding Energy	Area	RSF	Area/RSF	
C	1s	283,27	566	1	566	C=CH
		285,15	2951,2	1	2951,2	C=CCl
		289,41	899,4	1	899,4	Carboxyl
O	1s	530,84	1061,8	2,93	362,38908	Hf-O
		532,53	5602,2	2,93	1912,0137	org. C-O
Cl	2p	201,01	1072	2,29	468,12227	organic Cl
Hf	4f 7/2	17,82	2376,6	4,2	565,85714	HfO2
	4f 5/2	19,49	1879,4	3,32	566,08434	

Scanning Electron Microscopy and Energy Dispersive X-ray Spectroscopy (EDX) Analyses of Hf-HHU-2

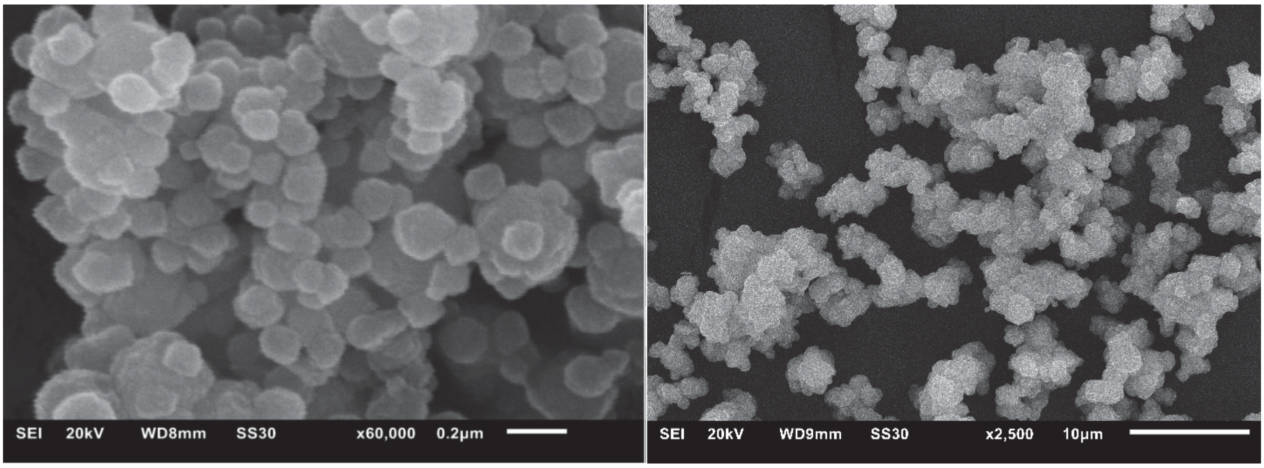

Figure S7. SEM images of Hf-HHU-1 (left) and Hf-HHU-2 (right).

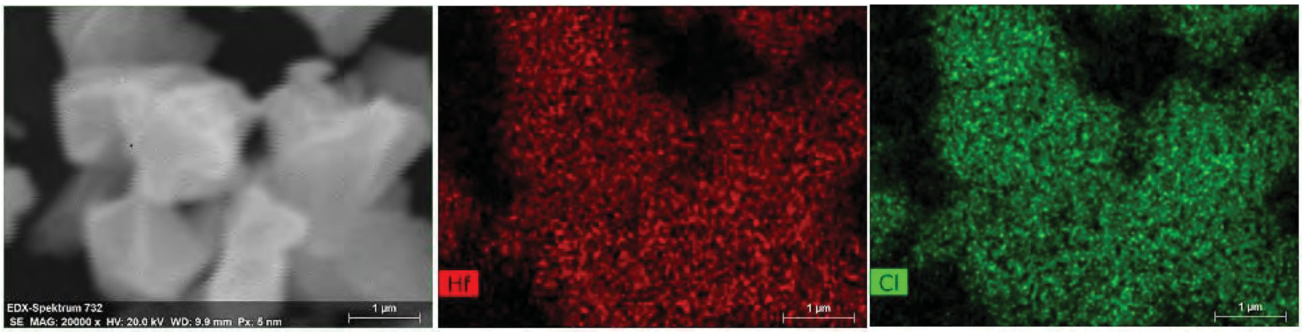

Figure S8. SEM and EDX elemental maps of Hf-HHU-2.

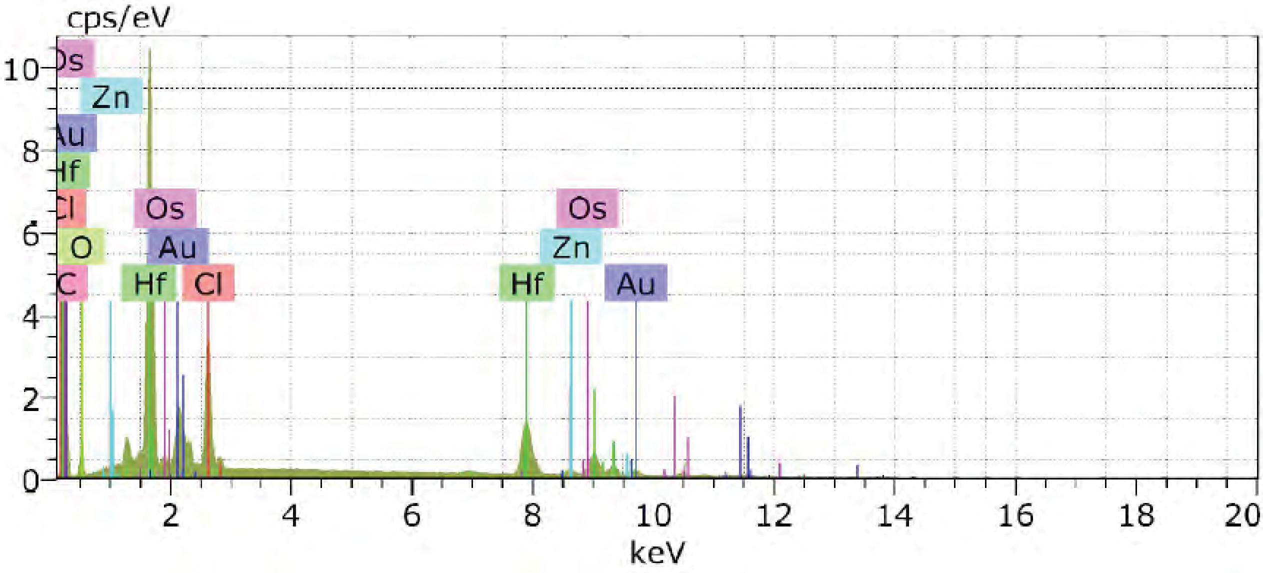

Figure S9. EDX spectrum of Hf-HHU-2.

Table S2. Atomic and Weight % of C, O, Cl and Hf for Hf-HHU-2

Element [a]	atom#	Series	mass fraction [wt.%]	mass fraction [norm. wt.%]	atom fraction [norm. At.%]	standard deviation for wt.% (1 Sigma)
C	6	K-Serie	20.84	23.39	64.75	3.15
O	8	K-Serie	6.39	7.17	14.90	1.10
Hf	72	L-Serie	45.90	50.60	9.42	1.28
Cl	17	K-Serie	8.86	9.94	9.32	0.33
Au	79	L-Serie	5.93	6.66	1.12	0.27
Os	76	K-Serie	1.94	2.17	0.38	0.12
F	9	K-Serie	0.05	0.054	0.09	0.06
		Summe:	89.11	100	100	

[a] The element signals for Au stem from the sputtering and brass sample holder. Os and F signals are probably from reactants impurities.

Thermogravimetric Analyses of Hf-HHU-1, -2

A weight loss of ~5% corresponds to the evaporation of the solvent in Hf-HHU-1 and Hf-HHU-2. The main weight loss of 29% and 26% in Hf-HHU-1 and Hf-HHU-2 respectively, corresponds to the decomposition of the linker, with the remaining ~65 or ~70 wt%, respectively being close to the expected residue for HfO_2 (calc. 64 wt% for Hf-HHU-1) or an oxychloride "$Hf_2O_3Cl_2$" (calc 71 wt% for Hf-HHU-2). We note that there is also residual carbon in the black product at 600 °C as the TGA was performed under N_2.

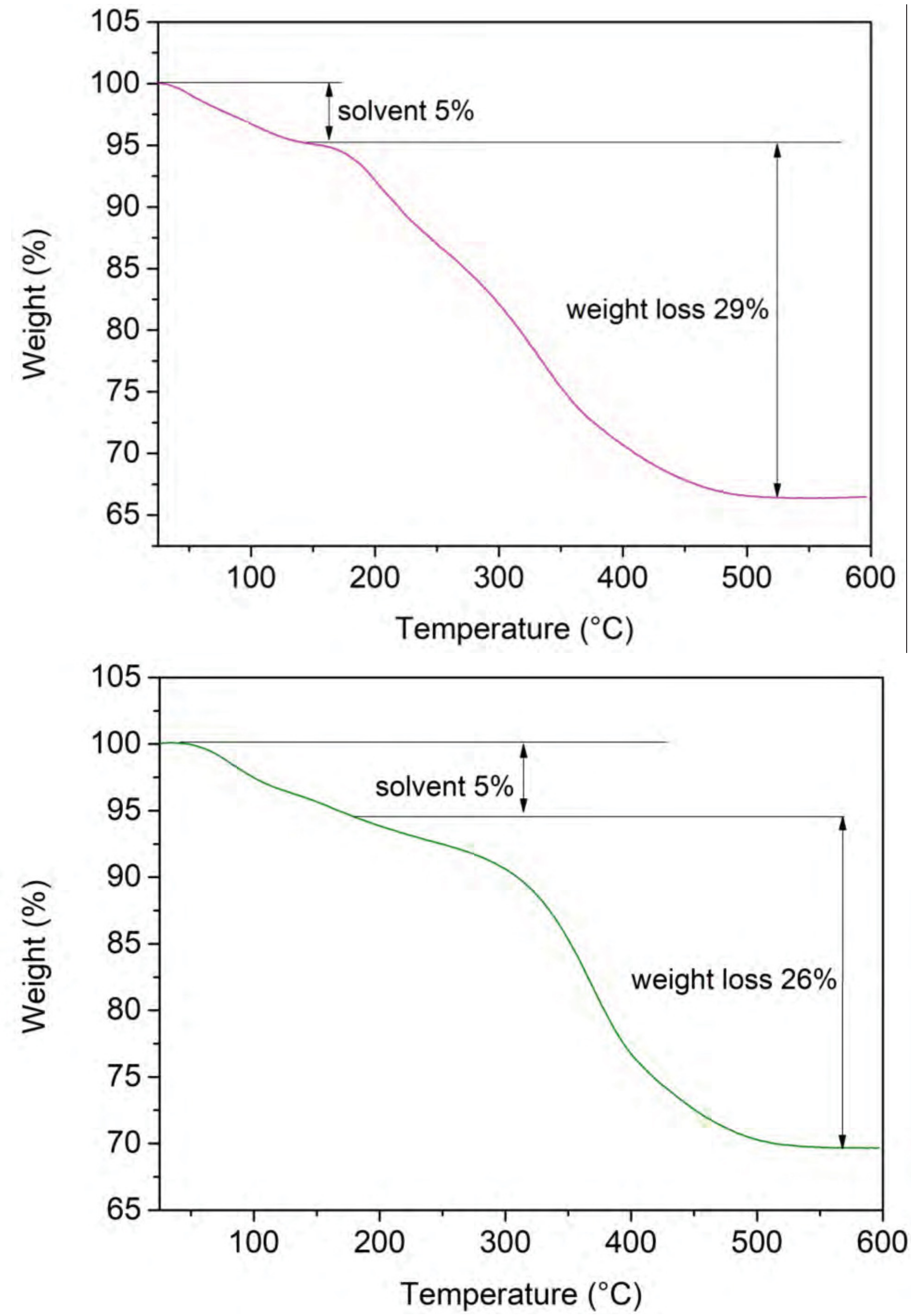

Figure S10. TGA trace of Hf-HHU-1 (top) and Hf-HHU-2 (bottom) (before activation) conducted under nitrogen.

Chemical Stability Tests of Hf-HHU-1, -2

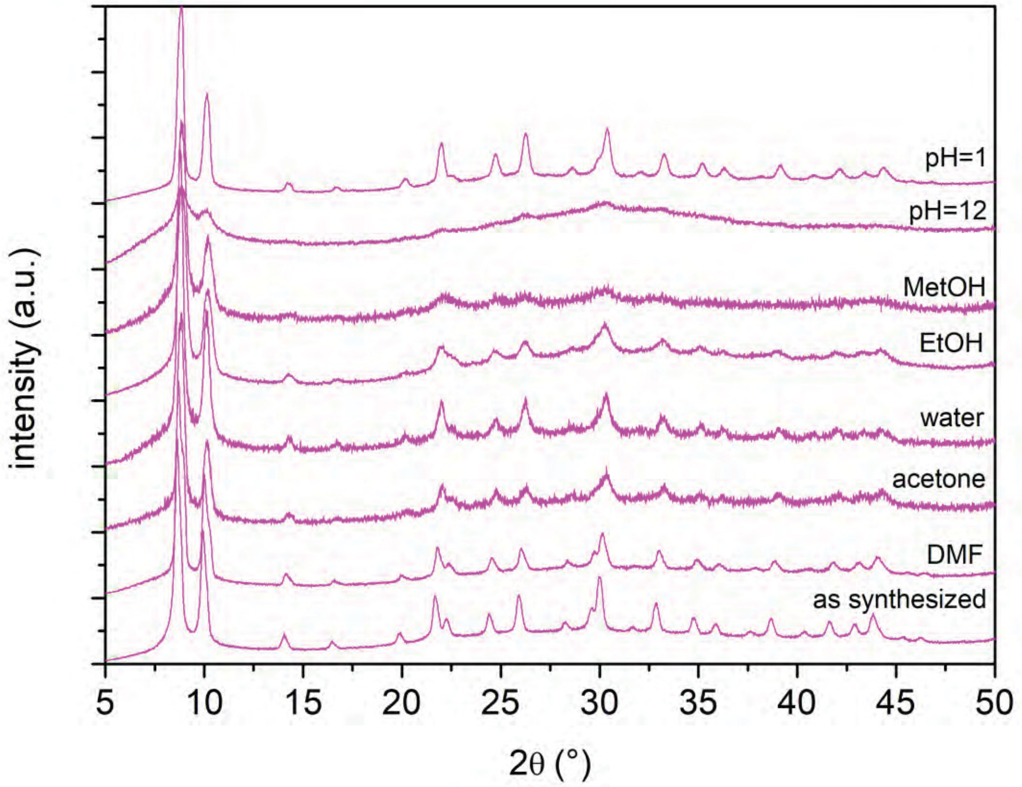

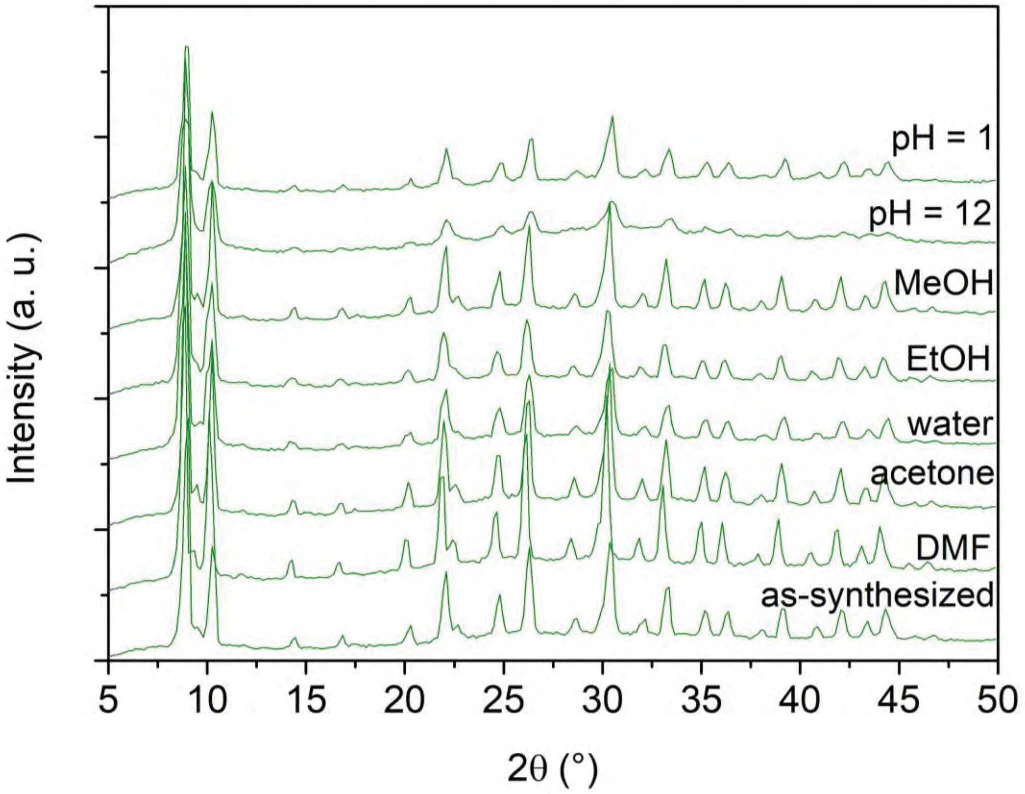

Figure S11. PXRD of Hf-HHU-1 (top) and Hf-HHU-2 (bottom) after stirring in various solvent and solutions for 24 h.

After activation by solvent exchange and supercritical drying, the PXRD shows that the framework of Hf-HHU-1 collapses at a temperature above 100 °C. The initial weight loss in the TG of the activated sample up to about 120 °C is water adsorbed from air during sample handling before the thermal analysis, as this material is highly hydrophilic. At a relative humidity of $P/P_0 = 0.4$ (typical ambient air humidity) the supercritically activated Hf-HHU-1 has a water uptake of about 12 wt%. The mass loss due to decomposition starts at about 200 °C.

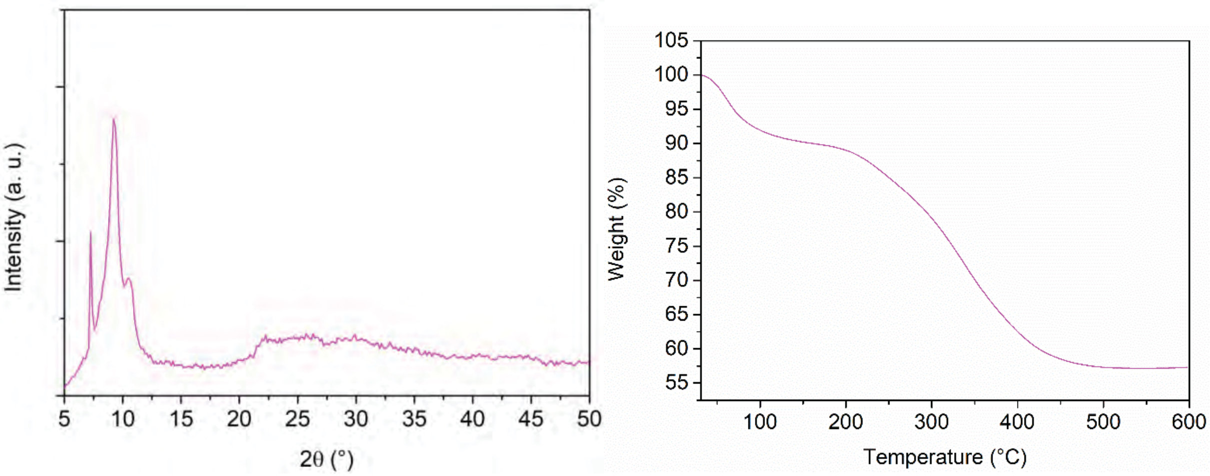

Figure S12. PXRD pattern (left) and thermogravimetric curve (right) of Hf-HHU-1 after activation by solvent exchange and supercritical drying and heating in vacuum at 120 °C.

Structure Details of Hf-HHU-1, -2

In view of structure refinement, PXRD pattern was measured in transmission geometry on a STOE Stadi MP, equipped with a Dectris Mythen detector and using monochromated CuKα1 radiation, and could be successfully indexed using TOPAS academics[3] with cubic F-centered cells (a = 17.854(3) Å, extinction conditions suitable for space group $Fm\bar{3}m$). A suitable starting model for Rietveld refinement was established using the crystal structure of the terephthalate UiO-66 as a starting point. The lateral atoms of the benzene core of the linker molecules were removed after imposing the indexed cell parameters and the structure was optimized by force-field calculation using the universal force field as implemented in the Materials Studio software.[4]

No constraints but only distance restraints were utilized for the refinement of Hf-HHU-1. However, the atoms of the framework structure are all located on special positions, and therefore the degrees of freedom are very limited.

The thus obtained model was refined by Rietveld methods using TOPAS. Residual electron density inside the pores was identified by Fourier synthesis and attributed to guest molecules, modelled by oxygen atoms of refinable occupancy. These guest atoms (Gn) should be considered placeholders for any kind of solvent molecules. All atoms were freely refined using one temperature factor for the framework and one temperature factor for the guest atoms, respectively. Some relevant parameters are summarized in Table S3 and the final plot is shown in Figure S13.

Table S3. Selected Parameters for the Rietveld Refinement of Hf-HHU-1.

Compound	Hf-HHU-1
Crystal system	cubic
Space group	$Fm\bar{3}m$
$a = b = c$ / Å	17.8529(6)
$\alpha = \beta = \gamma$ / °	90
V / Å^3	5690.2(5)
R_{wp} / %	6.2
R_{Bragg} / %	2.4
GoF	2.9

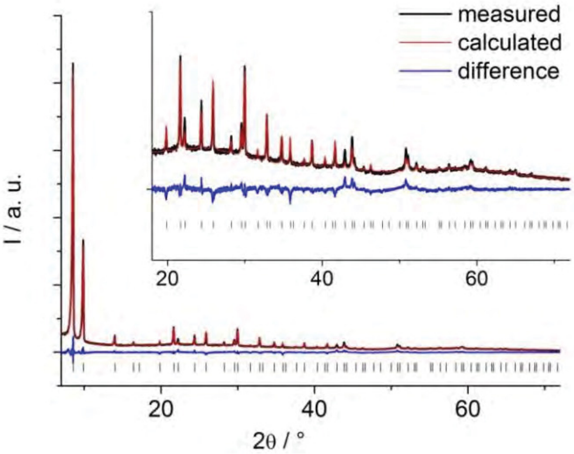

Figure S13. Final Rietveld plot of Hf-HHU-1. The black curve represents the measured data, the red curve is the theoretical data and the blue curve indicates the difference. Vertical black bars mark the allowed Bragg reflection positions.

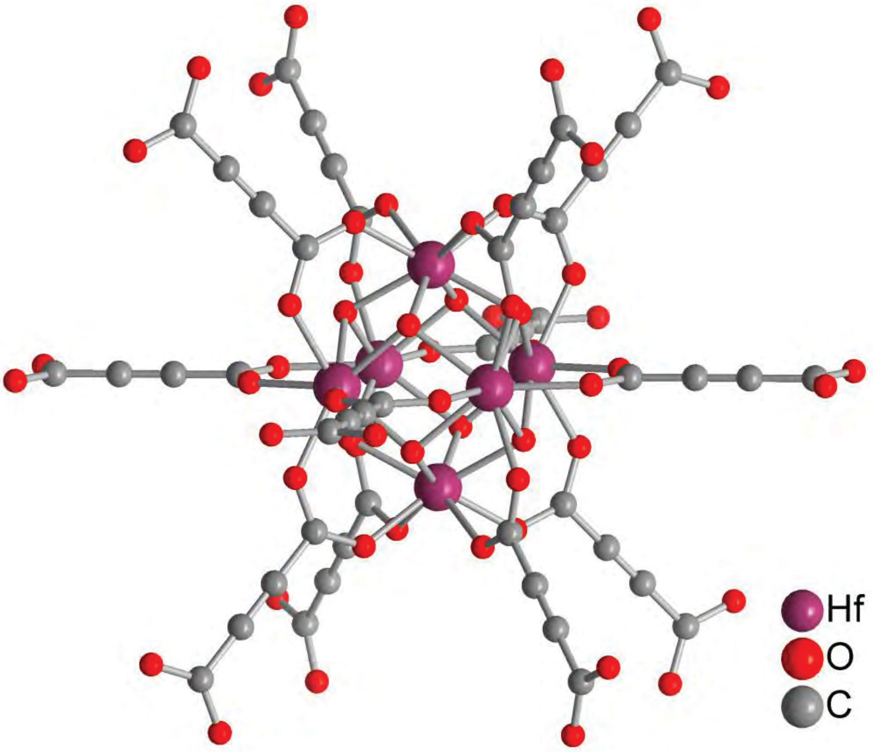

Figure S14. Secondary building units of the octahedral clusters {$Hf_6(O)_4(OH)_4$} with the 12 surrounding and connecting acetylenedicarboxylate linkers.

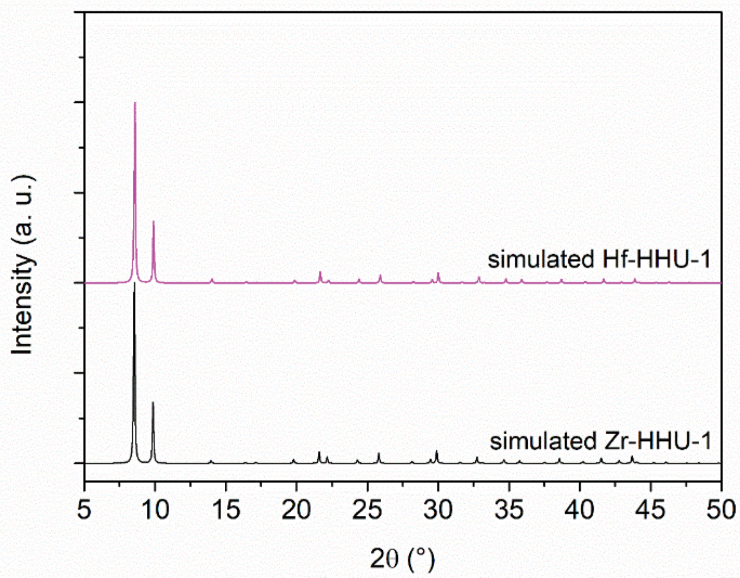

Figure S15. Simulated PXRD pattern of Hf-HHU-1 compared with simulated PXRD pattern of Zr-HHU-1.[5]

Cif file for Hf-HHU-1

```
data_HfADC
# start Validation Reply Form
_vrf_EXPT005_HfADC
;
```

```
PROBLEM: _exptl_crystal_description is missing
RESPONSE: Structure determined from PXRD data.
;
_vrf_ATOM007_HfADC
;
PROBLEM: _atom_site_aniso_label is missing
RESPONSE: Structure determined from PXRD data, isotropoc refinement.
;
_vrf_GEOM001_HfADC
;
PROBLEM: _geom_bond_atom_site_label_1 is missing
RESPONSE: Structure determined from PXRD data, value not given.
;
_vrf_GEOM002_HfADC
;
PROBLEM: _geom_bond_atom_site_label_2 is missing
RESPONSE: Structure determined from PXRD data, value not given
;
_vrf_GEOM003_HfADC
;
PROBLEM: _geom_bond_distance is missing
RESPONSE: Structure determined from PXRD data, value not given
;
_vrf_GEOM006_HfADC
;
PROBLEM: _geom_angle_atom_site_label_2 is missing
RESPONSE: Structure determined from PXRD data, value not given
;
_vrf_GEOM007_HfADC
;
PROBLEM: _geom_angle_atom_site_label_3 is missing
RESPONSE: Structure determined from PXRD data, value not given
;
_vrf_PLAT029_HfADC
;
PROBLEM: _diffrn_measured_fraction_theta_full value Low .      0.000 Why?
RESPONSE: Structure determined from PXRD data, Rietveld plot given in manuscript.
;
_vrf_PLAT183_HfADC
;
PROBLEM: Missing _cell_measurement_reflns_used Value ....     Please Do !
RESPONSE: Structure determined from PXRD data, cell not measured separately.
;
_vrf_PLAT184_HfADC
;
PROBLEM: Missing _cell_measurement_theta_min Value ......     Please Do !
RESPONSE: Structure determined from PXRD data, cell not measured separately.
;
_vrf_PLAT185_HfADC
;
PROBLEM: Missing _cell_measurement_theta_max Value ......     Please Do !
RESPONSE: Structure determined from PXRD data, cell not measured separately.
;
_vrf_PLAT197_HfADC
;
PROBLEM: Missing _cell_measurement_temperature Datum ....     Please Add
RESPONSE: Structure determined from PXRD data, cell not measured separately.
;
_vrf_PLAT880_HfADC
;
PROBLEM: N0 datum for _diffrn_reflns_number ............     Please Do !
RESPONSE: Structure determined from PXRD data, Rietveld plot given in manuscript.
;
_vrf_PLAT881_HfADC
;
PROBLEM: No Datum for _diffrn_reflns_av_R_equivalents ...     Please Do !
RESPONSE: Structure determined from PXRD data.
;
```

```
# Added during the CSD deposition process: Monday 13 May 2019 05:29 PM
# end Validation Reply Form

_chemical_name_mineral           Hf-UiO-66-ADC
_chemical_formula_sum           'C56.74 Hf24 O168.83'
_chemical_formula_weight         7666.47
_cell_length_a                  17.85289(55)
_cell_length_b                  17.85289(55)
_cell_length_c                  17.85289(55)
_cell_angle_alpha                 90
_cell_angle_beta                 90
_cell_angle_gamma                  90
_cell_volume                    5690.17(52)
_cell_formula_units_Z            1
_symmetry_cell_setting           cubic
_symmetry_space_group_name_H-M   'F m -3 m'
_symmetry_Int_Tables_number      225
_space_group_name_Hall           '-F 4 2 3'

loop_
_symmetry_equiv_pos_as_xyz
'-x, -y, -z'
'-x, -y, z'
'-x, -z, -y'
'-x, -z, y'
'-x, z, -y'
'-x, z, y'
'-x, y, -z'
'-x, y, z'
'-y, -x, -z'
'-y, -x, z'
'-y, -z, -x'
'-y, -z, x'
'-y, z, -x'
'-y, z, x'
'-y, x, -z'
'-y, x, z'
'-z, -x, -y'
'-z, -x, y'
'-z, -y, -x'
'-z, -y, x'
'-z, y, -x'
'-z, y, x'
'-z, x, -y'
'-z, x, y'
'z, -x, -y'
'z, -x, y'
'z, -y, -x'
'z, -y, x'
'z, y, -x'
'z, y, x'
'z, x, -y'
'z, x, y'
'y, -x, -z'
'y, -x, z'
'y, -z, -x'
'y, -z, x'
'y, z, -x'
'y, z, x'
'y, x, -z'
'y, x, z'
'x, -y, -z'
'x, -y, z'
'x, -z, -y'
'x, -z, y'
'x, z, -y'
'x, z, y'
'x, y, -z'
```

```
'x, y, z'
'-x+1/2, -y+1/2, -z'
'-x+1/2, -y+1/2, z'
'-x+1/2, -z+1/2, -y'
'-x+1/2, -z+1/2, y'
'-x+1/2, z+1/2, -y'
'-x+1/2, z+1/2, y'
'-x+1/2, y+1/2, -z'
'-x+1/2, y+1/2, z'
'-y+1/2, -x+1/2, -z'
'-y+1/2, -x+1/2, z'
'-y+1/2, -z+1/2, -x'
'-y+1/2, -z+1/2, x'
'-y+1/2, z+1/2, -x'
'-y+1/2, z+1/2, x'
'-y+1/2, x+1/2, -z'
'-y+1/2, x+1/2, z'
'-z+1/2, -x+1/2, -y'
'-z+1/2, -x+1/2, y'
'-z+1/2, -y+1/2, -x'
'-z+1/2, -y+1/2, x'
'-z+1/2, y+1/2, -x'
'-z+1/2, y+1/2, x'
'-z+1/2, x+1/2, -y'
'-z+1/2, x+1/2, y'
'z+1/2, -x+1/2, -y'
'z+1/2, -x+1/2, y'
'z+1/2, -y+1/2, -x'
'z+1/2, -y+1/2, x'
'z+1/2, y+1/2, -x'
'z+1/2, y+1/2, x'
'z+1/2, x+1/2, -y'
'z+1/2, x+1/2, y'
'y+1/2, -x+1/2, -z'
'y+1/2, -x+1/2, z'
'y+1/2, -z+1/2, -x'
'y+1/2, -z+1/2, x'
'y+1/2, z+1/2, -x'
'y+1/2, z+1/2, x'
'y+1/2, x+1/2, -z'
'y+1/2, x+1/2, z'
'x+1/2, -y+1/2, -z'
'x+1/2, -y+1/2, z'
'x+1/2, -z+1/2, -y'
'x+1/2, -z+1/2, y'
'x+1/2, z+1/2, -y'
'x+1/2, z+1/2, y'
'x+1/2, y+1/2, -z'
'x+1/2, y+1/2, z'
'-x+1/2, -y, -z+1/2'
'-x+1/2, -y, z+1/2'
'-x+1/2, -z, -y+1/2'
'-x+1/2, -z, y+1/2'
'-x+1/2, z, -y+1/2'
'-x+1/2, z, y+1/2'
'-x+1/2, y, -z+1/2'
'-x+1/2, y, z+1/2'
'-y+1/2, -x, -z+1/2'
'-y+1/2, -x, z+1/2'
'-y+1/2, -z, -x+1/2'
'-y+1/2, -z, x+1/2'
'-y+1/2, z, -x+1/2'
'-y+1/2, z, x+1/2'
'-y+1/2, x, -z+1/2'
'-y+1/2, x, z+1/2'
'-z+1/2, -x, -y+1/2'
'-z+1/2, -x, y+1/2'
'-z+1/2, -y, -x+1/2'
```

```
'-z+1/2, -y, x+1/2'
'-z+1/2, y, -x+1/2'
'-z+1/2, y, x+1/2'
'-z+1/2, x, -y+1/2'
'-z+1/2, x, y+1/2'
'z+1/2, -x, -y+1/2'
'z+1/2, -x, y+1/2'
'z+1/2, -y, -x+1/2'
'z+1/2, -y, x+1/2'
'z+1/2, y, -x+1/2'
'z+1/2, y, x+1/2'
'z+1/2, x, -y+1/2'
'z+1/2, x, y+1/2'
'y+1/2, -x, -z+1/2'
'y+1/2, -x, z+1/2'
'y+1/2, -z, -x+1/2'
'y+1/2, -z, x+1/2'
'y+1/2, z, -x+1/2'
'y+1/2, z, x+1/2'
'y+1/2, x, -z+1/2'
'y+1/2, x, z+1/2'
'x+1/2, -y, -z+1/2'
'x+1/2, -y, z+1/2'
'x+1/2, -z, -y+1/2'
'x+1/2, -z, y+1/2'
'x+1/2, z, -y+1/2'
'x+1/2, z, y+1/2'
'x+1/2, y, -z+1/2'
'x+1/2, y, z+1/2'
'-x, -y+1/2, -z+1/2'
'-x, -y+1/2, z+1/2'
'-x, -z+1/2, -y+1/2'
'-x, -z+1/2, y+1/2'
'-x, z+1/2, -y+1/2'
'-x, z+1/2, y+1/2'
'-x, y+1/2, -z+1/2'
'-x, y+1/2, z+1/2'
'-y, -x+1/2, -z+1/2'
'-y, -x+1/2, z+1/2'
'-y, -z+1/2, -x+1/2'
'-y, -z+1/2, x+1/2'
'-y, z+1/2, -x+1/2'
'-y, z+1/2, x+1/2'
'-y, x+1/2, -z+1/2'
'-y, x+1/2, z+1/2'
'-z, -x+1/2, -y+1/2'
'-z, -x+1/2, y+1/2'
'-z, -y+1/2, -x+1/2'
'-z, -y+1/2, x+1/2'
'-z, y+1/2, -x+1/2'
'-z, y+1/2, x+1/2'
'-z, x+1/2, -y+1/2'
'-z, x+1/2, y+1/2'
'z, -x+1/2, -y+1/2'
'z, -x+1/2, y+1/2'
'z, -y+1/2, -x+1/2'
'z, -y+1/2, x+1/2'
'z, y+1/2, -x+1/2'
'z, y+1/2, x+1/2'
'z, x+1/2, -y+1/2'
'z, x+1/2, y+1/2'
'y, -x+1/2, -z+1/2'
'y, -x+1/2, z+1/2'
'y, -z+1/2, -x+1/2'
'y, -z+1/2, x+1/2'
'y, z+1/2, -x+1/2'
'y, z+1/2, x+1/2'
'y, x+1/2, -z+1/2'
```

```
'y, x+1/2, z+1/2'
'x, -y+1/2, -z+1/2'
'x, -y+1/2, z+1/2'
'x, -z+1/2, -y+1/2'
'x, -z+1/2, y+1/2'
'x, z+1/2, -y+1/2'
'x, z+1/2, y+1/2'
'x, y+1/2, -z+1/2'
'x, y+1/2, z+1/2'
loop_
_atom_site_label
_atom_site_type_symbol
_atom_site_fract_x
_atom_site_fract_y
_atom_site_fract_z
_atom_site_occupancy
_atom_site_B_iso_or_equiv
Hf1 Hf -0.36723(23) 0.5 0 1 9.38(19)
O1 O -0.42437(96) 0.42437(96) -0.07563(96) 1 9.38(19)
O2 O -0.30662(52) 0.39682(45) 0 1 9.38(19)
C1 C -0.33050(93) 0.33050(93) 0 0.591(28) 9.38(19)
C2 C -0.2736(14) 0.2736(14) 0 0.591(28) 9.38(19)
G1 O 0.4382(24) 0.3679(20) 0.3679(20) 0.225(19) 1.0(25)
G2 O 0.1794(51) 0.184(10) 0.1794(51) 0.0350(81) 1.0(25)
G3 O 0.3275(31) 0.2155(18) 0.7845(18) 0.179(11) 1.0(25)
G4 O 0.5 0.5 0.5 0.232(66) 1.0(25)


_diffrn_ambient_temperature      298
_diffrn_measurement_device_type  'STOE Stadi P Cu Ka1'
_diffrn_radiation_wavelength     1.540598
_refine_special_details          'Structure determined from PXRD data.'
_ccdc_publ_extra_info
;

Reason for no structure factor data deposited:

Structure determined from PXRD data.
;
```

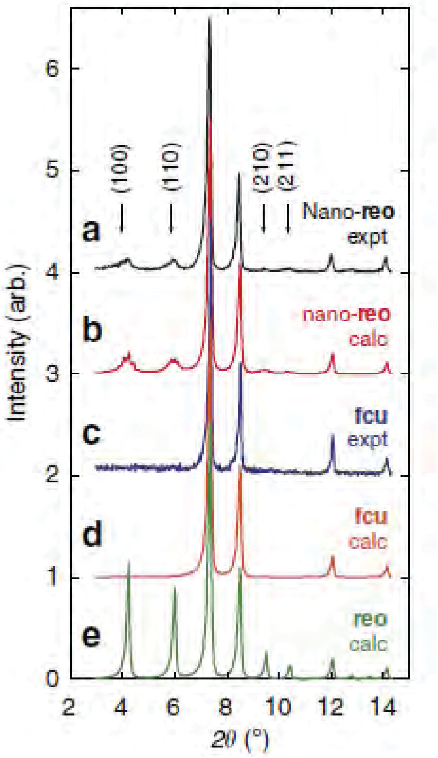

Figure S16. Original Figure caption, taken from ref.[6]: Chemical control over defect nanoregion concentration and domain size. (a) The experimental low-angle X-ray diffraction pattern of UiO-66(Hf), measured over the angular range 3–15° ($\lambda = 1.541$Å), consists of a sharp Bragg scattering component with reflections obeying the conditions expected for the face-centred-cubic lattice illustrated in Fig. 1 and a less-intense diffuse scattering component centred on 'forbidden' reflection positions associated with a primitive cubic superstructure. The four most intense diffuse scattering peaks are highlighted by arrows. Conventional crystallographic analysis of this pattern is illustrated in Supplementary Fig. 29. (b) The corresponding diffraction pattern calculated from the reo defect nanoregion model described in the text: the intensities and peak widths of both Bragg and diffuse scattering contributions are quantitatively accounted for by this model. The experimental (c) and calculated (d) diffraction patterns for a defect-free fcu framework, showing the absence of diffuse scattering features. (e) A long range- ordered reo model gives rise to superlattice peaks in the same positions as those observed in a, but simultaneously overestimates peak intensities and underestimates peak widths. Instead, the relative intensities and widths of the diffuse superlattice reflections measure defect concentration and domain size, respectively. Reprinted with permission from Cliffe, M. J.; Wan, W.; Zou, X.; Chater, P. A.; Kleppe, A. K.; Tucker, M. G.; Wilhelm, H.; Funnell, N. P.; Coudert, F.-X.; Goodwin, A. L. *Nat. Commun.* **2014**, *5*, Art. n. 4176. Copyright 2014 Springer Nature Publishing AG.

Comparison of Nitrogen and Water Vapor Sorption Characteristics of Hf-HHUs and Zr-HHUs

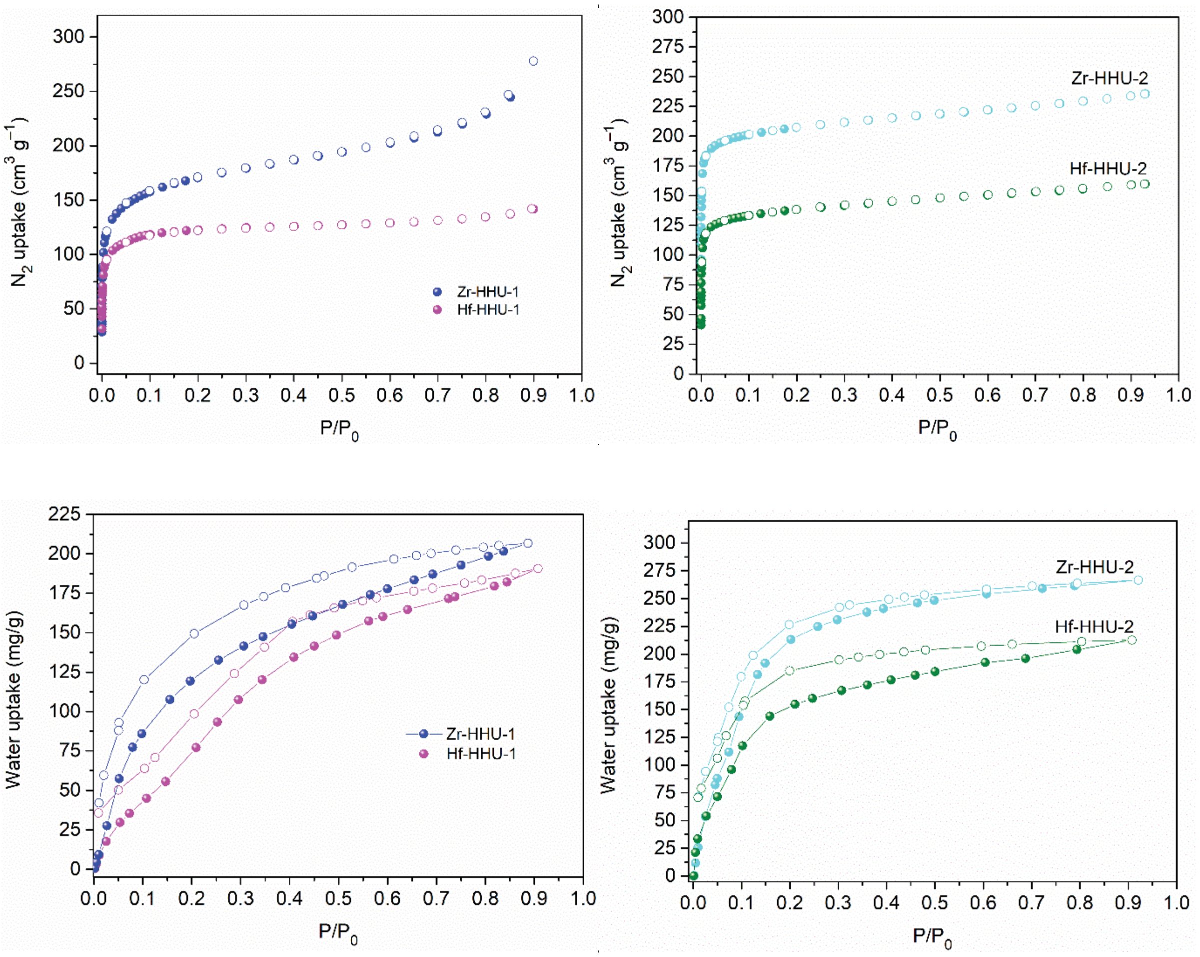

Figure S17. Experimental data of nitrogen sorption (at 77 K) and water sorption isotherms (at 293 K) for Hf-HHU-1, Zr-HHU-1, Hf-HHU-2 and Zr-HHU-2. Filled symbols are for adsorption, empty symbols for desorption.

Table S4. Specific Surface Area and Water Vapor Uptake Capacity for Hf-HHU-1 and Hf-HHU-2 Compared with their Zirconium Analogs Zr-HHU-1 and Zr-HHU-2.

Materials	Hf-HHU-1	Zr-HHU-1 [a]	Hf-HHU-2	Zr-HHU-2 [d]
N_2 uptake ($cm^3\ g^{-1}$) [b]	141	277	158	264
S_{BET} ($m^2\ g^{-1}$)	476	551	541	852
H_2O uptake ($mg\ g^{-1}$) [c]	190	205	212	267

[a] Data from ref. 5. [b] at $P/P_0 = 0.9$. [c] at $P/P_0 = 0.9$. [d] Zr-HHU-2 was obtained by an optimized synthesis with $ZrCl_4$ (akin to Hf-HHU-2 from $HfCl_4$ in this work) and therefore displays a better BET surface area than the materials which was previously reported with 460 $m^2\ g^{-1}$ in ref. 5.

Nitrogen and Water Sorption Isotherms of Hf-HHU-2 Containing Cluster Defect Nanodomains with reo Topology

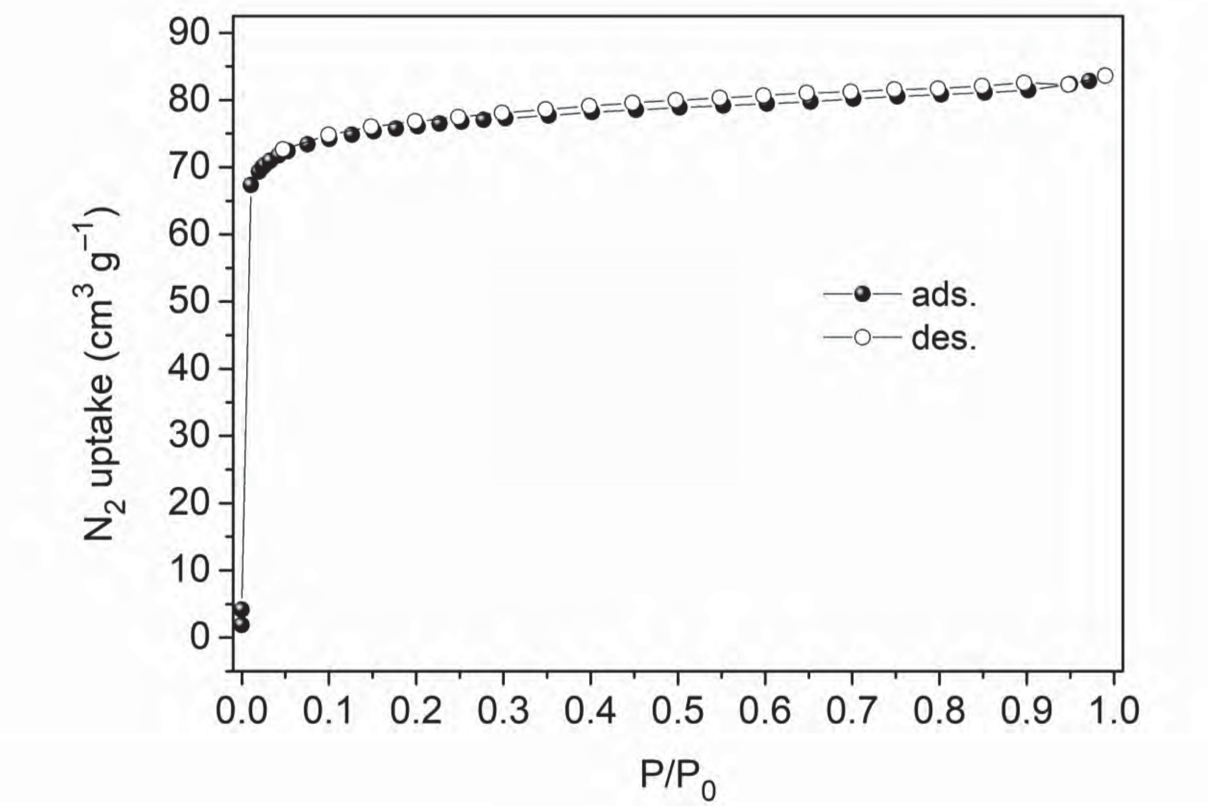

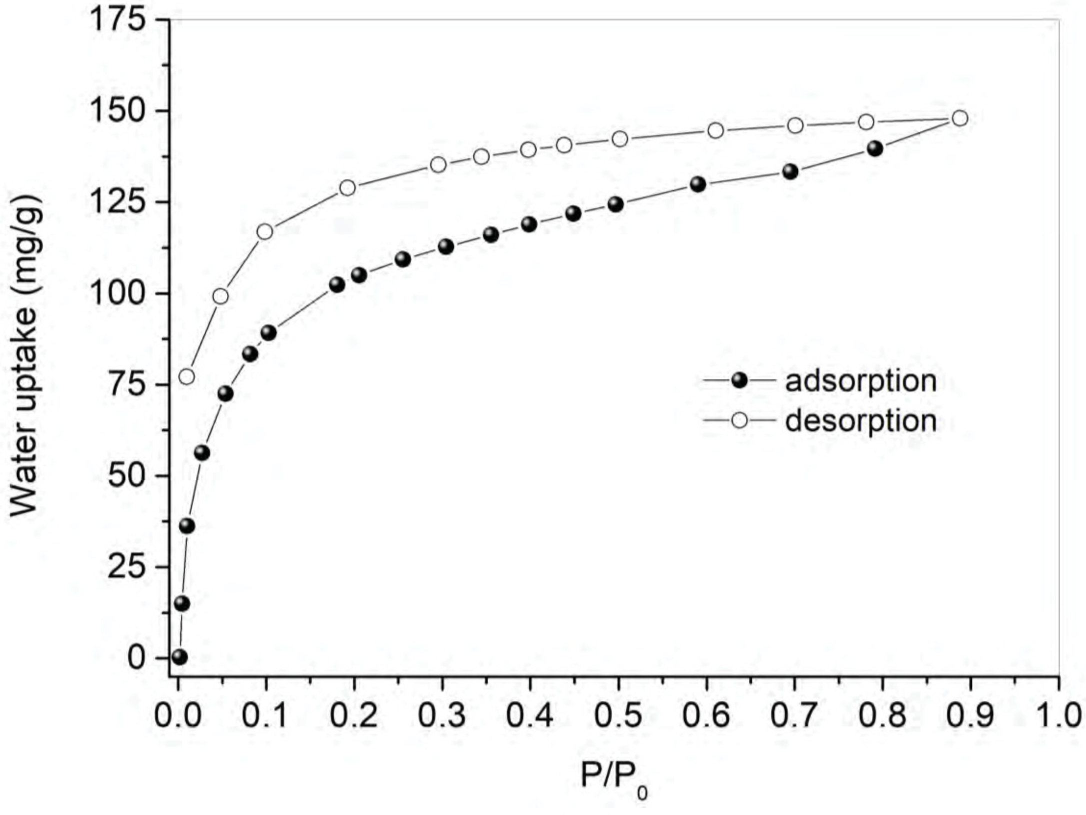

Figure S18. Nitrogen sorption isotherm at 77 K (top) and water sorption isotherm at 20 °C for Hf-HHU-2 containing defect nanodomains with reo topology (H-HHU-2_{defect}).

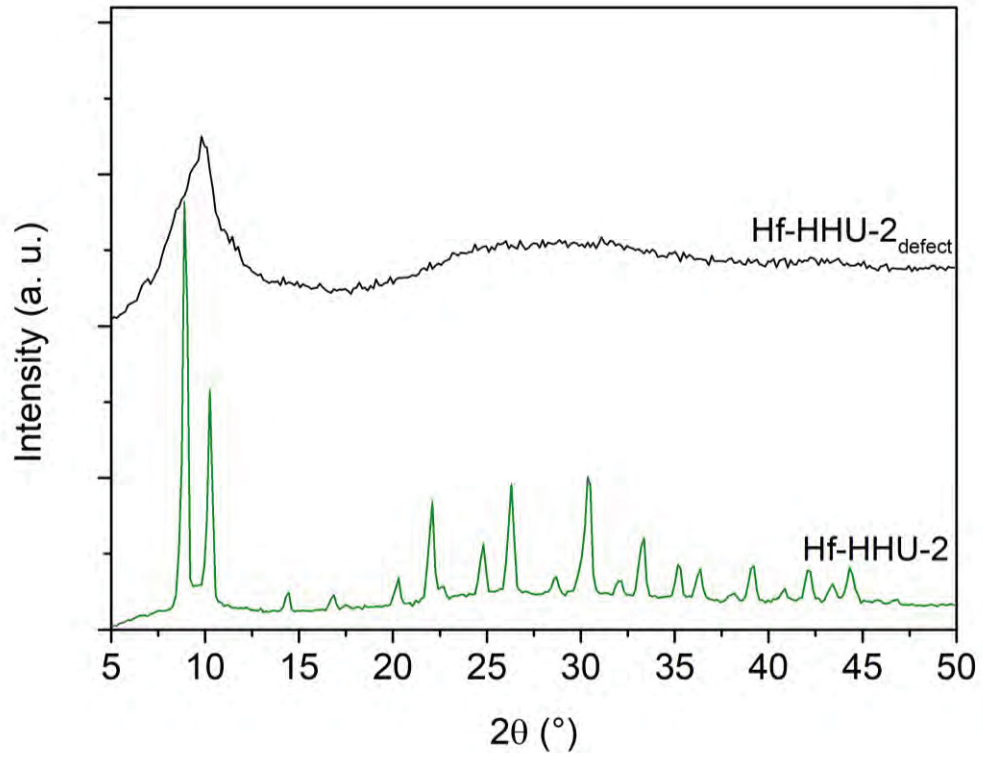

Figure S19. PXRD patterns after water sorption at 20 °C of Hf-HHU-2 and Hf-HHU-2$_{defect}$ (containing cluster defect nano-domains with **reo** topology). Hf-HHU-2 and Hf-HHU-2$_{defect}$ are synthesized from a reaction mixture with linker to $HfCl_4$ ratio of 3:1 and 1:1 respectively.

Iodine Adsorption for Hf-HHU-2

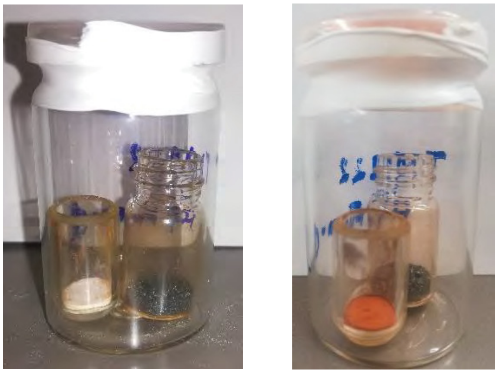

Figure S20. Pictures of the set-up of iodine adsorption for Hf-HHU-2, at the beginning of the experiment (left) and after some days (right).

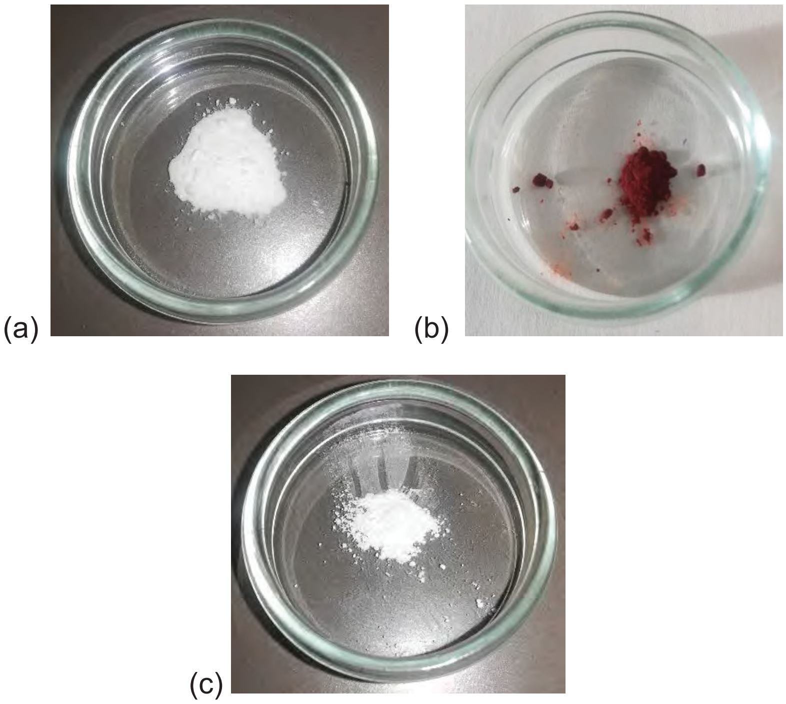

Figure S21. Pictures of Hf-HHU-2 samples before iodine adsorption (a) after iodine vapor loading (b) and after desorption in ethanol (c).

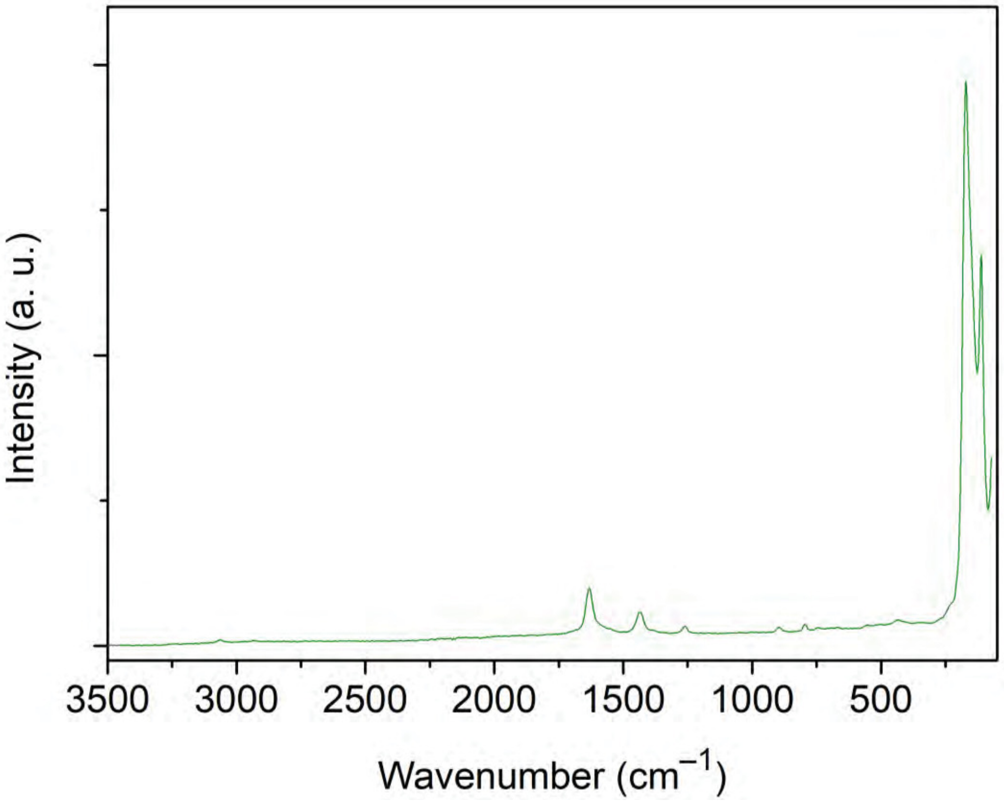

Figure S22. Raman spectra of iodine loaded Hf-HHU-2. The iodine vapor adsorption experiment was gravimetrically conducted at 20 °C for some days till the isotherm reached the plateau.

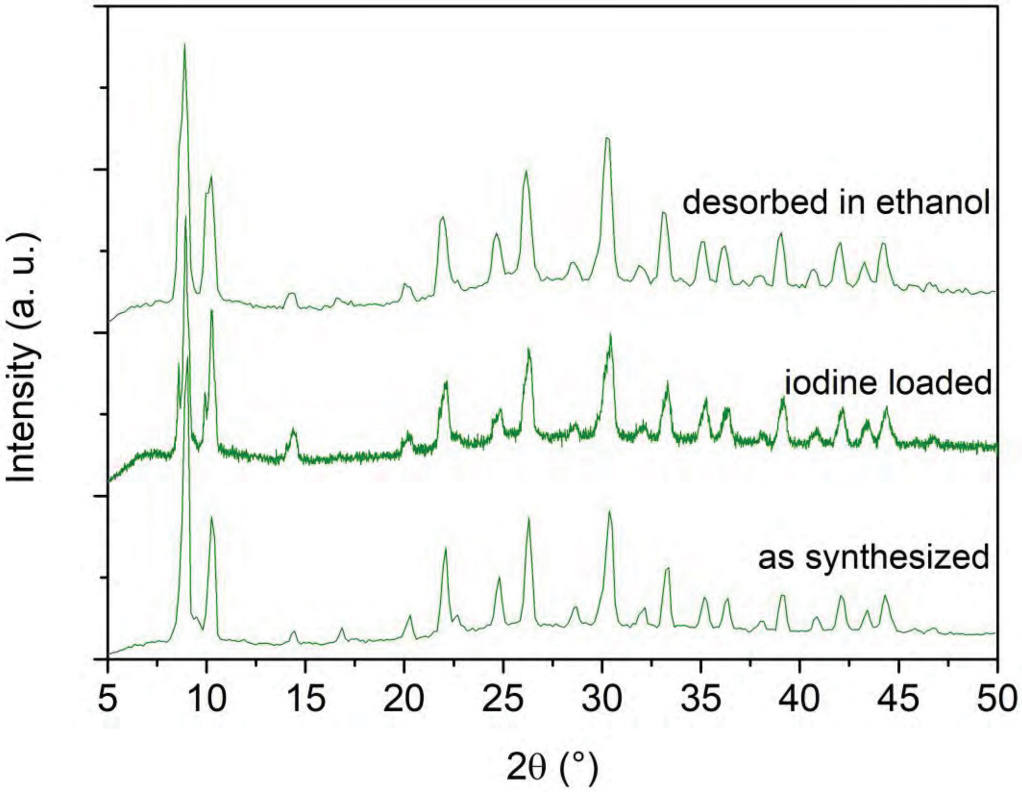

Figure S23. PXRD pattern of iodine-loaded Hf-HHU-2 and after desorption in ethanol, compared with the pattern of as-synthesized sample.

Determination of the Isosteric Heat of CO_2 Adsorption

The CO_2 isotherms experimentally obtained respectively at 273 K and 298 K were fitted with the Langmuir-Freundlich model (eq. 1). The fits are shown in Figure S19. The obtained fits were used to determine the pressure for each temperature corresponding to various CO_2 loadings. The isosteric heat of adsorption was finally calculated by applying the Clausius-Clapeyron equation (eq. 2).

$$q = q_{max} \cdot \frac{(k \cdot p)^t}{1 + (k \cdot p)^t} \qquad (1)$$

q is the gas amount adsorbed (mmol g^{-1}); q_{max} is the maximum loading; k is the affinity constant (bar^{-1}); t is the heterogeneity exponent; p is the pressure (kPa).

$$Q_{st} = -R\left(\frac{T_2 T_1}{T_2 - T_1}\right) ln \frac{P_2}{P_1} \qquad (2)$$

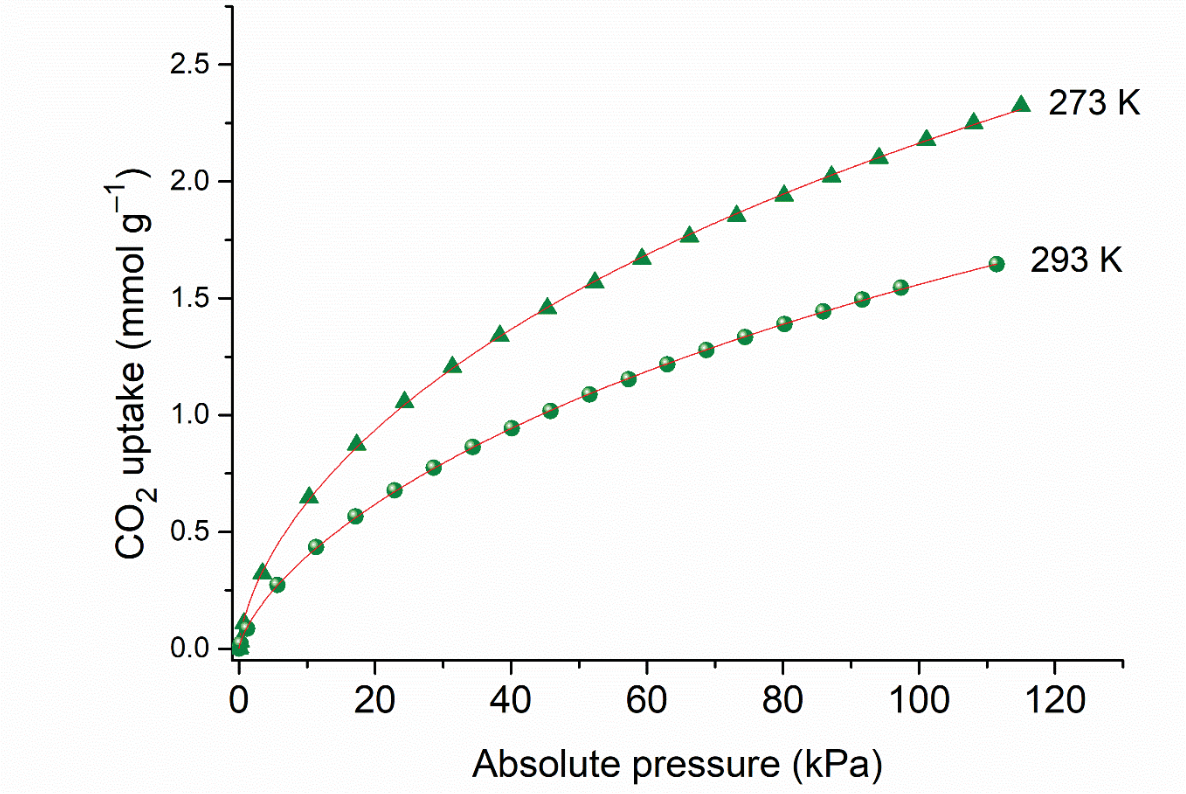

Figure S24. Fitting of CO_2 adsorption isotherms with the Langmuir-Freundlich model. Symbols for experimental data and red lines for simulated fits.

REFERENCES

---

(1) Bennett, A. E.; Rienstra, C. M.; Auger, M.; Lakshmi, K. V.; Griffin, R. G. Heteronuclear Decoupling in Rotating Solids. *J. Chem. Phys*. **1995**, *103*, 6951-6958.

(2) Roy, P.; Schaate, A.; Behrens, P.; Godt, A. Post-Synthetic Modification of Zr-Metal–Organic Frameworks through Cycloaddition Reactions. *Chem. Eur. J*. **2012**, *18*, 6979-6985.

(3) Topas Academics 4.2; Coelho Software: Brisbane, 2007.

(4) Accelrys Materials Studio Version 5.0, San Diego, CA, **2009**.

---

(5) Matemb Ma Ntep, T. J.; Reinsch, H.; Moll, B.; Hastürk, E.; Gökpinar, S.; Breitzke, H.; Schlüsener, C.; Schmolke, L.; Buntkowsky, G.; Janiak, C. Realizing the Potential of Acetylenedicarboxylate by Functionalization to Halofumarate in Zr^{IV} Metal–Organic Frameworks. *Chem. Eur. J*. **2018**, *24*, 14048 – 14053.

(6) Cliffe, M. J.; Wan, W.; Zou, X.; Chater, P. A.; Kleppe, A. K.; Tucker, M. G.; Wilhelm, H.; Funnell, N. P.; Coudert, F.-X.; Goodwin, A. L. Correlated Defect Nanoregions in a Metal–Organic Framework. *Nat. Commun.* **2014**, *5*, Art. n. 4176.

2.3 Acetylenedicarboxylate-based cerium(IV) metal-organic framework with fcu topology: a potential material for air cleaning from toxic halogen vapors

Tobie J. Matemb Ma Ntep, Helge Reinsch, Jun Liang and Christoph Janiak

Dalton Trans. **2019**, *48*, 15849–15855.

DOI: 10.1039/c9dt03518d

Impact factor 2018: 4.052

Cerium(IV)-metal-organic frameworks having the same **fcu** net topology as analogous MOFs based on zirconium have been recently discovered. These MOFs are composed of octahedral $[Ce_6(\mu_3\text{-}O)_4(\mu_3\text{-}OH)_4]$ secondary building units each connected to twelve linear dicarboxylate linkers. The particularity of these materials is the ease of their synthesis within few minutes ranging between 15 to 30 min. The redox activity of the Ce^{IV} within the framework makes also Ce(IV)-MOFs ideal candidates for applications in redox-catalysis and photocatalysis. The fact that zirconium and hafnium UiO-type MOFs were obtained using the simple acetylenedicarboxylate linker, was strongly indicative that an acetylenedicarboxylate-based Ce^{IV}-MOF with the same structure as Zr-HHU-1 and Hf-HHU-1 could also be obtained. A further discovery was made relative to the synthesis of this new cerium(IV) acetylenedicarboxylate with **fcu** topology. The material was synthesized at room temperature in water only, and did not use mono-carboxylic acid modulation. This is of great advantage not only because the pores can be completely evacuated by supercritical drying, but also because it would enable to have a real representation of the properties of Adc-based **fcu** MOFs. The new Adc-based **fcu** Ce^{IV}-MOF denoted as Ce-HHU-1 was structurally characterized by PXRD and Rietveld refinement. The nitrogen sorption was performed on an activated sample to attest the permanent microporosity of the material obtained. The water vapor adsorption, CO_2 adsorption and energetics, and molecular halogen vapor (Br_2 and I_2) adsorption were performed to assess the effect of the triple-bond in Ce-HHU-1. Ce-HHU-1 can indeed be considered as a framework of - ≡ - triple-bonds that are connected at the $Ce_6O_4(OH)_4$ clusters. Detailed results of this work are found in the article that follows.

Author´s contribution to the work:

- Idea and setting of the synthesis procedure.
- Synthesis and preparation of samples for further characterizations.
- Characterizations including PXRD experiments, TGA, chemical stability test, determination of the amount of missing linker defects from TGA curve.
- Nitrogen sorption and determination of porosity parameters, other gas sorption (H_2O and CO_2) experiments.
- Br_2 and I_2 sorption experiments.
- Samples activation by supercritical CO_2 drying prior characterizations and MOF digestion/preparation prior liquid NMR analysis.
- Fitting of adsorption isotherms and determiation of the isosteric heat of CO_2 adsorption.
- Writing of the manuscript, drawing of figures and responses to reviewers during the review process.

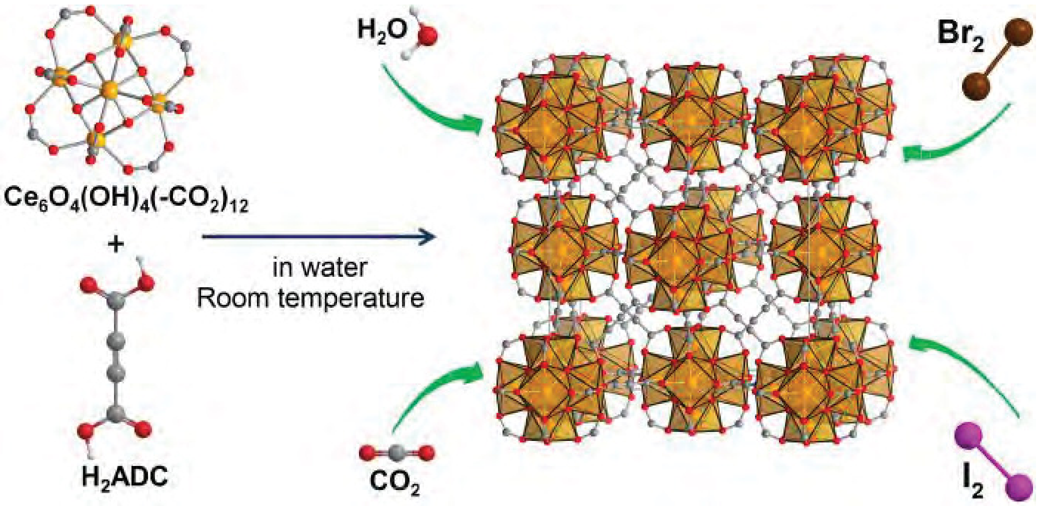

Dalton
Transactions

PAPER

Cite this: *Dalton Trans.*, 2019, **48**, 15849

Acetylenedicarboxylate-based cerium(IV) metal–organic framework with fcu topology: a potential material for air cleaning from toxic halogen vapors†

Tobie J. Matemb Ma Ntep,[a] Helge Reinsch, [b] Jun Liang[a,c] and
Christoph Janiak *[a]

Received 30th August 2019,
Accepted 1st October 2019

DOI: 10.1039/c9dt03518d

rsc.li/dalton

The most contracted cerium(IV)-based metal–organic framework (MOF) with **fcu** topology incorporating an alkyne-based linker, namely acetylenedicarboxylate (ADC), was synthesized under green conditions in water at room temperature and thoroughly characterized. The structure of this new MOF, denoted as Ce-HHU-1, was determined from powder X-ray diffraction data and Rietveld refinement and is made up of octahedral $[Ce_6O_4(OH)_4]^{12+}$ clusters, each of which is connected to other inorganic units by twelve ADC linkers to give a porous network with **fcu** topology analogous with UiO-66. The permanent microporosity of Ce-HHU-1 was confirmed by nitrogen sorption, meanwhile its high hydrophilicity was displayed by a type I water vapor sorption isotherm. The adsorption of CO_2 in Ce-HHU-1 features a remarkably high zero-coverage isosteric heat of adsorption of 47 kJ mol^{-1}, attributed to the presence of the $-C{\equiv}C-$ triple-bond in the framework. The latter also allows for Ce-HHU-1 to capture and irreversibly chemisorb Br_2 vapors, as well as both chemi- and physisorb I_2 vapors in an effective manner, making this material potentially applicable for air cleaning from toxic halogen vapors.

Introduction

Metal–organic frameworks (MOFs) based on cerium(IV) (Ce(IV)-MOFs) have recently attracted scientific attention due to the redox activity of Ce(IV), yielding MOFs applicable in redox-catalysis,[1] and photocatalysis.[2] Constructed by connecting Ce-oxido clusters by organic ligands into porous materials, Ce-MOFs are usually obtained by easy synthetic route within few minutes. Since the first report in 2015 by Lammert *et al.* of conditions to stabilize Ce(IV) cations in a MOF,[3] many Ce-MOFs have been synthesized displaying various net topologies including **reo**, **spn**, **scu**, **she**, **scq** and **fcu**, depending on the employed linker geometry.[4,5] However, Ce-MOFs with the **fcu** topology like UiO-66 are by far the most representative.[6] Their structure consists of octahedral $[Ce_6O_4(OH)_4]^{12+}$ secondary building units (SBUs), which are twelvefold connected to other units by linear dicarboxylate linkers, forming an expanded cubic close-packed porous framework.[7] In this regard, many linear dicarboxylate linkers have been used including benzene-1,4-dicarboxylate, fumarate, 2,2′-bipyridine-5,5′-dicarboxylate, pyridine-2,5-dicarboxylate, napththalene-2,6-dicarboxylate, biphenyl-4.4′-dicarboxylate.[3,4] However, no Ce-MOF based on acetylenedicarboxylate (ADC) as the shortest straight linear alkyne-based dicarboxylate linker (Scheme 1) is yet reported.

Very few ADC-based MOFs are known. Serre *et al.* obtained the first Eu(III)-acetylenedicarboxylate open framework, which showed irreversible pore contraction upon pore evacuation by dehydration.[8] Tranchemontagne *et al.* synthesized Zn-acetylenedicarboxylate, the smallest member of IRMOF series

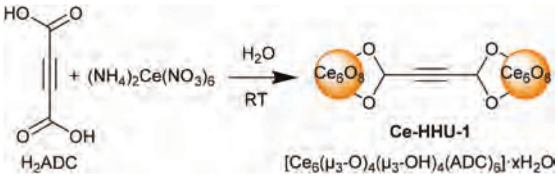

Scheme 1 Reaction of acetylenedicarboxylic acid to the UiO-type MOF Ce-HHU-1.

---

[a] *Institut für Anorganische Chemie und Strukturchemie, Heinrich-Heine-Universität Düsseldorf, Universitätsstraße 1, D-40225 Düsseldorf, Germany. E-mail: janiak@hhu.de*

[b] *Institut für Anorganische Chemie, Christian-Albrechts-Universität zu Kiel, Max-Eyth-Straße 2, 24118 Kiel, Germany*

[c] *Hoffmann Institute of Advanced Materials, Shenzhen Polytechnic, 7098 Liuxian Blvd, Nanshan District, Shenzhen 518055, China*

† Electronic supplementary information (ESI) available: Additional information on PXRD, IR, Raman, TGA, Rietveld refinement, halogen adsorption, isosteric heat of CO_2 adsorption. CCDC 1946853. For ESI and crystallographic data in CIF or other electronic format see DOI: 10.1039/c9dt03518d

(IRMOF-0), albeit as non-porous material due to double-interpenetration and trapped guest solvent molecules that could not be removed.[9] Gramm *et al.* also synthesized a series of three-dimensional rare-earth acetylenedicarboxylate-based coordination polymers,[10] so extending a previous work of Michaelides *et al.*[11] However, none of these works could prove the permanent porosity of the obtained ADC-based coordination polymers. Obviously, despite its simplicity as linear linker, obtaining acetylenedicarboxylate-based metal–organic frameworks with experimentally proven permanent porosity had been a challenge in the MOF field. Nevertheless, we recently reported the synthesis and porosity studies of an acetylenedicarboxylate-based zirconium-MOF having the **fcu** topology, namely Zr-HHU-1 (HHU stands for Heinrich-Heine-University Düsseldorf). This work was the first report of an ADC-based MOF presenting experimentally assessed permanent porosity.[12]

Employing the ADC linker in the construction of MOFs is of great interest not only because it provides MOFs spaced solely by linear carbon arrays (hydrogen-free linker) but also because of the functionalizable –C≡C– triple-bond (Scheme 1). We demonstrated that this could involve an *in situ* hydrohalogenation to halogen functionalized MOFs.[12] In addition, the alkyne function could be the basis for post-synthetic modification of the constructed ADC-based MOF *via* addition reactions. Post-synthetic halogenation of integral unsaturated C–C bonds are known for Zr- and Hf-MOFs constructed from 4,4′-ethynylene-dibenzoate and 4,4′-(buta-1,3-diyne-1,4-diyl)-dibenzoate linkers.[13] Furthermore, the presence of –C≡C– triple bonds in the porous material could enhance the adsorption affinity/capacity of some gases like CO_2, as well as vapors like water and molecular halogens.[12,14]

To broaden the scope of porous acetylenedicarboxylate-based MOFs containing M(IV) cations, we herein report the synthesis, structural characterization, porosity and gas/vapor sorption properties of a new **fcu** Ce(IV)-MOF based on the simple ADC linker (Scheme 1). We also investigate the adsorption of bromine and iodine vapors in the new material, in view of its application for air cleaning from these toxic halogen vapors.

Experimental

Materials and methods

Cerium(IV) ammonium nitrate [$(NH_4)_2Ce(NO_3)_6$, purity 99%] was obtained from Acros Organics; acetylenedicarboxylic acid (H_2ADC, purity 97%) was obtained from abcr; bromine (Br_2, technical grade) from Merck Schuchardt OHG, and iodine (I_2, purity 99.5%) from Grüssing.

Powder X-ray diffraction (PXRD) patterns were recorded with the Brucker D2 Phaser diffractometer using a Cu-Kα1/α2 radiation with λ = 1.5418 Å at 30 kV. Diffractograms were obtained on a flat silicon layer sample holder, with 2θ angles ranging within 5–50° at a scan rate of 0.0125° s^{-1}.

The **infrared (IR)** spectrum was obtained on a Bruker FT-IR Tensor 37 Spectrometer in the 4000–550 cm^{-1} region with 2 cm^{-1} resolution as KBr disk. The **Raman** spectra were measured on a Bruker MultiRAM-FT Raman spectrometer equipped with a Nd:YAG-laser (wavelength 1064 nm).

Scanning electron microscopy (SEM) images were obtained using a Jeol JSM-6510LV QSEM advanced electron microscope with a LaB_6 cathode at 5–20 keV. The samples for SEM imaging were coated with gold using a Jeol JFC 1200 fine-coater (20 mA for 25 s).

Thermogravimetric analysis (TGA) was carried out on a Netzsch TG209 F3 Tarsus device under synthetic air atmosphere and heating at a ramp rate of 5 K min^{-1} to 600 °C.

Liquid ^{13}C NMR spectra were measured with a Bruker Avance III-300 (300 MHz). Prior to solution NMR analysis, 20 mg of Ce-HHU-1-Br_2 were dissolved in 0.5 mL of DMSO-d_6. For Ce-HHU-1-I_2, 20 mg of iodine-desorbed MOF were suspended in DMSO-d_6 (0.65 mL) and 5 drops of DCl (35 wt% in D_2O) were added. After about 1 h, the yellowish formed solution was introduced in the NMR tube for the analysis.

Nitrogen and CO_2 sorption isotherms were measured with a Micromeritics ASAP 2020 automatic gas sorption analyzer at 77 K (N_2), 273 K and 293 K (CO_2). The Brunauer–Emmett–Teller (BET) specific surface area and pore volume were evaluated from the nitrogen physisorption isotherms.

Water sorption isotherm was obtained using a VSTAR™ vapor sorption analyzer from Quantachrome.

Water-based synthesis of Ce-HHU-1 at ambient temperature

In a 25 mL glass vial, 364 mg (3.2 mmol) of acetylenedicarboxlic acid were dissolved in 12 mL of water. 2 mL of an aqueous solution of cerium ammonium nitrate (0.533 M) was added under stirring. The yellowish precipitate, which was formed instantly under mixture of the two solutions, was stirred for 15 min and separated from the mother liquor by centrifugation. The solid product was then washed twice with water and twice with ethanol and then centrifuged.

The activated sample was obtained by supercritical CO_2 ($scCO_2$) drying of the as-synthesized material, followed by outgassing under dynamic vacuum for 16 h at 40 °C. The use of supercritical CO_2 drying as activation procedure was adopted because of the low thermal stability of Ce-HHU-1 (stable only until about 120 °C, from TGA, Fig. S4, ESI†). We experienced in our previous works that the analogous frameworks of Zr-HHU-1 and Hf-HHU-1 collapse over conventional activation by heating at temperatures above 100 °C under vacuum.[12] Since the acetylenedicarboxylate linker is thermally labile, the supercritical CO_2 drying enables to avoid high temperatures for de-solvating/outgassing the pores of Ce-HHU-1. Elemental analysis of the activated sample: calcd for $Ce_6C_{24}H_4O_{32}$ = $[Ce_6O_4(OH)_4(OOC\text{-}C{\equiv}C\text{-}COO)_6]$: C 17.52%, H 0.24%; found: C 18.33%, H 1.09%. Yield: 270 mg (92%) based on the cerium salt.

Bromine adsorption

30 mg of activated Ce-HHU-1 were distributed in a small open vial, and a small amount of bromine was introduced in another open vial (see Fig. 7). The two vials were transferred in a vessel that was sealed to ensure a closed system. The sealed vessel was allowed to stand at room temperature over a week.

Iodine adsorption

About 40 mg of activated sample of Ce-HHU-1 were distributed in a small open vial, while about 100 mg I_2 crystals were distributed in a second open vial. The two vials were transferred together in a vessel that was sealed to ensure a closed system and stored at room temperature (see Fig. S9 in ESI†). Iodine uptake was measured gravimetrically after regular adsorption times.

Results and discussion

Synthesis and characterization

The new acetylenedicarboxylate-based cerium(IV)–metal–organic framework termed as Ce-HHU-1 of formula $[Ce_6(\mu_3\text{-}O)_4(\mu_3\text{-}OH)_4(ADC)_6]\cdot xH_2O$, was quantitatively obtained immediately after mixing aqueous solutions of acetylenedicarboxylic acid and cerium(IV) ammonium nitrate (Scheme 1). It should be noted that early syntheses of Ce(IV)-MOFs were performed in a DMF/water solvent mixture with at times addition of a monocarboxylic acid modulator like acetic or formic acid. In the case of Ce-HHU-1, the synthesis is carried out in water only and requires neither organic solvents like DMF, nor monocarboxylic acid modulator. Furthermore, although a water-based synthesis of Ce(IV)-MOF was recently reported at about 100–110 °C,[15] our synthesis takes place at room temperature and within a shorter reaction time, making the synthesis of Ce-HHU-1 even greener, as it consumes no energy from heating. This easy synthesis would also enable to produce Ce-HHU-1 at a large scale and competitive cost. This aspect is very important considering industrial production of this material towards commercial applications. The production of metal–organic frameworks in a clean, fast and economical way is a current challenge to take MOFs from laboratories to industries towards practical applications.[16]

Interestingly, Ce-HHU-1 displays a very high crystallinity in spite of its very rapid formation. SEM images of Ce-HHU-1 (Fig. S15, ESI†) reveal that the obtained product is made of agglomerated crystallites. Individual crystals have a size of about 100 nm, with no specific shape. The PXRD pattern of the obtained yellow microcrystalline powder of Ce-HHU-1 resembles that of zirconium acetylenedicarboxylate (Zr-HHU-1) (Fig. 1 and Fig. S1 in ESI†). However, the reflections in Ce-HHU-1 are slightly shifted to lower values compared to those of Zr-HHU-1. This indicates that the two MOFs are analogues, with Ce-HHU-1 having a slightly larger cell parameter, which is consistent with a larger ionic radius of Ce^{4+} (0.97 Å) in comparison to Zr^{4+} (0.84 Å).[17]

The strong band in the Raman spectrum at 2225 cm^{-1} (Fig. S2 in ESI†) is ascribed to the stretching vibration of the –C≡C– triple-bond of the ADC linker. The bands at 1600 cm^{-1} and 1371 cm^{-1} in the infrared spectrum (Fig. S3 in ESI†) are due to asymmetric and symmetric vibrations of coordinated carboxylate of the linker respectively.

The thermogravimetric analysis (Fig. S4, ESI†) shows that Ce-HHU-1 is thermally stable to about 120 °C. After this temperature, the material is decomposed in two steps to yield a solid residue that was identified by PXRD to be CeO_2 (see PXRD of residue in Fig. S5, ESI†). Ce-HHU-1 is thermally less stable than Zr-HHU-1 (180 °C).[12] This is expected, as UiO-type Ce(IV)-MOFs feature lower thermal stability compared to their zirconium analogues.[3] Furthermore, the vast majority of ADC-based coordination polymers/complexes feature low thermal stability (<250 °C) with some even decomposing in air at room temperature.[18] An exception is that of Sr-ADC for which a thermal stability of up to 440 °C was observed.[19] This relatively low thermal stability is attributable to the thermal liability of H_2ADC linker. Solid acetylenedicarboxylic acid decomposes at 180 °C. However, Ce-HHU-1 has a good hydrolytic and chemical stability, as it maintains its crystallinity after stirring in water, acidic solution (pH = 1) and various solvents at room temperature for 24 h (Fig. S6 and S7, ESI†). Unfortunately, Ce-HHU-1 would degrade in an alkaline solution (pH = 12) under the same treatment.

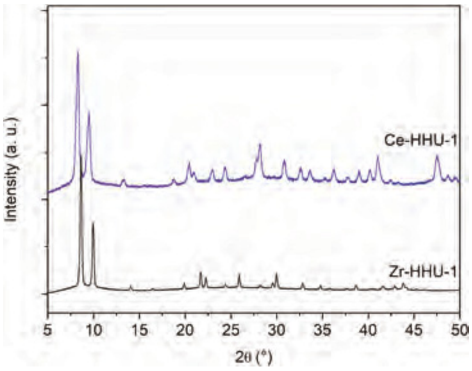

Fig. 1 Powder X-ray diffractogram of Ce-HHU-1 compared to Zr-HHU-1. The patterns are similar with that of Ce-HHU-1 being slightly shifted to lower 2θ angle values.

The analysis of the TG curve reveals that the obtained Ce-HHU-1 contains no missing linker defects. This result is in accordance with other reports of Ce(IV)-MOFs synthesized without monocarboxylic acid modulator.[4] Missing ligand defective sites in UiO-type Zr-MOFs are mainly due to the use of monocarboxylic acid modulators. Indeed, a defect free UiO-66 MOF was obtained by Lillerud *et al.* from a synthesis done without monocarboxylic acid modulator.[20]

Structure

The structure of Ce-HHU-1 was determined by means of Rietveld refinement from powder diffraction data obtained in transmission geometry on a STOE Stadi MP, equipped with a Dectris Mythen detector and using monochromated CuKα1 radiation. The indexation was done using TOPAS academics[21] (details in ESI†). Some relevant parameters are summarized in Table 1 and the final plot is shown in Fig. 2. Crystallographic data for the structure of Ce-HHU-1 have been deposited with the Cambridge Crystallographic Data Center (CCDC 1946853†).

The structure of Ce-HHU-1 consists of a face centered cubic **fcu** net topology in space group $Fm\bar{3}m$ like UiO-66.[7] Its frame-

Table 1 Selected parameters for the Rietveld refinement of Hf-HHU-1

Compound	Ce-HHU-1
Crystal system	Cubic
Space group	$Fm\bar{3}m$
$a = b = c$/Å	19.1733(6)
$\alpha = \beta = \gamma$/°	90
V/Å^3	7048.4(6)
R_{wp}/%	6.6
R_{Bragg}/%	3.0
GoF	2.1

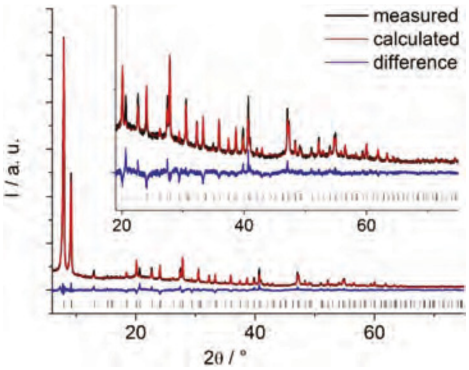

Fig. 2 Final Rietveld plot for Ce-HHU-1. The black curve represents the measured data, the red curve is the theoretical data and the blue curve indicates the difference. Vertical black bars mark the allowed Bragg reflection positions.

work is built up of octahedral $[Ce_6(\mu_3\text{-}O)_4(\mu_3\text{-}OH)_4]$ SBUs each connected to other units by twelve ADC linkers. This results in a porous network having tetrahedral cages of 5.8 Å diameter and octahedral cages of 9.6 Å diameter. Pores are accessible through triangular windows of about 4 Å diameter (Fig. 3). Ce-HHU-1 can therefore be regarded as the most contracted **fcu** Ce(IV)-MOF incorporating an alkyne-based linker, that is a framework of –C≡C– triple bonds joined at Ce_6O_8 SBUs.

Porosity, water vapor and CO_2 adsorption

The porosity of Ce-HHU-1 was assessed by nitrogen sorption experiment conducted with an activated (solvent evacuated) sample at 77 K. The obtained isotherm is of type I (Fig. 4), corresponding to a permanently microporous material.[22] The calculated BET surface area and micropore volume amount to 793 m^2 g^{-1} and 0.24 cm^3 g^{-1} respectively. These values are comparable with the BET surface area and micropore volume previously reported for cerium(IV) fumarate Ce-UiO-66-Fum (S_{BET} = 732 m^2 g^{-1}, V_{Pmicro} = 0.3 cm^3 g^{-1}).[3] This is in agreement with comparable sizes of ADC and Fum linkers. It is worth noting that the surface area of Ce-HHU-1 is larger than that we previously obtained for Zr-HHU-1 (570 m^2 g^{-1}).[12] This could be explained by the fact that Ce-HHU-1 is synthesized in water without modulator, which could have enabled a better evacuation of its pores, whereas Zr-HHU-1 was synthesized in DMF and using acetic acid as crystallization modulator.

The water sorption isotherm obtained at 20 °C exhibits a type I isotherm similar to that of Zr-HHU-1 (Fig. 5),[12] revealing the high hydrophilicity of the material. This is in agreement with their analogous compositions and structures. The water uptake capacity of about 208 mg g^{-1} is in agreement with the micropore volume. It is worth noting that the crystallinity of Ce-HHU-1 was maintained after the water sorption experiment with only small loss in the surface area (793 m^2 g^{-1} before and 731 m^2 g^{-1} after water sorption). The high hydrophilicity and water uptake capacity of Ce-HHU-1 indicate that this material can be applied for dehumidification/desiccation purpose.[23]

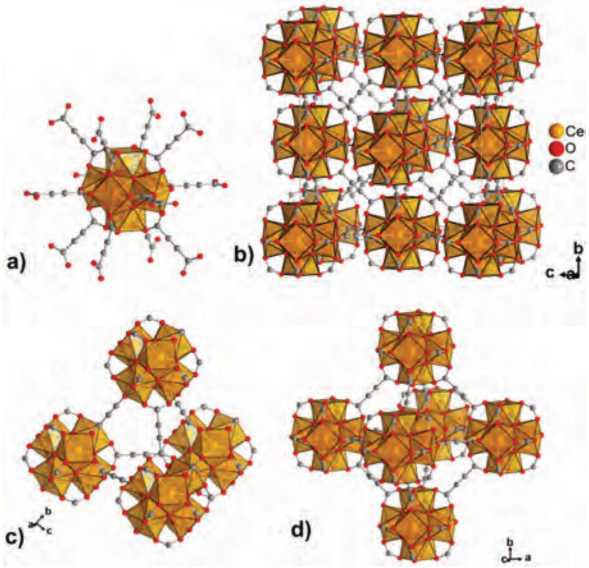

Fig. 3 (a) Secondary building unit of $\{Ce_6O_4(OH)_4\}$ with the twelve surrounding and connecting acetylenedicarboxylate linkers and the edge-sharing square-antiprismatic Ce_6O_8 polyhedra (b) fcc packing diagram of the **fcu** network in Ce-HHU-1 (c) tetrahedral cage (d) octahedral cage.

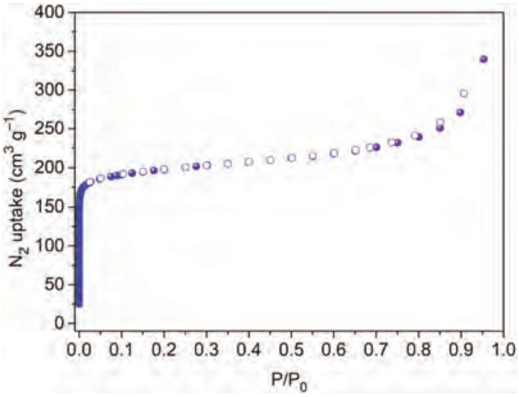

Fig. 4 Nitrogen sorption isotherm for Ce-HHU-1 at 77 K (filled symbols: adsorption; empty symbols: desorption).

The CO_2 sorption isotherms of Ce-HHU-1 obtained at 273 and 293 K respectively (Fig. 6a), exhibit a type I shape which is in agreement with its microporous nature. The CO_2 uptake capacity at 1 bar amounts to 3.2 and 2.5 mmol g^{-1} at 273 K and 293 K respectively. We note that the CO_2 uptake capacity

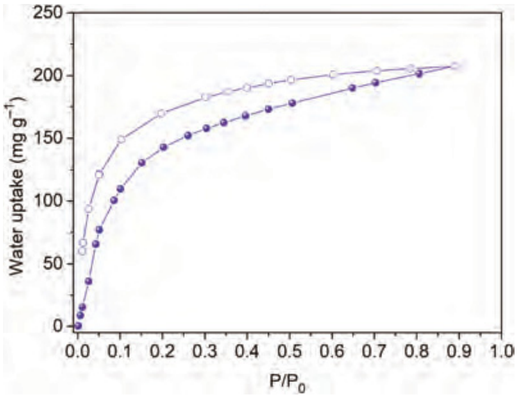

Fig. 5 Water vapor sorption isotherm for Ce-HHU-1 at 20 °C (filled symbols: adsorption; empty symbols: desorption).

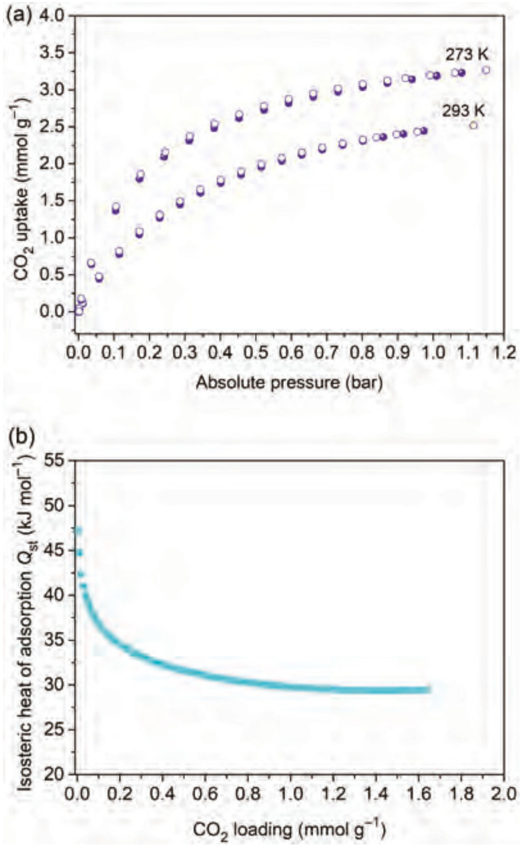

Fig. 6 (a) CO_2 sorption isotherms at 273 K and 293 K. (b) Plot of isosteric heat of CO_2 adsorption with loading for Ce-HHU-1 (filled symbols: adsorption; empty symbols: desorption).

of Ce-HHU-1 is higher than most reports of CO_2 adsorption in Ce(IV)-based MOFs (see Table S1 in ESI†). Its uptake is also comparable with those of Zr-UiO-66 (2.3 mmol g^{-1}), Zr-UiO-NH_2 (2.6 mmol g^{-1}) and Zr-UiO-67 (2.51 mmol g^{-1}) under ambient (293 K, 1 bar) conditions.[24,25] Thus, Ce-HHU-1 has an interesting CO_2 adsorption capability and can therefore be considered a prospective material for CO_2 capture and storage. The isosteric heat of absorption Q_{st} calculated using the Clausius Clapeyron equation from isotherms obtained at 273 K and 293 K is plotted in Fig. 6b (see calculation details in ESI†). The zero coverage heat of adsorption Q^0_{st} of about 47 kJ mol^{-1} is higher than that reported for UiO-66 (28 kJ mol^{-1}), zirconium and hafnium fumarate (19–29 kJ mol^{-1}) for example.[26] Such a high heat of adsorption was previously attributed to the synergistic effect of pore size reduction, μ_3-OH groups on metal-clusters and most especially to the –C≡C– triple-bond in the framework.[12]

Adsorption of bromine and iodine vapors

The capital importance of elemental halogens (mostly Cl_2 and Br_2) in industry contrasts with their hazardous nature due to their high toxicity, volatility and corrosiveness.[27] It is of great importance to find solid materials that can capture bromine and chlorine in case of spillage and leakage or for routine safety of workers and installations in halogen production units.[28] Many studies highlight the negative impact of bromine on human health and its contribution to ozone layer depletion.[29]

The presence of the alkyne function within the framework of Ce-HHU-1 prompted us to investigate its adsorption properties towards halogen vapors. When placed in a closed vessel with a small amount of bromine, 30 mg of Ce-HHU-1 completely adsorb and clean up the vessel space from the brownish smog, as well as empty the bromine container within few days (Fig. 7). Surprisingly, the material is transformed into a new highly crystalline and light yellow product showing no trace of the red-brownish color of Br_2 (Fig. 7). The product Ce-HHU-1-Br_2 has a completely different structure as seen from the PXRD patterns (Fig. 8). This indicates that Br_2 is completely irreversibly chemisorbed by Ce-HHU-1. The liquid NMR analysis reveals that the new adduct contains the 2,3-dibromofumarate linker (see Fig. S10 in ESI†). This indicates that the triple-bond of ADC in Ce-HHU-1 undergoes a solid state dibromination leading to a dibromoalkene-based coordination polymer/complex in a microcrystalline-to-microcrystalline fashion. The new compound is soluble in water and other organic solvents, suggesting that the $Ce_6O_4(OH)_4$ cluster is also altered by reacting with Br_2. However, the determination of the

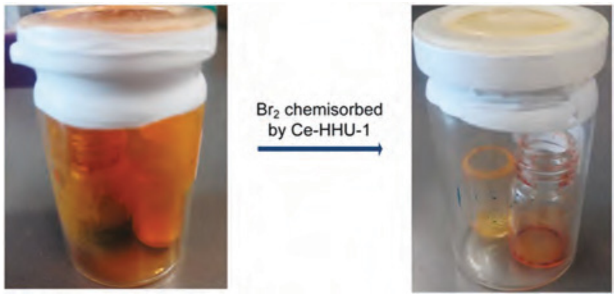

Fig. 7 Photographs of the set-up for bromine vapor adsorption with Ce-HHU-1. A complete clean-up of the vessel from bromine is observed after some days.

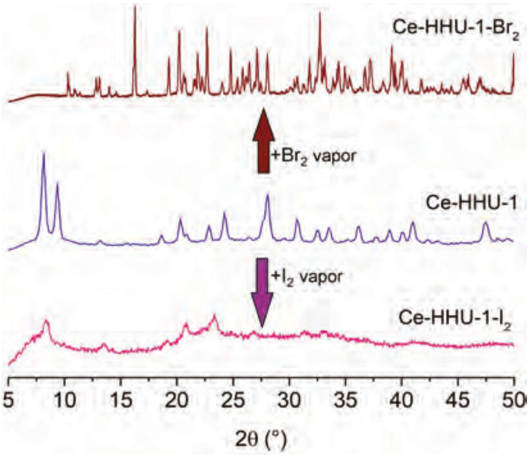

Fig. 8 Powder X-ray diffractograms of Ce-HHU-1, compared to adducts obtained after iodine and bromine vapor adsorption.

exact structure of Ce-HHU-1-Br_2 is out of the scope of this work. We anticipate that a similar chemisorption with Ce-HHU-1 could also take place with chlorine vapor.

Ce-HHU-1 has high ability for fixation of bromine vapor and can therefore be used in filtration sets like gas masks, or can be applied to clean polluted air from toxic bromine gas. We note that scarce reports are found where a solid material like Ce-HHU-1 can chemisorb bromine vapor and clean spaces polluted by this toxic vapor.

The adsorption of molecular iodine (I_2) vapor was also conducted gravimetrically with an activated sample of Ce-HHU-1 at room temperature. The adsorption of I_2 was evidenced by a progressive color change of Ce-HHU-1 from yellow to brown (Fig. S11, ESI†). The curve of iodine uptake with time (Fig. 9) shows that Ce-HHU-1 has an iodine adsorption capacity of about 0.8 g g^{-1}. In the Raman spectrum of iodine loaded sample I_2@Ce-HHU-1 (Fig. S13, ESI†), a decrease in intensity of the band related to the triple bond at 2225 cm^{-1} is observed, as well as the increase of the band at 1600 cm^{-1} suggesting a partial transformation of some triple-bonds to double-bonds. The ^{13}C NMR spectrum of the digested washed sample post-iodine sorption (Fig. S12, ESI†) has three peaks at 167, 91, and 85 ppm corresponding to the carbon of the carboxylate, the iodine substituted olefinic carbon and of the triple-bond respectively. In addition, new distinct bands at 1000, 800, 717, 522 cm^{-1} appear in the Raman spectrum (Fig. S13, ESI†) which correspond to the formation of new bonds, notably the ═C–I bond. It is worth noting that the new bands remain after full I_2 desorption by washing over one week. The washing consisted in stirring I_2@Ce-HHU-1 in ethanol for a week, changing the solvent twice each day. The aforementioned observations indicate that iodine is both physisorbed and chemisorbed in Ce-HHU-1. The chemisorption consists of a diiodination of some of the –C≡C– triple bonds of the ADC linker to a diiodofumarate linker. The PXRD pattern of the iodine-loaded sample (Fig. 8) shows that the framework collapses upon adsorption of iodine to a poorly crystalline phase. The adsorption of I_2 in Ce-HHU-1, therefore results in the solid state diiodination of some of the triple-bonds in the framework.

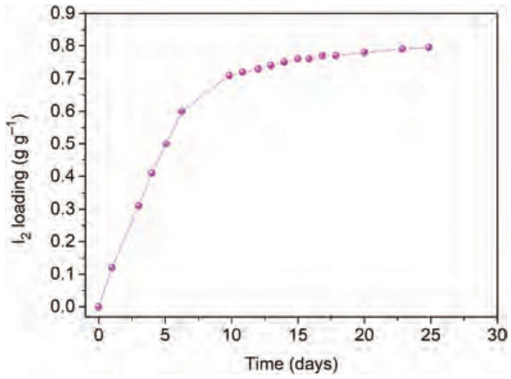

Fig. 9 Plot of iodine vapor adsorption with time for Ce-HHU-1.

The Raman spectrum of I_2@Ce-HHU-1 presents also very strong bands at 169 and 111 cm^{-1} (Fig. S13, ESI†). These bands are characteristics for I_5^- and I_3^- polyiodides respectively.[30] Interestingly, these bands persist in the thoroughly washed sample, although slightly shifted (159 and 110 cm^{-1} for I_5^- and I_3^- respectively) with reduced intensity. This indicates the formation of stable polyiodide ions from the interaction of I_2 with covalently bonded I (═C–I···I_2). The iodine adsorption and storage capacity of Ce-HHU-1 demonstrates the potential application of this material for radioactive I_2 sequestration.

Conclusions

This work establishes the potential of the acetylenedicarboxylate linker in the construction of permanently porous metal–organic frameworks. The new UiO-type MOF (Ce-HHU-1) based on acetylenedicarboxylate linker and Ce(IV) cations has successfully been synthesized and structurally characterized by Rietveld refinement. Its permanent microporosity has been demonstrated by nitrogen sorption experiment, while its high hydrophilicity is evidenced from the water sorption isotherm of type I. This material features a high isosteric heat of CO_2 adsorption attributable to the effect of the triple-bond. Ce-HHU-1 is a good halogen vapor adsorbent, of which bromine undergoes a complete chemical fixation to a new crystalline material *via* halogenation of the triple-bond. The later property makes Ce-HHU-1 a potential material for application in the capture of hazardous halogen vapors.

Conflicts of interest

There are no conflicts to declare.

Acknowledgements

We thank the German Academic Exchange Service (DAAD) for funding to TJMMN through grant no. 57214225 and the

Federal Ministry of Education and Research (BMBF) for project Optimat, grant no. 03SF0492C. We also thank Mr. Bastian Moll for conducting the Raman spectroscopy measurements.

References

1 (*a*) S. Smolders, K. A. Lomachenko, B. Bueken, A. Struyf, A. L. Bugaev, C. Atzori, N. Stock, C. Lamberti, M. B. J. Roeffaers and D. E. De Vos, *ChemPhysChem*, 2018, **19**, 373–378; (*b*) X.-J. Hong, C.-L. Song, Y. Yang, H.-C. Tan, G.-H. Li, Y.-P. Cai and H. Wang, *ACS Nano*, 2019, **13**, 1923–1931.

2 X.-P. Wu, L. Gagliardi and D. G. Truhlar, *J. Am. Chem. Soc.*, 2018, **140**, 7904–7912.

3 M. Lammert, M. T. Wharmby, S. Smolders, B. Bueken, A. Lieb, K. A. Lomachenko, D. De Vos and N. Stock, *Chem. Commun.*, 2015, **51**, 12578–12581.

4 M. Lammert, C. Glißmann, H. Reinsch and N. Stock, *Cryst. Growth Des.*, 2017, **17**, 1125–1131.

5 S. Smolders, A. Struyf, H. Reinsch, B. Bueken, T. Rhauderwiek, L. Mintrop, P. Kurz, N. Stock and D. E. De Vos, *Chem. Commun.*, 2018, **54**, 876–879.

6 (*a*) R. Dalapati, B. Sakthivel, A. Dhakshinamoorthy, A. Buragohain, A. Bhunia, C. Janiak and S. Biswas, *CrystEngComm*, 2016, **18**, 7855–7864; (*b*) K. A. Lomachenko, J. Jacobsen, A. L. Bugaev, C. Atzori, F. Bonino, S. Bordiga, N. Stock and C. Lamberti, *J. Am. Chem. Soc.*, 2018, **140**, 17379–17383.

7 J. H. Cavka, S. Jakobsen, U. Olsbye, N. Guillou, C. Lamberti, S. Bordiga and K. P. Lillerud, *J. Am. Chem. Soc.*, 2008, **130**, 13850–13851.

8 C. Serre, J. Marrot and G. Férey, *Inorg. Chem.*, 2005, **44**, 654–657.

9 D. J. Tranchemontagne, J. R. Hunt and O. M. Yaghi, *Tetrahedron*, 2008, **64**, 8553–8557.

10 V. K. Gramm, A. Schuy, M. Suta, C. Wickleder, C. Sternemann and U. Ruschewitz, *Z. Anorg. Allg. Chem.*, 2018, **644**, 127–135.

11 A. Michaelides and S. Skoulika, *Cryst. Growth Des.*, 2005, **5**, 529–533.

12 (*a*) T. J. Matemb Ma Ntep, H. Reinsch, B. Moll, E. Hastürk, S. Gökpinar, H. Breitzke, C. Schlüsener, L. Schmolke, G. Buntkowsky and C. Janiak, *Chem. – Eur. J.*, 2018, **24**, 14048–14053; (*b*) T. J. Matemb Ma Ntep, H. Reinsch, C. Schlüsener, A. Goldman, H. Breitzke, B. Moll, L. Schmolke, G. Buntkowsky and C. Janiak, *Inorg. Chem.*, 2019, **58**, 10965–10973.

13 (*a*) R. J. Marshall, S. L. Griffin, C. Wilson and R. S. Forgan, *J. Am. Chem. Soc.*, 2015, **137**, 9527–9530; (*b*) R. J. Marshall, S. L. Griffin, C. Wilson and R. S. Forgan, *Chem. – Eur. J.*, 2016, **22**, 4870–4877.

14 Z. Yan, Y. Yuan, Y. Tian, D. Zhang and G. Zhu, *Angew. Chem., Int. Ed.*, 2015, **54**, 12733–12737.

15 (*a*) R. D'Amato, A. Donnadio, M. Carta, C. Sangregorio, D. Tiana, R. Vivani, M. Taddei and F. Costantino, *ACS Sustainable Chem. Eng.*, 2019, **7**, 394–402; (*b*) J. Jacobsen, B. Achenbach, H. Reinsch, S. Smolders, F.-D. Lange, G. Friedrichs, D. De Vos and N. Stock, *Dalton Trans.*, 2019, **48**, 8433–8441; (*c*) S. Waitschat, D. Fröhlich, H. Reinsch, H. Terraschke, K. A. Lomachenko, C. Lamberti, H. Kummer, T. Helling, M. Baumgartner, S. Henninger and N. Stock, *Dalton Trans.*, 2018, **47**, 1062–1070.

16 (*a*) H. Reinsch, *Eur. J. Inorg. Chem.*, 2016, 4290–4299; (*b*) S. Wang and C. Serre, *ACS Sustainable Chem. Eng.*, 2019, **7**, 11911–11927.

17 R. Shannon, *Acta Crystallogr., Sect. A: Cryst. Phys., Diffr., Theor. Gen. Crystallogr.*, 1976, **32**, 751–767.

18 (*a*) H. Billetter, F. Hohn, I. Pantenburg and U. Ruschewitz, *Acta Crystallogr., Sect. C: Cryst. Struct. Commun.*, 2003, **59**, 130–131; (*b*) I. Pantenburg and U. Ruschewitz, *Z. Anorg. Allg. Chem.*, 2002, **628**, 1697–1702; (*c*) U. Ruschewitz and I. Pantenburg, *Acta Crystallogr., Sect. C: Cryst. Struct. Commun.*, 2002, **58**, 483–484; (*d*) I. Stein and U. Ruschewitz, *Z. Anorg. Allg. Chem.*, 2010, **636**, 400–404; (*e*) A. Schuy, I. Stein and U. Ruschewitz, *Z. Anorg. Allg. Chem.*, 2010, **636**, 1026–1031; (*f*) S. Busch, I. Stein and U. Ruschewitz, *Z. Anorg. Allg. Chem.*, 2012, **638**, 2098–2101.

19 F. Hohn, I. Pantenburg and U. Ruschewitz, *Chem. – Eur. J.*, 2002, **8**, 4536–4541.

20 G. C. Shearer, S. Chavan, J. Ethiraj, J. G. Vitillo, S. Svelle, U. Olsbye, C. Lamberti, S. Bordiga and K. P. Lillerud, *Chem. Mater.*, 2014, **26**, 4068–4071.

21 Coelho Software, *Topas Academics 4.2*, 2007.

22 M. Thommes, K. Kaneko, A. V. Neimark, J. P. Olivier, F. Rodriguez-Reinoso, J. Rouquerol and K. S. W. Sing, *Pure Appl. Chem.*, 2015, **87**, 1051–1069.

23 (*a*) P. Guo, A. G. Wong-Foy and A. J. Matzger, *Langmuir*, 2014, **30**, 1921–1925; (*b*) P. Kenfack Tsobnang, E. Hastürk, D. Fröhlich, E. Wenger, P. Durand, J. Lambi Ngolui, C. Lecomte and C. Janiak, *Cryst. Growth Des.*, 2019, **19**, 2869–2880.

24 Y. Lin, C. Kong, Q. Zhang and L. Chen, *Adv. Energy Mater.*, 2017, **7**, 1601296.

25 P. Xydias, I. Spanopoulos, E. Klontzas, G. E. Froudakis and P. N. Trikalitis, *Inorg. Chem.*, 2014, **53**, 679–681.

26 (*a*) Z. Hu, Y. Peng, Z. Kang, Y. Qian and D. Zhao, *Inorg. Chem.*, 2015, **54**, 4862–4868; (*b*) Z. Hu, I. Castano, S. Wang, Y. Wang, Y. Peng, Y. Qian, C. Chi, X. Wang and D. Zhao, *Cryst. Growth Des.*, 2016, **16**, 2295–2301.

27 P. Coleman, R. Mascarenhas and P. Rumsby, *A Review of the Toxicity and Environmental Behaviour of Bromine in Air*, Environment Agency, Rio House, Waterside Drive, Aztec West, Almondsbury, Bristol, BS32 4UD, 2005.

28 R. C. Liimatainen and W. J. Mecham, *J. Air Pollut. Control Assoc.*, 1956, **6**, 17–49.

29 (*a*) B. J. Finlayson-Pitts, F. E. Livingston and H. N. Berko, *Nature*, 1990, **343**, 623–625; (*b*) G. Lammel, A. Röhrl and H. Schreiber, *Environ. Sci. Pollut. Res.*, 2002, **9**, 397–404.

30 (*a*) I. D. Yushina, B. A. Kolesovb and E. V. Bartashevicha, *New J. Chem.*, 2015, **39**, 6163–6170; (*b*) P. Deplano, J. R. Ferraro, M. L. Mercuri and E. F. Trogu, *Coord. Chem. Rev.*, 1999, **188**, 71–95; (*c*) E. M. Nour, L. H. Chen and J. Laane, *J. Phys. Chem.*, 1986, **90**, 2841–2846.

Electronic Supplementary Material (ESI) for Dalton Transactions.

Electronic Supplementary Information (ESI)

Acetylenedicarboxylate-based cerium(IV) metal-organic framework with fcu net topology: A potential material for air cleaning from toxic halogen vapors

Tobie J. Matemb Ma Ntep,[a] Helge Reinsch,[b] Jun Liang,[a,c] and Christoph Janiak *[a]

[a] Institut für Anorganische Chemie und Strukturchemie, Heinrich-Heine-Universität Düsseldorf, Universitätsstraße 1, D-40225 Düsseldorf, Germany

[b] Institut für Anorganische Chemie, Christian-Albrechts-Universität, Max-Eyth-Straße 2, 24118 Kiel, Germany

[c] Hoffmann Institute of Advanced Materials, Shenzhen Polytechnic, 7098 Liuxian Blvd, Nanshan District, Shenzhen 518055, China

* Corresponding author: E-mail: janiak@uni-duesseldorf.de; Fax: + 49-211-81-12287; Tel: +49-211-81-12286
Additional email addresses:
tobie.matemb.ma.ntep@uni-duesseldorf.de; hreinsch@ac.uni-kiel.de; liangj@hhu.de

Table of contents

Comparison of simulated PXRD patterns of fcu cerium acetylenedicarboxylate MOF Ce-HHU-1 and zirconium acetylenedicarboxylate Zr-HHU-1

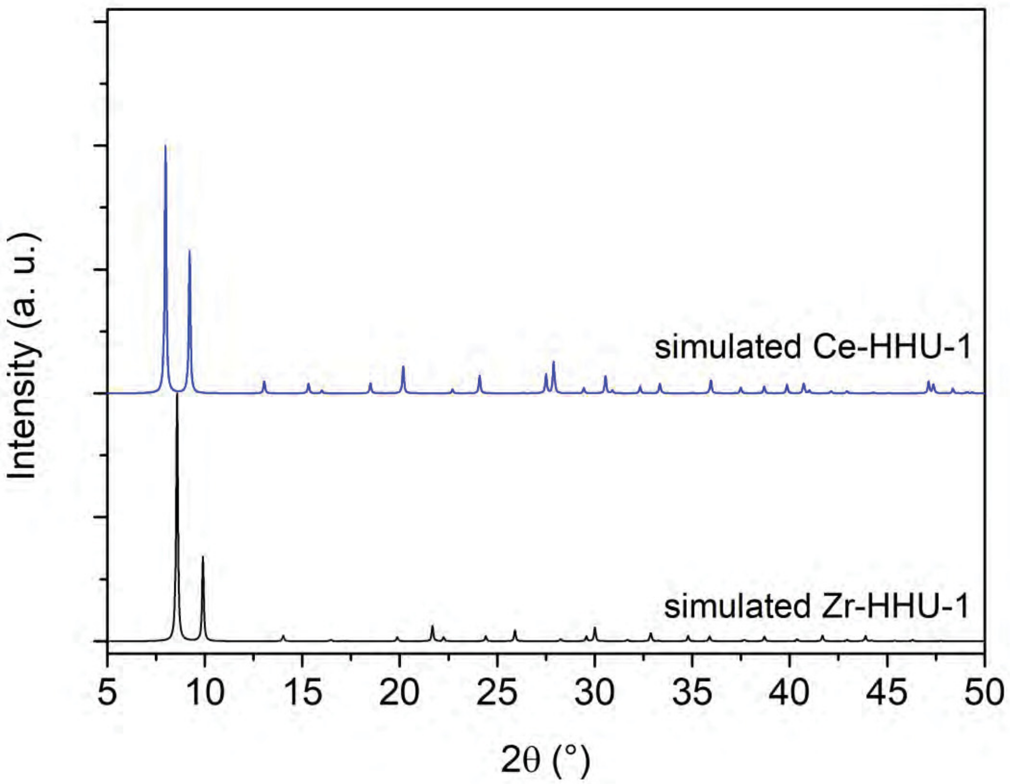

Fig. S1 Simulated PXRD pattern of Ce-HHU-1 in comparison with the simulated PXRD pattern of Zr-HHU-1.

Infrared and Raman spectroscopy of fcu cerium acetylenedicarboxylate MOF Ce-HHU-1

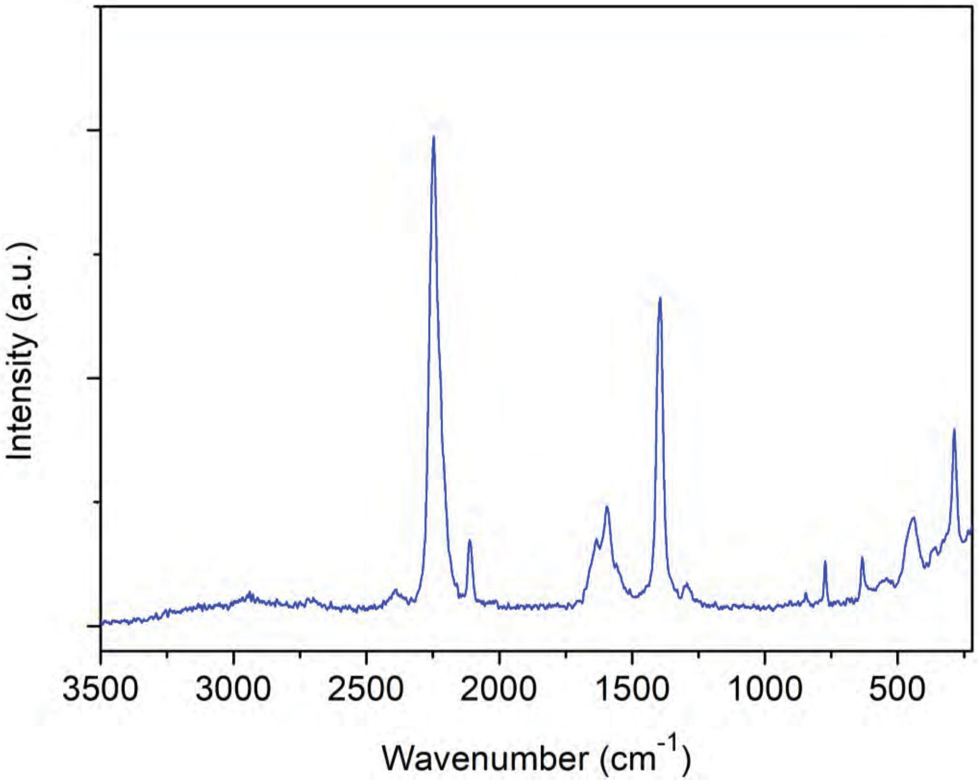

Fig. S2 Raman spectrum of Ce-HHU-1. The strong band at 2225 cm^{-1} is ascribed to the vibration of the C≡C triple-bond of acetylenedicarboxylate.

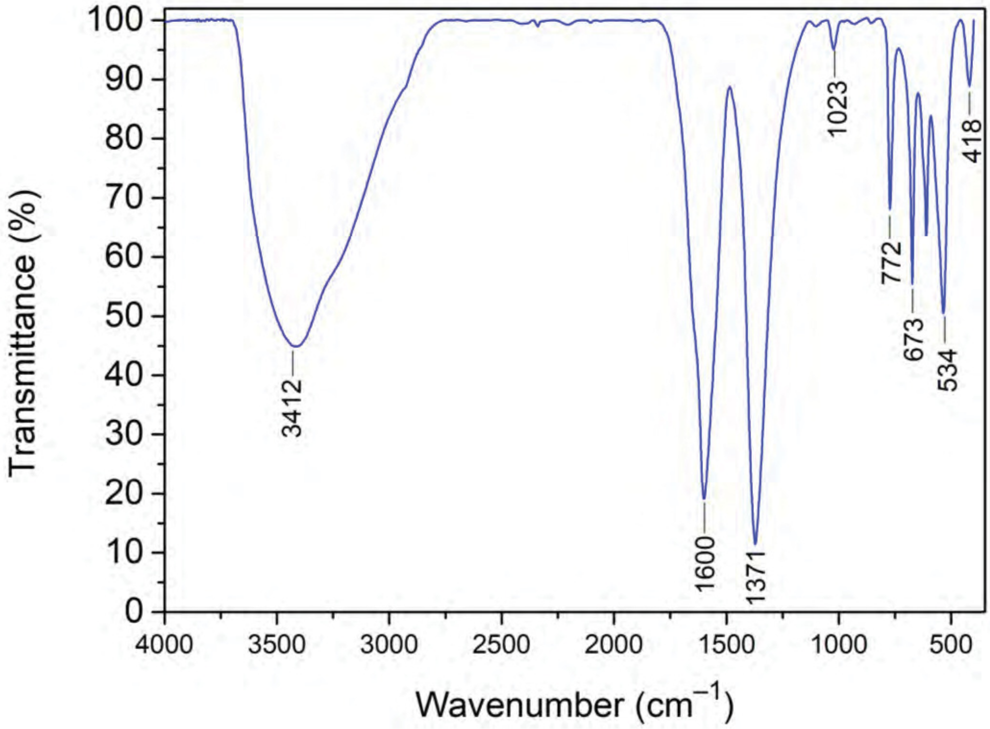

Fig. S3 Infrared spectrum of cerium(IV) acetylenedicarboxylate MOF Ce-HHU-1.

Thermogravimetric analysis of Ce-HHU-1 with missing linker defect calculation

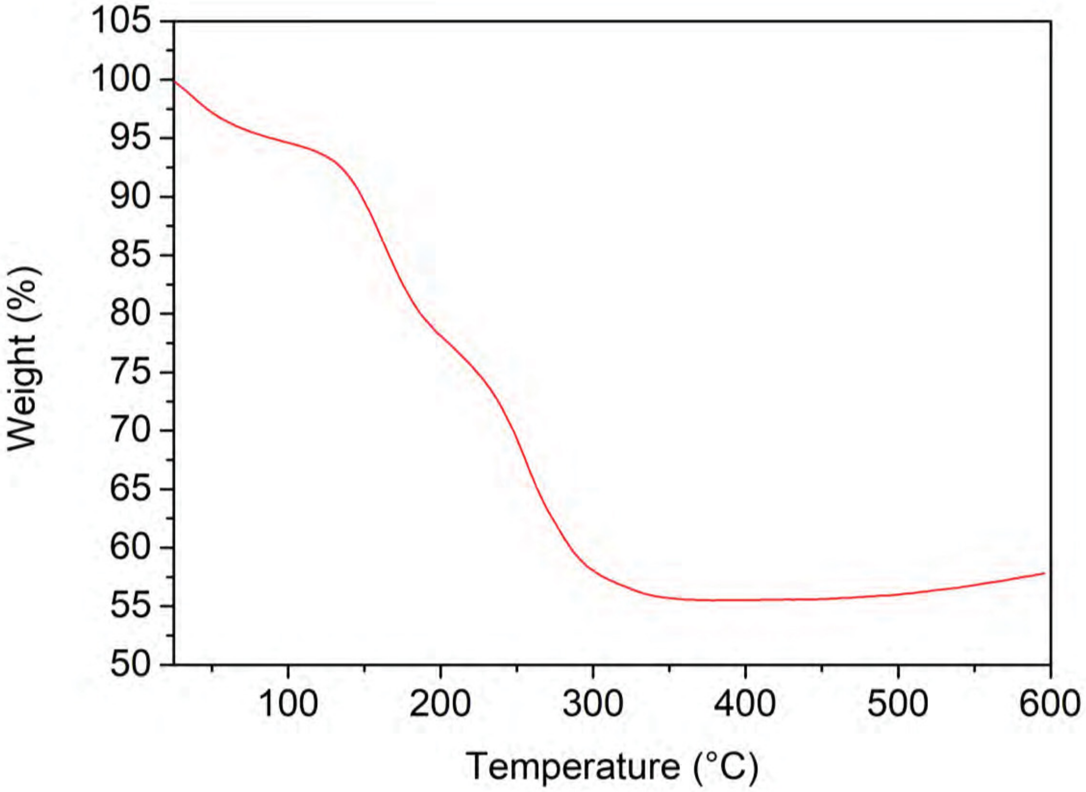

Fig. S4 Trace of the thermogravimetric analysis under air at a heating rate of 5 K min^{-1} for Ce-HHU-1. The slight rise of the TGA curve in the temperature range 500-600 °C is a measurement artifact, which we frequently observe with our Netzsch TGA. The origin of this artifact could not be elucidated. Hence, this rise should not be given a particular attention. A possibility could be the instability of the thermobalance in this temperature range during the measurement. Further, the rise of the TGA curve happened after complete decomposition of Ce-HHU-1 and has therefore no effect on the thermogram profile of Ce-HHU-1. The more so, as the final solid residue was identified as CeO_2 which is expected already at 350 °C, in agreement with the thermal decomposition profile of for example Ce-UiO-66 and Ce-Fum.[1]

- Missing linker defect calculation (according to Shearer *et al.*[2])

The ideal (defect-free) Ce-HHU-1 (Ce-ADC) MOF formula is $[Ce_6O_4(OH)_4(ADC)_6]$.

The complete decomposition of ideal Ce-HHU-1 would yield $6CeO_2$ solid residue.

Mass of solid residue: $6\times M(CeO_2) = 1032.66$ g mol^{-1}

Molar mass of ideal Ce-HHU-1: $M[Ce_6O_6(ADC)_6] = 1644.97$ g mol^{-1}, a factor of 1.5929 higher than the solid residue.

The ideal plateau of MOF should then be found at 159.3% on the TG trace normalized to 100% solid residue i.e $Wt_{\text{ideal plat.}} = 159.3\%$ and $W_{\text{end}} = 100\%$ (see Fig. S4b).

The experimental plateau of the TG curve is found at $Wt_{\text{exp.plat.}} \approx 161\%$.

A value for expected weight loss per ADC linker out of $NL_{\text{ideal}} = 6$ linkers is:

$Wt_{\text{pL.teo}} = (Wt_{\text{ideal plat.}} - W_{\text{end}}) / NL_{\text{ideal}} = (159.29 - 100) / 6 = 9.88\%$

The number of experimental linkers per Ce_6 cluster is:

$NL_{exp.} = 6 - x = (Wt_{exp.\ plat.} - W_{end}) / Wt_{pL.theo} = (160.8 - 100) / 9.88 = 6.15 \approx 6$ which implies no occurrence of missing linker defects in the framework of Ce-HHU-1 obtained. This conclusion is in agreement with the result of the CHN elemental analysis.

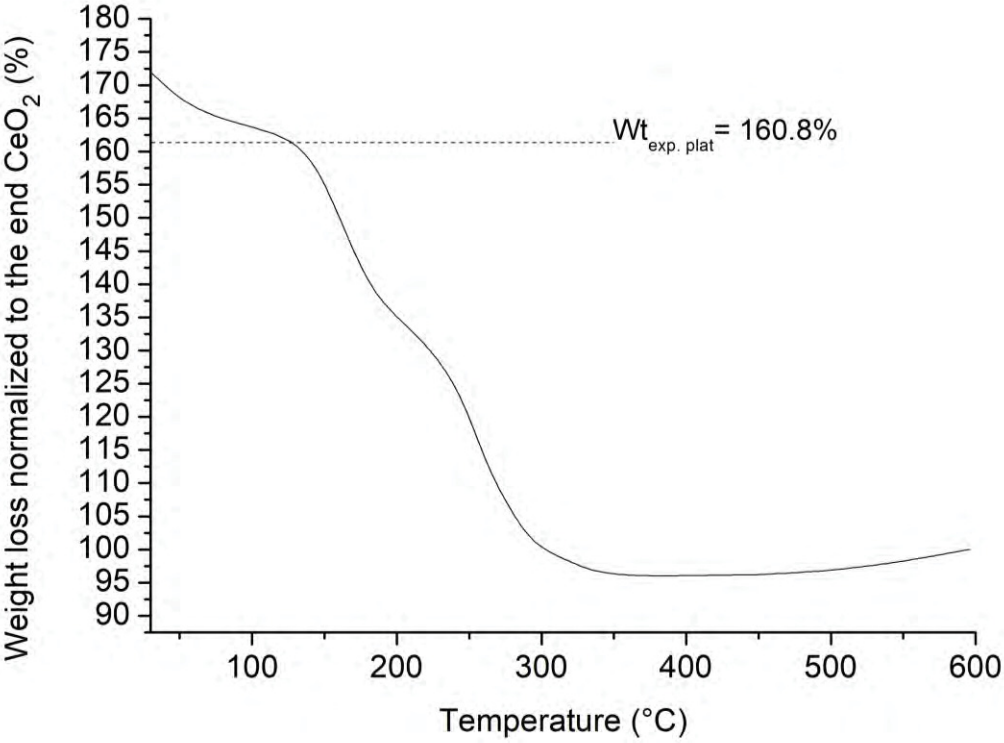

Fig. S4b Normalized TGA curve of Ce-HHU-1.

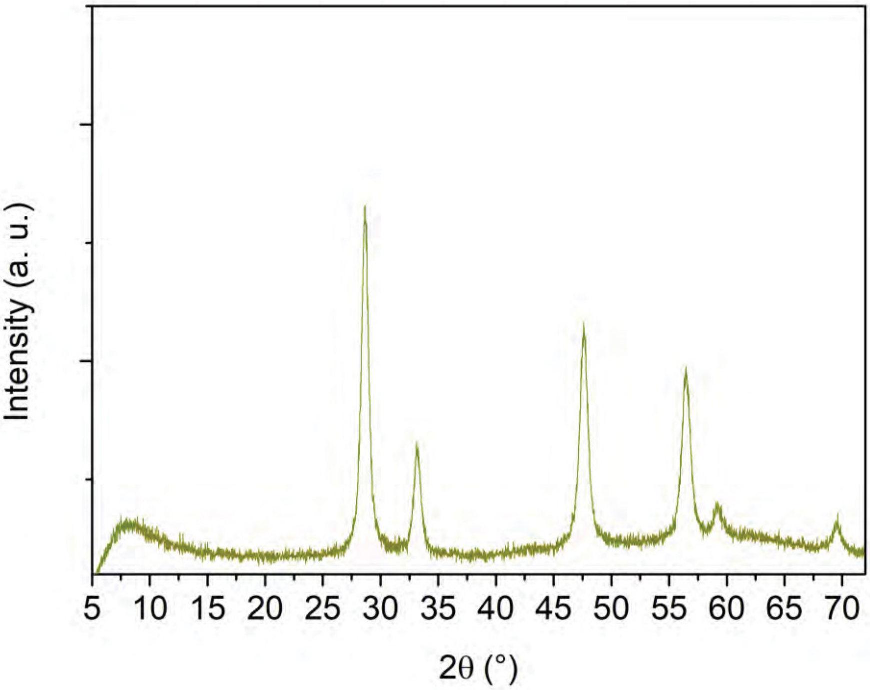

Fig. S5 PXRD pattern of the solid residue after TGA analysis. The pattern corresponds to the cubic fluorite-type phase of CeO_2.[3]

PXRD patterns of the chemical stability test for Ce-HHU-1

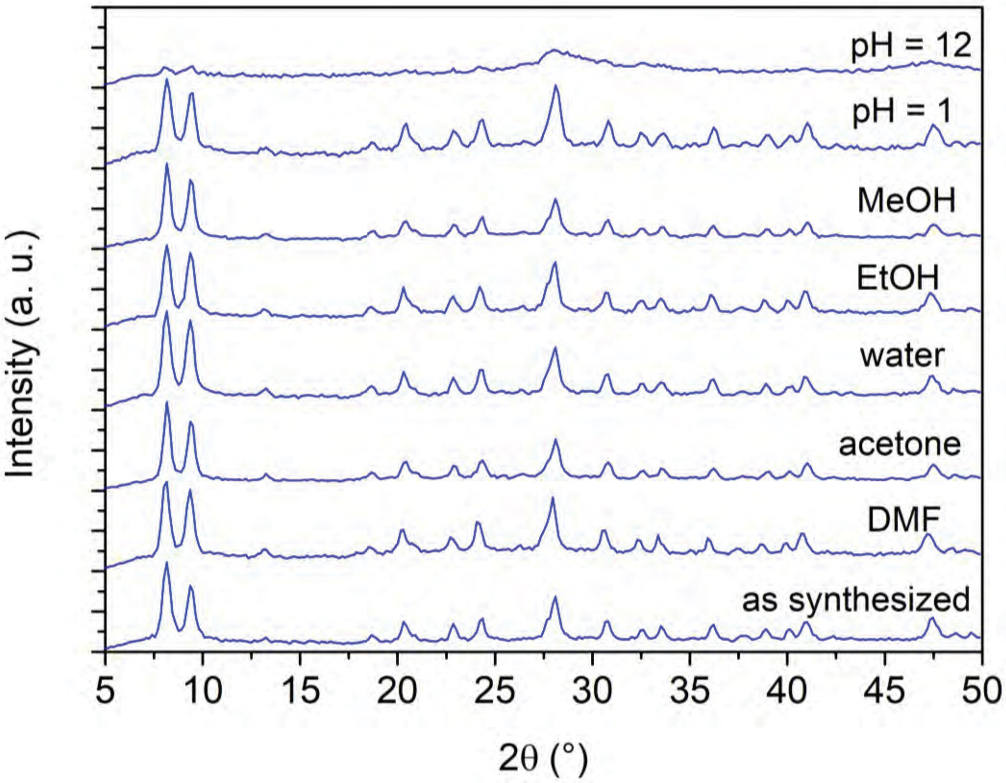

Fig. S6 PXRD patterns of Ce-HHU-1 after stirring 24 h at room temperature in various solvents and solutions (top). PXRD of Ce-HHU-1 after water sorption experiment (bottom).

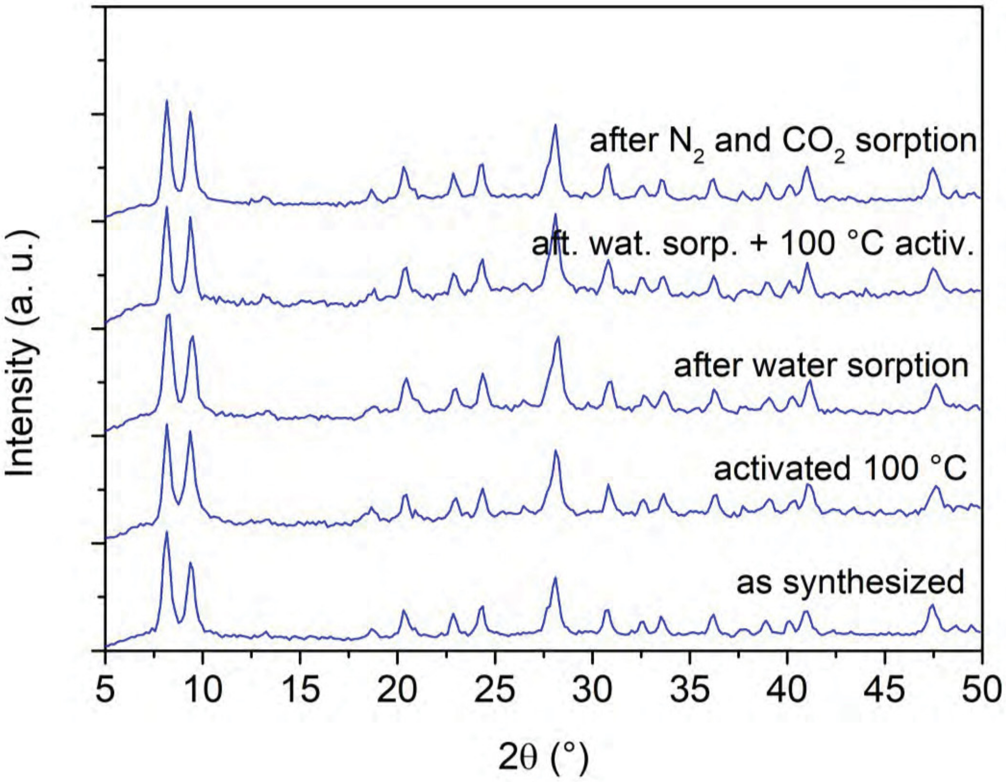

Fig. S7 PXRD patterns of Ce-HHU-1 after activation at 100 °C, after water and gas sorption.

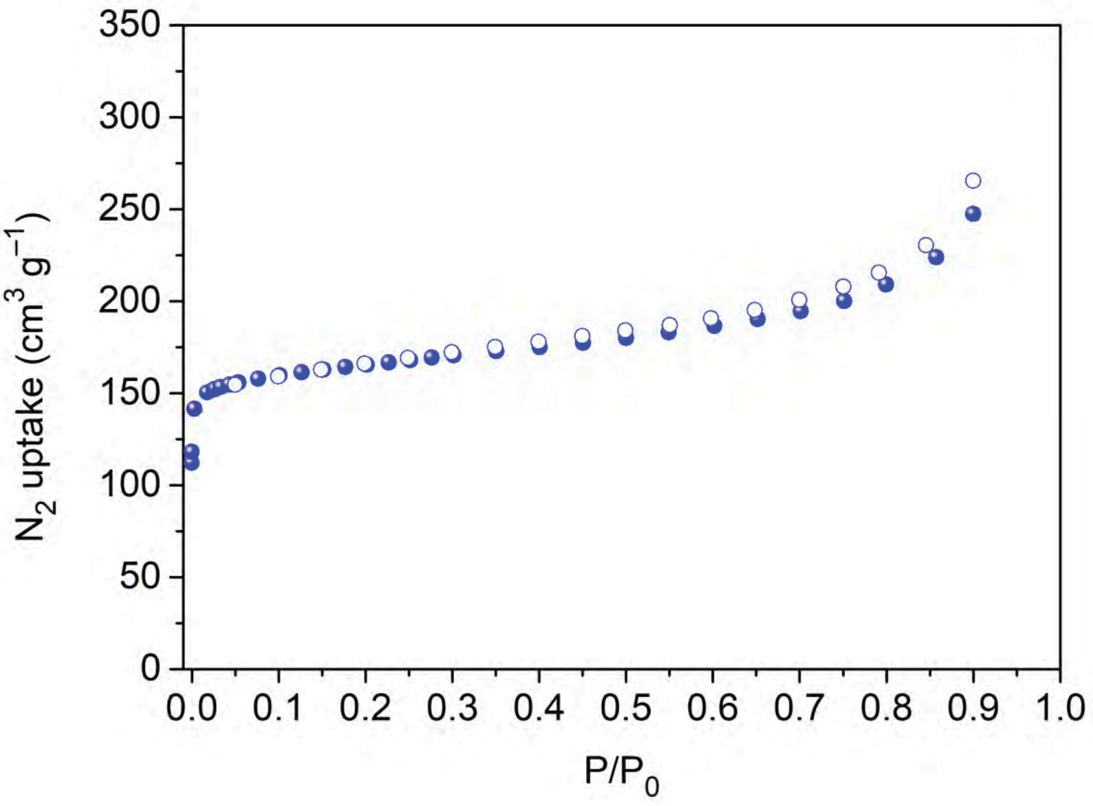

Fig. S8 Nitrogen sorption isotherm of Ce-HHU-1 after water sorption, followed by activation at 100 °C under vacuum.

Method of structure determination by Rietveld refinement for Ce-HHU-1

For the refinement of Ce-HHU-1 structure, the crystal structure of Hf-HHU-1 was used as starting model for the Rietveld refinement after exchanging the Hf atoms for Ce atoms and superimposing the cell parameter deduced from the position of the second peak (hkl = 200). All atoms were freely refined using one temperature factor for the framework and one temperature factor for the guest atoms, respectively. The occupancy of the linker molecules was also freely refined. Residual electron density inside the pores was identified by Fourier synthesis and attributed to guest molecules, modeled by oxygen atoms of refinable occupancy. These guest atoms (G*n*) should be considered placeholders for any kind of solvent molecules. The linker occupancy converged to ≈ 0.69. It must be mentioned that the modeling of the guest atoms could easily affect this and thus this value should be carefully interpreted. Some relevant parameters are summarized in Tab. 1 and the final plot is shown in Fig. 2. Crystallographic data for the structural analyses of Ce-HHU-1 have been deposited with the Cambridge Crystallographic Data Centre (CCDC 1946853).

Tab. S1 Summary of some reported CO_2 uptake capacity of Ce(IV)-based MOFs .

Materials	S_{BET} (m^2 g^{-1})	CO_2 uptake (mmol g^{-1}, 273 K)	CO_2 uptake (mmol g^{-1}, 293 K)	Structure	Ref
Ce-HHU-1	793	3.2	2.5	fcu	This work
Ce-UiO-66-$(CH_3)_2$	845	1.5	1.0	fcu	4
F_4_UiO-66(Ce)	641	2.5	1.5	fcu	5
F_4_MIL-140A(Ce)	320	2.1	1.9	MIL-140	2
Ce-UiO-66-N_3	835	2.6	–	fcu	6
Ce-UiO-66-NO_2	819	3.7	–	fcu	3
Ce-CCA	1210	1.6	–	fcu	7

CCA = 4-carboxycinnamate

Bromine adsorption for Ce-HHU-1

Fig. S9 Photograph of the product obtained after bromine vapour adsorption on Ce-HHU-1.

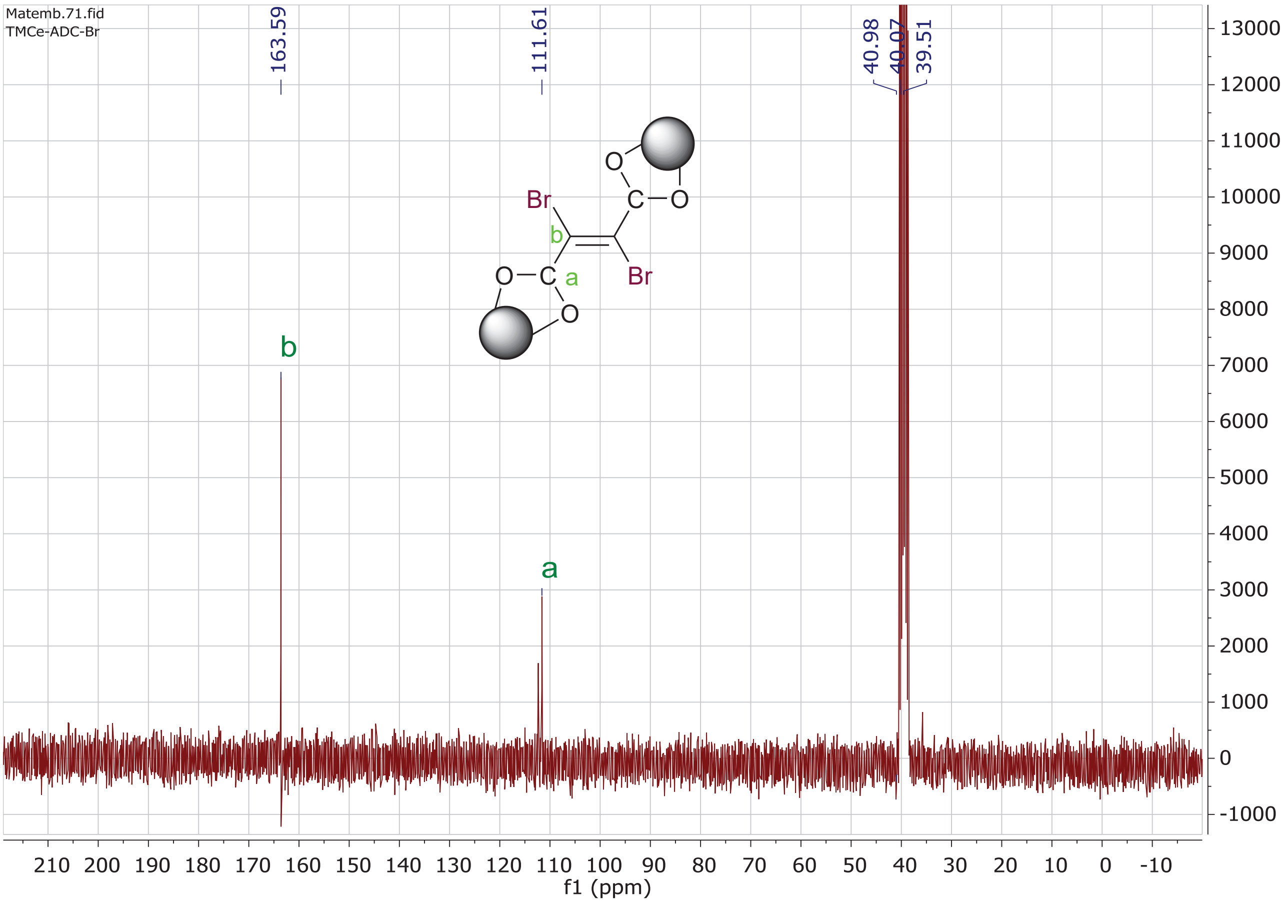

Fig. S10 Liquid ^{13}C NMR spectrum of product obtained after bromine vapor adsorption onto Ce-HHU-1 (Ce-HHU-1-Br$_2$).

Iodine adsorption for Ce-HHU-1

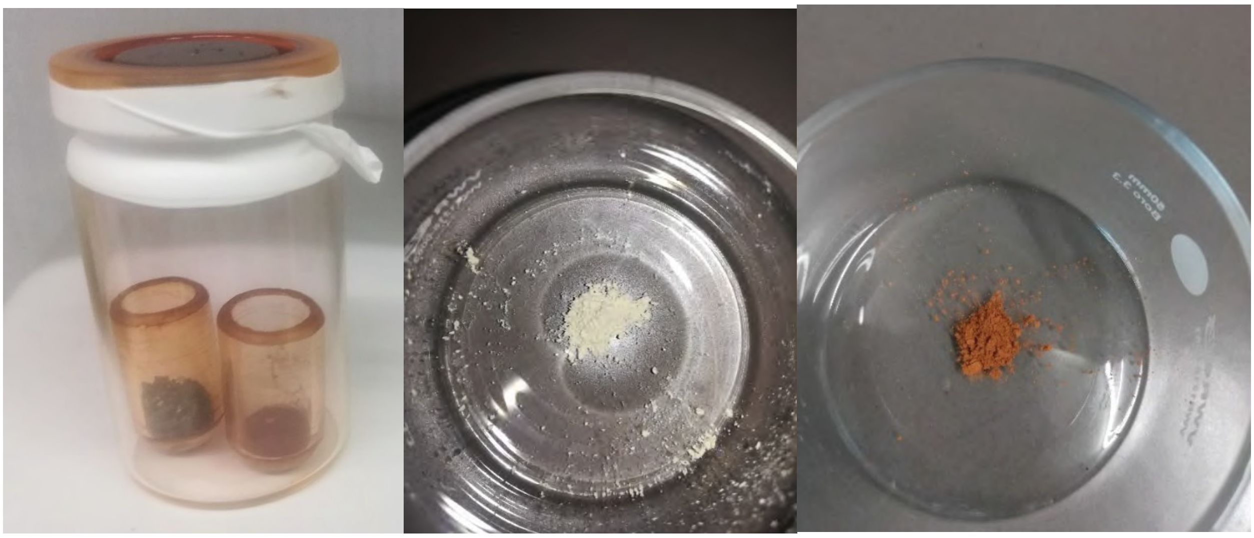

Fig. S11 Photographs of the set up for iodine adsorption (left), Ce-HHU-1 before iodine adsorption (middle) and after iodine loading (right).

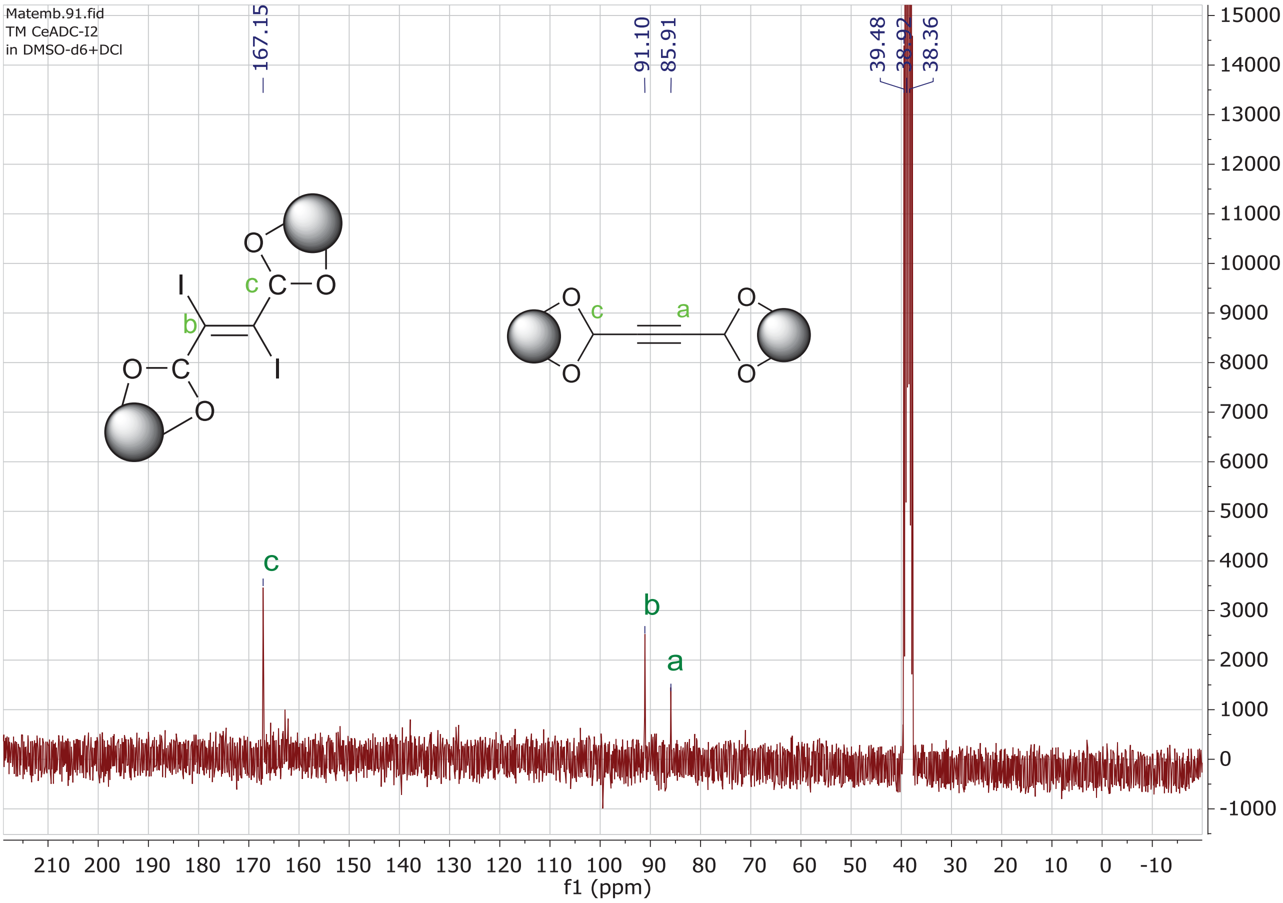

Fig. S12 Liquid ^{13}C NMR spectrum of Ce-HHU-1-I_2 after iodine desorption (washing) in ethanol over a week to a colorless supernatant washing solvent.

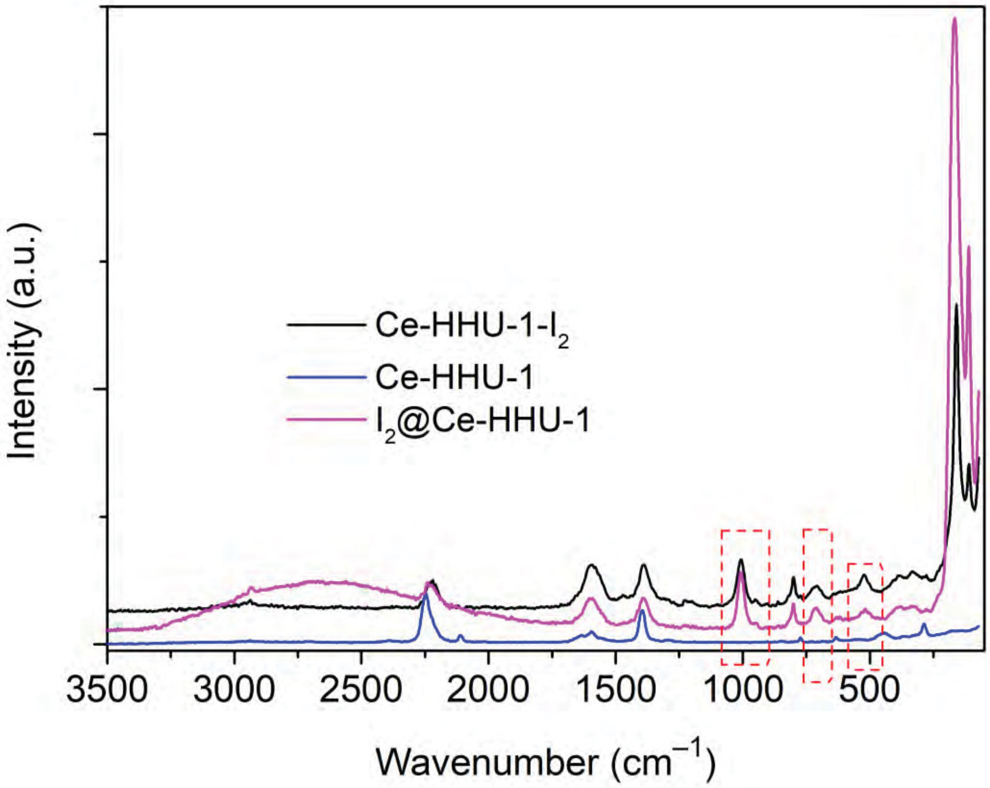

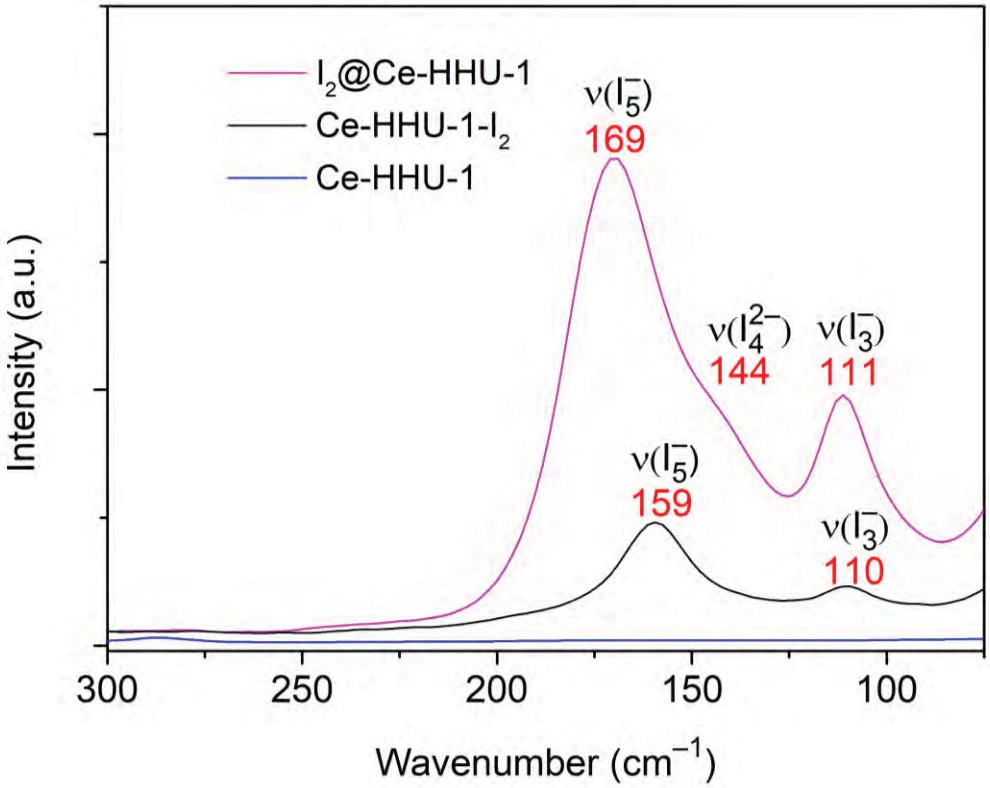

Fig. S13 Raman spectra of activated Ce-HHU-1 (blue), iodine-loaded I_2-Ce-HHU-1 (pink) and desorbed/ethanol washed Ce-HHU-1-I_2. Spectra in the 3500-50 cm^{-1} range (top) and in the 300-50 range (bottom).

Determination of the isosteric heat of CO_2 adsorption

The CO_2 isotherms experimentally obtained respectively at 273 K and 298 K were fitted with the Langmuir-Freundlich model (eq. 1). The fits are shown in Figure S14. The obtained fits were used to determine the pressure for each temperature corresponding to various CO_2 loadings. The isosteric heat of adsorption was finally calculated by applying the Clausius-Clapeyron equation (eq. 2).

$$q = q_{max} \cdot \frac{(k \cdot p)^t}{1 + (k \cdot p)^t} \qquad (1)$$

q is the gas amount adsorbed (mmol g^{-1}); q_{max} is the maximum loading; k is the affinity constant (bar^{-1}); t is the heterogeneity exponent; p is the pressure (kPa).

$$Q_{st} = -R\left(\frac{T_2 T_1}{T_2 - T_1}\right) ln \frac{P_2}{P_1} \qquad (2)$$

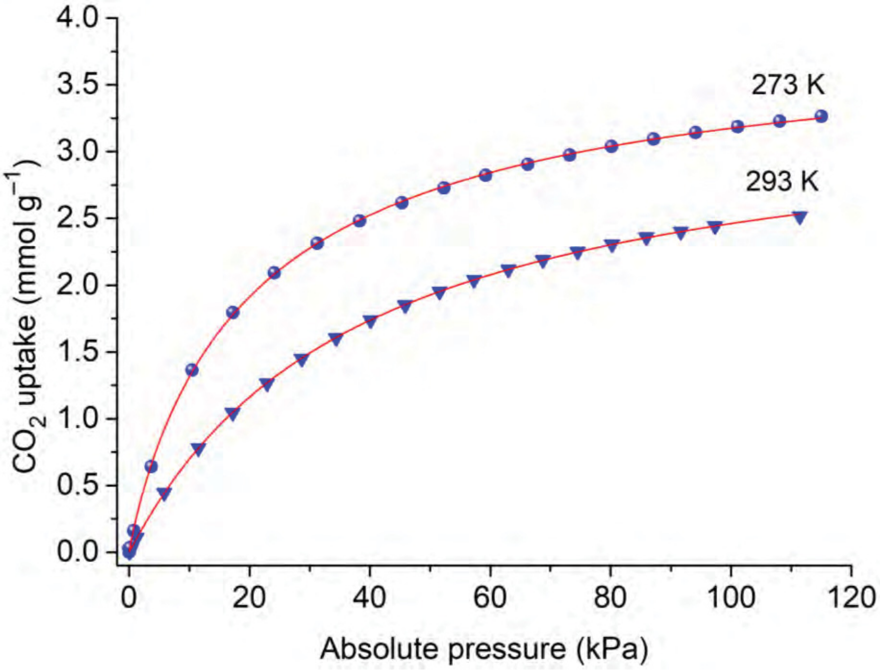

Fig. S14 Fitting of CO_2 adsorption isotherms with the Langmuir-Freundlich model. Symbols for experimental data and red lines for simulated fits.

Scanning electron microscopy (SEM)

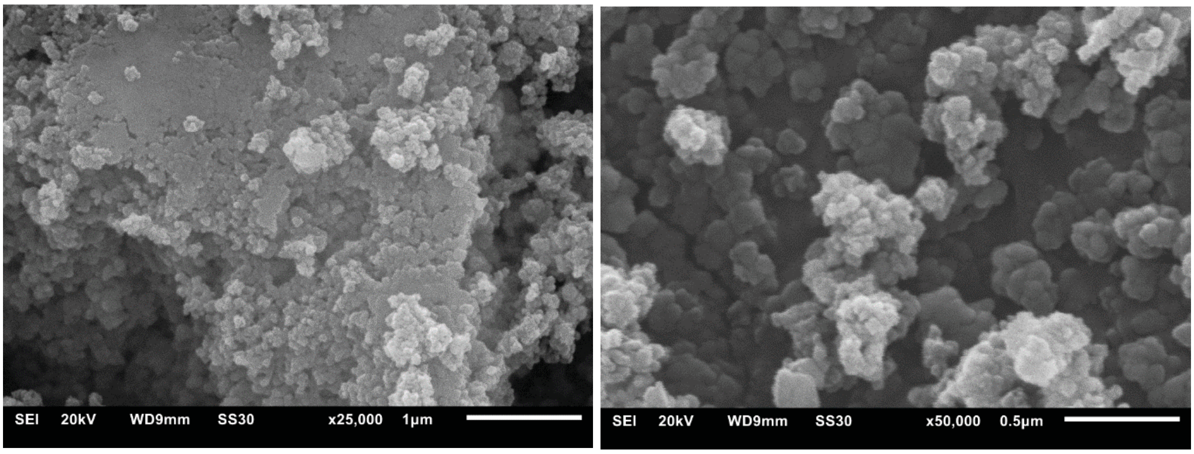

Fig. S15 Scanning electron micrographs (SEM) of Ce-HHU-1.

REFERENCES

---

1 M. Lammert, M. T. Wharmby, S. Smolders, B. Bueken, A. Lieb, K. A. Lomachenko, D. De Vos and N. Stock, *Chem. Commun.*, 2015, **51**, 12578–12581.
2 G. C. Shearer, S. Chavan, S. Bordiga, S. Svelle, U. Olsbye and K. P. Lillerud, *Chem. Mater.*, 2016, **28**, 3749-3761.
3 L. Zhang, W. Zou, K. Ma, Y. Cao, Y. Xiong, S. Wu, C. Tang, F. Gao and L. Dong, *J. Phys. Chem. C*, 2015, **119**, 1155−1163.
4 R. Dalapati, B. Sakthivel, A. Dhakshinamoorthy, A. Buragohain, A. Bhunia, C. Janiak and S. Biswas, *CrystEngComm*, 2016, **18**, 7855–7864.
5 R. D’Amato, A. Donnadio, M. Carta, C. Sangregorio, D. Tiana, R. Vivani, M. Taddei and F. Costantino, *ACS Sustainable Chem. Eng.*, 2019, **7**, 394−402.
6 A. Buragohain and S. Biswas, *CrystEngComm*, 2016, **18**, 4374–4381.
7 M. SK, M. Grzywa, D. Volkmer and S. Biswas, *Microporous Mesoporous Mat.*, 2017, **237**, 275–281.

2.4 Facile in situ halogen functionalization via triple-bond hydrohalogenation: enhancing sorption capacities through halogenation to halofumarate-based Zr(IV)-metal-organic frameworks

Tobie Matemb Ma Ntep, Hergen Breitzke, Laura Schmolke, Carsten Schlüsener, Bastian Moll, Simon Millan, Niels Tannert, Ilias El Aita, Gerd Buntkowsky and Christoph Janiak

Chem. Mater. **2019**, *31*, 21, 8629-8638.

DOI: 10.1021/acs.chemmater.9b00524

Impact factor 2018: 10.15

After unexpectedly discovering the chloro-functionalization of zirconium fumarate (MOF-801) via in situ hydrochlorination of acetylenedicarboxylic acid, when reacting with zirconium chloride ($ZrCl_4$) in water, an inquiry came up to know if this facile route could lead to other halogen functionalization of MOF-801 by using corresponding zirconium halides. The reaction was therefore repeated by reacting acetylenedicarboxylic acid with zirconium bromide ($ZrBr_4$) and zirconium iodide (ZrI_4), respectively. This led to the formation of three isostructural halogen-functionalized MOF-801, namely HHU-2-Cl, HHU-2-Br and HHU-2-I. The three MOFs have the same structure as MOF-801, in which octahedral $[Zr_6O_4(OH)_4]^{12+}$ clusters are connected with each other by halofumarate (chlorofumarate, bromofumarate and iodofumarate) linkers into microporous materials with **fcu** topology. Their thermal and chemical stabilities were evaluated, as well as their porosity, gas (CO_2, SO_2 and CH_4) and water vapor sorption properties. HHU-2-Cl was further evaluated for its potential application for adsorption thermal batteries (ATB), by testing its stability over five consecutive water vapor ad-/desorption cycles, the determination of the heat of water adsorption and heat storage capacity, as well as the determination of the kinetic of water adsorption. Detailed results of this work are found in the article that follows.

Author´s contribution to the work:

- Idea and setting of the synthesis procedures.
- Synthesis and preparation of the samples for further characterization.

- Characterizations including PXRD experiment, TGA, chemical stability test, nitrogen sorption and porosity parameters determination, other gas/vapor sorption (H_2O, CO_2, SO_2 and CH_4) experiments.
- Organization of other analyses (Raman, ssNMR, SEM-EDX and XPS), data analysis/interpretations and treatment.
- Experimental investigation of the mechanism of the in situ hydrohalogenation.
- Samples activation prior characterizations and MOF digestion prior liquid NMR analysis.
- Determination of the amount of missing linker defects from solution NMR.
- Fitting of water adsorption isotherms and determination and plot of the isosteric heat of water adsorption from isotherms at three different temperatures. Calculation of the heat storage capacity.
- Determination of the kinetics model from time dependent water sorption. Calculation of kinetics parameters.
- Writing of the manuscript, drawing of figures and responses to reviewers during the review process.

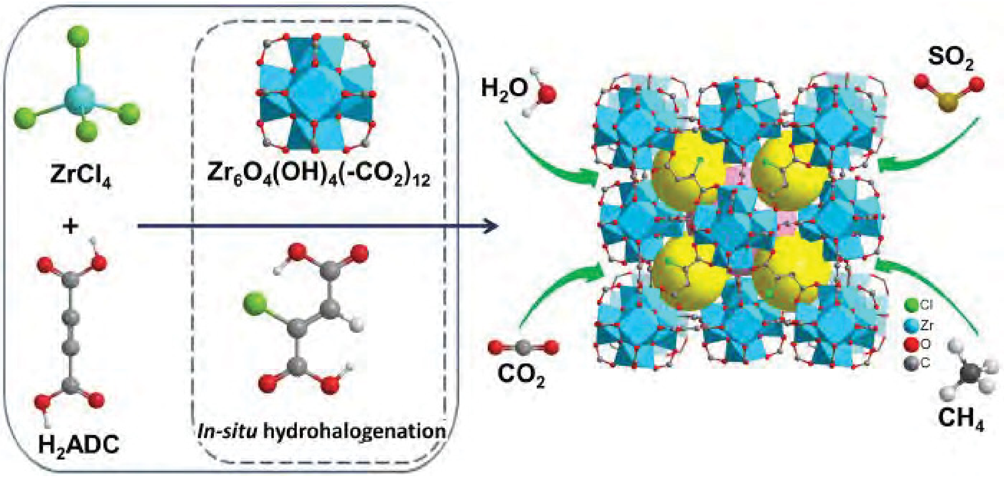

CHEMISTRY OF MATERIALS
Article
Cite This: Chem. Mater. 2019, 31, 8629−8638
pubs.acs.org/cm

Facile in Situ Halogen Functionalization via Triple-Bond Hydrohalogenation: Enhancing Sorption Capacities through Halogenation to Halofumarate-Based Zr(IV)-Metal-Organic Frameworks

Tobie Matemb Ma Ntep,[†] Hergen Breitzke,[‡] Laura Schmolke,[†] Carsten Schlüsener,[†] Bastian Moll,[†] Simon Millan,[†] Niels Tannert,[†] Ilias El Aita,[§] Gerd Buntkowsky,[‡] and Christoph Janiak*,[†]

[†]Institut für Anorganische Chemie, Heinrich-Heine-Universität Düsseldorf, D-40204 Düsseldorf, Germany

[‡]Eduard-Zintl-Institut für Anorganische und Physikalische Chemie, Technische Universität Darmstadt, Alarich-Weiss-Straße 4, D-64287 Darmstadt, Germany

[§]Institut für Pharmazeutische Technologie und Biopharmazie, Heinrich-Heine-Universität Düsseldorf, D-40225 Düsseldorf, Germany

Supporting Information

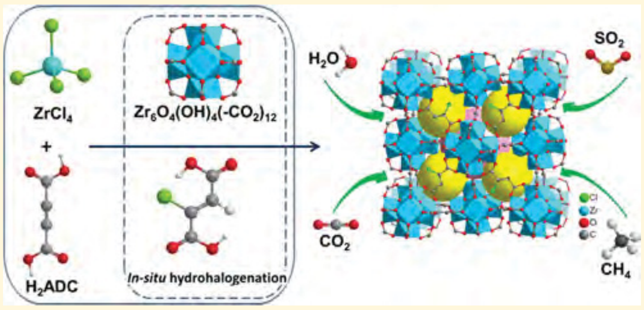

ABSTRACT: Surface halogenation is an important means to tune or improve functionalities of solid-state materials. However, this concept has been hardly explored and exploited in the engineering of metal-organic frameworks (MOFs). Here, a facile approach to obtain halo-functionalized derivatives of zirconium fumarate (MOF-801) is developed by reacting zirconium halides (ZrX$_4$; X = Cl, Br, I) in water with acetylenedicarboxylic acid. The latter quantitatively undergoes an unusual in situ linker transformation into halofumarate via trans addition of HX to the −C≡C− triple bond. This HX addition and MOF formation happen in a one-pot reaction, that is, the in situ generated halogenated linker reacts with zirconium ions in solution to yield three microporous HHU-2-X MOFs (X = Cl, Br, I) with an **fcu** topology, containing UiO-type [Zr$_6$O$_4$(OH)$_4$] secondary building units 12-fold connected by halofumarate linkers. The halogen (Cl) groups in HHU-2-Cl result in increased hydrophilicity for water vapor sorption as well as increased gas uptakes of 21% SO$_2$, 24% CH$_4$, 44% CO$_2$, and 154% N$_2$ when compared to the non-halogenated MOF-801. The tuning of the inner surface chemistry is realized to yield multipurpose adsorbent materials for enhanced gas and vapor uptakes over their non-halogenated analogues. The gas sorption properties of the chlorinated HHU-2-Cl material indicate its suitability for CO$_2$, N$_2$, and SO$_2$ capture and separation, while its water sorption profile yields a high heat storage capacity of 500 kJ kg^{-1}, making it promising for adsorption-based thermal batteries and dehumidification applications.

INTRODUCTION

Metal-organic frameworks (MOFs) are porous materials consisting of organic ligands coordinatively connected to metal clusters into a three-dimensional network.[1,2] MOFs promise a wide range of technological applications, such as gas storage and separation,[3−6] catalysis,[7−9] adsorption-driven chillers and heat pumps,[10,11] proton conduction,[12−14] and water harvesting from air.[15] Decorating the inner surface of MOFs with polar groups has been proven to be an effective means to tune their affinity for gas/vapor molecules in view of target applications, with amino-, carboxyl-, hydroxyl-, and nitro-functionalization dominating the field.[16,17] Substituting linkers with electron-withdrawing halogens was shown to have a multiplicative effect on the Lewis acid catalysis with MOFs.[18] Yet, astonishingly few studies of the effect of halogen-decorated pores on the gas/vapor adsorption properties of MOFs are reported.[19−22] At the same time, the necessity that synthesis methods and functionalization approaches should economize time and cost, as well as ensure sustainability, is increasingly becoming an essential issue, as MOFs are progressively shifting from laboratories to industry.[23]

Alkyne-containing ligands pose platforms to halo-functionalize a MOF via halogenation reactions on the triple bond.[24] Marshall et al. demonstrated that post-halogenation of linker-integral −C≡C− bonds was possible in zirconium(IV)-based MOFs containing alkyne moieties, with retention of structure topology. They reported the postsynthetic bromination of the UiO-type 4,4′-(ethyne-1,2-diyl)dibenzoate-based Zr-MOF to an isostructural 4,4′-(1,2-dibromoethene-1,2-diyl)dibenzoate-based MOF.[24,25] However, halogenated MOFs obtained by

Received: February 4, 2019
Revised: October 8, 2019
Published: October 9, 2019

ACS Publications

DOI: 10.1021/acs.chemmater.9b00524
Chem. Mater. 2019, 31, 8629−8638

direct reaction of prefunctionalized ligands are also known. For example, Meek et al. reported the synthesis of a series of halogenated versions of MOF-5 using halogenated terephthalic acid as starting ligands.[26] In principle, an in situ transformation of an alkyne-containing linker into a halo-substituted alkene-containing linker and subsequent/simultaneous MOF formation should be an interesting approach to halo-functionalized MOFs. This was observed in the formation of copper(II) chlorofumarate and lithium hydrogen iodofumarate coordination polymers, starting from acetylenedicarboxylic acid.[27,28] Such an approach would have benefits of reducing synthesis steps, time, and cost, as well as yielding materials that might not be obtained by direct synthesis or postmodification.[29]

For acetylenedicarboxylate (ADC), being the shortest alkyne-containing dicarboxylate linker, we recently communicated a strategy to synthesize a chloro-functionalized version of zirconium(IV) fumarate via in situ hydrochlorination of the −C≡C− triple bond of acetylenedicarboxylic acid (H_2ADC) to chlorofumarate (Scheme 1).[30] This discovery prompted us to investigate here the generation of other halo- (bromo-, iodo-)functionalized versions of zirconium fumarate by the same strategy but with some amendment in the first synthesis procedure. Thereby, we verify that bromine and iodine can also be successfully hydrohalogenated to acetylenedicarboxylic acid. This could not be necessarily inferred from the reported hydrochlorination, as it is known that changing reaction conditions in the synthesis of MOFs (and especially the metal source) can yield no or other products as targeted.[31] The hydrohalogenation approach should be of wider interest not only because of its environmental friendliness (water as solvent, low reaction temperature, short reaction time, and high yield) but also because it presents an easy access to halofumarate-based MOFs for which linkers as acids are otherwise very expensive. As a matter of fact, 50 mg (!) of 2-chlorofumaric acid presently cost 144 €, compared to 25 g H_2ADC for 210 € at Sigma-Aldrich, while 2-bromofumaric acid and 2-iodofumaric acid do not appear to be commercially available.

Scheme 1. Reaction of Acetylenedicarboxylic Acid to Halofumarate-Based UiO-Type MOFs HHU-2-Cl, HHU-2-Br, and HHU-2-I by in Situ Hydrohalogenation

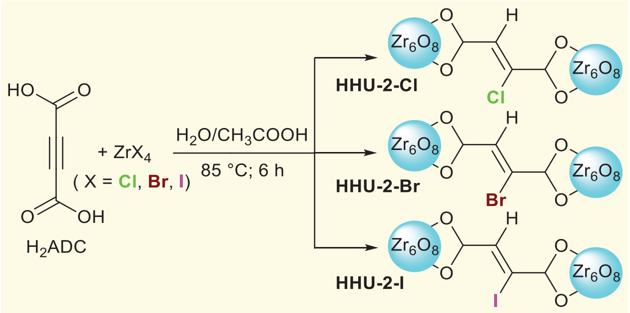

Zr-fumarate, which is named MOF-801, crystallizes in an **fcu** net topology, consisting of octahedral $[Zr_6O_4(OH)_4]$ secondary building units (SBUs) each connected by 12 fumarate linkers to yield a three-dimensional framework with octahedral cages of 7.4 Å diameter and two slightly differently sized tetrahedral cages with pore diameters 4.8 and 5.6 Å, respectively [Figure S1 in the Supporting Information (SI)].[32] This material features high chemical and thermal stability like the parent UiO-66 and was studied for its potential application in water harvesting from air and adsorption cooling.[33,34] To date, only two functionalized versions of MOF-801 have been reported, namely, zirconium mesaconate, which has a methyl-substituted fumarate linker,[35] and our Zr-chlorofumarate, which was named HHU-2.[30] Functionalizing the fumarate linker with polar and not very sterically hindering groups such as halogens should be of great interest in tuning or enhancing the properties of the underlying Zr-fumarate (MOF-801) material. This hydrohalogenation of H_2ADC (Scheme 1) also provides a basis to investigate the effect of halogen functionality on the hydrophilicity of MOFs and their gas adsorption capacity and selectivity. So far, there have been limited studies to demonstrate that aryl or aliphatic halogen groups provide any enhancement of low-pressure gas/vapor uptake and/or affinity.[22]

We herein report the synthesis of three novel halo- (i.e., chloro-, bromo-, and iodo-)functionalized Zr-fumarates, that is, halo-functionalized MOF-801, having chlorofumarate, bromofumarate, and iodofumarate as linkers, following our recent communication of the in situ formed Zr-chlorofumarate, HHU-2. Their thorough characterization and possible applications in water-sorption-based thermal batteries, gas (SO_2, CH_4, CO_2, and N_2) storage and separation are investigated, as well as the mechanism of the in situ functionalization leading to these halogenated materials.

■ EXPERIMENTAL SECTION

Materials and Methods. Zirconium chloride ($ZrCl_4$, purity 99%), zirconium bromide ($ZrBr_4$, purity 99%), and acetylenedicarboxylic acid (H_2ADC, purity 97%) were obtained from Alfa Aesar. Zirconium iodide (ZrI_4, purity 99.99%) was obtained from Sigma-Aldrich, acetic acid (purity 100%) from VWR Chemicals, and methanol (analytical reagent grade) from Fisher Chemical. All chemicals were used without further purification.

Infrared (IR) spectra were obtained on a Bruker FT-IR Tensor 37 spectrometer in the 4000−550 cm^{-1} region with 2 cm^{-1} resolution as KBr disks.

Raman spectra were obtained on a Bruker MultiRAM-FT Raman spectrometer equipped with a Nd:YAG laser (wavelength 1064 nm). All Raman spectra were measured in the solid state for 2500 scans with a laser power between 10 and 20 mW.

Powder X-ray diffraction (PXRD) data were collected on a Bruker D2 Phaser diffractometer using Cu $K\alpha_1/\alpha_2$ radiation with $\lambda = 1.5418$ Å at 30 kV covering 2θ angles in the range 5−50° over a time of 1 h, that is, 0.0125° s^{-1}. Diffractograms were obtained on a flat silicon layer sample holder, where the beam spot was strongly broadened at low angles, so that only a fraction of the reflected radiation reached the detector, which led to low relative intensities measured at $2\theta < 7°$.

Thermogravimetric analyses (TGA) were carried out at a ramp rate of 5 °C min^{-1} in N_2 flow with a Netzsch Thermo-Microbalance Apparatus TG 209 F3 Tarsus.

Scanning electron microscopy (SEM) images were obtained using a JEOL JSM-6510LV QSEM advanced electron microscope with a LaB_6 cathode at 5−20 keV. The microscope was equipped with a Bruker Xflash 410 silicon drift detector for energy-dispersive X-ray (EDX) spectroscopy element analysis. The samples for SEM imaging were coated with gold using a JEOL JFC 1200 fine-coater (20 mA for 25 s).

X-ray photoelectron spectroscopy, XPS (ESCA), measurements were performed with a Fisons/VG Scientific ESCALAB 200X XP spectrometer, operating at 70−80 °C, a pressure of 7.0×10^{-9} bar, and a sample angle of 33°. Spectra were recorded using polychromatic Al $K\alpha$ excitation (11 kV, 20 mA) and an emission angle of 0°. Calibration of the XPS was achieved by recording spectra with Al $K\alpha$

X-rays from clean samples of copper, silver, and gold at 50 and 10 eV pass energies and comparison with reference values.

Conventional cross-polarized magic-angle spinning (CP MAS) solid-state NMR measurements were carried out at room temperature on a Bruker AVANCE II+ spectrometer at 400 MHz proton resonance frequency, employing a Bruker 4 mm double resonance probe. ^{13}C CP MAS spectra were recorded utilizing ramped CP MAS sequences at a spinning rate of 8 kHz. Contact time was set to 1.5 ms and two-pulse phase-modulated (tppm) decoupling with a 15° phase jump was applied during data acquisition.[36] ^{13}C spectra were referenced with respect to tetramethylsilane (TMS). Frequency-switched Lee Goldburg (FSLG) CP MAS heteronuclear correlation (HETCOR) spectra were recorded at 8 kHz and contact times of 500 μs and 1500 μs. The tppm decoupling sequence with a 15° phase jump was applied during data acquisition. ^{1}H spectra were recorded utilizing FSLG homonuclear decoupling, applying the same LG field strength and step width as those for the FSLG-HETCOR spectra. ^{1}H shift values of the direct dimension of these spectra were utilized to reference the indirect dimensions of the FSLG-HETCOR spectra. The direct dimensions of the ^{1}H spectra were referenced with respect to TMS. Solution ^{1}H, ^{13}C, heteronuclear single quantum coherence, and heteronuclear multiple bond correlation spectra were measured with a Bruker Avance III-300 at 300 MHz frequency. Prior to solution NMR analysis, an activated sample of HHU-2-X and zirconium fumarate MOF was digested as follows: 15 mg of MOF and 10 mg of cesium fluoride were suspended in dimethyl sulfoxide-d_6 (0.65 mL). Five drops of aqueous DCl (35 wt % in D_2O) were added. As soon as the light yellow/white solid of MOF had dissolved (after 15−30 min), 12 mg K_2CO_3 was added to neutralize the acid.[37]

Water vapor sorption isotherms were measured at 20 °C on a VSTAR vapor sorption analyzer from Quantachrome. An accurately weighed amount (about 25 mg) of the activated sample was introduced into the measuring cell and connected to the analysis port of the analyzer. Gravimetric water vapor sorption isotherms were measured using a Projekt Messtechnik SPS11 gravimetric vapor sorption analyzer. The weight of the dried powder (≈150 mg) was constantly monitored with a high-resolution microbalance (±0.1 μg) under pure water vapor pressures. The kinetic curve was obtained by measuring the real-time mass change at a fixed relative humidity (RH) of 30% at 25 °C.

For gas sorption studies, nitrogen, carbon dioxide (CO_2), and sulfur dioxide isotherms were measured on a Quantachrome Autosorb iQ MP at 77 K (N_2) and 293 K (N_2, CO_2, SO_2), respectively. The temperature of 77 K was set by a liquid nitrogen bath, whereas 293 K was set by a temperature-controlled water bath. The specific surface area was calculated from the nitrogen sorption isotherms using the Brunauer−Emmett−Teller (BET) equation. Nonlinear density functional theory (NLDFT) calculations for pore size distributions were done with the NovaWin 11.03 software using the "N_2 at 77 K on carbon, slit pore, NLDFT equilibrium" model. Methane (CH_4) isotherms were measured at 293 K using a Micromeritics ASAP 2020 automatic gas sorption analyzer equipped with oil-free vacuum pumps (ultimate vacuum $<10^{-8}$ mbar) and valves, which guaranteed contamination-free measurements. The sample was connected to the preparation port of the sorption analyzer and degassed under vacuum until the outgassing rate, i.e., the rate of pressure rise in the temporarily closed manifold with the connected sample tube, was less than 2 μTorr min^{-1} at the specified temperature of 120 °C. After weighing, the sample tube was then transferred to the analysis port of the sorption analyzer. All gases for the sorption measurements were of ultrapure grades (99.999%, 5.0).

For safety precautions of toxic SO_2, a Dräger Pac 6000 SO_2 detector (1−100 ppm) was used in close range to the sorption device. The exhaust of the Quantachrome sorption instrument was directed to a hood for safe removal of desorbed gases.

Synthesis Procedure. All three HHU-2-X compounds (X = Br, Cl, I) were obtained following the same acetic acid modulated synthesis. Typically, 1 mmol $ZrCl_4$ (233 mg), $ZrBr_4$ (411 mg), or 0.5 mmol ZrI_4 (300 mg) was dissolved in a solvent mixture containing 2.5 mL of water and 2.5 mL of acetic acid. Then, 1 or 2 mmol (114 or 228 mg) of acetylenedicarboxylic acid was added to the solution. The resulting clear mixture was introduced into a 10 mL screw-capped Duran glass vial and stored for 6 h in an oven preheated at 85 °C. After cooling to room temperature, the precipitate was separated from the mother liquor by centrifugation, and re-dispersed in and centrifuged from distilled water (3 × 10 mL) and methanol (3 × 10 mL). Afterward, the product was dried in air. Yield: 243 mg (86%) for HHU-2-Cl; 296 mg (94%) for HHU-2-Br; and 121 mg (76%) for HHU-2-I based on the zirconium salt.

The washed and dried as-synthesized samples were heated for 6 h at 120 °C under dynamic vacuum (10^{-4} mbar) to yield activated samples, prior to various further characterizations.

■ RESULTS AND DISCUSSION

Synthesis and Characterizations. The reaction of acetylenedicarboxylic acid with zirconium chloride ($ZrCl_4$) in water at 85 °C in the presence of acetic acid unexpectedly yielded, within 1 h, the new MOF HHU-2 of the ideal formula, $[Zr_6(\mu_3\text{-O})_4(\mu_3\text{-OH})_4(\text{Fum-Cl})_6]\cdot$solv (Fum = fumarate/*trans*-1,2-ethylenedicarboxylate).[30] For differentiation, HHU-2 is named HHU-2-Cl, as the reaction was repeated using zirconium bromide and iodide as the metal source, yielding the new MOFs, HHU-2-Br and HHU-2-I, respectively, of ideal formulae $[Zr_6(\mu_3\text{-O})_4(\mu_3\text{-OH})_4(\text{Fum-X})_6]\cdot$solv (X = Br, I) (Scheme 1) (HHU stands for Heinrich-Heine-University Düsseldorf). Although a rapid formation of products was observed, the reaction was allowed to continue for 6 h to ensure maximum yield. Reaction yields reached up to 94% yield based on the zirconium salt. It should be noted that the synthesis was carried out only in water and did not require dimethylformamide or organic solvents.

The transformation of the initial ADC linker into a halofumarate was first discerned by Raman spectroscopy analysis. The −C≡C− triple bond in alkyne-containing molecules, such as acetylenedicarboxylic acid, displays in Raman spectroscopy a characteristic very strong stretching band at about 2230 cm^{-1}.[38] In the diagnostic Raman spectra (Figure 1), complete disappearance of the −C≡C− stretching band at 2225 cm^{-1} was observed. This observation suggested an addition reaction to the acetylenedicarboxylic acid triple bond, giving a new double-bond-containing linker. The bands at 681, 744, and 672 cm^{-1} in the infrared spectra (Figure S6 in SI) are attributable to the C−Cl, C−Br, and C−I stretching vibrations in HHU-2-Cl, HHU-2-Br, and HHU-2-I, respectively.[39,40]

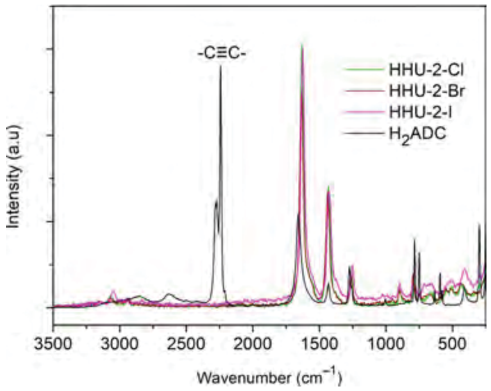

Figure 1. Raman spectra of HHU-2-Cl, HHU-2-Br, and HHU-2-I in comparison to acetylenedicarboxylic acid. The band at 2225 cm^{-1} has disappeared in the spectra of HHU-2-X.

Solid-state (^1H and ^{13}C) NMR (ssNMR) spectroscopy analysis was conducted to further investigate the nature of the linkers in the new HHU-2-X materials.[41−43] For HHU-2-Cl, using $ZrOCl_2$ as the metal salt[30] and again with $ZrCl_4$, the $^1H-^{13}C$ FSLG-HETCOR spectrum (Figures 2 and S7) unambiguously elucidated the linker as a substituted chlorofumarate.[30]The ssNMR spectra showed additional signals attributable to the coordinated acetate modulator and methanol used as the exchange solvent (Figure 2), as the analysis was conducted on a nonactivated sample. Solid-state and liquid NMR analyses of HHU-2-Br and HHU-2-I also clearly identify a monosubstituted fumarate as the linker (see details in the SI).

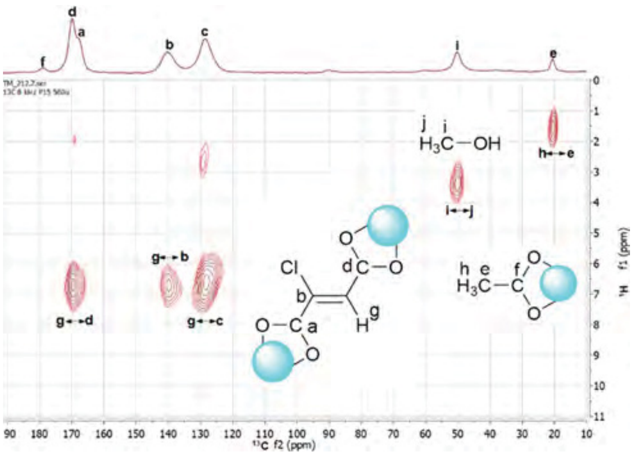

Figure 2. $^1H-^{13}C$ FSLG-HETCOR CP MAS of HHU-2-Cl at 8 kHz spinning speed and 500 μs contact time.

To prove hydrohalogenation (addition of HBr, HCl, and HI, respectively, and thereby exclude addition of H_2O), X-ray photoelectron spectroscopy (XPS) was conducted on all materials. The presence of organic chlorine in HHU-2-Cl was shown through the Cl 2p peak at 201.65 eV binding energy (Figure S14 in the SI). The presence of bromine in HHU-2-Br was shown through Br 3d peaks at 70.61 ($3d_{5/2}$) and 71.66 ($3d_{3/2}$) eV binding energies (Figure S17), and the presence of organic iodine in HHU-2-I was shown through the couple of I 3d peaks at 621.67 ($3d_{3/2}$) and 632.95 ($3d_{5/2}$) eV binding energies (Figure S21). All of these values are indicative of C−X bound organic chlorine, bromine, and iodine in HHU-2-Cl, HHU-2-Br, and HHU-2-I, respectively. The signal of free halide ions would occur at 198 eV for Cl^-, at 68.4 and 68.9 eV for Br^-, and at 618.6 and 630.1 eV for I^-.[44−46]

Scanning electron microscopy (SEM) with energy-dispersive X-ray (EDX) spectroscopy elemental mapping (Figures 3, S25, and S28) confirms the even distribution of Cl, Br, I, and Zr across the entire samples of HHU-2-Cl, HHU-2-Br, and HHU-2-I, respectively. The presence of a proton bonded to the C═C double bond in the ^1H NMR analysis also excludes a dihalogenation reaction of the alkyne triple bond.

The mechanism of HHU-2-X formation most likely consists of zirconium halogenide (ZrX_4; X = Cl, Br, I) reacting with acetic acid and water to produce hydrogen halogenide HX. Afterward, a trans hydrohalogenation (addition of produced HX) of the −C≡C− bond takes place with acetylenedicarboxylic acid to give halofumaric acid, followed by formation of the new MOF through acetate-to-halofumarate ligand exchange (see details and Scheme S1 in the Supporting Information).

The thermal stability of HHU-2-X was assessed by thermogravimetric analysis under a nitrogen atmosphere. TGA traces (Figures S37−S39 in the SI) indicate that HHU-2-Cl and HHU-2-Br are thermally stable till about 300 °C, slightly less than MOF-801 (400 °C), unlike HHU-2-I, which is stable only till about 180 °C.

Structural Description and Defect Elucidation of HHU-2-X. All three HHU-2-X (X = Br, Cl, I) materials were obtained as highly microcrystalline powders. The PXRD patterns of the three materials are similar to each other and resemble that of unsubstituted MOF-801 (Figure 4), indicating that they are isostructural with this UiO-type metal-organic framework.

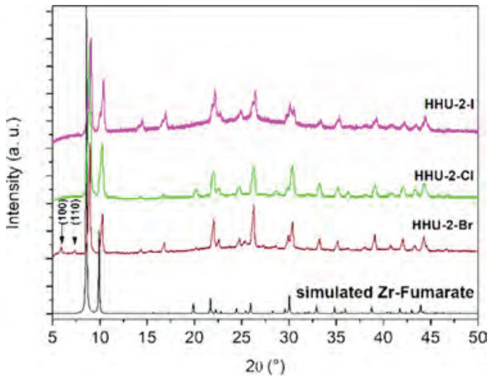

Figure 4. PXRD patterns of HHU-2-X (X = Br, Cl, I) in comparison with the MOF-801 simulated pattern from deposited cif-file under CCDC 1002676. The sample for HHU-2-Br was obtained from a 1:1 H_2ADC-to-Zr-salt molar ratio, and the other two samples were obtained from a 2:1 ratio (see text for explanation). See Figure S30 for PXRDs of other respective ratios.

Similar to MOF-801, the HHU-2-X structures consist of octahedral $[Zr_6O_4(OH)_4]^{12+}$ secondary building units (SBUs) each 12-fold connected by chlorofumarate (HHU-2-Cl), bromofumarate (HHU-2-Br), or iodofumarate (HHU-2-I)

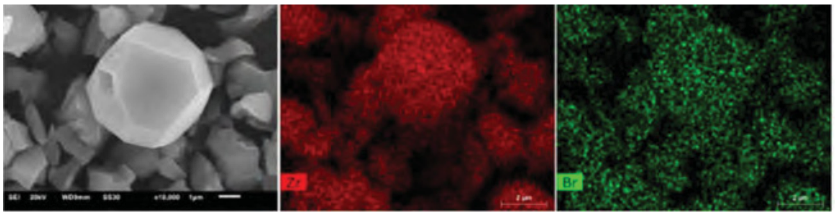

Figure 3. SEM image of microcrystals with Zr- and Br-EDX elemental maps for HHU-2-Br, showing uniform and concomitant distribution of Zr (red) and Br (green) over the entire sample.

linkers into a three-dimensional porous framework with an **fcu** net topology (Figure 5).

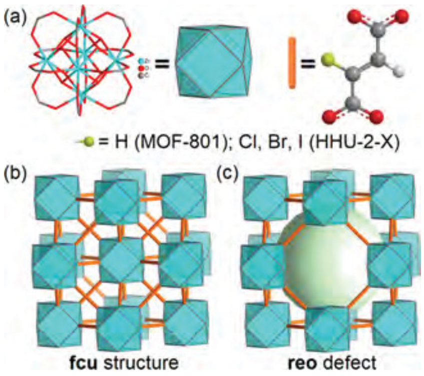

Figure 5. Structure depiction of HHU-2-X and MOF-801. (a) $Zr_6O_4(OH)_4$ cluster as polyhedra and connecting linkers as rod yield (b) an **fcu** topology network and eventually (c) defective missing cluster regions with a **reo** topology.

It is worth noting that the H_2ADC-to-Zr-salt molar ratio in the synthesis mixture was found to have an impact on the PXRD pattern of the obtained materials. When the molar ratio was 1:1, two less intense diffuse reflections appeared at 5.9 and 7.3° 2θ angles (see the example for HHU-2-Br in Figure 4). These reflections do not appear in the PXRD patterns of materials obtained from a 2:1 ratio, that is, with excess linker (HHU-2-Cl and -I in Figure 4; HHU-2-Br in Figure S32a in the SI).

Similar diffuse forbidden reflections in the PXRD pattern have already been reported for UiO-66 (Hf, Zr) but not yet for any fumarate-based Zr-MOF.[47,48] These reflections, which are forbidden for the face-centered cubic **fcu** structure, reveal the presence of correlated defect nanoregions with a **reo** topology (Figure 5c). These defects were associated with missing linkers and clusters in the MOF structure. Variation in the H_2ADC-to-Zr-salt molar ratio can thus be exploited to induce correlated defect nanoregions in HHU-2-X MOFs. Cluster defects in these materials could have an effect on the material properties and serve as a basis for postsynthetic modification.[49] However, even samples not containing cluster-defective nanodomains do contain some missing linker defect sites. This is substantiated by the occurrence of the acetate modulator in HHU-2-X, as revealed by ssNMR analyses. The amount of linker defects can be calculated from the acetate-to-linker ratio using the signal integration in the solution ^1H NMR spectra (see the SI for details) to be 0.7, 0.9, and 1.4 missing linkers per $\{Zr_6\}$-cluster for HHU-2-Cl, HHU-2-Br, and HHU-2-I, respectively. This means that for HHU-2-Cl, for example, there are $(6 - 0.7) = 5.3$ linkers in its average formula unit and only $(5.3 \times 2) = 10.6$ linkers coordinated to its average $\{Zr_6\}$-cluster. Zirconium-based MOFs are known to tolerate such a range of defect amounts without compromising their stabilities.[50]

Porosity and Water Sorption Properties. *Nitrogen Sorption.* Experiments at 77 K (Figure S30) yield a composition of reversible type I isotherms in the low partial pressure region and type II or type III for high relative pressure for the three materials,[51] establishing their permanent microporosity. The Brunauer–Emmett–Teller (BET) surface areas were calculated to be 852, 620, and 327 $m^2\ g^{-1}$ for HHU-2-Cl, HHU-2-Br, and HHU-2-I, respectively. The total pore volumes were calculated to be 0.41, 0.31, and 0.18 $cm^3\ g^{-1}$ (Table 1). The reversible increasing uptake at high P/P_0 as in a type II or type III isotherm is traced to monolayer–multilayer adsorption in the interparticle macropores. BET surface areas and pore volumes of HHU-2-X are lower than those of MOF-801 ($S_{BET} = 939\ m^2\ g^{-1}$, $V_{pore} = 0.43\ cm^3\ g^{-1}$, Table 1, see Figure S3 in SI). This is in accordance with the introduction of halogen functions at the pore surface, thereby reducing both the surface area and the pore volume compared to MOF-801. The order of reduction of surface area and pore volume of the new MOFs relative to MOF-801 follows the trend of increasing atomic size of the grafted halogen atoms (atomic radius in nanometers: $r_{Cl} = 0.099 < r_{Br} = 0.111 < r_I = 0.128$).

Interestingly, there is an inversion in the relative N_2 capacities of HHU-2-Cl and MOF-801 at 77 and 293 K, respectively (Table 2). At 77 K, HHU-2-Cl has a lower N_2 uptake (11.87 mmol g^{-1}) compared to MOF-801 (13.20 mmol g^{-1}), whereas this trend is reversed at 293 K. This shows that at a temperature of 77 K, the physisorption of nitrogen on these MOF surfaces is the dominating process, yielding adsorption capacities, which reflect the surface area and porosity. At a high temperature, the adsorption capacity is directed instead by the chemical affinity of materials with nitrogen molecules, in which the quadrupole moment of N_2 may play a role. Hence, HHU-2-Cl with its polar inner surface will have a higher nitrogen affinity and uptake than nonfunctionalized MOF-801.

Water Uptake. With respect to the previous communication on the water sorption of HHU-2-Cl,[30] we have not only measured the water sorption profiles for HHU-2-Br and HHU-2-I here, but added for HHU-2-Cl, the water adsorption energetics and kinetics, as well as the multicycle adsorption–desorption stability. It is expected that the presence of polar halogen functions on the inner surface of the HHU-2 MOFs should result in increased hydrophilicity relative to MOF-801. To investigate this, water vapor sorption experiments were carried out at 20 °C. All three MOFs display a water sorption isotherm close to type Ib and two uptake steps at low P/P_0 until 0.2 (Figure 6).

The exceptional high hydrophilicity in the order HHU-2-Cl > -Br > -I is disclosed by an early and steep water uptake in the low relative pressure range, $0 < P/P_0 < 0.1$. The isotherms

Table 1. Summary of Surface Area, Porosity Characteristics, and Water Capacities of HHU-2-X and MOF-801

materials	BET surface area,[a] $m^2\ g^{-1}$	total pore volume,[b] $cm^3\ g^{-1}$	micropore volume,[c] $cm^3\ g^{-1}$	water uptake,[d] mg g^{-1}
HHU-2-Cl	852	0.41	0.275	267
HHU-2-Br	620	0.31	0.19	236
HHU-2-I	327	0.18	0.10	173
MOF-801	939	0.43	0.30	339

[a] Obtained from seven adsorption points in the pressure range $P/P_0 = 0.001–0.05$. [b] Derived at $P/P_0 = 0.9$ for pores smaller than 20 nm. [c] Volume that originates only from micropores, obtained by the $V–t$ method with thickness method "DeBoer". [d] Uptake at $P/P_0 = 0.9$.

DOI: 10.1021/acs.chemmater.9b00524
Chem. Mater. 2019, 31, 8629–8638

Table 2. Summary of Gas Sorption Capacities of HHU-2-X and MOF-801 at 293 K and 1 bar

materials	CO_2 ($cm^3\ g^{-1}$, mmol g^{-1}, wt %)[a]	N_2 ($cm^3\ g^{-1}$, mmol g^{-1}, wt %)[a]	SO_2 ($cm^3\ g^{-1}$, mmol g^{-1}, wt %)[a]	CH_4 ($cm^3\ g^{-1}$, mmol g^{-1}, wt %)[a]
HHU-2-Cl	79.95	8.28	236.19	16.08
	3.28	0.34	9.69	0.66
	12.61	0.94	38.28	1.04
HHU-2-Br	44.60	1.95	147.95	10.72
	1.83	0.08	6.07	0.44
	7.45	0.22	28.00	0.70
MOF-801	55.57	3.16	195	12.91
	2.28	0.13	8.00	0.53
	9.11	0.36	33.88	0.84

[a] The three units from left to right refer to the given values from top to bottom.

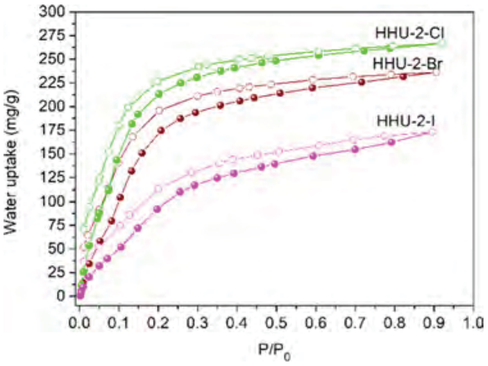

Figure 6. Water vapor ad- and desorption isotherms of HHU-2-Cl, HHU-2-Br, and HHU-2-I at 20 °C (filled symbols adsorption, empty symbols desorption).

reach their plateaus between 0.1 and 0.3 relative humidity, and the water capacities of HHU-2-X at $P/P_0 = 0.9$ are 267, 236, and 173 mg g^{-1} for HHU-2-Cl, HHU-2-Br, and HHU-2-I, respectively (Table 1).

The hydrophilicity of HHU-2-X is higher than that of nonfunctionalized MOF-801 with its S-shaped isotherm (see Figure S36 in the SI), as the start of the water uptake is shifted from 0.1 relative pressure in MOF-801 to near 0 in HHU-2-X. Comparatively, the lower hydrophilicity when going from C−Cl to C−I (HHU-2-Cl > HHU-2-Br > HHU-2-I) is revealed by a shift of the saturation point to higher humidity (Figure S35 in the SI). Conversely, with increasing electronegativity (polarity) of the halogen atoms, there is an increasing water−adsorbent interaction, and hence, an increasing uptake at lower relative pressure. The introduction of halogen atoms on the pore surface of MOFs is a means of adjusting the hydrophilicity. It is worth noting that the increase of hydrophilicity by halogen does not result in water isotherms with irreversible and incomplete desorption branches, as is observed for MOFs bearing hydrophilic −OH groups. Although the desorption loop does not fully close at low partial pressure, which is an indication that part of the water is retained by stronger hydrogen bonding, the water can, however, be fully removed by evacuation for 1 h at 100 °C under vacuum, with the activated sample then showing again the full water uptake capacity (Figure S41, SI).

In particular, the water uptakes for HHU-2-Cl and HHU-2-Br of 10.7 and 8.4 mmol g^{-1}, respectively, at relative humidity as low as 15% make these materials good candidates for dehumidification applications at an already low water vapor concentration.[52] An application-oriented example for such dehumidification would be the dehydration of natural gas.[53,54] For this, the material should have, at the same time, a low methane adsorption capacity, which would be the case for HHU-2-X (Figure S44 in the SI and Table 2).

Water sorption can be the basis for thermal batteries. The power to operate on-board air-conditioning systems is significant in both gasoline and electrically driven vehicles. Conventional compressor air conditioners substantially reduce the driving range of electric vehicles (EVs) and increase the fuel consumption and greenhouse gas emissions in gasoline vehicles. Research efforts are being made to develop more efficient methods for on-board air conditioning.[55,56]

Adsorption-based thermal batteries (ATBs) were recently introduced as an alternative to traditional air conditioners, for delivering both heating and cooling in vehicles. The advantage of ATBs is that they use for operation primary thermal energy sources, such as thermal solar energy or the excess heat released from engines. Their principle is based on cyclic water adsorption/desorption on and from a porous material, upon exchange of heat between a cold source and a hot source without use of electricity or fossil fuel (Figure 7). It is, therefore, evident that the efficiency of the thermal battery will fundamentally depend on the performance of the applied adsorbent material.[57] Most importantly, the adsorbent material should achieve a high water uptake at a low relative pressure ($P/P_0 = 0.1$) to reduce the need to incorporate a compressor in the system. Also, the adsorption of water on the material should release a large amount of heat to achieve high heat storage capacity (C_{HS}). The hydrothermal and multicyclic ad-/desorption stability of the applied adsorbent should be ensured as well.

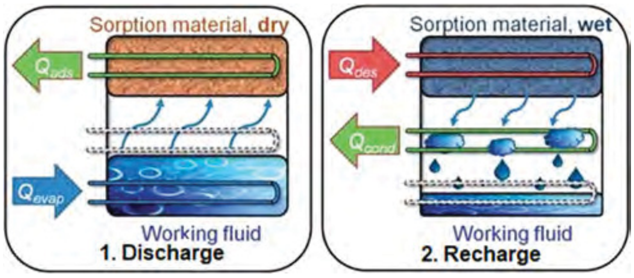

Figure 7. Working principle of an adsorption-based thermal battery. The thermal battery is charged with a temperature difference, just like an electric battery is charged with a voltage difference.

The early water uptake of HHU-2-Cl with a working capacity of 0.15 g g^{-1} at $P/P_0 = 0.1$ prompted us to evaluate this material for thermal battery applications. To assess the hydrolytic stability of HHU-2-Cl upon cyclic water sorption, the ad-/desorption experiment was carried out over five consecutive cycles, showing no loss of water adsorption capacity or crystallinity (see Figure S38 and S41 in the SI). The cycle conditions consisted of adsorption at 25 °C and desorption at 100 °C under vacuum. These conditions correspond to a vacuum tight system and regeneration temperature of 100 °C. The heat of water adsorption (ΔH_{ads}) for HHU-2-Cl was calculated by applying the Clausius−Clapeyron equation (eq S3 in the SI) using the water sorption isotherms obtained at 20, 30, and 40 °C, respectively (Figure S42).

The plot of isosteric heat of water adsorption with increasing water loading is shown in Figure 8a. For uptakes between 25 and 180 mg g^{-1}, the heat of adsorption is at about 60 kJ mol^{-1}, which is well above the latent heat of vaporization of water (40.7 kJ mol^{-1}). This value and the plot profile are comparable with the isosteric heat of water adsorption of MOF-801 within the same uptake range, where also the heat of adsorption increases notably during pore filling (Figures S46 and S47, SI).[58] This behavior has apparently not yet been addressed and clarified in the literature. We suggest that it might be due to the rearrangement to stable water clusters at higher pore filling.

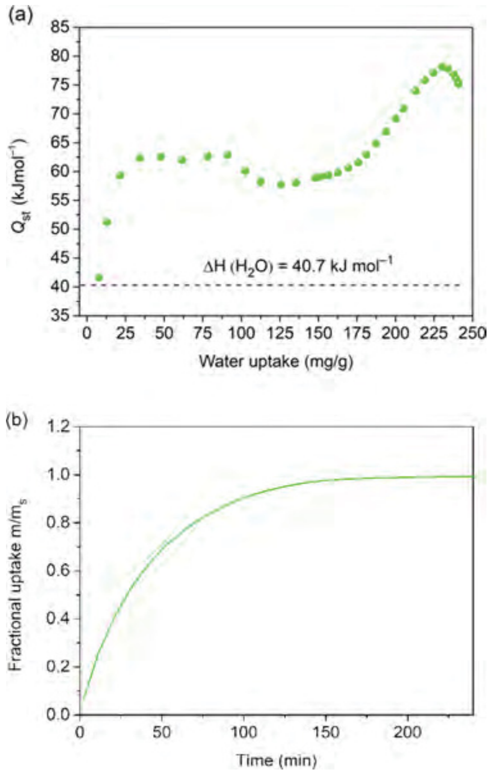

Figure 8. (a) Plot of isosteric heat of adsorption and (b) kinetic curve of water adsorption at 25 °C and 30% RH for HHU-2-Cl.

Kinetics of Water Adsorption. The kinetics of water adsorption on the porous material is also a figure of importance when it comes to assess the influence of the applied adsorbent performance on the heat exchanger efficiency. The water adsorption experiment was conducted gravimetrically to investigate the kinetics of water adsorption in HHU-2-Cl. Figure 8b shows the plot of the fractional water uptake (ratio of the mass, *m*, of water adsorbed at time *t* by the mass, m_s, at saturation) with time. The material reaches the saturation equilibrium in less than 150 min at 25 °C and 30% relative humidity, which indicates a fast kinetics when compared to some other adsorbents such as aluminum fumarate, CAU-10, and MIL-101 (all >340 min) under the same conditions.[59] The kinetics of water adsorption on HHU-2-Cl is consistent with the Fickian diffusion model. The diffusion constant k_D was calculated to be 2.80×10^{-5} and 4.22×10^{-5} s^{-1} for short- and long-time adsorption, respectively (see method and calculation details in the SI). The corresponding diffusivity, *D*, using the average particle radius, R_p, of 5.5 μm is 1.27×10^{-11} and 8.43×10^{-12} cm^2 s^{-1}.

Heat Storage Capacity. In view of their use for climate control in electric vehicles (EVs) and hybrid electric vehicles, the American Department of Energy (DOE) had set the minimum heat storage capacity for ATBs to be 2.5 kWh as the target and maximum weight of the heat exchanger system to be 35 kg.[60]

The heat storage capacity (C_{HS}) for HHU-2-Cl was calculated to be 500 kJ kg^{-1} (0.133 kWh kg^{-1}) at a relative pressure $P/P_0 = 0.1$ (calculation details in the SI). This means that 18 kg of HHU-2-Cl (out of 35 kg required for the system by the DOE) could achieve the targeted minimum heat storage capacity of 2.5 kWh, set by the American Department of Energy (DOE) for thermal batteries.[60] This makes HHU-2-Cl a promising material applicable in adsorption-based thermal batteries.

SO_2 and CO_2 Adsorption. The presence of polar groups in HHU-2-X pores should also affect their gas sorption capacity and/or selectivity. While functionalization of MOFs with polar groups would rationally be expected to enhance gas affinity of the framework, this does not always apply to gas uptake capacities. The pore occupancy by functional groups usually results in reduced porosity, surface area, and gas uptake capacities. It is even more challenging for MOFs having quite small pores, such as MOF-801, for which enhancement of gas adsorption capacities through halogen functionalization may not have been readily anticipated.[61−63] To investigate the effect of halogen functionalities on the gas adsorption properties of the new materials, SO_2, CO_2, and N_2 sorption capacities of HHU-2-X (X = Cl, Br) were compared to those of MOF-801 at 293 K. The isotherms obtained for both materials are shown in Figures 9 and S45 (in the SI). SO_2 sorption of HHU-2-X and MOF-801 displays type I isotherms, with a noticeable large hysteresis loop between the SO_2 adsorption and desorption branches in the case of HHU-2-Cl and HHU-2-Br. Meanwhile, nitrogen sorption of the three MOFs shows

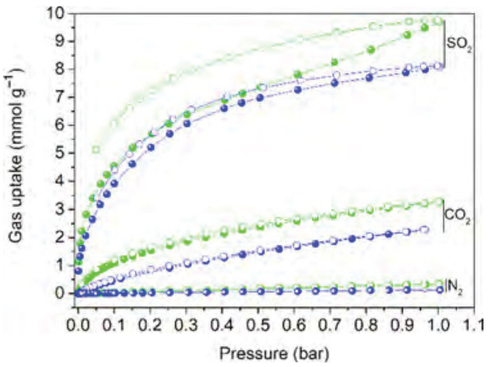

Figure 9. CO_2, N_2, and SO_2 sorption isotherms of HHU-2-Cl (green symbols) and MOF-801 (blue symbols) at 293 K (see Figure S43 in the SI for the respective isotherms of HHU-2-Br).

the expected very low uptake. Gas adsorption capacities of HHU-2-X and MOF-801 at 293 K and 1 bar are summarized in Table 2. Noteworthy is that HHU-2-Cl features higher SO_2, CH_4, CO_2, and N_2 capacities compared to the parent MOF-801 in spite of its quite lower surface area. This interesting increase of about 21% (SO_2), 24% (CH_4), 44% (CO_2), and 154% (N_2) in gas uptake is attributable to the presence of the polar chloro-functionality in the HHU-2-Cl pores. The large hysteresis loop observed in the SO_2 sorption isotherm of HHU-2-Cl unlike MOF-801, further indicates a strong SO_2−MOF interaction. This behavior is consistent with the increase in hydrophilicity earlier observed in the water adsorption profile. A PXRD measurement after SO_2 sorption of HHU-2-Cl verified the unchanged crystalline nature of the MOF, ruling out any noticeable decomposition. The nitrogen sorption experiment at 77 K confirms the pore accessibility of the materials post-SO_2-exposure, although with a slight decrease in surface area (see Figure S31 and Table S7 in the SI).

When normalized to the surface area, gas adsorption capacities of HHU-2-Br (CO_2: 3.0 μmol m^{-2}, SO_2: 9.8 μmol m^{-2}, and CH_4: 0.7 μmol m^{-2}) are also higher than those of MOF-801 (CO_2: 2.4 μmol m^{-2}, SO_2: 8.5 μmol m^{-2}, and CH_4: 0.5 μmol m^{-2}). These results strongly indicate that the presence of halogen functionalities considerably enhances both gas affinity and uptakes in metal-organic frameworks under practically applicable conditions.

The calculation of linker defects (see the SI for details) reveals that MOF-801 also contains missing linker defects (1.2 linker defects per $\{Zr_6\}$-cluster in the unit formula) like HHU-2-Cl (0.7 linker defects). The difference reported above for HHU-2-Cl and MOF-801 for water and gas adsorption affinities and capacities is, therefore, not due to the linker defects in HHU-2-Cl but due to some other factor, namely, the presence of the chloro-function decorating the surface of HHU-2-Cl, since both materials have the same range of defects. Furthermore, halogen atoms in molecular entities are, on account of their high electronegativity, the basis of inter- and intra-molecular interactions known as halogen bonding.[64]

While CO_2 is considered to be the main greenhouse gas, SO_2 is an acidic gas responsible for environmental pollution leading to acid rain and photochemical smog as well as human respiratory diseases.[65,66] Therefore, removal of these generated toxic gases from flue gas is one of the main challenges in the power and chemical industries. Among several clean-up technologies of flue gases, capturing by advanced adsorbent materials was suggested as a cost- and energy-saving solution.[67]

The CO_2 adsorption capacity of HHU-2-Cl under ambient conditions (293 K and 1 bar) of 3.28 mmol g^{-1} is higher than those of UiO-66 (2.3 mmol g^{-1}) and UiO-66−NH_2 (2.6 mmol g^{-1}) under the same conditions.[68] Thus, with a quite moderate surface area, HHU-2-Cl is among the MOFs of the UiO-type family with the highest (maybe it has the highest) CO_2 uptake capacity at 293 K and 1 bar (Table S9, SI).

The SO_2 uptake capacity of 9.7 mmol g^{-1} for HHU-2-Cl is among the highest reported at 293 K and 1 bar.[69] With a quite moderate surface area, HHU-2-Cl is already counted among the MOFs with the highest SO_2 uptake capacity per weight. Noteworthily, HHU-2-Cl has the highest SO_2 uptake capacity per surface area, even ahead of MOFs reported as having record uptakes per weight at 293 K and 1 bar (Table S10, SI). Both HHU-2-Cl and MOF-801 show a high gas adsorption capacity for molecules with larger quadrupole moment and polarizability, CO_2 vs N_2 (CO_2: 43.0×10^{-27} esu^{-1} cm^{-1} and 29.1×10^{-25} cm^{-3}; N_2: 15.2×10^{-27} esu^{-1} cm^{-1} and 17.4×10^{-25} cm^{-3}),[70] and even more for dipolar molecules (SO_2). This is clearly due to the presence of μ_3-O and μ_3-OH groups on Zr-oxoclusters, inducing gas affinity by μ_3-O···C(S)=O and O−C(S)=O···H−O− interactions. These interactions are visibly reinforced by −Cl···C(S)=O interactions in HHU-2-Cl. In comparison to SO_2 and CO_2 uptakes, HHU-2-Cl and MOF-801 adsorb only a small amount of N_2 at 293 K and 1 bar. This indicates selective SO_2 and CO_2 adsorption over N_2 and, therefore, the potential of HHU-2-Cl and MOF-801 for selective capture and storage of these harmful gases. Although HHU-2-Br displays lower gas adsorption capacities as compared to HHU-2-Cl and MOF-801, it still features higher SO_2/N_2 and CO_2/N_2 selectivity than MOF-801.

■ CONCLUSIONS

We have established the in situ hydrohalogenation of acetylenedicarboxylic acid in water as a time-, cost-effective, and sustainable approach to introduce chloro-, bromo-, and iodo-functionalities in MOF pores. This approach was clearly illustrated by the production of the three chloro-, bromo-, and iodo-MOFs, HHU-2-Cl, -Br, and -I, respectively, as functionalized derivatives of zirconium fumarate (MOF-801). The inclusion of halogen functionalities in MOF pores was found to have significant beneficial consequences on the comparative sorption properties. The water sorption profiles of the new HHU-2 materials are close to a type I isotherm and give a heat storage capacity of 500 kJ kg^{-1} at 0.1 relative humidity (in the case of zirconium chlorofumarate), indicating the applicability of these materials in dehumidification/desiccation and thermal batteries. A remarkable increase was also noticed in the CH_4, CO_2, N_2, and SO_2 adsorption capacities of HHU-2-Cl over MOF-801 under ambient conditions, indicating suitability of the chlorinated material for noxious gas capture from flue gas. Concerning gas uptake, this work also demonstrates that one does not always need MOFs with very large, sophisticated, and expensive linkers to achieve high sorption performance. Short, simple, and relatively inexpensive linkers (such as in situ formed chlorofumarate with an appropriate MOF structure) can yield functionalized ultramicroporous adsorbents, which could perform superior to more porous MOFs regarding both gas adsorption affinity and capacity for various applications. We hence broaden the scope of MOF functionalization and believe that the reported hydrohalogenation approach could be extended by using other alkyne-containing linkers and other metal ions such as aluminum, as well as for fluoro-functionalization.

■ ASSOCIATED CONTENT

Ⓢ Supporting Information

The Supporting Information is available free of charge on the ACS Publications website at DOI: 10.1021/acs.chemmater.9b00524.

> IR, Raman, NMR, XPS, EDX spectra; gas/water sorption isotherms; PXRD patterns of stability tests; TGA, SEM images; EDX maps; functionalization mechanism, heat, and kinetics of water adsorption (PDF)

■ AUTHOR INFORMATION

Corresponding Author

*E-mail: janiak@uni-duesseldorf.de.

ORCID

Gerd Buntkowsky: 0000-0003-1304-9762
Christoph Janiak: 0000-0002-6288-9605

Notes

The authors declare no competing financial interest.

■ ACKNOWLEDGMENTS

We thank the German Academic Exchange Service (DAAD) for funding to T.M.M.N. and the Federal Ministry of Education and Research (BMBF) for project Optimat, grant no. 03SF0492C.

■ REFERENCES

(1) Janiak, C.; Vieth, J. K. MOFs, MILs and More: Concepts, Properties and Applications for Porous Coordination Networks (PCNs). *New J. Chem.* **2010**, *34*, 2366−2388.

(2) Yaghi, O. M.; O'Keeffe, M.; Ockwig, M. W.; Chae, H. K.; Eddaoudi, M.; Kim, K. Reticular Synthesis and the Design of New Materials. *Nature* **2003**, *423*, 705−714.

(3) Lin, Y.; Kong, C.; Zhang, Q.; Chen, L. Metal-Organic Frameworks for Carbon Dioxide Capture and Methane Storage. *Adv. Energy Mater.* **2017**, *7*, No. 1601296.

(4) Suh, M. P.; Park, H. J.; Prasad, T. K.; Lim, D.-W. Hydrogen Storage in Metal−Organic Frameworks. *Chem. Rev.* **2012**, *112*, 782−835.

(5) Sumida, K.; Rogow, D. L.; Mason, J. A.; McDonald, T. M.; Bloch, E. D.; Herm, Z. R.; Bae, T.-H.; Long, J. R. Carbon Dioxide Capture in Metal−Organic Frameworks. *Chem. Rev.* **2012**, *112*, 724−781.

(6) Li, J.-R.; Kuppler, R. J.; Zhou, H.-C. Selective Gas Adsorption and Separation in Metal−Organic Frameworks. *Chem. Soc. Rev.* **2009**, *38*, 1477−1504.

(7) Zhu, L.; Liu, L._X.; Jiang, H.-L.; Sun, L.-B. Metal−Organic Frameworks for Heterogeneous Basic Catalysis. *Chem. Rev.* **2017**, *117*, 8129−8176.

(8) Huang, Y.-B.; Liang, J.; Wang, X.-S.; Cao, R. Multifunctional Metal−Organic Framework Catalysts: Synergistic Catalysis and Tandem Reactions. *Chem. Soc. Rev.* **2017**, *46*, 126−157.

(9) Farrusseng, D.; Aguado, S.; Pinel, C. Metal−Organic Frameworks: Opportunities for Catalysis. *Angew. Chem., Int. Ed.* **2009**, *48*, 7502−7513.

(10) Henninger, S. K.; Habib, H. A.; Janiak, C. MOFs as Adsorbents for Low Temperature Heating and Cooling Applications. *J. Am. Chem. Soc.* **2009**, *131*, 2776−2777.

(11) Jeremias, F.; Fröhlich, D.; Janiak, C.; Henninger, S. K. Water and Methanol Adsorption on MOFs for Cycling Heat Transformation processes. *New J. Chem.* **2014**, *38*, 1846−1852.

(12) Yoon, M.; Suh, K.; Natarajan, S.; Kim, K. Proton Conduction in Metal−Organic Frameworks and Related Modularly Built Porous Solids. *Angew. Chem., Int. Ed.* **2013**, *52*, 2688−2700.

(13) Shimizu, G. K. H.; Taylor, J. M.; Kim, S. Proton Conduction with Metal-Organic Frameworks. *Science* **2013**, *341*, 354−355.

(14) Ramaswamy, P.; Wong, N. E.; Shimizu, G. K. H. MOFs as Proton Conductors − Challenges and Opportunities. *Chem. Soc. Rev.* **2014**, *43*, 5913−5932.

(15) Kalmutzki, M. J.; Diercks, C. S.; Yaghi, O. M. Metal−Organic Frameworks for Water Harvesting from Air. *Adv. Mater.* **2018**, No. 1704304.

(16) Wang, H.; Peng, J.; Li, J. Ligand Functionalization in Metal−Organic Frameworks for Enhanced Carbon Dioxide Adsorption. *Chem. Rec.* **2016**, *16*, 1298−1310.

(17) Zhang, J.; Yao, S.; Liu, S.; Liu, B.; Sun, X.; Zheng, B.; Li, G.; Li, Y.; Huo, Q.; Liu, Y. Enhancement of Gas Sorption and Separation Performance via Ligand Functionalization within Highly Stable Zirconium-Based Metal−Organic Frameworks. *Cryst. Growth Des.* **2017**, *17*, 2131−2139.

(18) Vermoortele, F.; Vandichel, M.; Van de Voorde, B.; Ameloot, R.; Waroquier, M.; Van Speybroeck, V.; De Vos, D. E. Electronic Effects of Linker Substitution on Lewis Acid Catalysis with Metal−Organic Frameworks. *Angew. Chem., Int. Ed.* **2012**, *51*, 4887−4890.

(19) Meek, S. T.; Teich-McGoldrick, S. L.; Perry, J. J., IV; Greathouse, J. A.; Allendorf, M. D. Effects of Polarizability on the Adsorption of Noble Gases at Low Pressures in Monohalogenated Isoreticular Metal−Organic Frameworks. *J. Phys. Chem. C* **2012**, *116*, 19765−19772.

(20) Devic, T.; Salles, F.; Bourrelly, S.; Moulin, B.; Maurin, G.; Horcajada, P.; Serre, C.; Vimont, A.; Lavalley, J.-C.; Leclerc, H.; Clet, G.; Daturi, M.; Llewellyn, P. L.; Filinchuk, Y.; Férey, G. Effect of the Organic Functionalization of Flexible MOFs on the Adsorption of CO_2. *J. Mater. Chem.* **2012**, *22*, 10266−10273.

(21) Hulvey, Z.; Sava, D. A.; Eckert, J.; Cheetham, A. K. Hydrogen Storage in a Highly Interpenetrated and Partially Fluorinated Metal−Organic Framework. *Inorg. Chem.* **2011**, *50*, 403−405.

(22) Das, A.; D'Alessandro, D. M. Tuning the Functional Sites in Metal−Organic Frameworks to Modulate CO_2 Heats of Adsorption. *CrystEngComm* **2015**, *17*, 706−718.

(23) Reinsch, H. "Green" Synthesis of Metal-Organic Frameworks. *Eur. J. Inorg. Chem.* **2016**, 4290−4299.

(24) Marshall, R. J.; Griffin, S. L.; Wilson, C.; Forgan, R. S. Single-Crystal to Single-Crystal Mechanical Contraction of Metal−Organic Frameworks through Stereoselective Postsynthetic Bromination. *J. Am. Chem. Soc.* **2015**, *137*, 9527−9530.

(25) Marshall, R. J.; Griffin, S. L.; Wilson, C.; Forgan, R. S. Stereoselective Halogenation of Integral Unsaturated C−C Bonds in Chemically and Mechanically Robust Zr and Hf MOFs. *Chem. − Eur. J.* **2016**, *22*, 4870−4877.

(26) Meek, S. T.; Perry, J. J., IV; Teich-McGoldrick, S. L.; Greathouse, J. A.; Allendorf, M. D. Complete Series of Monohalogenated Isoreticular Metal_Organic Frameworks: Synthesis and the Importance of Activation Method. *Cryst. Growth Des.* **2011**, *11*, 4309−4312.

(27) Billetter, H.; Pantenburg, I.; Ruschewitz, U. Copper(II) Chlorofumarate Trihydrate. *Acta Crystallogr., Sect. E: Struct. Rep. Online* **2006**, *62*, m881−m883.

(28) Billetter, H.; Pantenburg, I.; Ruschewitz, U. Lithium Hydrogen Iodofumarate Monohydrate. *Acta Crystallogr., Sect. E: Struct. Rep. Online* **2005**, *61*, m1857−m1859.

(29) Zhang, X.-M. Hydro(solvo)thermal in situ Ligand Syntheses. *Coord. Chem. Rev.* **2005**, *249*, 1201−1219.

(30) Matemb Ma Ntep, T. J.; Reinsch, H.; Moll, B.; Hastürk, E.; Gökpinar, S.; Breitzke, H.; Schlüsener, C.; Schmolke, L.; Buntkowsky, G.; Janiak, C. Realizing the Potential of Acetylenedicarboxylate by Functionalization to Halofumarate in Zr(IV) Metal−Organic Frameworks. *Chem. − Eur. J.* **2018**, *24*, 14048−14053.

(31) Feng, L.; Chen, R.; Hou, S.; Chen, W.; Huang, H.; Wang, Y.; Wu, Y.-n.; Li, F. Common but Differentiated Flexible MIL-53(Al): Role of Metal Sources in Synthetic Protocol for Tuning the Adsorption Characteristics. *J. Mater. Sci.* **2019**, *54*, 6174−6185.

(32) Furukawa, H.; Gándara, F.; Zhang, Y.-B.; Jiang, J.; Queen, W. L.; Hudson, M. R.; Yaghi, O. M. Water Adsorption in Porous Metal−Organic Frameworks and Related Materials. *J. Am. Chem. Soc.* **2014**, *136*, 4369−4381.

(33) Kim, H.; Yang, S.; Rao, S. R.; Narayanan, S.; Kapustin, E. A.; Furukawa, H.; Umans, A. S.; Yaghi, O. M.; Wang, E. N. Water Harvesting from Air with Metal-Organic Frameworks Powered by Natural Sunlight. *Science* **2017**, *356*, 430−434.

(34) Solovyeva, M. V.; Gordeeva, L. G.; Krieger, T. A.; Aristov, Y. I. MOF-801 as a Promising Material for Adsorption Cooling: Equilibrium and Dynamics of Water Adsorption. *Energy Convers. Manage.* **2018**, *174*, 356−363.

(35) Sk, M.; Bhowal, S.; Biswas, S. Synthesis, Characterization, Stability, and Gas Adsorption Characteristics of a Highly Stable Zirconium Mesaconate Framework Material. *Eur. J. Inorg. Chem.* **2015**, 3317−3322.

DOI: 10.1021/acs.chemmater.9b00524
Chem. Mater. 2019, 31, 8629−8638

(36) Bennett, A. E.; Rienstra, C. M.; Auger, M.; Lakshmi, K. V.; Griffin, R. G. Heteronuclear Decoupling in Rotating Solids. *J. Chem. Phys.* **1995**, *103*, 6951−6958.

(37) Roy, P.; Schaate, A.; Behrens, P.; Godt, A. Post-Synthetic Modification of Zr-Metal−Organic Frameworks through Cycloaddition Reactions. *Chem. − Eur. J.* **2012**, *18*, 6979−6985.

(38) Yan, Z.; Yuan, Y.; Tian, Y.; Zhang, D.; Zhu, G. Highly Efficient Enrichment of Volatile Iodine by Charged Porous Aromatic Frameworks with Three Sorption Sites. *Angew. Chem., Int. Ed.* **2015**, *54*, 12733−12737.

(39) De Lorenzi, A.; Giorgianni, S.; Bini, R. High-Resolution FTIR Spectroscopy of the C−Cl Stretching Mode of Vinyl Chloride. *Mol. Phys.* **1999**, *96*, 101−108.

(40) Hunt, G. R.; Wilson, M. K. Infrared Spectra and Potential Constants of Some Monohaloacetylenes. *J. Chem. Phys.* **1961**, *34*, 1301−1306.

(41) Rossini, A. J.; Zagdoun, A.; Lelli, M.; Canivet, J.; Aguado, S.; Ouari, O.; Tordo, P.; Rosay, M.; Maas, W. E.; Copéret, C.; Farrusseng, D.; Emsley, L.; Lesage, A. Dynamic Nuclear Polarization Enhanced Solid-State NMR Spectroscopy of Functionalized Metal−Organic Frameworks. *Angew. Chem., Int. Ed.* **2012**, *51*, 123−127.

(42) Lucier, B. E. G.; Chen, S.; Huang, Y. Characterization of Metal−Organic Frameworks: Unlocking the Potential of Solid-State NMR. *Acc. Chem. Res.* **2018**, *51*, 319−330.

(43) Grünberg, B.; Emmler, T.; Gedat, E.; Shenderovich, I.; Findenegg, G. H.; Limbach, H.-H.; Buntkowsky, G. Hydrogen Bonding of Water Confined in Mesoporous Silica MCM-41 and SBA-15 Studied by ^{1}H Solid-State NMR. *Chem. − Eur. J.* **2004**, *10*, 5689−5696.

(44) Li, Y.; Chen, H.; Voo, L. Y.; Ji, J.; Zhang, G.; Zhang, G.; Zhang, F.; Fan, X. Synthesis of Partially Hydrogenated Graphene and Brominated Graphene. *J. Mater. Chem.* **2012**, *22*, 15021−15024.

(45) Papirer, E.; Lacroix, R.; Donnet, J.-B.; Nan, G.; Fioux, P. XPS Study of the Halogenation of Carbon black−Part 2. Chlorination. *Carbon* **1995**, *33*, 63−72.

(46) Hai-Fang, W.; Xiao-Yong, D.; Jing, W.; Xing-Fa, G.; Geng-Mei, X.; Zu-Jin, S.; Zhen-Nan, G.; Yuan-Fang, L.; Yu-Liang, Z. XPS Study of C−I Covalent Bond on Single-walled Carbon Nanotubes (SWNTs). *Acta Phys.-Chim. Sin.* **2004**, *20*, 673−675.

(47) Shearer, G. C.; Chavan, S.; Bordiga, S.; Svelle, S.; Olsbye, U.; Lillerud, K. P. Defect Engineering: Tuning the Porosity and Composition of the Metal−Organic Framework UiO-66 via Modulated Synthesis. *Chem. Mater.* **2016**, *28*, 3749−3761.

(48) Cliffe, M. J.; Wan, W.; Zou, X.; Chater, P. A.; Kleppe, A. K.; Tucker, M. G.; Wilhelm, H.; Funnell, N. P.; Coudert, F.-X.; Goodwin, A. L. Correlated Defect Nanoregions in a Metal−Organic Framework. *Nat. Commun.* **2014**, *5*, No. 4176.

(49) Taddei, M. When Defects Turn into Virtues: The Curious Case of Zirconium-Based Metal-Organic Frameworks. *Coord. Chem. Rev.* **2017**, *343*, 1−24.

(50) Yuan, S.; Qin, J.-S.; Lollar, C. T.; Zhou, H.-C. Stable Metal−Organic Frameworks with Group 4 Metals: Current Status and Trends. *ACS Cent. Sci.* **2018**, *4*, 440−450.

(51) Thommes, M.; Kaneko, K.; Neimark, A. V.; Olivier, J. P.; Rodriguez-Reinoso, F.; Rouquerol, J.; Sing, K. S. W. Physisorption of Gases, with Special Reference to the Evaluation of Surface Area and Pore Size Distribution (IUPAC Technical Report). *Pure Appl. Chem.* **2015**, *87*, 1051−1069.

(52) Tsobnang, P. K.; Hastürk, E.; Fröhlich, D.; Wenger, E.; Durand, P.; Ngolui, J. L.; Lecomte, C.; Janiak, C. Water Vapor Single-Gas Selectivity via Flexibility of Three Potential Materials for Autonomous Indoor Humidity Control. *Cryst. Growth Des.* **2019**, *19*, 2869−2880.

(53) Gandhidasan, P.; Al-Farayedhi, A. A.; Al-Mubarak, A. A. Dehydration of Natural Gas Using Solid Desiccants. *Energy* **2001**, *26*, 855−868.

(54) Cadiau, A.; Belmabkhout, Y.; Adil, K.; Bhatt, P. M.; Pillai, R. S.; Shkurenko, A.; Martineau-Corcos, C.; Maurin, G.; Eddaoudi, M. Hydrolytically Stable Fluorinated Metal-organic Frameworks for Energy-Efficient Dehydration. *Science* **2017**, *356*, 731−735.

(55) Li, T. X.; Xu, J. X.; Yan, T.; Wang, R. Z. Development of Sorption Thermal Battery for Low-Grade Waste Heat Recovery and Combined Cold and Heat Energy Storage. *Energy* **2016**, *107*, 347−359.

(56) Scapino, L.; Zondag, H. A.; Van Bael, J.; Diriken, J.; Rindt, C. C. M. Sorption Heat Storage for Long-Term Low-Temperature Applications: A Review on the Advancements at Material and Prototype scale. *Appl. Energy* **2017**, *190*, 920−948.

(57) Narayanan, S.; Li, X.; Yang, S.; Kim, H.; Umans, A.; McKay, I. S.; Wang, E. N. Thermal Battery for Portable Climate Control. *Appl. Energy* **2015**, *149*, 104−116.

(58) Kim, H.; Cho, H. J.; Narayanan, S.; Yang, S.; Furukawa, H.; Schiffres, S.; Li, X.; Zhang, Y.-B.; Jiang, J.; Yaghi, O. M.; Wang, E. N. Characterization of Adsorption Enthalpy of Novel Water-Stable Zeolites and Metal-Organic Frameworks. *Sci. Rep.* **2016**, *6*, No. 19097.

(59) Teo, H. W. B.; Chakraborty, A. Water Adsorption on Various Metal Organic Framework. *IOP Conf. Ser.: Mater. Sci. Eng.* **2017**, *272*, No. 012019.

(60) Advanced Research Projects Agency-DOE, HEATS Program Overview. https://arpa-e.energy.gov/sites/default/files/documents/files/HEATS_ProgramOverview.pdf (accessed Oct, 2016).

(61) Reimer, N.; Bueken, B.; Leubner, S.; Seidler, C.; Wark, M.; De Vos, D.; Stock, N. Three Series of Sulfo-Functionalized Mixed-Linker CAU-10 Analogues: Sorption Properties, Proton Conductivity, and Catalytic Activity. *Chem. − Eur. J.* **2015**, *21*, 12517−12524.

(62) Yang, Q.; Wiersum, A. D.; Llewellyn, P. L.; Guillerm, V.; Serre, C.; Maurin, G. Functionalizing Porous Zirconium Terephthalate UiO-66(Zr) for Natural Gas Upgrading: a Computational Exploration. *Chem. Commun.* **2011**, *47*, 9603−9605.

(63) Reinsch, H.; Waitschat, S.; Stock, N. Mixed-linker MOFs with CAU-10 Structure: Synthesis and Gas Sorption Characteristics. *Dalton Trans.* **2013**, *42*, 4840−4847.

(64) Cavallo, G.; Metrangolo, P.; Milani, R.; Pilati, T.; Priimagi, A.; Resnati, G.; Terraneo, G. The Halogen Bond. *Chem. Rev.* **2016**, *116*, 2478−2601.

(65) Keith, D. W. Why Capture CO_2 from the Atmosphere? *Science* **2009**, *325*, 1654−1655.

(66) Rezaei, F.; Rownaghi, A. A.; Monjezi, S.; Lively, R. P.; Jones, C. W. SO_x/NO_x Removal from Flue Gas Streams by Solid Adsorbents: A Review of Current Challenges and Future Directions. *Energy Fuels* **2015**, *29*, 5467−5486.

(67) Savage, M.; Cheng, Y.; Easun, T. L.; Eyley, J. E.; Argent, S. P.; Warren, M. R.; Lewis, W.; Murray, C.; Tang, C. C.; Frogley, M. D.; Cinque, G.; Sun, J.; Rudić, S.; Murden, R. T.; Benham, M. J.; Fitch, A. N.; Blake, A. J.; Ramirez-Cuesta, A. J.; Yang, S.; Schröder, M. Selective Adsorption of Sulfur Dioxide in a Robust Metal−Organic Framework Material. *Adv. Mater.* **2016**, *28*, 8705−8711.

(68) Lin, Y.; Kong, C.; Zhang, Q.; Chen, L. Metal-Organic Frameworks for Carbon Dioxide Capture and Methane Storage. *Adv. Energy Mater.* **2017**, *7*, No. 1601296.

(69) Cui, X.; Yang, Q.; Yang, L.; Krishna, R.; Zhang, Z.; Bao, Z.; Wu, H.; Ren, Q.; Zhou, W.; Chen, B.; Xing, H. Ultrahigh and Selective SO_2 Uptake in Inorganic Anion-Pillared Hybrid Porous Materials. *Adv. Mater.* **2017**, *29*, No. 1606929.

(70) Zhang, Z.; Zhao, Y.; Gong, Q.; Li, Z.; Li, J. MOFs for CO_2 Capture and Separation from Flue Gas Mixtures: the Effect of MultiFunctional Sites on their Adsorption Capacity and Selectivity. *Chem. Commun.* **2013**, *49*, 653−661.

Supporting Information

Facile in Situ Halogen Functionalization via Triple-Bond Hydrohalogenation: Enhancing Sorption Capacities through Halogenation to Halofumarate-Based Zr(IV)-Metal-Organic Frameworks

Tobie Matemb Ma Ntep,[†] Hergen Breitzke,[‡] Laura Schmolke,[†] Carsten Schlüsener,[†] Bastian Moll,[†] Simon Millan,[†] Niels Tannert,[†] Ilias El Aita,[§] Gerd Buntkowsky,[‡] and Christoph Janiak*,[†]

[†] Institut für Anorganische Chemie und Strukturchemie, Heinrich-Heine-Universität Düsseldorf, Universitätsstraße 1, D- 40225 Düsseldorf, Germany

[‡] Eduard-Zintl-Institut für Anorganische und Physikalische Chemie, Technische Universität Darmstadt, Alarich-Weiss-Straße. 4, D-64287 Darmstadt, Germany

[§] Institut für Pharmazeutische Technologie und Biopharmazie, Heinrich-Heine-Universität Düsseldorf, D- 40225 Düsseldorf, Germany

* Corresponding author: E-mail: janiak@uni-duesseldorf.de; Fax: + 49-211-81-12287; Tel: +49-211-81-12286

Additional email addresses:
tobie.matemb.ma.ntep@uni-duesseldorf.de; breitzke@chemie.tu-darmstadt.de; laura.schmolke@uni-duesseldorf.de; carsten.schluesener@uni-duesseldorf.de; bastian.moll@uni-duesseldorf.de; simon.millan@uni-duesseldorf.de; elaita@uni-duesseldorf.de; gerd.buntkowsky@chemie.tu-darmstadt.de

Table of contents:

Zirconium fumarate, MOF-801 structure description, synthesis and characterization

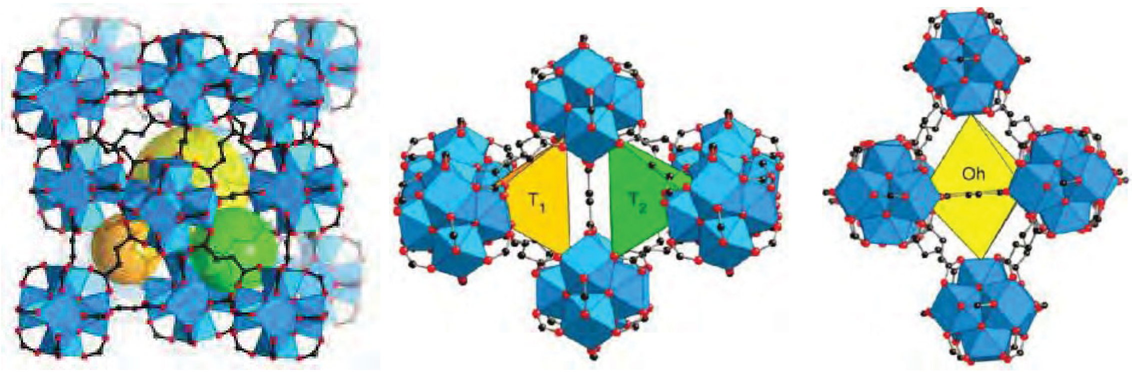

Figure S1. fcc packing diagram of the **fcu** framework in zirconium fumarate, MOF-801 (left) with tetrahedral T (middle) and octahedral Oh (right) cages.[1]

Synthesis procedure of zirconium fumarate, MOF-801. Zirconium fumarate, MOF-801 was synthesized according to a previously reported procedure.[2] 233 mg (1 mmol) of zirconium chloride ($ZrCl_4$) were dissolved in a solvent mixture of water/formic acid (20 ml/ 8.578 mL). 348 mg (3 mmol) of fumaric acid (H_2Fum) were added and ultrasonicated for 3 minutes. The resulting mixture was sealed in a Teflon lined autoclave and stored in an oven at 120 °C for 24 h. The obtained white precipitate was centrifuged from its mother liquor and redispersed three times in 20 mL of water followed by centrifugation. Afterwards the product was redispersed and centrifuged three times in 20 mL of methanol.

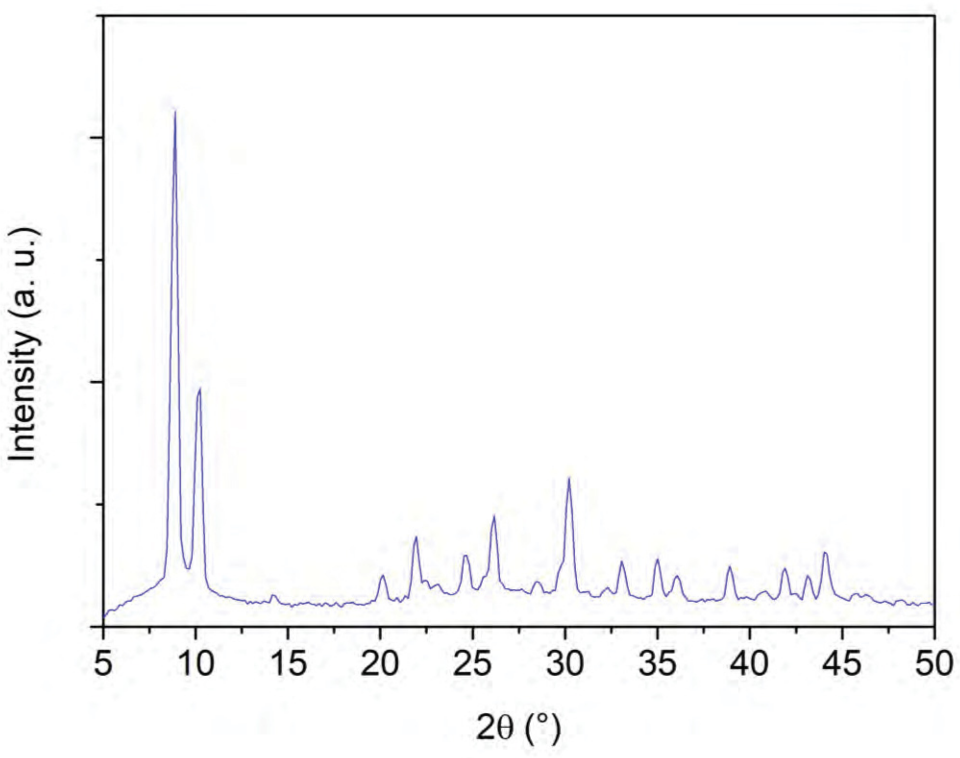

Figure S2. PXRD pattern of as-synthesized zirconium fumarate, MOF-801.

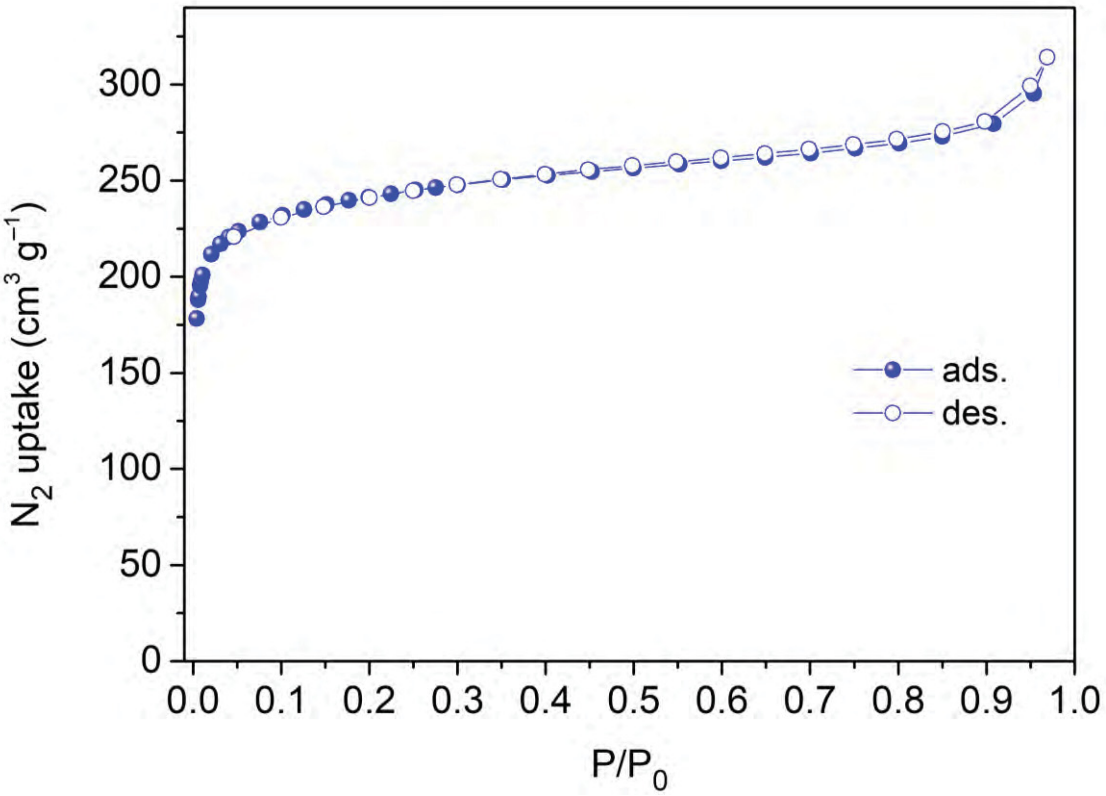

Figure S3. Nitrogen sorption isotherm of zirconium fumarate, MOF-801 at 77K.

Raman spectroscopy of zirconium fumarate, MOF-801

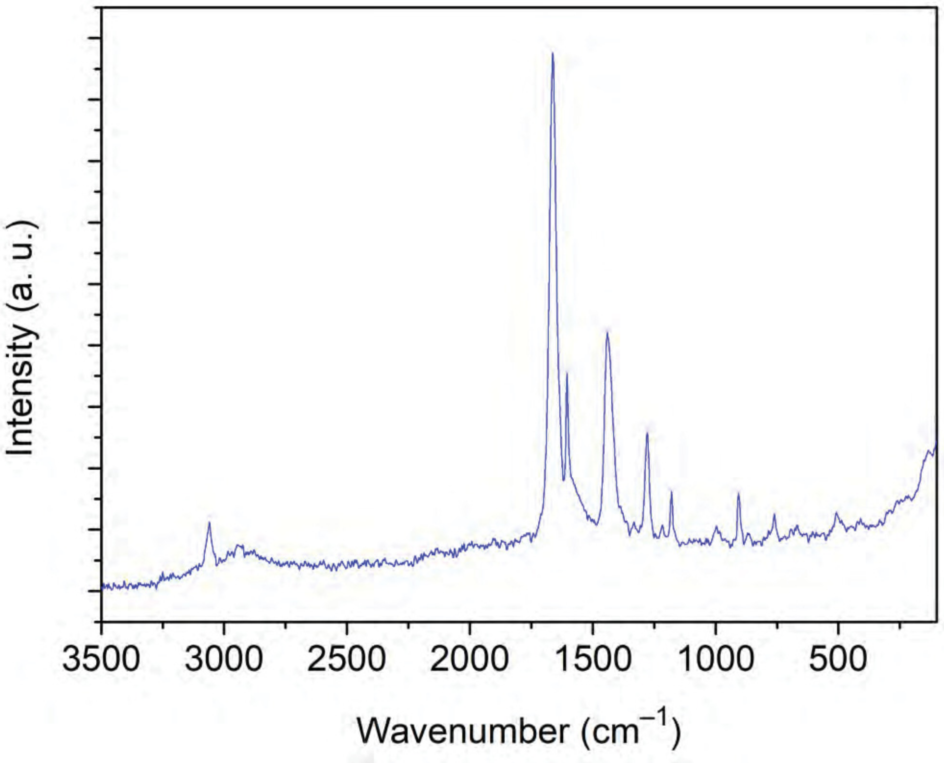

Figure S4. Raman spectrum of zirconium fumarate, MOF-801.

Solution NMR spectroscopy of acetic acid modulation synthesized zirconium fumarate, MOF-801

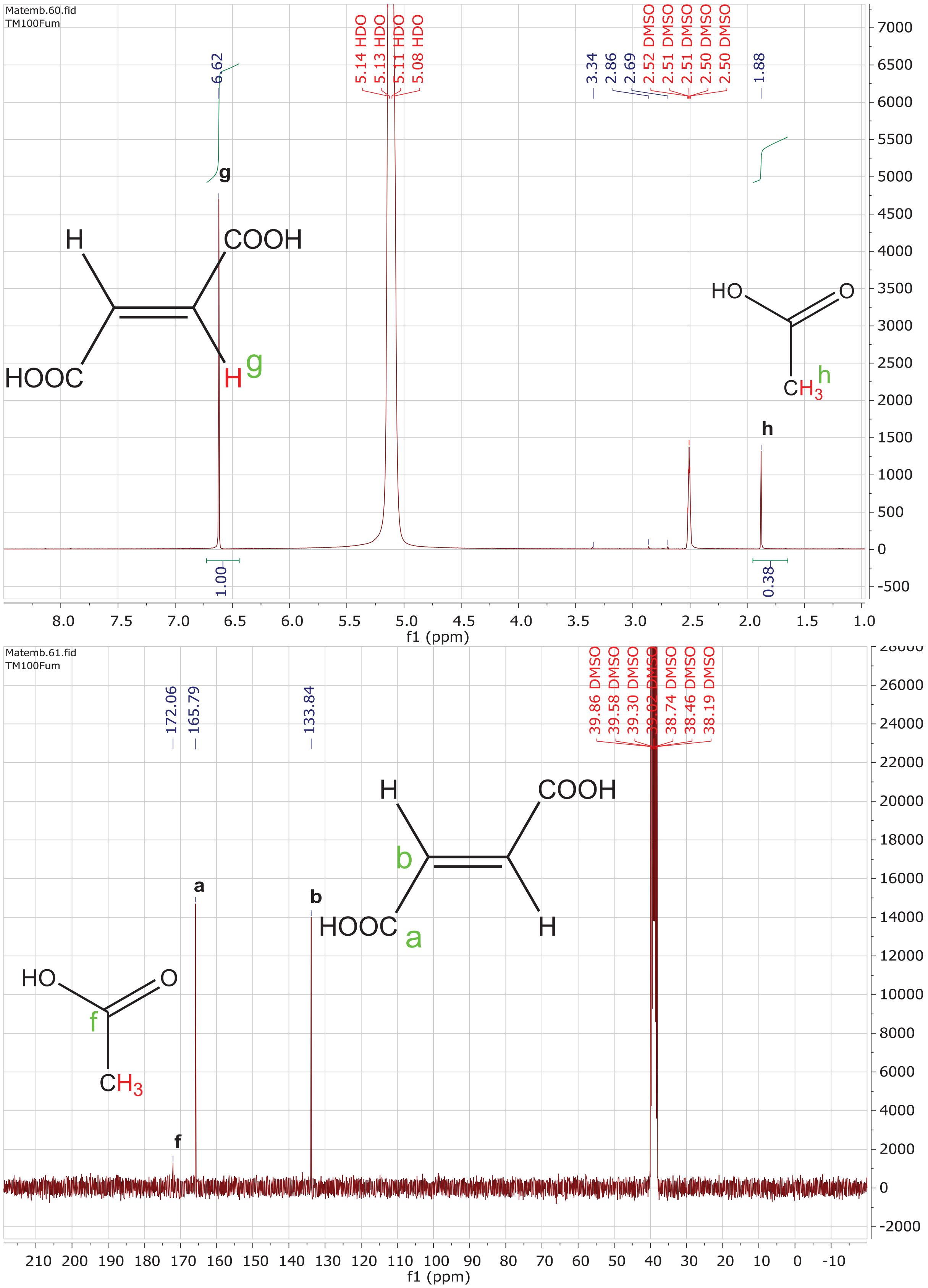

Figure S5. Solution ^1H (top) and ^{13}C (bottom) NMR spectra of digested zirconium fumarate, MOF-801 in DMSO-d_6. This sample was synthesized by acetic acid modulation for comparison purpose with HHU-2-X spectra.

Determination of linker defects amount for MOF-801

$$\frac{Acetate}{Fum}\,\text{molar ratio} = \frac{\left(\frac{Integration\ of\ acetate\ signal}{Number\ of\ protons\ per\ acetate}\right)}{\left(\frac{Integration\ of\ Fum\ signal}{Number\ of\ protons\ per\ Fum}\right)} = \left(\frac{Integ.of\ acet.}{3}\right) \times \left(\frac{2}{Integ.of\ Fum}\right)$$

$$= \left(\frac{0.38}{3}\right) \times \left(\frac{2}{1}\right)$$

Hence, the acetate to fumarate molar ratio is calculated to 0.25 for MOF-801

Considering the unit formula $[Zr_6O_4(OH)_{4+x}(Fum)_{6-x}(Ac)_x]$ where *x* is the number of missing linker on the $\{Zr_6\}$-cluster per unit formula:

$$\frac{Ac}{Fum}\,\text{molar ratio} = m_R = \frac{x}{6-x}\,, \qquad \text{which leads to} \quad x = \frac{6 \times m_R}{1 + m_R}$$

The amount of missing linker per $\{Zr_6\}$-cluster in the unit formula for MOF-801 is 1.2 missing linker per zirconium cluster.

Infrared spectroscopy of HHU-2-X

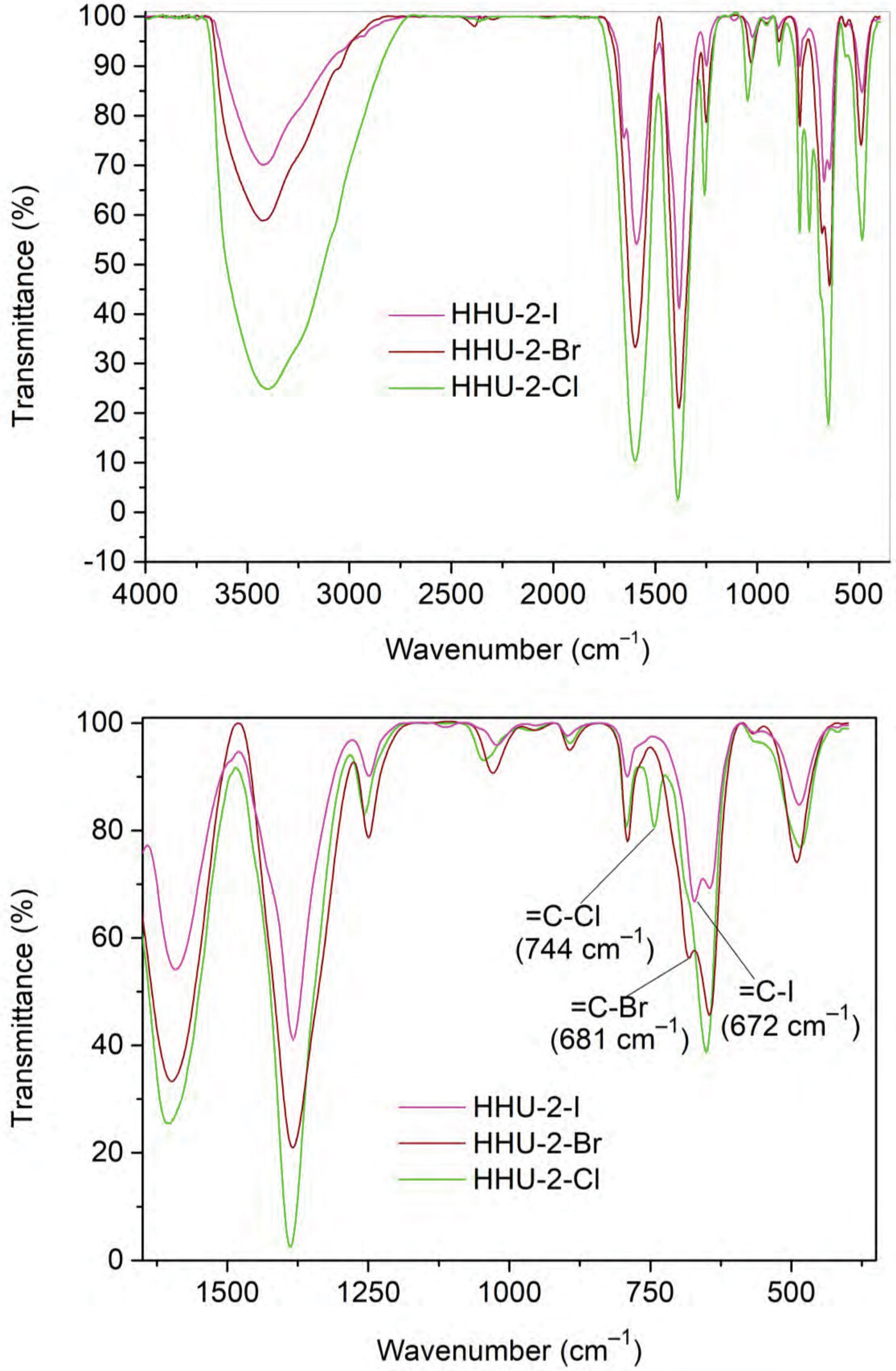

Figure S6. IR spectra of HHU-2-X (X = Cl, Br, I) in the wavenumber range 4000–400 cm^{-1} (top) and 1700–400 cm^{-1} (bottom).

Solid-state and solution ^1H and ^{13}C NMR spectroscopy of HHU-2-X

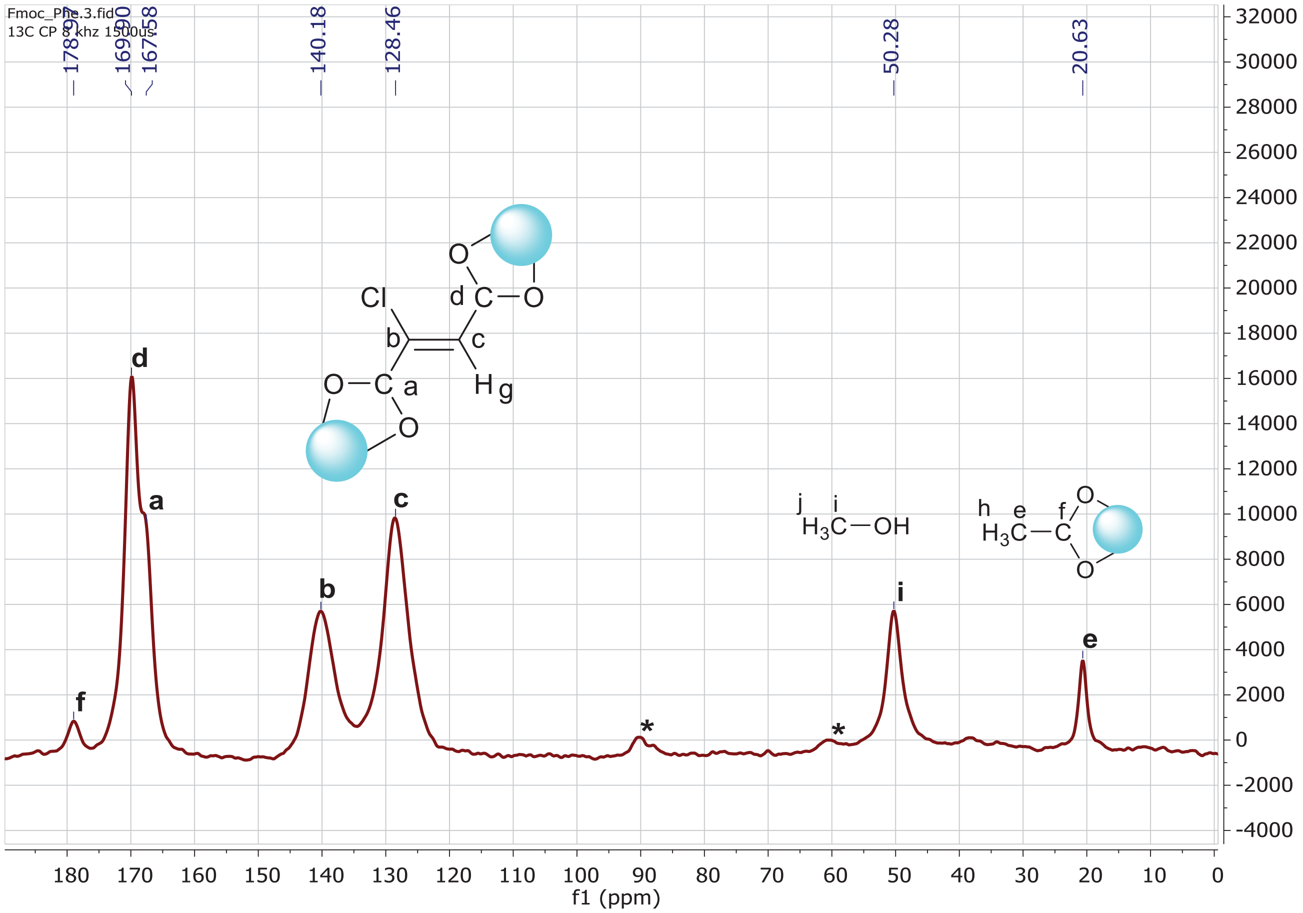

Figure S7. ^{13}C CP MAS solid-state NMR spectrum at 12 kHz spinning speed and 1500 µs contact time of HHU-2-Cl. The stars indicate spinning sidebands.

In Figure S7, the ^{13}C NMR signals at about 140 and 130 ppm chemical shift can be attributed to two carbons of a non-symmetrically bonded C=C double bond. The signal at 170 ppm in the ^{13}C ssNMR displays a shoulder. This is assigned to the carbon atoms of the two different carboxylate groups, appearing at slightly different chemical shifts. This is consistent with the non-symmetrically bonded nature of the double bond. The ^1H dimension shows a signal at about 6.9 ppm, which is correlated to all four carbon atoms and corresponds to one proton bonded to the C=C double bond. Furthermore, the $^1H/^{13}C$ correlation of 1.5 to 20 ppm is assigned to a terminal coordinated CH_3COO modulator ligand. Its carboxylate ^{13}COO signal at about 180 ppm is seen in the ^{13}C CP MAS spectrum but the CH_3-C correlation is too weak to show in the FSLG-HETCOR experiment (Figure 2 in the main text). Two additional correlated signals at 3.3 and 50 ppm in the ^1H and ^{13}C spectra, respectively, are attributable to CH_3 from the methanol solvent in the pores of the sample. The absence of correlation of these signals with any other ligand signals shows that they do not belong to the framework structure of HHU-2-Cl but present uncoordinated solvent. For HHU-2-Br the ^{13}C NMR ssNMR signals are not well resolved but the overall pattern in the FSLG-HETCOR spectrum agrees with HHU-2-Cl (Figure. S9 in SI).

Solution NMR analysis was conducted on the activated and digested sample of HHU-2-I (see SI for details). In the ^{1}H NMR spectrum of HHU-2-I (Figure S11 in SI), the peaks at about 7.4 and 1.83 ppm chemical shift are ascribed to a proton bonded to an olefinic carbon (=C–H) and the protons of $–CH_3$ group of acetic acid modulator, respectively. In the ^{13}C spectrum (Figure S11 in SI) the peaks at 165 and 164 ppm are ascribed to carbons of linker carboxylates. They appear at slightly different chemical shifts because of the non-symmetrical nature of the linker. The peak at 138 ppm is due to the olefinic carbon bonded to a proton. The carbon bonded to iodine atom (=C-I) appears at about 103 ppm chemical shift. These assignments are confirmed by their respective correlations observed in the HSQC (Heteronuclear Multiple Quantum Correlation) and HMBC (Heteronuclear Multiple Bond Correlation) spectra (Figure S12).

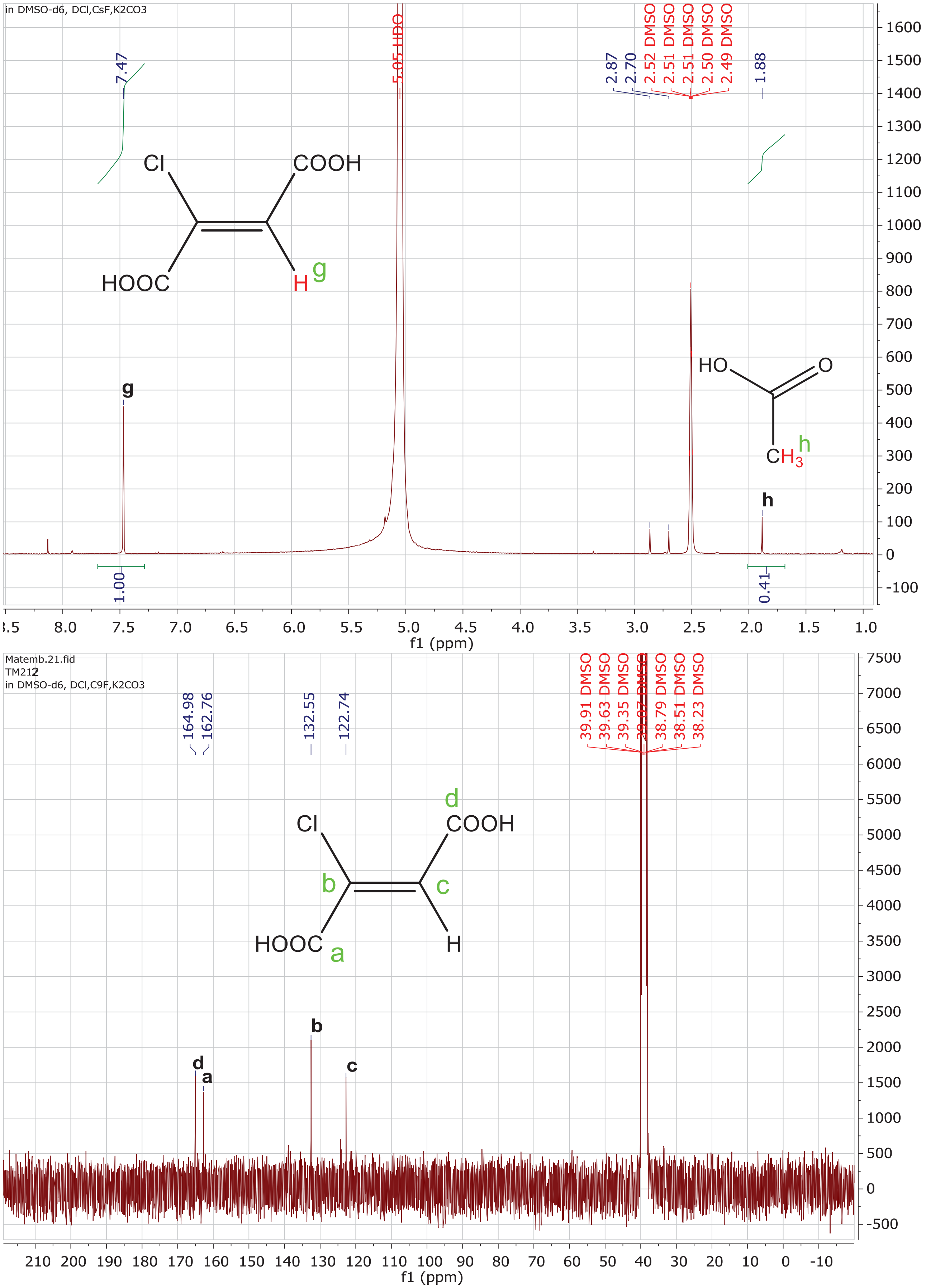

Figure S8. Solution ^{1}H (top) and ^{13}C (bottom) NMR spectra of digested HHU-2-Cl in DMSO-d_6.

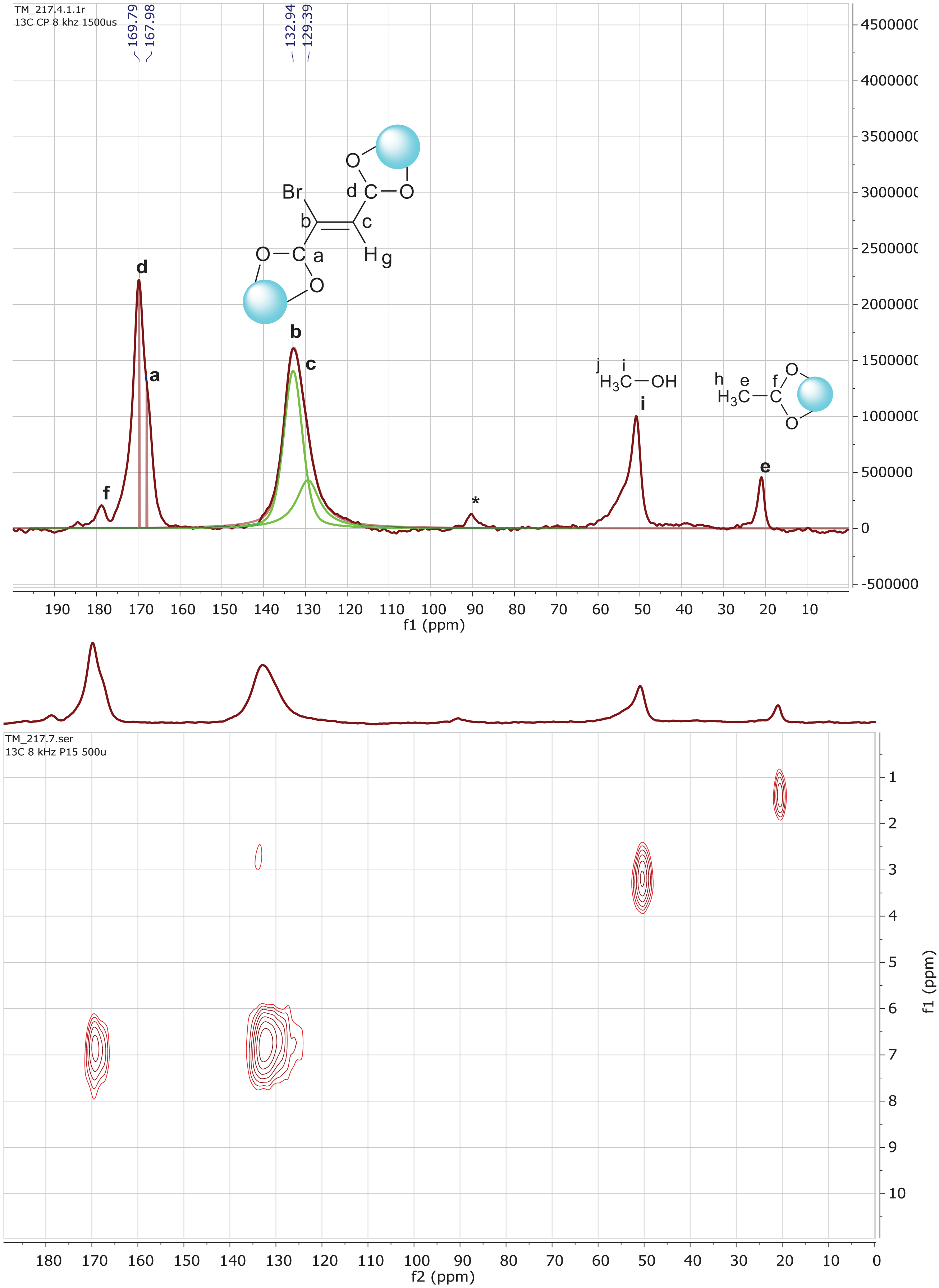

Figure S9. (a) ^{13}C CP MAS solid-state NMR spectrum and (b) ^{1}H-^{13}C FSLG-HETCOR CP MAS at 12 kHz spinning speed and 500 µs contact time of HHU-2-Br. The star indicates a spinning sideband.

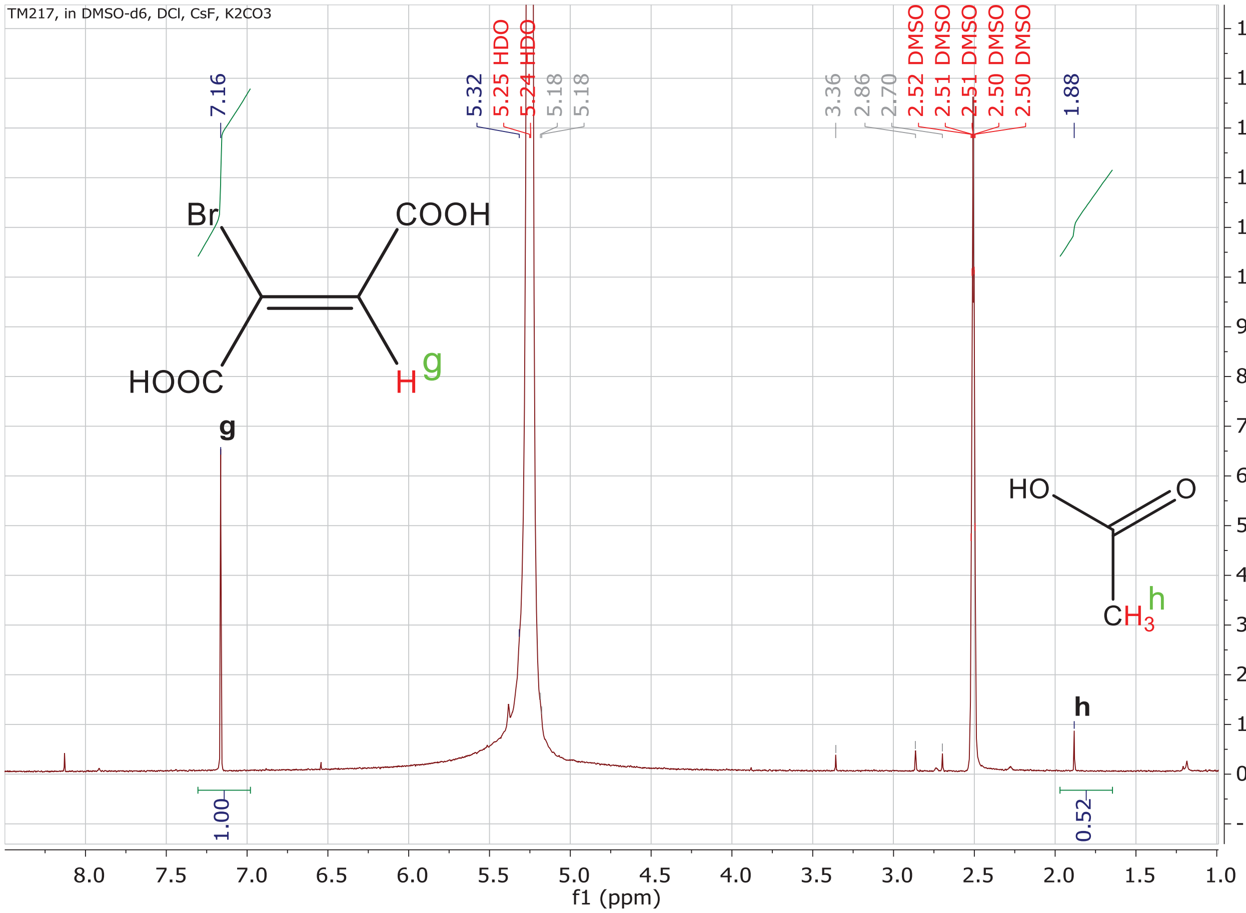

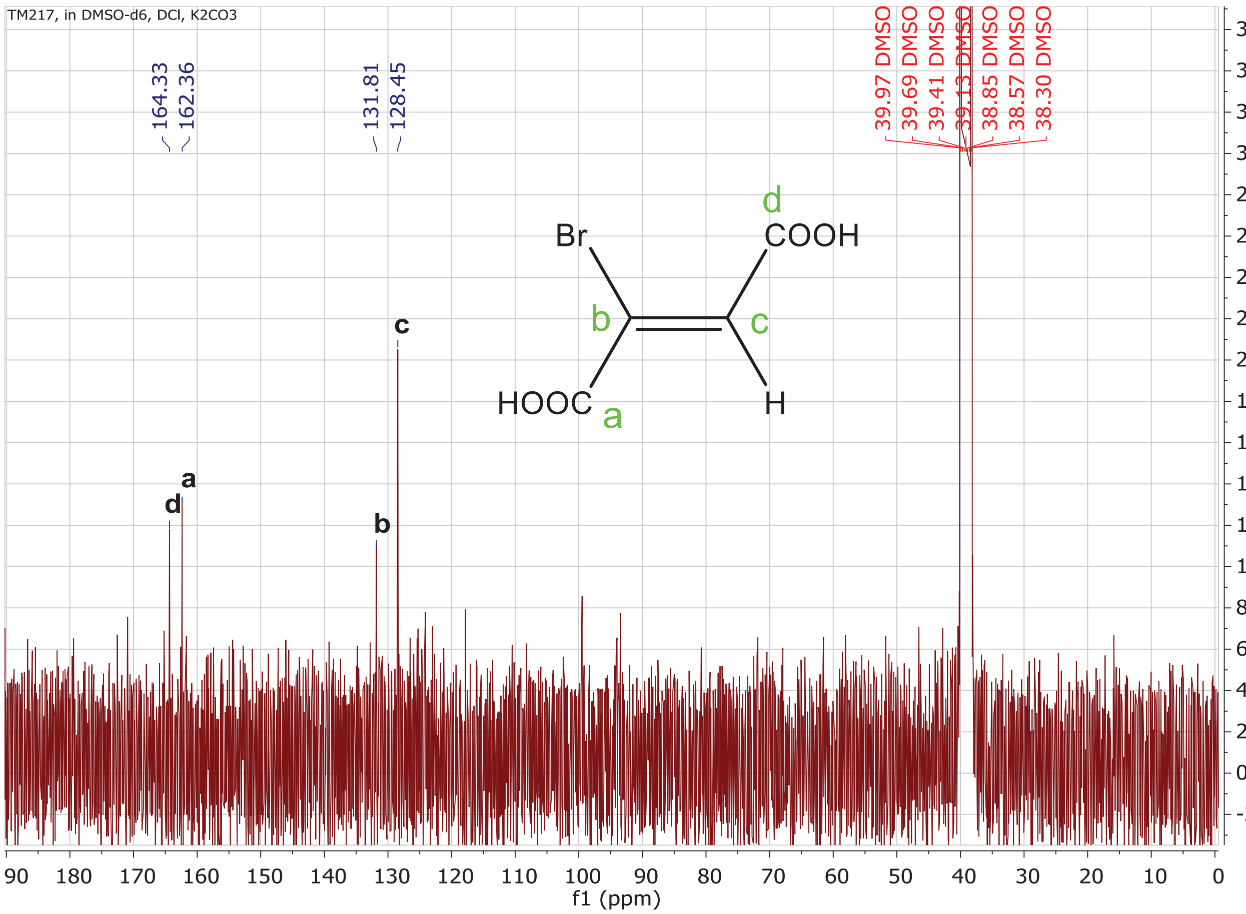

Figure S10. Solution ^{1}H (top) and ^{13}C (bottom) NMR spectra of digested HHU-2-Br in DMSO-d$_6$.

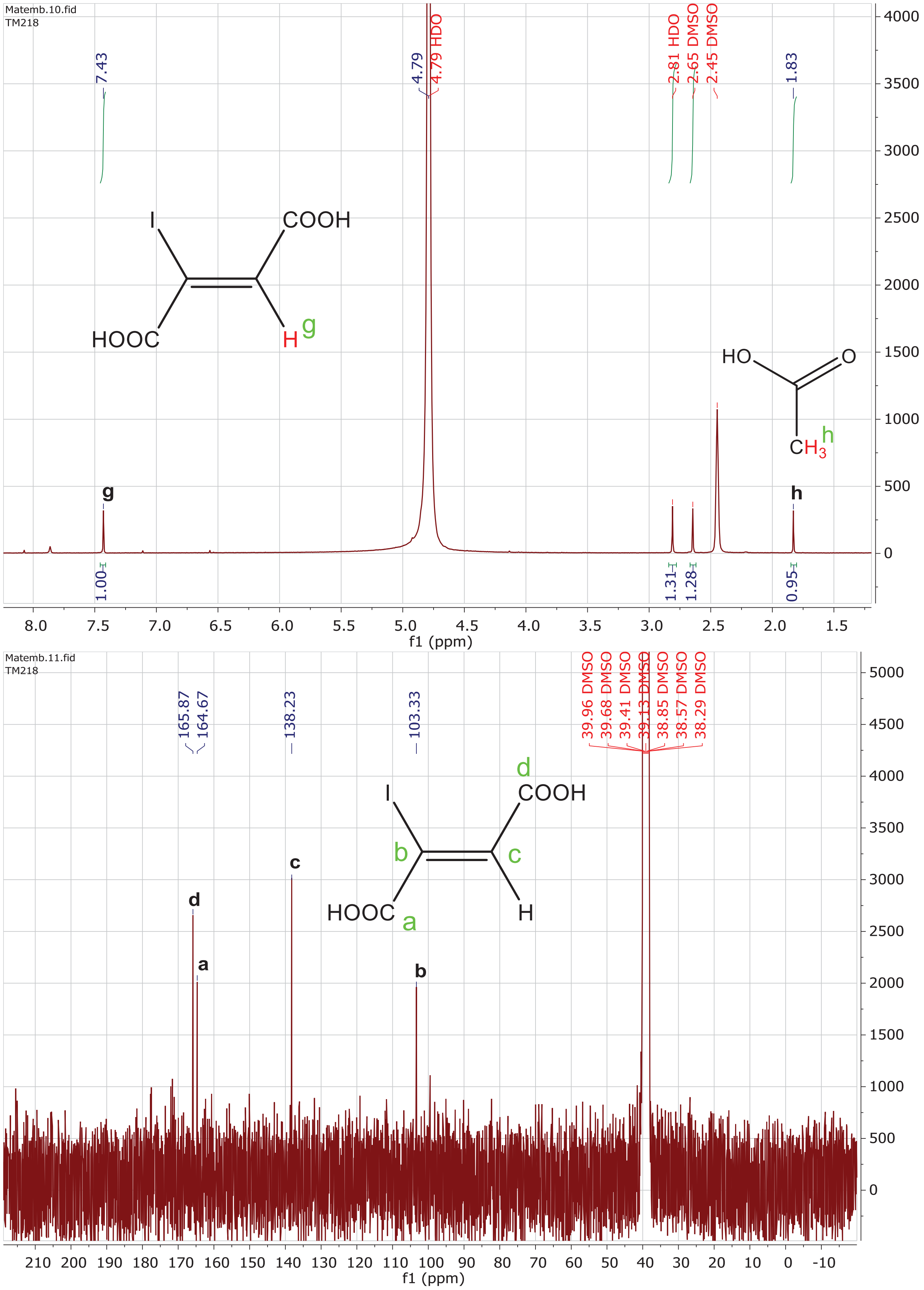

Figure S11. Solution ^{1}H (top) and ^{13}C (bottom) NMR spectra of digested HHU-2-I in DMSO-d_6.

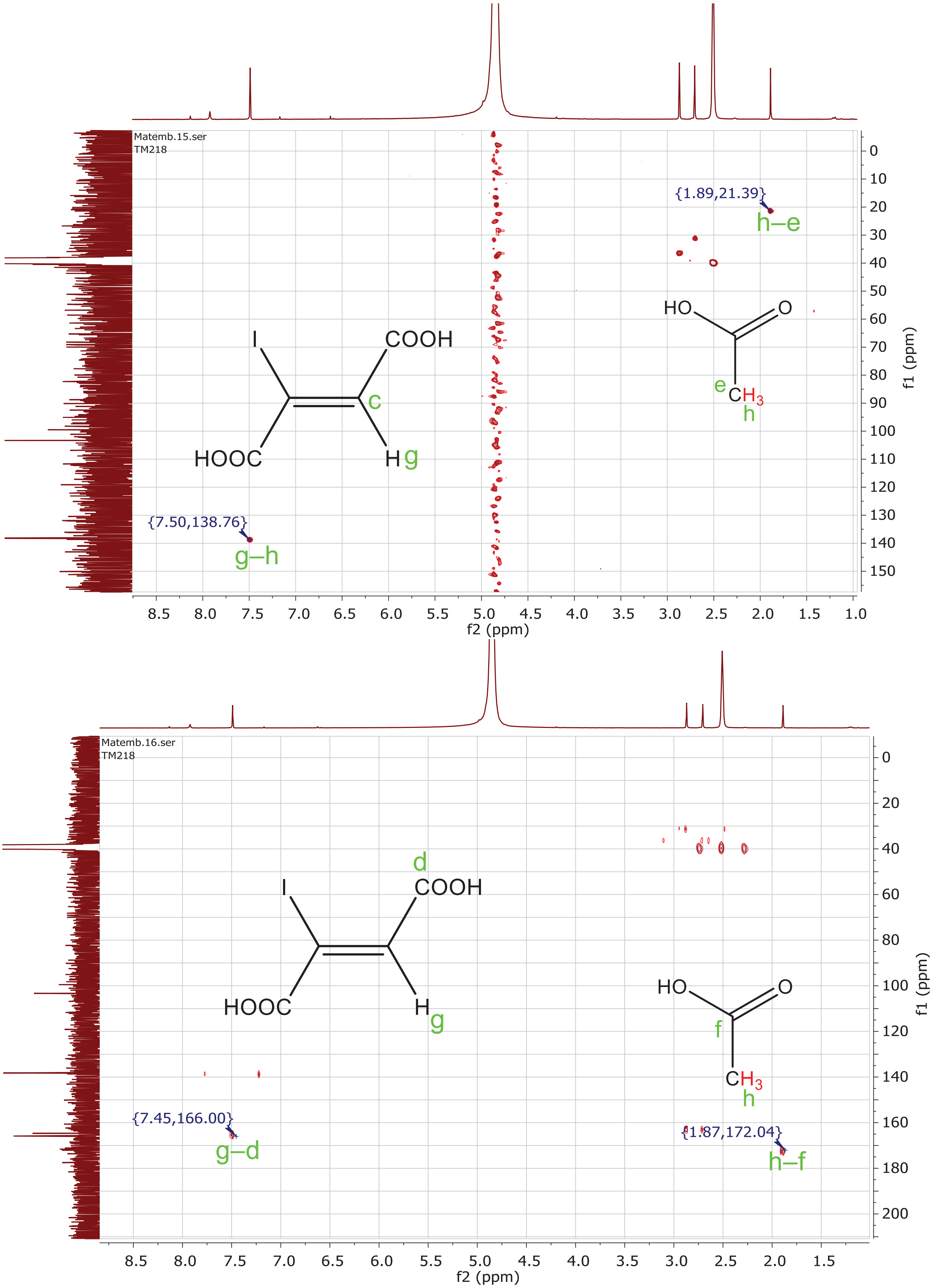

Figure S12. 2D ^{1}H-^{13}C HSQC (top) and HMBC (bottom) NMR spectra of digested HHU-2-I in DMSO-d$_6$. HSQC = Heteronuclear Multiple Quantum Correlation, HMBC = Heteronuclear Multiple Bond Correlation.

HSQC correlates the chemical shift of protons with chemical shift of the directly bonded carbons. HMBC gives correlations between protons and carbons that are separated by two or three bonds (direct one-bond correlations are suppressed).

Prior to solution NMR analysis, an activated sample of HHU-2-X and zirconium MOF was digested as follows: 15 mg of MOF and 10 mg CsF (caesium fluoride) were suspended in DMSO-d_6 (0.65 mL). 2 drops of aqueous DCl (35 wt% in D_2O) was added. As soon as the light yellow/white solid of MOF had dissolved (after 5-15 min), 12 mg K_2CO_3 was added to neutralize the acid.

Determination of acetate to halofumarate (Fum-X) linker ratio in HHU-2-X MOFs from solution ^{1}H NMR

$$\frac{Acetate}{Fum-\mathrm{x}}\,\text{molar ratio} = \frac{\left(\dfrac{Integration\ of\ acetate\ signal}{Number\ of\ protons\ per\ acetate}\right)}{\left(\dfrac{Integration\ of\ Fum-X\ signal}{Number\ of\ protons\ per\ Fum-X}\right)}$$

$$= \left(\frac{Integ.\,of\ acet.}{3}\right)\times\left(\frac{1}{Integ.\,of\ Fum-X}\right)$$

Hence, respective acetate to linker molar ratios are calculated to 0.136, 0.173 and 0.316 for HHU-2-Cl, HHU-2-Br and HHU-2-I.

Considering the unit formula $[Zr_6O_4(OH)_{4+x}(\text{Fum-X})_{6-x}(Ac)_x]$ where *x* is the number of missing linker on the $\{Zr_6\}$-cluster per unit formula:

$$\frac{Ac}{Fum-\mathrm{x}}\,\text{molar ratio} = m_R = \frac{x}{6-x}\ , \qquad \text{which leads to}\ \ x = \frac{6\times m_R}{1+m_R}$$

Corresponding amount of missing linker per $\{Zr_6\}$-cluster in the unit formula is 0.7, 0.9 and 1.4 missing linker per zirconium cluster for HHU-2-Cl, HHU-2-Br and HHU-2-I respectively.

X-ray Photoelectron Spectroscopy (XPS) of HHU-2-X

Another I_{3d} signal was observed in the iodine spectrum at 620.8 ($3d_{3/2}$) and 630.85 ($3d_{5/2}$) eV (Figure S21). The peak positions are consistent with Zr bound iodide in place of μ_3-OH groups at the {Zr_6} clusters as was previously reported[3] or coordinated at missing linker sites. Fitting the XPS C 1s spectrum reveals three components which can be assigned to carboxylate carbon –COO (~288 eV), and the two C-H and C-X bound double-bonded carbon C=C (~284 and ~285-286 eV respectively). The high resolution O 1s spectrum (Figure S15) shows two components attributable to the carboxylate oxygen C-O (533 eV) and the oxygen of the zirconium cluster Zr-O (532 eV).[4,5] The deconvoluted Zr spectrum shows two peaks at 183.48 and 185.79 eV binding energy, corresponding respectively to $3d_{3/2}$ and $3d_{5/2}$ components of zirconium in the oxidation state Zr^{IV}.[3]

a) HHU-2-Cl

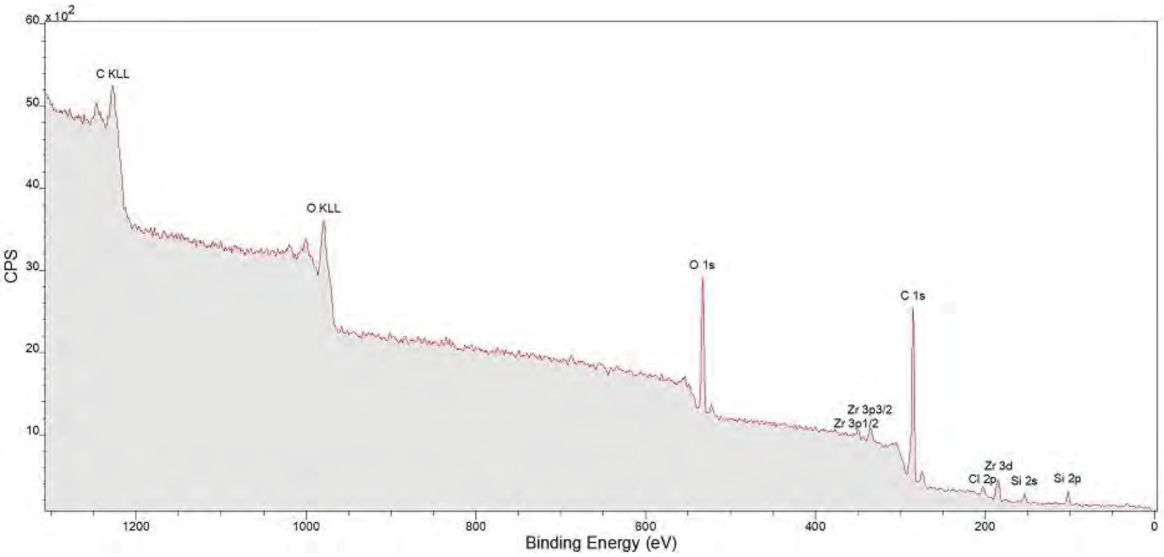

Figure S13. XPS survey spectrum of HHU-2-Cl surface.

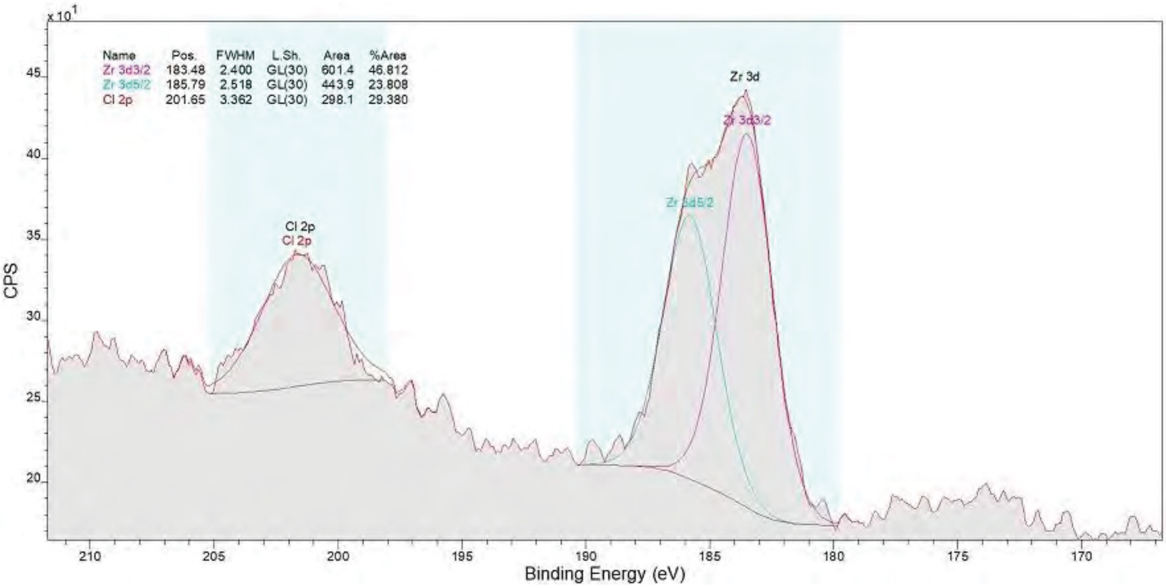

Figure S14. High resolution XPS core-level spectrum of HHU-2-Cl (Zr-Fum-Cl) in the region of Cl 2p and Zr 3d.

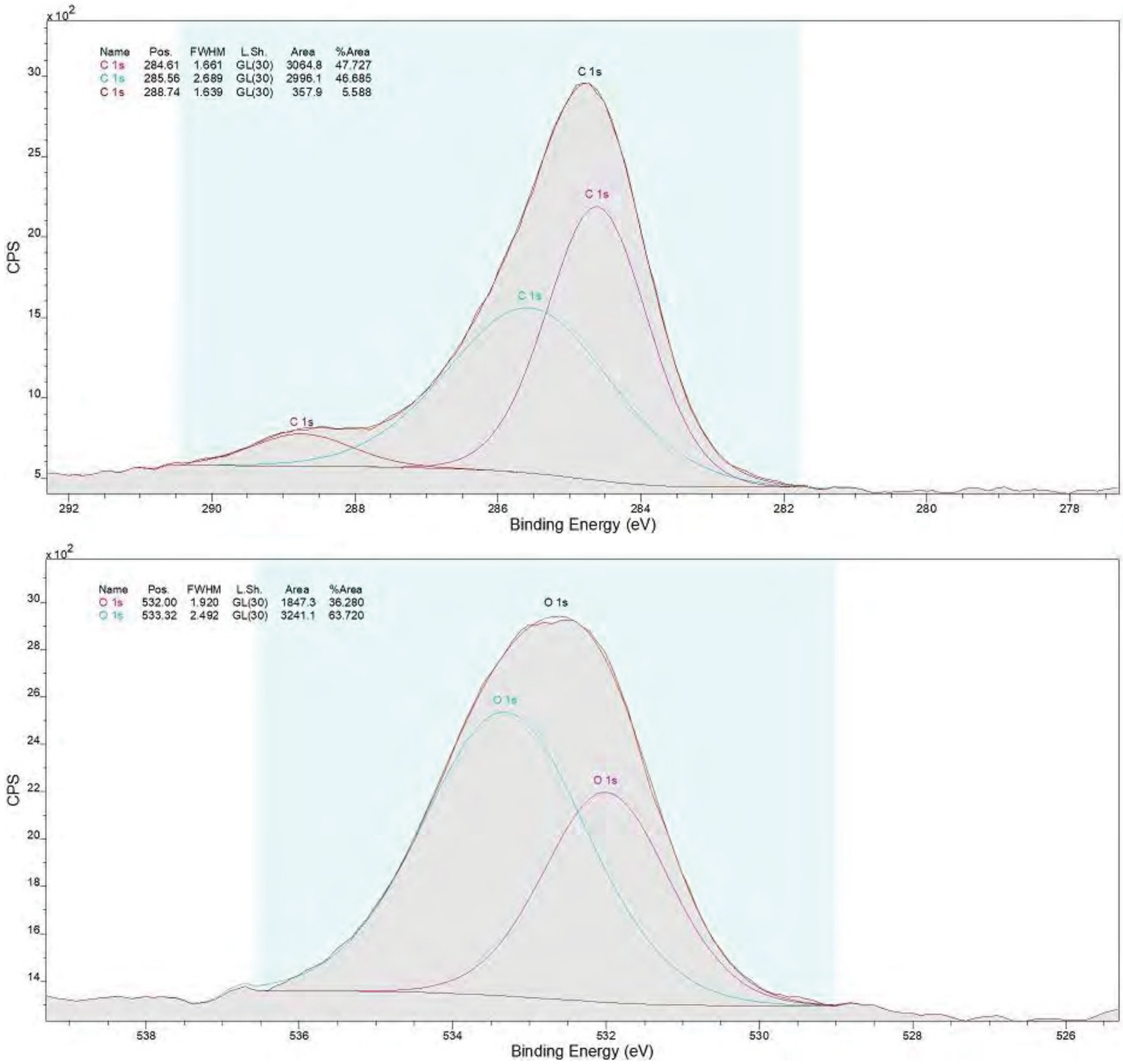

Figure S15. High resolution XPS core-level spectrum of HHU-2-Cl in the region of C 1s and O 1s.

Table S1. XP spectrum peak assignments of HHU-2-Cl

Element	Orbital	Binding Energy	Area	RSF	Area/RSF	
C	1s	284,61	3064,8	1	3064,8	C=CH
		285,56	2996,1	1	2996,1	C=CCl
		288,74	357,9	1	357,9	Carboxyl
O	1s	532	1847,3	2,93	630,47782	Zr-O
		533,32	3241,1	2,93	1106,1775	org. C-O
Cl	2p	201,65	298,1	2,29	130,17467	organic Cl
Zr	3d 3/2	183,48	601,4	2,87	209,54704	Zr-O
	3d 5/2	185,79	443,9	4,17	106,45084	

b) HHU-2-Br

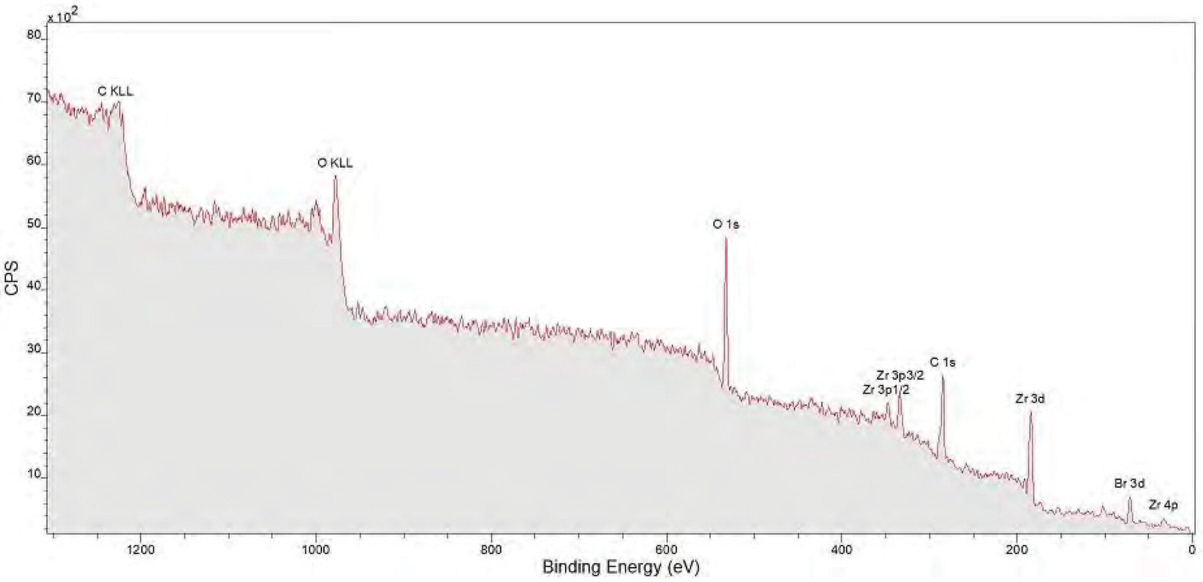

Figure S16. XPS survey spectrum of HHU-2-Br surface.

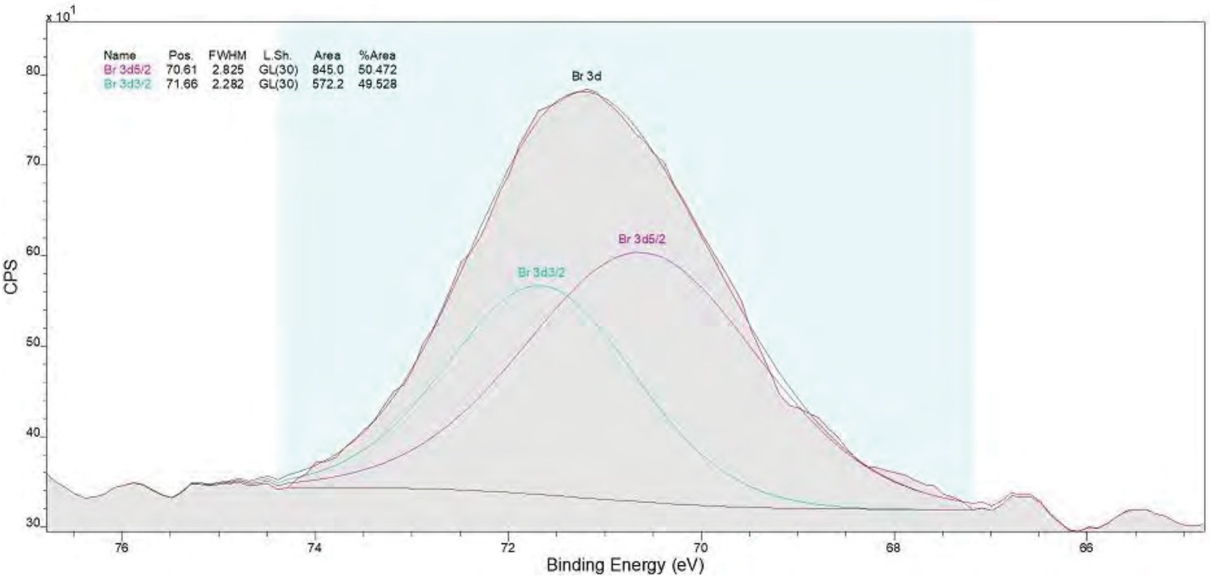

Figure S17. High resolution XPS core-level spectrum of HHU-2-Br in the region of Br 3d.

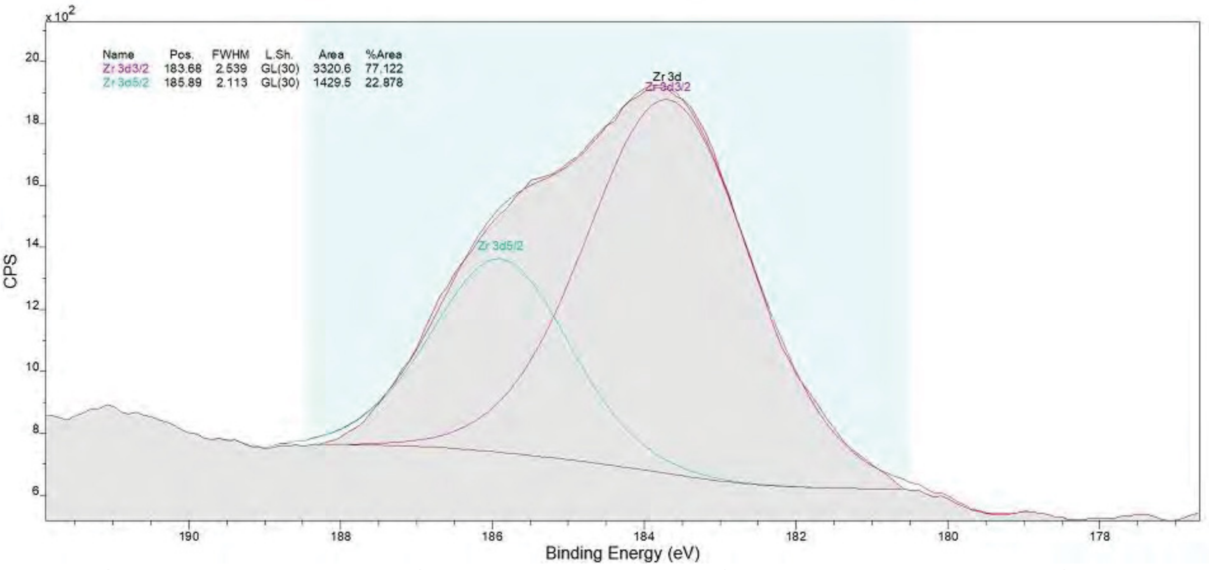

Figure S18. High resolution XPS core-level spectrum of HHU-2-Br in the region of Zr 3d.

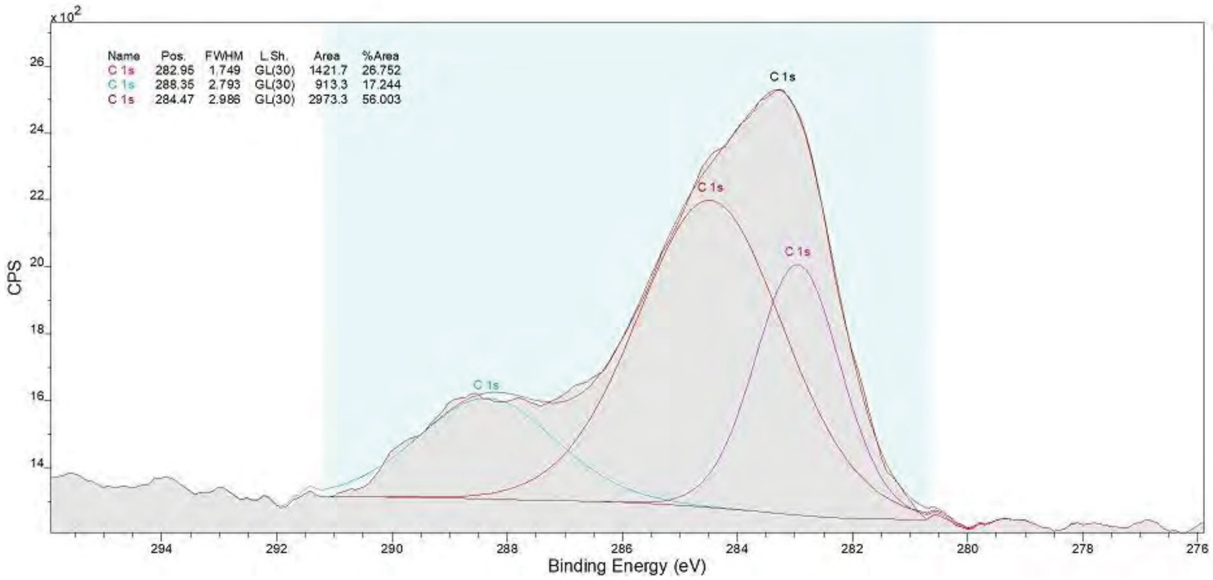

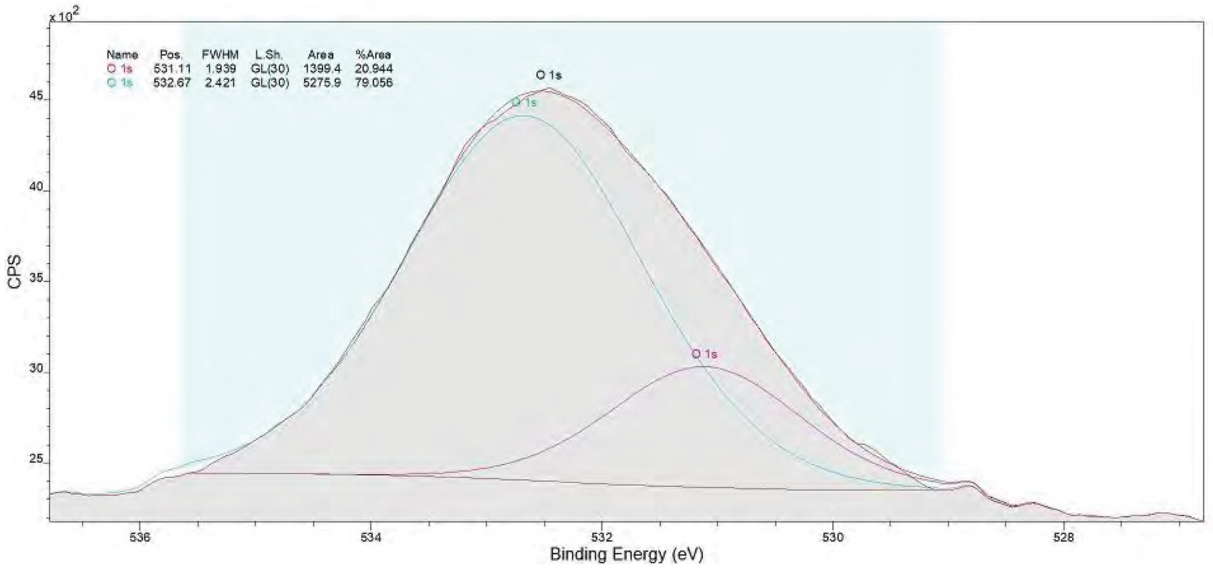

Figure S19. High resolution XPS core-level spectrum of HHU-2-Br in the region of C 1s and O 1s.

Table S2. XP spectrum peak assignments of HHU-2-Br

Element	Orbital	Binding Energy	Area	RSF	Area/RSF	
C	1s	282,95	1421,7	1	1421,7	C=*C*H
		284,47	2973,3	1	2973,3	C=*C*Br
		288,35	913,3	1	913,3	Carboxyl
O	1s	531,11	1399,4	2,93	477,61092	Zr-O
		532,67	5275,9	2,93	1800,6485	org. C-O
Br	3d 5/2	70,61	845	1,68	502,97619	C-Br
	3d 3/2	71,66	572,2	1,16	493,27586	
Zr	3d 3/2	183,68	3320,6	2,87	1157,0035	Zr-O
	3d 5/2	185,89	1429,5	4,17	342,80576	

c) HHU-2-I

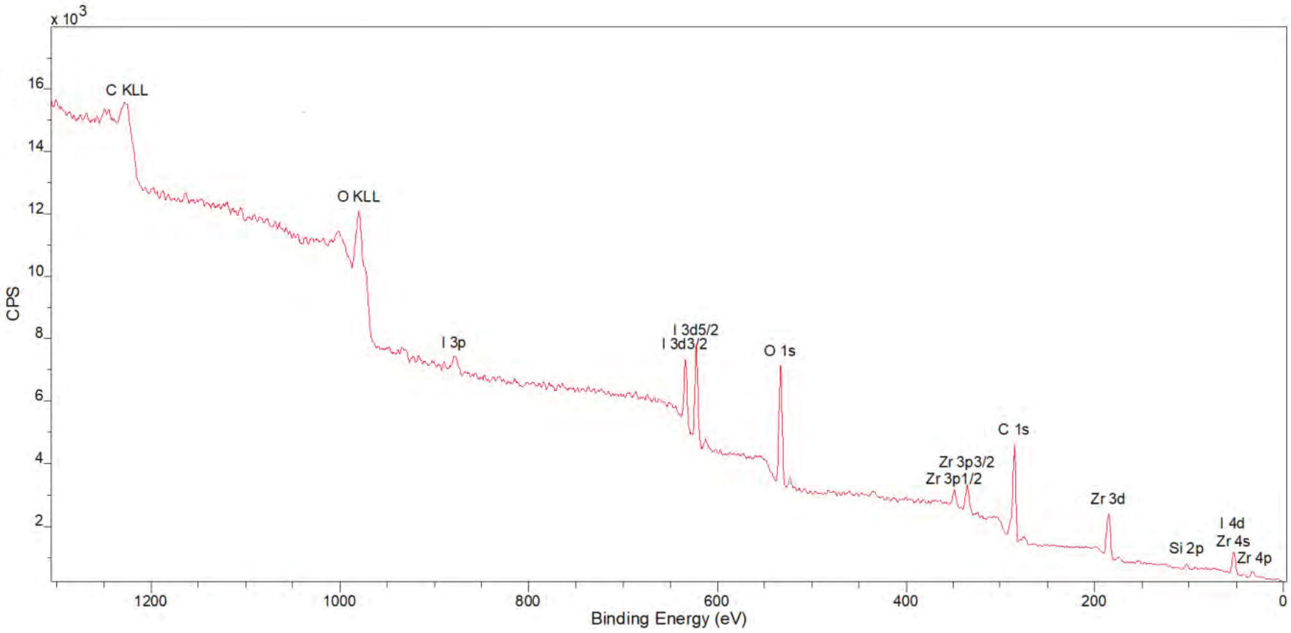

Figure S20. XPS survey spectrum of HHU-2-I surface.

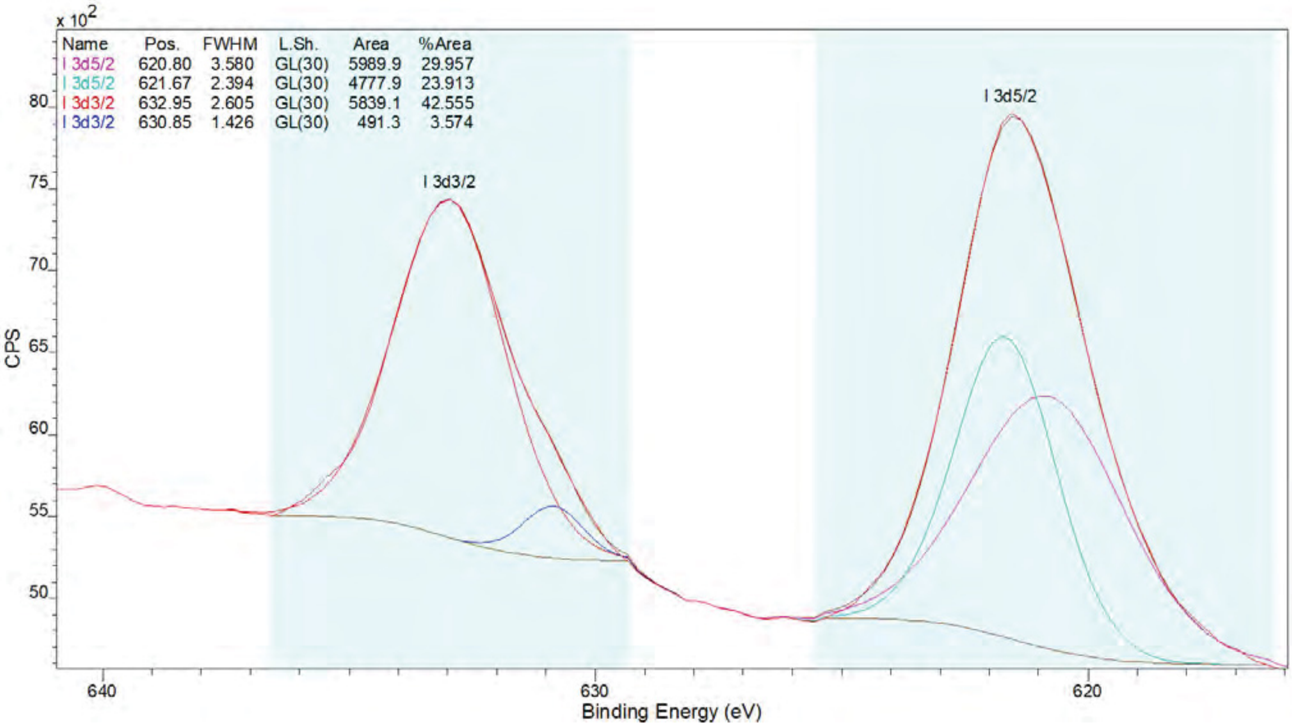

Name	Pos.	FWHM	L.Sh.	Area	%Area
I 3d5/2	620.80	3.580	GL(30)	5989.9	29.957
I 3d5/2	621.67	2.394	GL(30)	4777.9	23.913
I 3d3/2	632.95	2.605	GL(30)	5839.1	42.555
I 3d3/2	630.85	1.426	GL(30)	491.3	3.574

Figure S21. High resolution XPS core-level spectrum of HHU-2-I in the region of I 3d.

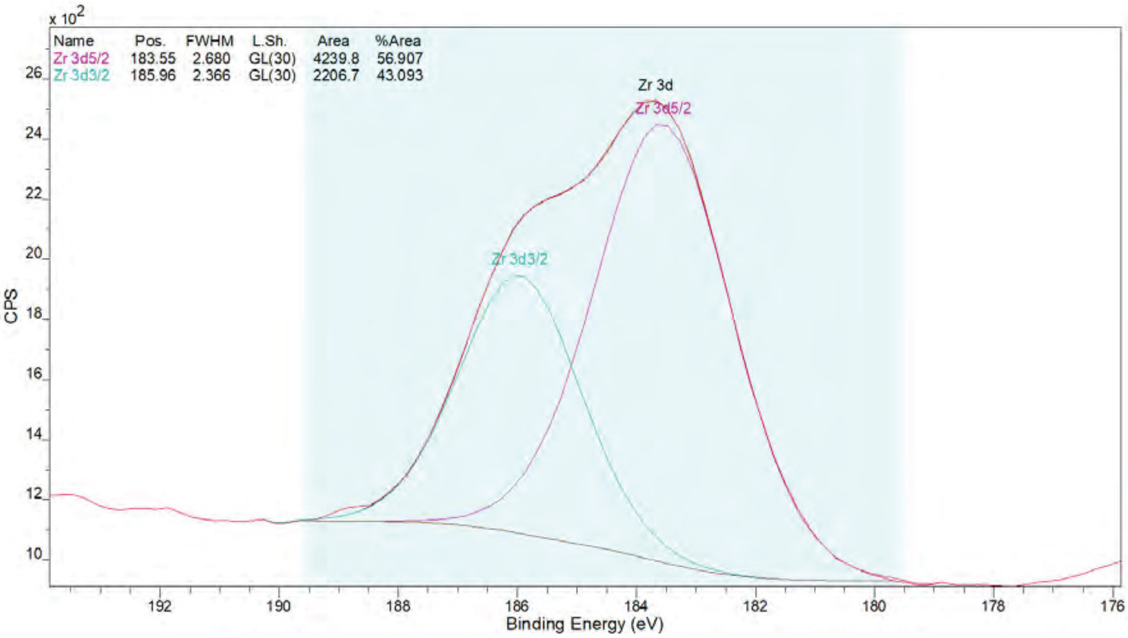

Name	Pos.	FWHM	L.Sh.	Area	%Area
Zr 3d5/2	183.55	2.680	GL(30)	4239.8	56.907
Zr 3d3/2	185.96	2.366	GL(30)	2206.7	43.093

Figure S22. High resolution XPS core-level spectrum of **HHU-2-I** in the region of Zr 3d.

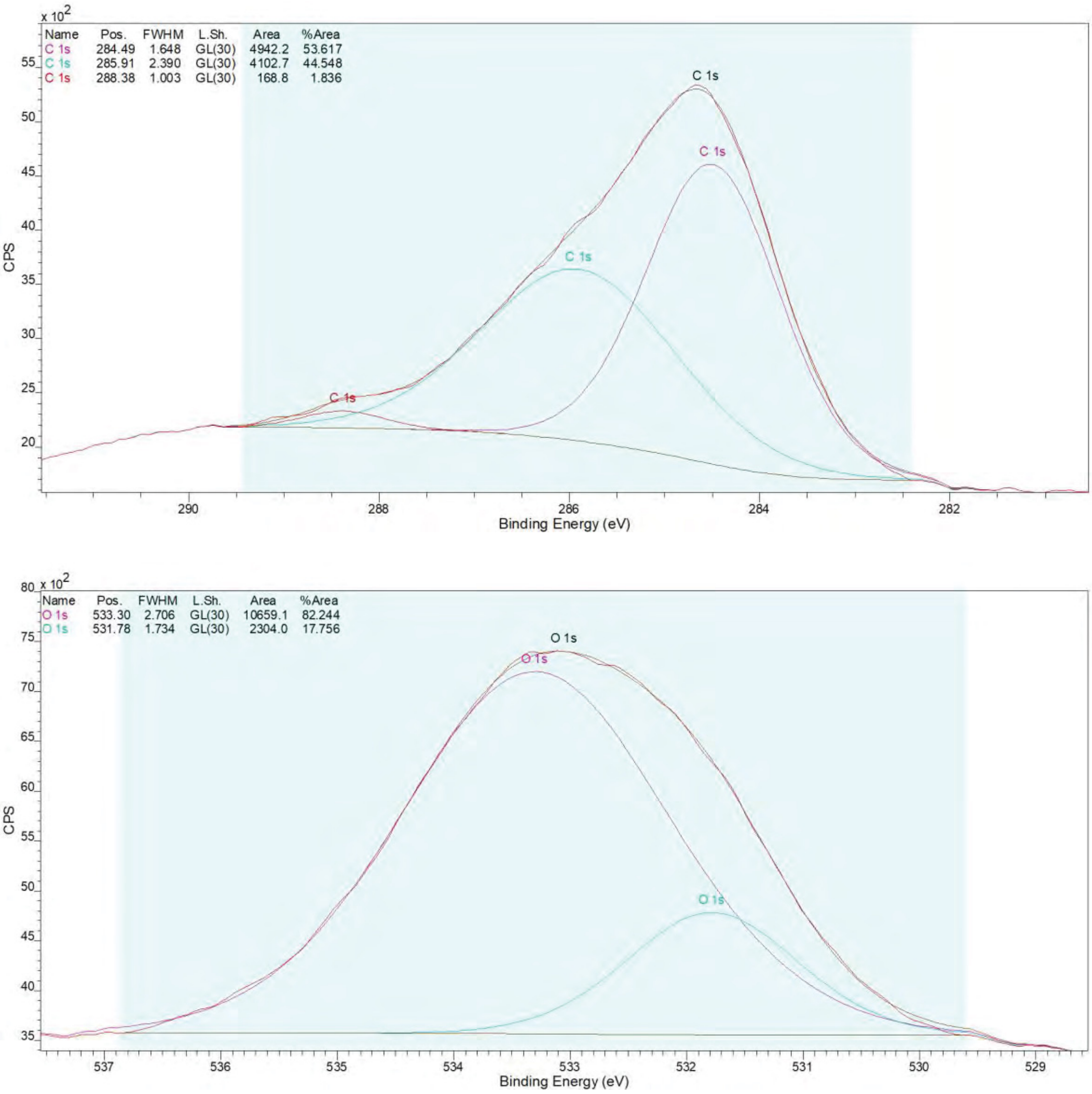

Name	Pos.	FWHM	L.Sh.	Area	%Area
C 1s	284.49	1.648	GL(30)	4942.2	53.617
C 1s	285.91	2.390	GL(30)	4102.7	44.548
C 1s	288.38	1.003	GL(30)	168.8	1.836

Name	Pos.	FWHM	L.Sh.	Area	%Area
O 1s	533.30	2.706	GL(30)	10659.1	82.244
O 1s	531.78	1.734	GL(30)	2304.0	17.756

Figure S23. High resolution XPS core-level spectrum of HHU-2-I in the region of C 1s and O 1s.

Table S3. XP spectrum peak assignments of HHU-2-I

Element	Orbital	Binding Energy	Area	RSF	Area/RSF	
C	1s	284,49	4942,2	1	4942,2	C=*C*H
		285,91	4102,7	1	4102,7	C=*C*-I
		288,38	168,8	1	168,8	Carboxyl
O	1s	531,78	2304	2,93	786,34812	Zr-O
		533,3	10659,1	2,93	3637,9181	org. C-O
I	3d 5/2	620,8	5989,9	19,9	301	TM-I ?
	3d 5/2	621,67	4777,9	19,9	240,09548	C-I
	3d 3/2	630,85	49,3	13,8	3,5724638	
	3d 3/2	632,95	5839,1	13,8	423,12319	C-I
Zr	3d 3/2	183,55	4239,8	2,87	1477,2822	Zr-O
	3d 5/2	185,96	2206,7	4,17	529,18465	

Scanning electron microscopy images and EDX spectroscopy

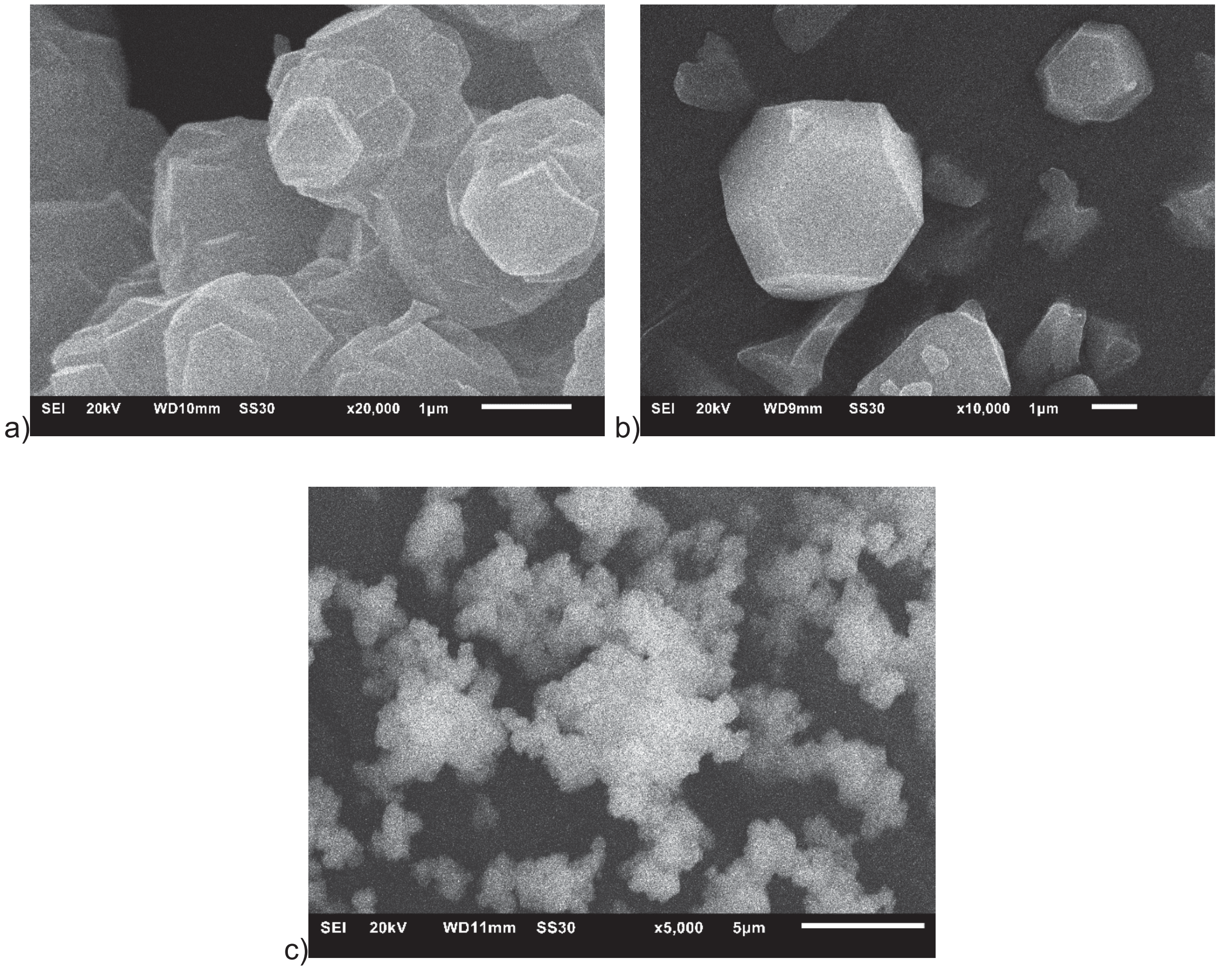

Figure S24. SEM images of (a) HHU-2-Cl, (b) HHU-2-Br and (c) HHU-2-I

a) HHU-2-Cl (Zr-Fum-Cl)

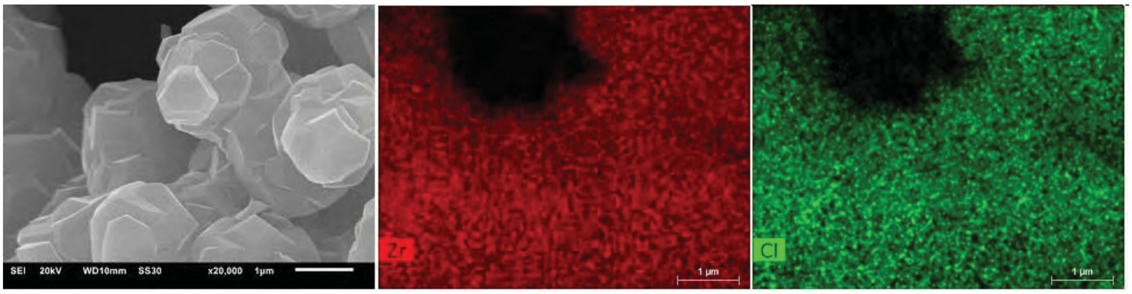

Figure S25. SEM image of microcrystals with Zr- and Cl-EDX elemental maps for HHU-2-Cl showing uniform and concomitant distribution of Zr (red) and Cl (green) over the entire sample.

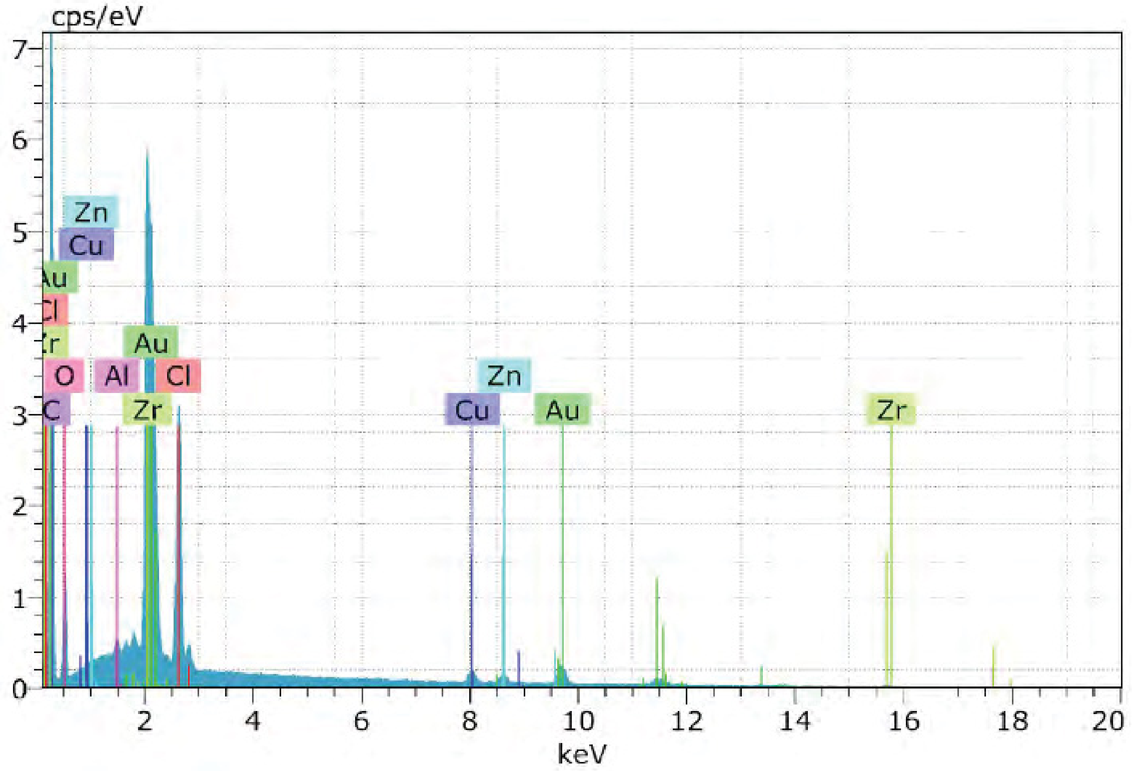

Figure S26. EDX spectrum of HHU-2-Cl

Table S4. Atom and Weight % of C, O, Cl and Zr for **HHU-2-Cl**

Element [a]	atom#	Series	mass fraction [wt.%]	atom fraction [norm. wt.%]	atom fraction [norm. At.%]	standard deviation for wt.% (1 Sigma)
C	6	K-Series	64.19	58	83	5
O	8	K-Series	9.89	9	10	1.6
Zr	40	L-Series	15.97	14.5	2.7	0.6
Cl	17	K-Series	6.07	5.5	2.7	0.2
Au	79	L-Series	11.47	10.5	0.9	0.4
Cu	29	K-Series	1.37	1.24	0.33	0.08
Zn	30	K-Series	1.21	1.10	0.29	0.08
Al	13	K-Series	0.16	0.15	0.01	0.04
		Sum:	110.37	100	100	

[a] The element signals for Au, Cu, Zn, Al stem from the sputtering and brass sample holder.

b) HHU-2-Br (Zr-Fum-Br)

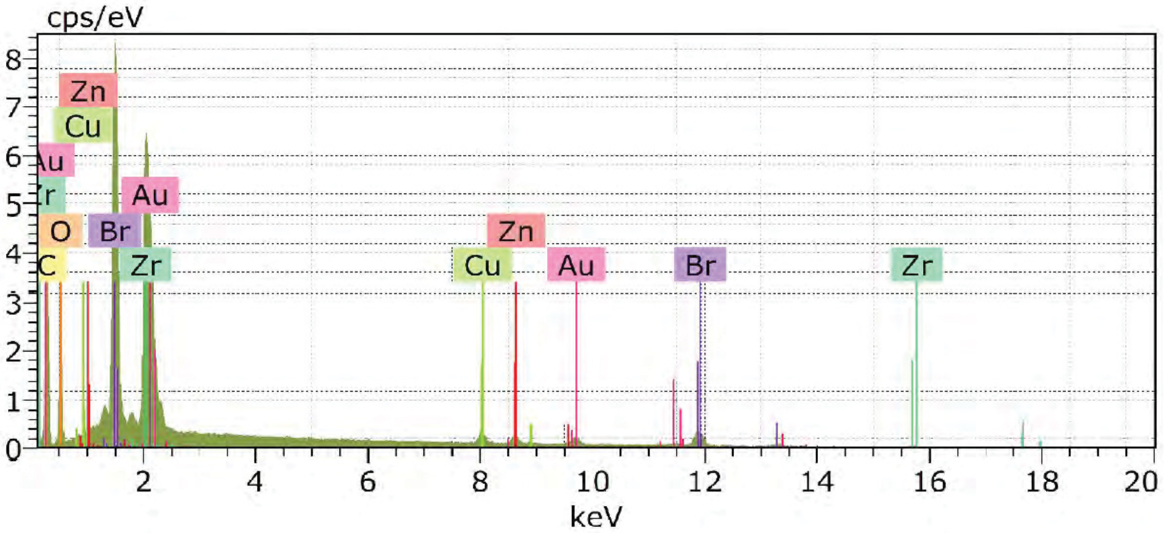

Figure S27. EDX spectrum of HHU-2-Br.

Table S5. Atom and Weight % of C, O, Br and Zr for **HHU-2**-Br

Element [a]	atom#	Series	mass fraction [wt.%]	atom fraction [norm. wt.%]	atom fraction [norm. At.%]	standard deviation for wt.% (1 Sigma)
C	6	K-Series	34	38.2	71.4	5
O	8	K-Series	10.14	11.4	16	1.6
Zr	40	L-Series	18.8	21.1	5.2	0.8
Br	35	K-Series	16.42	18.5	5.2	0.6
Cu	29	K-Series	2.12	2.4	0.8	0.1
Au	79	L-Series	5.9	6.6	0.8	0.3
Zn	30	K-Series	1.6	1.9	0.6	0.1
		Summe:	89.04	100	100	

[a] The element signals for Au, Cu, Zn stem from the sputtering and brass sample holder.

d) HHU-2-I (Zr-Fum-I)

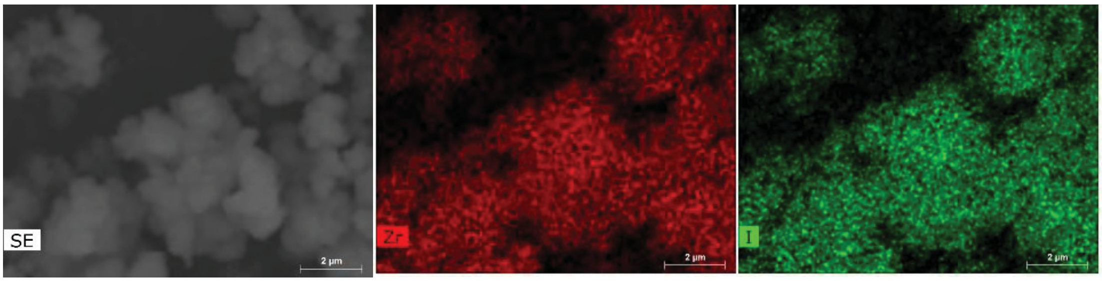

Figure S28. SEM image of microcrystals with Zr- and I-EDX elemental maps for HHU-2-I showing uniform and concomitant distribution of Zr (red) and I (green) over the entire sample.

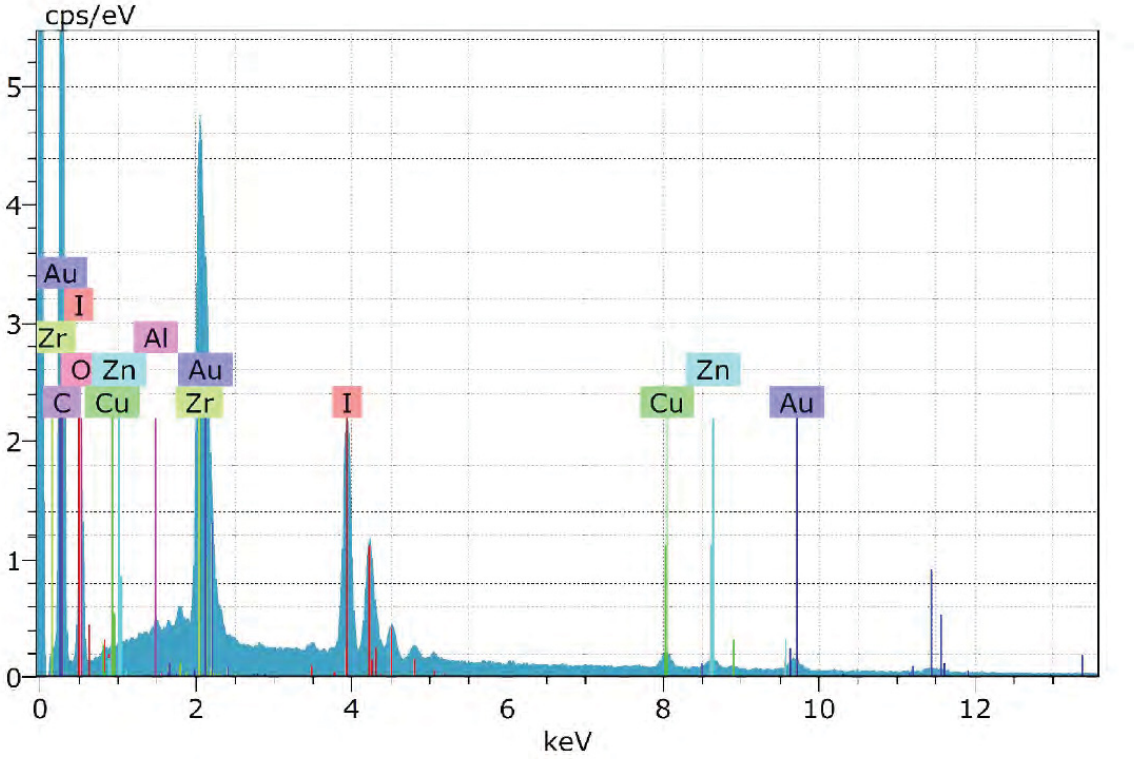

Figure S29. EDX spectrum of HHU-2-I.

Table S6. Atom and Weight % of C, O, I and Zr for HHU-2-I

Element [a]	atom#	Series	mass fraction [wt.%]	atom fraction [norm. wt.%]	atom fraction [norm. At.%]	standard deviation for wt.% (1 Sigma)
C	6	K-Series	42.4	44.2	79.3	5.4
O	8	K-Series	8.13	8.5	11.4	1.3
Zr	40	L-Series	14.4	15	3.6	0.6
I	53	L-Series	19.7	20.5	3.5	0.6
Au	79	L-Series	7.7	8	0.9	0.3
Cu	29	K-Series	2.2	2.3	0.8	0.1
Zn	30	K-Series	1.5	1.5	0.5	0.1
Al	13	K-Series	0.2	0.2	0.1	0.04
		Summe:	96.04	100	100	

[a] The element signals for Au, Cu, Zn stem from the sputtering and brass sample holder.

Nitrogen sorption and porosity of HHU-2-X

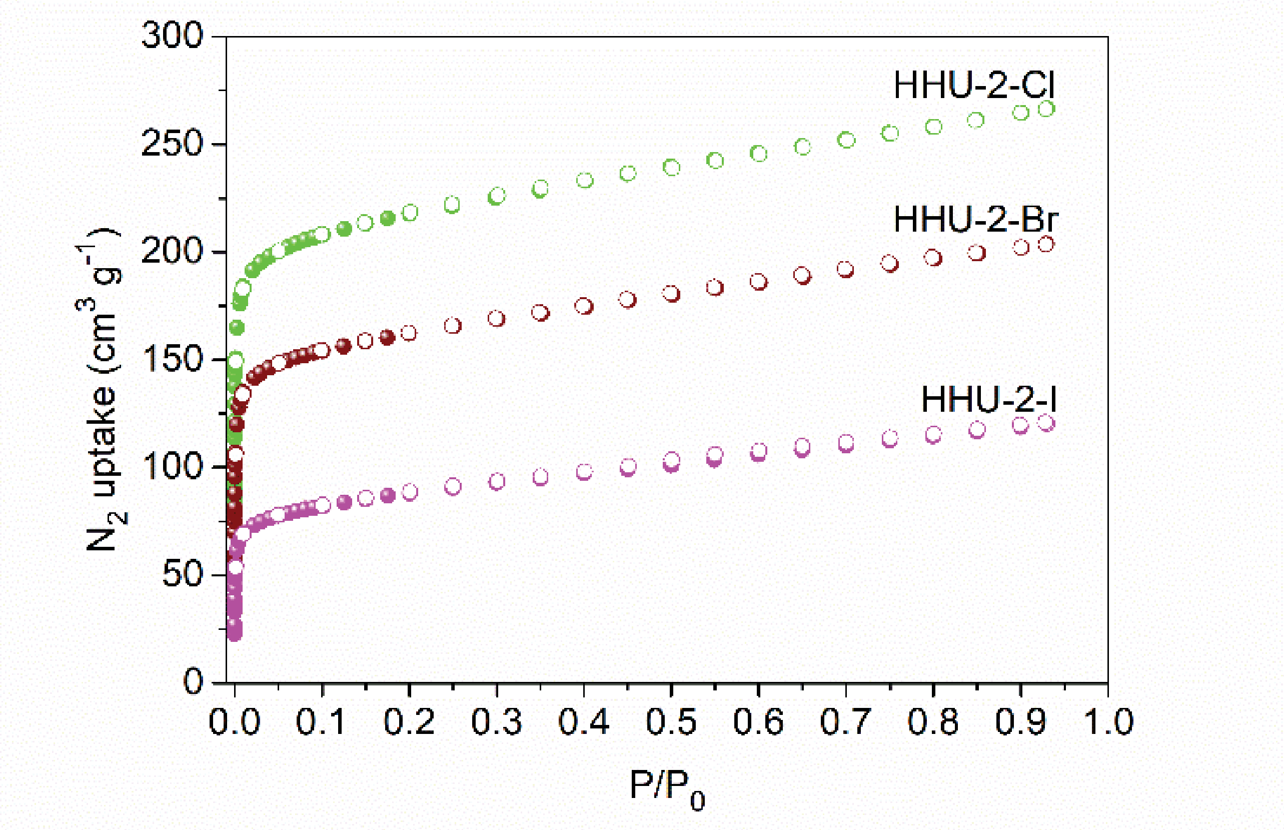

Figure S30. Nitrogen sorption isotherms of HHU-2-Cl, HHU-2-Br and HHU-2-I at 77K (filled symbols adsorption, empty symbols desorption).

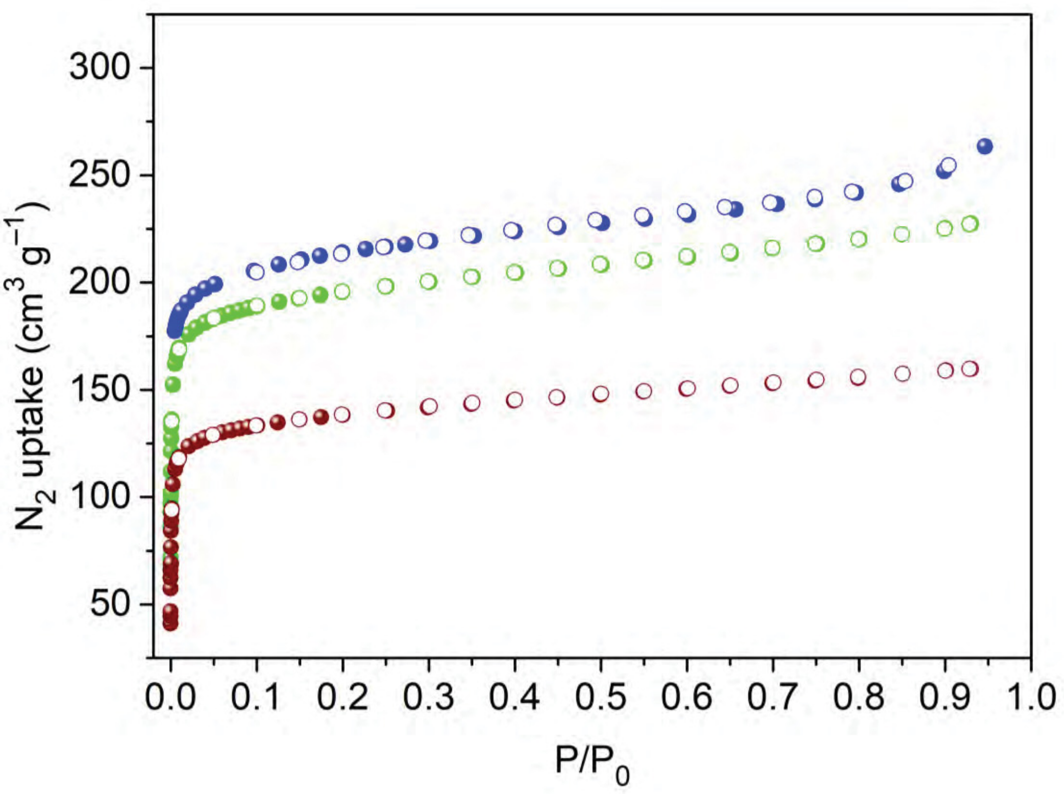

Figure S31. N_2 sorption (77 K) isotherms of MOF-801 (blue) HHU-2-Cl (green) and HHU-2-Br (brown) post SO_2 sorption experiment. adsorption (closed symbols), desorption (open symbols).

Table S7. BET specific surface area of HHU-2-Cl, -Br and MOF-801 before and after SO_2 sorption experiment .

Materials	S_{BET} (m^2 g^{-1}) before SO_2 sorption	S_{BET} (m^2 g^{-1}) after SO_2 sorption	% loss of surface area
HHU-2-Cl	852	767	10.0%
HHU-2-Br	620	530	14.5%
MOF-801	939	827	11.9%

PXRD patterns of HHU-2-Cl and HHU-2-Br obtained from different H_2ADC linker to Zr salt ratios

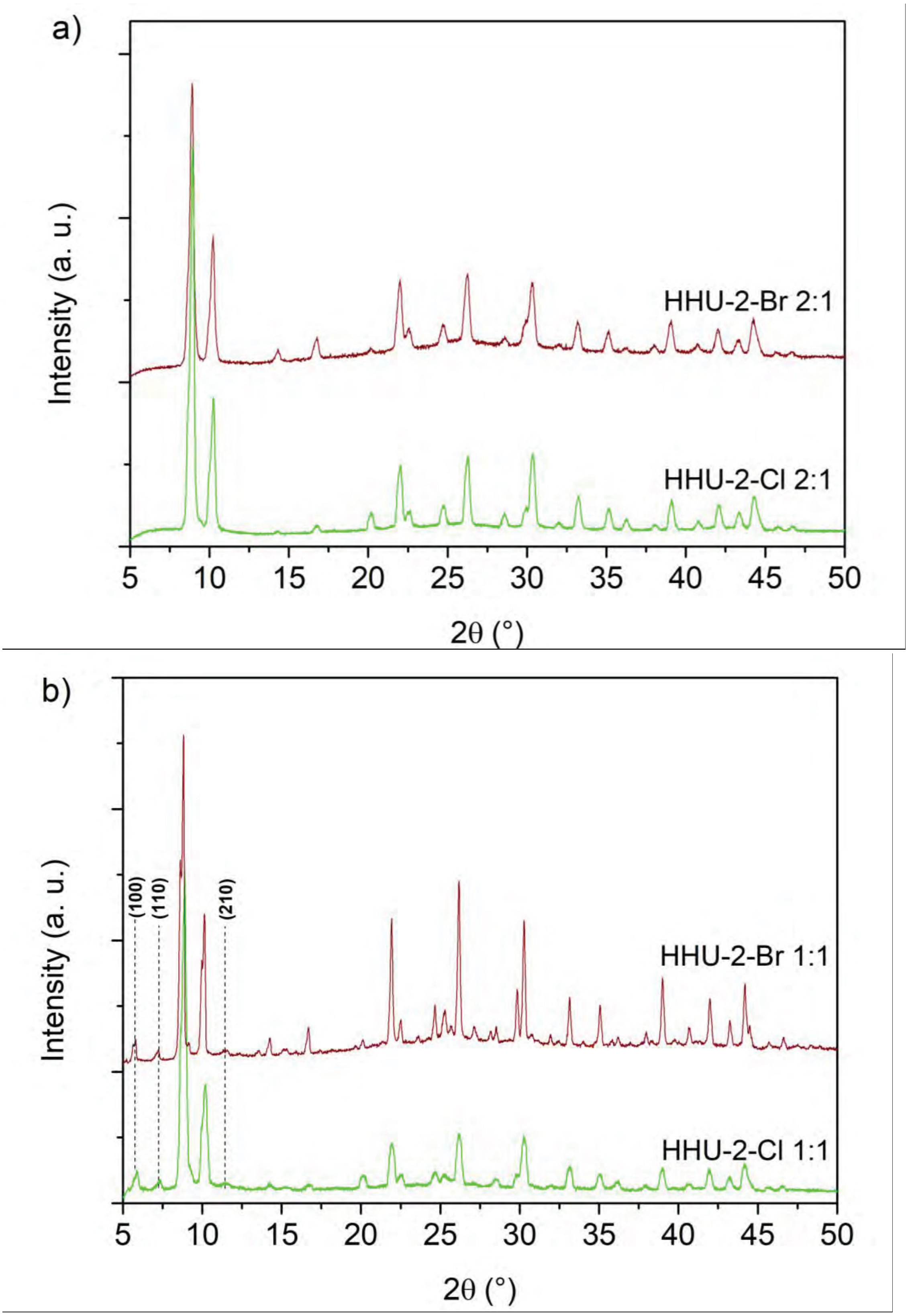

Figure S32. PXRD patterns of HHU-2-X (x = Cl, Br) obtained from reaction mixtures containing (a) 2:1 and (b) 1:1 H_2ADC to Zr-salt molar ratio. 1:1 molar ratio mixture yield materials with **fcu** topology containing correlated defect nanoregions with **reo** topology.

Mechanism of in situ functionalization / Functionalization mechanism

The mechanism of the in-situ transformation of acetylenedicarboxylic acid to halofumarate in the HHU-2-X Zr(IV)-MOFs was investigated. It was observed that the reaction is fast, with first MOF product precipitates forming as early as after 20 min of reaction time (Figure S33). Considering the essential role of acetic acid modulation for this reaction, we suppose that, as previously reported for the modulated synthesis of Zr-MOFs, acetic acid reacts with zirconium ions to form soluble monomeric $\{Zr_6O_4(OH)_4(CH_3COO)_{12}\}$ clusters, producing aqueous HCl, HBr or HI solutions (Scheme 2).[6,78] Then the formation of a Zr-acetylenedicarboxylate MOF can result from acetate to acetylenedicarboxylate ligand exchange on the clusters, followed by hydrohalogenation of the -C≡C- bond in the intermediary Zr-acetylenedicarboxylate MOF (HHU-1, see route 1 in Scheme S1). Alternatively, hydrohalogenation of the -C≡C- bond can take place with acetylenedicarboxylic acid to give halofumaric acid, followed by formation of the new MOF through acetate to halofumarate ligand exchange (see route 2 of Scheme S1). We experimentally observed that MOF formation more likely follows route 2. In fact, a Raman spectroscopy analysis conducted on the first product precipitate for HHU-2-Br obtained after about 20 min of reaction, shows the absence of the -C≡C- band at 2225 cm^{-1} (Figure S34 in SI). This strongly suggests that the triple bond is already transformed when the MOF is forming. A post-synthetic hydrohalogenation according to route 1 should have still shown some unreacted -C≡C- bonds. Further, the hydrohalogenation is trans-stereoselective and the addition reaction does not proceed to the single bond. Trans configuration is necessary for the **fcu** net topology of the obtained MOF. This topology is in principle obtained with more or less linear linkers like fumarate. A cis addition would yield a V-shaped thermodynamically less stable halomaleate isomer linker. It is rationally not expected that a maleate linker or mixture with fumarate yields a unique **fcu-** phase MOF topology. Furthermore, the rapid transformation of acetylenedicarboxylic acid into chlorofumaric acid (as the more thermodynamically stable trans-adduct) was previously reported, when reacting H_2ADC with $LaCl_3$ in aqueous solution.[9]

Scheme S1. Mechanism of formation for halofumarate-based Zr-MOF from intermediate Zr-acetate clusters and acetylenedicarboxylic acid by in-situ hydrohalogenation of the acid before MOF formation (highlighted in yellow).

$$6\ ZrX_4 + 6\ H_3CCOOH + 20\ H_2O \longrightarrow [Zr_6O_4(OH)_4(OOCCH_3)_{12}] + 24\ HX$$

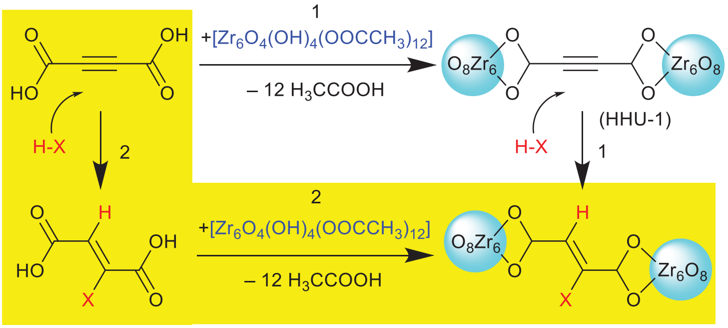

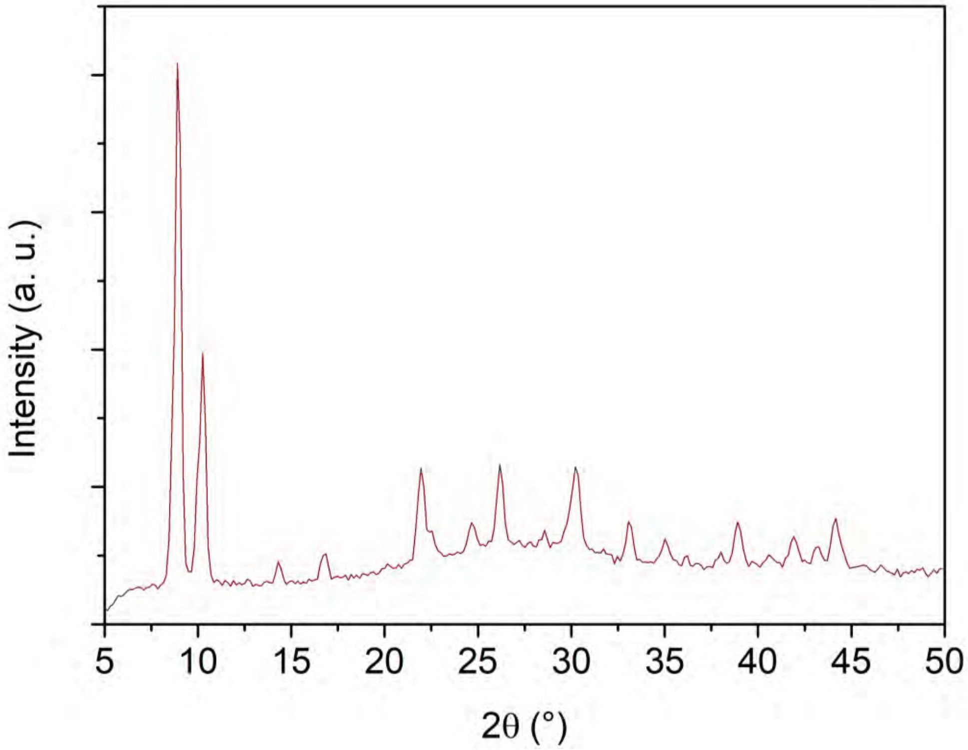

Figure S33. PXRD pattern of HHU-2-Br sample collected after 20 min reaction time. The rapid MOF formation with high crystallinity is observed.

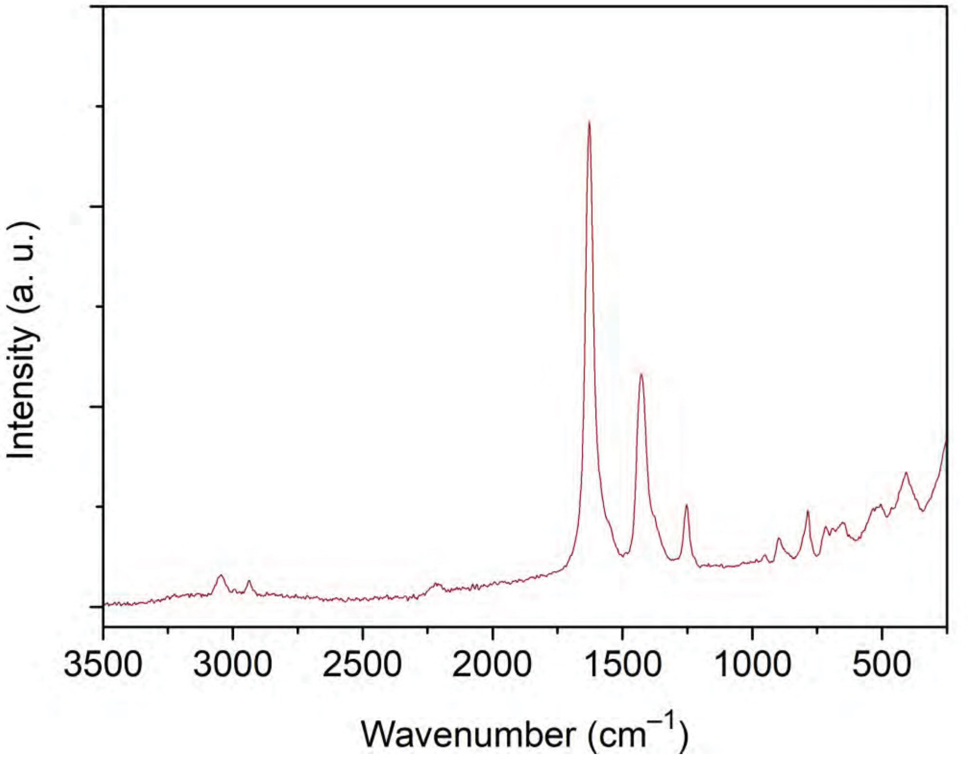

Figure S34. Raman spectrum of HHU-2-Br sample collected after 20 min reaction time. The strong band of -C≡C- triple bond at 2250 cm^{-1} Raman shift has already disappeared after 20 min reaction.

Water sorption of HHU-X and zirconium fumarate, MOF-801

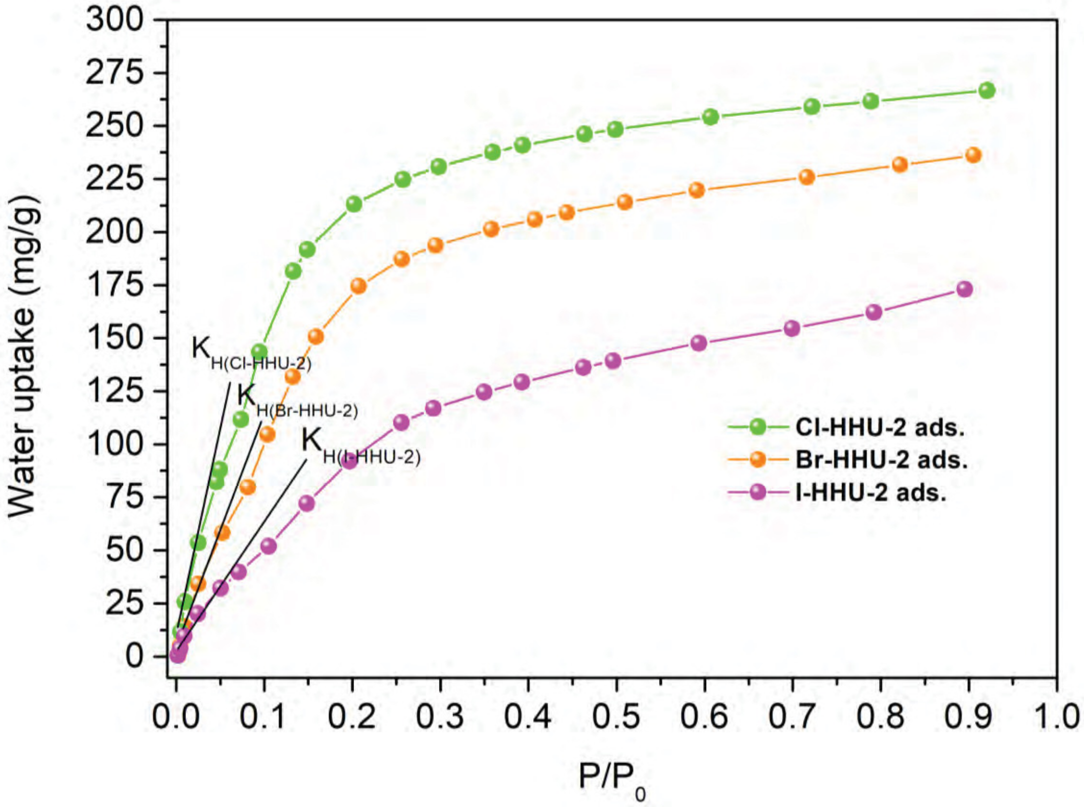

Figure S35. Water adsorption isotherms of HHU-2-X (X = Cl, Br, I) showing Henry's constants of respective MOFs, that is the initial slope of isotherms.

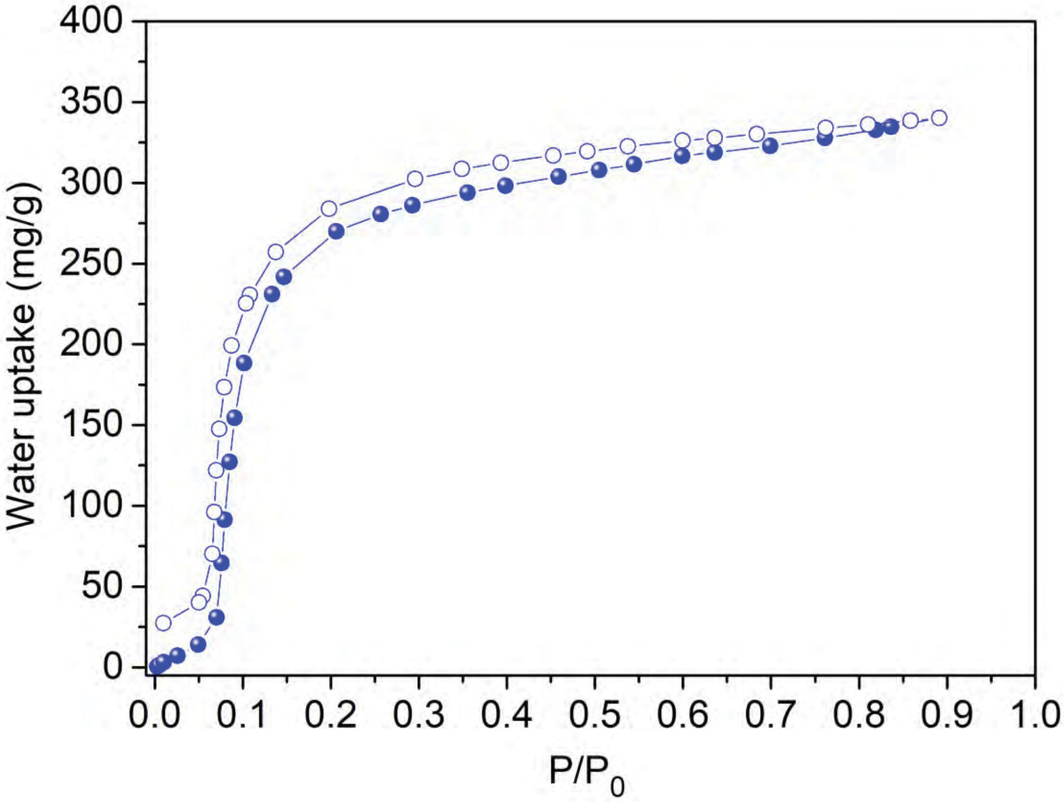

Figure S36. Water sorption isotherm of zirconium fumarate, MOF-801. The isotherm displays a type V S-shaped isotherm.

Hydrothermal and chemical stabilities

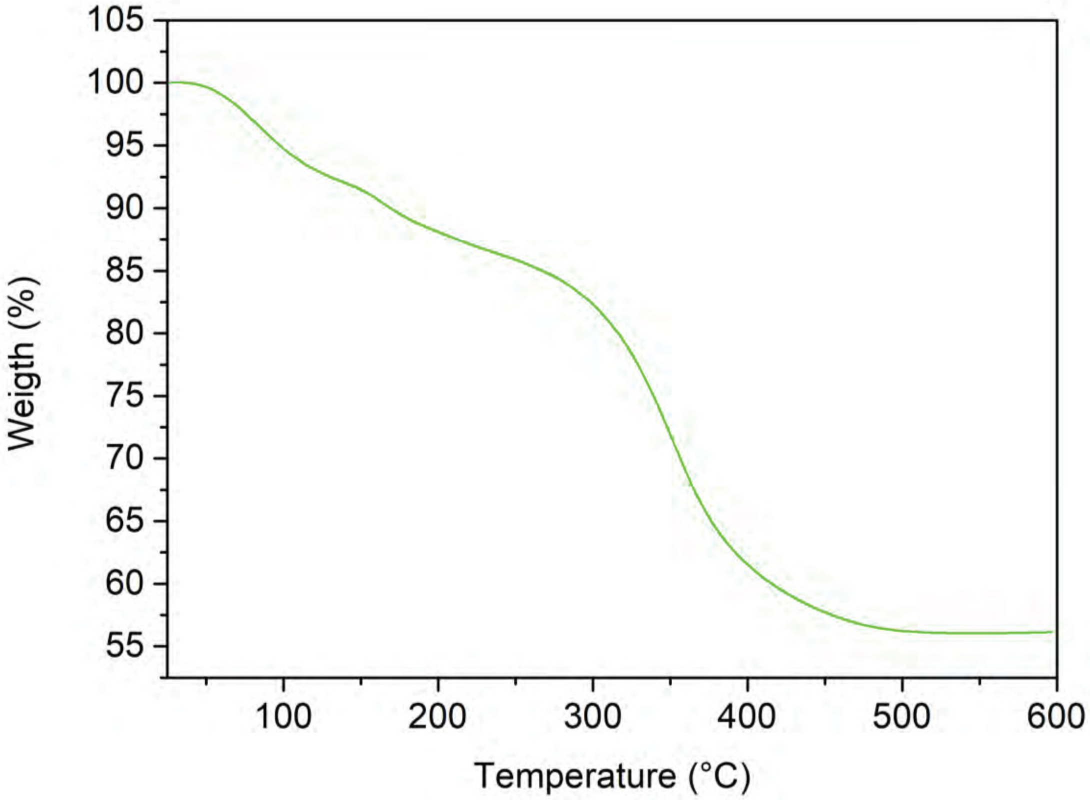

Figure S37. TG trace of HHU-2-Cl (Zr-Fum-Cl)

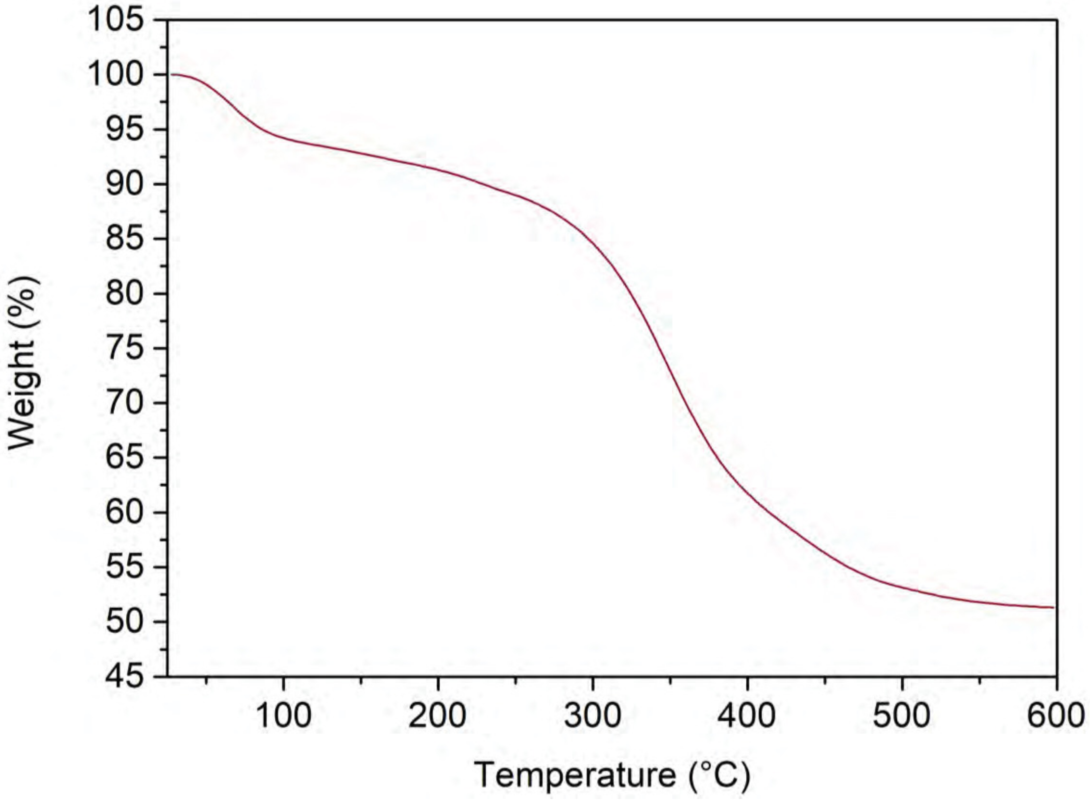

Figure S38. TG trace of HHU-2-Br.

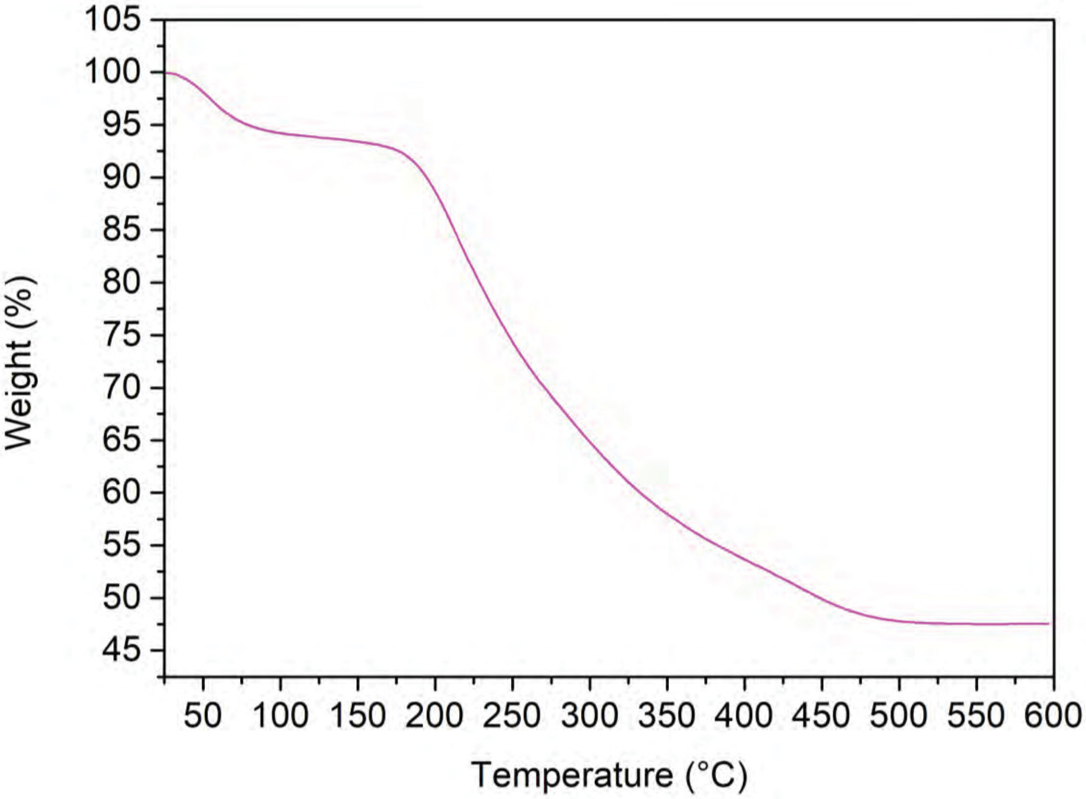

Figure S39. TG trace of HHU-2-I.

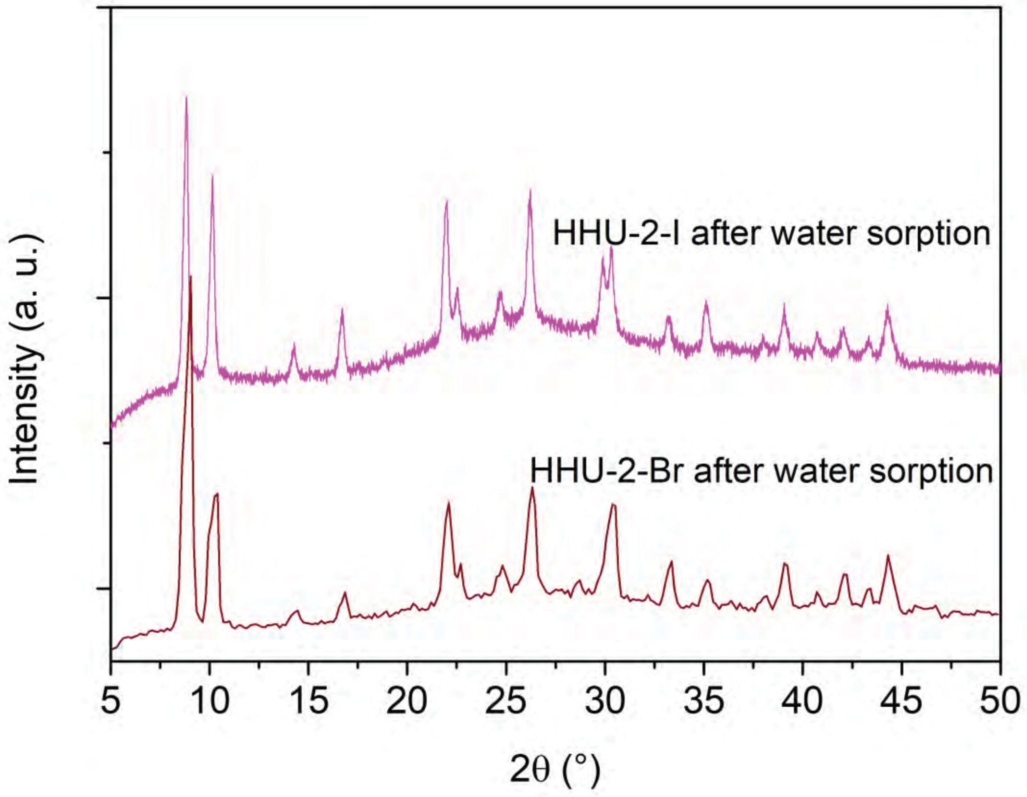

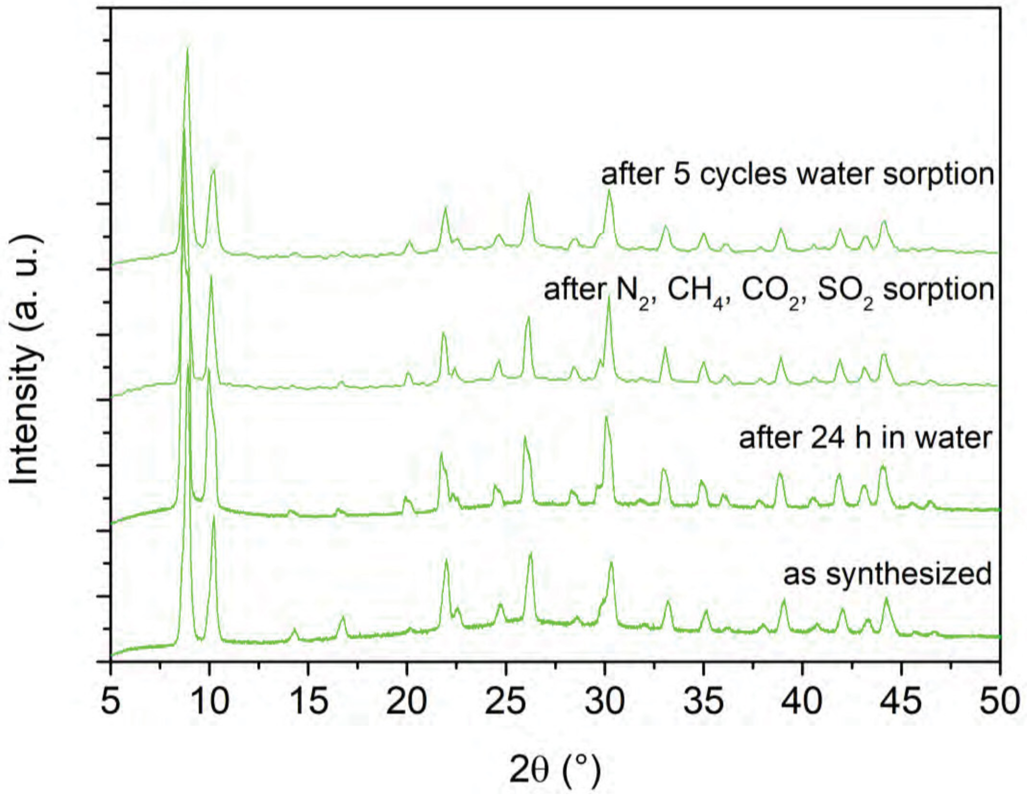

Figure S40. PXRD patterns of HHU-2-Cl after five cycles water sorption, after gases sorption and after stirring 24 h in water at room temperature. The sample retains its crystallinity after all these experiments, which ascertains its hydrothermal/ chemical stability.

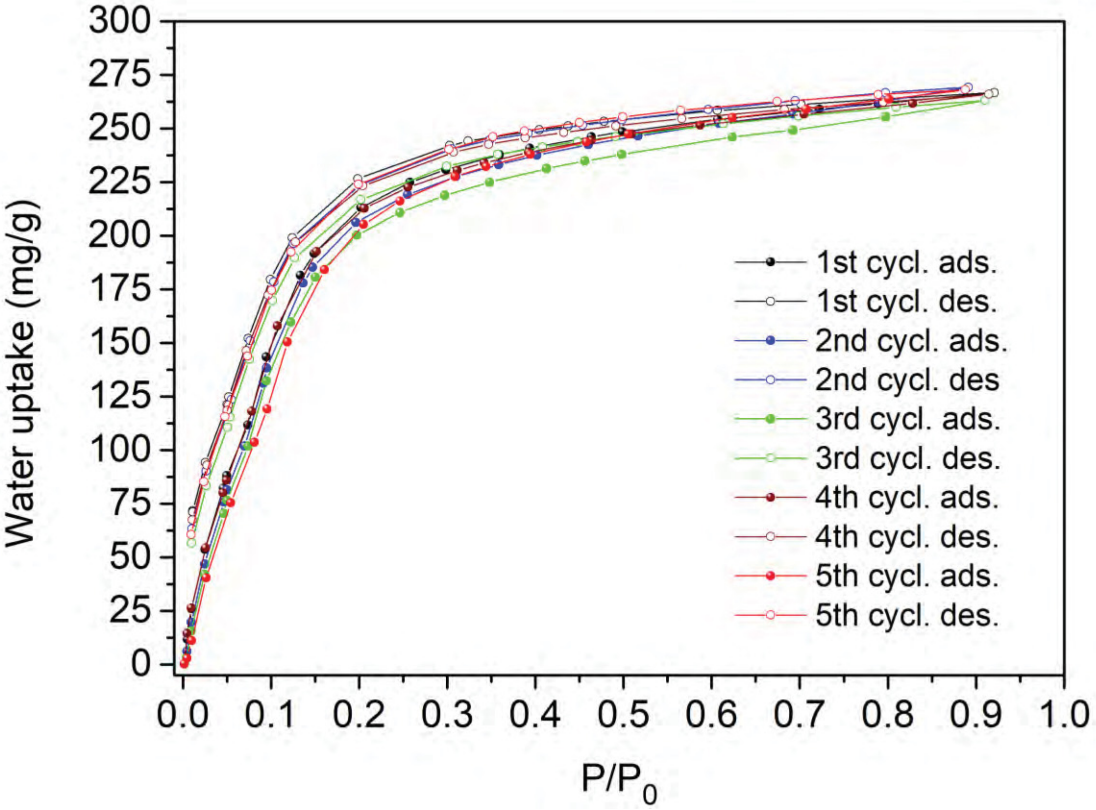

Figure S41. Cycle performance of water uptake in HHU-2-Cl at 20 °C. The sample was regenerated by evacuation for 1 h at 100 °C under vacuum between subsequent cycles.

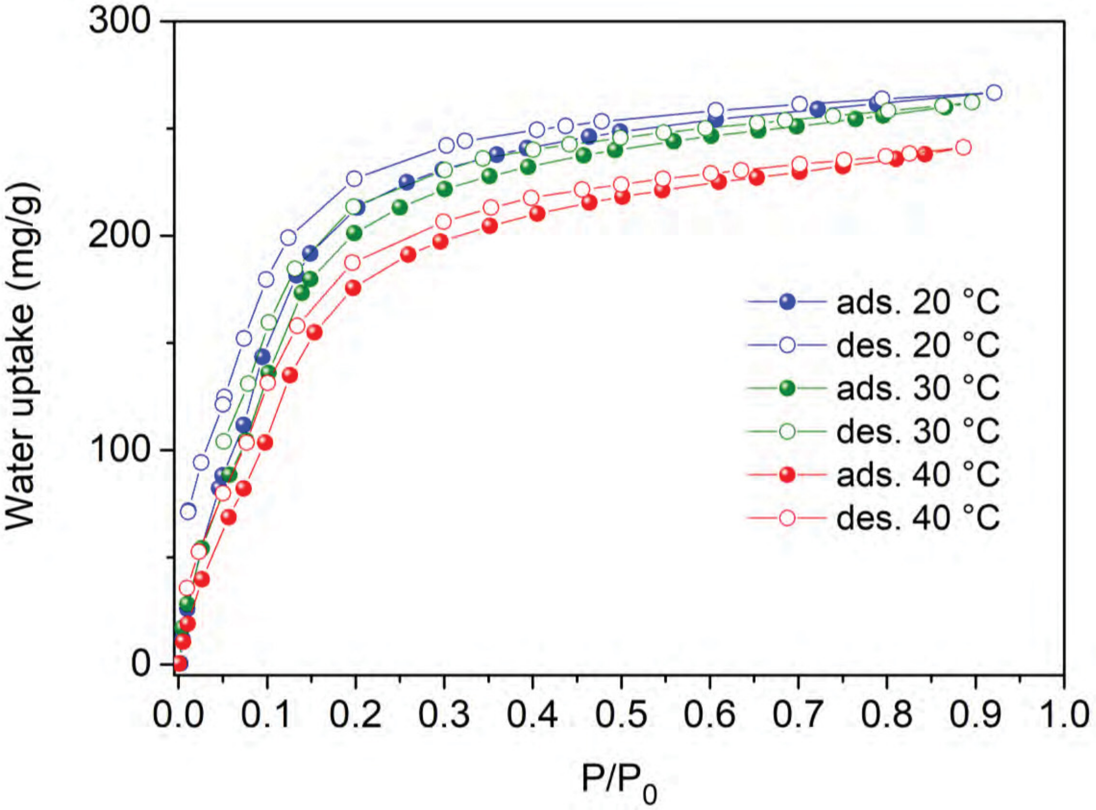

Figure S42a. Water sorption isotherms of HHU-2-Cl measured at 20, 30 and 40 °C.

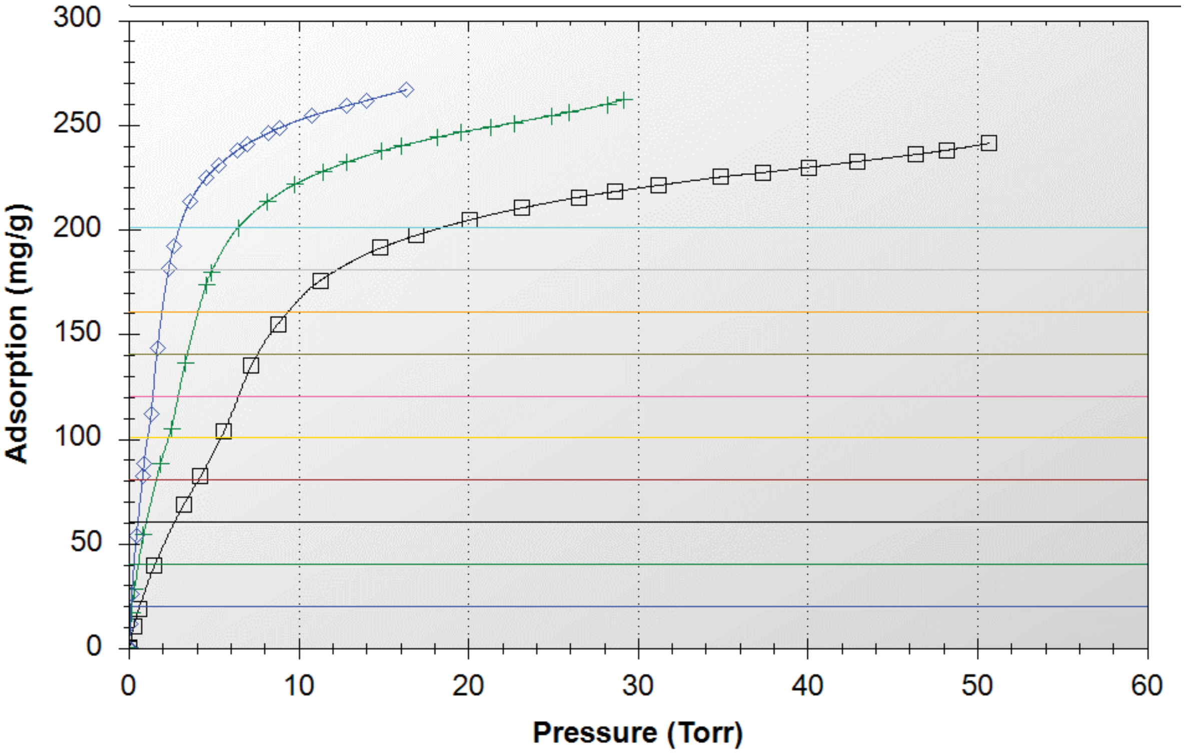

Figure S42b. Water adsorption isotherms of HHU-2-Cl at 20 (blue), 30 (green) and 40 °C (black) used for determination of the isosteric heat of adsorption. Symbols represent experimental isotherms and line represents isotherms fits.

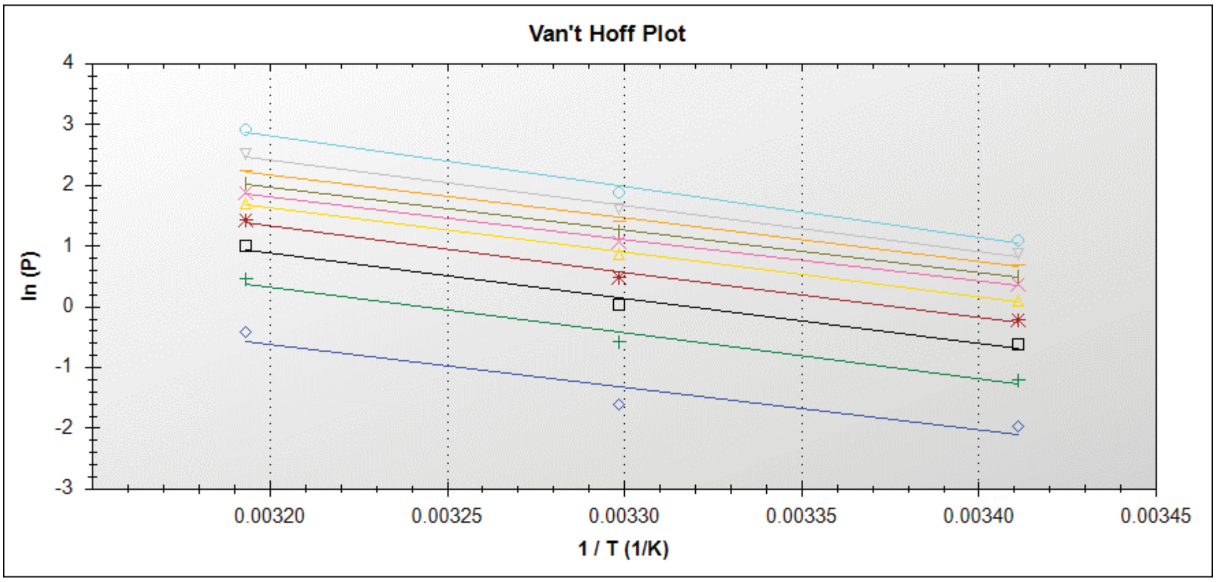

Figure S42c. Water adsorption isosters for HHU-2-Cl, confirming the accuracy of the heat of adsorption as evidenced by the linearity in the isosters.

Heat of water adsorption and heat storage capacity for application in adsorption thermal batteries

$$\Delta H_{ads} = -R\ln\left(\frac{P_2}{P_1}\right)\frac{T_1 \cdot T_2}{T_2 - T_1} \qquad \text{(S3)}$$

where R is the ideal gas constant, P_1 and P_2 are two pressures of same isostere obtained at adsorption temperatures T_1 and T_2 respectively.

$$C_{HS} = \frac{\Delta H_{ads} \cdot \Delta w}{M_w} \qquad \text{(S4)}$$

where ΔH_{ads} is the heat of water adsorption, Δw is the working capacity and M_w is the molar weight of water.

$$C_{HS} = \frac{\Delta H_{ads} \cdot \Delta w}{M_w} = \frac{60\ kJ\ mol^{-1} \cdot 0.15\ g\ g^{-1}}{0.018\ kg\ mol^{-1}} = 500\ kJ\ kg^{-1} = \frac{500}{3600}\ kWh\ kg^{-1} = 0.138\ kWh\ kg^{-1}$$

The heat Q stored in the material is proportional to the heat storage capacity C_{HS} and mass $m_{adsorbent}$ of the material.

$$\mathrm{Q} = m_{adsorbent} \times C_{HS}$$

The calculated mass needed to provide a targeted heat Q = 2.5 *kWh* is therefore:

$$m_{adsorbent} = \frac{\mathrm{Q}}{C_{HS}} = \frac{2.5\ kWh}{0.138\ kWh\ kg^{-1}} = 18.11\ kg$$

The heat storage capability of MOF-801 was estimated to 1.8 kWh for an arbitrary adsorbent mass of 15 kg.[6] However, the calculation was performed based on an assumed efficiency of 65 %, which makes a direct comparison with the result obtained for HHU-2-Cl not evident.

Kinetics of water adsorption for HHU-2-Cl

The adsorption kinetics was estimated using the Fickian diffusion (FD) model.[10] The FD model gives a relation between the uptake and time for which simplified expressions are given by equation S1 at long times[11] and by equation S2 at short times.[12]

$$\frac{m}{m_s} = 1 - \frac{6}{\pi^2} exp\left(-\frac{\pi^2 D \cdot t}{R_p^2}\right) \qquad \text{(S1)}$$

$$\frac{m}{m_s} = 6\sqrt{\frac{D \cdot t}{\pi R_p^2}} \qquad \text{(S2)}$$

where D is the apparent water diffusivity and R_p is the average radius of adsorbent. $k_D = D/R_p^2$ is the diffusion constant.

Plots of $ln(1\text{-}m/m_s)$ versus time (Figure S43 in SI) and m/m_s versus square root of time (Figure S43 in SI), turn out to be both linear in the long time and short time region. Thus, the kinetics of water adsorption on HHU-2-Cl is consistent with the FD model. The diffusion constant k_D after ~2500 s (41 min) was estimated from the slope of the $ln(1\text{-}m/m_s)$ *vs t* plot to about 4.22×10^{-5} s^{-1} (see below for calculation details). At the very beginning up to ~ 36 min the diffusion constant k_D is about 2.80×10^{-5} s^{-1}. The corresponding diffusivity using the average particle radius R_p of 5.5 µm is 1.27×10^{-11} cm^2 s^{-1} and 8.43×10^{-12} cm^2 s^{-1} for short and long time adsorption respectively.

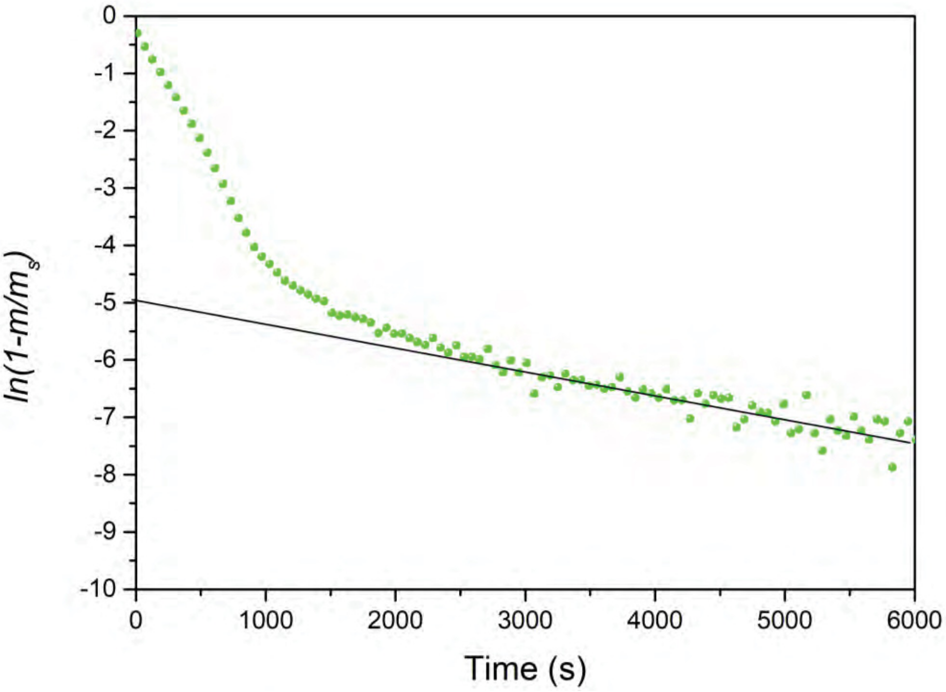

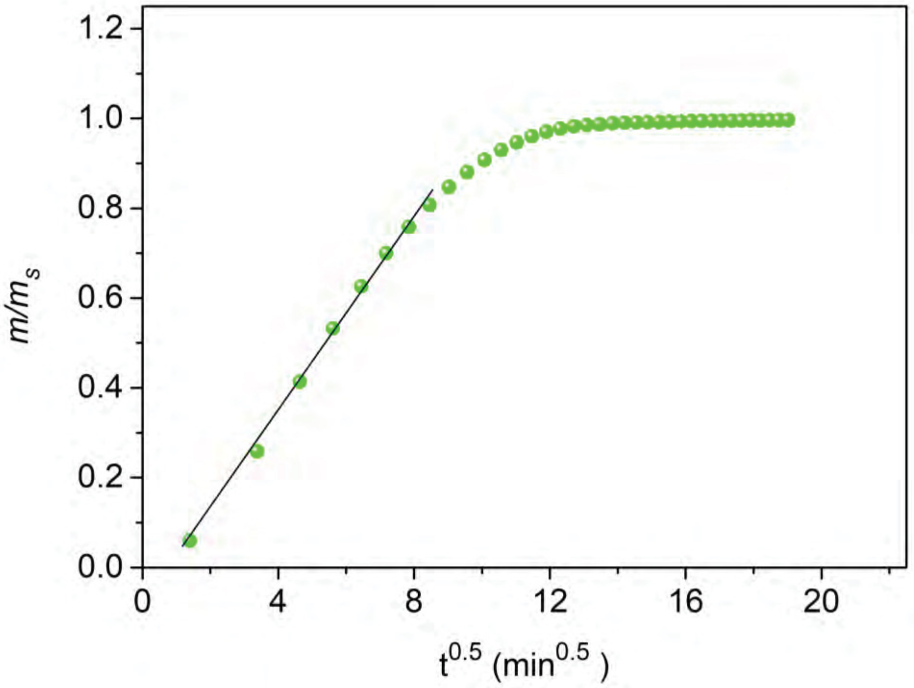

Figure S43. (Top) plot of *ln(1-m/m$_s$)* versus adsorption time and (Bottom) plot of fractional mass uptake versus square root adsorption time for the HHU-2-Cl-water pair at 25 °C and 30 % RH.

The Fickian diffusion (FD) model[10] is used to estimate the adsorption kinetics of assorted adsorbent-refrigerant pair. The simplified expression of the uptake dependence with time is given by equation S1 in the long time region:[11] $\frac{m}{m_s} = 1 - \frac{6}{\pi^2} exp\left(-\frac{\pi^2 D\cdot t}{R_p^2}\right)$ (S1), where t is the adsorption time. m and m_s are mass of water adsorbed at time t and at saturation (m_∞) respectively. D is the apparent water diffusivity and R_p is the average adsorbent grains radius.

Linearization of equation 1 gives equation S2: $ln\left(1 - \frac{m}{m_s}\right) = ln\left(\frac{6}{\pi^2}\right) - \pi^2\left(\frac{D}{R_p^2}\right)t$ (S2), where $k_D = \frac{D}{R_p^2}$ is the diffusion time constant.

The plot of $ln\left(1 - \frac{m}{m_s}\right)$ $vs\ t$ gives at long adsorption times a straight line of slope

$$-\pi^2\left(\frac{D}{R_p^2}\right) = -\pi^2 k_D = \frac{\Delta\left[ln\left(1-\frac{m}{m_s}\right)\right]}{\Delta t} = \frac{-2.5}{6000} = -4.16 \times 10^{-4}\ s^{-1}$$

and therefore $k_D = \frac{D}{R_p^2} = \frac{4.16\times10^{-4}\ s^{-1}}{\pi^2} = 4.22 \times 10^{-5}\ s^{-1};\ D = k_D \times R_p^2 = 1.27 \times 10^{-11}\ \mathrm{cm\ s^{-1}}$

The linearity deviation of $ln\left(1 - \frac{m}{m_s}\right)$ $vs\ t$ plot at the early stage of adsorption was reported to be due to effects of generation of heat adsorption at early stage of the adsorption.[12] The early stage then corresponds to a non-isothermal kinetics.

The slope *A* from the short-time equation for the plot of $\frac{m}{m_s}$ $vs\ \sqrt{t}$

$$\frac{m}{m_s} = 6\sqrt{\frac{D\cdot t}{\pi R_p^2}} = A \times \sqrt{t}$$

$$A = \frac{6}{\sqrt{\pi}}\sqrt{\frac{D}{R_p^2}} = \frac{6}{\sqrt{\pi}}\sqrt{k_D} = \frac{\Delta\left(\frac{m}{m_s}\right)}{\Delta\left(\sqrt{t}\right)} = \frac{0.64346}{5.79171} = 0.111\ min^{-0.5}$$

$k_D = \frac{\pi A^2}{36} = 0.0016\ min^{-1} = 2.8 \times 10^{-5}\ s^{-1};\ D = k_D \times R_p^2 = 8.47 \times 10^{-12}\ \mathrm{cm\ s^{-1}}$ (the average particle radius of HHU-2-Cl was estimated to 5.5 µm from the following SEM image:

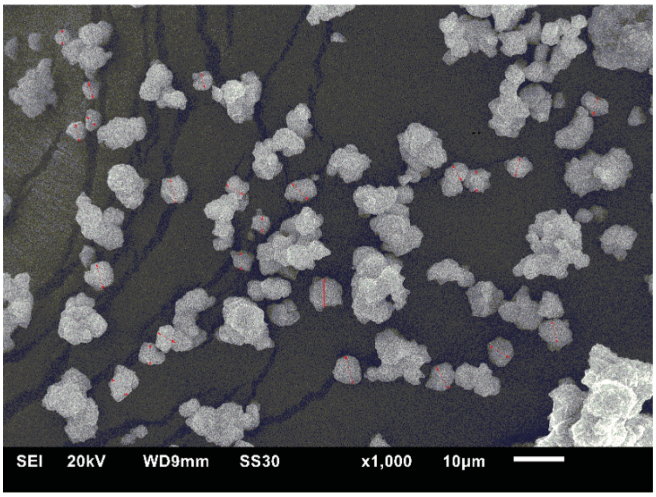

Gas sorption properties of HHU-2-X

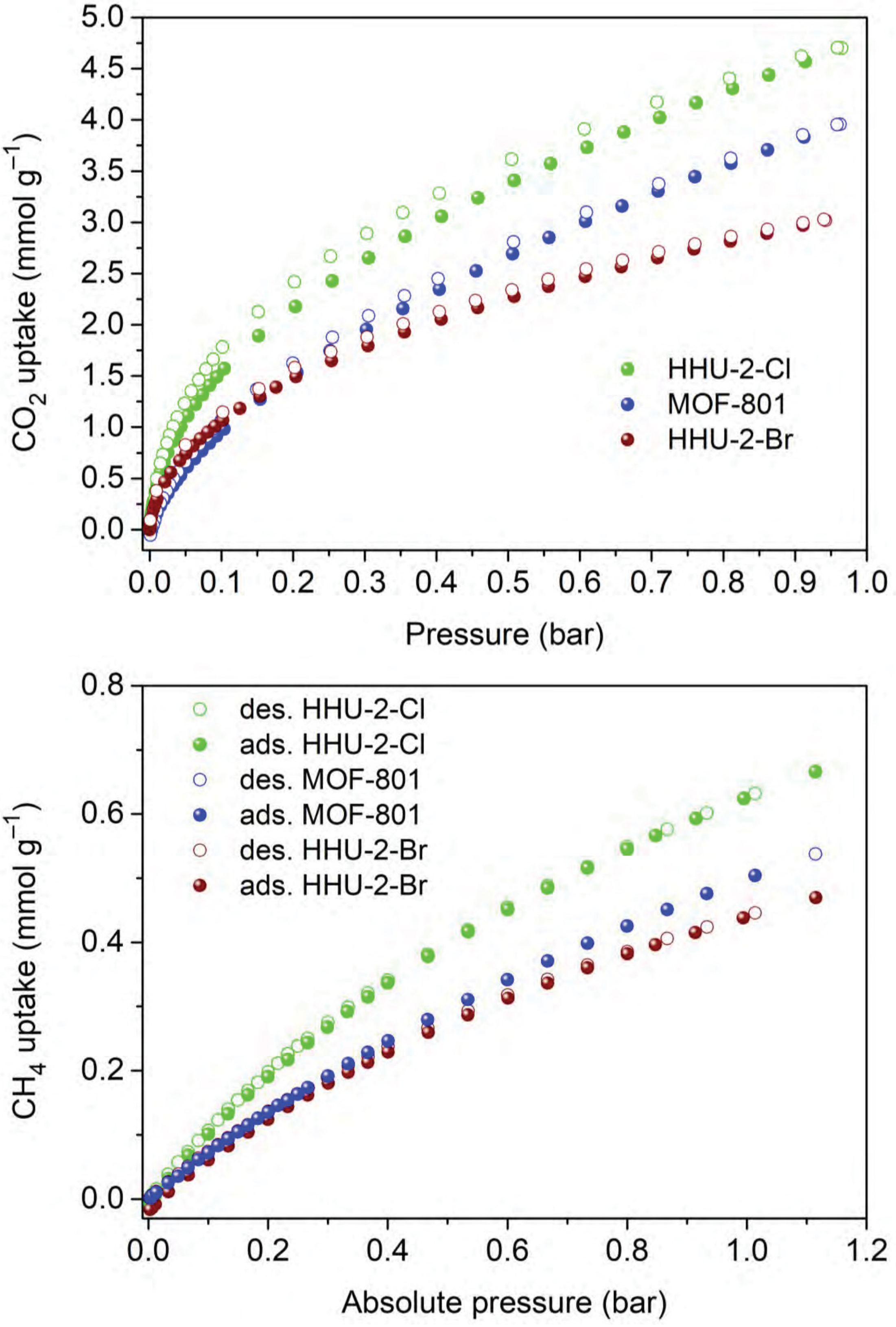

Figure S44. Sorption isotherms of CO_2 at 273 K (top) and CH_4 at 293 K (bottom) for HHU-2-X and MOF-801.

At pore sizes close to the kinetic diameter of N_2 (~3.64 Å) the diffusion limitation at 77 K can prevent an uptake of N_2. This can be alleviated by using CO_2 (kinetic diameter 3.30 Å) as an adsorbate at 273 K which ensures faster equilibration.[13-16] This is also due to the saturation pressure of CO_2 at 0 °C being ~26141 Torr and pressures necessary for micropore filling and analysis are already achieved in the range of moderate absolute pressures (1–760 Torr). Therefore, CO_2 adsorption at 273 K versus N_2 adsorption at 77 K can give adsorption in pores of smaller sizes that are accessible to CO_2 molecules but not to N_2.

Table S8. Summary of CO_2 uptakes and porosity analysis from CO_2 sorption at 273 K for HHU-2-Cl, HHU-2-Br and MOF-801

Materials	Uptake ($cm^3\ g^{-1}$, $mmol\ g^{-1}$, wt%)	Total pore volume,[a] ($cm^3\ g^{-1}$)	DFT micropore volume,[b] ($cm^3\ g^{-1}$)	DFT surface area ($m^2\ g^{-1}$)
HHU-2-Cl	105.28 4.7 17.13	0.22	0.058	184
HHU-2-Br	67.65 3.02 11.73	0.143	0.044	131
MOF-801	88.70 3.96 14.83	0.187	0.031	88

[a] Pore volume corresponding to the last measured uptake point at about 1 bar. [b] Micropore volume for pores smaller than 15 Å (1.5 nm) diameter, from the CO_2 NL-DFT model at 273 K.

Table S9. CO_2 adsorption capacity of UiO-type MOFs at 293 K and 1bar.

Materials	S_{BET} ($m^2\ g^{-1}$)	CO_2 uptake ($mmol\ g^{-1}$)	Ref.
HHU-2-Cl	852	3.28	This work
UiO-66	1331	2.3	17
UiO-66-NH_2	1057	2.6	17
UiO-67	1996	2.51	18
UiO-67-SO_2	1442	2.88	18
$Zr_6O_4(OH)_4(EDDC)_6$	2496	2.63 (273 K)	19
$Zr_6O_4(OH)_4(EDDC)_6$-NH_2	2619	2.46 (273 K)	19

Table S10. MOFs with high SO_2 adsorption capacity per weight and surface area.

Materials	S_{BET} ($m^2\ g^{-1}$)	SO_2 uptake (mmol g^{-1})	SO_2 uptake (μmol m^{-2})	Remarks	Ref
HHU-2-Cl	852	9.7	11.38		This work
MOF-177	4100	25.7	6.26	Record 2019	20
MMF-601	3644	12.3	3.37	Record 2018	21
MMF-300(In)	1071	8.28	7.73		22
Ni(bdc)(ted)$_{0.5}$	1783	9.97 (1.13 bar)	5.59		23

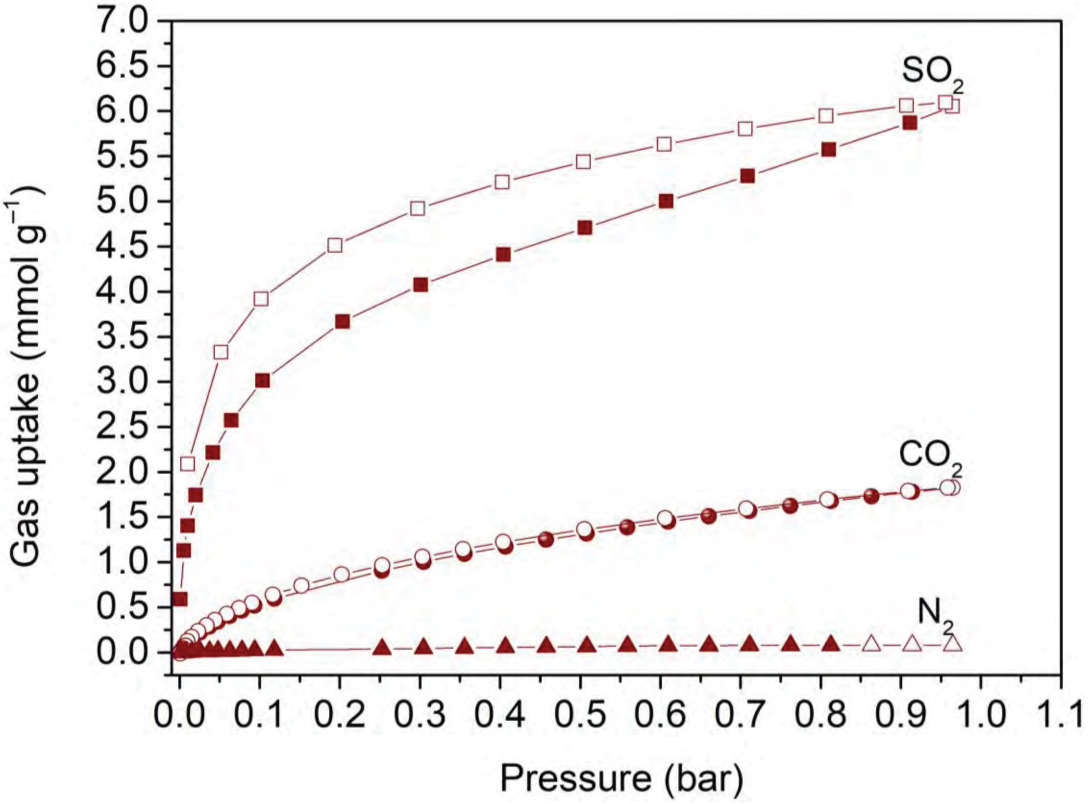

Figure S45. SO_2 and CO_2 and N_2 sorption isotherms of HHU-2-Br at 293 K. adsorption (closed symbols), desorption (open symbols).

Plots of isosteric heat of water adsorption for MOF-801 and MOF-841 in the literature

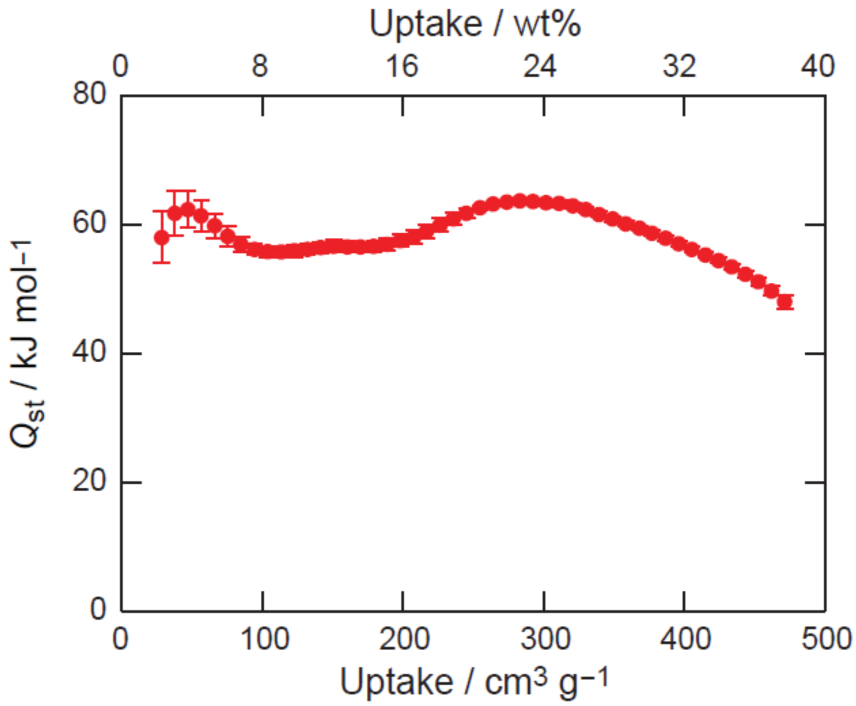

Figure S46. Plot of isosteric of heat of water adsorption of zirconium fumarate (MOF-801). Reprinted with permission from Furukawa, H.; Gándara, F.; Zhang, Y-B.; Jiang, J.; Queen, W. L.; Hudson, M. R.; Yaghi, O. M. *J. Am. Chem. Soc.* **2014**, *136*, 4369-4381. Copyright 2014 American Chemical Society.

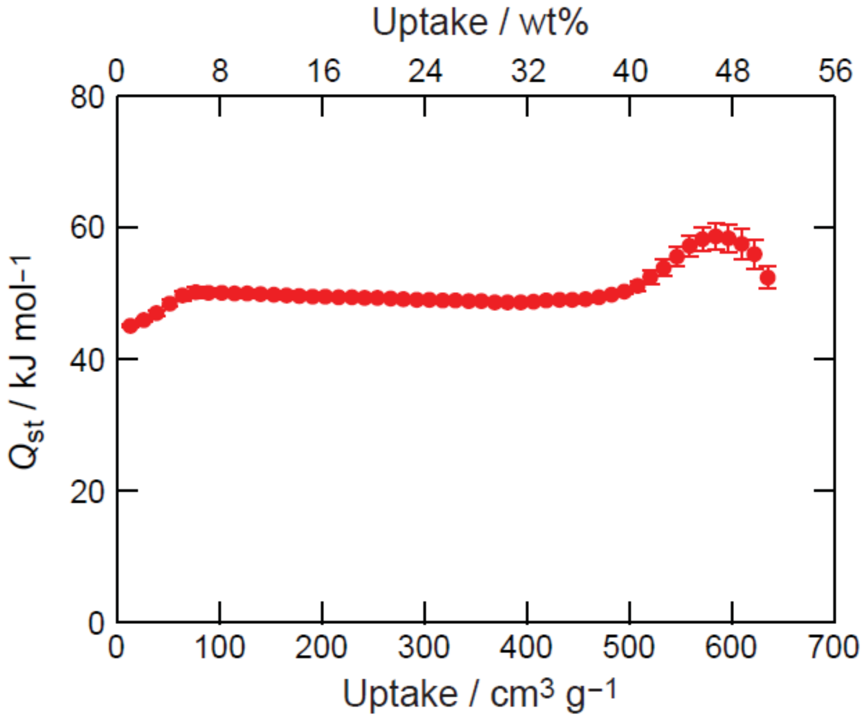

Figure S47. Plot of isosteric of heat of water adsorption of MOF-841. Reprinted with permission from Furukawa, H.; Gándara, F.; Zhang, Y-B.; Jiang, J.; Queen, W. L.; Hudson, M. R.; Yaghi, O. M. *J. Am. Chem. Soc.* **2014**, *136*, 4369-4381. Copyright 2014 American Chemical Society.

The prominent increase in heat of water adsorption at pore filling in these robust and non-flexible MOFs has not yet clearly been justified. It could be due to rearrangement of stable water clusters during pore filling.

REFERENCES

(1) Furukawa, H.; Gándara, F.; Zhang, Y-B.; Jiang, J.; Queen, W. L.; Hudson, M. R.; Yaghi, O. M. Water Adsorption in Porous Metal-Organic Frameworks and Related Materials. *J. Am. Chem. Soc.* **2014**, *136*, 4369-4381.

(2) Zahn, G.; Schulze, H. A.; Lippke, J.; Konig, S.; Sazama, U.; Fröba, M.; Behrens, P. A Water-Born Zr-Based Porous Coordination Polymer: Modulated Synthesis of Zr-Fumarate MOF. *Micropor. Mesopor. Mater.* **2015**, *203*, 186–194.

(3) Ke, F.; Peng, C.; Zhang, T.; Zhang, M.; Zhou, C.; Cai, H.; Zhu, J.; Wan, X. Fumarate-Based Metal-Organic Frameworks as a New Platform for Highly Selective Removal of Fluoride from Brick Tea. *Sci. Rep*. **2018**, *8*, 939.

(4) Alexander, S.; Morrow, L.; Lord, A. M.; Dunnilla, C. W.; Barron, A. R. pH-Response Octylamine Coupling Modification of Carboxylated Aluminium Oxide Surfaces. *J. Mater. Chem. A* **2015**, *3*, 10052–10059.

(5) Zhan, G.; Zeng, H. C. Synthesis and Functionalization of Oriented Metal-Organic Framework Nanosheets: Toward a Series of 2D Catalyst. *Adv. Funct. Mater*. **2016**, *26*, 3268–3281.

(6) Guillerm, V.; Gross, S.; Serre, C.; Devic, T.; M. Bauer, Férey, G. A Zirconium Methacrylate Oxocluster as Precursor for the Low-Temperature Synthesis of Porous Zirconium(IV) Dicarboxylates. *Chem. Commun*. **2010**, *46*, 767–769.

(7) Schaate, A.; Roy, P.; Godt, A.; Lippke, J.; Waltz, F.; Wiebcke, M.; Behrens, P. Modulated Synthesis of Zr-Based Metal-Organic Frameworks: From Nano to Single Crystals. *Chem. Eur. J.* **2011**, *17*, 6643 – 6651.

(8) Gutov, O. V.: Molina, S.; Escudero-Adán, E. C.; Shafir, A. Modulation by Amino Acids: Toward Superior Control in the Synthesis of Zirconium Metal-Organic Frameworks *Chem. Eur. J.* **2016**, *22*, 13582 – 13587.

(9) Huskens, J.; Peters, J. A.; van Bekkum, H. The Addition of Hydroxyl Compounds to Unsaturated Carboxylic Acids Homogeneously Catalysed by Lanthanide(III). *Tetrahedron* **1993**, *15*, 3149-3164.

(10) Ruthven, D. M. Principles of Adsorption and Adsorption Processes, Wiley: New York, 1984.

(11) El-Sharkawy, I. I.; Uddin, K.; Miyazaki, T.; Saha, B. B.; Koyama, S.; Miyawaki, J.; Seong-Ho Yoon, S.-H. Adsorption of Ethanol onto Parent and Surface Treated Activated Carbon Powders *Int. J. Heat Mass Transfer* **2014**, *73*, 445–455.

(12) Aristov, Y. I.; Tokarev,M. M.: Freni, A.; Glaznev, I. S.; Restuccia, G. K. Kinetics of Water Adsorption on Silica Fuji Davison RD. *Micropor. Mesopor. Mater*. **2006**, *96*, 65–71.

(13) Bhunia, A.; Boldog, I.; Möller, A.; Janiak, C. Highly Stable Nanoporous Covalent Triazine-Based Frameworks with an Adamantane Core for Carbon Dioxide Sorption and Separation. *J. Mater. Chem. A* **2013**, *1*, 14990–14999.

(14) Dey, S.; Bhunia, A.; Boldog, I.; Janiak, C. A Mixed-Linker Approach Towards Improving Covalent Triazine-Based Framework for CO_2 Capture and Separation. *Micropor. Mesopor. Mater.* **2017**, *241*, 303–315.

(15) Dey, S.; Bhunia, A.; Breitzke, H.; Groszewicz, P. B.; Buntkowsky, G.; Janiak, C. Two Linkers Are Better than One: CO_2 Capture and Separation with Porous Covalent Triazine-Based Frameworks from Mixed Nitrile Linkers. *J. Mater. Chem. A* **2017**, *5*, 3609–3620.

(16) Guo, F.; Chen, C.; Wang, K; Zhang, Q.; Lin, Z. Supramolecular Templating Approach for the Solvent-Free Synthesis of Open-Framework Metal Oxalates. *Inorg. Chem*. **2016**, *55*, 7817-7819.

(17) Lin, Y.; Kong, C.; Zhang, Q.; Chen, L. Metal-Organic Frameworks for Carbon Dioxide Capture and Methane Storage. *Adv. Energy Mater*. **2017**, *7*, 1601296.

(18) Xydias, P.; Spanopoulos, I.; Klontzas, E.; George E. Froudakis, G. E.; Trikalitis, P. N. Drastic Enhancement of the CO_2 Adsorption Properties in Sulfone-Functionalized Zr- and Hf-UiO-67 MOFs with Hierarchical Mesopores. *Inorg. Chem*. **2014**, *53*, 679−681.

(19) Zhang, J.; Yao, S.; Liu, S.; Liu, B.; Sun, X.; Zheng, B.; Li, G.; Li, Y.; Huo, Q.; Liu, Y. Enhancement of Gas Separation Performance via Ligand Functionalization within Highly Stable Zirconium-Based Metal-Organic Framework. *Cryst. Growth Des*. **2017**, *17*, 2131−2139.

(20) Brandt, P.; Nuhnen, A.; Lange, M.; Möllmer, J.; Weingart, O.; Janiak, C. Metal−Organic Frameworks with Potential Application for SO_2 Separation and Flue Gas Desulfurization *ACS Appl. Mater. Interfaces* **2019**, *11*, 17350−17358.

(21) Carter, J. H.; Han, X.; Moreau, F. Y.; da Silva, I.; Nevin, A.; Godfrey, H. G. W.;Tang, C. C.; Yang, S.; Schröder, M. Exeptional Adsorption and Binding of Sulfur Dioxide in a Robust Zirconium-Based Metal-Organic Framework. *J. Am. Chem. Soc*. **2018**, *140*, 15564−15567.

(22) Savage, M.; Cheng, Y.; Easun, T. L.; Eyley, J. E.; Argent, S. P.; Warren, M. R.; Lewis, W.; Murray, C.; Tang, C. C.; Frogley, M. D.; Cinque, G.; Sun, J.; Rudić, S.; Murden, R. T.; Benham, M. J.; Fitch, A. N.; Blake, A. J.; Ramirez-Cuesta, A. J.; Yang, S.; Schröder, M. Selective Adsorption of Sulfur Dioxide in a Robust Metal-Organic Framework Material. *Adv. Mater.* **2016**, *28*, 8705–8711

(23) Tan, K.; Canepa, P.; Gong, Q.; Liu, J.; Johnson, D. H.; Dyevoich, A.; Thallapally, P. K.; Thonhauser, T.; Li, J.; Chabal, Y. J. Mechanism of Preferential Adsorption of SO_2 into Two Microporous Paddle Wheel Frameworks M(bdc)(ted)$_{0.5}$. *Chem. Mater*. **2013**, *25*, 4653−4662.

2.5 Halogen functionalization of aluminum fumarate metal-organic framework via in situ hydrochlorination of acetylenedicarboxylate

Tobie J. Matemb Ma Ntep, Wei Wu, Hergen Breitzke, Carsten Schlüsener, Bastian Moll, Laura Schmolke, Gerd Buntkowsky and Christoph Janiak

Aust. J. Chem. **2019**, *72*, 835–841. (Contribution upon invitation to the special issue for Professor Richard Robson in commemoration of his seminal contribution to science, in particular to the foundation of MOF chemistry)

DOI: 10.1071/CH19221

Impact factor 2018: 1.2

Several synthesis attempts to obtain an acetylenedicarboxylate-based aluminum MOF were unsuccessful. However, the modulated synthesis with acetic acid modulator yielded a chlorofunctionalized aluminum fumarate with the same MIL-53-type structure as aluminum fumarate (MIL-53-Fum). The new material was formed by in situ hydrochlorination of acetylenedicarboxylic acid when reacting with aluminum chloride ($AlCl_3$). The new material denoted as MIL-53-Fum-Cl is the first reported functionalized version of aluminum fumarate with the MIL-53 topology. MIL-53-Fum-Cl is made of *trans*-corner-sharing AlO_6 octahedra chains connected together by chlorofumarate linkers to form a porous framework having one-dimensional channels with lozenge-shaped section. The adsorption properties of MIL-53-Fum-Cl were investigated, revealing that decorating the pores of MIL-53-Fum with chloro-functions also results in an increased CO_2, CH_4 and H_2 capacities and/or affinities. An increase in the selective adsorption of CO_2 over CH_4 was also noticed in MIL-53-Fum-Cl compared to MIL-53-Fum. However, the water sorption profile does not yield the targeted stepwise S-shape, and the material featured a low hydrolytic stability due a large number of missing linker defects, resulting from the modulated synthesis employed. MIL-53-Fum-Cl would therefore not be a good candidate as adsorbent applicable for heat transformation applications. This work shows that the halogen functionalization of MOFs via in situ hydrohalogenation of acetylenedicarboxylate is extendable to all other metal cations. Detailed results of this work are contained in the article that follows.

Author´s contribution to the work:

- Idea and setting of the synthesis procedures.
- Characterizations including PXRD experiment, TGA, chemical stability test, nitrogen sorption and determination of porosity parameters, other gas/vapor sorption (H_2O, CO_2, H_2 and CH_4) experiments.
- Organization of other analyses (Raman, ssNMR, SEM-EDX and XPS), data analysis/interpretations and treatment.
- Samples activation prior characterizations and MOF digestion prior liquid NMR analysis.
- Determination of the amount of missing linker defects from liquid NMR. Determination of the amount of missing linker defects from TGA curve.
- Fitting of CO_2 adsorption isotherms, determination and plot of the isosteric heat of CO_2 adsorption from isotherms at two different temperatures. Calculation of the IAST (ideal adsorption solution theory) CO_2 versus CH_4 selectivity.
- Writing of the manuscript, drawing of figures and responses to reviewers during the review process.

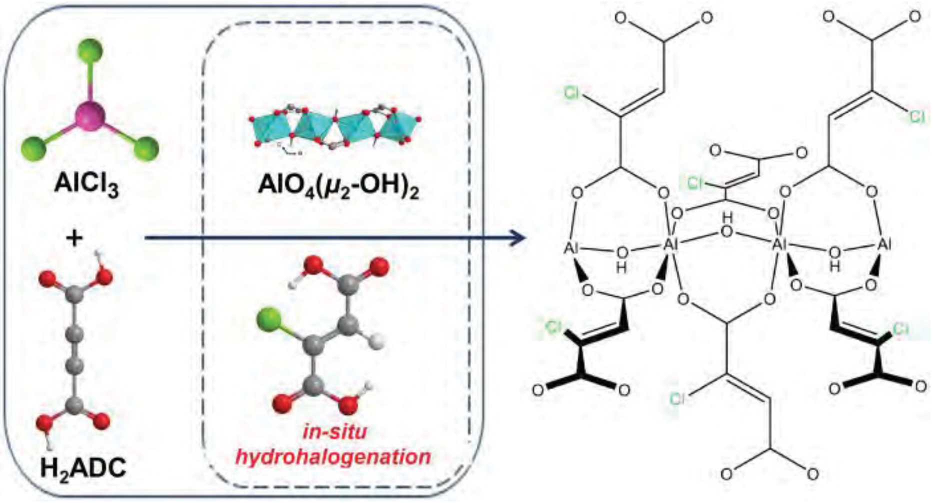

CSIRO PUBLISHING
RESEARCH FRONT
Aust. J. Chem. **2019**, *72*, 835–841
https://doi.org/10.1071/CH19221
Full Paper

Halogen Functionalization of Aluminium Fumarate Metal–Organic Framework via In Situ Hydrochlorination of Acetylenedicarboxylic Acid*

Tobie J. Matemb Ma Ntep,[A] *Wei Wu,*[A] *Hergen Breitzke,*[B]
Carsten Schlüsener,[A] *Bastian Moll,*[A] *Laura Schmolke,*[A]
Gerd Buntkowsky,[B] *and Christoph Janiak*[A,C]

[A]Institut für Anorganische Chemie, Heinrich-Heine-Universität Düsseldorf, D-40204 Düsseldorf, Germany.
[B]Eduard-Zintl-Institut für Anorganische und Physikalische Chemie, Technische Universität Darmstadt, Alarich-Weiss-Straße. 4, D-64287 Darmstadt, Germany.
[C]Corresponding author. Email: janiak@uni-duesseldorf.de

The successful chloro-functionalization of aluminium fumarate (MIL-53-Fum) was achieved by in situ hydrochlorination of acetylenedicarboxylic acid on reaction with aluminium chloride resulting in the formation of the aluminium chlorofumarate metal–organic framework (MIL-53-Fum-Cl = [Al(OH)(Fum-Cl)]) in a one-pot reaction. The chloro functional groups decorating the pores enhance gas (CO$_2$, CH$_4$, and H$_2$) sorption capacities and affinity compared with the non-functionalized MIL-53-Fum. The functionalization also results in a 2-fold increase in the selective adsorption of CO$_2$ over CH$_4$ compared with MIL-53-Fum.

Manuscript received: 13 May 2019.
Manuscript accepted: 9 August 2019.

Introduction

Composed of metal units that are bridged by organic ligands into porous networks, metal–organic frameworks (MOFs) allow for various functional groups to be introduced into the material, hence tuning of the chemistry of their pore surface to meet specific properties and potential applications.[1] Such functionalization of MOFs can be done pre-synthetically, post-synthetically or in situ.[2] For the latter, linker or cluster functionalization and MOF formation occur in a one-pot reaction, which offers the advantage of reducing synthesis steps and cost when compared with post-synthetic modification, as well as yields products that might at times not be obtained by direct synthesis.[3]

We recently reported the halogen functionalization of MOFs via in situ hydrohalogenation of linkers containing alkyne moieties.[4] More precisely, chlorofumarate-based UiO-type zirconium MOF was obtained by in situ hydrohalogenation of the triple bond of acetylenedicarboxylic acid. Aluminium-based MOFs are of great interest owing to the lightness and low toxicity of aluminium, as well as the abundance of its sources. Aluminium fumarate was one of the first commercialized Al-MOFs owing to its easy and inexpensive synthesis route at large scale.[5] Owing to its high thermal, chemical, and hydrothermal stability, aluminium fumarate holds promise for adsorption-based heat transformation applications,[6] adsorption of fluoride from water,[7] carbon dioxide capture from wet gas stream,[8] shape-based separation of hydrocarbons,[9] and as anode material for lithium ion batteries.[10] Aluminium fumarate, commercialized under the trademark Basolite A520, is also named MIL-53-Fum because it is isostructural with the aluminium terephthalate MOF MIL-53(-BDC).[11] The MIL-53 framework is built up from chains of *trans*-corner-sharing AlO$_6$ octahedra, linked together by fumarate to form lozenge-shaped one-dimensional channels having a cross-section of $\sim 5.7 \times 6.0$ Å^2 (Fig. 1).[12]

The short fumarate linker in this material yields narrow pores (ultramicroporous MOF), which are beneficial with respect to the optimum adsorption of some gases and vapours like CO$_2$ and water. For example, the Al-fumarate MOF (MIL-53-Fum) and the Zr-fumarate MOF (MOF-801) both display an S-shaped water sorption isotherm. The high hydrophilicity of these MOFs is demonstrated by a water step at a low relative pressure range of $P/P_0 = 0.2$–0.3 (for MIL-53-Fum) and 0.05–0.1 (for MOF-801) favourable for application in thermally driven adsorption heat exchangers.[13,14] This hydrophilicity was attributed to the small pores, which dictate easy water molecule interaction with the framework and formation of hydrogen bonds between neighbouring water molecules.[15] Also, the short fumarate linker enables minimization or even cancelling of the hysteresis loop between the water adsorption and desorption branches in MIL-53-Fum and MOF-801 compared with what is observed for their respective terephthalate parents MOFs

---

*Dedicated to Professor Richard Robson in commemoration of his seminal contribution to science.

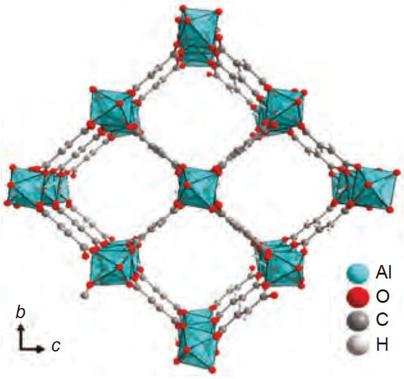

Fig. 1. Structure of aluminium fumarate (MIL-53-Fum) framework.

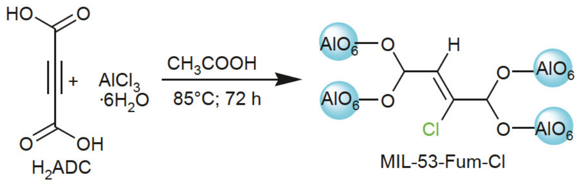

Scheme 1. Reaction of acetylenedicarboxylic acid to form MIL-53-type aluminium chlorofumarate MOF via in situ hydrochlorination.

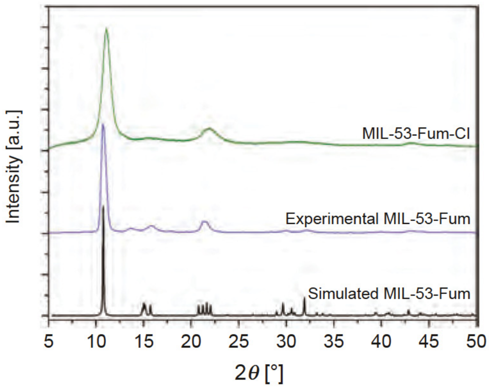

Fig. 2. PXRD pattern of MIL-53-Fum-Cl compared with experimental and simulated patterns of aluminium fumarate (as-synthesized MIL-53-Fum). See Supplementary Material for further information on the PXRD of MIL-53-Fum.

MIL-53-BDC and UiO-66.[15,16] Further, the small pore system in ultramicroporous MOFs is the basis for cost-effective selective removal of CO_2 from flue gas as well as for the selective exclusion of branched paraffins.[17,18] Introducing moderately sized polar functional groups (chlorine for instance) into the pore system of MIL-53-Fum is of interest to improve its sorption capacity without compromising its gas selectivity. Surprisingly, no functionalized version of MIL-53-Fum has yet been reported. Reinsch et al. recently described the synthesis of an Al-MOF based on the short methylfumarate linker (MIL-68Mes).[19] However, grafting a CH_3 group to the fumarate linker yielded an Al-MOF with the structure of MIL-68,[20] unlike the MIL-53-type structure of aluminium fumarate. Thus, synthesizing a functionalized version of MIL-53-Fum remains a non-accessed research area to explore.

Herein, we report the synthesis of the new aluminium chlorofumarate MOF (MIL-53-Fum-Cl), which is isoreticular with the well-known aluminium fumarate. As MIL-53-Fum-Cl is obtained by in situ generation of the chlorofumarate linker, the nature of the latter is examined along with the porosity and vapour and gas sorption properties of the new material.

Results and Discussion

The reaction in DMF of acetylenedicarboxylic acid (H_2ADC) with aluminium chloride hexahydrate in the presence of acetic acid modulator after 72 h at 85°C yielded a light brown–yellowish microcrystalline powder, designated MIL-53-Fum-Cl (Scheme 1).

The powder X-ray diffraction pattern (PXRD) of the material obtained is similar to that of aluminium fumarate (MIL-53-Fum) (Fig. 2), thus revealing their isostructural nature.

Poor crystallinity is well known for MIL-53-Fum (Basolite A520),[12] and hence can also be expected for the analogue MIL-53-Fum-Cl. However, the fairly broad reflections in the PXRD pattern of MIL-53-Fum-Cl also derive from the very small particle size of the obtained material (see SEM image below). Conducting the synthesis using formic acid as modulator produced no improvement on the PXRD pattern (see PXRD pattern in Fig. S17, Supplementary Material).

In addition, a slight shift of reflections in the PXRD pattern of MIL-53-Fum-Cl can be a result of its flexibility (as in MIL-53-Fum). The position of the lowest reflection and the one at ~21° 2θ shift slightly depending on the degree of hydration and number of guests in the pores (see Fig. S12 in the Supplementary Material, where the position of these reflections varies with the solvent in the material). The PXRD patterns of MIL-53-Fum-Cl treated with different solvents show variable shifts of the strongest reflections at ~11° and 21° 2θ angles depending on the nature of the solvent in the pores of the material (Fig. S12). This supports the notion of the slight flexibility of MIL-53-Fum-Cl. Its flexibility is more noticeable than was previously observed for MIL-53-Fum.[12,13] This could mean that the chlorofunctionalization of MIL-53-Fum induces an increased flexibility in its framework. At the same time, the introduction of the chloro functional group can result in a slight change in the unit cell parameters with respect to MIL-53-Fum.[21]

It was observed that conducting the reaction without addition of acetic acid did not yield any solid product. This shows that acetic acid plays an important role in the formation of the new material. The role of monocarboxylic acids (formic, acetic, benzoic acid) has been clearly elucidated for the modulated synthesis of Zr-MOFs and Hf-MOFs,[22] whereas few Al-MOFs have been obtained by the modulated synthesis approach.[23] However, the mechanism of modulation remains to be studied in the case of Al-MOFs.

The Raman spectrum (Fig. 3) of MIL-53-Fum-Cl shows the disappearance of the strong band at 2250 cm^{-1} relative to the spectrum of the initial H_2ADC linker. This band is characteristic of the stretching vibrations of the –C≡C– triple bond. The disappearance of this band indicates the transformation of the –C≡C– triple bond during MOF formation. The band at ~3100 cm^{-1} is ascribed to the =C–H vibration. In the IR spectrum (Fig. S1, Supplementary Material), the bands at 1616 and 1414 cm^{-1} correspond respectively to the asymmetric and symmetric stretching mode of coordinated carboxylate (–COO). Their respective wavenumber values, within the same range with those obtained for aluminium fumarate (ν_{as} 1606 cm^{-1} and ν_s 1424 cm^{-1}), (Fig. S2, Supplementary

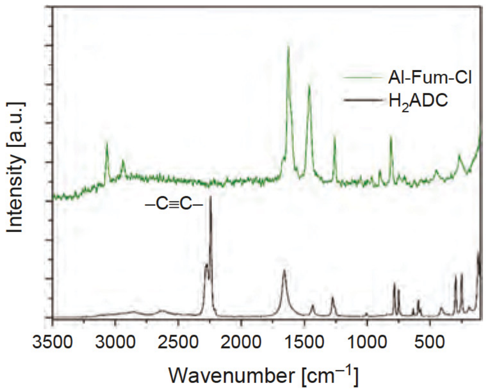

Fig. 3. Raman spectrum of MIL-53-Fum-Cl compared with the spectrum of the initial acetylenedicarboxylic acid ligand. A complete disappearance of the band at 2225 cm^{-1} is noted.

Material) suggest the same coordination mode of linkers in both materials. The band at 748 cm^{-1} in the IR spectrum of MIL-53-Fum-Cl is attributable to the vibration of the C–Cl bond.[24]

Solid-state NMR (ssNMR) analysis gives more insight into the nature of the linker in the new MOF. The peaks at 130 and 140 ppm in the ^{13}C spectrum (Fig. 4a) are ascribed to two non-symmetrically bonded olefinic carbon atoms (C=C). One olefinic carbon atom is bonded to a proton with a chemical shift at 6.9 ppm, as revealed by their correlation in the ^{1}H–^{13}C frequency switched Lee Goldburg heteronuclear correlation (FSLG HETCOR) spectrum (Fig. 4c). This chemical shift is confirmed by homonuclear decoupled 2D FSLG proton spectra, recorded with the same parameters as for the FLSG HECTOR spectra. Fig. S4 (Supplementary Material) depicts the projection on the indirect dimension of this spectrum. The peak at 170 ppm with a shoulder is ascribed to the two carboxylate carbon atoms of the linker. The ssNMR analysis also reveals the presence of the acetate modulator in the framework. The peak at 20 ppm in the ^{13}C spectra is due to the acetate –CH_3 group, while its carboxylate group –COO yields the peak at 180 ppm. This suggests the coexistence of defective sites within the material, where the acetate modulator is partly coordinated in place of the linker. This type of defect is well known for example in UiO-type MOFs obtained by monocarboxylic acid modulation.[25] The ^{1}H ssNMR spectrum (Fig. 4b) presents three peaks at 6.9, 2.1, and 1.6 ppm attributable to the olefinic proton, the proton of the bridging μ-OH, and the methyl protons of acetate respectively. The correlation peak at ~170 ppm(^{13}C)/2 ppm(^{1}H) in the HETCOR spectrum recorded at 500 μs (Fig. S4) results from the long-range interaction between the proton of the bridging μ-OH and the carboxylate of the linker, as they are both connected to the same aluminium centre. If this interpretation holds true, this correlation should be absent in HETCOR spectra recorded with lower contact times, i.e. in HETCOR spectra that are only sensitive to short-range interactions. Fig. 4c depicts the HETCOR spectrum recorded with 200 μs contact time, where this correlation is indeed absent. Note that some peaks may slightly shift or split owing to different build-up times during the cross-polarization process, and also that cross-polarization spectra are not quantitative.

The number of defects was determined from the liquid ^{1}H NMR analysis of a digested sample of MIL-53-Fum-Cl as ~0.4 missing Fum-Cl linker per unit formula of MIL-53-Fum-Cl ([Al(OH)(Fum-Cl)]) (see details in Supplementary Material). The number of missing linkers obtained from NMR analysis is confirmed by its estimation from thermogravimetric analysis (TGA) (see details in Supplementary Material).

From the X-ray photoelectron (XP) spectrum (Fig. S8, Supplementary Material), the presence of chlorine is observed in MIL-53-Fum-Cl. The peak at ~200 eV binding energy accounts for an organic chlorine.[26] Thus, there has been formation of a C–Cl bond during the reaction. This chlorine atom is obviously bonded to the second olefinic carbon atom that was observed in the ssNMR analysis (signal b in Fig. 4a). Peaks at 73.7 and 74.5 eV binding energy are due to Al–O and Al–OH respectively.[27] Scanning electron microscopy (SEM) energy-dispersive X-ray spectroscopy (EDX) elemental mapping (Fig. 5) further shows the presence of chlorine homogenously distributed over the whole MIL-53-Fum-Cl sample range. The molar atomic aluminium to chlorine (Al : Cl) ratio of ~1 : 0.7 (from EDX, details in Supplementary Material) is different from the expected 1:1 ratio for an ideal MIL-53-type MOF (ideal formula: [Al(OH)(linker)]). This is however in agreement with the occurrence of ~0.4 missing linker per formula unit of the synthesized MIL-53-Fum-Cl.

The aforementioned analysis results indicate a transformation of the reacting acetylenedicarboxylic acid molecule into a chlorofumarate linker in the newly formed MOF (Scheme 1). A *trans* hydrochlorination (addition of HCl) on the –C≡C– triple bond of acetylenedicarboxylic acid has taken place. HCl is produced in situ during the reaction of $AlCl_3$ with water or with the acetic acid modulator to an intermediate aluminium hydroxide acetate $Al(OH)(OOCCH_3)_2$. The MOF is subsequently formed from the substitution of the acetate by the chlorofumate (see Scheme 2). This suggested mechanism is corroborated by the presence of missing linkers whose sites are occupied instead by coordinated acetate from incomplete substitution. Moreover, the basic aluminium acetate $Al(OH)(ac)_2{\cdot}xH_2O$ has previously been reported as a precursor for the synthesis of Al-MOFs.[28] An equivalent mechanism was also studied for monocarboxylic acid-modulated synthesis of Zr-MOFs and Hf-MOFs.[21]

A similar transformation has previously been found for the formation of a chlorofumarate-based UiO-type Zr-MOF (HHU-2) from acetylenedicarboxylic acid reacting with zirconium chloride.[4]

Structural information could be obtained from ^{27}Al ssNMR spectroscopy analysis. The ^{27}Al ssNMR spectrum of activated MIL-53-Fum-Cl (Fig. 6) exhibits a peak at –13 ppm corresponding to an octahedral six-coordinate Al–O.[29] MIL-53-Fum-Cl is therefore constructed of AlO_6 octahedra. The shoulder displayed at −13 ppm indicates the presence of two slightly different Al sites, and is due to the asymmetry of the chlorofumarate linker and to the presence of linker defective sites with coordinated acetate. Furthermore, the presence of the Al–OH group is seen in the XP spectrum (Fig S8, Supplementary Material). Analogously with the formula of MIL-53-type MOFs like aluminium fumarate, the ideal formula of the desolvated material is [Al(OH)(OOC–HC=CCl–COO)] ([Al(OH)(Fum-Cl)]). Its exact formula, taking into account the number of linker defects from liquid NMR, is $[Al(OH)_{1.4}(OOC{-}HC{=}CCl{-}COO)_{0.6}(OOCCH_3)_{0.4}]$. It is worth noting that the number of defects in materials obtained from a monocarboxylic acid-modulation synthesis usually depends on the relative amount of modulator used. Therefore, the linker defects ratio may vary from one synthesis batch to the other.

The thermal stability from TGA under air (Fig. S10, Supplementary Material) shows that MIL-53-Fum-Cl is stable to ~300°C. Its stability is lower than that of MIL-53-Fum, which

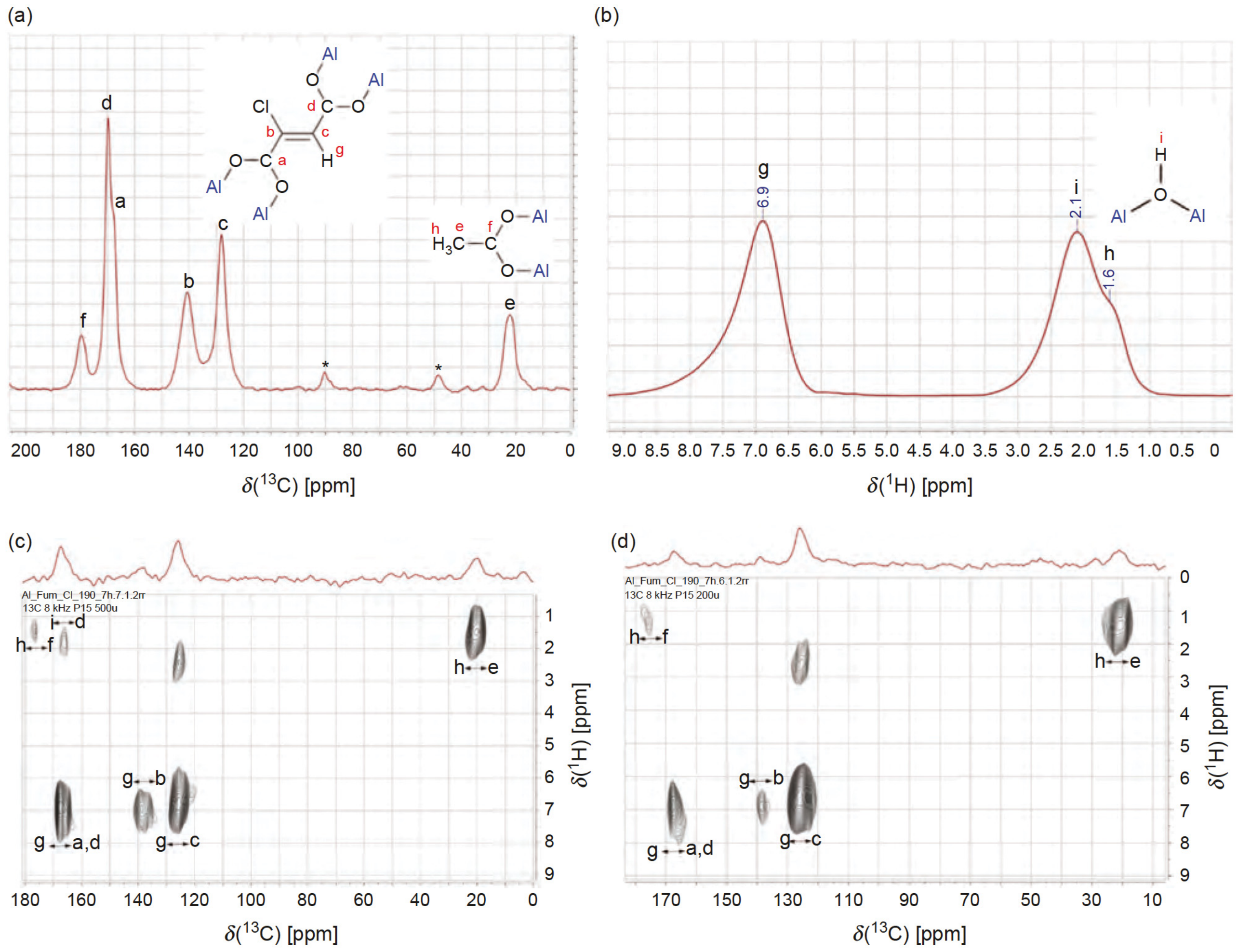

Fig. 4. (a) ^{13}C CP-MAS, and (b) ^{1}H CP-MAS solid-state spectrum. (c, d) ^{1}H-^{13}C FSLG-HETCOR CP MAS of desolvated MIL-53-Fum-Cl at 8 kHz spinning speed, and (c) 500 µs, and (d) 200 µs contact time (* spinning side bands). See Supplementary Material for further information (Figs S4–S6).

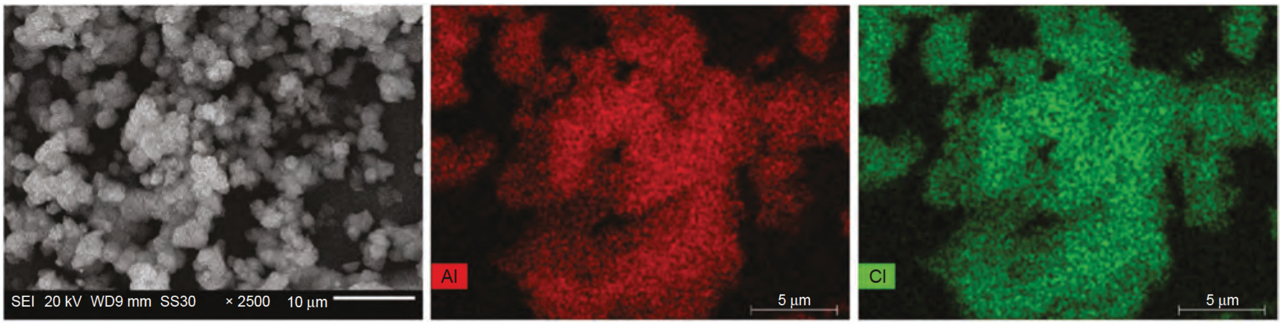

Fig. 5. SEM image and EDX elemental maps of MIL-53-Fum-Cl showing uniform distribution of Cl and Al over the entire sample. Cl and Al are mapped green and red respectively.

is stable to ∼400°C, but is still within the same range. Also, the chemical stability of MIL53-Fum-Cl is lower than that of MIL-53-Fum. The crystallinity of MIL-53-Fum-Cl was slightly altered after stirring in water or aqueous NaOH (pH 12) for 24 h at room temperature. The material completely dissolved in aqueous HCl (pH 1) to give a colourless solution. However, MIL-53-Fum-Cl was found to be stable in ethanol, methanol, DMF, and acetone with the same treatments (see Fig. S12 in Supplementary Material for details). The lower chemical stability can be attributed to the presence of a large number of linker defective sites that are occupied by coordinated acetate instead, as revealed in the ssNMR analysis. A synthesis method that considerably reduces the number of defects is expected to provide higher chemical stability. It has been demonstrated with highly chemically stable MOFs like UiO-66 that a large number of defects compromises their stability.[30]

The Brunauer–Emmett–Teller (BET) surface area of MIL-53-Fum-Cl was evaluated from nitrogen adsorption experiments

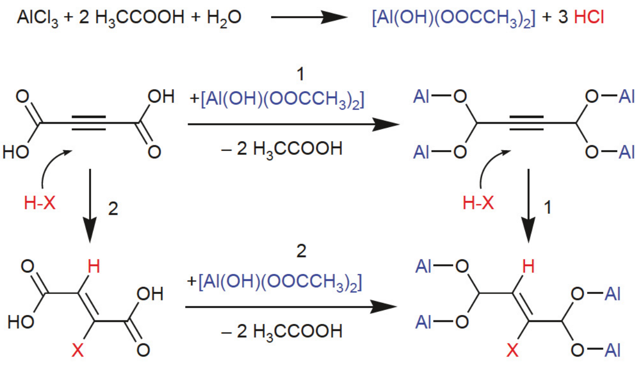

Scheme 2. Plausible mechanism of MIL-53-Fum-Cl formation via in situ hydrochlorination of the triple bond of H_2ADC, through path 1 or 2.

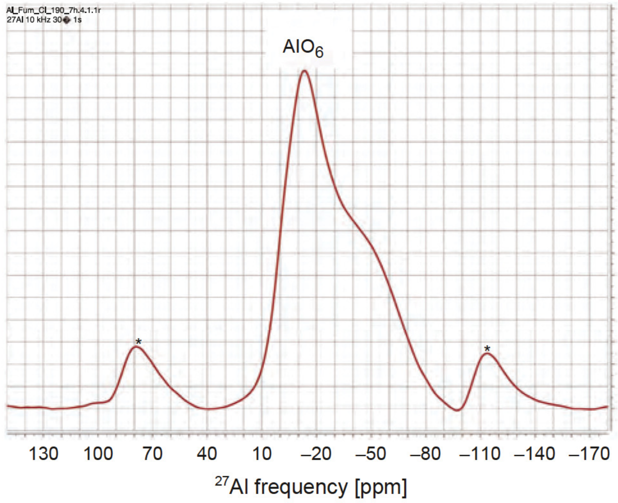

Fig. 6. ^{27}Al magic-angle-spinning (MAS) spectrum of desolvated MIL-53-Fum-Cl (* spinning side bands).

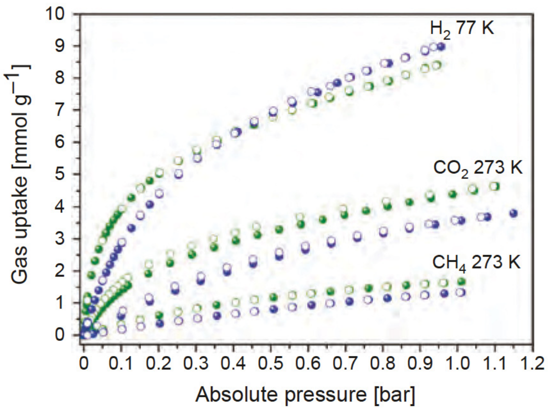

Fig. 7. Hydrogen (77 K), CO_2 (273 K), and methane (273 K) sorption isotherms for MIL-53-Fum-Cl (green) compared with MIL-53-Fum (blue) (filled symbols: adsorption; empty symbols: desorption).

as 800 $m^2\,g^{-1}$, while micropore and total pore volumes were calculated as 0.21 and 0.48 $cm^3\,g^{-1}$ respectively (see Fig. S13, and details in Supplementary Material). Its surface area and micropore volume are smaller than that of aluminium fumarate MIL-53-Fum (1021 $m^2\,g^{-1}$ and 0.48 $cm^3\,g^{-1}$). This is in agreement with pore occupancy by the chlorine atoms resulting in a decrease of surface area and micropore volume.

Sorption experiments of carbon dioxide at 273 K, methane at 273 K, and hydrogen at 77 K established the microporosity of MIL-53-Fum-Cl as they display type I isotherms (Fig. 7).[31] The CO_2 adsorption capacity of MIL-53-Fum-Cl at 273 K and 1 bar (100 kPa) is 4.6 mmol g^{-1}. This value is higher than the CO_2 adsorption capacity of MIL-53-Fum (3.6 mmol g^{-1}) which has a surface area of 984 $m^2\,g^{-1}$. Thus, there is a 27 % increase in the CO_2 adsorption capacity of MIL-53-Fum-Cl compared with the non-functionalized MIL-53-Fum.

The CH_4 adsorption capacity of MIL-53-Fum-Cl at 273 K and 1 bar is 1.5 mmol g^{-1}, corresponding to a 15 % increase in comparison with that of MIL-53-Fum (1.3 mmol g^{-1}).

The H_2 adsorption capacity of MIL-53-Fum-Cl is 8.40 mmol g^{-1} at 77 K and 1 bar and is slightly lower than that of MIL-53-Fum (8.97 mmol g^{-1}) under the same conditions. A summary of the porosity characteristics and gas adsorption capacities of MIL-53-Fum-Cl and MIL-53-Fum is given in Table 1. This is expected as hydrogen uptake capacity at 77 K is known to strongly depend on the surface area of the adsorbent.[32] However, when normalized to the BET surface area, the H_2 sorption capacity of MIL-Fum-Cl (10.5 μmol m^{-2}) is still higher than that of MIL-53-Fum (9.1 μmol m^{-2}). Furthermore, all CO_2, CH_4, and H_2 adsorption isotherms display a higher initial slope and uptake compared with MIL-53-Fum, indicating a higher affinity for these gases. The affinity constants for MIL-53-Fum-Cl obtained from the Toth model fits of CO_2, CH_4, and H_2 isotherms are 2.73, 1.34, and 2.18 bar^{-1} respectively (see Supplementary Material for details). These values are higher than those obtained with MIL-53-Fum (1.09, 0.41, 1.87 bar^{-1} for CO_2, CH_4, and H_2 respectively). The increased gas sorption capacity and affinity in MIL-53-Fum-Cl compared with MIL-53-Fum is indicative of stronger CO_2–, CH_4–, or H_2–MOF interactions. This is confirmed by the higher isosteric heat of CO_2 adsorption (Q_{st}) in MIL-53-Fum-Cl (average 35 kJ mol^{-1}) compared with the Q_{st} of 22 kJ mol^{-1} obtained for MIL-53-Fum (Fig. S16, Supplementary Material). The zero-coverage isosteric heat of CO_2 adsorption (Q_{st}^0) in MIL-53-Fum-Cl is much higher, reaching a value of 55 kJ mol^{-1} (see details of calculation and plots of Q_{st} in the Supplementary Material). These observations can rationally be attributed to the presence of polar chloro functional groups on the pore surface of MIL-53-Fum-Cl, inducing $C–Cl\cdots O{=}C{=}O$, $C–Cl\cdots C{=}O$, and $C–Cl\cdots H–H$ interactions. Halogen atoms as molecular entities are, on account of their high electronegativity, the basis of inter- and intramolecular interactions known as halogen bonding.[33] However, the pore confinement due to steric occupation by chlorine atoms could also be contributing to the observed CO_2 adsorption enhancement in MIL-53-Fum-Cl.[34]

The CO_2 versus CH_4 selectivity was calculated for a 50 : 50 (v/v) CO_2/CH_4 mixture at 273 K and 1 bar pressure. Applying IAST (ideal adsorbed solution theory) calculations on Toth-fitted isotherms yielded a selectivity of CO_2 over CH_4 ($S_{CO2/CH4}$) value of 8.5 for MIL-53-Fum-Cl, approximately twice the value of 4.5 for MIL-53-Fum (calculation details in the Supplementary Material).

MIL-53-Fum-Cl shows a non-reversible S-shaped water vapour adsorption isotherm with a considerable hysteresis loop between the adsorption and desorption branches (Fig. 8). In the case of MIL-53-Fum, the S-shaped water adsorption isotherm is characterized by a steep increase in the narrow pressure range $P/P_0 = 0.2–0.3$, with the isotherm reaching a plateau, and uptake

Table 1. Summary of surface area, porosity characteristics, water uptake, and gas adsorption capacities of MIL-53-Fum-Cl and MIL-53-Fum

Material	S_{BET}^{A} [$m^2\,g^{-1}$]	$V_{micropore}^{B}$ [$cm^3\,g^{-1}$]	H_2 uptake^{C} [$mmol\,g^{-1}$]	CO_2 uptake^{C} [$mmol\,g^{-1}$]	CH_4 uptake^{C} [$mmol\,g^{-1}$]	H_2O uptake^{D} [$mg\,g^{-1}$]
MIL-53-Fum-Cl	800	0.21	8.4	4.6	1.5	300
MIL-53-Fum	984	0.33	8.97	3.6	1.3	410

^{A}Specific surface area (S_{BET}) obtained from five adsorption points in the pressure range $P/P_0 = 0.001–0.05$.
^{B}Micropore volume ($V_{micropore}$) that originates only from micropores, obtained by volume–thickness (V-t) method with 'Deboer' thickness method.
^{C}At 273 K, 1 bar.
^{D}Uptake at $P/P_0 = 0.9$.

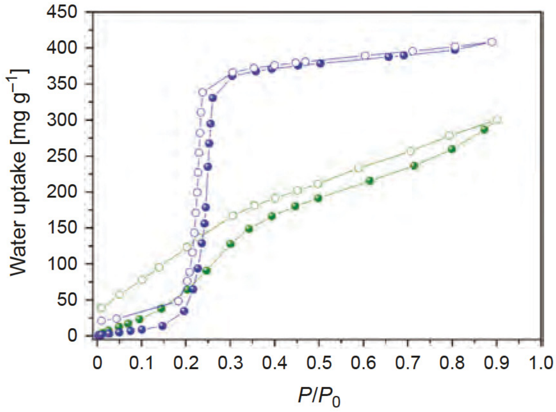

Fig. 8. Water vapour sorption isotherms of MIL-53-Fum-Cl (green) in comparison with MIL-53-Fum (blue) at 20°C (filled symbols: adsorption; empty symbols: desorption).

capacity of 410 mg g^{-1} at $P/P_0 = 0.9$. Unlike MIL-53-Fum, MIL-53-Fum-Cl shows a fairly gradual water uptake without reaching a plateau to a water uptake capacity of 300 mg g^{-1} at $P/P_0 = 0.9$. The water adsorption behaviour of MIL-53-Fum-Cl can be explained by strong H_2O–MOF interactions due to the presence of polar chlorine groups on the surface. The different shape of the desorption branch relative to the adsorption one indicates partial deterioration of the framework during water sorption. This was verified by a decrease in the surface area after water sorption from 800 to 570 m^2 g^{-1}, although the PXRD pattern post water sorption showed retention of crystallinity (see Fig. S12 in Supplementary Material).

Conclusions

In summary, the in situ hydrohalogenation of acetylenedicarboxylic acid in the presence of $AlCl_3{\cdot}6H_2O$ under acetic acid modulation was shown to be a route for obtaining chloro-functionalized aluminium fumarate. The modified aluminium fumarate (MIL-53-Fum-Cl) features enhanced gas uptake capacity, affinity, and CO_2 versus CH_4 selectivity relative to the non-functionalized MOF, which highlights the benefit of chlorination. This synthesis of the first functionalized version of aluminium fumarate paves the way to other possible functionalization of this important adsorbent as a means to improving its properties.

Supplementary Material

Experimental details including materials used, syntheses, methods; infrared, Raman, NMR, EDX, and XP spectra; PXRD in the chemical stability test; nitrogen sorption isotherms; fitting of gas adsorption isotherms, and selectivity calculations are available on the Journal's website.

Conflicts of Interest

The authors declare no conflicts of interest.

Acknowledgements

We thank the German Academic Exchange Service (DAAD) for funding to TJMMN and the German Federal Ministry of Education and Research (BMBF) for project Optimat, grant no. 03SF0492C.

References

[1] (a) H. Furukawa, K. E. Cordova, M. O'Keeffe, O. M. Yaghi, *Science* **2013**, *341*, 1230444. doi:10.1126/SCIENCE.1230444
(b) C. Janiak, J. K. Vieth, *New J. Chem.* **2010**, *34*, 2366. doi:10.1039/C0NJ00275E

[2] (a) S. M. Cohen, *Chem. Rev.* **2012**, *112*, 970. doi:10.1021/CR200179U
(b) K. K. Tanabe, S. M. Cohen, *Chem. Soc. Rev.* **2011**, *40*, 498. doi:10.1039/C0CS00031K
(c) A. Torrisi, R. G. Bell, C. Mellot-Draznieks, *Cryst. Growth Des.* **2010**, *10*, 2839. doi:10.1021/CG100646E
(d) S. Chavan, J. G. Vitillo, M. J. Uddin, F. Bonino, C. Lamberti, E. Groppo, K.-P. Lillerud, S. Bordiga, *Chem. Mater.* **2010**, *22*, 4602. doi:10.1021/CM1005899

[3] (a) X. Kong, T. He, Y. Zhang, X. Wu, S. Wang, M. Xu, G. Si, J. J. Li, *Chem. Sci.* **2019**, *10*, 3949. doi:10.1039/C9SC00178F
(b) X.-M. Zhang, *Coord. Chem. Rev.* **2005**, *249*, 1201. doi:10.1016/J.CCR.2005.01.004

[4] T. J. Matemb Ma Ntep, H. Reinsch, B. Moll, E. Hastürk, S. Gökpinar, H. Breitzke, C. Schlüsener, L. Schmolke, G. Buntkowsky, C. Janiak, *Chem. – Eur. J.* **2018**, *24*, 14048. doi:10.1002/CHEM.201802838

[5] M. Gaab, N. Trukhan, S. Maurer, R. Gummaraju, U. Müller, *Microporous Mesoporous Mater.* **2012**, *157*, 131. doi:10.1016/J.MICROMESO.2011.08.016

[6] (a) F. Jeremias, D. Fröhlich, C. Janiak, S. K. Henninger, *RSC Adv.* **2014**, *4*, 24073. doi:10.1039/C4RA03794D
(b) H. Kummer, F. Jeremias, A. Warlo, G. Füldner, D. Fröhlich, C. Janiak, R. Gläser, S. K. Henninger, *Ind. Eng. Chem. Res.* **2017**, *56*, 8393. doi:10.1021/ACS.IECR.7B00106

[7] S. Karmakar, J. Dechnik, C. Janiak, S. De, *J. Hazard. Mater.* **2016**, *303*, 10. doi:10.1016/J.JHAZMAT.2015.10.030

[8] J. A. Coelho, A. M. Ribeiro, A. F. P. Ferreira, S. M. P. Lucena, A. E. Rodrigues, D. C. S. de Azevedo, *Ind. Eng. Chem. Res.* **2016**, *55*, 2134. doi:10.1021/ACS.IECR.5B03509

[9] B. Bozbiyik, J. Lannoeye, D. E. De Vos, G. V. Baron, J. F. M. Denayer, *Phys. Chem. Chem. Phys.* **2016**, *18*, 3294. doi:10.1039/C5CP06342F

[10] Y. Wang, Q. Qu, G. Liub, V. S. Battaglia, H. Zheng, *Nano Energy* **2017**, *39*, 200. doi:10.1016/J.NANOEN.2017.06.007

[11] T. Loiseau, C. Serre, C. Huguenard, G. Fink, F. Taulelle, M. Henry, T. Bataille, G. Férey, *Chem. – Eur. J.* **2004**, *10*, 1373. doi:10.1002/CHEM.200305413

[12] E. Alvarez, N. Guillou, C. Martineau, B. Bueken, B. Van de Voorde, Cl. Le Guillouzer, P. Fabry, F. Nouar, F. Taulelle, D. de Vos, J.-S. Chang,

K. H. Cho, N. Ramsahye, T. Devic, M. Daturi, G. Maurin, C. Serre, *Angew. Chem. Int. Ed.* **2015**, *54*, 3664. doi:10.1002/ANIE.201410459

[13] F. Jeremias, D. Fröhlich, C. Janiak, S. K. Henninger, *RSC Adv.* **2014**, *4*, 24073. doi:10.1039/C4RA03794D

[14] M. V. Solovyeva, L. G. Gordeeva, T. A. Krieger, Y. I. Aristov, *Energy Convers. Manage.* **2018**, *174*, 356. doi:10.1016/J.ENCONMAN.2018.08.032

[15] H. Furukawa, F. Gándara, Y.-B. Zhang, J. Jiang, W. L. Queen, M. R. Hudson, O. M. Yaghi, *J. Am. Chem. Soc.* **2014**, *136*, 4369. doi:10.1021/JA500330A

[16] J. Canivet, J. Bonnefoy, C. Daniel, A. Legrand, B. Coasne, D. Farrusseng, *New J. Chem.* **2014**, *38*, 3102. doi:10.1039/C4NJ00076E

[17] S. Shalini, S. Nandi, A. Justin, R. Maitya, R. Vaidhyanathan, *Chem. Commun.* **2018**, 13472. doi:10.1039/C8CC03233E

[18] A. H. Assen, Y. Belmabkhout, K. Adil, P. M. Bhatt, D.-X. Xue, H. Jiang, M. Eddaoudi, *Angew. Chem. Int. Ed.* **2015**, *54*, 14353. doi:10.1002/ANIE.201506345

[19] H. Reinsch, T. Homburg, N. Heidenreich, D. Fröhlich, S. Hennninger, M. Wark, N. Stock, *Chem. – Eur. J.* **2018**, *24*, 2173. doi:10.1002/CHEM.201704771

[20] (a) S.-H. Lo, C.-H. Chien, Y.-L. Lai, C.-C. Yang, J. J. Lee, D. S. Raja, C.-H. Lin, *J. Mater. Chem. A Mater. Energy Sustain.* **2013**, *1*, 324. doi:10.1039/C2TA00030J

(b) K. Barthelet, J. Marrot, G. Férey, D. Riou, *Chem. Commun.* **2004**, 520. doi:10.1039/B312589K

(c) Q. Yang, S. Vaesen, M. Vishnuvarthan, F. Ragon, C. Serre, A. Vimont, M. Daturi, G. De Weireld, G. Maurin, *J. Mater. Chem.* **2012**, *22*, 10210. doi:10.1039/C2JM15609A

[21] (a) H. Reinsch, S. Waitschat, S. M. Chavan, K. P. Lillerud, N. Stock, *Eur. J. Inorg. Chem.* **2016**, 4490. doi:10.1002/EJIC.201600295

(b) M. Lammert, M. T. Wharmby, S. Smolders, B. Bueken, A. Lieb, K. A. Lomachenko, D. De Vos, N. Stock, *Chem. Commun.* **2015**, 12578. doi:10.1039/C5CC02606G

[22] (a) G. Wißmann, A. Schaate, S. Lilienthal, I. Bremer, A. M. Schneider, P. Behrens, *Microporous Mesoporous Mater.* **2012**, *152*, 64. doi:10.1016/J.MICROMESO.2011.12.010

(b) O. V. Gutov, S. Molina, E. C. Escudero-Adán, A. Shafir, *Chem. – Eur. J.* **2016**, *22*, 13582. doi:10.1002/CHEM.201600898

(c) A. Schaate, P. Roy, A. Godt, J. Lippke, F. Waltz, M. Wiebcke, P. Behrens, *Chem. – Eur. J.* **2011**, *17*, 6643. doi:10.1002/CHEM.201003211

[23] (a) S.-H. Lo, C.-H. Chien, Y.-L. Lai, C.-C. Yang, J. J. Lee, D. S. Raja, C.-H. Lin, *J. Mater. Chem. A Mater. Energy Sustain.* **2013**, *1*, 324. doi:10.1039/C2TA00030J

(b) E. D. Bloch, D. Britt, C. Lee, C. J. Doonan, F. J. Uribe-Romo, H. Furukawa, J. R. Long, O. M. Yaghi, *J. Am. Chem. Soc.* **2010**, *132*, 14382. doi:10.1021/JA106935D

(c) H. W. B. Teo, A. Chakraborty, S. Kayal, *Microporous Mesoporous Mater.* **2018**, *272*, 109. doi:10.1016/J.MICROMESO.2018.06.016

(d) W. Liang, L. Li, J. Hou, N. D. Shepherd, T. D. Bennett, D. M. D'Alessandro, V. Chen, *Chem. Sci.* **2018**, *9*, 3508. doi:10.1039/C7SC05175A

[24] A. De Lorenzi, S. Giorgianni, R. Bini, *Mol. Phys.* **1999**, *96*, 101.

[25] (a) G. C. Shearer, S. Chavan, S. Bordiga, S. Svelle, U. Olsbye, K. P. Lillerud, *Chem. Mater.* **2016**, *28*, 3749. doi:10.1021/ACS.CHEMMATER.6B00602

(b) G. C. Shearer, S. Chavan, J. Ethiraj, J. G. Vitillo, S. Svelle, U. Olsbye, C. Lamberti, S. Bordiga, K. P. Lillerud, *Chem. Mater.* **2014**, *26*, 4068. doi:10.1021/CM501859P

[26] E. Papirer, R. Lacroix, J.-B. Donnet, G. Nan, P. Fioux, *Carbon* **1995**, *33*, 63. doi:10.1016/0008-6223(94)00111-C

[27] M. R. Alexander, G. E. Thompson, G. Beamson, *Surf. Interface Anal.* **2000**, *29*, 468. doi:10.1002/1096-9918(200007)29:7<468::AID-SIA890>3.0.CO;2-V

[28] N. Tannert, S.-J. Ernst, C. Jansen, H.-J. Bart, S. K. Henninger, C. Janiak, *J. Mater. Chem. A Mater. Energy Sustain.* **2018**, *6*, 17706. doi:10.1039/C8TA04407D

[29] (a) M. Haouas, F. Taulelle, C. Martineau, *Prog. Nucl. Magn. Reson. Spectrosc.* **2016**, *94–95*, 11. doi:10.1016/J.PNMRS.2016.01.003

(b) P. Soubayrol, G. Dana, *Magn. Reson. Chem.* **1996**, *34*, 638. doi:10.1002/(SICI)1097-458X(199608)34:8<638::AID-OMR926>3.0.CO;2-5

(c) D. Muller, W. Gessner, *Chem. Phys. Lett.* **1981**, *79*, 59. doi:10.1016/0009-2614(81)85288-8

[30] A. W. Thornton, R. Barbarao, A. Jain, F. Trouselet, F.-X. Coudert, *Dalton Trans.* **2016**, 4352. doi:10.1039/C5DT04330A

[31] M. Thommes, K. Kaneko, A. V. Neimark, J. P. Olivier, F. Rodriguez-Reinoso, J. Rouquerol, K. S. W. Sing, *Pure Appl. Chem.* **2015**, *87*, 1051. doi:10.1515/PAC-2014-1117

[32] M. P. Suh, H. J. Park, T. K. Prasad, D.-W. Lim, *Chem. Rev.* **2012**, *112*, 782. doi:10.1021/CR200274S

[33] G. Cavallo, P. Metrangolo, R. Milani, T. Pilati, A. Priimagi, G. Resnati, G. Terraneo, *Chem. Rev.* **2016**, *116*, 2478. doi:10.1021/ACS.CHEMREV.5B00484

[34] (a) Q. Wang, J. Bai, Z. Lu, Y. Pan, X. You, *Chem. Commun.* **2016**, 443. doi:10.1039/C5CC07751F

(b) Q.-G. Zhai, X. Bu, X. Zhao, D.-S. Li, P. Feng, *Acc. Chem. Res.* **2017**, *50*, 407. doi:10.1021/ACS.ACCOUNTS.6B00526

Supplementary Material

Halogen Functionalization of Aluminium Fumarate Metal-Organic Framework via in-situ Hydrochlorination of Acetylenedicarboxylic Acid

Tobie J. Matemb Ma Ntep,[A] Wei Wu,[A] Hergen Breitzke,[B] Carsten Schlüsener,[A] Bastian Moll,[A] Laura Schmolke,[A] Gerd. Buntkowsky [B] and Christoph Janiak[A,C]

[A] Institut für Anorganische Chemie und Strukturchemie, Heinrich-Heine-Universität Düsseldorf, Universitätsstraße 1, D- 40225 Düsseldorf, Germany

[B] Eduard-Zintl-Institut für Anorganische und Physikalische Chemie, Technische Universität Darmstadt, Alarich-Weiss-Straße. 4, D-64287 Darmstadt, Germany

[C] Corresponding author: E-mail: janiak@uni-duesseldorf.de; Fax: + 49-211-81-12287; Tel: +49-211-81-12286

Additional email addresses:
tobie.matemb.ma.ntep@uni-duesseldorf.de; wei.wu@uni-duesseldorf.de; breitzke@chemie.tu-darmstadt.de; laura.schmolke@uni-duesseldorf.de; carsten.schluesener@uni-duesseldorf.de; bastian.moll@uni-duesseldorf.de; gerd.buntkowsky@chemie.tu-darmstadt.de

Table of contents

Materials, syntheses and methods

Acetylenedicarboxylic acid Acetylenedicarboxylic acid (H_2ADC, purity 97%) was purchased from Alfa Aesar; aluminium chloride hexahydrate ($AlCl_3$, purity 99%) was purchased from Janssen Chimica; N,N-dimethylformamide (DMF, analytical reagent grade) and Ethanol (analytical reagent grade) were purchased from Fischer Chemical; acetic acid (purity >99%) was purchased from VWR Chemicals. All reagents were used as purchased, without further purification.

Synthesis procedure of aluminium chlorofumarate (MIL-53-Fum-Cl)

Al-MIL-53-Fum-Cl was synthesized by mixing $AlCl_3{\cdot}6H_2O$ (483 mg, 2 mmol), H_2ADC (228 mg, 2 mmol), 50 mL DMF and 5 mL acetic acid as modulator in a 100 mL Duran bottle with a screw cap, which was heated at 85 °C for 72 h. light brown/yellowish powder was isolated from brown mother liquor by centrifugation and washed three times with fresh 5mL DMF, followed by washing three times with 5mL ethanol. After centrifugation, the product was allowed to dry at room temperature in air. The as-synthesized material was heated 7h at 150 °C under dynamic vacuum to yield the activated material. Yield = 296 mg (77%) based on the aluminium salt.

Synthesis procedure of aluminium fumarate (MIL-53-Fum)

Aluminium fumarate was synthesized according to a previously reported method.[1] In short, 513 mg of $Al_2(SO_4)_3{\cdot}18H_2O$, 179 mg fumaric acid and 92 mg urea were dissolved in 5 mL water, sealed in a Teflon lined autoclave and heated for 32 h at 110 °C in an oven. The resulting powder was washed with water and ethanol. It was activated by heating 7 h at 150 °C under dynamic vacuum.

Methods

All **powder X-ray (PXRD)** patterns were acquired using a Bruker D2 Phaser diffractometer equipped with a flat sample holder (also a flat silicon, low background sample holder). The devise operates with Cu $K\alpha_1/\alpha_2$ radiation $\lambda = 1.5418$ Å at 30 kV covering 2theta angles 5-50° over a time of 1 h, that is 0.0125 °/sec.

Raman spectroscopy was executed on a Bruker MultiRAM-FT Raman spectrometer equipped with a Nd:YAG-laser (wavelength 1064 nm). All Raman spectra were measured in solid state for 2500 scans with a laser power between 10-20 mW.

Infrared spectroscopy was done using a Bruker FT-IR Tensor 37 Spectrometer in the 4000-550 cm^{-1} region with 2 cm^{-1} resolution as KBr disks.

Thermogravimetric analysis (TGA) was performed using a Netzsch TG 209 F3 Tarsus thermal analyser under an air flow with a heating rate of 5 °C min^{-1}.

Conventional **CP MAS solid state NMR** measurements were carried out at room temperature on a Bruker AVANCE II+ spectrometer at 400 MHz proton resonance frequency, employing a Bruker 4 mm double resonance probe. ^{13}C CP MAS spectra were recorded utilizing ramped CP-MAS sequences at spinning rates of 8 kHz. Contact time was set to 1.5 ms and tppm decoupling with a 15° phase jump was applied during data acquisition.[2] ^{13}C spectra were referenced with respect to

TMS (tetramethylsilane). Frequency switched Lee Goldburg (FSLG) CP MAS HETCOR spectra were recorded at 8 kHz and contact times of 2 ms, 500 µs and 200 µs. The tppm decoupling sequence with a 15° phase jump was applied during data acquisition. ^{1}H spectra were recorded utilizing FSLG homonuclear decoupling, applying the same LG field strength and step width as for the FSLG HETCOR spectra. ^{1}H shift values of the direct dimension of these spectra were utilized to reference the indirect dimensions of the FSLG HETCOR spectra. The direct dimensions of the ^{1}H spectra were referenced with respect to TMS.

Liquid ^{1}H, ^{13}C NMR spectra were measured with a Bruker Avance III-300 (300 MHz). Prior to solution NMR analysis, an activated sample of MIL-53-Fum-Cl was digested as follows: 20 mg of MOF were suspended in water free DMSO-d_6 (0.65 mL). 5 drops of DCl (35 wt% in D_2O) were added. After 3 h, the yellowish supernatant solution was separated from the decanted white solid of aluminium oxide and introduced in the NMR tube for analysis.

X-ray photoelectron spectroscopy (XPS) was performed with an ULVAC-PHI VersaProbe II microfocus X-ray photoelectron spectrometer. The spectra were recorded using polychromatic aluminum Kα X-ray source (1486.8 eV) and referenced to the carbon 1s orbital with a binding energy of 284.8 eV. Fitting of the experimental XP spectra was done with the program CasaXPS, version 2.3.19PR1.0, copyright 1999-2018 Casa Software Ltd.

Scanning electron microscopy (SEM) images were obtained using a Jeol JSM-6510LV QSEM advanced electron microscope with a LaB_6 cathode at 5–20 keV. The samples for SEM imaging were coated with gold using a Jeol JFC 1200 fine-coater (20 mA for 25 s).

For **gas sorption studies** N_2, H_2, CH_4 and CO_2 isotherms were measured on a Quantachrome Autosorb iQ MP at 77 K (N_2, H_2) and 273 K (CH_4, CO_2), respectively. The specific surface area was calculated from the nitrogen sorption isotherms using the Brunauer-Emmett-Teller (BET) equation. All gases for the sorption measurements were of ultrapure grades (99.999%, 5.0).

Water vapor sorption isotherms were measured gravimetrically at 20 °C on a VSTAR^{TM} vapor sorption analyzer (Model number Vstar4-0000-1000-XS) from Quantachrome. For this purpose, about 25 mg of activated sample were introduced in the measuring cell and connected to the analysis port of the analyzer.

Infrared and Raman spectra of MIL-53-Fum-Cl and MIL-53-Fum

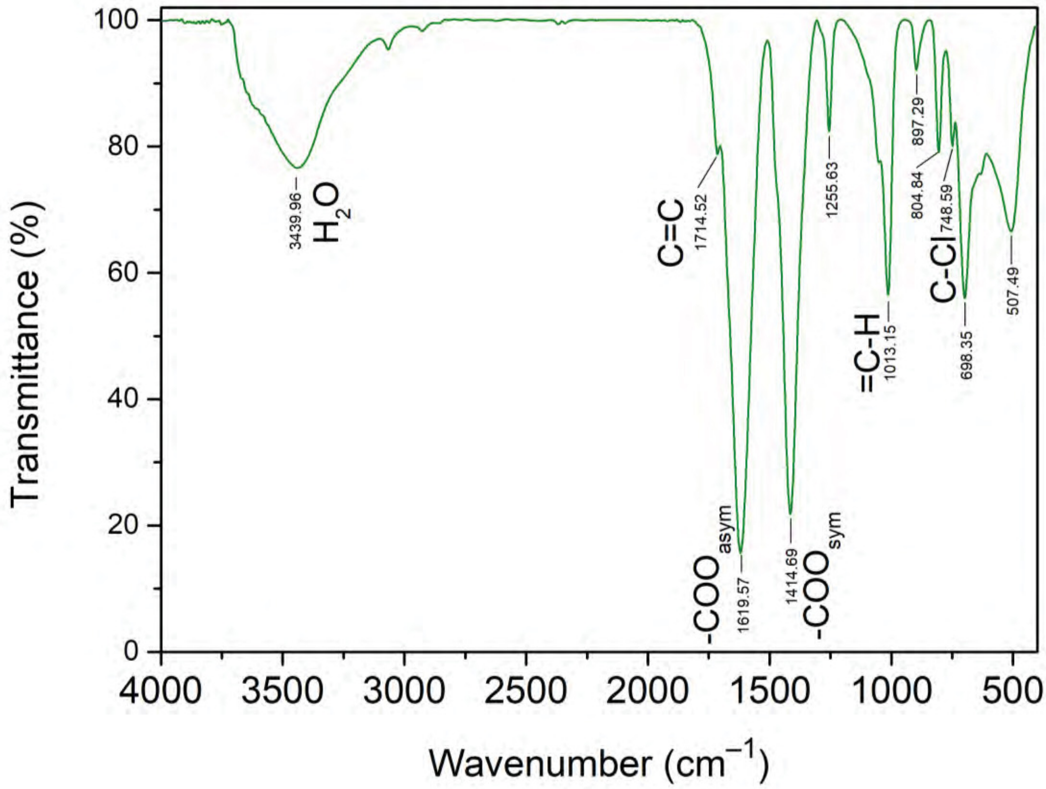

Fig. S1 Infrared spectrum of MIL-53-Fum-Cl.

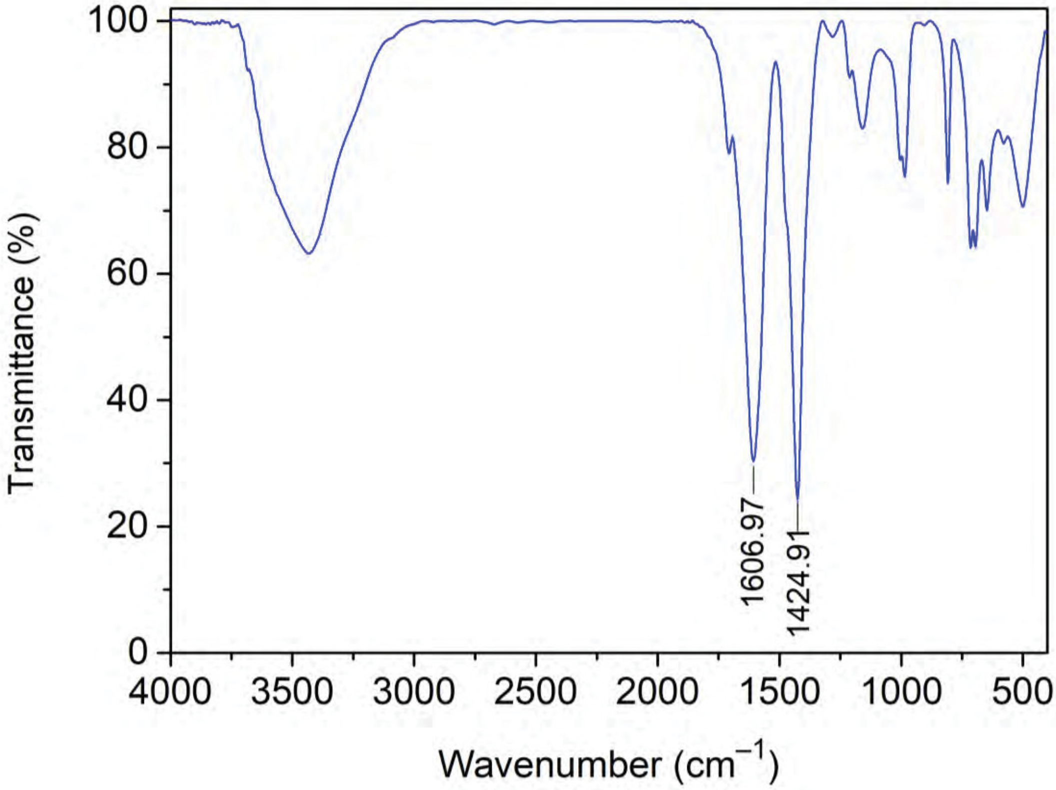

Fig. S2 Infrared spectrum of aluminium fumarate (MIL-53-Fum).

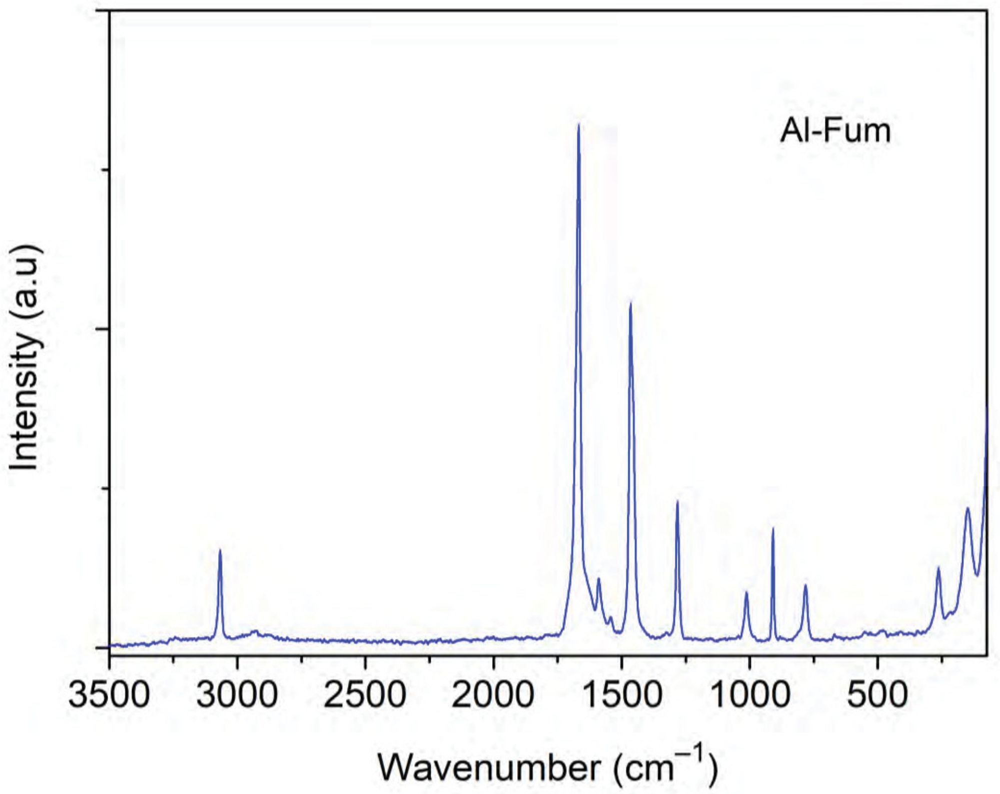

Fig. S3 Raman spectrum of aluminium fumarate.

Solid-state ^{1}H spectrum of MIL-53-Fum-Cl

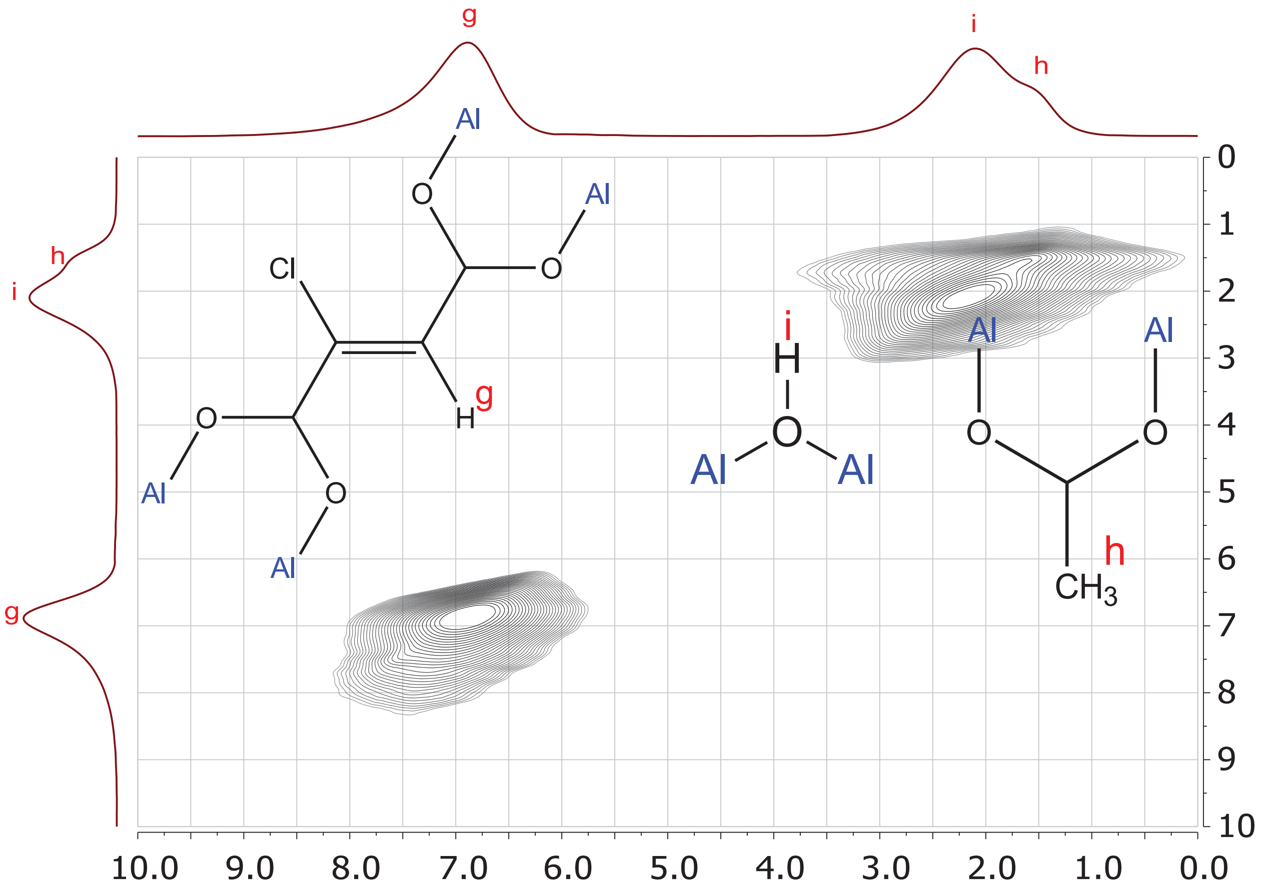

Fig. S4 Homonuclear decoupled 2D FSLG proton (^{1}H-^{1}H) spectrum at 8 kHz spinning speed and 200 μs contact time of MIL-53-Fum-Cl.

Liquid ^{1}H and ^{13}C NMR spectra of MIL-53-Fum-Cl

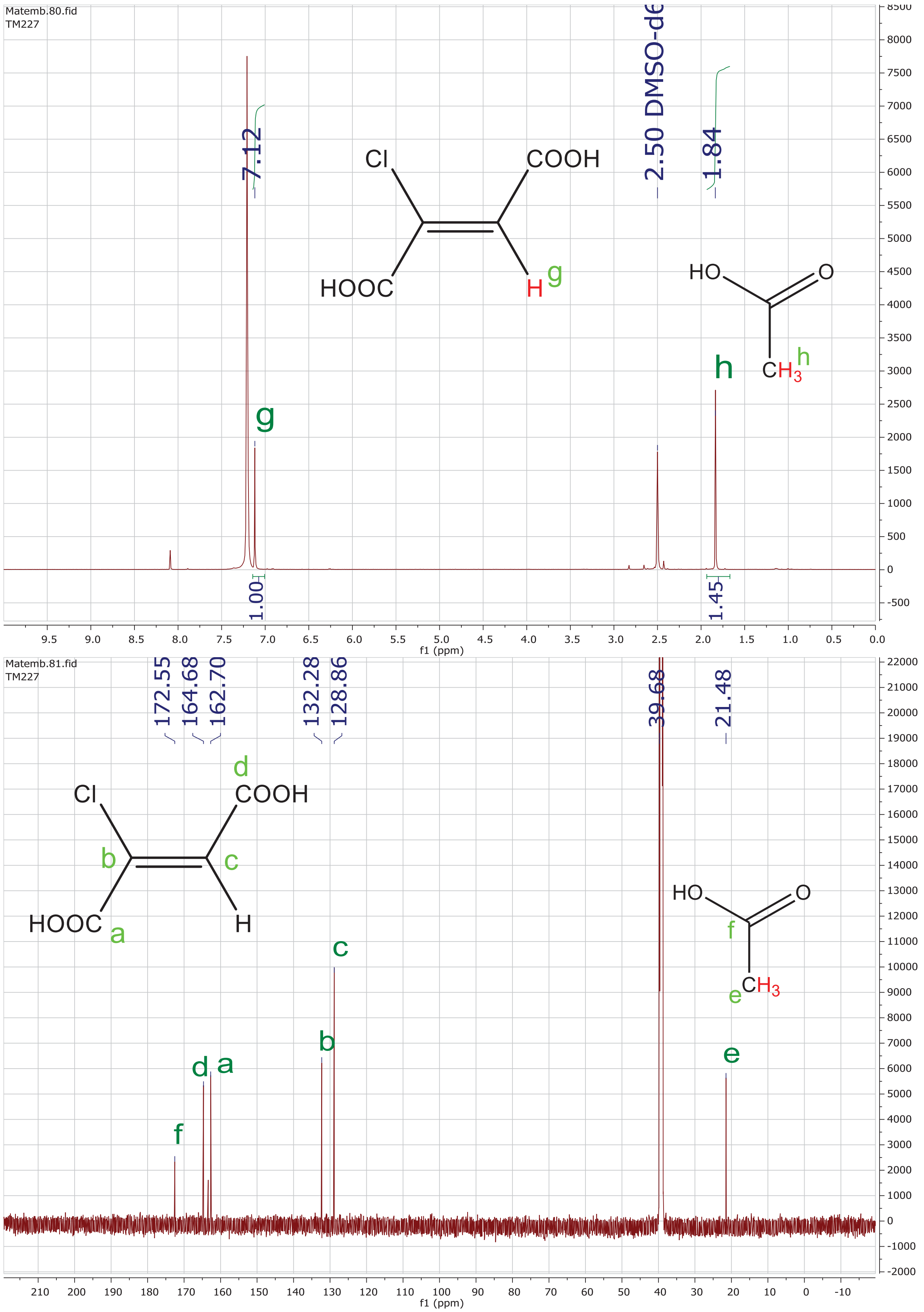

Fig. S5 Liquid ^{1}H (top) and ^{13}C (bottom) NMR spectra of digested Al-Fum-Cl in DMSO-d$_6$.

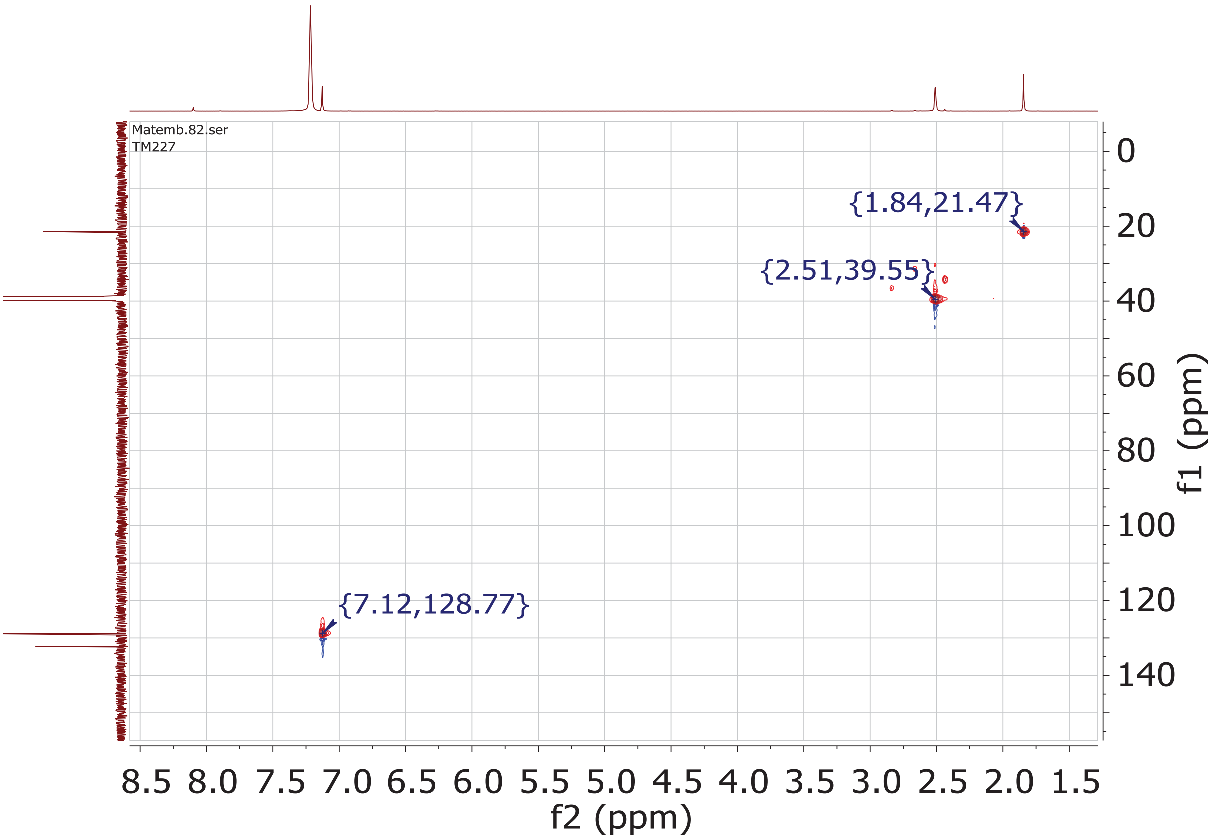

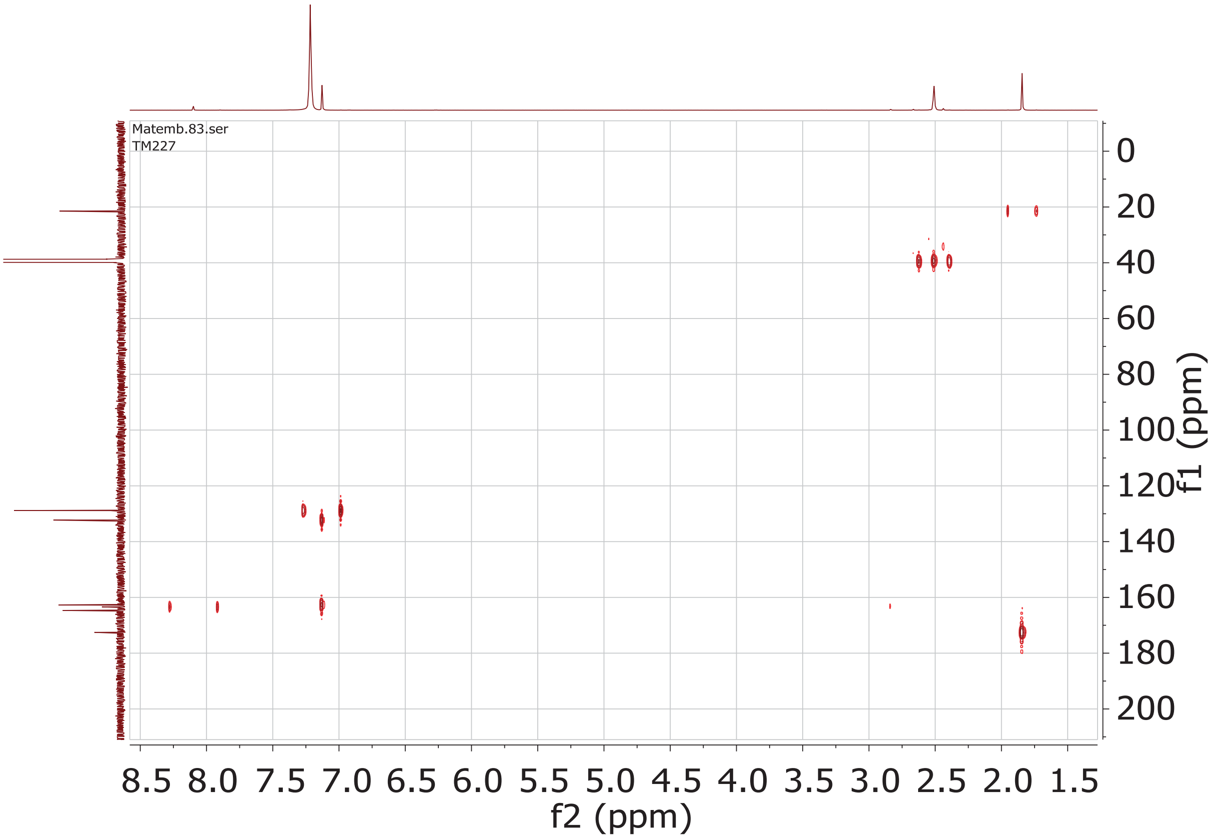

Fig. S6 2D ^{1}H-^{13}C HSQC (top) and HMBC (bottom) NMR spectra of digested MIL-53-Fum-Cl in water free DMSO-d_6. HSQC = Heteronuclear Multiple Quantum Correlation, HMBC = Heteronuclear Multiple Bond Correlation.

HSQC correlates the chemical shift of protons with chemical shift of the directly bonded carbons. HMBC gives correlations between protons and carbons that are separated by two or three bonds (direct one-bond correlations are suppressed).

Determination of missing linker ratio in MIL-53-Fum-Cl MOF from liquid ^{1}H NMR

$$\frac{Acetate}{Fum-Cl}\text{molar ratio} = \frac{\left(\frac{Integration\ of\ acetate\ signal}{Number\ of\ protons\ per\ acetate}\right)}{\left(\frac{Integration\ of\ Fum-Cl\ signal}{Number\ of\ protons\ per\ Fum-Cl}\right)}$$

$$= \left(\frac{Integ.of\ acet.}{3}\right) \times \left(\frac{1}{Integ.of\ Fum-Cl}\right)$$

Hence, the acetate to linker molar ratio is calculated to 0.689.

Considering the unit formula [Al(OH)$_{1+x}$ (Fum-Cl)$_{1-x}$(Ac)$_x$] where *x* is the number of missing linker per unit formula:

$$\frac{Ac}{Fum-\mathrm{x}}\text{molar ratio} = m_R = \frac{x}{1-x}\ , \qquad \text{which leads to} \quad x = \frac{m_R}{1+m_R}$$

The corresponding amount of missing linker per unit formula is 0.4.

Energy dispersive X-ray spectroscopy (EDX) of MIL-53-Fum-Cl

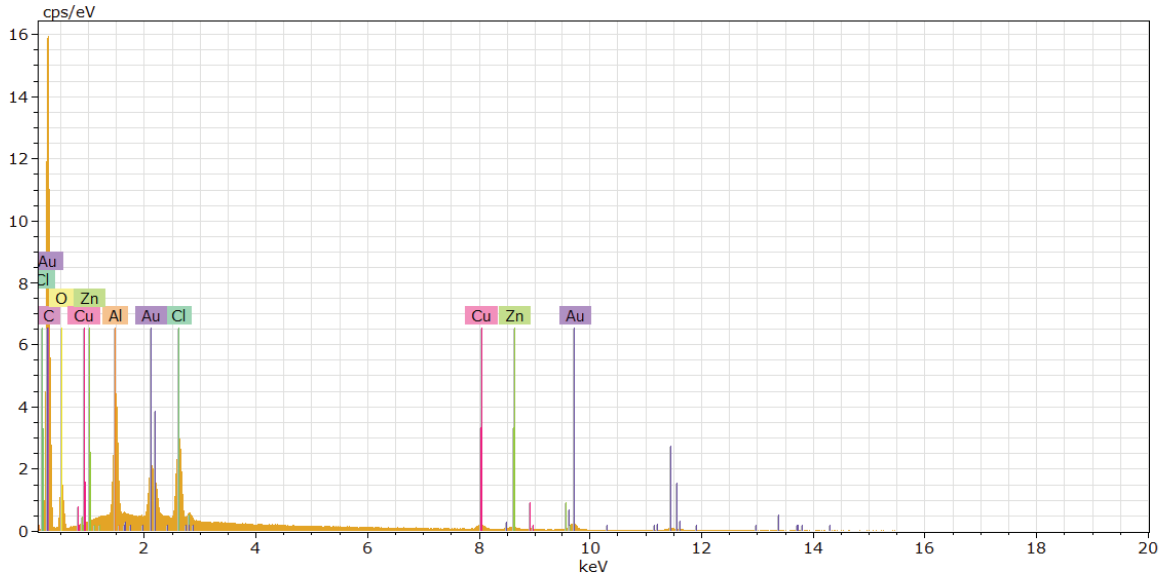

Fig. S7 EDX spectrum of MIL-53-Cl.

Table S1. Atom and Weight % of C, O, Cl and Al for MIL-53-Fum-Cl

Element [a]	atom#	Series	mass fraction [wt.%]	[norm. wt.%]	atom fraction [norm. At.%]	standard deviation for wt.% (1 Sigma)
C	6	K-Series	62.5	70.6	85.6	7.3
O	8	K-Series	9.8	11.1	10.1	1.5
Al	13	L-Series	2.8	3.12	1.7	0.2
Cl	17	L-Series	2.7	3.04	1.2	0.1
Au	79	L-Series	8.4	9.4	0.7	0.3
Cu	29	K-Series	1.3	1.5	0.3	0.1
Zn	30	K-Series	1	1.1	0.3	0.1
		Summe:	96.04	100	100	

[a] The element signals for Au, Cu, Zn stem from the sputtering and brass sample holder.

X-ray photoelectric spectroscopy (XPS) of MIL-53-Fum-Cl

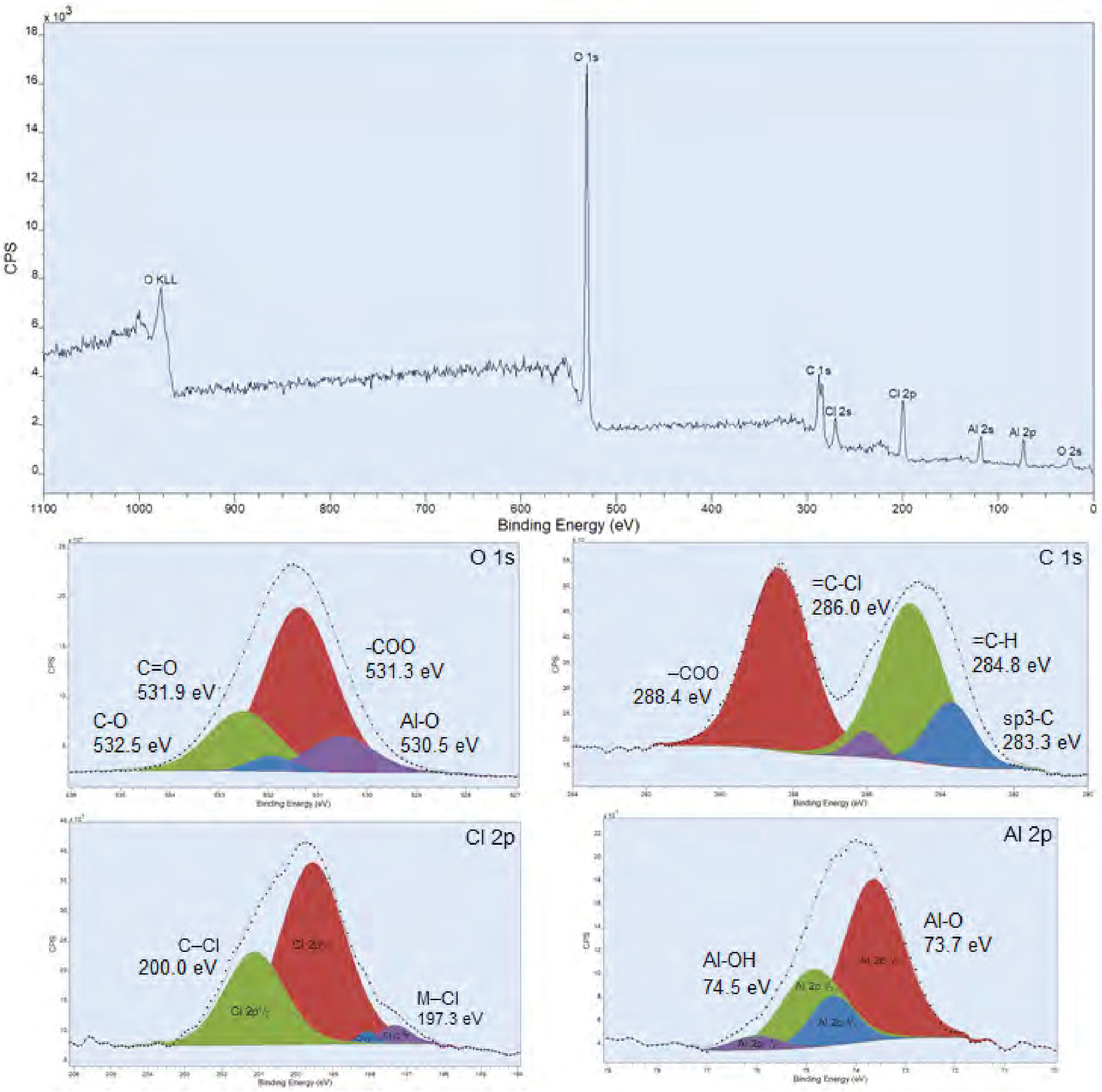

Fig. S8 XPS survey spectrum of MIL-53-Fum-Cl and high resolution core-level in the region of O 1s, C 1s, Cl 2p and Al 2p.

The structure of new material consists therefore of chains Al atoms bridged by two chlorofumarate linkers and one μ-OH (Fig. 3). The obtained material is therefore a chloro-functionalized version of aluminium fumarate, that is, MIL-53-Fum-Cl consists of *trans*-corner sharing AlO_6 octahedra, linked together by chlorofumarate to form lozenge-shaped one-dimensional chloro-decorated pores.

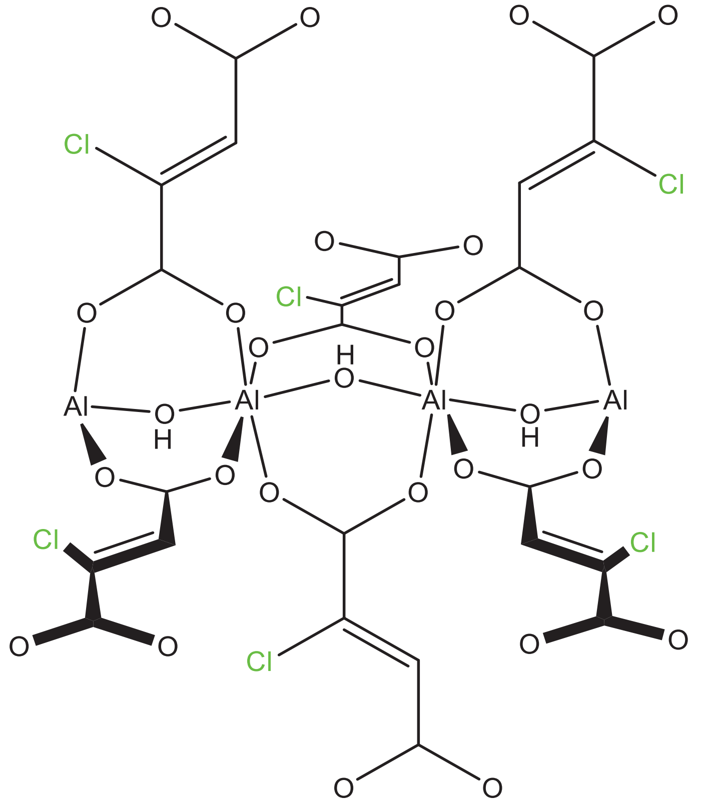

Fig. S9 Structural building block of MIL-53-Fum-Cl framework.

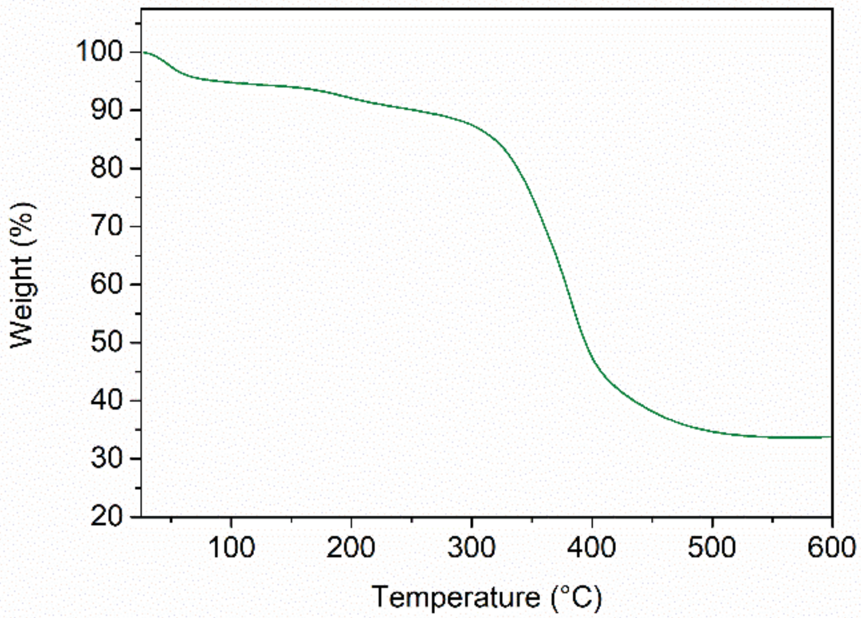

Fig. S10 Trace of thermogravimetric analysis under air for MIL-53-Fum-Cl.

Missing linker defect calculation

The ideal (defect-free) **MIL-53-Fum-Cl** (Al-Fum-Cl) MOF formula would be [Al(OH)(Fum-Cl)]

$$2\ \mathrm{Al(OH)(Fum\text{-}Cl)} + 11/2\ \mathrm{O_2} \xrightarrow{\qquad} \mathrm{Al_2O_3} + 8\ \mathrm{CO_2} + 2\ \mathrm{H_2O} + \mathrm{Cl_2}$$

The desolvated form Al(OH)(Fum-Cl) would yield 0.5 equivalents Al_2O_3 as a solid residue upon complete decomposition under air.

The equivalent mass of the solid residue would be: 0.5 × $M(Al_2O_3)$ = 50.98 g

The molar mass of ideal **MIL-3-Fum-Cl**: M[Al(OH)(Fum-Cl)] = 192.49 g mol^{-1}, is a factor of 3.78 higher than the solid residue.

The ideal plateau of the desolvated MOF should then be found at 378% on the TG trace normalized to 100% solid residue i.e $Wt_{\text{ideal plat.}}$ = 378% and W_{end} = 100% (Fig. S11).

The experimental plateau of the final desolvated MIL-53-Fum-Cl is found at a weight loss of $Wt_{\text{exp.plat.}}$ = 268% (Fig. S11).

A value for expected weight loss is:

$$Wt_{\text{pL.theo}} = (Wt_{\text{ideal plat.}} - W_{\text{end}}) = (378 - 100) / 6 = 278\%$$

The number of experimental linkers (x = number of linker deficiency) per formula unit is:

$NL_{\text{exp.}} = 1 - x = (Wt_{\text{exp. plat.}} - W_{\text{end}}) / Wt_{\text{pL.theo}} = (268 - 100) / 278 = 0.6$ and then the number of linker deficiency per formula unit is x = 0.4 which is the same value found from NMR analysis.

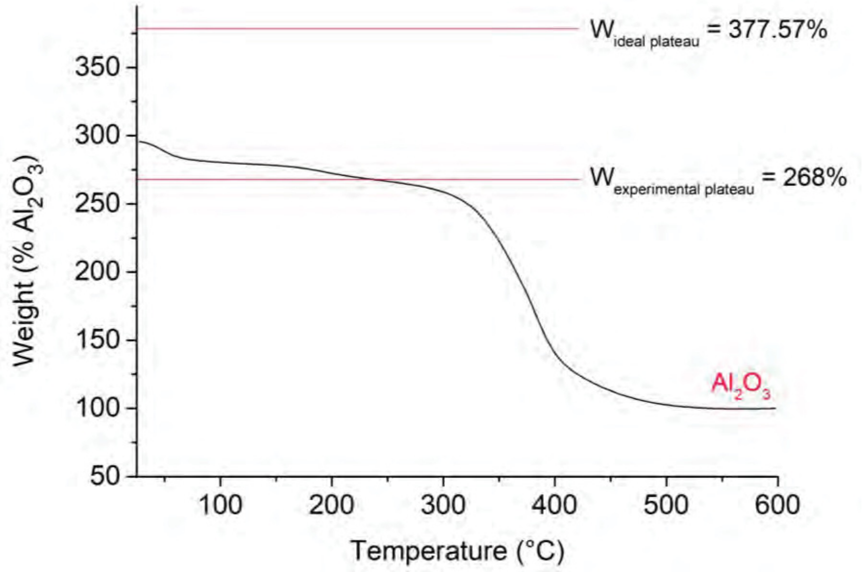

Fig. S11 Normalized TGA curve of MIL-53-Fum-Cl.

PXRD patterns of the chemical stability testing

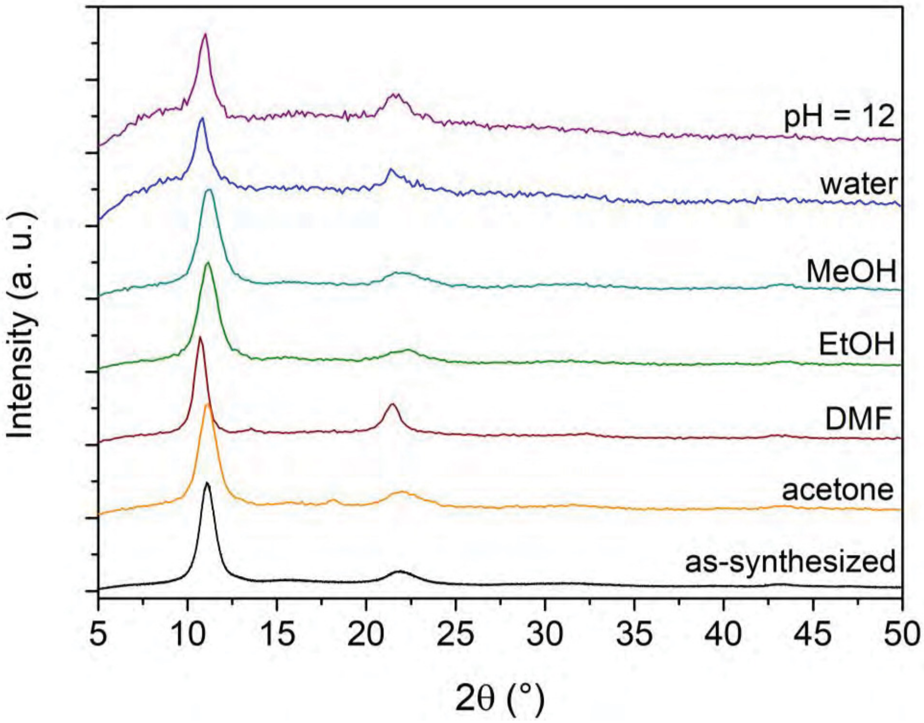

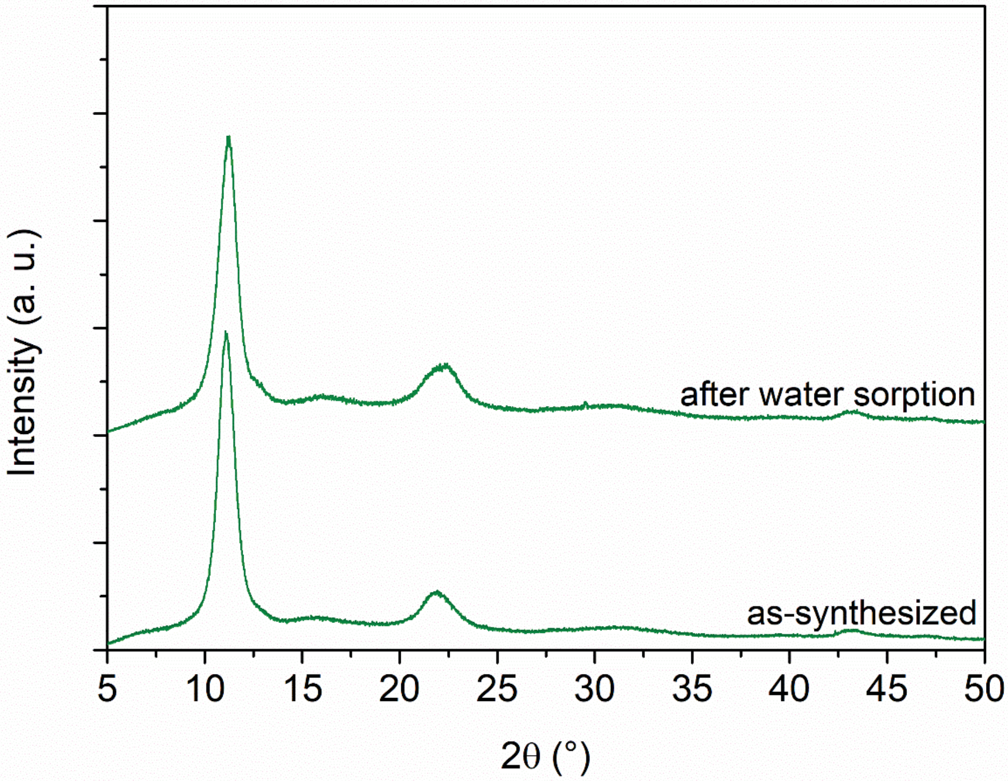

Fig. S12 PXRD patterns of MIL-53-Fum-Cl after stirring 24 h at room temperature in various solvents and solutions (top). PXRD of MIL-53-Fum-Cl after water sorption experiment (bottom).

Nitrogen sorption isotherms and porosities of MIL-53-Fum-Cl and MIL-53-Fum

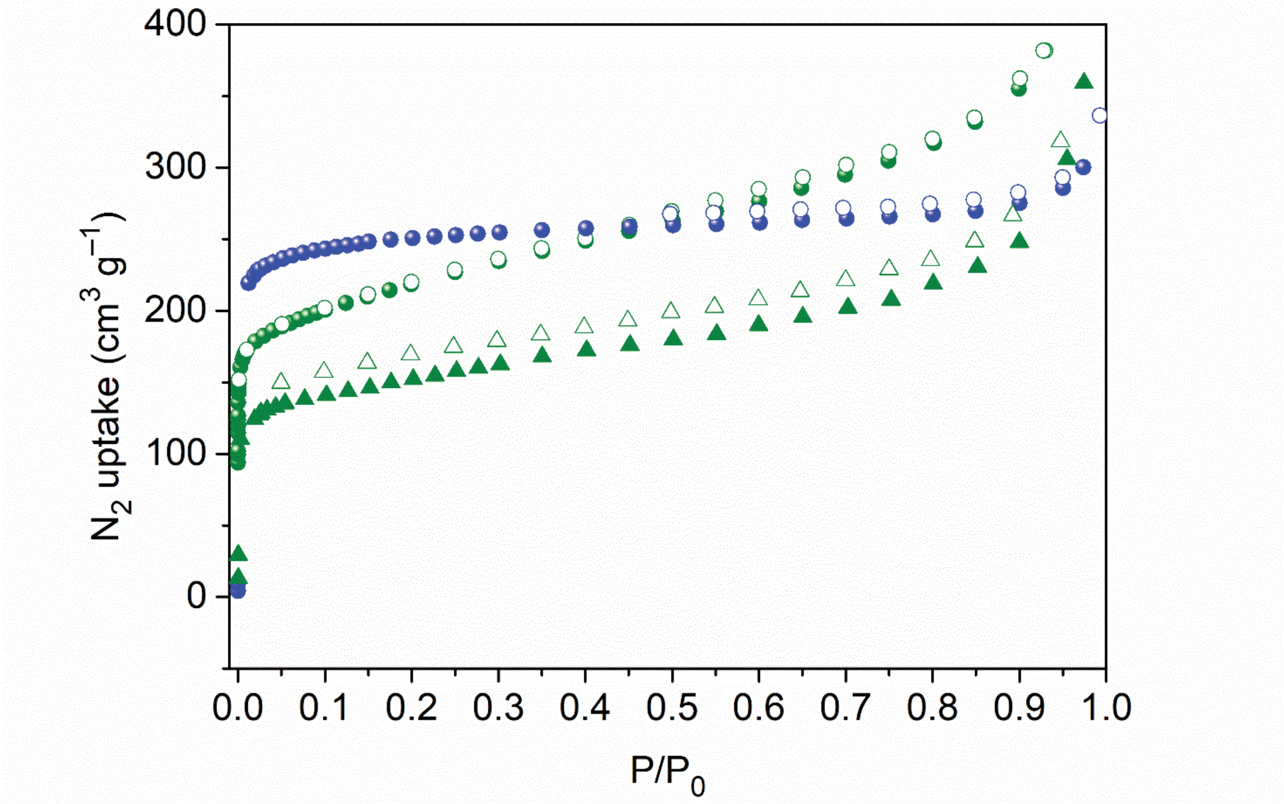

Fig. S13 Nitrogen sorption isotherms of MIL-53-Fum-Cl (green; circles before water sorption; triangle after water sorption) and MIL-53-Fum (blue) (filled symbols: adsorption; empty symbols: desorption).

For MIL-53-Fum-Cl the N_2 isotherm in Fig. S12 is of Type Ib at lower and Type II at higher relative pressure, the latter due to interparticle macropore condensation. The isotherm of aluminium fumarate (MIL-53-Fum) features a type I typical for microporous materials.

Table S2. Surface area and porosity parameters of MIL-53-Fum-Cl and MIL-53

Adsorptive	**S_{BET} (m^2g^{-1}) [a]**	**$S_{micro\text{-}BET}$ (m^2g^{-1}) [b]**	**S_{Ext} (m^2g^{-1}) [c]**	**$V_{pore\ (total)}$ (cm^3g^{-1}) [d]**	**$V_{pore\ (micro)}$ (cm^3g^{-1}) [e]**
MIL-53-Fum-Cl	800	551	249	0.48	0.21
MIL-53-Fum-Cl aft. wat. sorp.	570	315	255	0.38	0.12
MIL-53-Fum	982	864	118	0.42	0.33

[a] BET surface areas (S_{BET}) were obtained from five adsorption points in the pressure range pp_0^{-1}=0.001-0.05. [b] Micropore areas ($S_{micro\text{-}BET}$) were obtained by t-plot and V-t-method. [c] External area (S_{Ext}) refers to all area that does not originate from micropores and it includes meso- and macropores, i.e. pores > 2nm. Obtained by t-plot and V-t-method. [d] Total pore volumes ($V_{pore\ (total)}$) were derived at pp_0^{-1} = 0.95 for pores ≤ 20 nm. [e] Micropore volume ($V_{pore\ (micro)}$) refers to volume that originates only from micropores, obtained by V-t-method with thickness method 'DeBoer'. All correlation coefficients (r) within calculations were >0.999.

Fitting of CO_2, CH_4 and H_2 isotherms

Fits of adsorption isotherms were performed using the software **3P**Sim software.[3] **3P**Sim is a tool for interpretation and evaluation of experimental data from equilibrium and dynamic experiments. Several adsorption isotherm models including Henry, Toth, Freundlich, LAI, SIPS, Dual-site Langmuir, and DS Langmuir SIPS models. The isotherm model was validated based on the best correlation coefficient R^2. For the best fitting adsorption model, were calculated the affinity constant, the exponent and maximal loading. The Toth was the best fitting model for CO_2 and CH_4 isotherms, whereas the Sips model was the best to fit H_2 isotherms.

The Toth equation has the form is given by the equation 1

$$q = q_{max} \cdot \frac{k \cdot p}{[1 + (k \cdot p)^t]^{1/t}} \qquad (1)$$

Where q is the amount adsorbed, $q_{\max}$ is the amount adsorbed at saturation / maximal loading, p is the equilibrium pressure, k is the Toth constant and t the Toth exponent. k and t describe the heterogeneity of the adsorbent surface.[4]

The Sips equation is given by the equation 2

$$q = q_{max} \cdot \frac{(k \cdot p)^t}{1 + (k \cdot p)^t} \qquad (2)$$

q is the gas amount adsorbed (mmol g^{-1}); q_{max} is the maximum loading; k is the affinity constant (bar^{-1}); t is the heterogeneity exponent; p is the pressure (bar).

The obtained fits are shown in Fig. S14 and the different parameter obtained are presented in Table S3 below.

The IAST (ideal adsorbed solution theory) calculation was done with the multicomponent IAST-Toth model. The mole fraction of 0.5 was set for each gas and the parameters (affinity constant, saturation capacity, exponent) obtained from the Toth fit were given as input, as well as the total pressure of 1 bar. The respective adsorbed fractions of CO_2 (x_1) and CH_4 (x_2) were generated from which the selectivity was calculated using the formula:

$$S = \frac{x_1/x_2}{y_1/y_2}$$

y_1 and y_2 are the mole fractions respectively of CO_2 and CH_4 in the adsorptive i.e $y_1 = y_2 = 0.5$ for our 50:50 gas mixture. $x_1 = 0.895$ and $x_2 = 0.105$ for MIL-53-Fum-Cl; $x_1 = 0.819$ and $x_2 = 0.181$ for MIL-53-Fum.

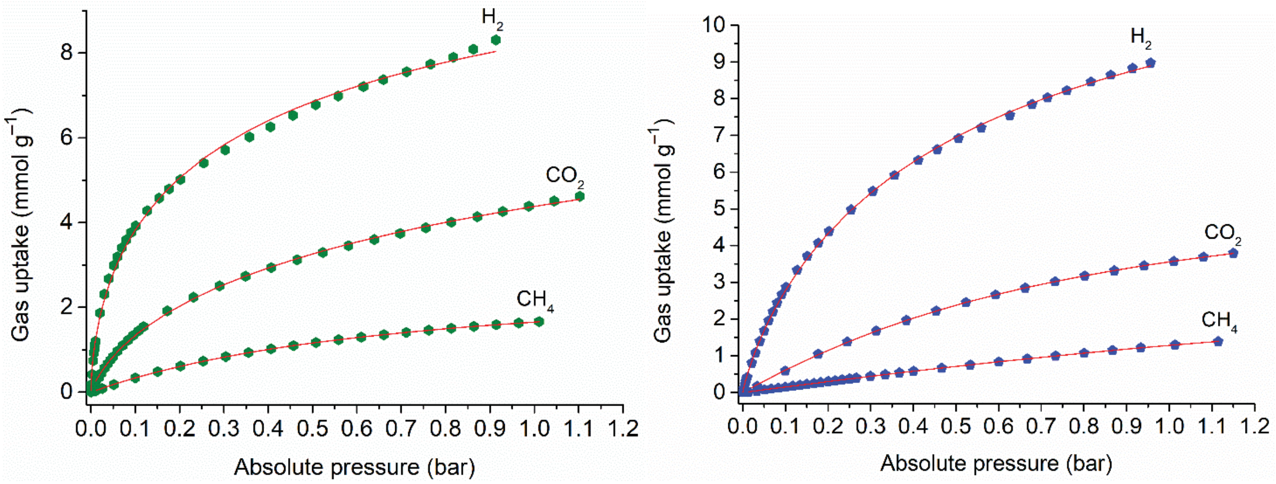

Fig. S14 Experimental CO_2, CH_4 and H_2 adsorption isotherms of MIL-53-Fum-Cl (green, left) and MIL-53-Fum, with corresponding Toth (CO_2 & CH_4, 273 K) or Sips (H_2, 77 K) model fits.

Table S3. Obtained Toth/Sips fitting parameters of CO_2 CH_4 and H_2 adsorption isotherms for MIL-53-Fum-Cl and MIL-53-Fum.

	MIL-53-Fum-Cl			**MIL-Fum**		
Gas	CO_2	CH_4	H_2	CO_2	CH_4	H_2
Toth/sips exponent	0.445	1.060	0.59	1.29	1.43	0.85
correlation coefficient R^2	0.999	0.999	0.998	0.999	0.999	0.999
affinity constant / bar^{-1}	2.73	1.34	2.18	1.09	0.41	1.87
maximal loading / mmol g^{-1} [a]	13.29	2.76	13.34	5.81	3.68	14.314

[a] amount adsorbed at saturation, that is maximal loading for the asymptotic curvature of the adsorption isotherm.

Determination of the isosteric heat of CO_2 adsorption

The CO_2 isotherms experimentally obtained respectively at 273 K and 298 K were fitted with the Langmuir-Freundlich model (eq. 1). The fits are shown in Fig. S15. The obtained fits were used to determine the pressure for each temperature corresponding to various CO_2 loadings. The isosteric heat of adsorption was finally calculated by applying the Clausius-Clapeyron equation (eq. 2).

$$q = q_{max} \cdot \frac{(k \cdot p)^t}{1 + (k \cdot p)^t} \qquad (1)$$

q is the gas amount adsorbed (mmol g^{-1}); q_{max} is the maximum loading; k is the affinity constant (bar^{-1}); t is the heterogeneity exponent; p is the pressure (kPa).

$$Q_{st} = -R\left(\frac{T_2 T_1}{T_2 - T_1}\right) ln\frac{P_2}{P_1} \qquad (2)$$

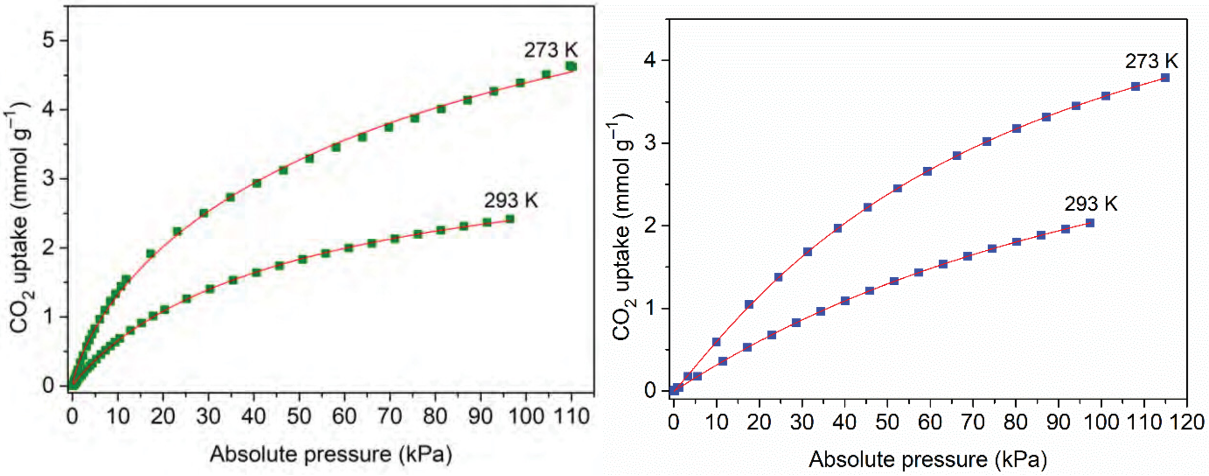

Fig. S15 Fitting of CO_2 adsorption isotherms with the Langmuir-Freundlich model for MIL-53-Fum-Cl (left, green) and MIL-53-Fum (right, blue). Symbols for experimental data and red lines for simulated fits.

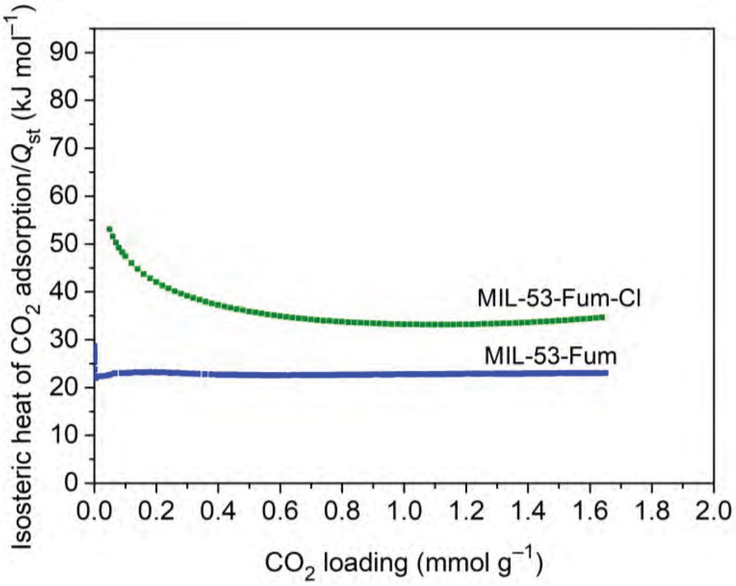

Fig. S16 Plot of isosteric heat of CO_2 adsorption for MIL-53-Fum-Cl (green) and MIL-53-Fum (blue) from isotherms data at 273 and 293 K.

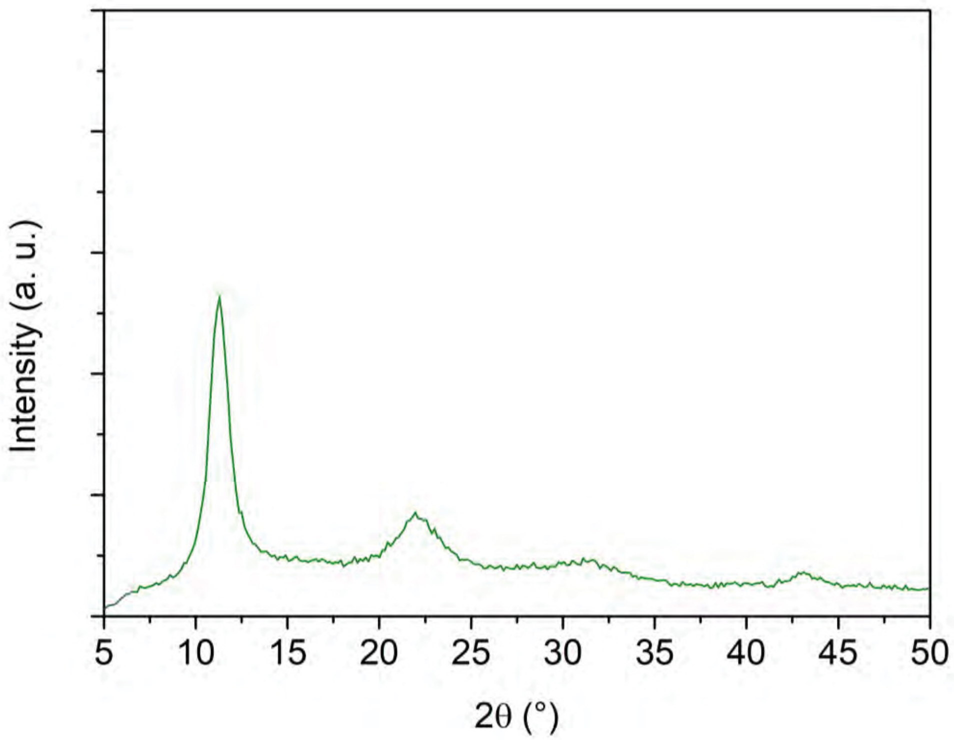

Fig. S17 PXRD pattern of MIL-53-Fum-Cl synthesized with formic acid modulator.

Discussion on the extra reflection at ~13° 2θ in the PXRD pattern of MIL-53-Fum

Examination of experimental PXRDs in the literature for MIL-53-Fum (= aluminium fumarate) and the related Ga-fumarate can exhibit a reflection at ~13° and ~15° 2θ angle. Often but not always the reflection at ~13° disappears and the reflection at ~15° shifts to slightly lower angle upon activation or samples where the original solvent has been exchanged with water (Fig. S18-S19 in Suppl. Mater.). Noteworthy, activation of MIL-53-Fum with increasing temperature (re-)introduces the peak at ~13° when starting from a most likely water-containing sample which only showed one peak at 2θ slightly below 15° (Fig. S20 in Suppl. Mater.).

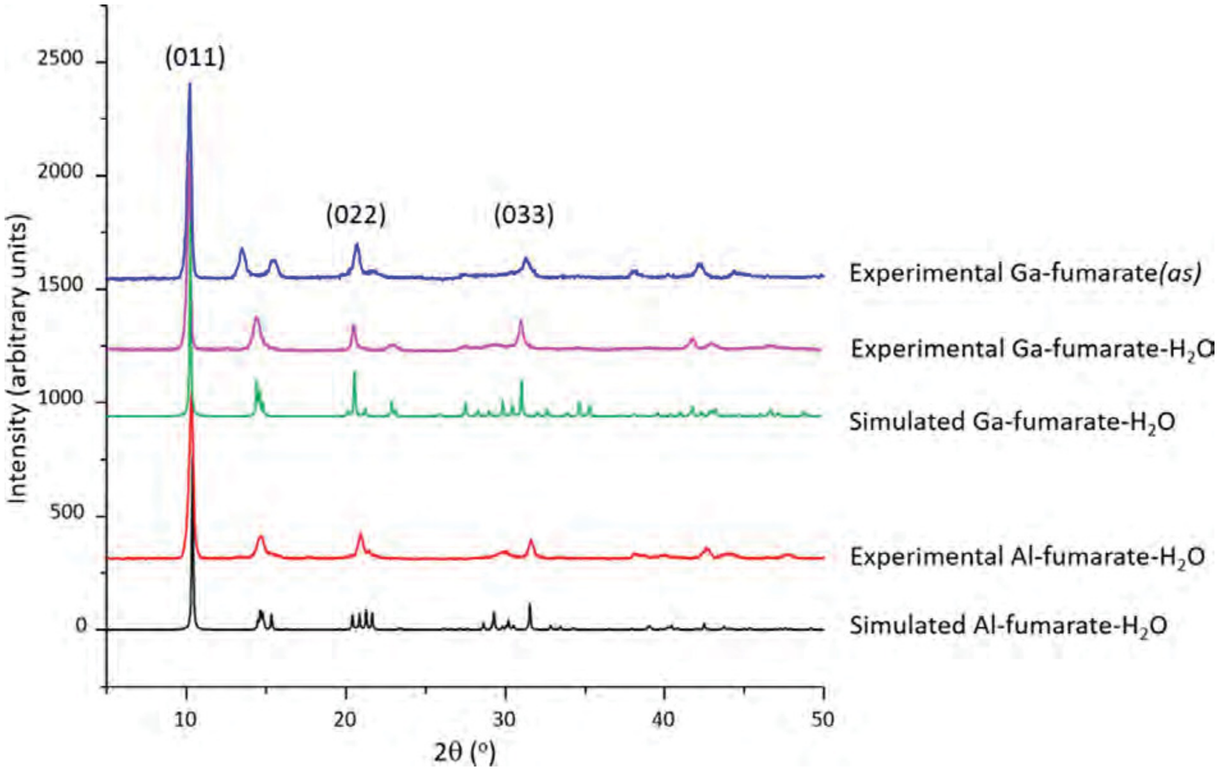

Fig. S18 Comparison of simulated and experimental PXRD patterns of Al- and Ga-fumarate MOFs, with select reflections labeled. The samples with water adsorbed within the channels are termed Al-fumarate−H_2O and Ga-fumarate−H_2O, respectively. The as-made sample of Ga-fumarate is referred to as Ga-fumarate(as). The 0kk reflections of Ga-fumarate−H_2O are shifted to lower angles versus those of Ga-fumarate(as), which indicates a small contraction of the MOF channel that propagates along the direction of the fumarate linker. Note the x-axis is truncated to exclude angles below 5°. Reprinted with permission from ref. Y. Zhang, B. E. G. Lucier S. M. McKenzie, M. Arhangelskis, A. J. Morris, T. Friščić, J. W. Reid, V. V. Terskikh, M. Chen, Y. Huang, *ACS Appl. Mater. Interfaces*, **2018**, *10*, 28582–28596. Copyright 2018 American Chemical Society.

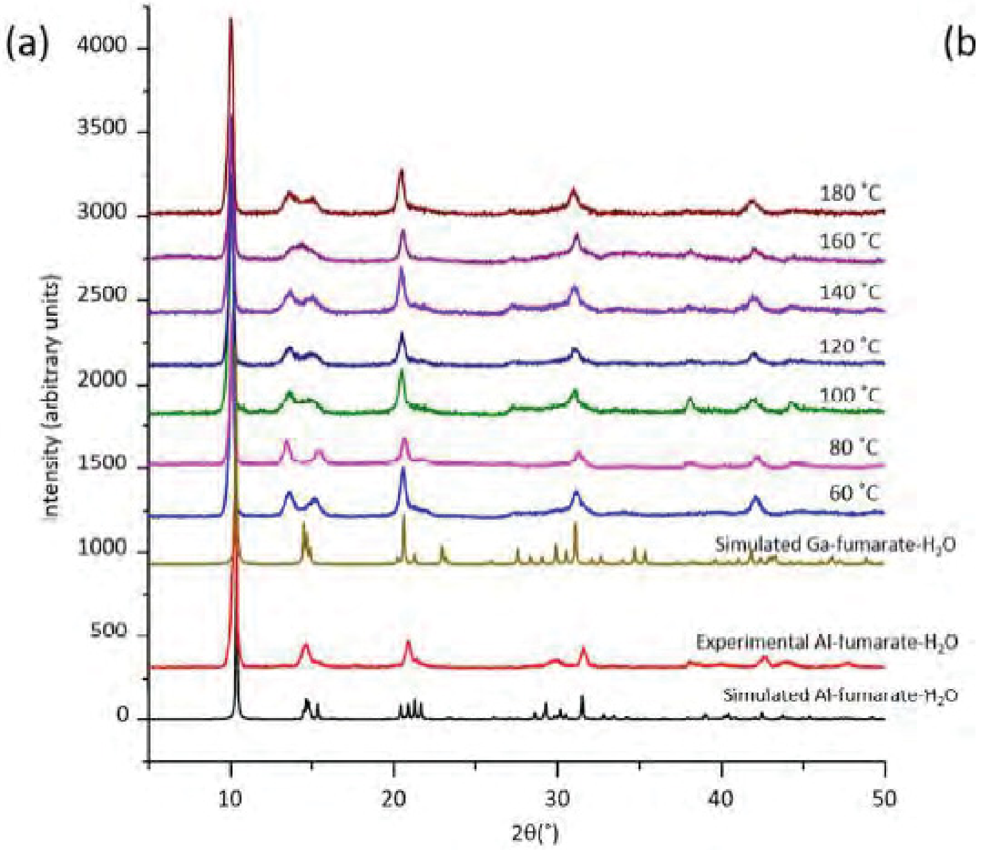

Fig. S19 The experimental PXRD patterns of as-synthesized Ga-fumarate prepared at temperatures ranging from 60 °C to 180 °C, along with experimental and simulated Al-fumarate-H_2O and simulated Ga-fumarate-H_2O PXRD patterns; all simulations were calculated from the corresponding crystal structures. Reprinted with permission from ref. Y. Zhang, B. E. G. Lucier S. M. McKenzie, M. Arhangelskis, A. J. Morris, T. Friščić, J. W. Reid, V. V. Terskikh, M. Chen, Y. Huang, *ACS Appl. Mater. Interfaces*, **2018**, *10*, 28582–28596. Copyright 2018 American Chemical Society.

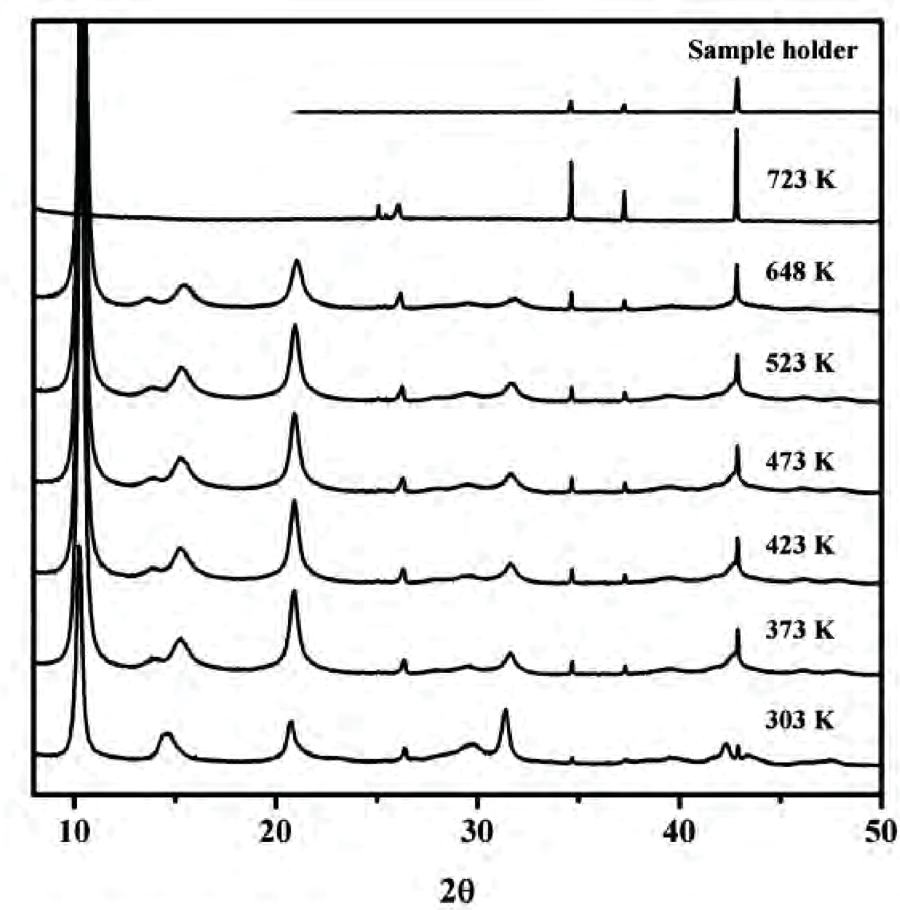

Fig. S20 PXRD of aluminium fumarate MOF at 303, 373, 423, 473, 523, 648 and 723 K and the sample holder (alumina). Reprinted with permission from ref. J. A. Coelho, A. Mafalda Ribeiro, A. F. P. Ferreira, S. M. P. Lucena, A. E. Rodrigues, D. C. S. de Azevedo, *Ind. Eng. Chem. Res*. **2016**, *55*, 2134−2143. Copyright 2016 American Chemical Society.

REFERENCES

---

[1] E. Alvarez, N. Guillou, C. Martineau, B. Bueken, B. Van de Voorde, Cl. Le Guillouzer, P. Fabry, F. Nouar, F. Taulelle, D. de Vos, J.-S. Chang, K. H. Cho, N. Ramsahye, T. Devic, M. Daturi, G. Maurin, C. Serre, *Angew. Chem. Int. Ed*. **2015**, *54*, 3664-3668.

[2] A. E. Bennett, C. M. Rienstra, M. Auger, K. V. Lakshmi, R. G. Griffin, Heteronuclear decoupling in rotating solids. *J. Chem. Phys*. **1995**, *103*, 6951-6958.

[3] 3P INSTRUMENTS, 3P sim, Version 1.1.0.7, Simulation and Evaluation Tool for mixSorb, 3P INSTRUMENTS 2018.

[4] A. P. Terzyk, J. Chatłas, P. A. Gauden, G. Rychlicki, P. Kowalczyk, *J. Colloid Interface Sci*. **2003**, *266*, 473-476.

2.6 Designing a new aluminum muconate metal-organic framework (MIL-53-Muc) as a methanol adsorbent for sub-zero temperature heat transformation applications

Tobie J. Matemb Ma Ntep, Helge Reinsch, Philipp P. C. Hügenell, Sebastian_Johannes Ernst, Emrah Hastürk, and Christoph Janiak

J. Mater. Chem. A. **2019**, *7*, 24973–24981.

DOI: 10.1039/c9ta07465a

Impact factor 2018: 10.15

The last step of this work was to investigate the influence on the vapor (water, alcohols) adsorption profile of elongating the fumarate linker into the *trans,trans*-muconate (Muc) linker. Meanwhile a UiO-type zirconium muconate MOF is already known, it was necessary to synthesize a new aluminum muconate MOF, as no such MOF was yet reported. Regarding the case of zirconium muconate (UiO-66-Muc) as an isoreticular expansion of zirconium fumarate (MOF-801), many attempts to synthesize this material in a good quality were unsuccessful. The synthesis of UiO-66-Muc is reported to be challenging and yields materials of poor crystallinity and very low porosity than expected. For example, Guillerm *et al.*[64] and Buragohain *et al.*[65] obtained this material with a BET surface area of 705 and 557 $m^2 g^{-1}$. The BET surface area of UiO-66-Muc should rationally largely exceed that of zirconium fumarate (990 $m^2 g^{-1}$), which is far to be the case. Gutov *et al.*[66] also obtained UiO-66-Muc single crystals, but did not provide any porosity characterization. However, the structure obtained in the latter work is conflicting with the formal in the configuration adopted by the Muc linker. Visibly, the zigzag nature of the *trans,trans*-muconate linker is not favorable for the construction of the **fcu** net topology like UiO-66. This point was recently demonstrated by Guillerm *et al.* who reported that Muc would preferably yield Zr-MOFs with the **bcu** net topology due to the zigzag (non-linear) shape of this linker.[67]

Unlike UiO-66-Muc, a new aluminum muconate MOF with the MIL-53 net topology like MIL-53-fum was successfully synthesized and evaluated for it applicability as adsorbent

---

[64] V. Guillerm, S. Gross, C. Serre, T. Devic, M. Bauer, G. Férey, *Chem. Commun*. **2010**, *46*, 767–769.

[65] A. Buragohain, S. Biswas, *Eur. J. Inorg. Chem*. **2015**, 2463–2468.

[66] O. V. Gutov, S. Molina, E. C. Escudero-Adán. A. Shafir, *Chem. Eur. J.* **2016**, *22*, 13582–13587.

[67] V. Guillerm, T. Grancha, I. Imaz, J. Juanhuix. D. Maspoch, *J. Am. Chem. Soc*. **2018**, *140*, 10153−10157.

for adsorption-based heat transformation applications (AHT). The stability and vapor sorption (water, methanol) were tested and revealed that the new MOF denoted has MIL-53-muc is a very promising adsorbent for AHT when paired with methanol as adsorptive.

The conclusion of this research is therefore that a twofold extension of the fumarate linker in the MIL-53-Fum structure is the best option of modification of this material to improve the efficiency of previously reported aluminum fumarate MOF (MIL-53-Fum) for AHT. However, the adsorptive has to be changed from water to methanol. It is worth mentioning that the water sorption isotherm profile of aluminum fumarate could also be improved just by producing the material from an appropriate synthesis route. The material produced from the synthesis route reported by Alvarez *et al.*[53] yields a water sorption isotherm with negligible hysteresis loop. The synthesis consists of reacting $Al_2(SO_4)_3$ with fumaric acid in water using urea as deprotonating/modulating agent instead of NaOH. A similar water sorption isotherm of aluminum fumarate without hysteresis was recently reported by Hanikel *et al.*[68] Their synthesis consists of reacting $AlCl_3$ with fumaric acid in water in the presence of KOH as deprotonating agent. The absence of hysteresis loop compared to what was observed by Jeremias *et al.*[55] was attributed to the larger crystallite size of the material obtained. A better performance of Al-MIL-53-Fum/water pair can therefore be anticipated. Detailed results of this work are contained in the article that follows.

Author´s contribution to the work:

- Idea and setting of the synthesis procedures.
- Synthesis and preparation of the samples for further characterization.
- Characterizations including PXRD experiments, TGA, chemical stability test, nitrogen sorption and determination of porosity parameters, other gas/vapor sorption (water, methanol) experiments.
- Five (05) cycles stability test of water ad-/desorption.
- Organization of other analyses (Raman, SEM and IR, multicycle methanol ad-/desorption stability test) and data analysis/interpretations and treatment.

---

[68] N. Hanikel, M. S. Prévot, F. Fathieh, E. A. Kapustin, H. Lyu, H. Wang, N. J. Diercks, T. G. Glover, O. M. Yaghi, *ACS Cent. Sci.* **2019**, *5* 1699−1706.

- Samples activation prior characterizations.
- Determination and plotting of the isosteric heat of water and methanol adsorption from isotherms measured at three different temperatures.
- Writing of the manuscript, drawing of figures and responses to reviewers during the review process.

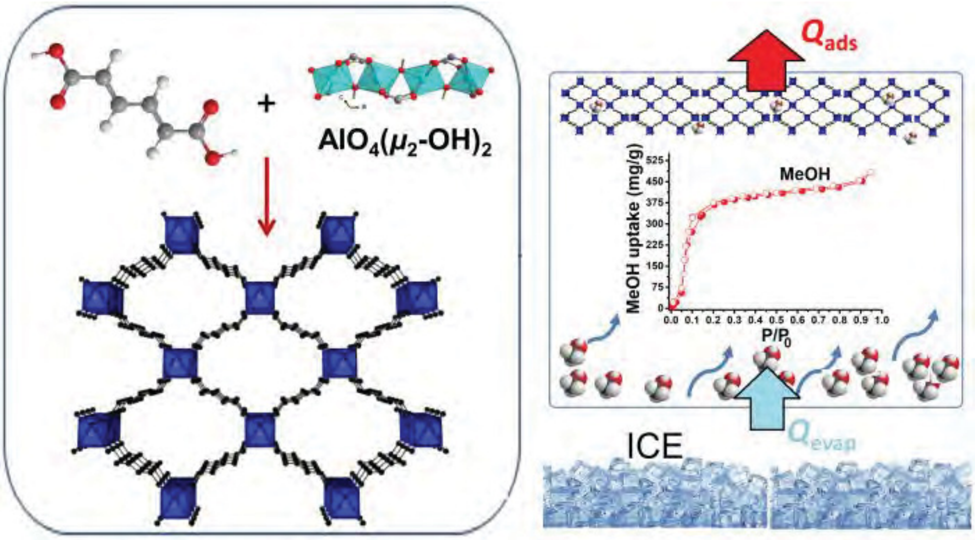

Journal of
Materials Chemistry A

PAPER

Cite this: *J. Mater. Chem. A*, 2019, **7**, 24973

Designing a new aluminium muconate metal–organic framework (MIL-53-muc) as a methanol adsorbent for sub-zero temperature heat transformation applications†

Tobie J. Matemb Ma Ntep,[a] Helge Reinsch,[b] Philipp P. C. Hügenell,[c] Sebastian-Johannes Ernst,[c] Emrah Hastürk[a] and Christoph Janiak *[a]

Employing methanol as an adsorbate can enable adsorption-driven heat pumps and chillers to operate at/or achieve temperatures below 0 °C, provided an appropriate pairing adsorbent is made available. By applying the principle of reticular chemistry, an isoreticular twofold expansion of aluminium fumarate was designed and synthesized using *trans*,*trans*-muconate as a linker to a new aluminium metal–organic framework (MOF) termed MIL-53-muc. MIL-53-muc is isostructural to the prototypical aluminium terephthalate (Al-MIL-53-BDC) and is therefore built from chains of *trans* corner-sharing $AlO_4(OH)_2$ octahedra connected by muconate linkers to a microporous network with lozenge-shaped one-dimensional pores. Featuring a high BET specific surface area of 1750 $m^2\ g^{-1}$, a type V (S-shaped) stepwise methanol adsorption isotherm in a 0.05–0.15 relative pressure range, a high methanol uptake capacity of about 0.5 g g^{-1} and methanol stability of over 50 assessed ad/desorption cycles, MIL-53-muc is revealed as a promising adsorbent applicable for adsorption-based heat transformation applications. The performance evaluation indicates that high coefficient of performance COP_H values above 1.5 could be reached for an evaporator operating at a temperature as low as −5 °C under heat pump conditions, while very low temperatures down to −10 °C could be achieved for refrigeration/ice making with COP_C values of up to 0.73 under cooling conditions. This makes MIL-53-muc/methanol outperform most other working pairs for adsorption-based cooling and heating applications under sub-zero temperature conditions. Furthermore, MIL-53-muc is hydrothermally stable and presents a favorable water sorption profile making this material also suitable for autonomous indoor humidity control applications.

Received 10th July 2019
Accepted 1st October 2019

DOI: 10.1039/c9ta07465a

rsc.li/materials-a

Introduction

Adsorption-based heat pumps (AHPs) and thermally driven adsorption chillers (TDCs) are air conditioning systems that have been introduced as sustainable and clean alternatives to traditional vapour-compression air systems operating on electricity or fossil fuels.[1] As AHPs and TDCs operate using solar heat or waste heat from industries, they can help to minimize electricity consumption.[2] Furthermore, unlike potentially ozone depleting chlorofluorocarbons (CFCs) used as the working fluid in compression heat exchangers, AHPs and TDCs use water, methanol or ethanol as coolants.[3]

The working principle of AHPs and TDCs is shown in Fig. 1. It is based on the evaporation and subsequent reversible adsorption of a coolant onto a porous material. The process releases heat during the working cycle and the fluid is desorbed and re-condensed by low temperature heating (solar heat or waste heat) during the regeneration cycle.[4]

The efficiency of AHPs and TDCs primarily depends on the performance of the applied adsorbent. The adsorbent should achieve high vapour uptakes at low relative pressures ($P/P_0 = 0.05$–0.3) with a stepwise isotherm (sigmoidal, S-shaped) featuring no or minor hysteresis. The material should also be stable over multiple adsorption–desorption cycles.[5,6] Although several types of materials have been applied for adsorption-based heat transformations including zeolites, silica gels, aluminium phosphates and activated carbons,[7] metal–organic frameworks (MOFs) are emerging as more promising materials for this application.[5,8] This is due to MOFs' high surface area and porosity, yielding higher

---

[a] *Institut für Anorganische Chemie und Strukturchemie, Heinrich-Heine-Universität Düsseldorf, Universitätsstraße 1, D- 40225 Düsseldorf, Germany. E-mail: janiak@uni-duesseldorf.de*

[b] *Institut für Anorganische Chemie, Christian-Albrechts-Universität zu Kiel, Max-Eyth-Straße 2, 24118 Kiel, Germany*

[c] *Fraunhofer Institute for Solar Energy Systems (ISE), Heidenhofstraße 2, 79110 Freiburg, Germany*

† Electronic supplementary information (ESI) available: IR and Raman spectra, TGA curve, PXRD patterns for the stability test, N_2 sorption and porosity, multicycle sorption stability, heat of adsorption, coefficient of performance. See DOI: 10.1039/c9ta07465a

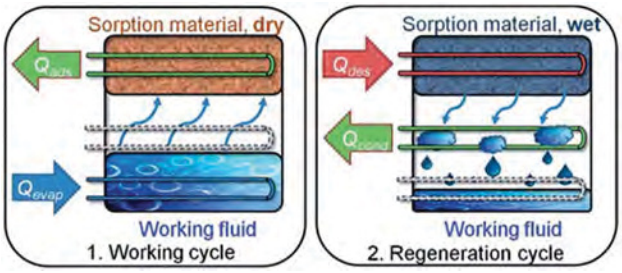

Fig. 1 Working principle of adsorption-based heat exchangers. In the working cycle (1), the coolant is evaporated by taking up the heat of evaporation Q_{evap} from the ambient. The fluid vapour is subsequently adsorbed on the porous material, releasing adsorption heat Q_{ads}. In the regeneration cycle (2), a driving heat Q_{des} is applied to the saturated adsorbent resulting in the desorption of the fluid. The desorbed vapours condense at a medium temperature level, releasing condensation heat Q_{cond}. Q_{evap} is exploited for cooling in TDCs, while Q_{ads} and Q_{cond} are exploited for heating in AHPs. The image was taken with permission from ref. 4.

fluid uptake capacities and the possibility to fine tune their pore size/shape and functionality.[9] As these materials are constructed by connecting metal clusters with organic ligands into porous networks, MOFs can be designed by a judicious choice of metal clusters and linkers to achieve a targeted fluid adsorption profile.[10] Designing MOFs to feature peculiar properties in view of their application for efficient heat transformation is hence a currently intensive research focus.[11] Aluminium-based MOFs have especially shown promise for this application owing to their high hydrothermal stability, the lightness and environmental friendliness of aluminium, and the availability of its sources.[12] Several Al-MOFs have been reported as good adsorbents for adsorption heat exchangers including aluminium fumarate,[13] CAU-10-H,[14] MIL-160,[15] and MIL-53-TDC.[16]

Depending on the working conditions and the aimed achievable performance of a heat exchanger, the choice of the adsorbent–adsorbate working pair is of key importance. A good combination of the adsorbent–coolant working pair can enable reaching a targeted adsorption profile.[17] In this respect, water has widely been used as the working fluid on account of its availability, high heat of evaporation and lack of toxicity.[18] However water presents some limitations under some heat transformation conditions like ice making. Water has a relatively high freezing point (0 °C) and cannot be used at sub-zero temperatures. Furthermore, the low saturation vapour pressure of water imposes that the system should be vacuum tight to provide very low pressures. These drawbacks can be addressed by using methanol as the refrigerant.[19] Methanol has a low freezing temperature (−97.6 °C) and can therefore be operated below 0 °C. Also, methanol has high saturation vapour pressure, which may result in faster mass transfer. Furthermore, the ease of regeneration due to its lower boiling point leads to faster adsorption–desorption cycles. In addition, the stability of MOFs under alcohol adsorption is less of an issue compared to water for which many MOFs are discarded for use in AHPs/TDCs on account of their poor hydrolytic stability. However, very few investigations of MOFs–methanol working pairs are reported.[20,21]

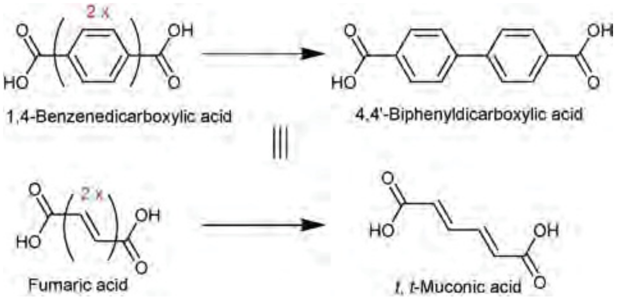

Scheme 1 Twofold extension of aliphatic fumaric acid to *t*,*t*-muconic acid, in analogy to 4-4′-biphenyldicarboxylic acid being the twofold extension of aromatic benzene-1,4-dicarboxylic acid.

Changing the working fluid usually makes adsorbents that were promising with water inappropriate for AHPs/ADCs. An example is that of methanol adsorption in aluminium fumarate (Al-Fum) which yields a type I isotherm, rather than the aimed type V S-shape obtained with water.[19] This therefore makes Al-Fum inappropriate for efficient heat transformations when paired with methanol. Taking advantage of the structural feature of Al-Fum, increasing the linker length by an isoreticular expansion should shift the step of the methanol sorption isotherm to higher relative pressure, on account of increased hydrophobicity. This could result in an S-shaped methanol sorption isotherm within the targeted relative pressure range, which is beneficial for sub-zero heat transformation. This should additionally increase the uptake capacity relative to Al-Fum. By using the principles of reticular chemistry,[22] such an isoreticular expansion could be achieved by replacing the fumarate linker with the *trans*,*trans*-muconate linker in the MIL-53 structure.[23] Muconic acid (*trans*,*trans*-1,3-butadiene-1,4-dicarboxylic acid = H_2muc) can be regarded as a twofold extension of the aliphatic fumarate linker analogous to 4,4′-biphenyldicarboxylate being a twofold extension of the aromatic 1,4-benzenedicarboxylate linker (see Scheme 1). Muconic acid is a renewable dicarboxylic acid that can be obtained from biomass.[24] This linker is therefore of interest for constructing MOFs in the context of sustainability underlying the use of adsorption-based heat exchangers.

The *trans*,*trans*-muconate linker had already been used to expand the structure of iron(III) fumarate (MIL-88A) to MIL-89 (ref. 25) and the structure of zirconium fumarate (MOF-801) to UiO-66-muc,[26] but to the best of our knowledge no report of muconate-based Al-MOFs is found.

We, herein, report the isoreticular twofold expansion of aluminium fumarate (Al-Fum) by using the aliphatic *trans*,*trans*-muconate dianion as a linker to a new MIL-53-muc MOF. The synthesis, thorough characterization, water sorption and especially methanol sorption are investigated for the intended application of this material as an adsorbent for sub-zero temperature adsorption-based heat transformations.

Experimental

Materials and methods

trans,*trans*-1,3-Butadiene-1,4-dicarboxylic acid (*t*,*t*-H_2muc, purity > 98%) and aluminium nitrate nonahydrate

($Al(NO_3)_3 \cdot 9H_2O$, purity > 98%) were obtained from Alfa Aesar; aluminium sulphate 18-hydrate ($Al_2(SO_4)_3 \cdot 18H_2O$, purity > 99%) was obtained from Applichem Panreac; dimethylformamide (DMF, analytical grade) was obtained from Fischer Chemical. All reagents were used as received.

Powder X-ray diffraction (PXRD) patterns were recorded on a Bruker D2 Phaser diffractometer using Cu $K\alpha_1/\alpha_2$ radiation with $\lambda = 1.5418$ Å at 30 kV, covering 2 theta angles 5–50° over a time of 1 h, that is, at a scan rate of $0.0125^\circ\ s^{-1}$. PXRD data for structure determination were collected in transmission geometry using a STOE Stadi MP diffractometer with monochromated $CuK\alpha_1$ radiation, equipped with a Dectris Mythen detector system.

Elemental analysis (CHN) was performed using a PerkinElmer 2400 series 2 elemental analyzer.

The *infrared (IR)* spectrum was obtained on a Bruker FT-IR Tensor 37 spectrometer in the 4000–550 cm^{-1} region with 2 cm^{-1} resolution as KBr disks. The *Raman* spectrum was obtained on a Bruker MultiRAM-FT Raman spectrometer equipped with a Nd:YAG-laser (wavelength 1064 nm). The measurements were executed in the solid state for 2500 scans with a laser power between 10 and 20 mW.

Thermogravimetric analysis (TGA) was carried out with a Netzsch Thermo-Microbalance Apparatus TG 209 F3 Tarsus, at a ramp rate of 5 °C min^{-1} under an air flow. *Scanning electron microscopy (SEM)* images were obtained using an ESEM Quanta 400 FEG SEM equipped with a secondary electron detector.

Vapour sorption isotherms of water and methanol were obtained using a VSTAR™ vapour sorption analyzer (Model number Vstar4-0000-1000-XS) from Quantachrome. For this purpose, about 25 mg of activated sample were introduced in the measuring cell and connected to the analysis port of the analyzer. The methanol used was of gradient grade (purity 99.85%) ChemSolute from Th. Geyer.

Nitrogen sorption isotherms were measured on a Quantachrome Autosorb iQ MP gas analyzer at 77 K. The Brunauer–Emmett–Teller (BET) specific surface area was evaluated from the nitrogen physisorption isotherms. The pore distribution traces were calculated using density functional theory (DFT) of NovaWin 11.03 software using the "N_2 at 77 K on carbon, slit pore, nonlinear density functional theory (NLDFT) equilibrium" model.

Synthetic procedures

Conventional solvothermal synthesis in an oven. 250 mg of *t*,*t*-muconic acid (1.76 mmol) and 600 mg of aluminium nitrate nonahydrate (1.6 mmol) were ultrasonically mixed in a water/DMF (5.6 mL/1.9 mL) solvent mixture. The obtained suspension was sealed in a 12 mL Teflon lined autoclave and placed for 3 h in an oven preheated at 120 °C. After cooling to room temperature, the yellow powder was decanted and separated from the brown mother liquor by centrifugation. The powder was afterwards washed three times by stirring (about 2 h each) in DMF and then three times in water. The product was finally centrifuged and dried in air.

Microwave assisted solvothermal synthesis. In a second synthesis route, 232 mg of *t*,*t*-muconic acid (1.63 mmol) and 1088 mg of aluminium sulphate octadecahydrate (1.63 mmol) were ultrasonically mixed in a water/DMF (7.5 mL/2.5 mL) solvent mixture. The obtained suspension was sealed in a 20 mL Pyrex glass tube, placed in a monowave (400 W) microwave reactor Anton Paar and heated for 1 h whilst stirring. After cooling, the product was separated from the mother liquor and washed the same way as aforementioned.

The activated sample was obtained by heating the dry as-synthesized sample at 150 °C for 12 h under dynamic vacuum (10^{-3} mBar). Elemental analysis of the activated sample: calcd for $[Al(OH)\ (C_6H_4O_4)] \cdot 0.25H_2O$: C 38.17%; H 2.91%. Found: C 38.21%; H 2.84%. The yield based on the aluminium salt: 200 mg, 66% from classical solvothermal synthesis and 240 mg, 78% from microwave assisted synthesis.

Synthesis of aluminium fumarate. Aluminium fumarate was synthesized according to a previously reported method.[27] In short, 513 mg of $Al_2(SO_4)_3 \cdot 18H_2O$, 179 mg fumaric acid and 92 mg urea were dissolved in 5 mL water, sealed in a Teflon lined autoclave and heated for 32 h at 110 °C in an oven. The resulting powder was washed with water and ethanol. It was activated by heating for 7 h at 150 °C under a dynamic vacuum. This synthesis procedure was adopted because it yields Al-Fum of high crystallinity. This is of importance for a rational comparison of the adsorption profile of Al-Fum with its twofold expansion MIL-53-muc. Water sorption in Al-Fum obtained by other synthetic routes usually displays a considerable hysteresis loop and capillary condensation effect at high P/P_0, which is rather the result of a poor crystallinity of the material than a reflection of structural features.[28]

Structural modelling and elucidation. Anticipating that extension of the fumarate linker to muconate would preserve the fundamental framework structure, we initially generated a structural model using force-field calculations. Thus the linker molecules in the aluminium fumarate structure were extended and the structure was energetically optimised using the universal force-field as implemented in Materials Studio.[29] This resulted in a model with a changed space-group symmetry ($C2/m$ compared to $P2_1/c$), which was subsequently superimposed. Based on the positions of the observed reflections, suitable unit cell parameters were deduced using the squared Bragg equation for monoclinic symmetry. After imposing these cell parameters and a second framework optimization by force-field calculations, the obtained model was refined by Rietveld methods using TOPAS academics.[30] The (half) linker molecule was considered as a rigid body and residual electron density inside the channels detected by Fourier synthesis was modelled as partially occupied oxygen atoms. Moreover, a preferred orientation along (110) had to be taken into account. However, one additional peak had to be considered as not being part of MIL-53-muc, indicating a crystalline impurity. Due to all these necessary corrections, the refined structure must be interpreted in any case only as a good model, since the low number of reflections and the limited crystallinity prevent a free refinement. The most important parameters are summarized in Table S1 and the Rietveld plot is shown in Fig. S5 (see the ESI†).

Multicycle methanol ad-/desorption experiment. The material MIL-53-muc was cycled using a DVS vacuum from Surface

Measurement Systems. The sample was cycled between 25 °C and 100 °C with methanol as the adsorbate at a relative pressure between 0.05 and $0.9P/P_0$. Before cycling, after 25 cycles and after 50 cycles, the material was examined for equilibrium conditions. Therefore, equilibrium points at 3%, 25%, 50%, 75% and 90% methanol moisture were approached. For the dry mass equilibrium points, the material was heated at 120 °C under vacuum.

Results and discussion

Synthesis

The new aluminium MOF termed MIL-53-muc of formula [Al(OH)(muc)] was synthesized solvothermally by reacting *t*,*t*-muconic acid with an aluminium salt in a water/DMF solvent mixture at 120 °C. The material was obtained as a yellowish microcrystalline powder with rectangular rod-like micro-crystals about 10 μm long (Fig. 2). Obtaining MIL-53-muc was successful by alternatively using aluminium sulphate ($Al_2(SO_4)_3 \cdot 18H_2O$) under microwave assisted heating for 1 h or aluminium nitrate ($Al(NO_3)_3 \cdot 9H_2O$) under conventional heating in an oven for 3 h (see the ESI† for details concerning the use of different Al salts).

Structure description

The powder X-ray diffraction (PXRD) pattern of MIL-53-muc is shown in Fig. 3. Its pattern broadly resembles that of aluminium fumarate (Al-Fum), except that the strongest reflection of MIL-53-muc is shifted to lower 2θ angle values. This is the first indication of their structural similarity, with MIL-53-muc featuring a larger lattice size, consistent with the longer linker compared to Al-Fum.

In the Raman spectrum of activated MIL-53-muc (Fig. S3 in ESI†), the strong band at 1644 cm^{-1} is assigned to the stretching vibration of C═C of the muconate linker, while the band at about 103 cm^{-1} is attributable to the Al–O stretching vibration. In the IR spectrum of the activated sample (Fig. S2, ESI†), the bands at 1570 and 1420 cm^{-1} correspond to the asymmetric and symmetric stretching modes of coordinated carboxylates of the linker (–COO), respectively. The C═C stretching vibration appears at about 1623 cm^{-1} and the olefinic C–H at 3052 cm^{-1}. The band at 3666 cm^{-1} is attributable to the structural μ_2-OH, characteristic for the corner-sharing chain of aluminium octahedra.

Being an analogue of the archetypical MIL-53 structure, the framework of MIL-53-muc is based on infinite chains of *trans*-corner sharing AlO_6-polyhedra which are connected *via* OH-groups. The remaining four oxygen atoms are part of carboxylate groups of the muconate linker. In this manner, each inorganic unit is connected to four adjacent infinite units, resulting in a framework with rhombic channels (Fig. 4). Their maximum diameter can be estimated to be 8 × 11 Å, based on the van der Waals radii of the framework.

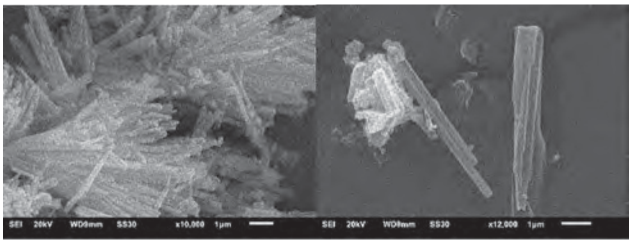

Fig. 2 SEM micrographs of MIL-53-muc.

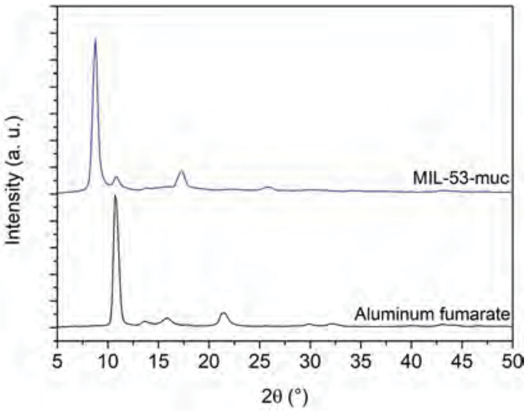

Fig. 3 Powder XRD pattern of MIL-53-muc (blue) in comparison with aluminium fumarate (black).

Porosity determination

The nitrogen sorption at 77 K exhibits a fully reversible type I isotherm according to the IUPAC classification (Fig. 5),[31] indicating the permanent microporosity of MIL-53-muc. The BET specific surface area, total pore volume and micropore volume were calculated to be 1750 $m^2\ g^{-1}$, 0.72 $cm^3\ g^{-1}$ and 0.52 $cm^3\ g^{-1}$, respectively. These values are quite higher than those of aluminium fumarate ($S_{BET} = 1021\ m^2\ g^{-1}$; $V_{micro} = 0.45$ from the literature).[13] The isoreticular expansion of aluminium fumarate to MIL-53-muc therefore results in about 70% increase in surface area. The average pore size was calculated to be about 0.9 nm (see Fig. S10 in the ESI†).

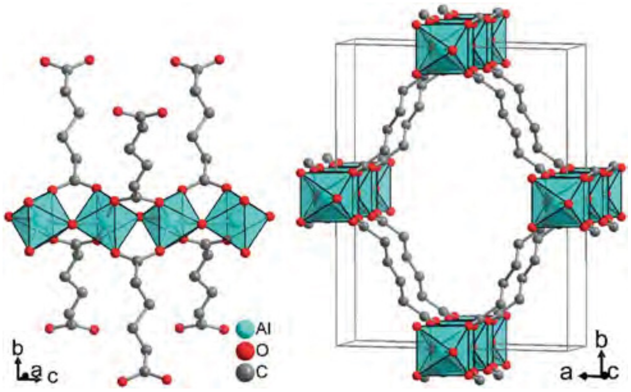

Fig. 4 Section of the 1D infinite chain of AlO_6 polyhedra (left) and the unit cell packing diagram (right) in the structure of MIL-53-muc (guest molecules are not shown and hydrogen atoms were not included in the Rietveld refinement).

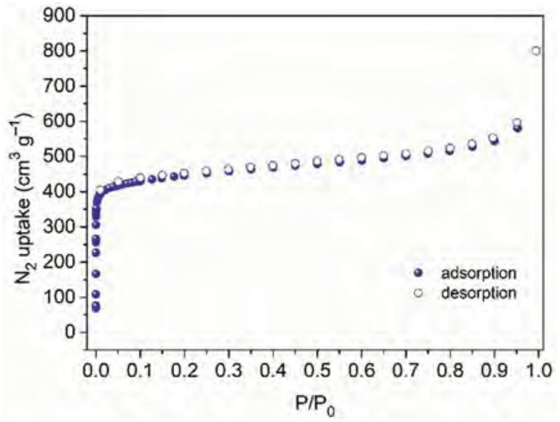

Fig. 5 Nitrogen sorption isotherm of MIL-53-muc at 77 K.

Water and methanol sorption

The water sorption experiment at 20 °C gives a type V (S-shaped) isotherm like aluminium fumarate (Fig. 6), which is in conformity with the same structure. However, some important differences are noticed: (i) the step of the water isotherm is shifted to higher relative pressures ($P/P_0 = 0.4$–0.6) compared to aluminium fumarate ($P/P_0 = 0.2$–0.3). The decreased hydrophilicity/increased hydrophobicity in MIL-53-muc can be traced back to the extension of the hydrophobic (organic chain) portion of the muconate linker. (ii) Unlike aluminium fumarate, there is a pronounced type H1 hysteresis loop between the adsorption and desorption branches in MIL-53-muc. (iii) The water uptake capacity of MIL-53-muc at $P/P_0 = 0.9$ amounts to 0.54 g g^{-1} and is in agreement with the micropore volume determined from the nitrogen sorption. This corresponds to a 35% increase in water uptake capacity compared to aluminium fumarate (0.4 g g^{-1} at $P/P_0 = 0.9$).

The isosteric heat of water adsorption $\Delta H_{\mathrm{ads}}(\mathrm{H_2O})$ was calculated by applying the Clausius–Clapeyron equation from water adsorption isotherms collected at 20, 30 and 40 °C, respectively. The plot of the heat of water adsorption (Fig. S16 in the ESI†) shows the same shape and trend as that previously reported for Al-Fum,[13] with an average value of 47–50 kJ mol^{-1} about 10% above the evaporation enthalpy of water (44 kJ mol^{-1}). This indicates that water adsorption in both materials occurs following the same mechanism.

Meanwhile aluminium fumarate features an ideal water sorption profile with respect to adsorption-driven heat transformation as previously reported,[13] MIL-53-muc rather falls short due to its relatively high hydrophobicity and wide hysteresis loop. Nevertheless, the water sorption profile of MIL-53-muc happens to be convenient for autonomous indoor moisture control application.[32] It was established that a good candidate material for such application should have (i) S-shaped water vapour sorption isotherms with adsorption and desorption branches separated in the 40–60% relative humidity (RH) range (recommended by the American Society of Heating, Refrigerating, and Air-Conditioning Engineers ASHRAE)[33] and (ii) a high water vapour uptake from the adsorption branch between 40% and 60% RH. These properties demonstrated by MIL-53-muc would enable the dual ability of starting to adsorb water as the RH exceeds 55% and starting to release water as the humidity level drops below 45%. Very few reported adsorbents like MIL-53-muc display these characteristics, among those that do are Y-shp-MOF-5, MCM-41 and Cr-soc-MOF-1.[32,34]

The methanol vapour sorption of MIL-53-muc yields also a sigmoidal shaped isotherm but with a negligible hysteresis loop (Fig. 7). The step of the isotherm is located within the narrow pressure range of 0.05–0.2 (inflexion point $\alpha = 0.08$; the inflexion point is defined as the relative pressure $\alpha = P/P_0$ at which half of the total adsorption capacity is reached),[19] achieving a methanol uptake capacity of about 0.5 g g^{-1} at $P/P_0 = 0.9$. Compared to aluminium fumarate which has a methanol adsorption isotherm with a type I profile and an uptake capacity of 0.32 g g^{-1}, the methanol sorption isotherm of MIL-53-muc is slightly shifted to higher relative pressure. The structure expansion therefore results in a 50% increase of the methanol uptake capacity for MIL-53-muc compared to Al-Fum.

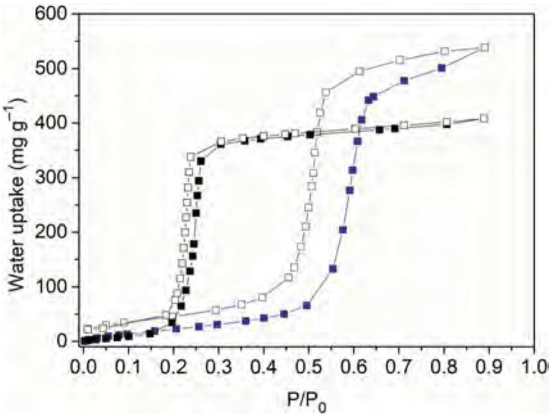

Fig. 6 Water vapour sorption isotherm of MIL-53-muc (blue) at 20 °C in comparison with aluminium fumarate (black) (filled symbols: adsorption; empty symbols: desorption).

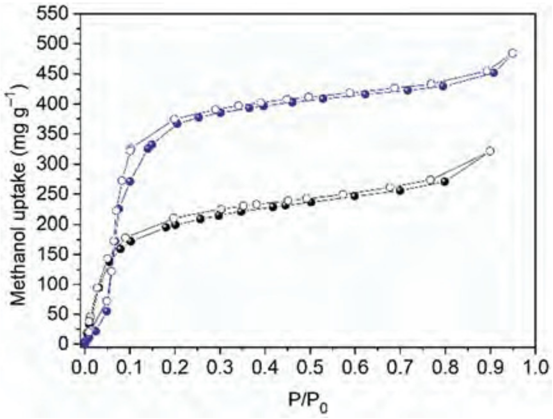

Fig. 7 Methanol vapour sorption isotherm of MIL-53-muc (blue) at 20 °C in comparison with aluminium fumarate (black) of MIL-53-muc (filled symbols: adsorption; empty symbols: desorption).

The methanol sorption profile of MIL-53-muc makes this material a suitable adsorbent for adsorption-driven heat transformation applications. The step position around $0.1P/P_0$ is especially favourable for adsorption thermal batteries (ATB) as it reduces the need to incorporate a compressor into the system. In this regard, the applied adsorbent should achieve a high heat storage capacity (C_{HS}).[35]

In order to evaluate the heat storage capacity C_{HS} of the MIL-53-muc–methanol pair, the isosteric heat of methanol adsorption ΔH_{ads}(MeOH) was determined using the Clausius–Clapeyron equation from methanol adsorption isotherms collected at 10 °C, 20 °C and 30 °C, respectively (calculation details for ΔH_{ads}(MeOH) and C_{HS} are in the ESI†). The plot of isosteric heat of methanol adsorption is shown in Fig. S17 (in the ESI†). It has an average value of 48 kJ for loading in the range of 100–320 mg g^{-1}. This value is well above the latent heat of methanol (34.4 kJ mol^{-1}). With a working capacity Δw of about 0.3 g g^{-1} (*vide infra*), the heat storage capacity was calculated to be 450 kJ kg^{-1} (0.125 kW h kg^{-1}).

Hydrothermal and chemical stabilities

The thermal and hydrolytic stabilities are basic requirements to use an adsorbent for many applications, especially for heat pumps and chillers.[36] This is due to elevated temperatures and the ubiquitous nature of water, even when water not the applied working fluid. The thermogravimetric analysis in air (Fig. S6†) reveals that MIL-53-muc is thermally robust, withstanding temperatures of up to 400 °C. Therefore, MIL-53-muc and aluminium fumarate have similar thermal stabilities. The PXRD pattern (Fig. S7 in the ESI†) of a sample stirred in water for 24 h reveals complete retention of its crystallinity, while both the crystallinity and water uptake capacity were retained over five consecutive water ad/desorption cycles (see Fig. S11 in the ESI†). Furthermore, PXRD patterns of MIL-53-muc samples after stirring for 24 h in solvents/solutions like acetone, DMF, ethanol, methanol, aqueous NaOH (pH = 12) and aqueous HCl (pH = 1) (Fig. S7 ESI†) also show retention of their crystalline phase. These observations show that MIL-53-muc is a material suitable for practical use.

Multicycle methanol sorption stability test

To assess the multicycle stability of MIL-53-muc, a multicycle sorption experiment under a pure methanol atmosphere was performed. The plots of temperature, relative pressure and relative uptake over time are shown in Fig. 8.

During the first 25 cycles, the material shows a maximum degradation of 5.6%. For the remaining 25 cycles, the equilibrium uptake during the isothermal measurement sequences reveals a maximum degradation of another 1.4% (shown in Fig. 8 and S12 in the ESI†). Over the entire 50 cycles, the material shows a degradation of 7%. The decrease in degradation over cycles indicates that this is not a continuous process. Therefore, the stability of Mil-53-muc towards methanol can be concluded. A cycling experiment over 50 cycles in water vapour (see Fig. S13 and related text in the ESI†) further indicated that MIL-53-muc is stable towards cyclic ad-/desorption stress.

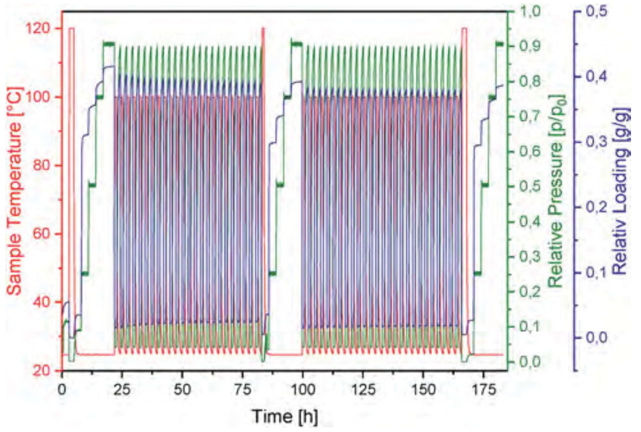

Fig. 8 Sample temperature in °C (red), relative pressure (green) and relative loading (blue) during the multicycle methanol ad/desorption experiment plotted over time.

Performance evaluation

In order to assess the performance of the working pair MIL-53-muc–methanol, achievable uptakes during the adsorption and desorption stage have been calculated for a variety of evaporator, middle and desorption temperatures making use of a Dubinin–Astakhov approach.[37] In general, two different applications can be thought of using methanol as the working fluid: a heat pump process enabling evaporator temperatures below 0 °C delivering heating temperatures of around 40 °C or an adsorption chiller process supplying freezing temperatures (*e.g.*, direct freezing of fish on ships).[21,38,39]

The heatmap of achievable uptakes during adsorption in Fig. 9 shows that MIL-53-muc can adsorb more than 0.3 g methanol per gram MOF for a broad range of temperatures. Even at temperatures as low as −5 °C and adsorption temperatures being sufficiently high to supply a floor radiation system (40 °C), a fairly high methanol uptake of 0.15 g g^{-1} can be achieved. For cooling applications, very low evaporator

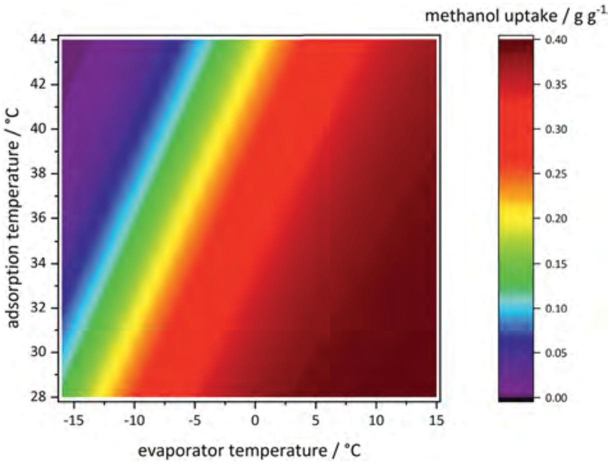

Fig. 9 Achievable methanol uptakes of MIL-53-muc during adsorption for different evaporator and adsorption temperatures calculated using a fitted Dubinin–Astakhov approach.

temperatures down to −10 °C can be reached for adsorption temperatures of 28 °C showing the huge potential of MIL-53-muc for freezing applications.

During desorption, the target is to dry the adsorbent as far as possible at the preferred middle temperature (meaning condenser and adsorption temperature) applying an as low as possible desorption temperature. The heatmap for achievable uptakes during the desorption stage is shown in Fig. 10. This plot indicates that temperatures of up to 120 °C have to be applied at a condenser temperature of 40 °C (heat pump mode) and the efficiency of a heat pump cycle can further be increased by applying a slightly lower condenser temperature of 35 °C and a thereby enabled lower desorption temperature of 110 °C. For a cooling process, a desorption temperature of slightly above 100 °C is sufficient to fully dry MIL-53-muc at condenser temperatures of around 28 °C.

These boundary temperatures define a process cycle and can be used to calculate the efficiency of such a process, the so-called coefficient of performance (COP). The COP is defined as the useable amount of heat per amount of heat that has to be spent for driving the process (eqn (1)) (see ref. 5, 19, 21 and 37 for further information):

$$\mathrm{COP_{HP}} = \frac{Q_{\mathrm{ads}} + Q_{\mathrm{cond}}}{Q_{\mathrm{des}}} \text{ and } \mathrm{COP_{C}} = \frac{Q_{\mathrm{evap}}}{Q_{\mathrm{des}}} \tag{1}$$

The thereby calculated COPs for heat pump conditions (middle temperature of 40 °C, a variety of evaporator temperatures and desorption temperatures) are plotted in Fig. 11. As can be seen, even at evaporator temperatures of around 0 °C, a comparably high $\mathrm{COP_{HP}}$ of over 1.6 can be reached for desorption temperatures of above 100 °C being in a range or slightly higher than other MOFs like CAU-3, ZIF-8, HKUST-1, MIL-53(Cr) or UiO-67 that have been investigated for the use in adsorption driven heat transformation with methanol as the working fluid before.[5,19,21] It is noteworthy that high COP values of almost 1.4 can still be reached for evaporator temperatures of around −10 °C.

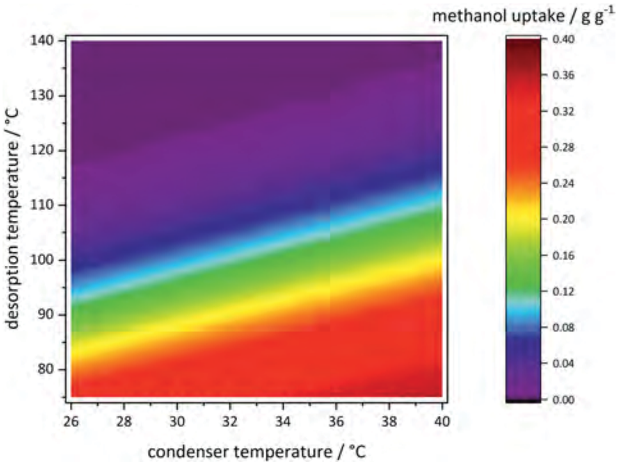

Fig. 10 Achievable methanol uptakes of MIL-53-muc during desorption for different condenser and desorption temperatures calculated using a fitted Dubinin–Astakhov approach.

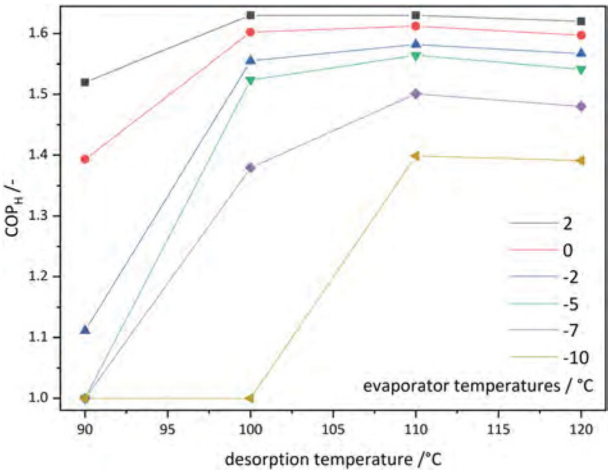

Fig. 11 Values of COP calculated for a middle temperature level of 40 °C and different evaporator and desorption temperatures.

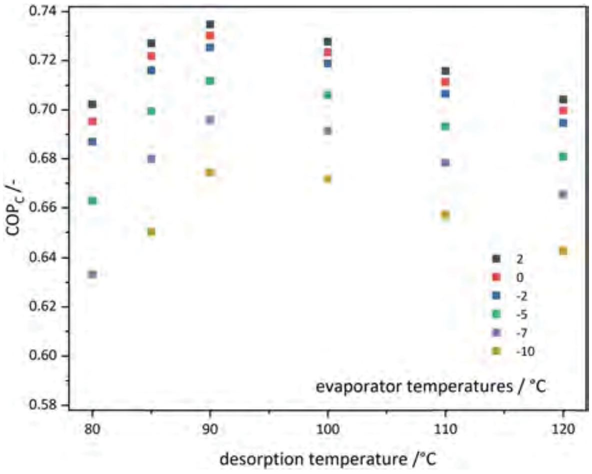

Fig. 12 Values of $\mathrm{COP_C}$ calculated for a middle temperature level of 28 °C and different evaporator and desorption temperatures.

Due to the comparably high methanol uptake within a demanded working window, also high values for $\mathrm{COP_C}$ can be reached (see Fig. 12). This large variety of feasible working windows along with the proven cycling stability towards methanol feature MIL-53-muc as a very promising material for applications that require evaporator temperatures of around or below 0 °C. Regarding the specific application for ice-making, the activated carbon–methanol pair was reported to be one of the best performing pairs with a $\mathrm{COP_C}$ of about 0.6, surpassing all (but limited) MOF–methanol pairs studied so far in this context.[5,40]

Interestingly, the $\mathrm{COP_C}$ value for the MIL-53-muc–methanol pair is over 0.7 under conditions for ice making ($T_{\mathrm{evap}} = -5$; $T_{\mathrm{ads}} = 25$ °C; $T_{\mathrm{des}} = 85$–105 °C) surpassing that of the activated carbon–methanol pair.[41]

Conclusions

In summary, we have successfully synthesized a twofold expansion of an aluminium fumarate metal–organic framework by replacing the fumarate linker by the *t*,*t*-muconate linker in the MIL-53 structure. The new microporous material termed MIL-53-muc possesses high hydrothermal and chemical stabilities. Featuring a reversible stepwise (S-shaped) isotherm of methanol adsorption with a relatively high methanol capacity, combined with a multicycle stability upon methanol adsorption–desorption, MIL-53-muc–methanol is disclosed to be a very promising adsorbent–adsorbate pair applicable for adsorption-based heat transformation applications. Furthermore, the methanol adsorption profile of MIL-53-muc allows reaching evaporator temperatures as low as −10 °C both in the heat pump and chilling modes with COP values of up to 1.6 at that temperature. These characteristics make MIL-53-muc a prominent material for heat transformation applications in the realm of temperatures below 0 °C, outclassing at the same time many materials reported for use in this context.

Conflicts of interest

There are no conflicts to declare.

Acknowledgements

We thank the German Academic Exchange Service (DAAD) for funding to TJMMN and the Federal Ministry of Education and Research (BMBF) for project Optimat, grant no. 03SF0492A/C.

References

1 (*a*) S. K. Henninger, H. A. Habib and C. Janiak, *J. Am. Chem. Soc.*, 2009, **131**, 2776–2777; (*b*) Y. I. Aristov, *Future Cities and Environment*, 2015, **1**, 10; (*c*) D. Lefebvre and F. H. Tezel, *Renewable Sustainable Energy Rev.*, 2017, **67**, 116–125.

2 R. Z. Wang and R. G. Oliveira, *Prog. Energy Combust. Sci.*, 2006, **32**, 424–458.

3 Y. Fan, L. Luo and B. Souyri, *Renewable Sustainable Energy Rev.*, 2007, **11**, 1758–1775.

4 F. Jeremias, D. Fröhlich, C. Janiak and S. K. Henninger, *New J. Chem.*, 2014, **38**, 1846–1852.

5 M. F. de Lange, K. J. F. M. Verouden, T. J. H. Vlugt, J. Gascon and F. Kapteijn, *Chem. Rev.*, 2015, **115**, 12205–12250.

6 M. H. Bagheri and S. N. Schiffres, *Langmuir*, 2018, **34**(4), 1908–1915.

7 (*a*) Y. I. Aristov, *Appl. Therm. Eng.*, 2013, **50**, 1610–1618; (*b*) S. K. Henninger, S.-J. Ernst, L. Gordeeva, P. Bendix, D. Fröhlich, A. D. Grekova, L. Bonaccorsi, Y. Aristov and J. Jaenchen, *Renewable Energy*, 2017, **110**, 59–68.

8 S. K. Henninger, F. Jeremias, H. Kummer and C. Janiak, *Eur. J. Inorg. Chem.*, 2012, 2625–2634.

9 (*a*) B. Li and B. Chen, *Chem*, 2016, **1**, 668–673; (*b*) H.-F. Zhang, M. Li, X.-Z. Wang, D. Luo, Y.-F. Zhao, X.-P. Zhou and D. Li, *J. Mater. Chem. A*, 2018, **6**, 4260–4265; (*c*) Q. Wang, J. Bai, Z. Lu, Y. Pan and X. You, *Chem. Commun.*, 2016, **52**, 443–452.

10 (*a*) H. Furukawa, K. E. Cordova, M. O'Keeffe and O. M. Yaghi, *Science*, 2013, **341**, 1230444; (*b*) C. Janiak and J. K. Vieth, *New J. Chem.*, 2010, **34**, 2366–2388.

11 (*a*) W. Li, X. Xia, M. Cao and S. Li, *J. Mater. Chem. A*, 2019, **7**, 7470–7479; (*b*) S. Wang, J. S. Lee, M. Wahiduzzaman, J. Park, M. Muschi, C. Martineau-Corcos, A. Tissot, K. H. Cho, J. Marrot, W. Shepard, G. Maurin, J.-S. Chang and C. Serre, *Nat. Energy*, 2018, **3**, 985–993; (*c*) E. Hastürk, S.-J. Ernst and C. Janiak, *Curr. Opin. Chem. Eng.*, 2019, **24**, 26–36.

12 M. Gaab, N. Trukhan, S. Maurer, R. Gummaraju and U. Müller, *Microporous Mesoporous Mater.*, 2012, **157**, 131–136.

13 (*a*) F. Jeremias, D. Fröhlich, C. Janiak and S. K. Henninger, *RSC Adv.*, 2014, **4**, 24073–24082; (*b*) H. Kummer, F. Jeremias, A. Warlo, G. Füldner, D. Fröhlich, C. Janiak, R. Gläser and S. K. Henninger, *Ind. Eng. Chem. Res.*, 2017, **56**, 8393–8398.

14 (*a*) D. Fröhlich, E. Pantatosaki, P. D. Kolokathis, K. Markey, H. Reinsch, M. Baumgartner, M. A. van der Veen, D. E. De Vos, N. Stock, G. K. Papadopoulos, S. K. Henninger and C. Janiak, *J. Mater. Chem. A*, 2016, **4**, 11859–11869; (*b*) D. Lenzen, P. Bendix, H. Reinsch, D. Fröhlich, H. Kummer, M. Möllers, P. P. C. Hügenell, R. Gläser, S. Henninger and N. Stock, *Adv. Mater.*, 2018, **30**, 1705869.

15 A. Permyakova, O. Skrylnyk, E. Courbon, M. Affram, S. Wang, U.-H. Lee, A. H. Valekar, F. Nouar, G. Mouchaham, T. Devic, G. De Weireld, J.-S. Chang, N. Steunou, M. Frère and C. Serre, *ChemSusChem*, 2017, **10**, 1419–1426.

16 N. Tannert, S.-J. Ernst, C. Jansen, H.-J. Bart, S. K. Henninger and C. Janiak, *J. Mater. Chem. A*, 2018, **6**, 17706–17712.

17 A. Freni, G. Maggio, A. Sapienza, A. Frazzica, G. Restuccia and S. Vasta, *Appl. Therm. Eng.*, 2016, **104**, 85–95.

18 S. K. Henninger, F. P. Schmidt and H.-M. Henning, *Appl. Therm. Eng.*, 2010, **30**, 1692–1702.

19 M. F. de Lange, B. L. van Velzen, C. P. Ottevanger, K. J. F. M. Verouden, L.-C. Lin, T. J. H. Vlugt, J. Gascon and F. Kapteijn, *Langmuir*, 2015, **31**, 12783–12796.

20 B. T. Nguyen, H. L. Nguyen, T. C. Nguyen, K. E. Cordova and H. Furukawa, *Chem. Mater.*, 2016, **28**, 6243–6249.

21 S.-J. Ernst, F. Jeremias, H.-J. Bart and S. K. Henninger, *Ind. Eng. Chem. Res.*, 2016, **55**, 13094–13101.

22 O. M. Yaghi, M. O'Keeffe, N. W. Ockwig, H. K. Chae, M. Eddaoudi and J. Kim, *Nature*, 2003, **423**, 705–714.

23 (*a*) F. Millange, C. Serre and G. Férey, *Chem. Commun.*, 2002, 822–823; (*b*) C. Serre, F. Millange, C. Thouvenot, M. Nogues, G. Marsolier, D. Louer and G. Férey, *J. Am. Chem. Soc.*, 2002, **124**, 13519–13526.

24 (*a*) J. M. Carraher, T. Pfennig, R. G. Rao, B. H. Shanks and J.-P. Tessonnier, *Green Chem.*, 2017, **19**, 3042–3050; (*b*) N. A. Rorrer, J. R. Dorgan, D. R. Vardon, C. R. Martinez, Y. Yang and G. T. Beckham, *ACS Sustainable Chem. Eng.*, 2016, **4**, 6867–6876; (*c*) A. Eudes, R. Berthomieu, Z. Hao, N. Zhao, V. T. Benites, E. E. K. Baidoo and D. Loquéa, *Metab. Eng.*, 2018, **46**, 13–19.

25 C. Serre, S. Surblé, C. Mellot-Draznieks, Y. Filinchuk and G. Férey, *Dalton Trans.*, 2008, 5462–5464.

26 (*a*) V. Guillerm, S. Gross, C. Serre, T. Devic, M. Bauer and G. Férey, *Chem. Commun.*, 2010, **46**, 767–769; (*b*) A. Buragohain and S. Biswas, *Eur. J. Inorg. Chem.*, 2015,

2463–2468; (*c*) O. V. Gutov, S. Molina, E. C. Escudero-Adán and A. Shafir, *Chem.–Eur. J.*, 2016, **22**, 13582–13587.

27 E. Alvarez, N. Guillou, C. Martineau, B. Bueken, B. Van de Voorde, C. Le Guillouzer, P. Fabry, F. Nouar, F. Taulelle, D. de Vos, J.-S. Chang, K. H. Cho, N. Ramsahye, T. Devic, M. Daturi, G. Maurin and C. Serre, *Angew. Chem., Int. Ed.*, 2015, **54**, 3664–3668.

28 N. Tannert, C. Jansen, S. Nießing and C. Janiak, *Dalton Trans.*, 2019, **48**, 2967–2976.

29 *Materials Studio Version 5.0*, Accelrys Inc., San Diego, 2009.

30 *Topas Academics 4.2*, Coelho Software, Brisbane, 2007.

31 M. Thommes, K. Kaneko, A. V. Neimark, J. P. Olivier, F. Rodriguez-Reinoso, J. Rouquerol and K. S. W. Sing, *Pure Appl. Chem.*, 2015, **87**, 1051–1069.

32 R. G. AbdulHalim, P. M. Bhatt, Y. Belmabkhout, A. Shkurenko, K. Adil, L. J. Barbour and M. Eddaoudi, *J. Am. Chem. Soc.*, 2017, **139**, 10715–10722.

33 ASHRAE, *Ventilation for Acceptable Indoor Air Quality (ANSI/ASHRAE Standard 62.1-2010)*, American Society of Heating, Refrigerating, and Air Conditioning Engineers, Atlanta, GA, 2010.

34 S. M. T. Abtab, D. Alezi, P. M. Bhatt, A. Shkurenko, Y. Belmabkhout, H. Aggarwal, Ł. J. Weseliński, N. Alsadun, U. Samin, M. N. Hedhili and M. Eddaoudi, *Chem*, 2018, **4**, 94–105.

35 (*a*) T. X. Li, J. X. Xu, T. Yan and R. Z. Wang, *Energy*, 2016, **107**, 347–359; (*b*) H. Furukawa, F. Gándara, Y.-B. Zhang, J. Jiang, W. L. Queen, M. R. Hudson and O. M. Yaghi, *J. Am. Chem. Soc.*, 2014, **136**, 4369–4381.

36 N. C. Burtch, H. Jasuja and K. S. Walton, *Chem. Rev.*, 2014, **114**, 10575–10612.

37 (*a*) F. Stoeckli, *Russ. Chem. Bull.*, 2001, **50**, 2265–2272; (*b*) L. Wang, J. Wu, R. Wang, Y. Xu, S. Wang and X. Li, *Appl. Therm. Eng.*, 2003, **23**, 1605–1617.

38 S. K. Henninger, M. Schicktanz, P. P. C. Hügenell, H. Sievers and H.-M. Henning, *Int. J. Refrig.*, 2012, **35**, 543–553.

39 H. Kummer, M. Baumgartner, P. P. C. Hügenell, D. Fröhlich, S. K. Henninger and R. Gläser, *Appl. Therm. Eng.*, 2017, **117**, 689–697.

40 (*a*) R. E. Critoph, *Sol. Energy*, 1988, **41**, 21–31; (*b*) R. E. Critoph, *Carbon*, 1989, **27**, 63–70.

41 (*a*) M. Pons and J. J. Guilleminot, *J. Sol. Energy Eng.*, 1986, **108**, 332–337; (*b*) L. W. Wang, J. Y. Wu, R. Z. Wang, Y. X. Xu, S. G. Wang and X. R. Li, *Appl. Therm. Eng.*, 2003, **23**, 1605–1617; (*c*) L. W. Wang, R. Z. Wang, Z. S. Lu, C. J. Chen, K. Wang and J. Y. Wu, *Carbon*, 2006, **44**, 2671–2680.

Electronic Supplementary Material (ESI) for Journal of Materials Chemistry A.
This journal is © The Royal Society of Chemistry 2019

Electronic Supplementary Information (ESI)

Designing the new aluminium muconate metal-organic framework (MIL-53-muc) as methanol adsorbent for sub-zero temperature heat transformation applications

Tobie J. Matemb Ma Ntep,[a] Helge Reinsch,[b] Philipp P. C. Hügenell,[c] Sebastian-Johannes Ernst,[c] Emrah Hastürk,[a] and Christoph Janiak *[a]

[a] Institut für Anorganische Chemie und Strukturchemie, Heinrich-Heine-Universität Düsseldorf, Universitätsstraße 1, D- 40225 Düsseldorf, Germany

[b] Institut für Anorganische Chemie, Christian-Albrechts-Universität zu Kiel, Max-Eyth-Straße 2, 24118 Kiel, Germany

[c] Fraunhofer Institue for Solar Enegy Systems (ISE), Heidenhofstraße 2, 79110 Freiburg, Germany

* Corresponding author: E-mail: janiak@uni-duesseldorf.de; Fax: + 49-211-81-12287; Tel: +49-211-81-12286
Additional email addresses:
tobie.matemb.ma.ntep@uni-duesseldorf.de; hreinsch@ac.uni-kiel.de; philipp.huegenell@ise.fraunhofer.de; sebastian-johannes.ernst@ise.fraunhofer.de; emrah.hastuerk@hhu.de;

Table of contents

Synthesis details

In order to obtain a muconate-based Al-MOF with MIL-53 structure, the initial syntheses were conducted by a conventional solvothermal route (without stirring) in a programmable oven and by microwave-assisted solvothermal heating using $Al_2(SO_4)_3 \cdot 18H_2O$ as the metal source in a H_2O/DMF solvent mixture. The choice of this salt was guided by the result previously obtained by Reinsch *et al.* for the synthesis of a MIL-53 type Al-MOF using the aliphatic adipate linker, which is close to the muconate linker.[1] We then realized that the targeted product was obtained under microwave conditions (under stirring). From the conventional solvothermal route in a programmable oven the product was mixed with an amorphous phase. For further trials in order to obtain the material also under solvothermal conditions in the oven, $Al(NO_3)_3 \cdot 9H_2O$ was used in place of $Al_2(SO_4)_3 \cdot 18H_2O$, which then yielded the pure expected phase of MIL-53-muc.

Infrared and Raman spectroscopy of MIL-53-muc and Aluminium fumarate

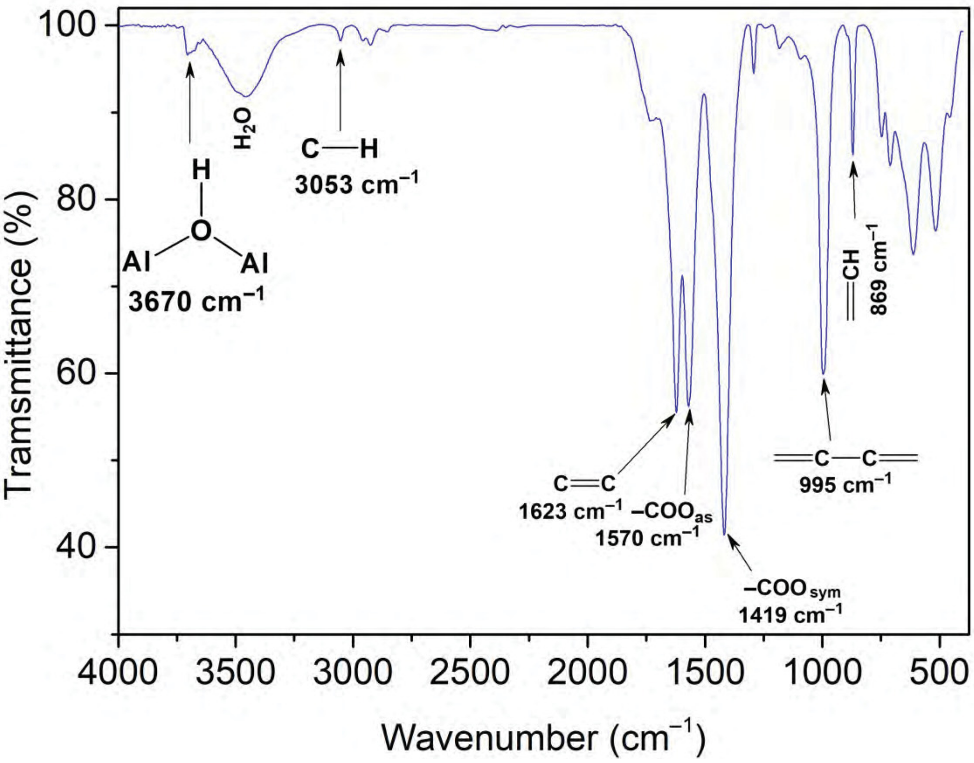

Fig. S1 Infrared spectrum of MIL-53-muc.

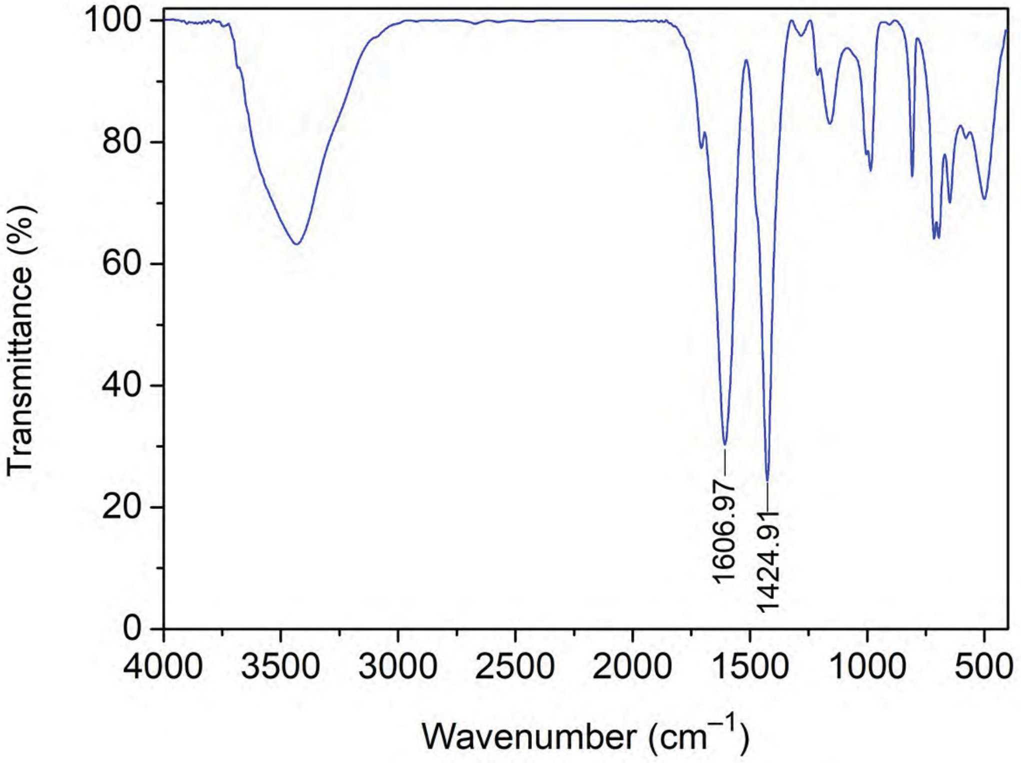

Fig. S2 Infrared spectrum of aluminium fumarate (Al-Fum).

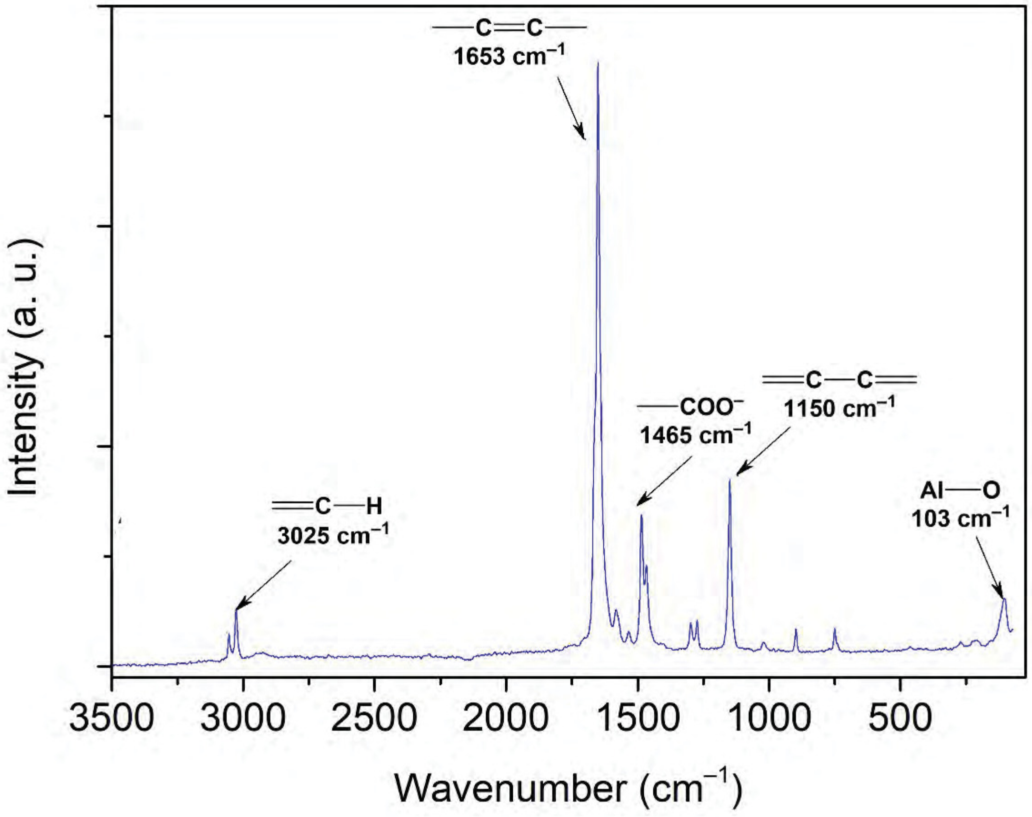

Fig. S3 Raman spectrum of MIL-53-muc.

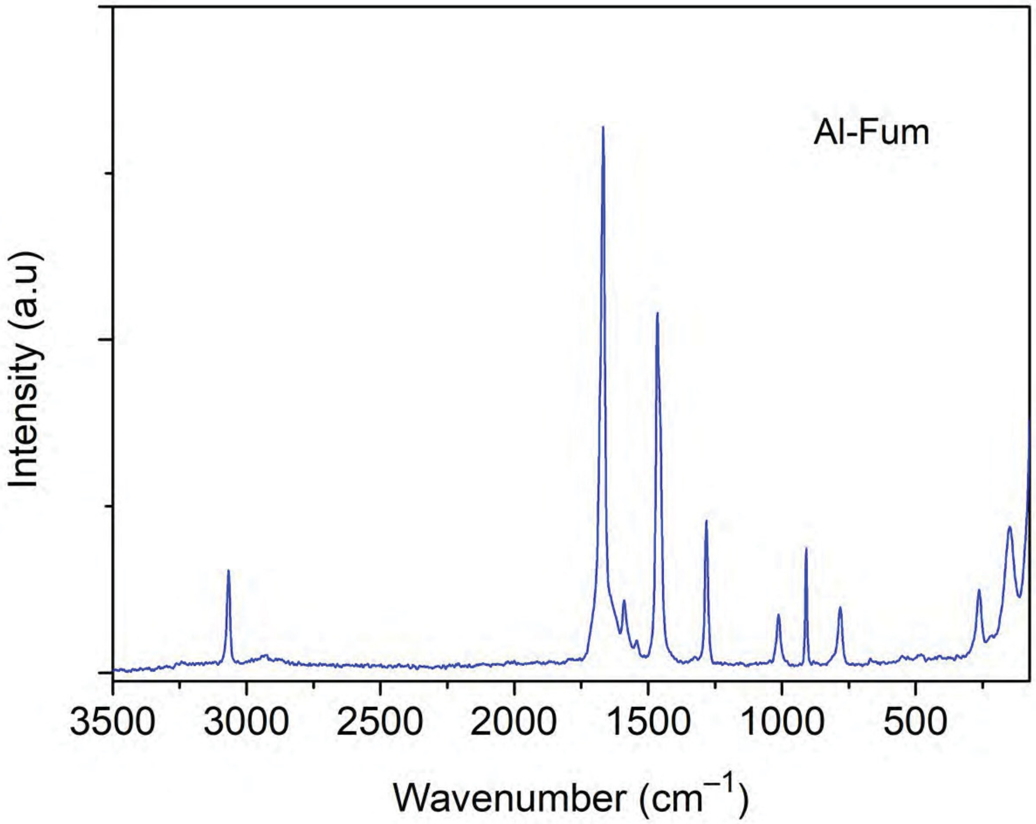

Fig. S4 Raman spectrum of aluminium fumarate.

Structure modelling and elucidation of MIL-53-muc

Except for the special position of several atoms, no parameters were fixed. The refined parameters comprise the non-special positions for the Al-O chains, the translational and rotational motion of the rigid body linker fragment as well as the position and occupancy of the atoms representing the occluded solvent molecules. Moreover, the cell parameters and general temperature factor were refined. These structural parameters aside, the background was modelled by a 12th order polynomial. Of course, the refinement included a peak shape function (Pseudo-Voigt), a scale factor and a zero error, and as described in the manuscript a preferred orientation was also modelled.

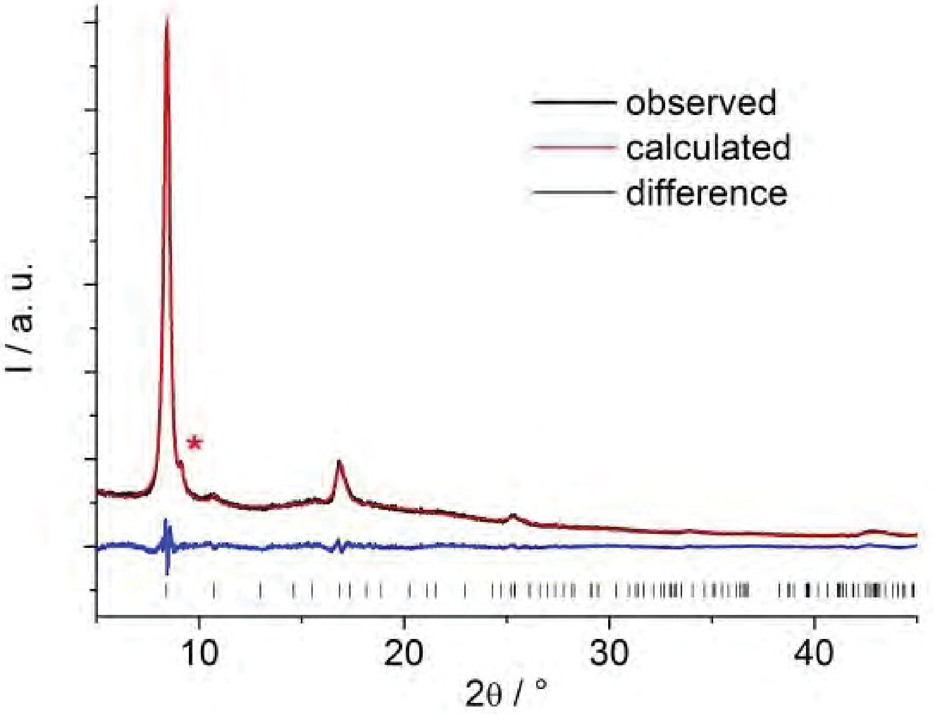

Fig. S5a Final Rietveld plot for MIL-53-muc. The black line represents measured data, the red line is the fit and the blue line indicates the difference curve. Vertical bars indicate the allowed peak positions. The red asterisk marks the shoulder of the first peak, attributed to a crystalline impurity.

Table S1 Selected relevant structure parameters for MIL-53-muc.

Compound	MIL-53-muc
Formula sum	[Al(OH) (O_2C-C_4H_4-CO_2)]
Space group	*C*2/*m*
Crystal system	monoclinic
Cell parameters	*a* = 14.71(3) Å
	b = 16.51(2) Å
	c = 6.53(2) Å
	α = 90°
	β = 68.1(2)°
	γ = 90°
R_{WP}	4.1 %
GoF	2.6
R_{Bragg}	0.3 %

Crystallographic Information File

```
data_structure
_symmetry_cell_setting           monoclinic
_symmetry_space_group_name_H-M   'C 2/m'
_symmetry_Int_Tables_number      12
_space_group_name_Hall           '-C 2y'
loop_
_symmetry_equiv_pos_site_id
_symmetry_equiv_pos_as_xyz
1 x,y,z
2 -x,y,-z
3 x,-y,z
4 -x,-y,-z
5 1/2+x,1/2+y,z
6 1/2-x,1/2+y,-z
7 1/2+x,1/2-y,z
8 1/2-x,1/2-y,-z
_cell_length_a                 14.71(3)
_cell_length_b                 16.513(18)
_cell_length_c                 6.535(18)
_cell_angle_alpha               90
_cell_angle_beta               68.1(2)
_cell_angle_gamma               90
_cell_volume                   1472.84
loop_
_atom_site_label
_atom_site_type_symbol
_atom_site_fract_x
_atom_site_fract_y
_atom_site_fract_z
Al1 Al 0 -0.5 -0.5
Al2 Al 0 -0.5 0
O1 O 0.062(10) -0.5 -0.30(5)
O2 O -0.09485 -0.42342 0.00103
O3 O -0.09845 -0.41843 -0.33648
C1 C -0.13045 -0.39935 -0.13705
C2 C -0.2162 -0.34879 -0.06949
C3 C -0.21942 -0.28117 0.03508
G1 O -0.62(4) -0.5 -0.1(2)
G2 O -0.58(3) -0.5 -0.5
```

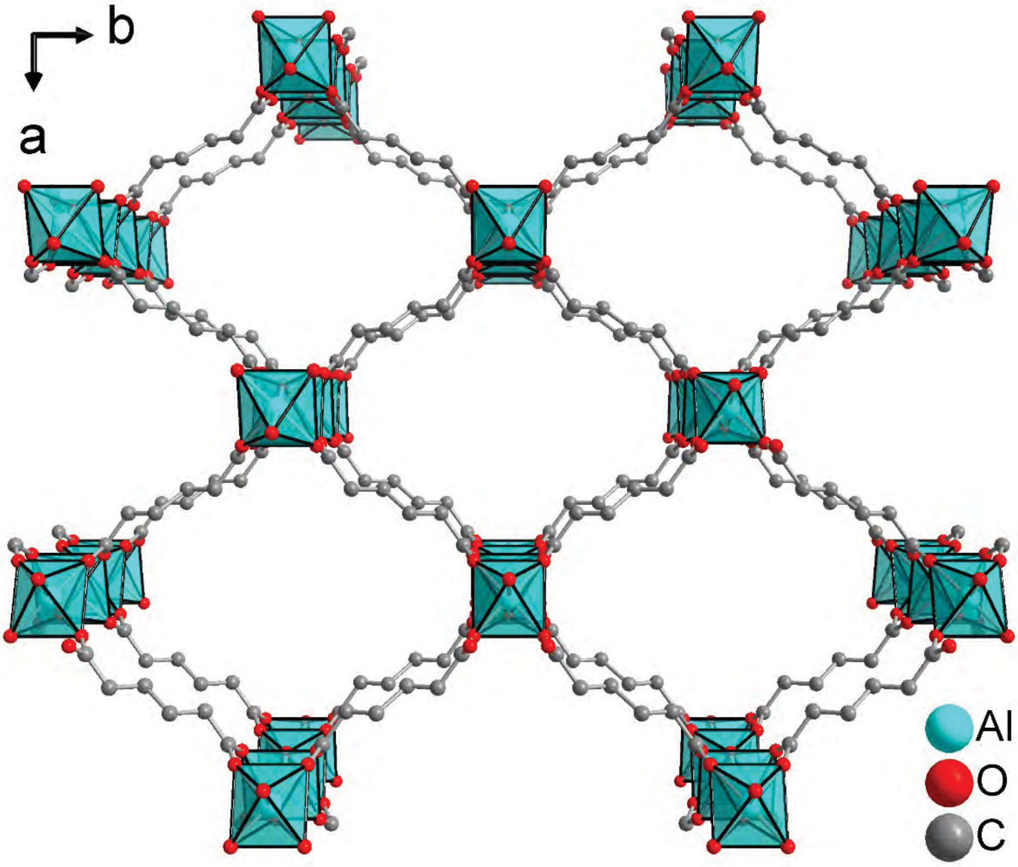

Fig. S5b Extended section of the packing diagram in the structure of MIL-53-muc (guest molecules are not shown and hydrogen atoms were not included in the Rietveld refinement).

Thermogravimetric analysis (TGA)

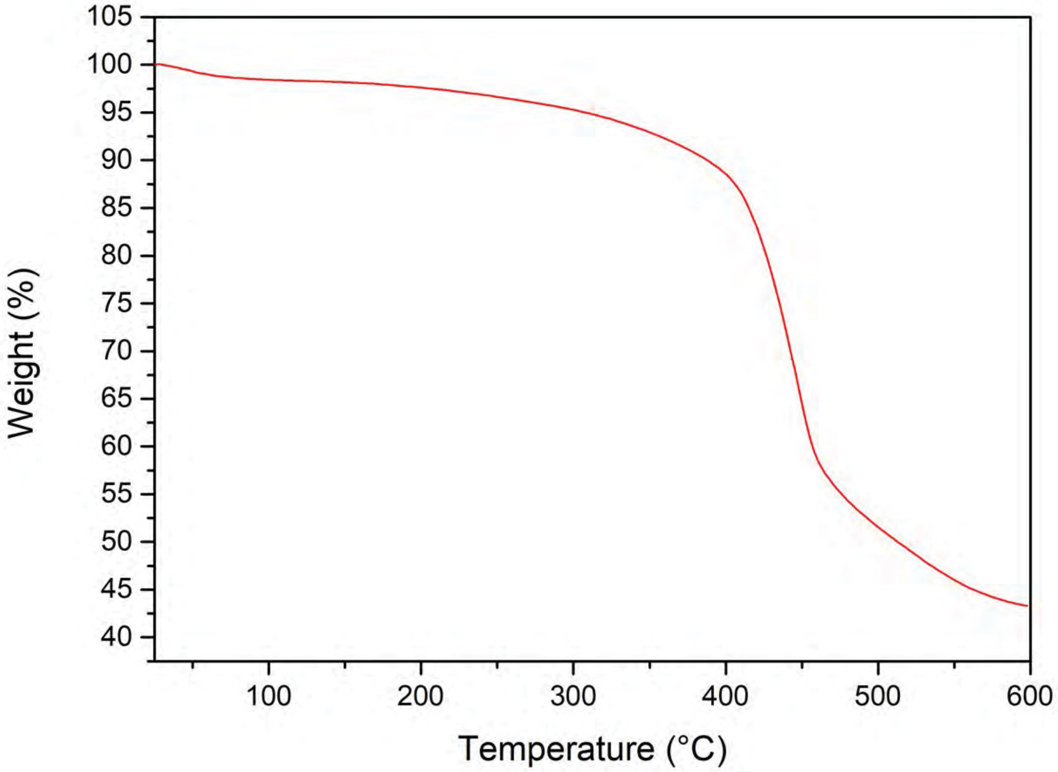

Fig. S6 Trace of thermogravimetry analysis conducted under air for MIL-53-muc.

PXRD patterns of the chemical stability testing

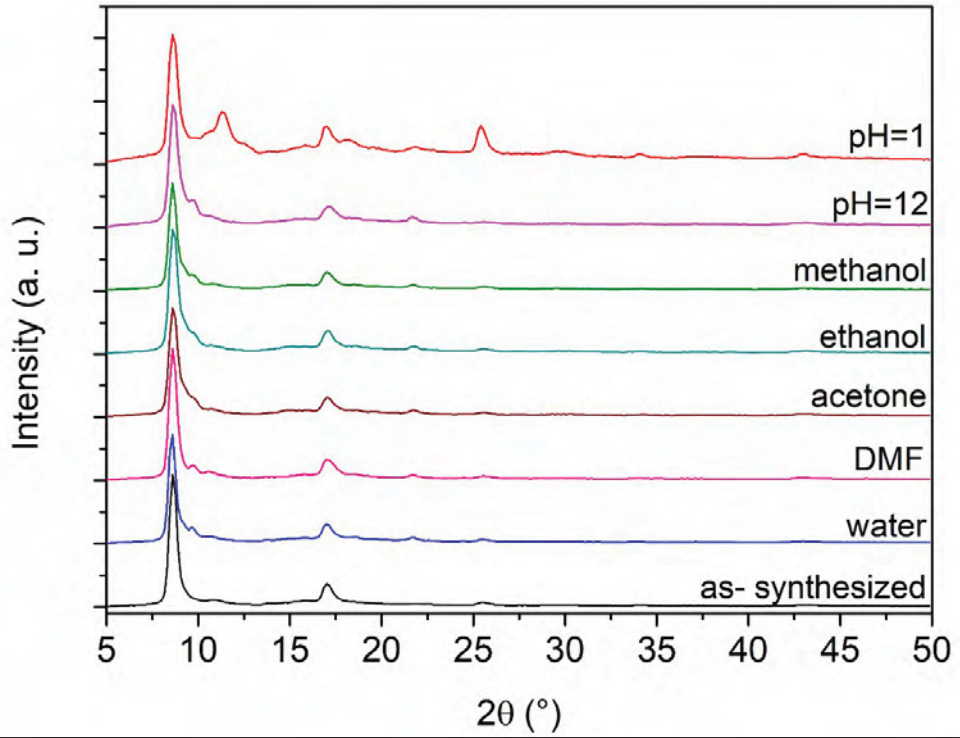

Fig. S7 PXRD patterns of MIL-53-muc after stirring 24 h at room temperature in various solvents and solutions.

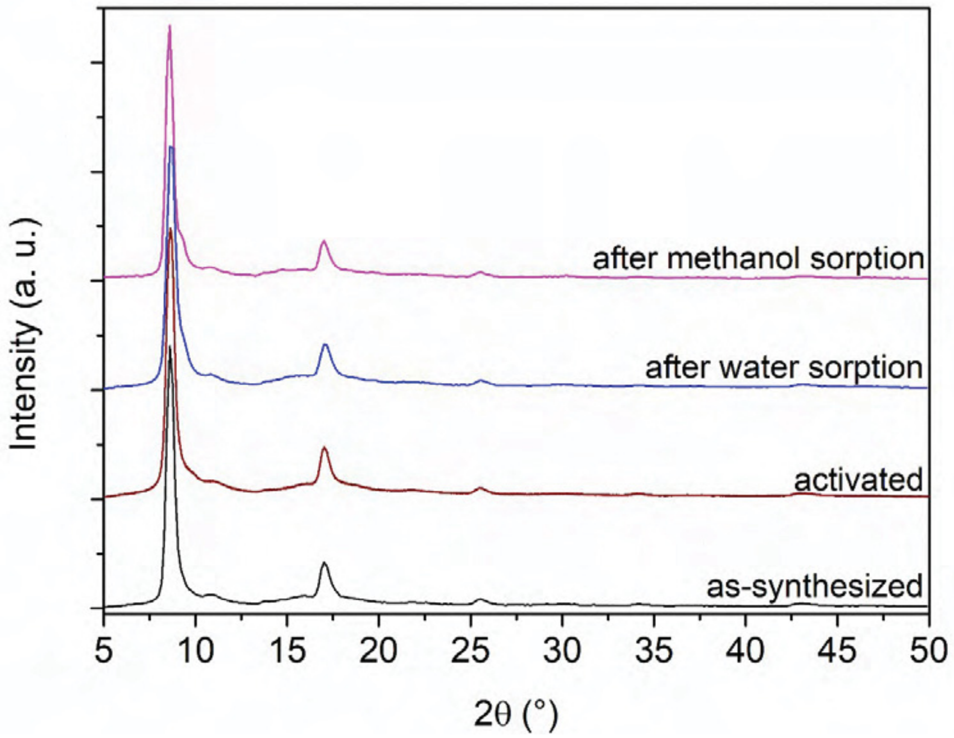

Fig. S8 PXRD patterns of MIL-53-muc after outgassing and after vapour sorption.

Nitrogen sorption and porosity analysis

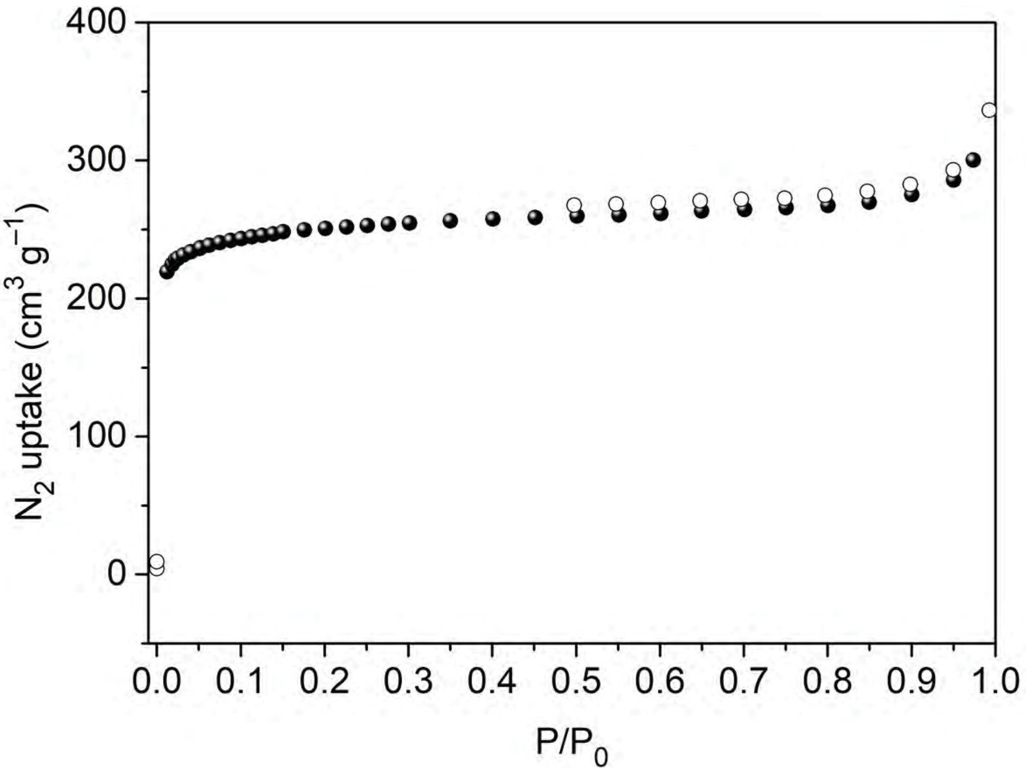

Fig. S9 Nitrogen sorption isotherms for aluminium fumarate (filled symbols: adsorption; empty symbols: desorption).

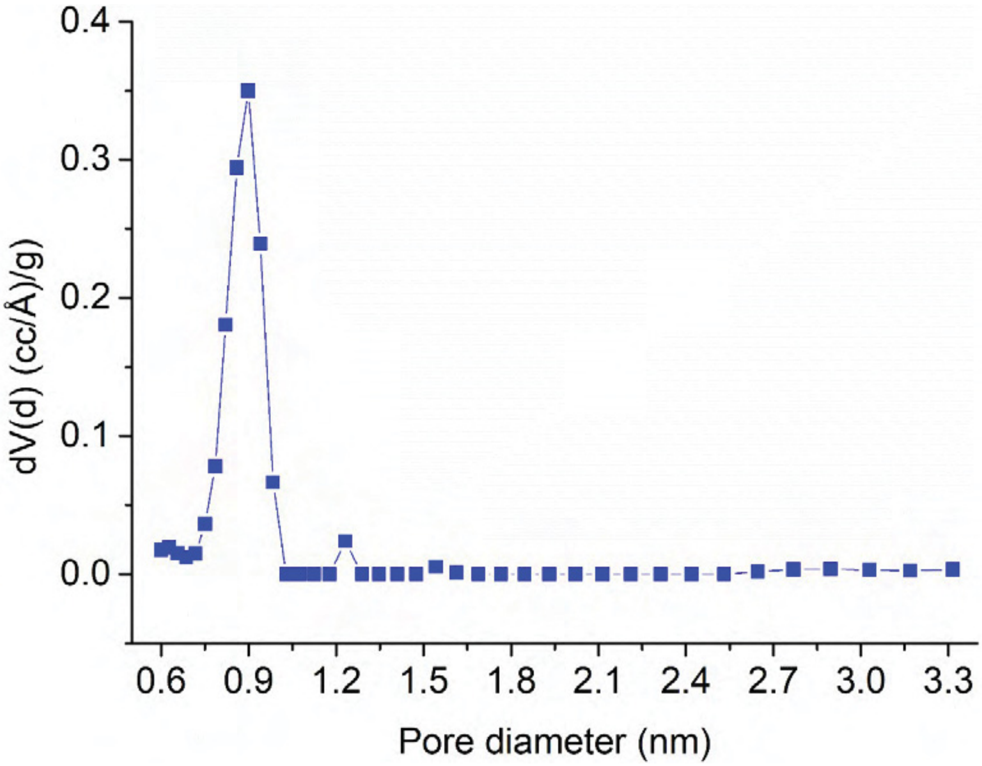

Fig. S10 Pore size distribution analysis for MIL-53-muc from N_2 sorption isotherm with the NLDFT model.

Table S2 Porosity parameters of MIL-53-muc

Materials	S_{BET} (m^2g^{-1}) [a]	$S_{micro\text{-}BET}$ (m^2g^{-1}) [b]	S_{Ext} (m^2g^{-1}) [c]	$V_{pore\ (total)}$ (cm^3g^{-1}) [d]	$V_{pore\ (micro)}$ (cm^3g^{-1}) [e]
MIL-53-Muc	1750	1530	220	0.72	0.52
Al-Fum	982	864	118	0.42	0.33

[a] BET surface areas (S_{BET}) were obtained from five adsorption points in the pressure range PP_0^{-1}=0.001-0.05. [b] Micropore areas ($S_{micro\text{-}BET}$) were obtained by t-plot and V-t-method. [c] External area (S_{Ext}) refers to all area that does not originate from micropores and it includes meso- and macropores, i.e. pores > 2nm. Obtained by t-plot and V-t-method. [d] Total pore volumes ($V_{pore\ (total)}$) were derived at PP_0^{-1}= 0.95 for pores ≤ 20 nm. [e] Micropore volume ($V_{pore\ (micro)}$) refers to volume that originates only from micropores, obtained by V-t-method with thickness method ‘DeBoer’. All correlation coefficients (r) in calculations were >0.999.

Multicycle adsorption-desorption stability tests

We would like to note that the water sorption isotherms in Fig. S11 (for a five-cycle water sorption stability test) were conducted with a sample obtained under slightly different synthesis conditions. This has resulted in a smaller hysteresis loop, indicating that the extent of the hysteresis (or the flexibility) depends on the synthetic route. This aspect is included in our current investigations and was already reported for the parent MIL-53-BDC. However, we do not expect the stability in itself to be different from the product obtained under our optimized synthesis.

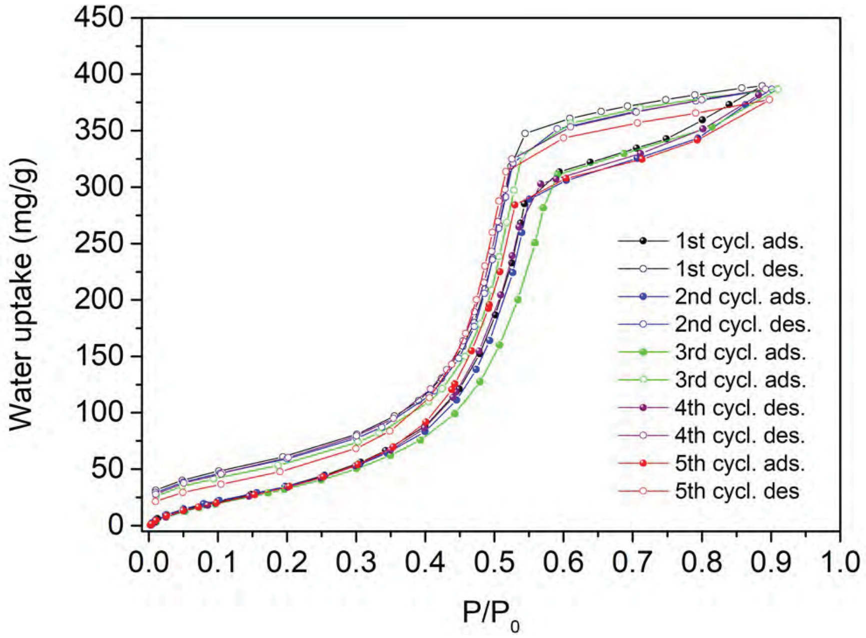

Fig. S11 Water sorption isotherms for MIL-53-muc, collected for five consecutive cycles. The water uptake capacity indicates the hydrolytic stability of MIL-53-muc.

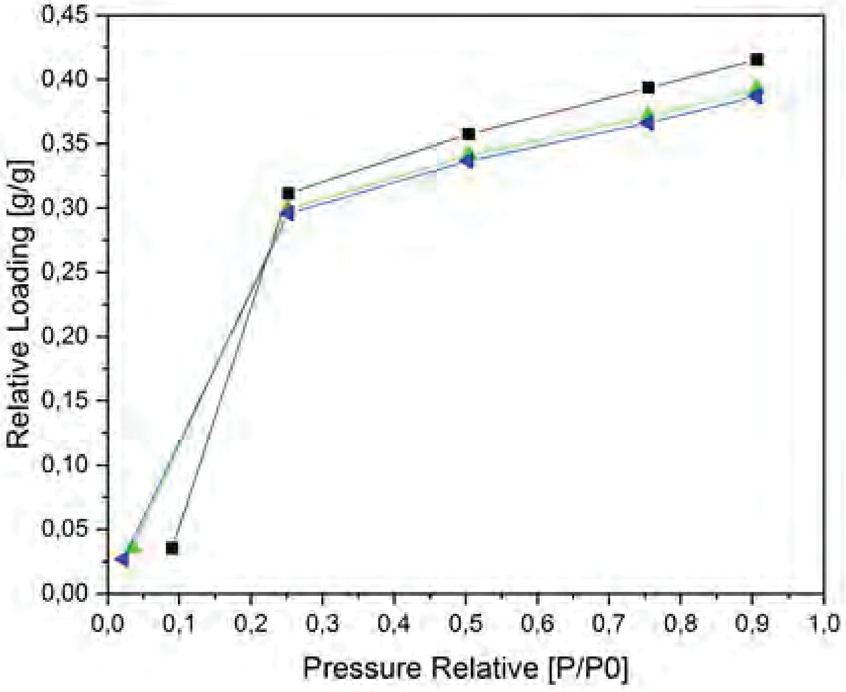

Fig. S12 Methanol adsorption isotherms measured after multicycle adsorption-desorption stability test. The black squares show the equilibrium points of the untreated sample MIL-53-muc. The green triangles correspond to the equilibrium points after 25 cycles and the blue triangles after 50 cycles.

Experimental

The 50-cycle stability in water vapor sorption was examined in a Setaram™ TGA-DSC-111. A humidified argon gas flow (40 °C, 76.3% relative humidity) was generated by a Setaram™ WetSys humidity controller and passed through the sample chamber, while the temperature of the sample chamber itself was varied. For multi-cycle ad-/desorption experiments, the temperature of the sample chamber was varied between 40 °C and 140 °C with a cycle time of 5 h for 50 cycles. Prior to and after the cycles, the sample was dried at 140 °C in a dry gas flow and then humidified.

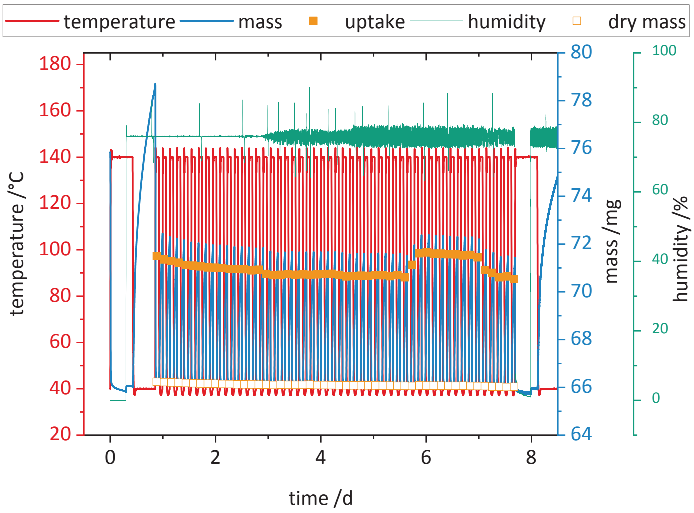

Fig. S13 50 cycles of adsorption and desorption of MIL-53-muc in a thermogravimetric analyzer. Red curve: temperature, blue curve: sample mass, green curve: humidity, filled orange squares: uptake, open orange squares: dry mass.

The cycle experiment whose results are depicted in Fig. S13 shows that the sample keeps its ability to adsorb water vapor over at least 50 cycles, though a small decrease of -1.3 % can be observed (orange squares). Further, the dry mass of the sample (open orange squares) stays pretty constant (-0.3 mass-%). Although the water vapor was slightly inconstant over the second half of the experiment, it is proven, that MIL-53-muc is not unstable in a humid atmosphere and over at least 50 cycles.

Isosteric heat of water and methanol adsorption

Making use of isotherms collected at three different temperatures (see Fig. S12 for water and Fig. 13 for methanol), the isosteric heat of adsorption was finally calculated by applying the Clausius-Clapeyron equation (eq. 1).

$$Q_{st} = -R\left(\frac{T_2T_1}{T_2-T_1}\right)ln\frac{P_2}{P_1} \qquad (1)$$

Q_{st} is the isosteric heat of adsorption (kJ mol^{-1}); T_1 and T_2 are two different temperatures at which isotherms are measured (K); P_1 and P_2 are two pressures at T_1 and T_2 respectively, corresponding to the same isostere (the same uptake).

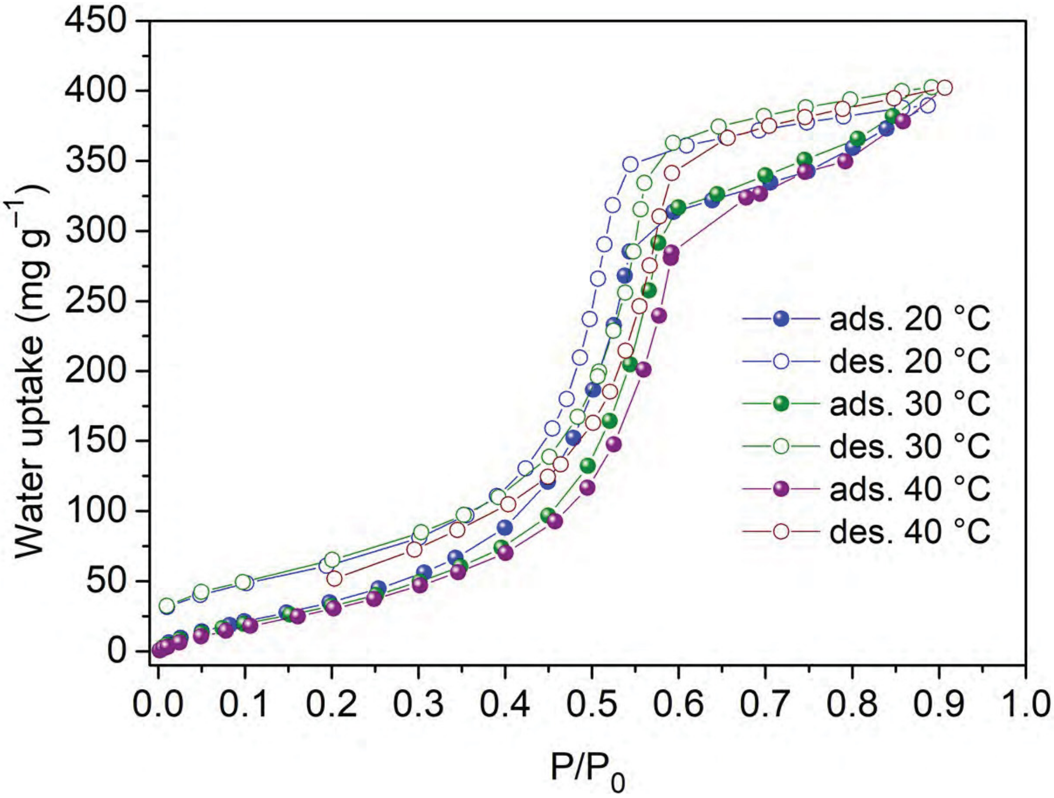

Fig. S14 Water sorption isotherms for MIL-53-muc collected at three different temperatures. On the page "Response to Review" please provide a separate point-by-point response to all comments in the collated report.

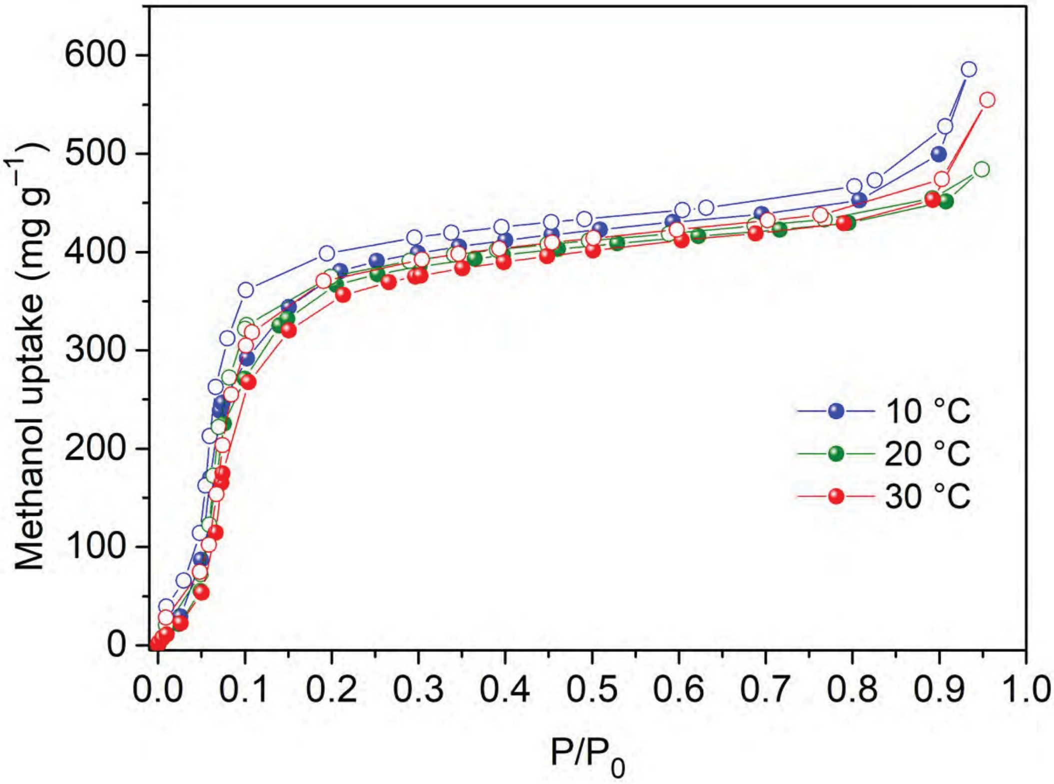

Fig. S15 Methanol sorption isotherms for MIL-53-muc, collected at three temperatures: 10 °C (blue), 20 °C (green) and 30 °C red (red).

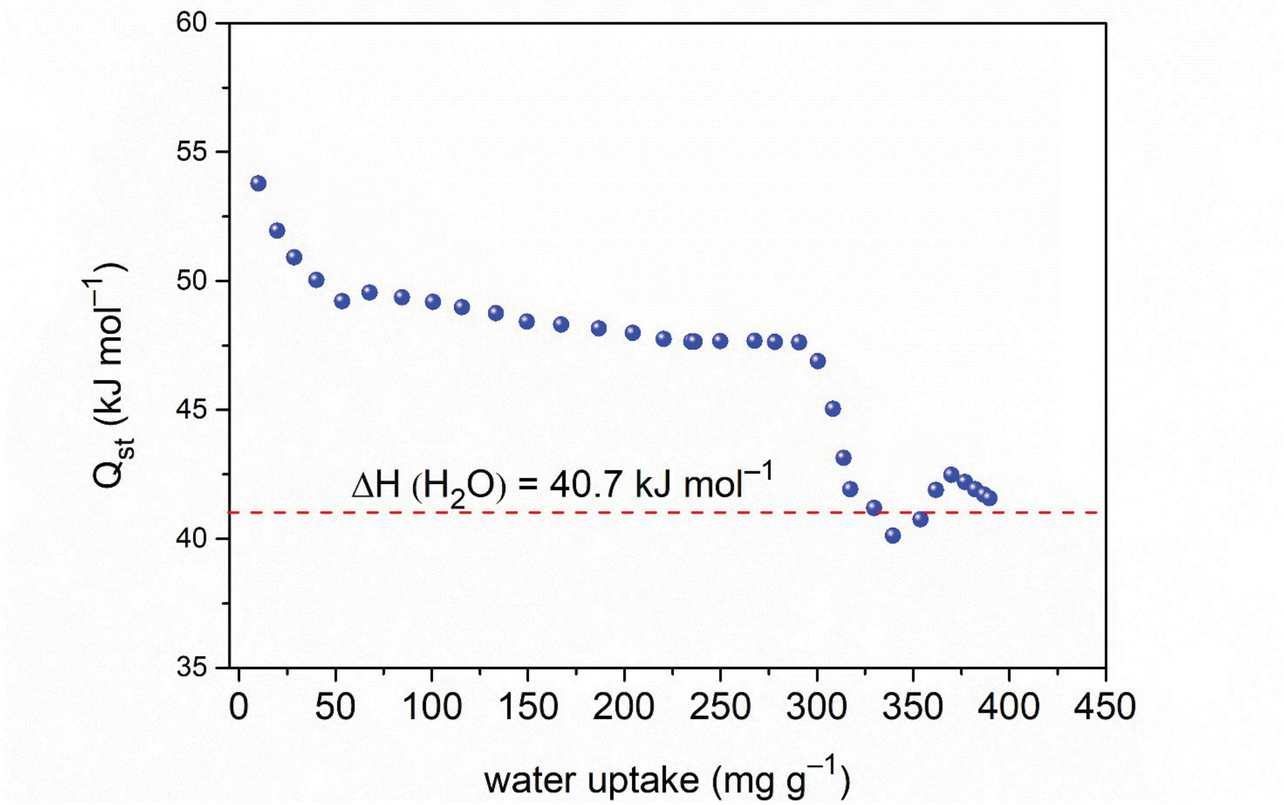

Fig. S16 Plot of the isosteric heat of water adsorption for MIL-53-muc.

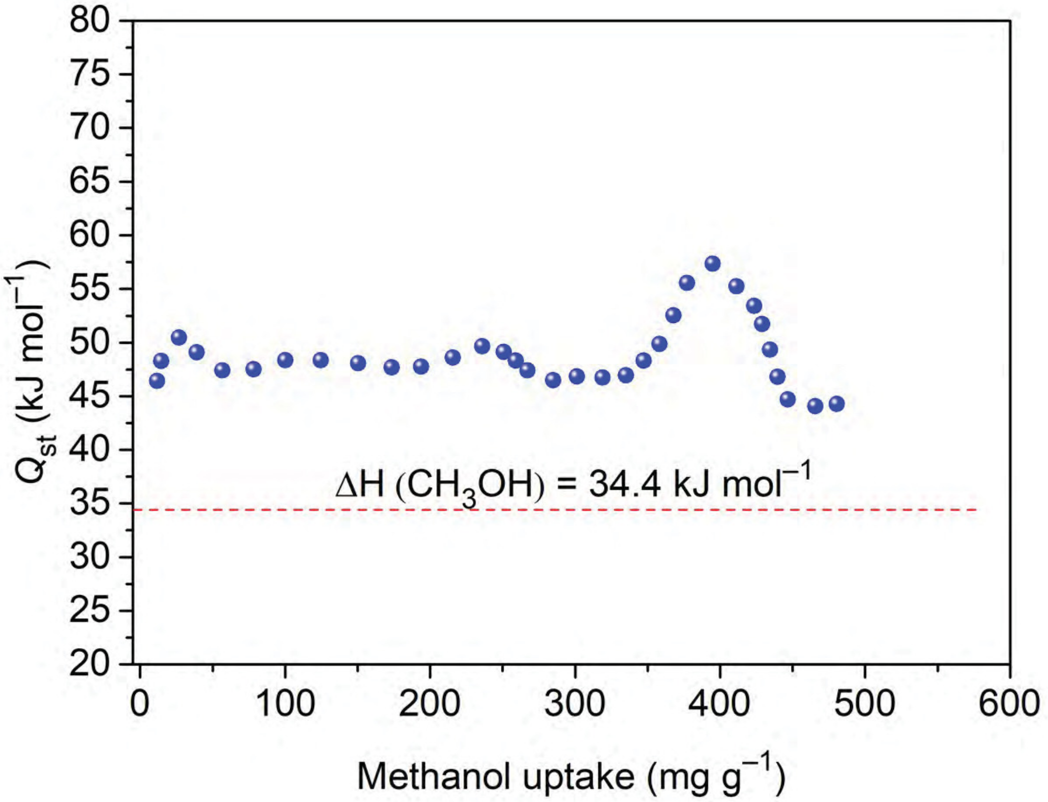

Fig. S17 Plot of the isosteric heat of methanol adsorption for MIL-53-muc.

Calculation of the heat storage capacity C_{HS} for MIL-53-muc

$$C_{HS} = \frac{\Delta H_{ads} \cdot \Delta w}{M_w} \qquad (2)$$

where ΔH_{ads} is the heat of water adsorption, Δw is the working capacity and M_w is the molar weight of methanol.

Calculations of methanol sorption performance for AHP and TDC applications

To assess the potential of the MIL-53-muc sample in adsorption heat transformation, the measured methanol adsorption data were fitted using a weighted-dual site Langmuir approach (wDSL).

$$X(p,T) = X_L(1 - w(p,T)) + X_U(p,T)w(p,T) \qquad (3)$$

$$X_L(p,T) = X_{L,\infty}\frac{b_L p}{1 + b_L p} \qquad (4)$$

$$X_U(p,T) = X_{U,\infty}\frac{b_U p}{1 + b_U p} + b_H p \qquad (5)$$

$$b_\alpha = b_{\alpha,\infty}\exp\left(\frac{E_\alpha}{RT}\right), \alpha = L,U,H \qquad (6)$$

$$w(p,T) = \left(\frac{\exp\left(\frac{\ln(p) - \ln(p_{step}(T))}{\sigma(T)}\right)}{1 + \exp\left(\frac{\ln(p) - \ln(p_{step}(T))}{\sigma(T)}\right)}\right)^\gamma \qquad (7)$$

$$\sigma(T) = \chi_1\exp\left(\chi_2\left(\frac{1}{T_0} - \frac{1}{T}\right)\right) \qquad (8)$$

$$p_{step}(T) = p_{step,0}\exp\left(\frac{-H_{Step}}{R}\left(\frac{1}{T_0} - \frac{1}{T}\right)\right) \qquad (9)$$

The methanol uptake at a certain pressure and temperature $X(p,T)$ is calculated from two Langmuir-terms (X_L and X_U), representing the adsorption before and after the step in the uptake. $w(p,T)$ is a weighting function that depends on the pressure p, the temperature T and the pressure p_{step} at which the uptake step occurs. Further symbols X_∞, b_α, E_α and $\chi_{1,2}$ represent fit parameters.[2,3]

COP calculation

The coefficient of performance (COP) for cooling can be defined as the ratio of evaporation enthalpy of the liquid phase and consumed heat for the desorption process:[4,5]

$$COP_C = \frac{Q_{evap}}{Q_{des} + Q_{IH}} \qquad (10)$$

In the numerator the evaporation enthalpy of methanol is used (34.4 kJ/mol). In the denominator the amounts of heat to apply for desorption (Q_{des}) and isosteric heating (Q_{IH}) of the adsorbent are added.

$$COP_{\mathrm{H}} = \frac{Q_{\mathrm{ads}} + Q_{\mathrm{cond}} + Q_{\mathrm{IC}}}{Q_{\mathrm{des}} + Q_{\mathrm{IH}}} \tag{11}$$

In the numerator the amounts of usable heat are summed up. It is the heat of adsorption (Q_{ads}), the heat from condensation (Q_{cond}) and the heat from isosteric cooling (Q_{IC}). In the denominator the amounts of heat to apply for desorption (Q_{des}) and isosteric heating (Q_{IH}) of the adsorbent are summarized.

The amounts of heat can be calculated from energy balances:

$$\mathrm{d}Q_{\mathrm{IH}} = m_{\mathrm{ads}} \cdot \left(c_{\mathrm{p,ads}} + X_{\mathrm{max}}\, c_{\mathrm{p,fl}}\right)\mathrm{d}T \tag{12}$$

$$\mathrm{d}Q_{\mathrm{des}} = m_{\mathrm{ads}} \cdot \left(c_{\mathrm{p,ads}} + X(p,T)c_{\mathrm{p,fl}}\right)\mathrm{d}T - m_{\mathrm{ads}}q_{\mathrm{st}}(T)\mathrm{d}X \tag{13}$$

$$Q_{\mathrm{evap}} = m_{\mathrm{ads}} \cdot \left(\Delta h_{\mathrm{vap}}(T_{evap}) - c_{\mathrm{p,g}}\left(\bar{T} - T_{\mathrm{evap}}\right)\right)(X_{\mathrm{max}} - X_{\mathrm{min}})) \tag{14}$$

$$\mathrm{d}Q_{\mathrm{ads}} = m_{\mathrm{ads}} \cdot \left(c_{\mathrm{p,ads}} + X(p,T)c_{\mathrm{p,fl}}\right)\mathrm{d}T - m_{\mathrm{ads}}q_{\mathrm{st}}(T)\mathrm{d}X \tag{15}$$

$$\mathrm{d}Q_{\mathrm{IC}} = m_{\mathrm{ads}} \cdot \left(c_{\mathrm{p,ads}} + X_{\mathrm{max}}\, c_{\mathrm{p,fl}}\right)\mathrm{d}T \tag{16}$$

$$Q_{\mathrm{cond}} = m_{\mathrm{ads}} \cdot \left(\Delta h_{\mathrm{vap}}(T_{evap}) - c_{\mathrm{p,g}}\left(\bar{T} - T_{\mathrm{evap}}\right)\right)(X_{\mathrm{max}} - X_{\mathrm{min}})) \tag{17}$$

Herein m_{ads} refers to the adsorbent mass, $c_{\mathrm{p,ads}}$, $c_{\mathrm{p,fl}}$ and $c_{\mathrm{p,g}}$ to the isobaric heat capacities of adsorbent, water and water vapor, $\bar{T}$ to the arithmetic mean temperature during desorption.

$$\bar{T} = 0.5\left(T_{\mathrm{des,max}} + T_{\mathrm{des,min}}\right) \tag{18}$$

Using the before described set of equations, the COP for a heat pump cycle was calculated for a heating temperature of 40 °C, and desired cold temperature of 10 °C and a variation of driving temperatures lower than 95 °C. As suggested by de Lange et al. and for the sake of comparability, the capacity of the adsorbent $c_{\mathrm{p,ads}}$ was assumed to 1 kJ/kg.[9]

REFERENCES

---

1 H. Reinsch, R. S. Pillai, R. Siegel, J. Senker, A. Lieb, G. Maurin and N. Stock, *Dalton Trans.*, 2016, **45**, 4179-4186.

2 M. Hefti, L. Joss, Z. Bjelobrk and M. Mazzotti, On the Potential of Phase-Change Adsorbents for CO_2 Capture by Temperature Swing Adsorption. *Faraday Discuss.*, 2016, **192**, 153–179.

3 S.-J. Ernst, M. Baumgartner, D. Fröhlich, H.-J. Bart and S. K. Henninger, Adsorbentien für sorptionsgestützte Klimatisierung, Entfeuchtung und Wassergewinnung. *Chem. Ing. Tech.*, 2017, **89**, 1650–1660.

4 M. F. de Lange, K. J. F. M. Verouden, T. J. H. Vlugt, J. Gascon and F. Kapteijn, Adsorption-Driven Heat Pumps: The Potential of Metal-Organic Frameworks. *Chem. Rev.*, 2015, **115**, 12205–12250.

5 S.-J. Ernst, F. Jeremias, H.-J. Bart and S. K. Henninger, Methanol Adsorption on HKUST-1 Coatings Obtained by Thermal Gradient Deposition. *Ind. Eng. Chem. Res.*, 2016, **55**, 13094–13101.

Conclusions

The aim of this research work was to investigate modifications of fumarate-based aluminum and zirconium MOFs, which would improve their adsorption performance, most especially as adsorbents for heat transformation applications. As a result of the work conducted between October 2016 and September 2019, a total of nine new MOFs were synthesized and fully characterized including:

- Three acetylenedicarboxylate-based UiO-type MOFs (Zr-HHU-1; Hf-HHU-1, Ce-HHU-1).
- Four halofumarate-based UiO-type MOFs (Zr-HHU-2-Cl, Zr-HHU-2-Br; Zr-HHU-2-I, Hf-HHU-2-Cl).
- Two aluminum MOFs with MIL-53-type structure, based on chlorofumarate (MIL-53-Fum-Cl) and *trans,trans*-muconate (MIL-53-Muc), respectively.

The Adc-based MOFs obtained in this work are the very first reported porous MOFs with experimentally accessed permanent porosity, which are based on this very simple linear dicarboxylate. The new Adc-based HHU-1 MOFs feature a very high hydrophilicity displayed by a type I water vapor sorption isotherm, which would require elevated desorption temperatures during the regeneration cycle of adsorption-based heat transformation. Meanwhile, these MOFs also have low thermal stability and would therefore deteriorate during the regeneration process. Linearizing the fumarate into the acetylenedicarboxylate linker is therefore not beneficial to improve the performance of MOF-801 or MIL-53-Fum toward AHT. Nevertheless, the presence of the $-\equiv-$ triple-bond in the framework is beneficial to improve the gas (CO_2 and H_2) affinity and these materials can be used for example in gas capture and storage whenever elevated temperatures are not involved. The triple-bond was experimentally disclosed to allow Adc-based MOFs to chemisorb Br_2 and I_2 vapor via halogenation reactions. This makes these materials useable for cleaning air from toxic halogen vapors. Substituting Zr^{IV} by Hf^{IV} or Ce^{IV} in the structure of Zr-HHU-1 does not make any improvement on the adsorption profile of the material with respect to applications for heat transformation.

An unexpected halofumarate formation via in situ hydrohalogenation of the $-\equiv\quad-$ bond of acetylenedicarboxylic acid during the MOF construction was discovered as a facile route to halogen-functionalization of MOFs. The combination of Raman spectroscopy, ssNMR, XPS, SEM-EDX spectroscopies was established as a powerful analysis set to determine this linker transformation in the obtained MOF. This approach, which was implemented for the synthesis of **fcu**-type zirconium chloro-, bromo-, iodofumarate MOFs, was also extended to produce **fcu**-type hafnium chlorofumarate and MIL-53-type aluminium chlorofumarate. The in situ functionalization occurs simply by reacting acetylenedicarboxylic acid with the corresponding metal halide in water. Defective nanodomains with **reo** tolopology can be introduced in the structure of halofumarate-based **fcu** Zr- and Hf-MOFs by variation of the linker to metal-salt molar ratio. It is expected that this approach could become a usual route to halogen functionalization of MOFs, starting from triple-bond containing linkers. Although the halogen functionalization does not improve the water uptake capacity of the halofumarate-based MOFs compared to the non-functionalized zirconium fumarate (MOF-801), the functionalization was revealed to increase the hydrophilicity of the MOF. This is therefore a means of adjusting the position of the water isotherm step to improve the performance of the material toward AHT. To this respect, the chloro-functionalized MOF-801 displays high hydrothermal stability and a high heat storage capacity, indicating its promise for application as adsorbent for adsorption thermal batteries. Furthermore, this material features an increased gas sorption capacity compared to MOF-801, which makes it to be a potential adsorbent applicable for CO_2, SO_2 and CH_4 capture and/or separation. Its good hydrothermal stability and hydrophilicity also indicate its potential usage for dehumidification purpose and water harvesting from air.

Finally, this work has shown that a twofold expansion of aluminum fumarate (MIL-53-Fum) is the best option for improving the performance of this material as adsorbent in the context of AHT. Especially when methanol is used as adsorptive, MIL-53-Muc features a better adsorption profile and capacity, while maintaining high multicycle methanol ad-/desorption stability. Furthermore, MIL-53-Muc/methanol pair gives access to AHT producing temperatures below 0 °C for applications like ice making. This working pair allows the deployment of a heat pump with evaporator temperature below 0 °C, enabling the usage even of ambient temperature during winter. Whereas adsorption heat pumps using water as working fluid are not operational at those temperatures. The aforementioned results were separately fully published as six scientific articles in peer reviewed journals, which constitute this cumulative thesis.

A concluding remark to this work is that the initial assessment of aluminum fumarate for AHT applications was very likely underestimated, since it was based on a material featuring a water sorption isotherm with considerable hysteresis loop and capillary condensation effect. This work reveals that a better synthesis approach yields a material displaying no hysteresis loop between the adsorption and desorption branches of the water sorption isotherm. A re-evaluation of aluminum fumarate for AHT application could therefore be envisaged. Another aspect requiring consideration is the long-term multicycle water ad-/desorption stability of MOF-801. Indeed the presence of large amount of missing linker and/or cluster defects in this material is a bottleneck limiting the exploitation of its otherwise very favorable water sorption profile toward AHT applications. This bottleneck is related to the sole modulated synthesis approach by which this material is obtained so far. It is therefore a necessity to find new synthesis routes that enable to produce a(n) (almost)defect-free MOF-801.